Developing Molecular Sensitisers for NiO-based p-Type Dye-Sensitised Solar Cells

Gareth H. Summers

A thesis submitted for the degree of
Doctor of Philosophy in Chemistry

School of Chemistry
Newcastle University
June 2018

Declaration

I declare that this thesis is my own work and that I have correctly acknowledged the work of others below. I certify that no part of the material offered has been previously submitted by me for a degree or other qualification in this or any other University.

In Chapter 3, Dr. Jean-François Lefebvre performed the synthesis and electrochemical characterisation of dye **3**, Dr. Christopher Wood performed the p-DSC measurements of dye **2** and Fiona Black performed the p-DSC measurements of dyes **1** and **3**-**5**. In Chapter 4, Dr. Christopher Wood performed the p-DSC measurements of dye **8**. They are all gratefully acknowledged for their assistance in this work.

Gareth Summers

Acknowledgements

I would like to take this time to thank the people who have made this PhD possible. First and foremost, I would like to express my gratitude to Dr. Elizabeth Gibson for giving me the opportunity to pursue this degree. It would not have been possible without all of her invaluable advice, guidance and support over the years. I have also been offered countless opportunities to travel and broaden my research interests over the years, for which I am very grateful.

I would also like to thank all of the members of Team Gibson, past and present, for making the lab an enjoyable atmosphere to work in; Jean-François, Charlotte, Chris, Fiona, Nathan and Nils. I truly enjoyed working alongside all of you. In particular, I would like to thank Dr. Jean-François Lefebvre, Dr. Christopher Wood and Fiona Black who have directly contributed to this work.

Thanks go to the technical and workshop staff who have worked to set up and keep our lab running after moving here. Special thanks must go to Dr. Corinne Wills, who was able to obtain NMR spectra for many of the poorly soluble samples I presented her with.

Many of the publications that came from this work would not have been possible without the help of collaborators, so for that I am appreciative. I would like to thank the group of Prof. Tönu Pullerits at Lund University for the use of their facilities and their hospitality (thanks for all the Fika). I would also like to thank the group of Prof. Athanassios Coutsolelos for hosting me during my short time working at the University of Crete. In particular, I would like to thank Vasilis Nikolaou, who made such a tremendous effort to make me feel so welcome during my visit. If I ever watch basketball again, I'll support Panathinaikos.

Finally, I would like to thank my family for their continued support and enthusiasm throughout all the stages of my education. Special thanks must go to Emma, as this thesis would not exist without the endless support she has given me throughout the duration of this PhD.

Abstract

The investigation of NiO-based p-type dye-sensitised solar cells (p-DSCs) has attracted significant research interest as they remain the limiting factor for highly efficient tandem-DSCs. As the dye is the part of a DSC that absorbs light and drives the production of a photocurrent, the development of new sensitisers is crucial to improve device efficiencies. Due to the typically low NiO film thickness used (*ca*. 1.5 µm), organic dyes with high extinction coefficients are needed to maximise light harvesting. When incorporated into a tandem-DSC, the NiO p-DSC will be in combination with a TiO_2 n-type DSC and should absorb a complementary wavelength range. As n-type devices have been optimised to harvest higher energy photons, for NiO we require dyes that can absorb across the longer-wavelength visible and near-IR regions. An anchoring unit, typically a group containing an acidic proton, is also essential for the dye to adsorb onto the semiconductor surface and to facilitate efficient charge transfer from NiO to the dye. In this thesis, novel BODIPY, indolium, porphyrin and indigo-based dyes have been synthesised and studied as sensitisers for p-DSCs. Each chapter focuses on a different aspect of dye design to provide an in-depth investigation into the requirements for an efficient device.

‘Push-pull’ dyes have been routinely used to construct efficient p-DSCs. These consist of electronic donor and acceptor groups, linked by a conjugated bridge, where the acceptor unit is spatially separated from the semiconductor surface. This is intended to promote a long-lived charge-separated state following electron transfer from NiO. A series of donor-acceptor BODIPY-triphenylamine dyes has been synthesised (**1-5**, Chapter 3) and characterised using spectroscopic and electrochemical techniques to investigate the effect of tuning donor-acceptor coupling on device efficiencies. When this coupling was limited, the lowest energy excitation was a π-π* transition localised on BODIPY, but as the coupling increased there was an increase in charge-transfer character. The dyes were integrated into p-DSCs and those with a π-π* transition localised on BODIPY performed modestly, with the performance largely unaffected by the nature of the donor/anchor group. The best performing dye had the highest degree of charge-transfer character and produced devices with efficiencies higher than the benchmark dye **P1** and comparable to other highly-performing dyes reported.

Many dyes used for p-DSCs contain a single carboxylic acid as an anchoring group. Multiple anchors are expected to increase dye stability and should induce a more rigid, structured dye monolayer. Dyes containing BODIPY or indolium acceptors and a novel

pyrrole-based multidentate anchoring system were synthesised (**6**-**8**, Chapter 4) and incorporated into p-DSCs. Modest performances were observed for the BODIPY dyes that has been attributed to poor charge transfer from NiO, while higher efficiencies were obtained for the indolium dye that was limited by a low extinction coefficient. Despite this, high dye loading was seen for the indolium dye which could have potential applications for co-sensitisation. The synthesis of these dyes was hindered by the difficult hydrolysis of the two methyl carboxylates situated on the pyrrole to form the anchoring unit. This prompted an investigation into developing alternative routes to introduce anchoring units as a final synthetic step.

While the BODIPY acceptors designed in Chapter 3 were successfully used to produce efficient devices, the most efficient dyes were those with higher charge-transfer character. These lacked most of the properties that attract interest toward BODIPYs, such as well-defined absorption/emission bands and high emission quantum yields. Therefore, the development of new acceptor groups was needed. Indigo derivatives have been routinely studied for their electron accepting properties and have found widespread use in organic photovoltaics. In Chapter 5, the development of dyes based on bay-annulated indigo is discussed. A major limitation to the synthesis was the poor solubility of the bay-annulated indigo core after halogenation. This was overcome by introducing solubilising branched chains to indigo prior to bay-annulation. A first-generation dye (**9**) containing a simple benzoic acid anchoring group was synthesised, characterised and investigated in p-DSCs. Somewhat low performances were obtained from these devices that has been attributed to low dye loading, likely due to the short anchor length compared to the bulky core. However, this study has proved the feasibility of bay-annulated indigo dyes for p-DSCs and has formed the initial groundwork to synthesise a more efficient dye.

The synthetic difficulties encountered in Chapters 4-5 prompted an investigation into alternative routes of introducing anchoring groups as a final synthetic step. This culminated in the synthesis of triazole-bridged porphyrins (**10**-**12**, Chapter 6) using ‘click’ chemistry, where a range of different anchors could be introduced in a facile manner. In this series, the anchoring groups consisted of a carboxylic acid, a phosphonic acid and coumarin 3-carboxylic acid. Dye adsorption onto NiO was investigated using adsorption isotherms and kinetic studies and the phosphonate was determined to have a higher affinity for NiO and a higher rate constant for adsorption. The dyes containing the phosphonic acid and coumarin anchoring groups exhibited higher dye loading than the carboxylic acid. Therefore, devices made using these dyes had a higher light harvesting efficiency and produced higher photocurrents. In this chapter, a new method of introducing various anchoring groups as a final synthetic step has been developed, which can open new strategies for dye design.

In conclusion, this thesis aimed to study the dye requirements for efficient p-type devices and provide guidelines for future dye design. Chapter 3 showed that higher device efficiencies were obtained with improved donor-acceptor coupling and Chapters 4 and 6 developed new routes for synthesising anchoring groups. The measurements carried out in Chapter 6 also showed that the phosphonate anchoring unit is more suitable for NiO that the widely used carboxylic acid group. A new acceptor based on indigo was developed for use in p-DSCs in Chapter 5 that could likely be improved using the anchoring groups designed in Chapter 6.

List of Publications

1. Bay annulated indigo as a new chromophore for p-type dye-sensitised solar cells. G. H. Summers and E. A. Gibson, *ChemPhotoChem*, 2018, **2**, 498-506.
2. A resonance Raman study of new pyrrole-anchoring dyes for NiO-sensitized solar cells. G. H. Summers, G. Lowe, J-F. Lefebvre, S. Ngwerume, M. Brautigam, B. Dietzek, J. E. Camp and E. A. Gibson, *ChemPhysChem*, 2017, **18**, 406-414.
3. Investigating interfacial electron transfer in dye-sensitized NiO using vibrational spectroscopy. F. A. Black, C. A. Clark, G. H. Summers, I. P. Clark, M. Towrie, T. Penfold, M. W. George and E. A. Gibson, *Phys. Chem. Chem. Phys.*, 2017, **19**, 7877-7885.
4. Charge-transfer dynamics at the dye–semiconductor interface of photocathodes for solar energy applications. F. A. Black, C. J. Wood, S. Ngwerume, G. H. Summers, I. P. Clark, M. Towrie, J. E. Camp and E. A. Gibson, *Faraday Discuss.*, 2017, **198**, 449–461.
5. Design and characterisation of BODIPY sensitizers for dye-sensitized NiO solar cells. G. H. Summers, J-F. Lefebvre, F. A. Black, E. S. Davies, E. A. Gibson, T. Pullerits, C. J. Wood and K. Zidek*, Phys. Chem. Chem. Phys.*, 2016, **18**, 1059-1070.
6. A comprehensive comparison of dye-sensitized NiO photocathodes for solar energy conversion. C. J. Wood, G. H. Summers, C. A. Clark, N. Kaeffer, M. Bräutigam, L. R. Carbone, L. D'Amario, K. Fan, Y. Farré, S. Narbey, F. Oswald, L. A. Stevens, C. D. J. Parmenter, M. W. Fay, A. La Torre, C. E. Snape, B. Dietzek, D. Dini, L. Hammarström, Y. Pellegrin, F. Odobel, L. Sun, V. Artero and E. A. Gibson, *Phys. Chem. Chem. Phys*., 2016, **18**, 10727-10738.
7. Increased photocurrent in a tandem dye-sensitized solar cell by modifications in push–pull dye-design. C. J. Wood, G. H. Summers, E. A. Gibson, *Chem. Commun.,* 2015, **51**, 3915-3918.
8. Ni Mg mixed metal oxides for p-type dye-sensitized solar cells. M. Zannotti, C. J. Wood, G. H. Summers, L. A. Stevens, M. R. Hall, C. E. Snape, R. Giovanetti, and E. A. Gibson, *ACS Applied Materials & Interfaces*, 2015, **7**, 24556-24565.

Table of Contents

Abbreviations

AM	- Air mass
APCE	- Absorbed photon to current conversion efficiency
BAI	- Bay-annulated indigo
BET	- Brunauer-Emmett-Teller
C_{CO}	- Capacitance at the FTO/NiO contact
$CDCl_3$	- Deuterated chloroform
C_e	- Dye bath concentration
C_{FTO}	- Double-layer capacitance at the FTO/electrolyte interface
$CHCl_3$	- Chloroform
Cheno	- Chenodeoxycholic acid
C_{NiO}	- Chemical capacitance of NiO
COSY	- Homonuclear correlation spectroscopy
C_{ox}	- Concentration of oxidised species
C_{Pt}	- Double-layer capacitance at the counter electrode
C_{red}	- Concentration of reduced species
CuAAC	- Copper-catalysed azide-alkyne cycloaddition
CV	- Cyclic voltammetry
$C_{60}PPy$	- N-methyl-2-(4’-pyridyl)-3,4-fulleropyrrolidine
δ	- NMR chemical shift
DCM	- Dichloromethane
DFT	- Density functional theory
ΔG_{inj}	- Driving force for NiO-dye charge transfer
ΔG_{reg}	- Driving force for reduced dye regeneration
DIPEA	- N,N-Diisopropylethylamine

DMF	- Dimethylformamide
DPP	- Diketopyrrolopyrrole
dppf	- 1,1'-Bis(diphenylphosphino)ferrocene
DPV	- Differential pulse voltammetry
DSC	- Dye-sensitised solar cell
EDOT	- 3,4-ethylenedioxythiophene
$E_{F,NiO}$	- Fermi-level of NiO
$E_{F,redox}$	- Redox potential of the electrolyte
$E_{ox}(S/S^+)$	- Ground state oxidation potential
E_{pa}	- Anodic peak potential
E_{pc}	- Cathodic peak potential
$E_{red}(S/S^-)$	- Ground state reduction potential
$E_{red}(S^*/S^-)$	- Excited state reduction potential
ESI	- Electrospray ionisation
$E_{VB(NiO)}$	- Energy of the NiO valence band
Fc/Fc^+	- Ferrocene/ferrocenium redox couple
FF	- Fill factor
FTO	- Fluorine-doped tin oxide
F108	- Poly(ethylene glycol)-block-poly(propylene glycol)-block-poly(ethylene glycol)
γ	- Diode non-ideality factor
HF	- Hartee-Fock
HMBC	- Heteronuclear multiple bond correlation
HOMO	- Highest occupied molecular orbital
HRMS	- High-resolution mass spectrometry
HSQC	- Heteronuclear single quantum coherence

η - Power conversion efficiency

η_{cc} - Charge collection efficiency

η_{inj} - Injection efficiency

η_{op} - Overpotential

η_{reg} - Regeneration efficiency

I_C - Internal conversion

I_{pa} - Anodic peak current

I_{pc} - Cathodic peak current

IPCE - Incident photon to current conversion efficiency

I_{SC} - Intersystem crossing

ITO - Indium tin oxide

J - Current density

J_{dark} - Dark current density

J_{inj} - Injected current density

J_{max} - Maximum current density

J_{SC} - Short-circuit current density

J_0 - Diode constant

K_B - Boltzmann constant

K_F - Freundlich isotherm constant

K_L - Langmuir isotherm constant

LHE - Light harvesting efficiency

LUMO - Lowest unoccupied molecular orbital

MeCN - Acetonitrile

NBS - N-Bromosuccinimide

NDI - Napthalene diimide

n-DSC	- n-Type dye-sensitised solar cell
NMR	- Nuclear magnetic resonance
N_{VB}	- Effective density of valence band states
n_{VB}	- Concentration of injected holes
Ω	- Resistance
OPV	- Organic photovoltaic
P	- Power
PCE	- Power conversion efficiency
PCM	- Polarisable continuum model
p-DSC	- p-Type dye-sensitised solar cell
PES	- Potential energy surface
$\Phi_{ph,AM1.5}$	- Photon flux (AM1.5 conditions)
P_{max}	- Maximum power point
PMI	- Perylene monoimide
ppm	- Parts per million
q	- Amount of dye adsorbed at a given time
q_e	- Amount of dye adsorbed at equilibrium conditions
Q_0	- Theoretical monolayer saturation capacity
R_{CO}	- Resistance at the FTO/NiO contact
R_{CT}	- Charge transfer resistance at the counter electrode
RDS	- Rapid discharge sintering
R_{FTO}	- Charge transfer resistance at the FTO/electrolyte interface
Γ_{max}	- Surface concentration at full monolayer coverage
R_{pt}	- Charge-transfer resistance at the platinised FTO counter electrode
r_{rec}	- Charge-transfer resistance for recombination

R_S - Total series resistance

r_t - Transport resistance of the NiO film

TBA - Tetrabutylammonium

TDDFT - Time-dependent density functional theory

TFA - Trifluoracetic acid

TMSBr - Trimethylsilyl bromide

TOF - Time-of-flight

TW - Terawatt

UV - Ultra-violet

V - Voltage

V_{OC} - Open-circuit voltage

V_{max} - Maximum voltage

VR - Vibrational relaxation

Chapter 1 – Introduction

1.1. Energy Context

Energy is crucial for sustaining human life on Earth and has always been the key to technological development. Since the industrial revolution, the use of fossil fuels over the past two and a half centuries has facilitated technological innovations and improved living standards for a large part of the global population. The majority of our energy needs are fulfilled by the consumption of fossil fuels (Figure 1.1), yet these are a diminishing resource that cannot be replenished in a suitable timescale. Furthermore, CO_2 release associated with the use of these fuel sources has been linked to damaging environmental changes in the form of global warming.[1,2] Consequently, policies are being put into place to reduce greenhouse gas emissions by developing the renewable energy sector.[3] While most of the energy demand is currently fulfilled by fossil fuels, the contribution from renewable sources is growing.

The global energy demand is projected to increase by ca. 50% to a continuous power consumption of 30 terawatts (TW) by 2050.[4] In comparison, the total power from sunlight that strikes the Earth is 120,000 TW. Projections from a decade ago calculated that covering 0.16% of the land on Earth with 10% efficient solar cells would provide 20 TW of energy.[4] Despite this abundance and the increased efficiency of commercial solar cells, solar sources today provide less than 0.5% of global primary energy demands and contribute less than 1% toward the production of electricity (which has a 22% contribution from renewable sources).[5]

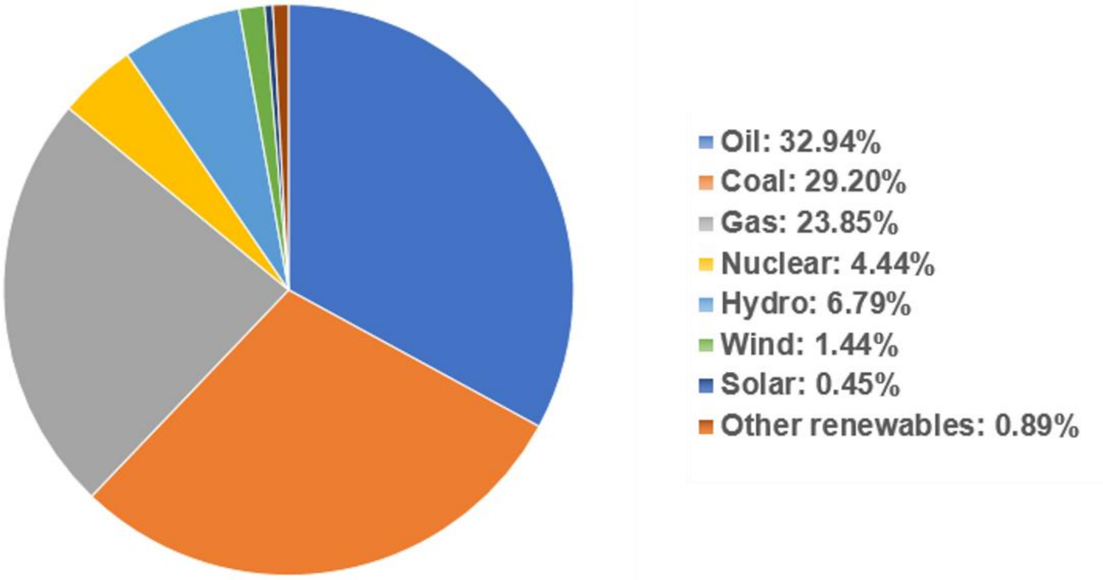

Figure 1.1. Primary energy consumption by source, 2015.[6]

1.2. Overview of photovoltaic technologies

Photovoltaics (PVs) refer to any devices capable of converting sunlight into electricity, which are often categorised within several ‘generations’ of technology. They operate by absorbing light, separating the subsequently formed opposing charges (electrons and holes) and extracting these charges to an external circuit.

First generation devices are based on silicon solar cells. Initially high manufacturing costs for these devices arose due to the stringent purity requirements for the silicon used, which limited their widespread use. However, these costs are decreasing as the solar industry continues to grow and they are the most prevalent type of commercial photovoltaic device. In a silicon photovoltaic, light absorption and charge separation occur in the same layer, separated by an internal electric field (a p-n junction). A certified record efficiency of 26.6% has been recently achieved for a silicon-based solar cell.[7] As silicon has an indirect band gap, a thick layer of absorber material is needed to produce efficient devices, which increases manufacturing costs.

Second generation devices aim to reduce manufacturing costs by using a more strongly absorbing material, thereby reducing the thickness of the absorber layer. Typically, this is performed by using materials with a direct band gap, such as cadmium telluride (CdTe) and copper indium gallium diselenide (CIGS). These have achieved certified record efficiencies of 22.1% and 22.6% for CdTe and CIGS respectively.[8] However, there are concerns regarding the natural abundance of these elements and the toxicity of cadmium.

The third generation of devices has been defined by Green[9] as anything capable of surpassing the Shockley-Queisser limit,[10] which includes multijunction devices and tandem cells. In these systems, multiple different solar cells, that are each optimised to absorb different regions of the solar spectrum, work in conjunction to reduce spectral losses. The highest conversion efficiency for any solar device was obtained for a multijunction device, which was certified at 46%.[11] However, the high cost and rare materials associated with these devices limits them to applications where the efficiency to weight ratio is crucial, such as for aerospace technologies.

The National Renewable Energy Laboratory (NREL) classify a selection of thin-film devices as ‘emerging photovoltaics’. This includes dye-sensitised solar cells (DSC), organic photovoltaics (OPV), quantum dot solar cells and perovskites. It also includes copper zinc tin sulphide (CZTS), an alternative to CdTe and CIGS solar cells, which uses more abundant materials. Most of these fall between the second and third generations, because they are thin-film technologies that can be integrated into a tandem device. The certified record efficiencies for the emerging photovoltaics mostly fall within a range of 10.6 – 13.4%.[8] Of these, rapid improvements have been made to perovskite solar cells.[12–14] The organometallic perovskite methylammonium lead iodide ($CH_3NH_3PbI_3$) was first used as a sensitiser in a liquid DSC in 2009, achieving a power conversion efficiency of 3.8%.[15] Since then, a tremendous effort has focussed on researching this field, including the use of alternative hole transporting materials,[16] new device architectures[17] and improved synthesis of the perovskite absorber.[18–20] The performance of these devices rapidly improved and a certified record efficiency of 22.1% was achieved in 2016.[8] Concerns remain over the stability and toxicity of these devices, which are two challenges that will have to be overcome for widespread implementation.

1.3. Development of DSCs

Dye-sensitised solar cells differ from Si-PVs in that the functions of charge separation and light absorption are separated and carried out by different components. Theoretically, this allows cheaper, lower purity materials to be used as defects are not such a prominent issue. The advantages of DSCs include using abundant materials, a simple manufacturing process and a wide choice of usable substrates. They do not perform as efficiently as silicon-based photovoltaics, so will struggle to compete for widespread conventional use. However, the angle of incident light is not critical and they have been shown to work under low-light conditions.[21] This means they have the potential for integration into windows or building materials and for use in indoor applications.

1.3.1. n-DSCs

The first major breakthrough in the development of n-type dye-sensitised solar cells (n-DSCs) was reported in 1991 by Brian O'Regan and Michael Grätzel.[22] In this work, a mesoporous film of TiO_2, sensitised with a ruthenium bipyridine dye, achieved a power conversion efficiency (PCE) of 7.10 - 7.90%. Since then, thousands of DSCs have been tested with different dyes, electrolytes and semiconductor morphologies.[23–

[25] The structure of a liquid-electrolyte DSC, or ‘Grätzel Cell’, is provided in Figure 1.2 and consists of the following components:

- A transparent, conductive glass electrode, typically fluorine-doped tin oxide (FTO) or, less commonly, indium tin oxide (ITO).
- A mesoporous metal oxide semiconductor with high surface area and porosity, typically TiO_2 for n-DSCs.
- A sensitising dye that absorbs across the visible-NIR region of light, capable of covalently anchoring to the semiconductor.
- A redox mediator, which is typically a combination of iodide/triiodide (I^-/I_3^-) in an organic solvent (most commonly acetonitrile).
- A counter electrode, which is typically another conductive glass electrode coated with a layer of platinum.

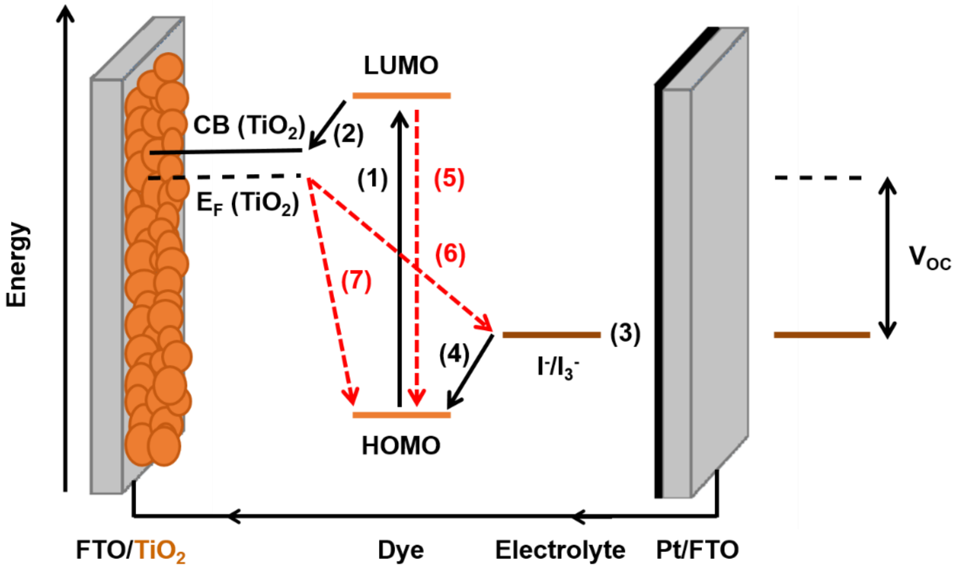

Figure 1.2. Schematic representation of the charge transfer processes occurring within a TiO_2-based n-DSC.

The charge transfer processes that occur in a n-DSC under operation are highlighted in Figure 1.2. These are as follows:

1) Photoexcitation of the dye (D) via the absorption of a photon to form an electronic excited state (D*):

$$D + h\nu \rightarrow D^*$$

Equation 1.1

2) Electron transfer from the excited dye to the conduction band of TiO_2 to form the oxidised dye (D^+):

$$D^* + TiO_2 \rightarrow D^+ + TiO_2|e^-$$

Equation 1.2

3) The electron diffuses through TiO_2 and into the external circuit where it reaches the counter electrode. Reduction of the oxidised species in the electrolyte then occurs at this electrode:

$$I_3{}^- + 2e^- \rightarrow 3I^-$$

Equation 1.3

4) Regeneration of the ground state of the dye by the reduced species in the electrolyte:

$$2D^+ + 3I^- \rightarrow 2D + I_3{}^-$$

Equation 1.4

These forward charge transfer processes are in competition with several recombination pathways:

5) Excited state decay of the dye (radiative and non-radiative):

$$D^* \rightarrow D + h\nu$$

Equation 1.5

6) Recombination of the injected electron within TiO_2 and the oxidised species in the redox electrolyte:

$$TiO_2|2e^- + I_3^- \rightarrow TiO_2 + 3I^-$$

Equation 1.6

7) Recombination of the oxidised dye and the injected electron within TiO_2:

$$TiO_2|e^- + D^+ \rightarrow TiO_2 + D$$

Equation 1.7

PCEs greater than 10% were soon achieved using the ruthenium dye **N3**[26] (Figure 1.3); the salt-analogue of this, **N719**, is still a routinely used benchmark dye for TiO_2-based n-DSCs. A wide variety of metal-based dyes have been studied for n-DSCs and these are often more efficient than organic dyes, despite the latter having higher extinction coefficients. Efficiencies of 12.3% and later 13% were achieved using porphyrin sensitisers (Figure 1.4) in conjunction with bipyridyl cobalt-based redox electrolytes.[27,28] Recently, a record efficiency of 14.3% has been achieved by co-sensitisation of an alkoxysilyl-anchored dye (**ADEKA-1**, Figure 1.5) and the organic dye **LEG4** with a cobalt-based electrolyte (optimised with eleven additives) and a FTO/Au/graphene nanoplatelet counter electrode.[29]

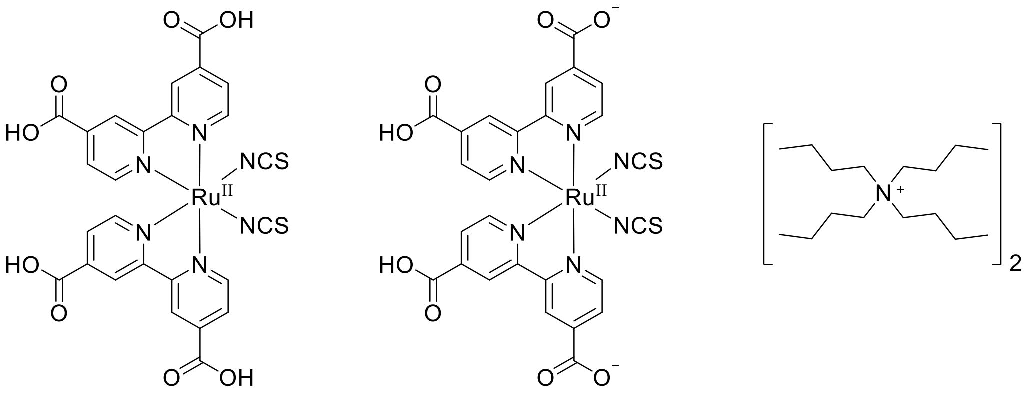

N3 **N719**

Figure 1.3. Molecular structure of highly efficient ruthenium dyes used for n-DSCs.

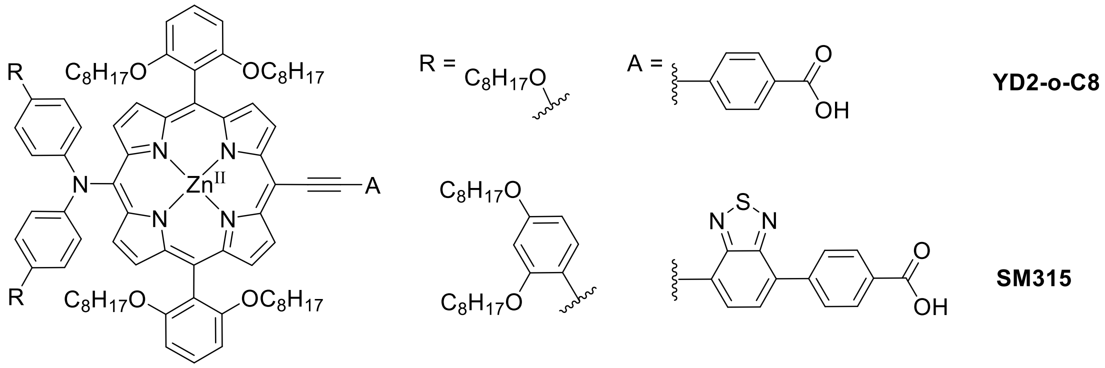

Figure 1.4. Molecular structure of the porphyrin dyes **YD2-o-C8** and **SM315**.

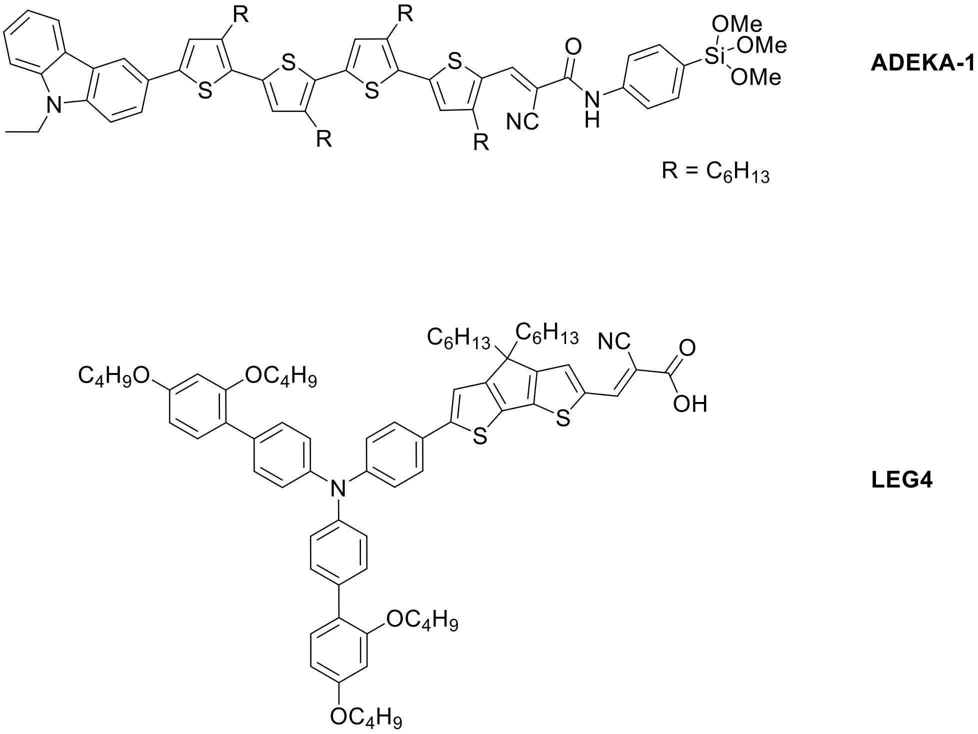

Figure 1.5. Molecular structure of the co-sensitised dyes, **ADEKA-1** and **LEG4**, used in the current record TiO$_2$ n-DSC.

1.3.2. p-DSCs

In 1999, Lindquist and co-workers published the first report of a p-type dye sensitised solar cell (p-DSC).[30] The cell was made using the same components as for a n-DSC, but the TiO$_2$ semiconductor was replaced with a layer of NiO, a p-type semiconductor. An overall PCE of 0.0076% was obtained using erythrosin B as a sensitiser. These devices operate in a similar fashion to n-DSCs, however, as the majority charge carriers in NiO are positive holes (h+), the electron flow occurs in the reverse direction. In a n-type device, electron transfer occurs from the excited dye into the conduction band of TiO_2. Conversely, for a p-type device electron transfer occurs from the valence band of NiO to the excited dye. A schematic representation of a NiO-based p-DSC is provided in Figure 1.6 and the individual components are discussed in more detail in the following section (**Chapter 1.4**).

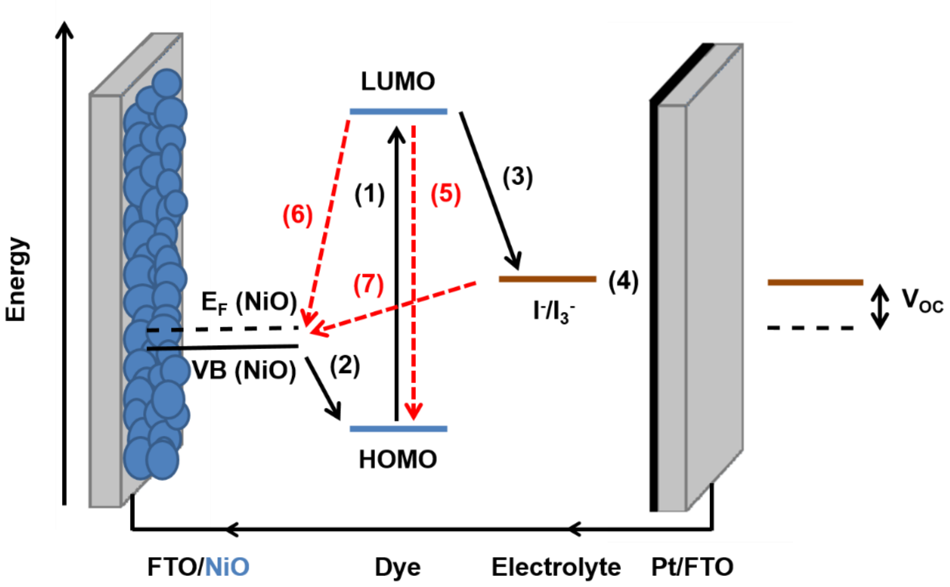

Figure 1.6. Schematic representation of the charge transfer processes occurring within a NiO-based p-DSC.

The charge transfer processes that occur in a p-DSC under operation are summarised in Figure 1.6. These are as follows:

1) Photoexcitation of the dye (D) via the absorption of a photon to form an electronic excited state (D*):

$$D + h\nu \rightarrow D^*$$

Equation 1.1

2) Electron transfer from the valence band of NiO to the excited dye (or hole transfer from the dye to NiO):

$$D^* + NiO \rightarrow D^- + NiO|h^+$$

Equation 1.8

3) Regeneration of the ground state of the dye by the oxidised species in the electrolyte:

$$2D^{-} + I_3^{-} \rightarrow 2D + 3\,I^{-}$$

Equation 1.9

4) Regeneration of the reduced species in the electrolyte at the counter electrode:

$$3\,I^{-} \rightarrow I_3^{-} + 2\,e^{-}$$

Equation 1.10

Again, these forward charge transfer processes are in competition with several recombination pathways:

5) Excited state decay of the dye (radiative and non-radiative):

$$D^{*} \rightarrow D + h\nu$$

Equation 1.5

6) Recombination between the reduced dye and a hole in NiO:

$$D^{-} + NiO|h^{+} \rightarrow D + NiO$$

Equation 1.11

7) Recombination of a hole in NiO with the reduced species in the electrolyte:

$$NiO|2h^{+} + 3I^{-} \rightarrow NiO + I_3^{-}$$

Equation 1.12

Regeneration of the reduced dye (process 3) is often simplified to Equation 1.9, but this process is thought to involve radical species.[31] The reduced dye is first regenerated by triiodide to form the diiodide radical (Equation 1.13). This undergoes disproportionation to form triiodide and iodide (Equation 1.14), the latter of which is regenerated at the counter electrode to supply an electron to the external circuit, quenching the hole in NiO (Equation 1.10).

$$D^{-} + I_3^{-} \rightarrow D + I_2^{\cdot -} + I^{\cdot}$$

Equation 1.13

$$2\,I_2^{\cdot -} \rightarrow I_3^{-} + I^{-}$$

Equation 1.14

Additionally, the redox electrolyte contributes to current generation by hole transfer into NiO. Triiodide can undergo photodissociation (Equation 1.15) to form the diiodide radical, which can accept an electron from NiO (Equation 1.16). This process can be observed by a contribution to the IPCE at 380 nm, which matches the absorption spectrum of triiodide.[31,32]

$$I_3^{-} + h\nu \rightarrow I_2^{\cdot -} + I^{\cdot}$$

Equation 1.15

$$I_2^{\cdot -} + NiO \rightarrow NiO|h^{+} + 2\,I^{-}$$

Equation 1.16

1.4. p-DSC components

1.4.1. Working electrodes

In a p-DSC, the working electrode is responsible for both providing a scaffold for the dye to adsorb onto and providing a conductive path for the migration of holes following charge separation. The majority of p-DSCs reported use NiO as a semiconductor material. NiO is a cubic semiconductor with a reported band-gap of between 3.4[33,34] and 4.3[35] eV, which is essentially transparent at low thicknesses, although some brown colour is present due to intrinsic Ni^{III} atoms that form during sintering.[36]

Various techniques are used to prepare NiO films[37,38] including sol-gel,[39] rapid discharge sintering (RDS),[40] hydrothermal[41] or screen-printing methods.[42] The most commonly used technique is the sol-gel method, due to its simplicity and reproducibility. A successful method for preparing mesoporous NiO films, which increases the surface area for dye adsorption, is to use triblock copolymers as templates in the sol-gel route. The method described by Sumikura *et al.*[39] is used to prepare F108-templated NiO films with thicknesses of 1-2 µm and crystal sizes of 16 nm (after sintering at 450 °C).[43]

While NiO is the most widely-studied p-type semiconductor for p-DSCs, other alternatives have been tested including $CuGaO_2$,[44–46] $CuCrO_2$,[47,48] CuO[49–51] and $NiCo_2O_4$.[52] While the efficiencies of devices made using these materials is typically lower than those reported for NiO, a PCE of 0.191% was recently obtained for nanorod structured CuO sensitised with phthalocyanines.[51] To tune the density of states/conductivity, NiO can be doped with other materials, for example Li[53] and Mg.[54,55]

1.4.2. Sensitisers

As the dye is the part of a DSC that absorbs light and drives the production of a photocurrent, the development of new sensitisers is crucial to improve device efficiencies. There are a number of criteria that need to be considered when designing new dyes:

- The dye must be capable of absorbing photons in the visible-NIR region, ideally with a broad absorption profile. Due to the typically low NiO film thicknesses used (ca. 1.5 µm), high extinction coefficients are needed to maximise light harvesting. As n-DSCs have been optimised to harvest higher energy photons, for NiO we require dyes that can absorb across the longer-wavelength visible and near-IR regions (to construct tandem devices).

- An anchoring unit, typically a group containing an acidic proton, is also essential for the dye to adsorb onto the semiconductor surface and to facilitate efficient charge transfer from NiO to the dye. Carboxylic acids are the most commonly used anchoring units,[56–58] but phosphonates[59,60] and pyridine[61–63] groups have also been used.

- The HOMO and LUMO levels of the dye need to be suitably positioned to promote efficient charge transfer and dye regeneration. The HOMO needs to be more positive than the valence band edge of NiO and the LUMO needs to be more negative than the redox potential of the electrolyte (with respect to redox potentials vs. NHE).
- As recombination between the excited dye molecules and holes in NiO is so prevalent for p-DSCs,[64,65] the dye structure should promote a long-lived charge-separated state. This is usually attempted by following a donor-acceptor 'push-pull' design, where electron density will be shuttled to the peripheries of the dye following charge transfer from NiO. This increases the spatial electron/hole separation.

The development of dyes and the push-pull design will be discussed in more depth in **Chapter 1.5**.

1.4.3. Electrolytes

In a DSC, the electrolyte is responsible for regenerating the ground state of the dye and transporting electrons to the counter electrode. Most p-DSCs use a liquid electrolyte, which is typically I^-/I_3^- or a metal complex-based redox shuttle, but recently a few solid-state p-DSCs have been reported.[66,67]

The most common liquid electrolyte is I^-/I_3^- (typically in the form of LiI and I_2 in acetonitrile) and this has been used for many high-efficiency devices.[57,68,69] However, despite its widespread use, there are several drawbacks to this electrolyte. The redox couple is strongly coloured and competes with the dye for light absorption, particularly at lower wavelengths (λ_{max} I_3^- = 380 nm, absorbs to ca. 450 nm).[70] Additionally, the small energy difference between the redox potential of this electrolyte and the Fermi level of NiO limits the open-circuit voltage (V_{OC}) of these devices (see **Chapter 2.5.2**). Cobalt (II/III) polypyridyl complexes have proved a promising alternative to the I^-/I_3^- redox couple, due to improved chemical stability, optical transparency and more negative redox potentials (vs. I^-/I_3^-). Also, the bulky size of these complexes can reduce recombination between the redox electrolyte and holes in NiO.[71] Devices made using cobalt-based electrolytes typically produce a higher PCE than I^-/I_3^- (when comparing the same dye) due to a higher V_{OC} (ca. 200-300 mV vs. 100 mV).[72,73] However, not all dyes can be used with transition metal-based electrolytes, as a long-lived charge-separated state is necessary for dye regeneration to compete with dye/NiO recombination. Most dyes used with these electrolytes contain a secondary electron acceptor, such as PMI or NDI, to generate long-lived radical species.[57,73] The PCE of devices made using the dye **PMI-6T-TPA**[58] (Figure 1.7) increased from 0.60% with the I^-/I_3^- redox couple to 1.20%[73] and 2.51%[74] using electrolytes based on $Co(en)_3$ and $Fe(acac)_3$ respectively.

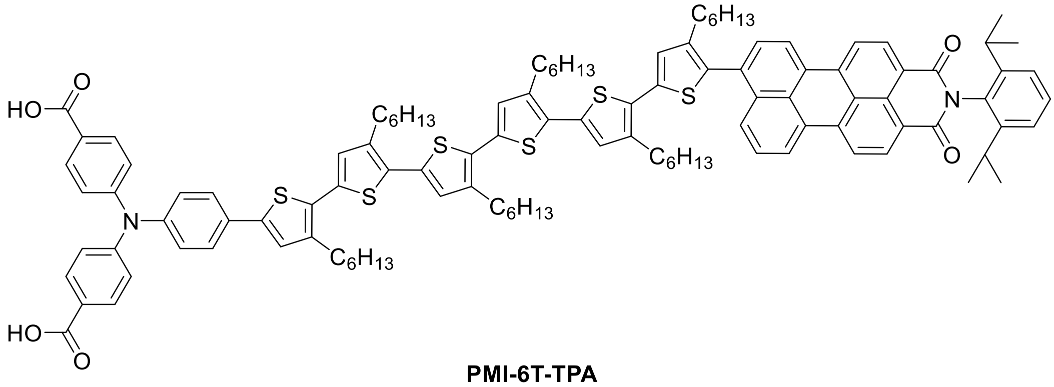

PMI-6T-TPA

Figure 1.7. Molecular structure of **PMI-6T-TPA**.

1.4.4. Counter electrodes

In a DSC, the counter electrode performs the role of regenerating the redox couple and shuttling the injected electrons to the working electrode so that the device can be cycled again. For both n-type and p-type devices, the most common material used for counter electrodes is a layer of platinum deposited on a conductive substrate.[75] Platinum is used because it is catalytically active toward the reduction of triiodide (for n-DSCs) and the oxidation of iodide (for p-DSCs), to ensure that the reaction occurs rapidly and at a low overpotential. The charge transfer resistance of the counter electrode (R_{CT}) is determined by the overpotential according to Equation 1.17.[76]

$$R_{CT} = {}^{\eta_{op}}/_{J}$$

Equation 1.17

Where η_{op} is the overpotential needed to drive the reaction at a specified current density (J). The charge transfer resistance will contribute to the series resistance of a DSC, so it is important to minimise this value to avoid significant efficiency losses.

Cobalt sulphide has been used as an alternative counter electrode material in p-DSCs.[77,78] Devices made using erythrosin B as a sensitiser performed similarly with a CoS counter electrode (PCE = 0.026%) compared to a Pt standard (PCE = 0.030%).[77] However, CoS performed poorly at higher current densities (> ca. 2 mA cm^{-2}) and there was a greater difference in efficiency for devices made using **P1** as a sensitiser (PCE = 0.07% for CoS and 0.11% for Pt).[78] This difference was attributed to an increased charge transfer resistance of CoS toward the oxidation of iodide compared to Pt (130 vs. 4.5 Ω).

1.5. Development of sensitisers for p-DSCs

Many research groups are working on designing new sensitisers to improve the efficiencies of p-DSCs, which has produced a wide range of publications.[79–81] Figure 1.9 provides a comparison of the DSC performances of around ninety dyes that have been designed for p-DSCs. Each data point represents a different dye; in cases where the same dye has been reported multiple times, the optimised system was plotted. Ruthenium refers to ruthenium complexes used as dyes and double acceptor/anchor refers to triphenylamine based push-pull dyes, with either one or two acceptor groups, depending on the configuration chosen (Figure 1.8). J_{SC} and V_{OC} refer to the short-circuit photocurrent density and open-circuit voltage respectively. These are two of the parameters used to compare solar cells and will be described in detail in a later section (**Chapter 2.5.2**). A detailed overview of the solar cell parameters, dye structures and references used to produce this figure is provided in Appendix 1.

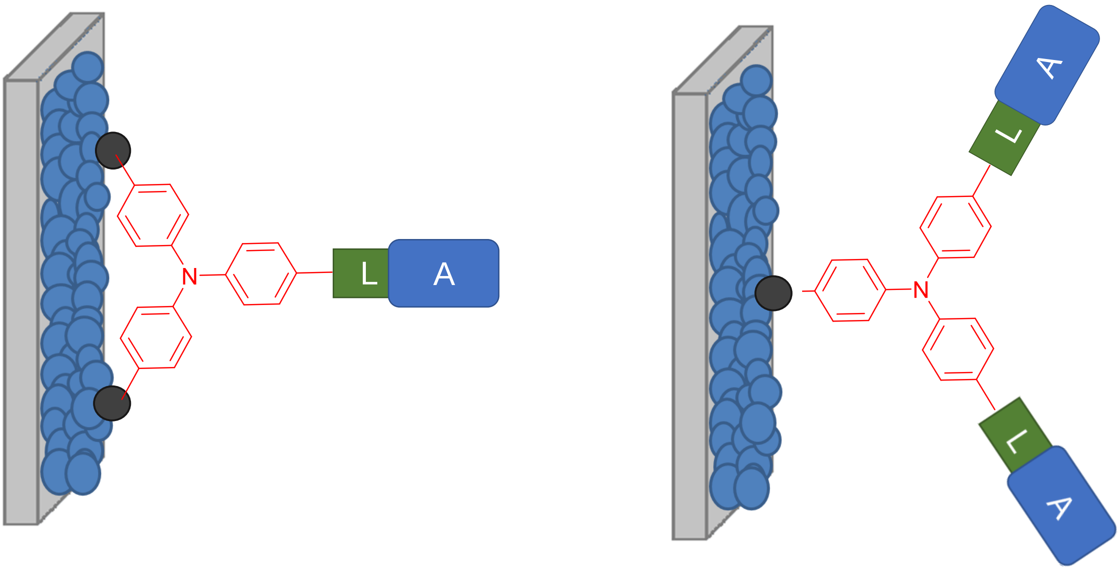

Figure 1.8. Schematic representation of triphenylamine ‘push-pull’ dyes bearing one or two acceptor groups. L = linker group and A = acceptor unit.

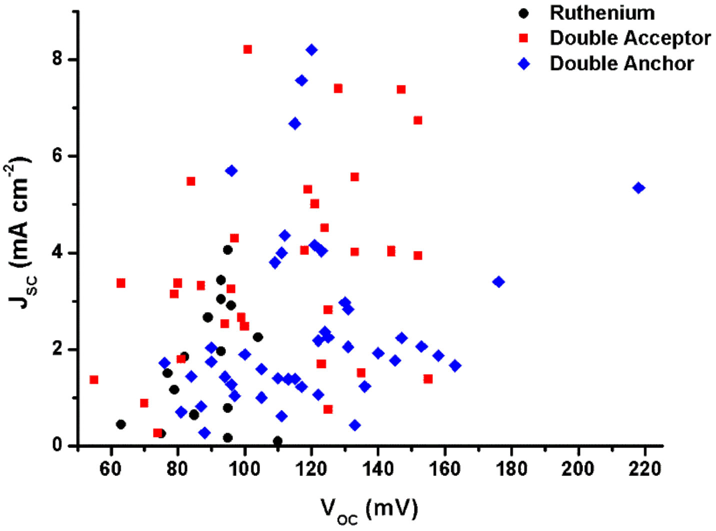

Figure 1.9. A comparison of p-DSC performances for various reported dyes tested with an I^-/I_3^- electrolyte.

In general, dyes based on ruthenium complexes perform worse than organic dyes, which is the opposite trend to the majority of n-DSCs. Organic dyes based on triphenylamine typically produce higher photocurrent densities with the double acceptor design, as appending the second chromophore typically increases the extinction coefficient. In comparison, the dyes with the double anchor design typically produce higher voltages. This is possibly due to improved dye loading, as the double anchored design could help to form a more compact dye monolayer on the NiO surface. Additionally, the linker groups for the double anchor design often contain long aliphatic chains, which can block the redox electrolyte from reaching the NiO surface. This reduces NiO/electrolyte recombination, leading to a higher hole concentration in the NiO valence band. This, in turn, can improve the voltages by increasing the potential difference between the Fermi level of the NiO valence band and the electrolyte redox potential.

1.5.1. Ruthenium complexes

In n-DSCs, ruthenium complexes are efficient sensitisers that outperformed organic dyes for a long time. One of the first ruthenium dyes tested as a sensitiser for NiO-based p-DSCs was the typical n-type dye **N719**.[42] A 'desensitising' effect was seen for NiO/**N719**, where the dyed devices performed worse than NiO alone (J_{SC} = 8 vs. 46 µA cm^{-2} for NiO/**N719** and NiO respectively). The authors postulated that **N719** was forming a dye-iodide complex, as has been reported previously for n-DSCs,[82] which can catalyse the oxidation of iodide. This could lead to enhanced electrolyte/NiO recombination in a p-type device. The fully protonated analogue **N3** was also tested in p-DSCs by Qin *et al.*,[83] who reported a negligible J_{SC} and no photocurrent response at monochromatic wavelengths that could be attributed to the dye. These dyes were thought to perform poorly as they were engineered to have higher electron densities at the semiconductor surface following excitation. This would promote electron transfer into the TiO_2 conduction band in an n-type device, but has the opposite effect of inhibiting NiO-dye electron transfer (and promoting dye^-/NiO recombination) in a p-type device.

However, while **N719** and **N3** did not prove suitable for use in a p-DSC, some ruthenium dyes have been more successful by adopting a donor-acceptor design. Figure 1.10 shows a selection of ruthenium dyes that have been used to produce photocurrent densities > 2 mA cm^{-2} when utilised in a p-DSC. Most of these (the **OX** series, **K1** and **SL1**) were designed with a triphenylamine donor, so that following excitation, electron density would be located on the ruthenium core, away from the NiO surface. This design, which was intended to inhibit charge recombination between the reduce dye molecules and holes in NiO, was successful in producing higher photocurrent densities. The dyes that produced a J_{SC} close to or higher than 3 mA cm^{-}

^{2} were **K1**,[84] **O3**,[85] **O18**[86] and **[Ru(bpy)$_2$(H5)]**[87] (J_{SC} = 2.91, 3.04, 3.43 and 4.06 mA cm^{-2} respectively). Interestingly, the highest performance (PCE = 0.139%) was obtained using the structurally simplest dye, **[Ru(bpy)$_2$(H5)]**. A structural analogue (**O11**[88]) has been previously reported for use in p-DSCs, which instead contained a carboxylic acid anchoring unit. With the carboxylic acid anchoring group, much lower device efficiencies were obtained (J_{SC} = 1.16 and PCE = 0.033% **O11** vs. J_{SC} = 4.06 mA cm^{-2} and PCE = 0.139% for **[Ru(bpy)$_2$(H5)]**), despite the apparent subtle structural difference. **[Ru(bpy)$_2$(H5)]** was isolated as a zwitterion,[60] so it is possible that the reduced electron density on ruthenium imparts some charge transfer character. This could increase the photocurrent density by reducing the recombination. A similar effect was reported for the ruthenium dyes with a carboxylic acid anchoring group by inserting additional phenyl groups between bipyridine and benzoic acid, thereby increasing the spatial separation between NiO and the ruthenium core.

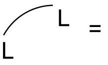

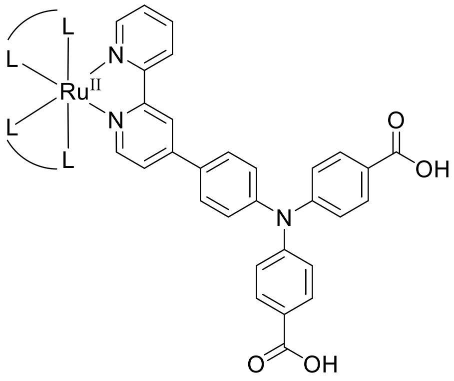

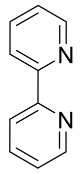

O3

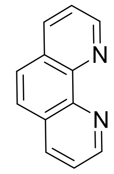

O13

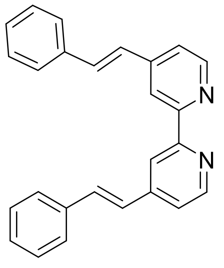

O18

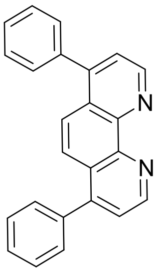

O17

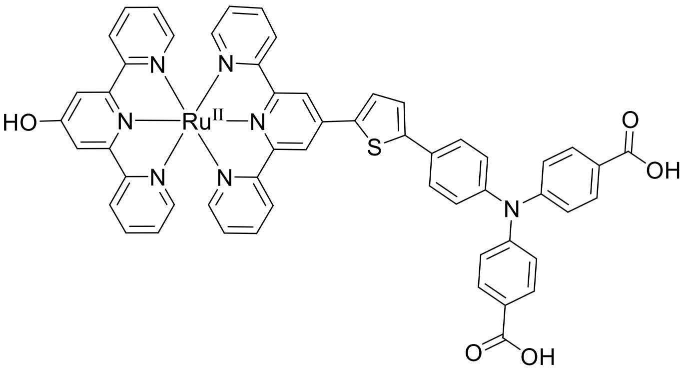

K1

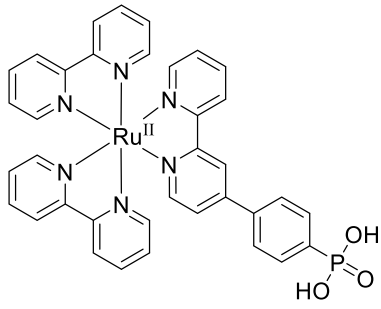

[Ru(bpy)$_2$(H5)]

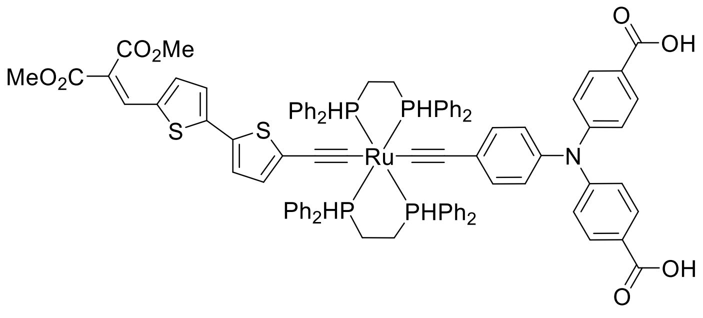

SL1

Figure 1.10. Molecular structure of ruthenium dyes used for NiO-based p-DSCs where J_{SC} > 2 mA cm^{-2}.[84–87,89]

1.5.2. Organic push-pull dyes

In early publications on NiO-based p-DSCs, commercial dyes such as coumarin 343 (**C343**) and erythrosin B were used as the sensitiser (Figure 1.11).[30,90–92] These served as proof-of-concept reports for dye-sensitised NiO as a photocathode, however, the devices were limited by low efficiencies. This was attributed to fast recombination between the reduced dye molecules and holes in NiO. The first time-resolved spectroscopic study of dye molecules adsorbed onto NiO was carried out using **C343**/NiO; electron transfer from NiO to the excited dye occurred on a timescale $\tau \approx$ 200 fs, compared to back recombination with the reduced dye $\tau \approx$ 20 ps.[91] Slowing down this recombination process is crucial to improving the performances of p-DSCs.

Coumarin 343 **Erythrosin B**

Figure 1.11. Molecular structures of coumarin 343 and erythrosin B, two commercial dyes used as sensitisers for NiO,

Morandeira and co-workers reported the first dye designed specifically for use in p-DSCs (**PMI-NDI**, Figure 1.12).[93] In this system, a long-lived charge separated state was formed in the presence of the naphthalene diimide (NDI) acceptor. The dyad achieved a quantum efficiency three times greater than the analogous dye without NDI. A variety of perylene based donor-acceptor dyads were tested with varying acceptor units (**NDI** or **C_{60}**, Figure 1.12)[94] and in each case higher performances were obtained with an acceptor group present. This was, again, attributed to an extension of the charge-separated state lifetime, by ca. 5 orders of magnitude, in the presence of an acceptor group. In a later publication, a p-DSC constructed using **PMI-NDI** sensitised NiO and a $Co^{II/III}$-based redox electrolyte obtained an overall PCE of 0.20%, in part due to a greatly increased V_{OC} of 350 mV.[72] This work highlighted the necessity of designing donor-acceptor dyes specifically engineered for NiO-based p-DSCs to increase device efficiencies (Figure 1.13).

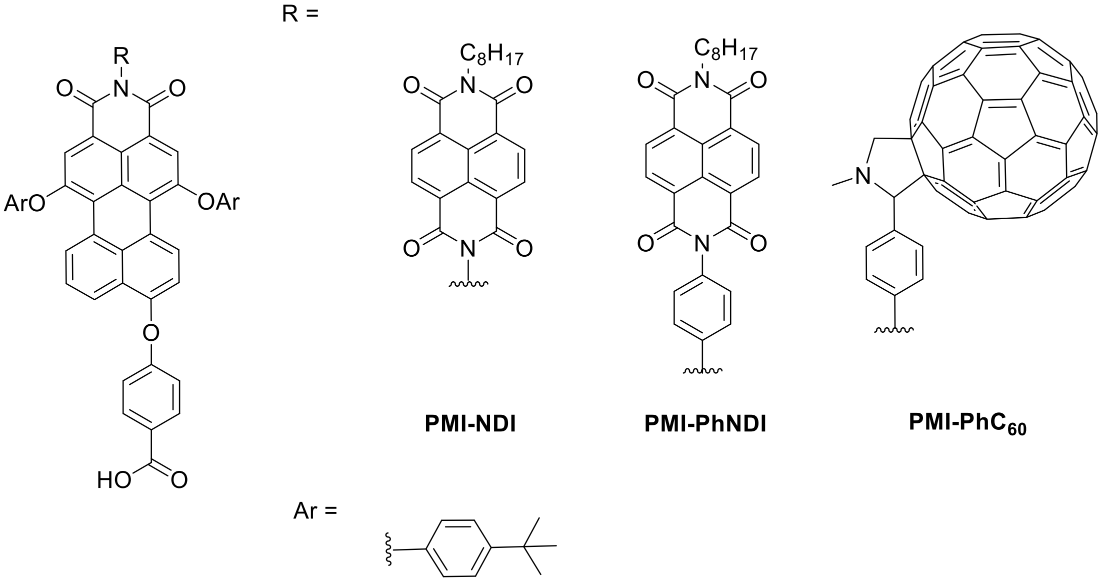

Figure 1.12. Molecular structure of PMI-acceptor dyads tested for p-DSCs.

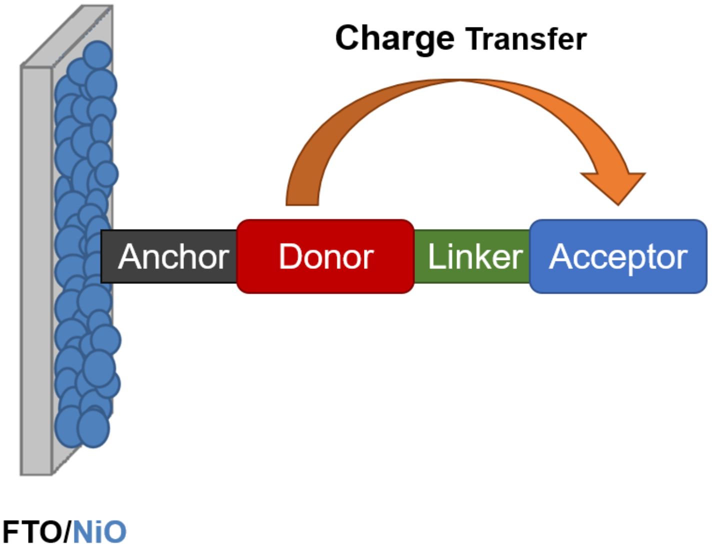

Figure 1.13. Schematic representation of the 'push-pull' design used for p-DSCs.

One of the first dyes to achieve a higher J_{SC} was the triphenylamine-based push-pull dye **P1** (Figure 1.14), the design of which heavily influenced the development of most subsequent dyes for p-DSCs. This combined a triphenylamine donor unit and two dicyanovinylene acceptors, linked using thiophene bridges, with a carboxylic acid anchoring group. In the initial publication,[83] **P1**/NiO p-DSCs produced a Jsc of 1.52 mA cm^{-2} and an IPCE of 18%, with an overall PCE of 0.05%. Devices made using **P1** were later optimised to give IPCEs of 35%[95] and then 53%[43], with a final PCE of 0.15%

obtained for the optimised system (J_{SC} = 5.48 mA cm^{-2}, V_{OC} = 84 mV, FF = 0.33, PCE = 0.15%).

Another highly efficient set of dyes (published at a similar time) is the **PMI-nT-TPA** series (Figure 1.15).[58] Here, a perylenemonoimide (PMI) acceptor is coupled to a triphenylamine donor by an oligothiophene spacer of varying length. The dyes are adsorbed onto NiO through two carboxylic acid groups on the triphenylamine donor. Increasing the oligothiophene length produced longer-lived charge separated states, which greatly increased device performances (PCE = 0.09%, 0.19% and 0.41% for n = 1, 2 and 3 respectively). While the J_{SC} for **PMI-6T-TPA** and **P1** were similar (J_{SC} = 5.35 vs. 5.48 mA cm^{-2}), the PCE was over twice as high for **PMI-6T-TPA** due to the larger V_{OC} (218 mV vs. 84 mV). The higher V_{OC} could be attributed to reduced electrolyte/NiO recombination, due to the presence of long sterically hindering alkyl chains. Alternatively, it could be due to differences in NiO preparation, as NiO films sensitised with **PMI-6T-TPA** were constructed using a screen printing paste prepared from NiO nanoparticles, instead of the sol-gel route used for **P1**. As mentioned previously, the PCE of p-DSCs constructed utilising **PMI-6T-TPA** increased from 0.60% with the I^-/I_3^- redox couple to 1.20%[73] and 2.51%[74] using electrolytes based on $Co(en)_3$ and $Fe(acac)_3$ respectively. The latter remains the record PCE for a NiO-based p-DSC.

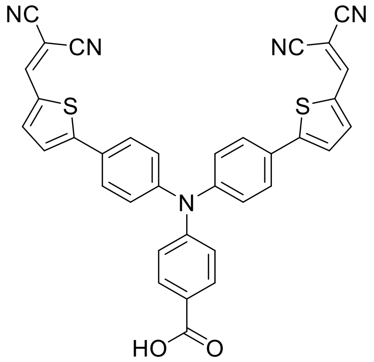

P1

Figure 1.14. Molecular structure of the triphenylamine push-pull dye **P1**.

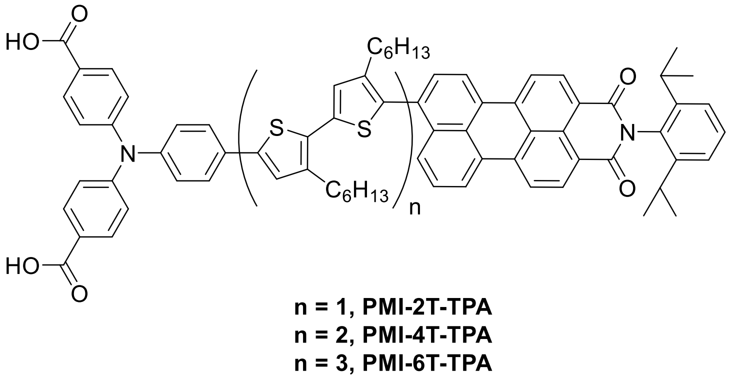

Figure 1.15. Molecular structure of the triphenylamine-perylene dyes **PMI-nT-TPA**.

The success of **P1** and **PMI-6T-TPA** sparked renewed interest into designing triphenylamine-based donor-acceptor dyes. Since these reports, the majority of dyes for p-DSCs contain either diphenylamine or triphenylamine donor groups. Triphenylamine has likely seen such widespread attention due to its strong electron-donating ability, ease of functionalisation and non-planar shape, which can help reduce aggregation. Due to these reasons, hundreds of arylamine-containing molecules have been designed for DSCs and organic solar cells.[96,97] Most new dye designs aim to modify the acceptor[68,69] or linker[98,99] groups, while there are only a few reports of modified anchoring structures.[59,61]

As mentioned previously, dyes with two acceptor groups tend to produce a higher J_{SC}. As shown in Figure 1.9, 65% of reported dyes with the double acceptor structure produced a $J_{SC} \geq 3$ mA cm^{-2}, compared to 26% for dyes with the double anchor structure. The structures of some of the dyes which generated the highest reported J_{SC} are provided in Figure 1.16 and Figure 1.17. The highest reported J_{SC} for a p-DSC was produced using **CAD3**[68] (J_{SC} = 8.21 mA cm^{-2}). This was based on the **P1** design, but had two cationic indolium groups as electron acceptors. This high performance was attributed to the strong absorption properties of the dye (λ_{max} = 614 nm, ε = 95,000 dm^3 mol^{-1} cm^{-1}) compared to related dyes with only one indolium acceptor (**CAD1** and **CAD2**)[100].

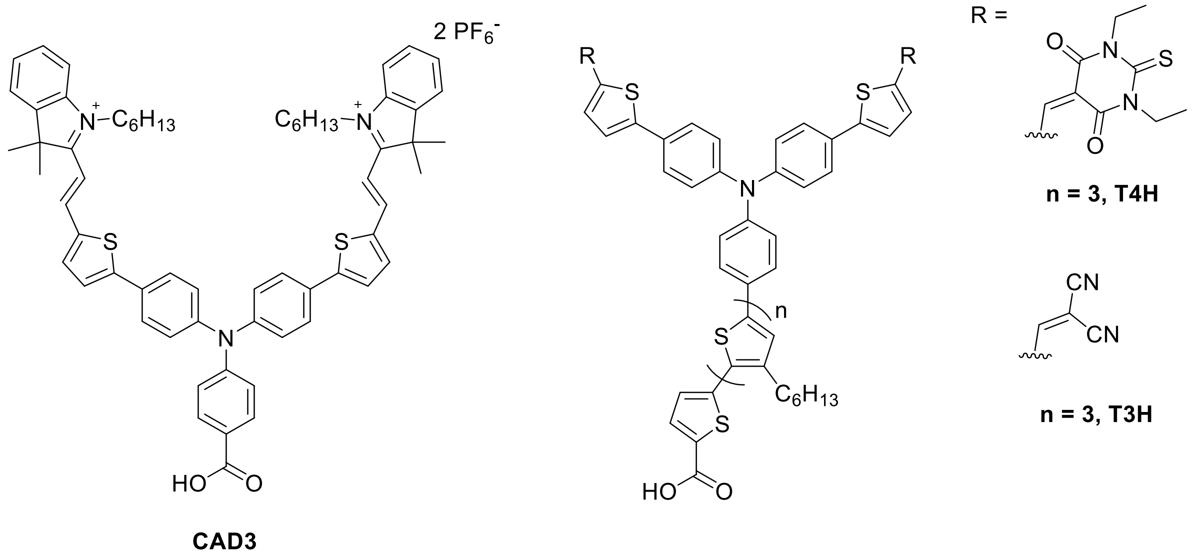

Figure 1.16. Molecular structure of highly performing push-pull dyes with the double acceptor design; **CAD3**,[68] **T3H**[101] and **T4H**.[103]

Yang and co-workers studied the effect of increasing the donor-anchor separation of the **P1** structure, by varying the oligothiophene length from four to six units.[101-103] The highest performance was achieved with four thiophenes (**T3H**). They found that, despite the increased conjugation length and stronger absorbance with five and six thiophenes, after four units the photocurrent decreased due to unfavourable charge transfer from NiO to the dye. Finally, using four thiophenes units as the optimum separation length, the dicyanovinylene acceptor groups were substituted for 1,3-diethyl-2-thiobarbituric acid (**T4H**).[103] A broader absorption profile was obtained that stretched further into the NIR, which resulted in a higher light harvesting ability of the device. Consequently, the device sensitised with **T4H** produced a higher J_{SC} than that which utilised **T3H**; J_{SC} = 5.57 and 6.74 mA cm^{-2} for **T3H** and **T4H** respectively. A higher V_{OC} of 152 mV, compared to 101 mV for **CAD3**, meant that **T4H** produced a higher overall PCE (PCE = 0.32% for **T4H** and 0.25% for **CAD3**).

The **BH** series (Figure 1.17)[104] was designed based on **PMI-6T-TPA**, with two oligothiophene-PMI acceptor groups and one carboxylic acid anchor. The presence of an additional acceptor increased molar extinction coefficients due to the extended conjugation (ε = 84,000 – 96,000 dm^3 mol^{-1} cm^{-1} for the **BH** series vs. 67,000 dm^3 mol^{-1} cm^{-1} for **PMI-6T-TPA**). The highest p-DSC performances were obtained with **BH4**, as although extinction coefficients increased with increasing oligothiophene length, the dye loading decreased. **BH6** had a dye loading three times lower than **BH4**, which decreased the J_{SC}. This is a different trend to the **PMI-nT-TPA** dyes, in which the J_{SC}

and overall PCE increased with increasing conjugation length. Dye loading for the **PMI-nT-TPA** series was not studied, but it is possible that the two anchoring groups induced a more ordered dye orientation on the NiO surface. Therefore, increasing the thiophene length would not significantly increase the overall ‘footprint’ of the dye. Whereas for the **BH** series, the long thiophene chains are orientated more horizontally and so increasing their length could reduce dye loading. Devices made with **BH4** produced higher photocurrents than both **PMI-4T-TPA** and **PMI-6T-TPA**. The overall performance of **BH4** was higher than **PMI-4T-TPA**, but lower than **PMI-6T-TPA**, due to a reduced V_{OC} (**BH4**; J_{SC} = 7.40 mA cm^{-2}, V_{OC} = 128 mV, FF = 0.30, PCE = 0.28%, **PMI-4T-TPA**; J_{SC} = 3.40 mA cm^{-2}, V_{OC} = 176 mV, FF = 0.32, PCE = 0.19%, **PMI-6T-NDI**; J_{SC} = 6.26 mA cm^{-2}, V_{OC} = 243 mV, FF = 0.39, PCE = 0.60%). While significant improvements were obtained for devices made using **PMI-6T-TPA** in conjunction with transition metal-based electrolytes, the **BH** series was only tested with I^-/I_3^-.

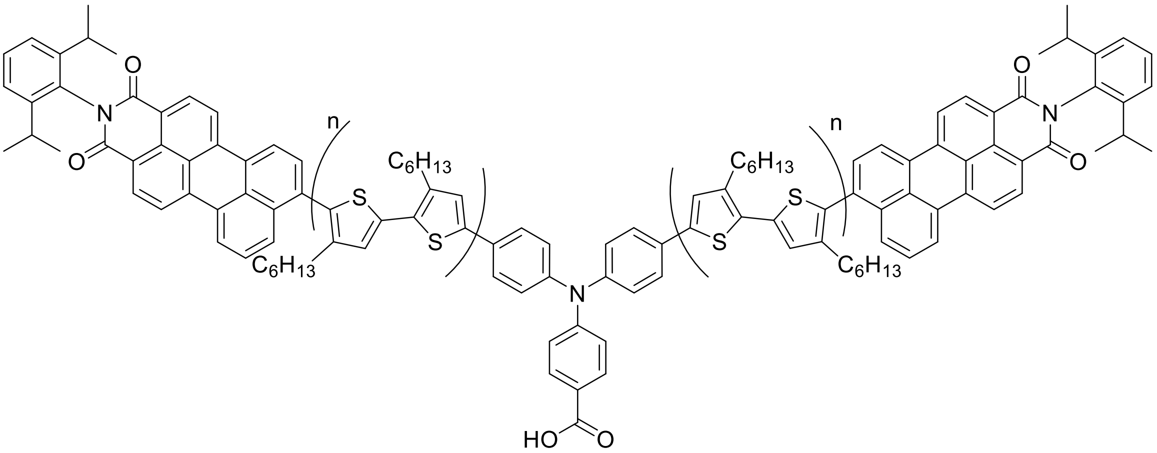

n = 1, BH2
n = 2, BH4
n = 3, BH6

Figure 1.17. Molecular structure of the **BH** dye series.[104]

Excluding the **PMI-nT-TPA** series, many dyes that adopt the double anchor design do not produce a high J_{SC}. However, a series of fluorene-bridged biphenylamine-perylenemonoimide dyes have been recently successful (Figure 1.18). In the **zzx-op** series, the fluorene bridge is directly appended to biphenylamine, which will improve donor/acceptor coupling.

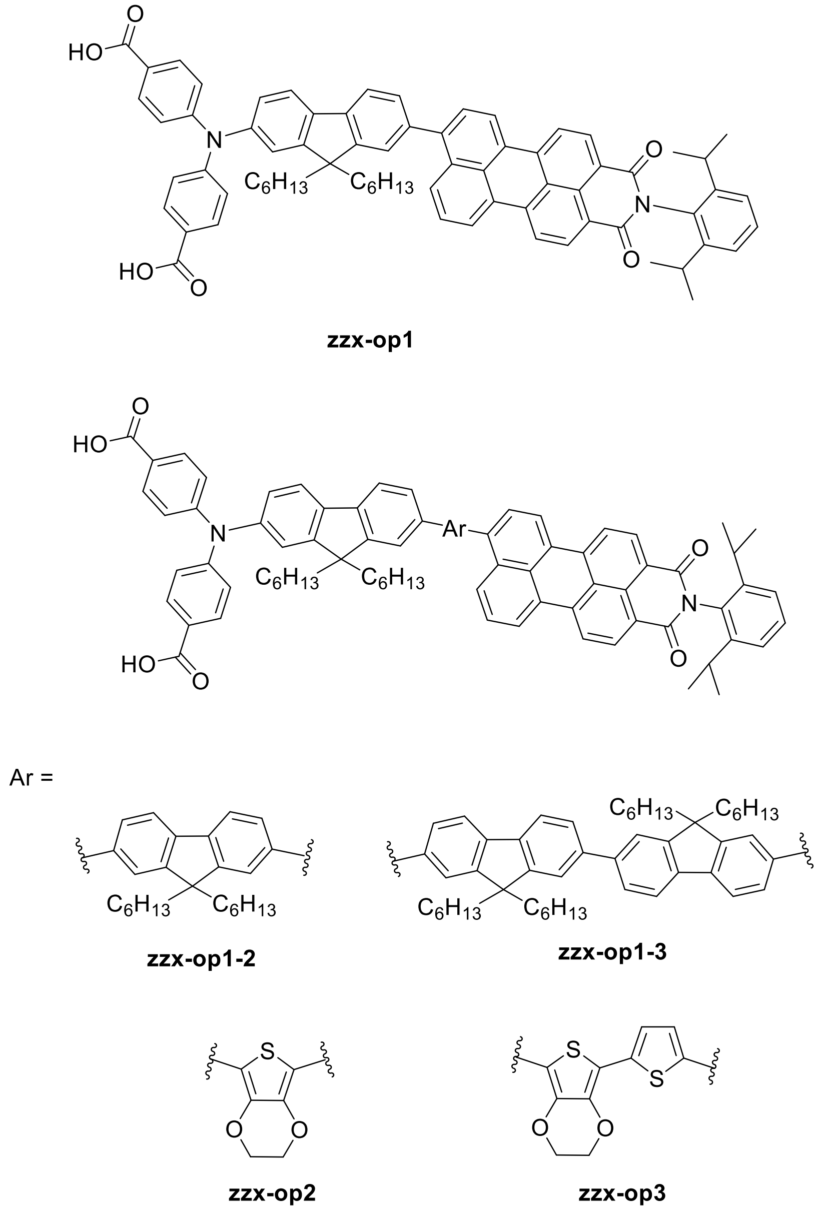

Figure 1.18. Molecular structure of the **zzx-op** series, a set of highly performing fluorene based push-pull dyes with the double anchor design.[98,99]

In the first publication by He *et al.*,[99] the linker groups were varied between fluorene (**zzx-op1**), fluorene-3,4-ethylenedioxythiophene (EDOT, **zzx-op2**) and fluorene-EDOT-thiophene (**zzx-op3**). There was a broader spectral coverage as the conjugation length increased, which was expected to increase the JSC. However, the JSC decreased in the order of 4.36 > 4.00 > 3.80 mA cm^{-2} (for **zzx-op1**, **zzx-op2** and **zzx-op3** respectively) as the spacer length increased. The VOC and fill factors of the devices were mostly unaffected (VOC and FF ranged from 109-112 mV and 0.36-0.38 respectively), therefore PCE decreased in the same trend of 0.18% > 0.16% > 0.15%.

These differences could not be rationalised on the basis of absorption properties or dye loading, as all three dyes had a similar dye loading of 2.09 – 2.15 x 10^{-7} mol cm^{-2}. The differences were therefore attributed to a decreasing driving force for charge transfer. As the conjugation length increased, the HOMO became more negative, which decreased the driving force. Injection quantum yields of 90% > 54% > 39% were calculated for **zzx-op1**, **zzx-op2** and **zzx-op3** respectively. From the basis of these measurements, they proposed that ≈ 0.80 eV of driving force is necessary for high charge transfer quantum yields. As fluorene proved to be the optimum linker unit, in a subsequent publication[98] they looked at extending the fluorene length (**zzx-op1-2** and **zzx-op1-3**). As the conjugation length was increased, the driving force for charge transfer remained mostly unaffected, but charge recombination to NiO was reduced. The highest efficiency was obtained with two fluorene spacers (**zzx-op1-2**, J_{SC} = 7.57 mA cm^{-2}, V_{OC} = 117 mV, FF = 0.40, PCE = 0.353%). This was attributed to a trade-off between increased donor/acceptor separation and the flexibility of the fluorene chain. As the fluorene bridge became longer, the increased spatial separation between the donor and acceptor groups would likely hinder recombination between the reduced dye and NiO. Conversely, with shorter chains the dyes could form a more compact layer, which could inhibit recombination between the electrolyte and NiO. **zzx-op1-2** was argued to have the correct chain length to balance these two factors, leading to the highest performances. Despite their similarities to the **PMI-nT-TPA** dyes, none of the **zzx-op** series were tested with transition metal-based electrolytes.

Both the **PMI-nT-TPA** and **zzx-op** dye series exemplify the double anchor design; triphenylamine or biphenylamine linked to PMI via a long, conjugated linker. A recently reported push-pull thienoquinoidal dye is the antithesis to this design, with a small conjugation length and little donor/acceptor separation (**QT-1**, Figure 1.19). Despite this, the dye produced one of the highest reported J_{SC} of 8.20 mA cm^{-2}. Coupled with a V_{OC} of 120 mV and a FF of 0.34, this dye had an overall PCE of 0.33% when tested with the I^-/I_3^- electrolyte. It also proved to be successful when used with a Co^{II}/Co^{III}-based electrolyte (J_{SC} = 6.5 mA cm^{-2}, V_{OC} = 226 mV, FF = 0.34, PCE = 0.50%), suggesting that the charge-separated state is long-lived. Little discussion was provided as to why these devices were so successful. Interestingly, it has a very similar structure to a previously reported dye, **O2**.[105] When employed in a p-DSC, **O2** performed only modestly (J_{SC} = 1.43 mA cm^{-2}, V_{OC} = 94 mV, FF = 0.37, PCE = 0.05%). This comparison highlights how fairly minor structural changes can have a large effect on device efficiencies.

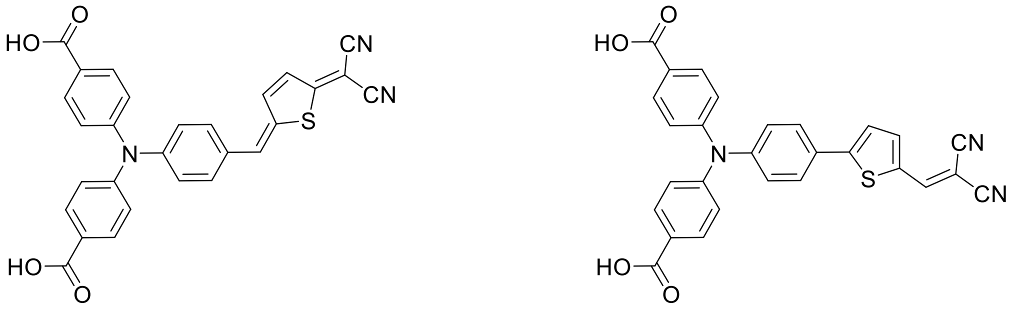

QT-1 **O2**

Figure 1.19. Molecular structure of **QT-1**[69] and the structurally similar dye **O2**.[105]

Lin and co-workers designed a series of arylamine-based dyes with a single acceptor unit and one or two carboxylic acid anchoring units, to directly probe the effect of multiple anchoring sites on device performances (Figure 1.20).[106,107] Comparing the two dyes with the 1,3-diethyl-2-thiobarbituric acid acceptor unit (**Lin-1** and **Lin-2**), devices made with the multi-anchored dye out-performed those made with the single-anchored dye (**Lin-1**; J_{SC} = 1.38 mA cm^{-2}, V_{OC} = 113 mV, FF = 0.34, PCE = 0.053%, **Lin-2**; J_{SC} = 2.18 mA cm^{-2}, V_{OC} = 122 mV, FF = 0.35, PCE = 0.092%). This improved performance was attributed to the second anchoring unit enhancing the binding strength between the dye and the semiconductor, thereby facilitating more efficient charge transfer. It was also suggested that the improvements were due to a suppression of the dark current of the device from more effective coverage of the NiO surface by the dye. However, a lower dye loading (1.54 x 10^{-7} mol cm^{-2} for **Lin-1** vs. 1.19 x 10^{-7} mol cm^{-2} for **Lin-2**) was observed for the dye containing two anchoring units. The same trend was seen for the squaraine dyes, with the double-anchored structure proving more efficient (**p-SQ1**; J_{SC} = 1.22 mA cm^{-2}, V_{OC} = 117 mV, FF = 0.37, PCE = 0.053%, **p-SQ2**; J_{SC} = 1.92 mA cm^{-2}, V_{OC} = 140 mV, FF = 0.42, PCE = 0.113%). Again, the improvements were attributed to a suppression of the dark current. In comparison to the first report, here the dye with two anchoring units had a higher dye loading (1.98 x 10^{-7} mol cm^{-2} for **p-SQ2** vs 1.07 x 10^{-7} mol cm^{-2} for **p-SQ1**), possibly due to a more compact dye monolayer brought about from the more rigid anchoring mode.

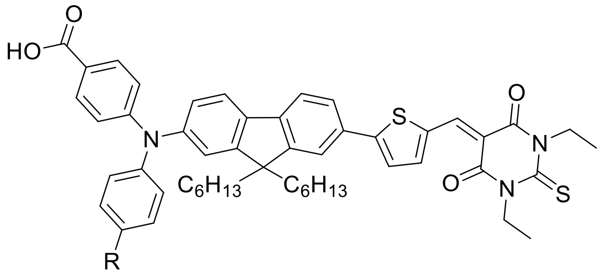

R = H, **Lin-1**

R = COOH, **Lin-2**

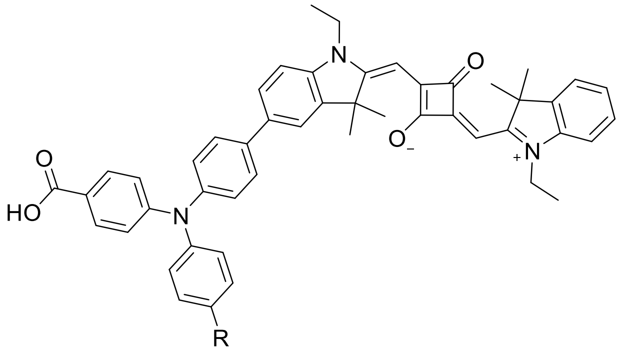

R = H, **p-SQ1**

R = COOH, **p-SQ2**

Figure 1.20. Molecular structure of arylamine dyes with one or two anchors designed for p-DSCs by the group of Lin.[106,107]

While triphenylamine-based push-pull dyes have dominated the p-DSC field since the work of Sun[83] and Bach,[58] very recently a publication by Odobel and co-workers described a highly efficient diketopyrrolopyrrole (DPP) dyad that does not contain an amine donor (Figure 1.21).[57] **Th-DPP-NDI** had a modest extinction coefficient of 37,000 dm^3 mol^{-1} cm^{-1}, lower than any of the other dyes that produced a high J_{SC}. Despite this, the average J_{SC} of NiO/**Th-DPP-NDI** devices was 7.38 mA cm^{-2} and the 'champion' device produced 8.2 mA cm^{-2}, which is comparable to the record dyes **CAD3** and **QT-1**. The NDI acceptor group is essential for these high performances, as **Th-DPP** produced only a negligible current response that could be attributed to the dye. It is possible that the success of this molecule will stimulate the design of more varied dyes for p-DSCs. These DPP dyes also serve as a prime example of how subtle structural modifications can have a significant effect on device performances. A DPP dyad with mixed phenyl/thiophene bridges (**DPP-NDI**) was previously reported by the same group and devices made using this dye obtained a J_{SC} of 1.79 mA cm^{-2}. The lower J_{SC}, coupled with a lower V_{OC} (V_{OC} = 147 and 91 mV for **Th-DPP-NDI** and **DPP-NDI** respectively), resulted in a PCE that was seven times lower than **Th-DPP-NDI** (PCE = 0.35% and 0.048% for **Th-DPP-NDI** and **DPP-NDI** respectively).

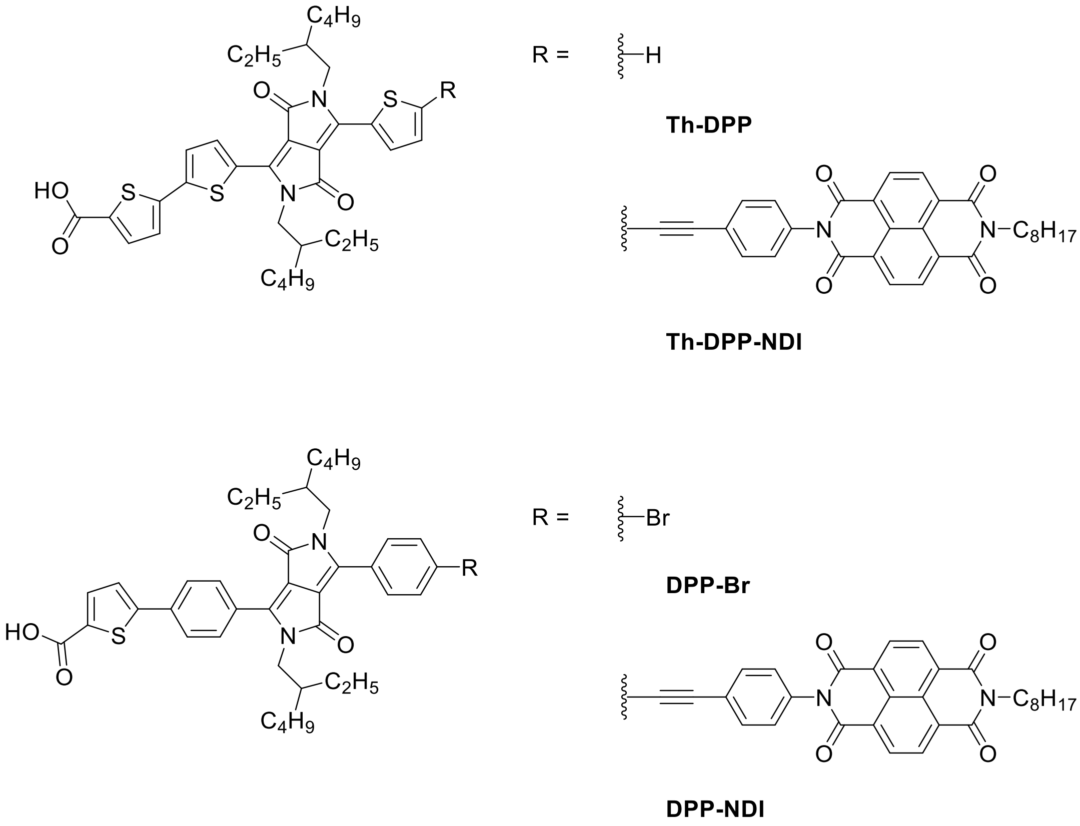

Figure 1.21. Molecular structure of DPP-dyads used for p-DSCs.[57,108]

1.6. Research Proposal

This thesis aims to study the requirements for efficient p-DSCs to provide guidelines for designing high-performing dyes. To this end, novel BODIPY, indolium, porphyrin and indigo-based dyes have been synthesised and studied as sensitisers for p-DSCs. Each chapter focuses on a different aspect of dye design, to provide an in-depth investigation into the requirements for an efficient device.

A series of push-pull triphenylamine-BODIPY dyes have been synthesised (**1-5**, Chapter 3) to investigate the effect of tuning donor-acceptor coupling on device efficiencies. In Chapter 4, a multidentate pyrrole-based anchoring system was developed. Three dyes containing BODIPY and indolium chromophores as spectroscopic handles were synthesised (**6-8**, Chapter 4) and incorporated into p-DSCs. Chapter 5 focuses on the functionalisation of bay-annulated indigo with an anchoring group. This is a recently designed chromophore used as a polymer for OPVs, which had not been previously tested as a small molecular sensitiser. Finally, an investigation into alternative routes of introducing anchoring groups as a final synthetic step was carried out. This culminated in the synthesis of triazole-bridged porphyrins (**10**-**12**, Chapter 6) using ‘click’ chemistry, where a range of different anchors could be introduced in a facile manner. The influence of the anchoring group on dye adsorption was studied using adsorption isotherms and kinetic measurements.

1.7. References

1 P. M. Cox, R. A. Betts, C. D. Jones, S. A. Spall and I. J. Totterdell, *Nature*, 2000, **408**, 184–187.

2 T. L. Root, J. T. Price, K. R. Hall, S. H. Scheider, C. Rosenzweig and J. A. Pounds, *Nature*, 2003, **421**, 57–60.

3 European Commission, *The roadmap for transforming the EU into a competitive, low-carbon economy by 2050*, 2011.

4 N. S. Lewis, G. Crabtree, A. J. Nozik, M. R. Wasielewski, P. Alivisatos, H. Kung, J. Tsao, E. Chandler, W. Walukiewicz, M. Spitler, R. Ellingson, R. Overend, J. Mazer, M. Gress, J. Horwitz, C. Ashton, B. Herndon, L. Shapard and R. M. Nault, *Basic Research Needs for Solar Energy Utilization. Report of the Basic Energy Sciences Workshop on Solar Energy Utilization, April 18-21, 2005*, 2005.

5 U.S. Energy Information Administration, *International Energy Outlook 2016*, 2016.

6 World Energy Council, *World Energy Resources*, 2016.

7 K. Yoshikawa, H. Kawasaki, W. Yoshida, T. Irie, K. Konishi, K. Nakano, T. Uto, D. Adachi, M. Kanematsu, H. Uzu and K. Yamamoto, *Nat. Energy*, 2017, **2**, 17032.

8 National Renewable Laboratory, Best Research-Cell Efficiencies, https://www.nrel.gov/pv/assets/images/efficiency-chart.png (Accessed 01/08/17).

9 M. A. Green, *Prog. Photovoltaics Res. Appl.*, 2001, **9**, 123–135.

10 W. Shockley and H. J. Queisser, *J. Appl. Phys.*, 1961, **32**, 510–519.

11 M. A. Green, Y. Hishikawa, W. Warta, E. D. Dunlop, D. H. Levi, J. Hohl-Ebinger

and A. W. Y. Ho-Baillie, *Prog. Photovoltaics Res. Appl.*, 2017, **25**, 668–676.

12 J.-P. Correa-Baena, A. Abate, M. Saliba, W. Tress, T. Jesper Jacobsson, M. Grätzel and A. Hagfeldt, *Energy Environ. Sci.*, 2017, **10**, 710-727.

13 H. J. Snaith, *J. Phys. Chem. Lett.*, 2013, **4**, 3623–3630.

14 M. A. Green, A. W. Y. Ho-Baillie and H. J. Snaith, *Nat. Photonics*, 2014, **8**, 506–514.

15 A. Kojima, K. Teshima, Y. Shirai and T. Miyasaka, *J. Am. Chem. Soc.*, 2009, **131**, 6050–6051.

16 L. Calió, S. Kazim, M. Grätzel and S. Ahmad, *Angew. Chem. Int. Ed.*, 2016, **55**, 14522–14545.

17 T. Liu, K. Chen, Q. Hu, R. Zhu and Q. Gong, *Adv. Energy Mater.*, 2016, **6**, 1600457.

18 C.-G. Wu, C.-H. Chiang, Z.-L. Tseng, M. K. Nazeeruddin, A. Hagfeldt and M. Grätzel, *Energy Environ. Sci.*, 2015, **8**, 2725–2733.

19 R. Fu, Y. Zhao, Q. Li, W. Zhou, D. Yu and Q. Zhao, *Chem. Commun.*, 2017, **53**, 1829–1831.

20 J. T.-W. Wang, Z. Wang, S. Pathak, W. Zhang, D. W. DeQuilettes, F. Wisnivesky-Rocca-Rivarola, J. Huang, P. K. Nayak, J. B. Patel, H. A. Mohd Yusof, Y. Vaynzof, R. Zhu, I. Ramirez, J. Zhang, C. Ducati, C. Grovenor, M. B. Johnston, D. S. Ginger, R. J. Nicholas and H. J. Snaith, *Energy Environ. Sci.*, 2016, **9**, 2892–2901.

21 M. Freitag, J. Teuscher, Y. Saygili, X. Zhang, F. Giordano, P. Liska, J. Hua, S. M. Zakeeruddin, J.-E. Moser, M. Grätzel and A. Hagfeldt, *Nat. Photonics*, 2017, **11**, 372–378.

22 B. O'Regan and M. Grätzel, *Nature*, 1991, **353**, 737–740.

23 A. Hagfeldt, G. Boschloo, L. Sun, L. Kloo and H. Pettersson, *Chem. Rev.*, 2010, **110**, 6595–6663.

24 L.-L. Li and E. W.-G. Diau, *Chem. Soc. Rev.*, 2013, **42**, 291–304.

25 M. Grätzel, *Acc. Chem. Res.*, 2009, **42**, 1788–1798.

26 M. K. Nazeeruddin, A. Kay, I. Rodicio, R. Humphry-Baker, E. Mueller, P. Liska, N. Vlachopoulos and M. Graetzel, *J. Am. Chem. Soc.*, 1993, **115**, 6382–6390.

27 A. Yella, H.-W. Lee, H. N. Tsao, C. Yi, A. K. Chandiran, M. K. Nazeeruddin, E. W.-G. Diau, C.-Y. Yeh, S. M. Zakeeruddin and M. Gratzel, *Science*, 2011, **334**, 629–634.

28 S. Mathew, A. Yella, P. Gao, R. Humphry-Baker, B. F. E. Curchod, N. Ashari-Astani, I. Tavernelli, U. Rothlisberger, M. K. Nazeeruddin and M. Grätzel, *Nat. Chem.*, 2014, **6**, 242–247.

29 K. Kakiage, Y. Aoyama, T. Yano, K. Oya, J. Fujisawa and M. Hanaya, *Chem. Commun.*, 2015, **51**, 15894–15897.

30 J. He, H. Lindström, A. Hagfeldt and S. Lindquist, *J. Phys. Chem. B*, 1999, **103**, 8940–8943.

31 E. A. Gibson, L. Le Pleux, J. Fortage, Y. Pellegrin, E. Blart, F. Odobel, A. Hagfeldt and G. Boschloo, *Langmuir*, 2012, **28**, 6485–6493.

32 C. J. Wood, C. A. McGregor and E. A. Gibson, *ChemElectroChem*, 2016, **3**, 1827–1836.

33 P. S. Patil and L. D. Kadam, *Appl. Surf. Sci.*, 2002, **199**, 211–221.

34 M. D. Irwin, D. B. Buchholz, A. W. Hains, R. P. H. Chang and T. J. Marks, *Proc. Natl. Acad. Sci.*, 2008, **105**, 2783–2787.

35 G. A. Sawatzky and J. W. Allen, *Phys. Rev. Lett.*, 1984, **53**, 2339–2342.

36 G. Boschloo and A. Hagfeldt, *J. Phys. Chem. B*, 2001, **105**, 3039–3044.

37 C. J. Wood, G. H. Summers, C. A. Clark, N. Kaeffer, M. Bräutigam, L. R. Carbone, L. D'Amario, K. Fan, Y. Farré, S. Narbey, F. Oswald, L. A. Stevens, C. D. J. Parmenter, M. W. Fay, A. La Torre, C. E. Snape, B. Dietzek, D. Dini, L. Hammarström, Y. Pellegrin, F. Odobel, L. Sun, V. Artero and E. A. Gibson, *Phys. Chem. Chem. Phys.*, 2016, **18**, 10727–10738.

38 D. Dini, Y. Halpin, J. G. Vos and E. A. Gibson, *Coord. Chem. Rev.*, 2015, **304–305**, 179–201.

39 S. Sumikura, S. Mori, S. Shimizu, H. Usami and E. Suzuki, *J. Photochem. Photobiol. A Chem.*, 2008, **199**, 1–7.

40 M. Awais, E. Gibson, J. G. Vos, D. P. Dowling, A. Hagfeldt and D. Dini, *ChemElectroChem*, 2014, **1**, 384–391.

41 Q. Wu, Y. Shen, L. Li, M. Cao, F. Gu and L. Wang, *Appl. Surf. Sci.*, 2013, **276**, 411–416.

42 A. Nattestad, M. Ferguson, R. Kerr, Y.-B. Cheng and U. Bach, *Nanotechnology*, 2008, **19**, 295304.

43 L. Li, E. A. Gibson, P. Qin, G. Boschloo, M. Gorlov, A. Hagfeldt and L. Sun, *Adv. Mater.*, 2010, **22**, 1759–1762.

44 A. Renaud, B. Chavillon, L. Le Pleux, Y. Pellegrin, E. Blart, M. Boujtita, T. Pauporté, L. Cario, S. Jobic and F. Odobel, *J. Mater. Chem.*, 2012, **22**, 14353-14356.

45 A. Renaud, L. Cario, P. Deniard, E. Gautron, X. Rocquefelte, Y. Pellegrin, E. Blart, F. Odobel and S. Jobic, *J. Phys. Chem. C*, 2014, **118**, 54–59.

46 M. Yu, G. Natu, Z. Ji and Y. Wu, *J. Phys. Chem. Lett.*, 2012, **3**, 1074–1078.

47 S. Powar, D. Xiong, T. Daeneke, M. T. Ma, A. Gupta, G. Lee, S. Makuta, Y. Tachibana, W. Chen, L. Spiccia, Y.-B. Cheng, G. Götz, P. Bäuerle and U. Bach, *J. Phys. Chem. C*, 2014, **118**, 16375–16379.

48 D. Xiong, W. Zhang, X. Zeng, Z. Xu, W. Chen, J. Cui, M. Wang, L. Sun and Y. B. Cheng, *ChemSusChem*, 2013, **6**, 1432–1437.

49 T. Jiang, M. Bujoli-Doeuff, Y. Farré, Y. Pellegrin, E. Gautron, M. Boujtita, L. Cario, S. Jobic and F. Odobel, *RSC Adv.*, 2016, **6**, 112765–112770.

50 O. Langmar, C. R. Ganivet, G. de la Torre, T. Torres, R. Costa and D. M. Guldi, *Nanoscale*, 2016, **8**, 17963–17975.

51 O. Langmar, C. R. Ganivet, A. Lennert, R. D. Costa, G. De La Torre, T. Torres and D. M. Guldi, *Angew. Chem. Int. Ed.*, 2015, **54**, 7688–7692.

52 Z. Shi, H. Lu, Q. Liu, K. Deng, L. Xu, R. Zou, J. Hu, Y. Bando, D. Golberg and L. Li, *Energy Technol.*, 2014, **2**, 517–521.

53 L. D’Amario, G. Boschloo, A. Hagfeldt and L. Hammarström, 2014, **46**, 1–12.

54 Z. Huang, X. Zeng, H. Wang, W. Zhang, Y. Li, M. Wang, Y.-B. Cheng and W. Chen, *RSC Adv.*, 2014, **4**, 60670–60674.

55 M. Zannotti, C. J. Wood, G. H. Summers, L. A. Stevens, M. R. Hall, C. E. Snape, R. Giovanetti and E. A. Gibson, *ACS Appl. Mater. Interfaces*, 2015, **7**, 24556–24565.

56 P. Qin, J. Wiberg, E. A. Gibson, M. Linder, L. Li, T. Brinck, A. Hagfeldt, B. Albinsson and L. Sun, *J. Phys. Chem. C*, 2010, **114**, 4738–4748.

57 Y. Farré, M. Raissi, A. Fihey, Y. Pellegrin, E. Blart, D. Jacquemin and F. Odobel, *ChemSusChem*, 2017, **10**, 2618–2625.

58 A. Nattestad, A. J. Mozer, M. K. R. Fischer, Y.-B. Cheng, A. Mishra, P. Bäuerle and U. Bach, *Nat. Mater.*, 2010, **9**, 31–35.

59 Y. Pellegrin, L. Le Pleux, E. Blart, A. Renaud, B. Chavillon, N. Szuwarski, M. Boujtita, L. Cario, S. Jobic, D. Jacquemin and F. Odobel, *J. Photochem. Photobiol. A Chem.*, 2011, **219**, 235–242.

60 F. Brunner, N. Marinakis, C. Wobill, M. Willgert, C. D. Ertl, T. Kosmalski, M. Neuburger, B. Bozic-Weber, T. Glatzel, E. C. Constable and C. E. Housecroft, *J. Mater. Chem. C*, 2016, **4**, 9823–9833.

61 J. Cui, J. Lu, X. Xu, K. Cao, Z. Wang, G. Alemu, H. Yuang, Y. Shen, J. Xu, Y. Cheng and M. Wang, *J. Phys. Chem. C*, 2014, **118**, 16433–16440.

62 Y. Dong, L. Wei, R. Fan, Y. Yang and P. Wang, *RSC Adv.*, 2016, **6**, 39972–39981.

63 G. Alemu, J. Cui, K. Cao, J. Li, Y. Shen and M. Wang, *RSC Adv.*, 2014, **4**, 51374–51380.

64 L. D’Amario, L. J. Antila, B. P. Rimgard, G. Boschloo and L. Hammarström, *J. Phys. Chem. Lett.*, 2015, **6**, 779–783.

65 R. J. Dillon, L. Alibabaei, T. J. Meyer and J. M. Papanikolas, *ACS Appl. Mater. Interfaces*, 2017, **9**, 26786-26796.

66 L. Zhang, G. Boschloo, L. Hammarström and H. Tian, *Phys. Chem. Chem. Phys.*, 2016, **18**, 5080–5085.

67 T. T. T. Pham, S. K. Saha, D. Provost, Y. Farré, M. Raissi, Y. Pellegrin, E. Blart, S. Vedraine, B. Ratier, D. Aldakov, F. Odobel and J. Bouclé, *J. Phys. Chem. C*, 2017, **121**, 129–139.

68 C. J. Wood, G. H. Summers and E. A. Gibson, *Chem. Commun.*, 2015, **51**, 3915–3918.

69 Q.-Q. Zhang, K.-J. Jiang, J.-H. Huang, C.-W. Zhao, L.-P. Zhang, X.-P. Cui, M.-J. Su, L.-M. Yang, Y.-L. Song and X.-Q. Zhou, *J. Mater. Chem. A*, 2015, **3**, 7695–7698.

70 P. Ho, S. Thogiti, Y. H. Lee and J. H. Kim, *Sci. Rep.*, 2017, **7**, 2272.

71 E. A. Gibson, A. L. Smeigh, L. Le Pleux, L. Hammarström, F. Odobel, G. Boschloo and A. Hagfeldt, *J. Phys. Chem. C*, 2011, **115**, 9772–9779.

72 E. A. Gibson, A. L. Smeigh, L. Le Pleux, J. Fortage, G. Boschloo, E. Blart, Y. Pellegrin, F. Odobel, A. Hagfeldt and L. Hammarström, *Angew. Chem. Int. Ed.*, 2009, **48**, 4402–4405.

73 S. Powar, T. Daeneke, M. T. Ma, D. Fu, N. W. Duffy, G. Götz, M. Weidelener, A. Mishra, P. Bäuerle, L. Spiccia and U. Bach, *Angew. Chem. Int. Ed.*, 2013, **52**, 602–605.

74 I. R. Perera, T. Daeneke, S. Makuta, Z. Yu, Y. Tachibana, A. Mishra, P. Bäuerle, C. A. Ohlin, U. Bach and L. Spiccia, *Angew. Chem. Int. Ed.*, 2015, **54**, 3758–3762.

75 S. Thomas, T. G. Deepak, G. S. Anjusree, T. A. Arun, S. V. Nair and A. S. Nair, *J. Mater. Chem. A*, 2014, **2**, 4474–4490.

76 G. Boschloo and A. Hagfeldt, *Acc. Chem. Res.*, 2009, **42**, 1819–1826.

77 M. Congiu, M. Bonomo, M. L. De Marco, D. P. Dowling, A. Di Carlo, D. Dini and C. F. O. Graeff, *ChemistrySelect*, 2016, **1**, 2808–2815.

78 M. Bonomo, M. Congiu, M. L. De Marco, D. P. Dowling, A. Di Carlo, C. F. O. Graeff and D. Dini, *J. Phys. D. Appl. Phys.*, 2017, **50**, 215501.

79 F. Odobel, Y. Pellegrin, E. A. Gibson, A. Hagfeldt, A. L. Smeigh and L. Hammarström, *Coord. Chem. Rev.*, 2012, **256**, 2414–2423.

80 F. Odobel and Y. Pellegrin, *J. Phys. Chem. Lett.*, 2013, **4**, 2551–2564.

81 M. Buchalska, J. Kuncewicz, E. Świętek, P. Łabuz, T. Baran, G. Stochel and W. Macyk, *Coord. Chem. Rev.*, 2013, **257**, 767–775.

82 J. N. Clifford, E. Palomares, M. K. Nazeeruddin, M. Grätzel and J. R. Durrant, *J.*

Phys. Chem. C, 2007, **111**, 6561–6567.

83 P. Qin, H. Zhu, T. Edvinsson, G. Boschloo, A. Hagfeldt and L. Sun, *J. Am. Chem. Soc.*, 2008, **130**, 8570–8571.

84 C. J. Wood, K. C. D. Robson, P. I. P. Elliott, C. P. Berlinguette and E. A. Gibson, *RSC Adv.*, 2014, **4**, 5782-5791.

85 Z. Ji, G. Natu and Y. Wu, *ACS Appl. Mater. Interfaces*, 2013, **5**, 8641–8648.

86 M. He, Z. Ji, Z. Huang and Y. Wu, *J. Phys. Chem. C*, 2014, **118**, 16518–16525.

87 N. Marinakis, M. Willgert, E. C. Constable and C. E. Housecroft, *Sustain. Energy Fuels*, 2017, **0**, 1–10.

88 Z. Ji, G. Natu, Z. Huang, O. Kokhan, X. Zhang and Y. Wu, *J. Phys. Chem. C*, 2012, **116**, 16854–16863.

89 S. Lyu, Y. Farré, L. Ducasse, Y. Pellegrin, T. Toupance, C. Olivier and F. Odobel, *RSC Adv.*, 2016, **6**, 19928–19936.

90 J. He, H. Lindström, A. Hagfeldt and S.-E. Lindquist, *Sol. Energy Mater. Sol. Cells*, 2000, **62**, 265–273.

91 A. Morandeira, G. Boschloo, A. Hagfeldt and L. Hammarström, *J. Phys. Chem. B*, 2005, **109**, 19403–19410.

92 S. Mori, S. Fukuda, S. Sumikura, Y. Takeda, Y. Tamaki, E. Suzuki and T. Abe, *J. Phys. Chem. C*, 2008, **112**, 16134–16139.

93 A. Morandeira, J. Fortage, T. Edvinsson, L. Le Pleux, E. Blart, G. Boschloo, A. Hagfeldt, L. Hammarström and F. Odobel, *J. Phys. Chem. C*, 2008, **112**, 1721–1728.

94 L. Le Pleux, A. L. Smeigh, E. Gibson, Y. Pellegrin, E. Blart, G. Boschloo, A. Hagfeldt, L. Hammarström and F. Odobel, *Energy Environ. Sci.*, 2011, **4**, 2075–2084.

95 P. Qin, M. Linder, T. Brinck, G. Boschloo, A. Hagfeldt and L. Sun, *Adv. Mater.*, 2009, **21**, 2993–2996.

96 M. Liang and J. Chen, *Chem. Soc. Rev.*, 2013, **42**, 3453–3488.

97 J. Wang, K. Liu, L. Ma and X. Zhan, *Chem. Rev.*, 2016, **116**, 14675-14725.

98 Z. Liu, W. Li, S. Topa, X. Xu, X. Zeng, Z. Zhao, M. Wang, W. Chen, F. Wang, Y.-B. Cheng and H. He, *ACS Appl. Mater. Interfaces*, 2014, **6**, 10614–22.

99 Z. Liu, D. Xiong, X. Xu, Q. Arooj, H. Wang, L. Yin, W. Li, H. Wu, Z. Zhao, W. Chen, M. Wang, F. Wang, Y. B. Cheng and H. He, *ACS Appl. Mater. Interfaces*, 2014, **6**, 3448–3454.

100 C. J. Wood, M. Cheng, C. A. Clark, R. Horvath, I. P. Clark, M. L. Hamilton, M. Towrie, M. W. George, L. Sun, X. Yang and E. A. Gibson, *J. Phys. Chem. C*, 2014, **118**, 16536–16546.

101 F. Wu, S. Zhao, C. Zhong, Q. Song and L. Zhu, *RSC Adv.*, 2015, **5**, 93652–93658.

102 L. Zhu, H. Bin Yang, C. Zhong and C. M. Li, *Dye. Pigment.*, 2014, **105**, 97–104.

103 F. Wu, L. Zhu, S. Zhao, Q. Song and C. Yang, *Dye. Pigment.*, 2016, **124**, 93–100.

104 K. A. Click, D. R. Beauchamp, B. R. Garrett, Z. Huang, C. M. Hadad and Y. Wu, *Phys. Chem. Chem. Phys.*, 2014, **16**, 26103–26111.

105 Z. Ji, G. Natu, Z. Huang and Y. Wu, *Energy Environ. Sci.*, 2011, **4**, 2818–2821.

106 C.-H. Chang, Y.-C. Chen, C.-Y. Hsu, H.-H. Chou and J. T. Lin, *Org. Lett.*, 2012, **14**, 4726–4729.

107 Y.-S. Yen, W.-T. Chen, C.-Y. Hsu, H.-H. Chou, J. T. Lin and M.-C. P. Yeh, *Org. Lett.*, 2011, **13**, 4930–4933.

108 Y. Farré, L. Zhang, Y. Pellegrin, A. Planchat, E. Blart, M. Boujtita, L. Hammarström, D. Jacquemin and F. Odobel, *J. Phys. Chem. C*, 2016, **120**, 7923–7940.

Chapter 2 – Theory and Experimental Methods

2.1. UV-visible Absorption Spectroscopy

Absorption spectroscopy has been used to study the photophysical properties of the dyes discussed in this thesis. The dye is the integral component of a DSC, that serves to produce a photocurrent by absorbing photons. Therefore, understanding where and how intensely the dye absorbs light is crucial for designing more efficient sensitisers. A schematic representation of the technique is provided in Figure 2.1.

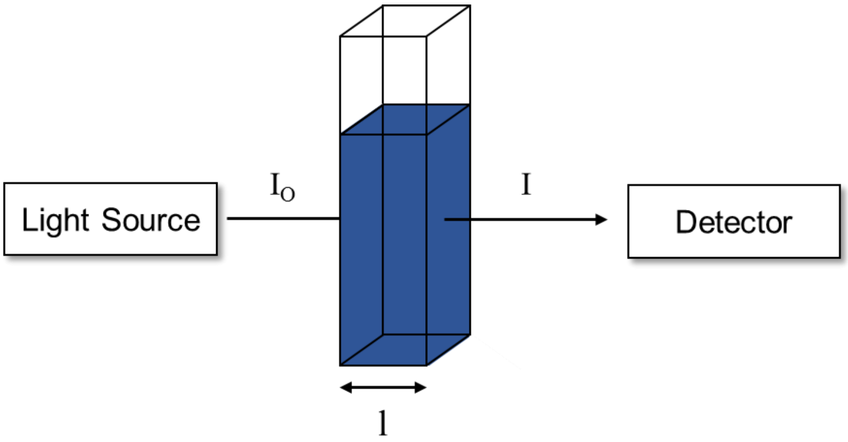

Figure 2.1. Schematic representation of the experimental setup for UV-visible absorption spectroscopy.

When a species absorbs radiation it becomes excited, with the nature of the excited state dependent on the wavelength of incoming radiation. UV-visible absorption spectroscopy measures the absorption of radiation between the visible and UV wavelength range. Here the energy of incoming radiation is large enough to promote transitions between electronic energy levels. UV-visible absorption spectroscopy is measured by passing light through a sample of known concentration and recording the attenuation. The intensity of the transmitted light (I) is compared to the intensity of the incident light (I_O) and the ratio of these gives the transmittance through the sample (T, Equation 2.1). This can be used to calculate the absorption of the sample using Equation 2.2.

Absorption can be treated quantitatively following the Beer-Lambert law (Equation 2.3). The calculated parameter, ε, describes how intensely light is absorbed and is a measure of the probability of an electronic transition occurring at the specified wavelength. The Beer-Lambert Law is only valid for a linear plot of absorption vs. concentration; this non-linearity can occur if there are interactions between molecules in solution (such as aggregation) or if there are losses from scattering or reflection (that could occur if the sample is not fully dissolved). For these reasons, UV-visible absorption spectroscopy is often recorded at low concentrations.

$$T(\lambda) = \frac{I(\lambda)}{I_O(\lambda)}$$

Equation 2.1.

$$A(\lambda) = -log_{10}T(\lambda)$$

Equation 2.2.

$$A = \varepsilon cl$$

Equation 2.3.

Where ε is the molar absorption coefficient, c is the sample concentration and l is the path length of the sample.

2.2. Photoluminescence Spectroscopy

Photoluminescence spectroscopy has been used to study the photophysics of the dyes in their excited states. This is important as the charge transfer processes that occur within a p-DSC involve the excited dye. In particular, photoluminescence spectroscopy has been used to determine the zero-zero energy (E_{0-0}), estimated as the intercept between the normalised absorption and emission spectra. This is used, alongside the redox potentials measured using electrochemistry, to calculate the driving force for charge transfer.

When a species absorbs an incoming photon, an electron is excited from the ground state to a higher energy excited singlet state (Figure 2.2 shows a potential energy diagram for an S_0 to S_1 excitation). There are two assumptions that are followed when describing electronic absorptions, the first of which is the Born-Oppenheimer approximation. This states that electronic motion and nuclear (vibrational and rotational) motion can be treated separately. This forms the basis of the Frank-Condon principle, which states that during an electronic transition, the nuclei of a molecule can be assumed to be fixed. Therefore, the transition can be represented as a vertical line on a potential energy diagram.

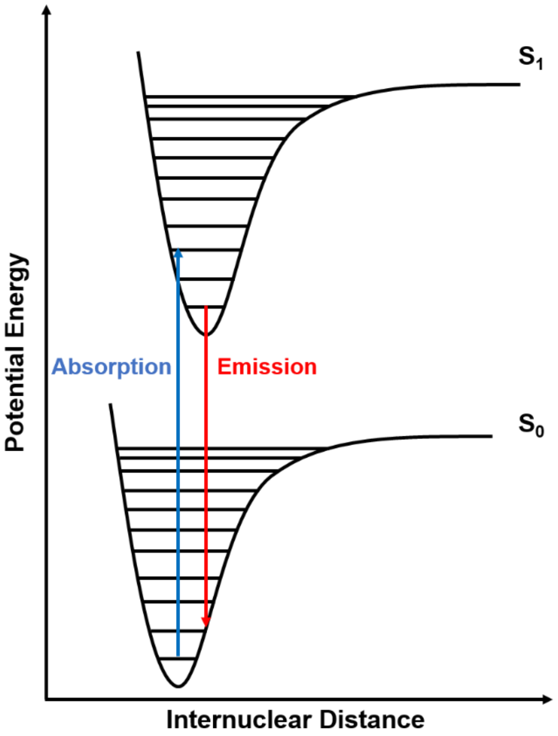

Figure 2.2. Potential energy diagram showing absorption and emission transitions from the lowest vibrational levels.

Following excitation, the excited species must lose this excess energy and relax to the ground state by a combination of radiative and non-radiative decay processes (Figure 2.3). Fluorescence, which is the emission of a photon from a singlet excited state, typically originates from the lowest energy excited state. Following excitation, internal conversion (from S_n to S_1) and vibrational relaxation occur on a faster timescale than fluorescence. Therefore, the emissive state is the lowest excited energy level, which is defined as Kasha’s rule. Emission from a triplet state is called phosphorescence, which is spin forbidden and occurs on a slower timescale than fluorescence. Typically, phosphorescence occurs due to intersystem crossing from an excited singlet state to a triplet state of lower energy.

Two different types of spectra have been discussed in this thesis; emission and excitation spectra. Emission spectra are recorded by measuring the emission intensity over a specified wavelength range, following monochromatic excitation at a fixed wavelength. An excitation spectrum is recorded by measuring the emission intensity at a fixed wavelength as a function of excitation wavelength.

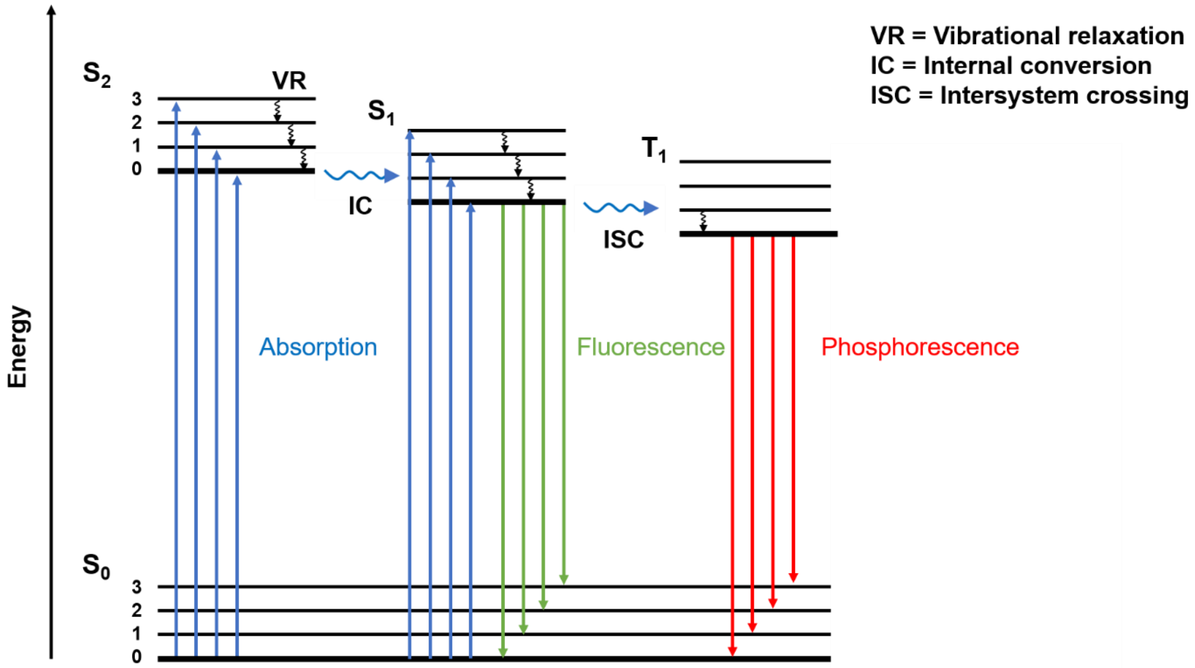

Figure 2.3. An example Jablonski diagram.

2.3. Electrochemistry

Electrochemistry is used to determine the frontier energy levels of the newly designed dyes and the reversibility of their redox processes. Alongside absorption and photoluminescence spectroscopy, it was used to calculate the driving force for the charge transfer processes that occur in a p-DSC. It is important to study the redox properties of the dyes to identify these driving forces. The HOMO of the dye must be more positive than the NiO valence band to facilitate electron transfer from NiO to the excited dye. Conversely, the dye LUMO must be more negative than the redox potential of the electrolyte. This is to promote efficient regeneration of the reduced dye by electron transfer to the redox electrolyte.

In this work, a three-electrode system has been used to perform electrochemistry (Figure 2.4).

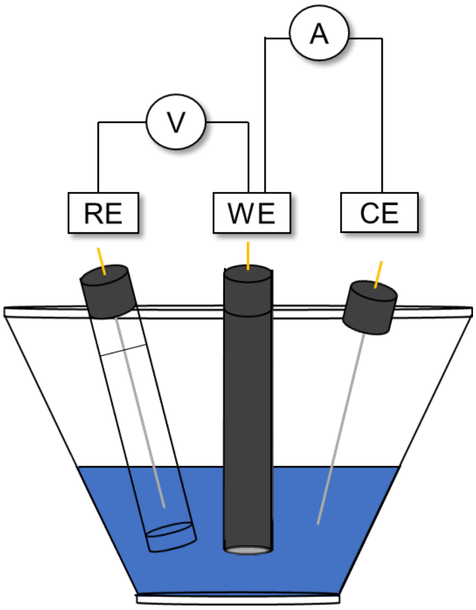

Figure 2.4. Schematic representation of a three-electrode electrochemical cell. RE = reference electrode, WE = working electrode and CE = counter electrode.

The three electrodes used, and their functions, are as follows:

1) Reference electrode; this is an electrode that has a known and stable electrode potential. To achieve this stability, a redox system is used with a saturated concentration of each component of the redox reaction. This electrode is used to provide a stable reference point for potential control between the working and reference electrodes. In this work, a Ag/Ag$^+$ pseudo-reference electrode has been used (the redox process for this electrode is provided in Equation 2.4). This is less stable than the commonly used Ag/AgCl reference electrode and so must be freshly prepared prior to use, but it is more compatible with non-aqueous measurements. The electrode consists of a silver wire immersed in an electrolyte solution of $AgNO_3$ (0.01M), with the solvent and supporting electrolyte the same as the solution to be measured. As the potential is unknown and dependent on the sample solution, measurements using a Ag/Ag$^+$ reference electrode are quoted relative to the redox potential of a known internal reference (the ferrocene/ferrocenium (Fc/Fc$^+$) redox couple has been used throughout this work).

$$Ag^+ + e^- \rightleftarrows Ag$$

Equation 2.4.

2) Working electrode; this is the electrode where the reaction of interest occurs. It needs to be inert, meaning that it does not generate a current in response to an applied potential and it should be stable over a wide potential range. Commonly used inert materials include gold, platinum, mercury and glassy carbon. Throughout this thesis a glassy carbon working electrode (diameter = 3 mm) has been used.

3) Counter electrode; this is used in conjunction with the working electrode to complete the electrical circuit in the cell. The surface area of the counter electrode must be higher than the area of the working electrode. This is so that the current flow at the counter electrode does not become a kinetic limitation to the process studied at the working electrode. For this reason, a platinum wire has been used.

In a three-electrode system, the electrodes are attached to a potentiostat, which ensures that current only flows between the counter and working electrodes. The potential difference between these two electrodes is controlled by holding the working electrode at an applied potential relative to the stable reference electrode. A supporting electrolyte is used to impart electrical conductivity to the solution. In this work, tetrabutyl ammonium (TBA) or Li perchlorate (ClO_4) and TBA hexafluorophosphate (PF_6) have been used. The redox properties of new dyes have been determined using cyclic voltammetry (CV) and differential pulsed voltammetry (DPV).

2.3.1. Cyclic Voltammetry

In cyclic voltammetry, the applied potential at the working electrode is cycled between two or more points (Figure 2.5). The potential is swept from an original value (E_1) to the first switching potential (E_2), where the sweep direction is reversed back to the original point. The sweep can then either stop at the initial potential or continue in this direction until a second switching potential is reached (E_3), after which the direction is reversed again back to the original point. The current is recorded during the potential sweep and plotted against the applied potential to give a cyclic voltammogram (Figure 2.6).

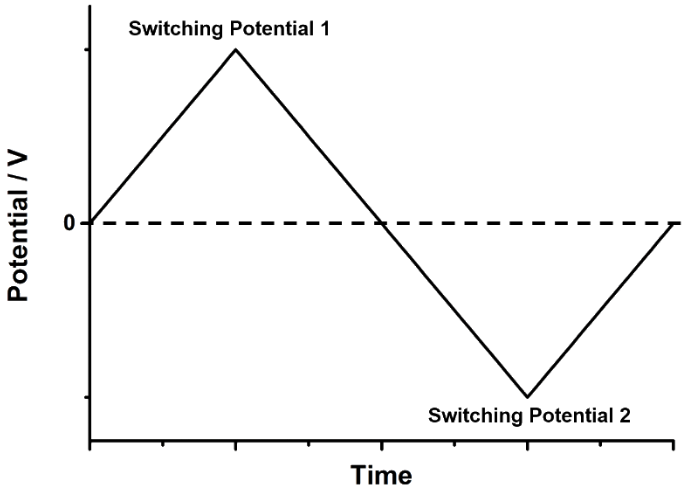

Figure 2.5. An example waveform used for cyclic voltammetry.

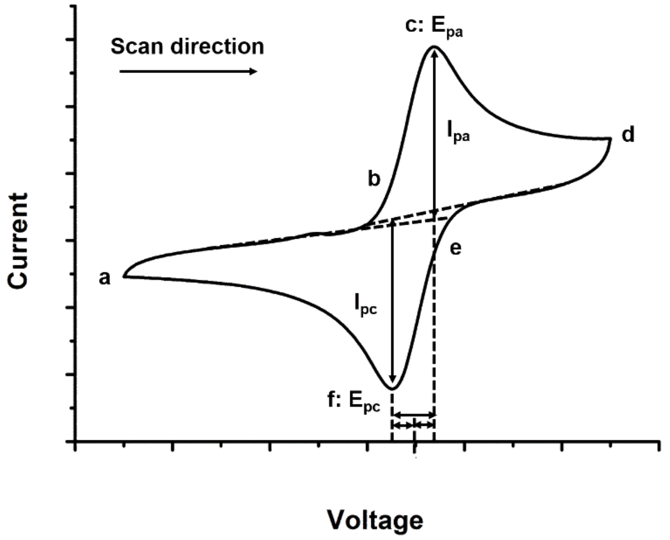

Figure 2.6. An example reversible cyclic voltammogram.

The characteristic shape of a reversible cyclic voltammogram is provided in Figure 2.6. A potential is swept from the initial potential (point a) to a more positive switching potential (point d). Initially there is no increase in current as the applied potential is not positive enough to oxidise the sample. At a certain point (b) the applied potential becomes sufficient to oxidise the sample and current flow increases. A maximum is reached (point c) when the entirety of the sample at the electrode surface is oxidised;

this point is called the anodic peak potential (E_{pa}). After this point the current flow starts to decrease, as fresh sample needs to diffuse to the electrode surface for oxidation (and current flow) to occur. When the applied potential reaches the specified switching point (d) the sweep direction is reversed. The oxidised sample remains oxidised until the applied potential is sufficient to drive reduction back to the ground state (point e). A current maximum is again reached (point f) when all of the oxidised sample at the electrode surface has been reduced; this point is called the cathodic peak potential (E_{pc}). Reduction and oxidation potentials are defined by their half-wave potentials ($E_{1/2}$) which are calculated using Equation 2.5.

$$E_{1/2} = \frac{(E_{pa} + E_{pc})}{2}$$

Equation 2.5.

Redox processes are typically described according to their reversibility. Equation 2.6 gives the one electron reduction of a species (A) to its reduced form ($A^{\cdot-}$)

$$A + ne^{-} \rightleftarrows A^{\cdot-} \rightarrow B$$

Equation 2.6.

For this reduction to be chemically reversible, the reduced species needs to be stable to reactions following electron transfer. It is chemically irreversible if a product (B) is formed, which cannot be converted to the original species by direct electron transfer. Electrochemical reversibility describes the rate of electron transfer between the working electrode and the solution. A process is reversible if this occurs on a sufficiently fast time scale, so that Nernstian equilibrium is attained at the electrode surface. For cyclic voltammetry, a reversible process can be characterised by the following rules:[1]

1) The anodic (I_{pa}) and cathodic (I_{pc}) peak currents are of equal intensity.

2) E_{pa} and E_{pc} are separated by 59/n mV (at 25 °C).

3) E_{pa} and E_{pc} are independent of scan rate.

2.3.2. Differential Pulse Voltammetry

When the redox potentials could not be determined using cyclic voltammetry (such as for irreversible or overlapping processes), they were instead measured using differential pulse voltammetry (DPV). An example waveform used for DPV is provided in Figure 2.7. Here a series of small pulses (of the same amplitude) are superimposed onto a stepped potential sweep. The current is sampled twice in each pulse period; once before the potential pulse is applied and again near the end of the pulse. The difference in current is recorded and plotted against the applied potential to give the voltammogram (Figure 2.8).

The peak potentials determined using DPV are analogous to $E_{1/2}$ for a reversible process determined by cyclic voltammetry. As background currents are subtracted during pulsed voltammetry (as they decay faster than faradaic currents), these techniques are more sensitive than cyclic voltammetry. The voltammogram will appear symmetric for a reversible process, but will be broader and more asymmetric when electron transfer is irreversible.

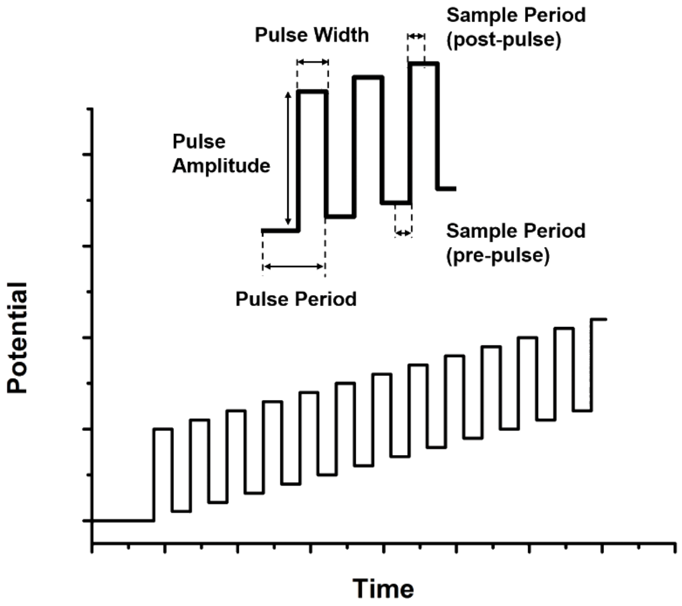

Figure 2.7. An example waveform used for differential pulse voltammetry.

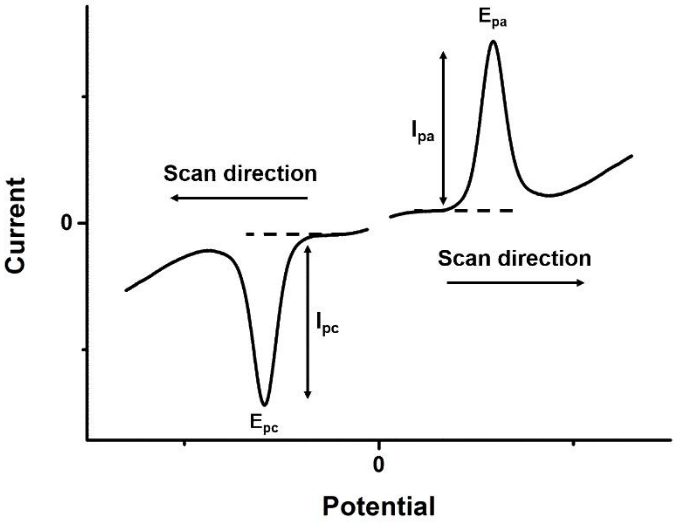

Figure 2.8. An example differential pulse voltammogram.

2.3.3. Driving Forces for Energy Transfer

The redox potentials determined using these two methods can be used to calculate driving forces for charge transfer. The driving force for electron transfer between NiO and the excited dye (ΔG_{inj}, Equation 2.7) is calculated using the Rehm-Weller equation. This equation is used to determine the driving force for photoinduced electron transfer between an electron donor (NiO) and an acceptor (sensitiser). The excited state reduction potential, $E_{red}(S^*/S^-)$, is obtained from the ground state reduction potential ($E_{red}(S/S^-)$) and E_{0-0} (the zero-zero energy, Equation 2.8).

$$\Delta G_{inj} = e[E_{VB}(NiO) - E_{red}(S^*/S^-)]$$

Equation 2.7

$$E_{red}(S^*/S^-) = E_{red}(S/S^-) + E_{0-0}$$

Equation 2.8.

Where e = electric charge and E_{VB}(NiO) = 0.54 V vs. NHE.[2]

The driving force for dye regeneration can be calculated from the difference between the reduction potential of the dye and the redox potential of the electrolyte (Equation 2.9).

$$\Delta G_{reg} = e[E(I_3^{-}/I_2^{\cdot -}) - E_{red}(S/S^{-})]$$

Equation 2.9.

Where $E(I_3^-/I_2^{\cdot -})$ = -0.19 V vs. NHE.[3]

2.4. Computational Studies

Throughout this thesis, computational chemistry has been used as a tool to aid the interpretation of experimental results. It has been used to calculate approximate HOMO/LUMO energy levels and to visualise molecular orbital distributions. It has also been used to predict electronic transitions. This is an important tool to aid dye design as it is useful to know where electron density is likely to be located following excitation.

Hybrid density functional theory (DFT) methods have been used in this thesis which are derived from *ab initio* calculations. These aim to find approximate solutions to the time independent Schrödinger equation (Equation 2.10). This defines the ground state position of all electrons in a given system.

$$\hat{H}\Psi = E\Psi$$

Equation 2.10.

$\hat{H}$ is a Hamiltonian operator which includes the kinetic energy of the electron and the energy of interaction of all the electrons. Ψ is the wavefunction which describes the probability that an electron will be in a specific location. The Hamiltonian acts on the wavefunction to determine the permitted energy levels, E, of the molecule. Ψ depends on the coordinates of each electron, therefore the electron configurations increase exponentially with each additional electron. Consequently, the Schrödinger equation cannot be solved for large systems (larger than hydrogen) and certain approximations have to be made when performing a calculation.

When a calculation is performed, a method/exchange correlation functional (for DFT methods) and a basis set are specified. The method acts as the Hamiltonian operator and the basis set acts as the wavefunction. Hybrid DFT methods (such as B3LYP, which has been used here) contain a mixture of Hartree-Fock (HF) and DFT conditions. The HF method treats electrons as independent systems in individual one spin orbitals per electron, moving in a uniform field. Electron correlation energy is ignored but electron exchange energy is calculated exactly. With DFT (such as the Kohn-Sham method), electron spin is ignored and the total energy is described by calculating electron density, rather than wavefunctions. Electrons are treated as independent and non-interacting and this method approximates both electron correlation and exchange energy.

DFT methods define the energy of a molecule as a function of electron density, which is itself a function of orbital positions. These orbitals are calculated from Kohn-Sham equations; these are similar to Hartree-Fock equations but contain an additional term called the exchange-correlation potential. Several approximations exist for this term including hybrid-DFT methods. A commonly used exchange functional is B3LYP, designed by Becke in 1992,[4] which includes a mixture of HF and DFT approaches to modelling electron-electron interactions. This is a widely used model due to its general applicability to many systems.[5,6]

The wavefunction gives the allowed orbital energies for all the electrons in a system. A basis set is a mathematical description of the wavefunction; it describes where the electrons can be located by overlapping model orbitals. Basis sets are primarily used to describe the orbitals of individual atoms, so polarisation (*) and diffuse (+) functions can be included to more accurately model molecules. Basis sets are described by nomenclature such as 3-21G, 6-21G, 6-31G, 6-311G etc. 6-31G* is commonly used due to a combination of low computational cost and accuracy, and has been used primarily in this thesis. In this basis set, each core orbital is described by six Gaussians and the valence orbital is composed of one three-Gaussian orbital and one single Gaussian orbital. The * defines polarisation of non-hydrogen atoms. As the numbers or added functions increase, the accuracy of the model increases, but this is at the expense of increased computational cost. For modelling heavy atoms, effective core potentials can be used to reduce computational cost by treating the core orbitals as a set potential and only explicitly modelling the valence orbitals. LANL2DZ[7–9] has been used to model Zn for the porphyrins of **Chapter 6**.

In this thesis, calculations have been used to optimise molecular geometries and model orbital locations. During a geometry optimisation, a starting geometry is proposed and a potential energy surface (PES) is formed. A PES describes the force (the first derivative of energy) as a function of molecular geometry. These net forces are calculated after each optimisation cycle, where bond lengths, angles and atomic coordinates are adjusted. When the force change is close to zero (as defined by the specified convergence criteria), a stationary point on the PES has been found. This stationary point could be an energy maximum, minimum or saddle point (which corresponds to a transition state). The second derivative of energy is determined using a frequency calculation, which computes the normal modes of vibration. The sign of these frequencies is used to determine if the stationary point is a minimum; if so, this will contain only positive frequencies, whereas a maximum or saddle point will be a mixture of positive and negative frequencies.

Geometries are initially optimised in a vacuum to reduce computational cost. To more accurately compare simulations with experimental results, the geometry is subsequently optimised in the presence of a solvent. Here, an implicit solvent model has been used, where the molecule is modelled in a homogenous polarizable medium, rather than interacting with explicitly modelled solvent molecules. The polarisable continuum model (PCM) has been used.[10]

Alongside optimised geometries and electron orbital densities, DFT has been used here to study the excited state properties of dyes. This is important as dye excitation provides the initial driving force for energy conversion. Time-dependent density functional theory (TDDFT) uses a time-dependent electronic density for the calculations and has been used to predict excited state energies and to simulate electronic absorption spectra.

2.5. Solar Cell Toolkit

2.5.1. p-DSC Fabrication

p-DSCs are constructed as shown in Figure 2.9, consisting of a NiO working electrode and a platinised counter electrode. Both electrodes are prepared using conductive fluorine-doped tin oxide (FTO) glass substrates. The counter electrode has a lower sheet resistance than the working electrode (8 vs. 15 Ω/square) but is less transparent.

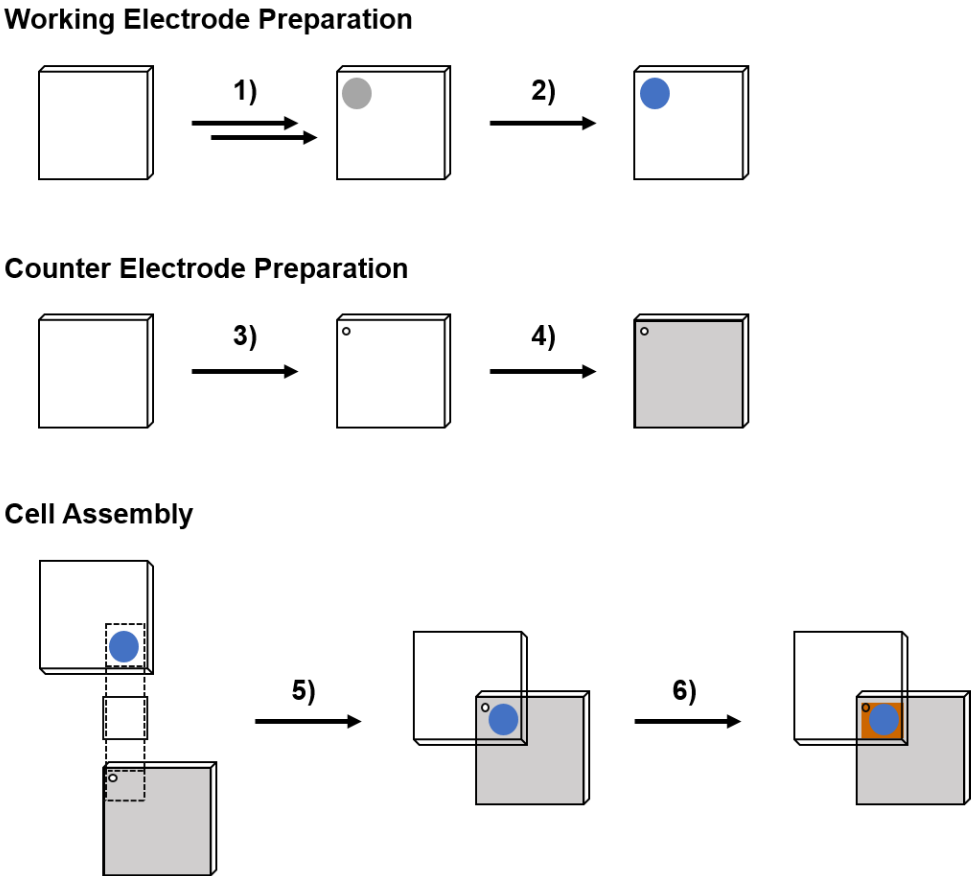

Figure 2.9. Schematic representation of electrode preparation and p-DSC construction.

Working electrode preparation:

1) A NiO precursor solution is prepared by mixing $NiCl_2$ and a templating polymer (F108) in ethanol/water. This is applied to the glass substrate (TEC 15) by doctor-blading, using Scotch tape as a frame to control the size of the electrode (0.18 cm^2). The electrode is sintered in an oven (at 450 °C) to remove the solvent/polymer template and drive the transformation of $Ni(OH)_2$ to NiO. This process is repeated as necessary to increase the NiO film thickness.

2) The bare NiO film is immersed in a solution of the dye (0.3 mM, typically in organic solvents such as acetonitrile) overnight for dye adsorption to occur. The films are rinsed in the same solvent as the dye bath to remove any physisorbed dye.

Counter electrode preparation:

3) A hole is drilled into FTO glass (TEC 8) that will allow the assembled cell to be filled with electrolyte.

4) The counter electrode is platinised using a solution of chloroplatinic acid ($H_2PtCl_6 \cdot 6H_2O$) in ethanol (4.8 mM). The solution is applied by drop-casting (10 µL cm^{-2}) and the electrode is annealed at 450 °C to evaporate any residual solvent and reduce the solution to a layer of Pt.

Cell assembly:

5) The two electrodes are assembled face-to-face, with the dyed NiO working electrode and the hole in the counter electrode surrounded by a 30 µm thick thermoplastic frame (Surlyn). Pressure is applied to the electrodes as they are heated on a hotplate (*ca.* 100 °C), melting the frame and adhering the glass together upon cooling.

6) The assembled solar cell is filled with electrolyte (1 M LiI and 0.1 M I_2 in acetonitrile) by back-filling. The cell is placed into a vacuum desiccator and a drop of electrolyte is applied to the pre-drilled hole. A vacuum is applied to remove the air from within the cell and when the vacuum is slowly released the electrolyte is drawn inside. The hole is sealed using a glass coverslip and a small piece of Surlyn.

2.5.2. J-V Measurements

For photovoltaic testing, all measurements must be carried out using a light source representative of solar irradiance. Figure 2.10 shows the AM1.5 solar spectrum, which is defined as the standard testing conditions for studying solar cells.

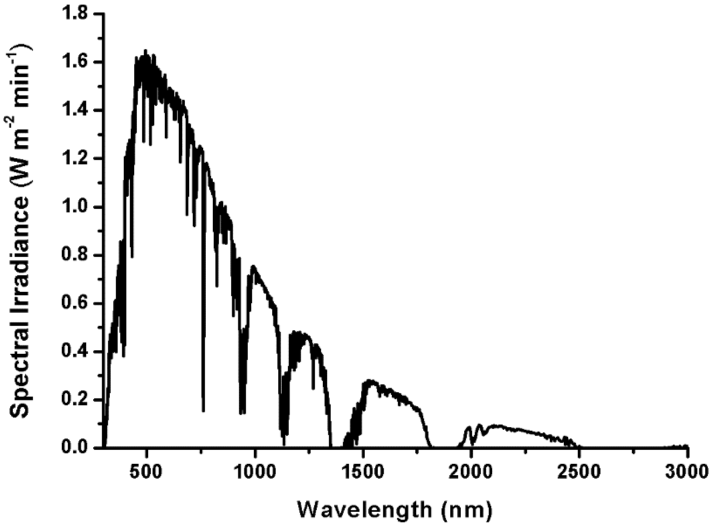

Figure 2.10. Solar spectrum (AM1.5).

The solar spectrum can be closely modelled as a blackbody emitter (at 5780K). Before it can reach the surface of the earth, solar radiation is partially absorbed by species in the atmosphere, which lead to the areas of lower irradiance. This absorption occurs primarily by water and carbon dioxide (in the IR region) and by ozone (in the UV). The path length through the atmosphere (and therefore the extent of absorption) is dependent on the incident angle of the sun. Solar spectra are characterised by the air mass coefficient (AM, Equation 2.11) which approximates the path length relative to the shortest possible path length (direct, overhead irradiation).

$$AM = \frac{1}{\cos \varphi}$$

Equation 2.11.

Where φ is the zenith angle, which is the angle from the sun and a vertical axis.

AM1.5 is defined as the standard condition for comparing solar cells and this corresponds to an incident angle of 48°. The intensity of this spectrum is normalised to 100 mW cm^{-2}.

Solar cell performances are typically compared via their overall power-conversion efficiency. This is determined by current-voltage relationships, which are measured using current density-voltage (J-V) curves. Typical J-V curves for a n-type and p-type device are provided in Figure 2.11 and Figure 2.12 respectively, which show how the key parameters are determined.

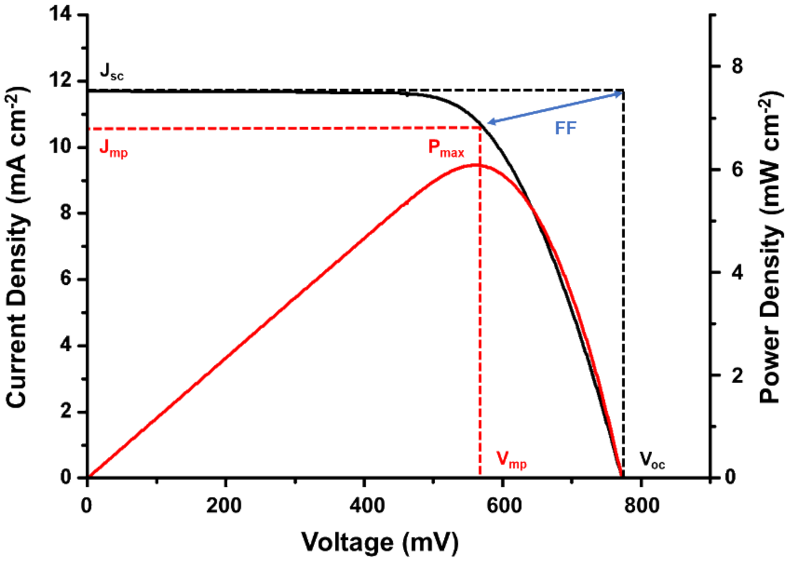

Figure 2.11. Sample J-V curve (black line) and overlaid calculated power density (red line) for a n-DSC. The key parameters used to describe DSCs are labelled.

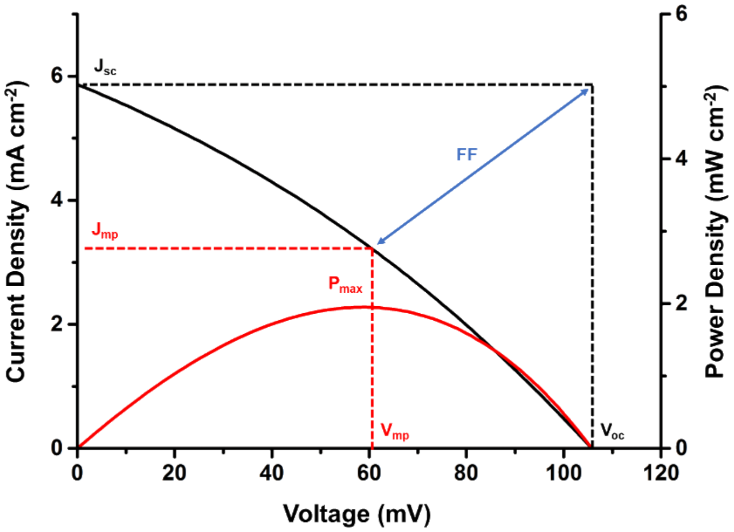

Figure 2.12. Sample J-V curve (black line) and overlaid calculated power density (red line) for a p-DSC. The key parameters used to describe DSCs are labelled.

During testing, the solar cell is illuminated (AM1.5, 100 mW cm^{-2}) and an applied potential is swept from open-circuit to short-circuit conditions while the corresponding current produced is recorded. When the voltage across the solar cell is equal to zero, the cell is at short circuit and the current flow is maximised. This is described as the short-circuit photocurrent density (J_{SC}), which can be determined from J at the V = 0 intercept. This is a measure of how efficiently the device converts incident photons into a collected current. It is dependent on many factors that will be discussed in the following section (**Chapter 2.5.3**).

When the solar cell is at open circuit, the external load resistance is high and no current can flow. The potential that develops is defined as the open-circuit photovoltage (V_{OC}). This can be determined from V at the $J = 0$ intercept. The photovoltage is defined as the difference in energy between the quasi-Fermi level of NiO ($E_{F,NiO}$) and the redox potential of the electrolyte ($E_{F,redox}$, Equation 2.12.).

$$V_{OC} = E_{F,NiO} - E_{F,redox}$$

Equation 2.12.

The Fermi level of NiO is dependent on the energy level of the valence band and the concentration of positive holes (Equation 2.13). The redox potential of the electrolyte is described by the Nernst equation and is dependent on the concentration of oxidised and reduced species present (Equation 2.14).

$$E_{F,NiO} = E_{VB} + \left(k_B T \times \ln\left(\frac{N_{VB}}{n_{VB}}\right)\right)$$

Equation 2.13.

$$E_{F,redox} = E^0_{F,redox} - \left(k_B T \times ln\left(\frac{C_{ox}}{C_{red}}\right)\right)$$

Equation 2.14.

Where E_{VB} is the energy of the valence band, k_B is the Boltzmann constant, N_{VB} is the effective density of valence band states, n_{VB} is the concentration of injected holes, $E^0_{F,redox}$ is the formal redox energy of the electrolyte, C_{ox} is the concentration of oxidised species and C_{red} is the concentration of reduced species.

While J_{SC} and V_{OC} describe the maximum attainable voltage and current density, no power is produced at either of these points. A plot of power (the product of J and V) versus photovoltage (Figure 2.11 and 2.12, red curves) is used to find the point where the maximum power is obtained. The power conversion efficiency (η) of a DSC can be calculated by the ratio of the maximum power output compared to the power input (Equation 2.15).

$$\eta = \frac{P_{out}}{P_{in}} = \frac{P_{max}}{P_{in}} = \frac{J_{SC} \times V_{OC} \times FF}{P_{in}}$$

Equation 2.15.

Equation 2.15 shows that P_{max} can be related to J_{sc} and V_{oc} by multiplication with the fill factor (FF). The fill factor is used to describe the shape of the JV-curve, which is the deviation from an ideal working cell ($P_{max} = J_{SC} * V_{OC}$). It is a measure of the losses occurring within a working device. These losses include shunt and series resistances, including recombination at the NiO surface/dye and the surface/electrolyte interfaces. Fill factors for p-DSCs are typically around half of those observed for n-DSCs, which is indicative of the increased recombination present in p-DSCs. The fill factor can be calculated by the ratio of P_{max} to the product of J_{SC} and V_{OC} (Equation 2.16).

$$FF = \frac{P_{max}}{J_{SC} \times V_{OC}} = \frac{J_{mp} \times V_{mp}}{J_{SC} \times V_{OC}}$$

Equation 2.16.

Figure 2.13 shows the electrical model that is used to describe DSCs, as described by Bisquert and co-workers.[11,12] A study by Wu *et al.* aimed to determine the dominant factors that cause low fill factors in NiO p-DSCs.[13] They proposed that the shunt resistance determines the horizontal flatness of the curve at short circuit conditions while the series resistance determines the vertical sharpness at open circuit conditions. The main contribution to series resistance is hole recombination with the electrolyte while recombination with the reduced dye was the dominating factor for shunt resistance. It was proposed that the major current loss and low FF are due to the recombination of holes in NiO with the reduced dye molecules. In comparison, the major contribution to series resistance in a n-DSC is from charge transfer processes at the exposed FTO/electrolyte interface.[14] Recombination in TiO_2 is much less prevalent in n-DSCs than the analogous processes in p-DSCs. Therefore, the recombination resistance is higher and this is not a major pathway for current losses. These combined factors lead to higher FFs for TiO_2-based devices.

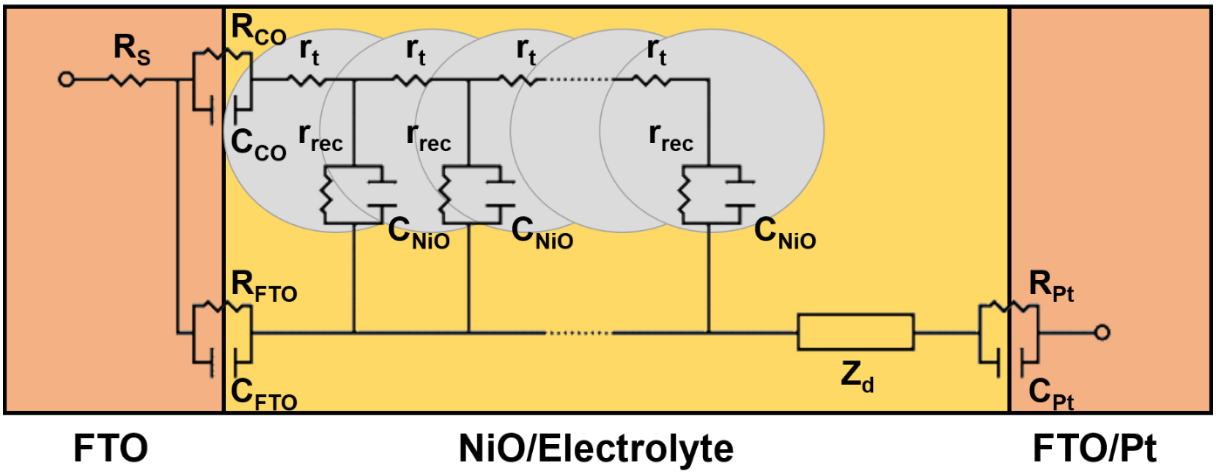

Figure 2.13. Electrical model used to describe a NiO p-DSC, adapted from the work of Bisquert *et al.*[11,12] R_S is the total series resistance, R_{CO} and C_{CO} are the resistance and capacitance at the FTO/NiO contact, R_{FTO} and C_{FTO} are the charge-transfer resistance and double-layer capacitance at the FTO/electrolyte interface, r_t is the transport resistance of the NiO film, r_{rec} is the charge-transfer resistance for recombination (with both the reduced dye and electrolyte with holes in NiO), C_{NiO} is the chemical capacitance of NiO, Z_d is the Warburg diffusion of the electrolyte and R_{Pt} and C_{Pt} are the charge-transfer resistance and double-layer capacitance at the counter electrode (platinised FTO).

2.5.3. IPCE Measurements

As mentioned previously, the J_{SC} is a measure of how efficiently a p-DSC converts photons into a collected current. It can be determined as a function of the absorbed photon-to-current conversion efficiency (APCE), by integrating the APCE spectrum relative to the wavelength of incident light (Equation 2.17). The APCE of a device is related to the incident photon-to-current conversion efficiency (IPCE, Equation 2.18 - Equation 2.19) by the devices light harvesting efficiency (LHE, Equation 2.20).

$$J_{SC} = \int APCE(\lambda) \times LHE(\lambda) \times e \times \phi_{ph,AM1.5}(\lambda)\, d(\lambda)$$

Equation 2.17.

$$IPCE(\lambda) = \frac{J_{SC}(\lambda)}{e\phi_{ph,AM1.5}} = LHE(\lambda) \times \eta_{inj}(\lambda) \times \eta_{reg} \times \eta_{CC}(\lambda)$$

Equation 2.18.

$$APCE(\lambda) = \frac{IPCE(\lambda)}{LHE(\lambda)}$$

Equation 2.19.

$$LHE(\lambda) = 1 - 10^{-A(\lambda)}$$

Equation 2.20.

Where e is the elementary charge, $\phi_{ph,AM1.5}$ is the photon flux for AM 1.5 illumination, η_{inj} is the charge injection efficiency, η_{reg} is the dye regeneration efficiency, η_{cc} is the charge collection efficiency and A is the absorption of the NiO film.

Photon to current conversion efficiencies are also defined as the quantum yields for conversion of a device. The IPCE is known as the external quantum yield and is a measure of the efficiency with which a dye converts incident photons into current. IPCE measurements are carried out by recording the photocurrent at short-circuit conditions over a range of monochromatic wavelengths. This is calibrated against a silicon photodiode which is used to quantify the photon flux at each wavelength. A plot of IPCE as a function of wavelength (Figure 2.14) will closely resemble the absorption profile of the dye adsorbed onto NiO. The APCE is defined as the internal quantum yield, which describes how efficiently absorbed photons are converted into current.

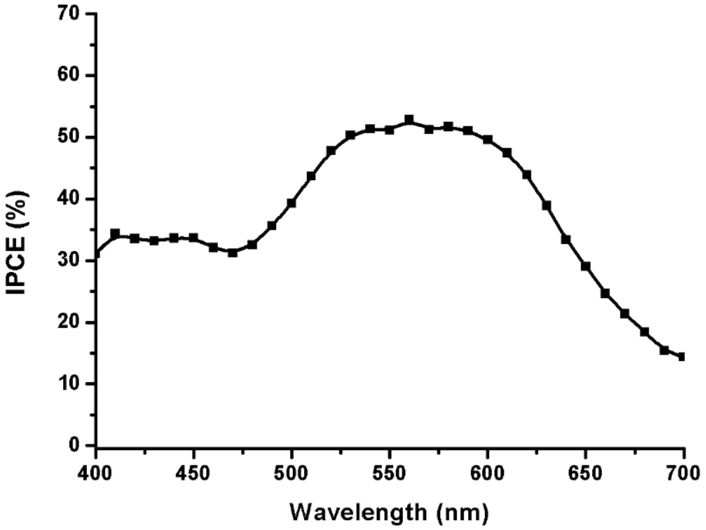

Figure 2.14. Example IPCE curve with the experimental data points shown (the limit of detection of this setup is 700nm, whereas the example dyed NiO film absorbs past this point).

The magnitudes of IPCE and APCE (and therefore J_{SC}) are determined by the various charge transfer efficiencies and the LHE;

1) η_{inj} is controlled by the competition between electron transfer from NiO to the excited dye and excited state decay of the dye.

2) η_{reg} is determined by the competition between regeneration of the reduced dye by the redox couple and recombination between the reduced dye molecules and holes in NiO.

3) η_{CC} is dependent on competition between the extraction of holes in NiO into the external circuit and the recombination of these holes in NiO with the electrolyte.

4) LHE is related to the absorption of the dyed NiO film, so is controlled by a combination of the molar absorption coefficient of the dye and dye loading onto NiO.

The net photocurrent of a device in operation is the difference between the injected and dark current (recombination) densities (Equation 2.21 - Equation 2.22).[15] Therefore, limiting the dark current[14] is crucial to increase device efficiencies. Dark currents can be measured by linear sweep voltammetry, as for JV curves, but without illumination. The current produced arises due to electron transfer from the electrolyte to NiO. Therefore, the dark currents of different dyes can be compared to investigate NiO/electrolyte recombination.

$$Net\ current = J_{inj} - J_{dark}$$

Equation 2.21.

$$J_{dark} = J_0 \left(e^{\frac{qV}{\gamma k_B T}} - 1 \right)$$

Equation 2.22.

Where J_{inj} is the injected current density, J_{dark} is the dark current density, J_0 is a constant that determines the diode dark current, V is the applied voltage and γ is a non-ideality factor.

2.5.4. Charge Extraction Measurements

Alongside J-V curves, a range of measurements exist to investigate the nature of charge and electron/hole lifetimes within a p-DSC. Two of these techniques that have been used in this thesis are charge extraction and charge lifetime measurements. Charge extraction experiments have been used to determine the amount of charge present within NiO as a function of voltage. This can be used in conjunction with charge lifetime measurements to study how hole lifetimes are effected by charge density. These measurements have been performed following a method reported by Duffy *et al.*[16]

In a charge extraction measurement (Figure 2.15), the cell is illuminated at open circuit until a steady state of charge is reached. The illumination is then turned off, causing a decay of charge due to recombination between NiO and the electrolyte. After a set delay time (which is varied to measure the extracted charge at various voltages), the cell is switched to short circuit and the charges remaining in the film are extracted. These steps are repeated with various delay times between turning off the illumination and switching to short circuit (Figure 2.16). As V_{OC} is the difference between $E_{F,NiO}$ and $E_{F,redox}$, at longer delay times the voltage is lower due to a reduced concentration of holes in the NiO valence band. The extracted charge is then integrated and plotted against voltage (an example plot is provided in Figure 2.17).

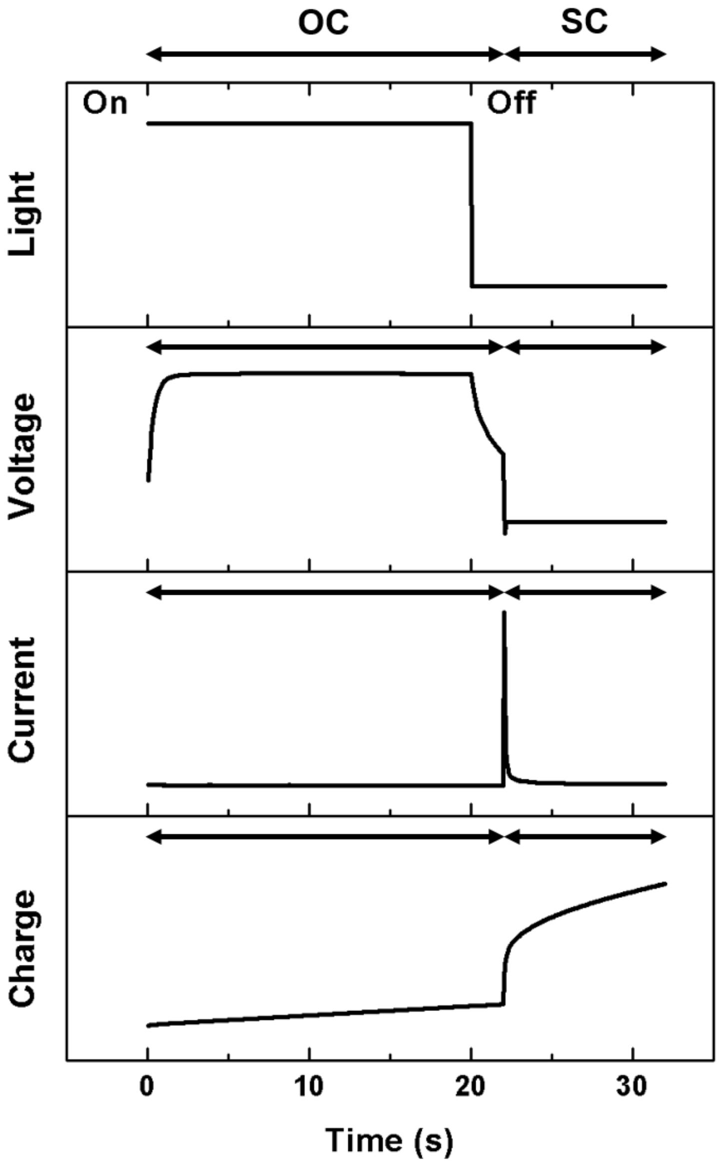

Figure 2.15. Relationship between on/off illumination and open/short-circuit conditions and the measurement of potential, current and charge.

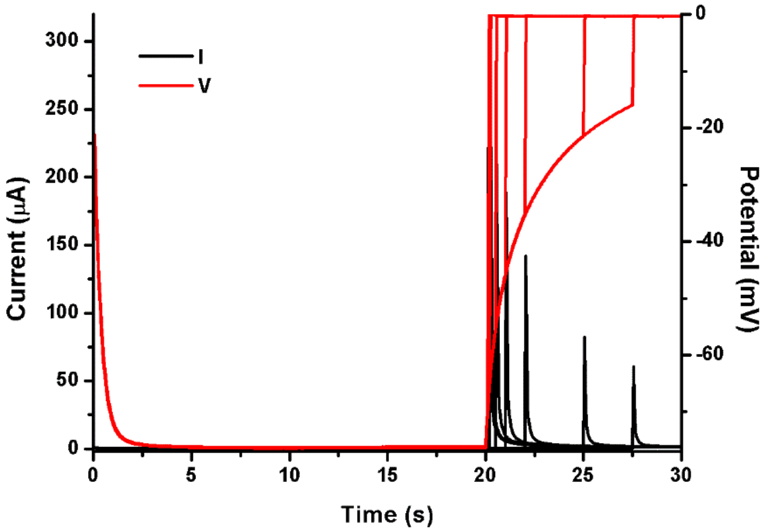

Figure 2.16. Overlaid current/potential measurements for an example charge extraction experiment, with various open to short circuit switching delays.

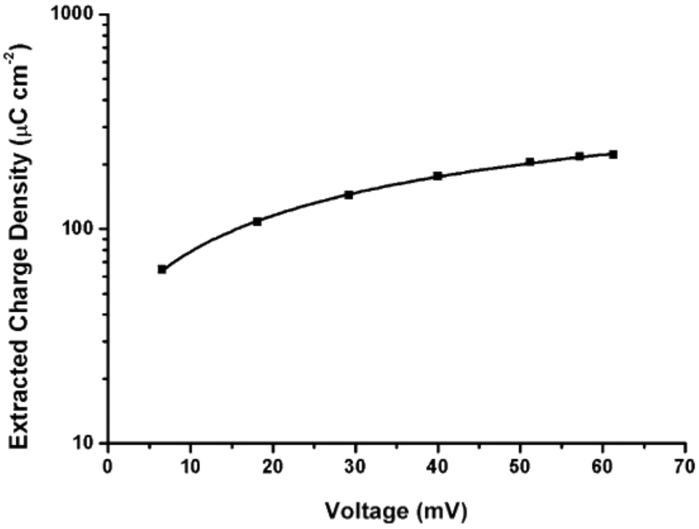

Figure 2.17. Example charge extraction plot.

2.5.5. Small Square Wave Modulated Photovoltage Measurements (SSWMPV)

Charge lifetimes have been investigated using SSWMPV methods. In this, a small square wave of light (with an intensity change of ca. 10%) is superimposed over a larger bias light and the resulting photovoltage is recorded under open circuit conditions (Figure 2.18). When the light intensity decreases, the only way for $E_{F,NiO}$ to decrease (due to a reduced hole concentration) is to recombine with the redox electrolyte. The voltage decays are fit to an exponential decay and the resulting hole lifetime is plotted against voltage (Figure 2.19). Hole lifetimes are shorter at higher light intensities (larger voltages), due to an increased hole concentration available to recombine with the electrolyte. As the lifetimes are recorded over a range of voltages, these can be compared to the working conditions of the p-DSC. By combining this measurement with charge extraction experiments, charge lifetimes can be plotted as a function of extracted charge density. This allows a comparison of systems with different rates of recombination.

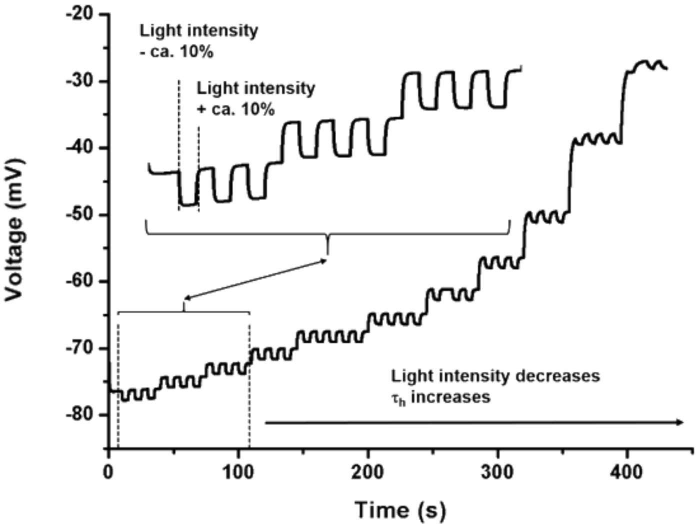

Figure 2.18. Relationship between voltage and light intensity for a charge-lifetime measurement.

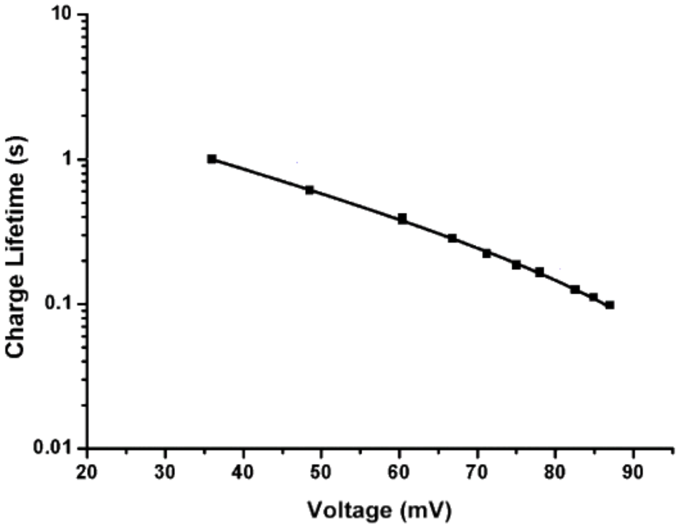

Figure 2.19. Example charge lifetime plot.

2.6. Experimental Details

2.6.1. General Methods

Products were characterised by ^{1}H NMR and ^{13}C NMR using a Bruker 300, 400, 500 or 700 MHz spectrometer at 25°C; chemical shifts (δ) are reported in parts per million (ppm) from low to high field and referenced to residual non-deuterated solvent. Standard abbreviations indicating multiplicity are used as follows: s = singlet; d = doublet; t = triplet; m = multiplet. High resolution mass spectrometry (HRMS) was carried out on a LC-MS system, based on a Bruker MicroTOF (Time of Flight) mass spectrometer using ElectroSpray Ionisation (ESI). Infrared spectroscopy was performed using a Varian 800 FT-IR spectrometer.

2.6.2. UV-visible Absorption Spectroscopy

UV-visible absorption spectroscopy measurements in solution were recorded on either a Perkin Elmer Lambda 25 UV-visible spectrometer, an Ocean Optics USB2000+ VIS-NIR fibre optic spectrometer or a Shimadzu UV-1800 UV spectrophotometer. All measurements were performed using a quartz cuvette with a path length of 1 cm.

2.6.3. Photoluminescence Spectroscopy

Photoluminescence spectroscopy measurements in solution were recorded on either a Gilden Photonics Fluorosens or a Shimadzu RF-6000 spectro fluorophotometer. All measurements were performed using a quartz cuvette with a path length of 1 cm. Quantum yields were determined by comparison to the emission spectra of Rhodamine 6G in ethanol ($\Phi_F = 0.95$).

2.6.4. Electrochemistry

Electrochemical studies were carried out using an IviumStat potentiostat controlled using IviumSoft. Redox potentials were determined using cyclic voltammetry and differential pulse voltammetry. All electrochemistry was performed under a nitrogen atmosphere, using a three-electrode setup, in a single compartment cell. A glassy carbon working electrode, a Pt wire secondary electrode and a saturated calomel or Ag/Ag^{+} (0.01 M $AgNO_3$ in acetonitrile) reference electrode were used. Measurements were typically carried out in anhydrous acetonitrile that had been purged with nitrogen. The sample had a concentration of 0.1 mM and 0.1 - 0.5 M supporting electrolyte was used. TBA ClO_4, Li ClO_4 or TBA PF_6 were used as supporting electrolytes. All redox potentials are quoted against the Fc/Fc^{+} couple used as an internal standard.

2.6.5. Computational Studies

DFT calculations were performed using Gaussian G03 on the University of Nottingham Minerva HPC or Gaussian G09 on the Pople Cluster at Newcastle University. Optimised geometries were first calculated in vacuum, then in solvent (using the PCM). Frequency calculations were used to check that the optimised geometries were true energy minima. Time-dependent DFT (TDDFT) calculations were then performed to calculate the electronic transitions. For the BODIPY, indolium and indigo-based dyes a B3LYP/6-31G(d) exchange functional and basis set combination was used. For the porphyrins B3LYP/6-311G(d,p) was used for C, H, N, O and P while B3LYP/LANL2DZ was used for Zn.

2.6.6. Solar Cell Measurements

Conductive glass substrates were cleaned using an ultrasonic bath for 15 minute intervals in various solvents; first in deionised water containing detergents, then in aqueous hydrochloric acid (0.01M) and finally in ethanol. A NiO precursor solution was prepared by dissolving anhydrous $NiCl_2$ (1 g) and the tri-block co-polymer Pluronic F108 (poly(ethylene glycol)-block-poly(propylene glycol)-block-poly(ethylene glycol)) (1 g) in ethanol (6 g) and Milli-Q water (3 g). Working electrodes were prepared by doctor-blading this precursor solution onto conductive glass substrates (Pilkington TEC15, sheet resistance 15 Ω/square) using Scotch tape as a spacer (0.18 cm^2 active area), followed by sintering in a Nabertherm B150 oven at 450 °C for 30 minutes. NiO films were prepared to a thickness of 1.52 (± 0.025) µm, measured using a Bruker DektakXT stylus profileometer and averaged over 5 samples. The NiO electrodes were soaked in a solution of the dye (typically 0.3 mM in acetonitrile) for 16 h at room temperature.

Platinised counter electrodes were prepared by drop-casting (10 µL cm^{-2}) a solution of $H_2PtCl_6{\cdot}6H_2O$ (4.8 mM in ethanol) onto conductive glass (Pilkington TEC8, sheet resistance 8 Ω/square) followed by annealing at 450 °C for 30 minutes. The two electrodes were assembled face-to-face using a 30 µm thick thermoplastic frame (Surlyn 1702, Dyesol). The electrolyte, containing LiI (1.0 M) and I_2 (0.1 M) in anhydrous acetonitrile, was introduced by vacuum back-filling through a pre-drilled hole in the counter electrode, which was sealed afterwards using a glass coverslip.

UV-visible absorption spectra of the dyes adsorbed onto NiO films were recorded using an Ocean Optics USB2000+ VIS-NIR fibre-optic spectrophotometer. Current-voltage measurements were performed using an Ivium CompactStat or IviumStat potentiostat under simulated sunlight (AM1.5) from an Oriel VeraSol-2 Class AAA LED Solar Simulator, with an intensity of 100 mW cm^{-2}. Incident photon-to-current conversion efficiencies (IPCE) were recorded using monochromatic light from a 300W Xe lamp (Oriel Newport) fitted with an AM1.5 filter, using a Cornerstone 130 1/8m monochromator and calibrated against a certified reference Si photodiode. Charge extraction and small square wave modulated photovoltage measurements were recorded under illumination from an LED light source (Ivium ModuLight).

2.7. References

1 A. J. Bard and L. R. Faulkner, *Electrochemical Methods: Fundamentals and Applications*, Wiley, 1980.

2 Z. Liu, D. Xiong, X. Xu, Q. Arooj, H. Wang, L. Yin, W. Li, H. Wu, Z. Zhao, W. Chen, M. Wang, F. Wang, Y. B. Cheng and H. He, *ACS Appl. Mater. Interfaces*, 2014, **6**, 3448–3454.

3 E. A. Gibson, L. Le Pleux, J. Fortage, Y. Pellegrin, E. Blart, F. Odobel, A. Hagfeldt and G. Boschloo, *Langmuir*, 2012, **28**, 6485–6493.

4 A. D. Becke, *J. Chem. Phys.*, 1993, **98**, 1372–1377.

5 D. Coskun, S. V. Jerome and R. A. Friesner, *J. Chem. Theory Comput.*, 2016, **12**, 1121–1128.

6 J. Tirado-Rives and W. L. Jorgensen, *J. Chem. Theory Comput.*, 2008, **4**, 297–306.

7 W. R. Wadt and P. J. Hay, *J. Chem. Phys.*, 1985, **82**, 284–298.

8 P. J. Hay and W. R. Wadt, *J. Chem. Phys.*, 1985, **82**, 270-283.

9 P. J. Hay and W. R. Wadt, *J. Chem. Phys.*, 1985, **82**, 299-310.

10 J. Tomasi, B. Mennucci and R. Cammi, *Chem. Rev.*, 2005, **105**, 2999–3094.

11 F. Fabregat-Santiago, J. Bisquert, G. Garcia-Belmonte, G. Boschloo and A. Hagfeldt, *Sol. Energy Mater. Sol. Cells*, 2005, **87**, 117–131.

12 Q. Wang, S. Ito, M. Grätzel, F. Fabregat-Santiago, I. Mora-Seró, J. Bisquert, T. Bessho and H. Imai, *J. Phys. Chem. B*, 2006, **110**, 25210–25221.

13 Z. Huang, G. Natu, Z. Ji, M. He, M. Yu and Y. Wu, *J. Phys. Chem. C*, 2012, **116**, 26239–26246.

14 F. Fabregat-Santiago, G. Garcia-Belmonte, I. Mora-Seró and J. Bisquert, *Phys. Chem. Chem. Phys.*, 2011, **13**, 9083–118.

15 F. Odobel, Y. Pellegrin, E. A. Gibson, A. Hagfeldt, A. L. Smeigh and L. Hammarström, *Coord. Chem. Rev.*, 2012, **256**, 2414–2423.

16 N. Duffy, L. Peter, R. M. G. Rajapakse and K. G. U. Wijayantha, *Electrochem. Commun.*, 2000, **2**, 658–662.

Chapter 3 – Tuning the Donor-Acceptor Electronic Communication in Triphenylamine-BODIPY Dyes

3.1. Introduction

3.1.1. Triphenylamine 'push-pull' dyes

The 'push-pull' design is commonly used for organic sensitisers in p-DSCs. In this system, the HOMO of the dye is localised on a donor unit anchored to NiO and the LUMO is localised on an acceptor unit at the periphery of the dye.[1,2] When the dye absorbs light, a charge transfer excited state is formed where the electron density moves from the donor to the acceptor. If the dye is adsorbed onto NiO, this promotes electron transfer from NiO to the dye. The donor-acceptor structure thus spatially separates the hole left in NiO from the electron located on the dye periphery. This spatial separation is expected to reduce charge recombination between the dye and the semiconductor, which will increase the J_{SC}.

Triphenylamine is commonly used as a donor moiety because it can be functionalised relatively easily and it has a non-planar arrangement that helps reduce π-π stacking.[3] An anchoring group is required to form covalent bonds with the NiO surface.[4] Carboxylic acid is widely used for p-DSCs[3,5] and there are a few examples of other groups that includes phosphonates,[6] catechol[7] and acetylacetone[8] anchors. π-linkers are typically included to improve electronic coupling between donor and acceptor units and to increase conjugation. A variety of π-linkers are reported in the literature, but the most commonly used are thiophene derivatives. These are often in the form of polythiophene chains, for example in the record dyes developed by Bach *et al.*[9,10] Finally, typical acceptor groups include malonitrile,[1,2,11] perylene monoimide,[12,13] fullerene[14] and indolium.[15]

Previous work in the Gibson group replaced the malonitrile acceptor units of the benchmark dye **P1**[1] with BODIPY moieties[16] (Figure 3.1). This change in structure increased the extinction coefficient of the dye (ε = 112,000 vs. 58,000 dm^3 mol^{-1} cm^{-1} for **1** and **P1** respectively). The lifetime of the charge-separated state was increased by several orders of magnitude (180 ns vs. 30 ps), despite little change in the driving force for charge transfer and recombination. However, despite these improvements, p-DSCs constructed using **1** performed worse than those previously reported for **P1**[17] (J_{SC} = 3.15 mA cm^{-2}, V_{OC} = 79 mV, η = 0.08%, IPCE = 28% for **1** vs. J_{SC} = 5.48 mA cm^{-2}, V_{OC} = 84 mV, η = 0.15%, IPCE = 64% for **P1**). Theoretical and experimental evidence suggested that the BODIPY acceptors had poor electronic coupling to the thiophene π-linkers (and subsequently the triphenylamine donor and semiconductor surface). This was attributed to steric hindrance from the methyl substituents in the 1 and 7-positions of the BODIPY core restricting rotation around the *meso*-coupled thiophene.

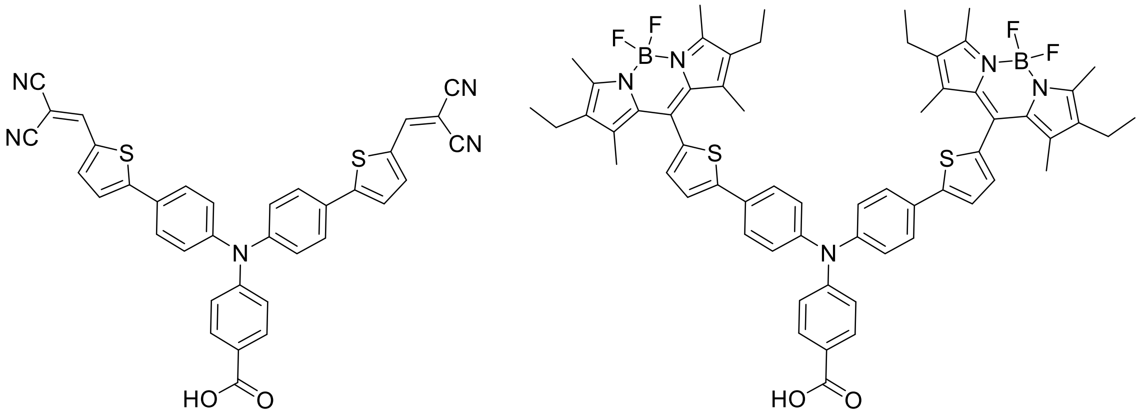

P1 **1**

Figure 3.1. Chemical structure of the triphenylamine-based push-pull dyes previously studied.

3.1.2. Motivation

The BODIPY group remains a promising acceptor group for further study, despite **1** performing worse than **P1**. While **1** had a long-lived charge-separated state, the decoupling of the dye HOMO and NiO surface lowered the charge transfer efficiency. In this chapter, dye **1** has been modified by synthesising the BODIPY unit using a mono α-substituted pyrrole. The new dye (**2**) is therefore less restricted around the *meso*-bond between the BODIPY and thiophene units. The aim was to tune electronic coupling between the donor and acceptor groups by reducing the steric hindrance. This was intended to increase the charge-transfer character of the dye, thereby increasing the efficiency of charge transfer from NiO to the HOMO of the dye.

Two dyes (**3** and **4**) have been designed and synthesised that do not contain the thiophene π-linker which is commonly used. These were developed to further study the influence that electronic coupling between the triphenylamine and BODIPY donor units has on the p-DSC performance. These were synthesised using both the sterically hindered 3-ethyl-2,4-dimethylpyrrole and a less hindered mono α-substituted pyrrole.

In these dyes, the anchoring unit was extended with the inclusion of an additional phenyl ring between triphenylamine and the carboxylic acid. This increases the spatial separation between the NiO surface and the BODIPY acceptors.

Finally, to investigate the performance of an isolated BODIPY without any charge-transfer character, a simple BODIPY (**5**) was synthesised using benzoic acid as an anchoring unit. This provides a benchmark to the more synthetically complicated dyes **1-4**.

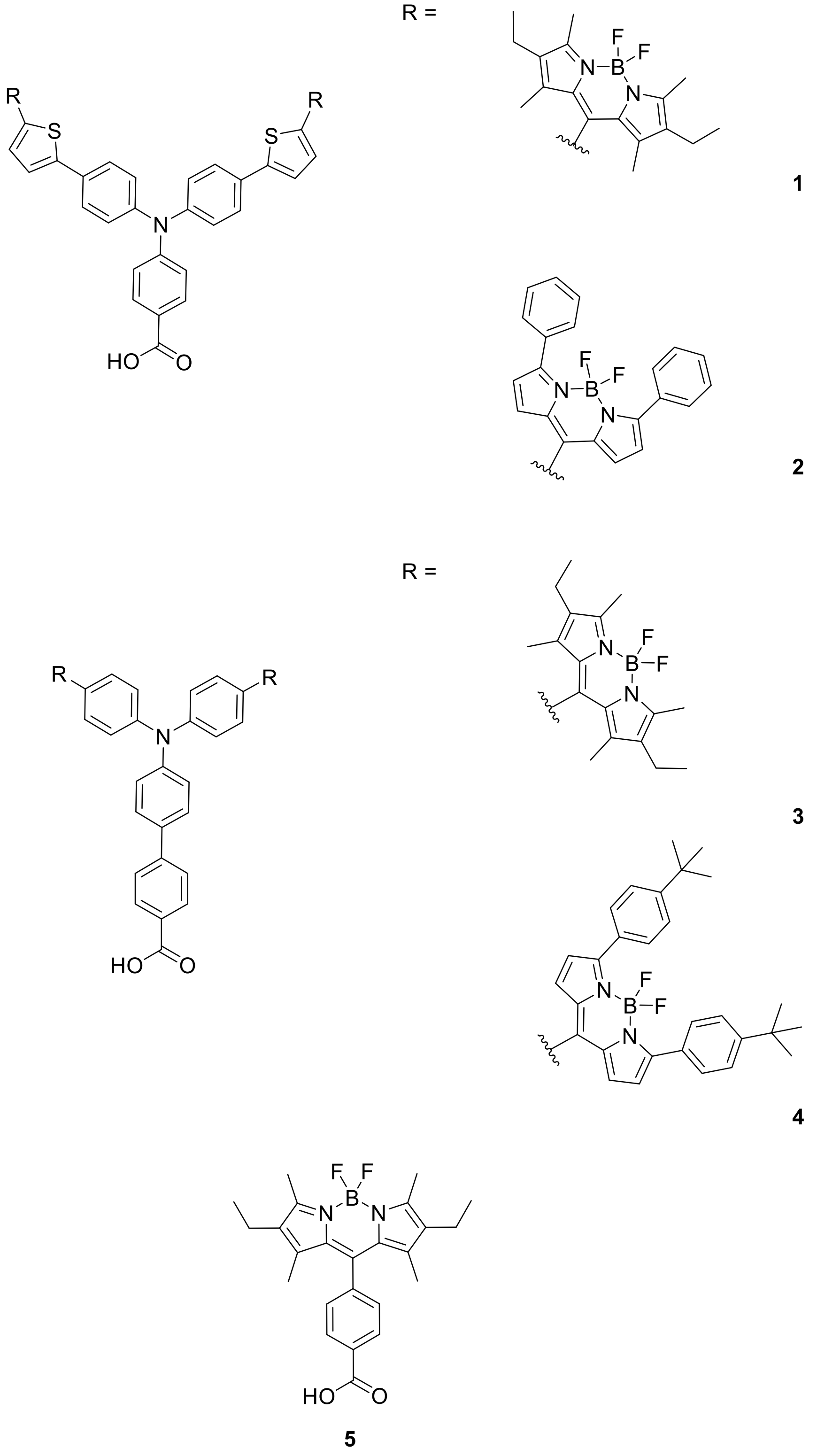

Figure 3.2. Chemical structure of the push-pull BODIPY dyes developed and studied in this chapter.

3.2. Results and Discussion

3.2.1. Synthesis

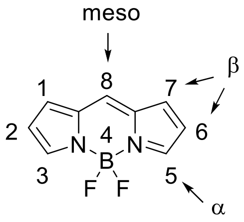

Figure 3.3. IUPAC numbering system for the BODIPY core.

When designing the pyrroles used to synthesise the less sterically hindered BODIPYs, it was important that they were substituted in the α-position (Figure 3.3). This was intended to block the formation of further condensed products, such as porphyrins, during the final acid-catalysed pyrrole condensation reaction. This was also to protect the radical ions that will be formed upon charge transfer from NiO against dimerisation or substitution, as the radical ions of unsubstituted BODIPYs are highly reactive.[18] Three proposed synthetic routes to α-substituted pyrroles are shown in Figure 3.4.

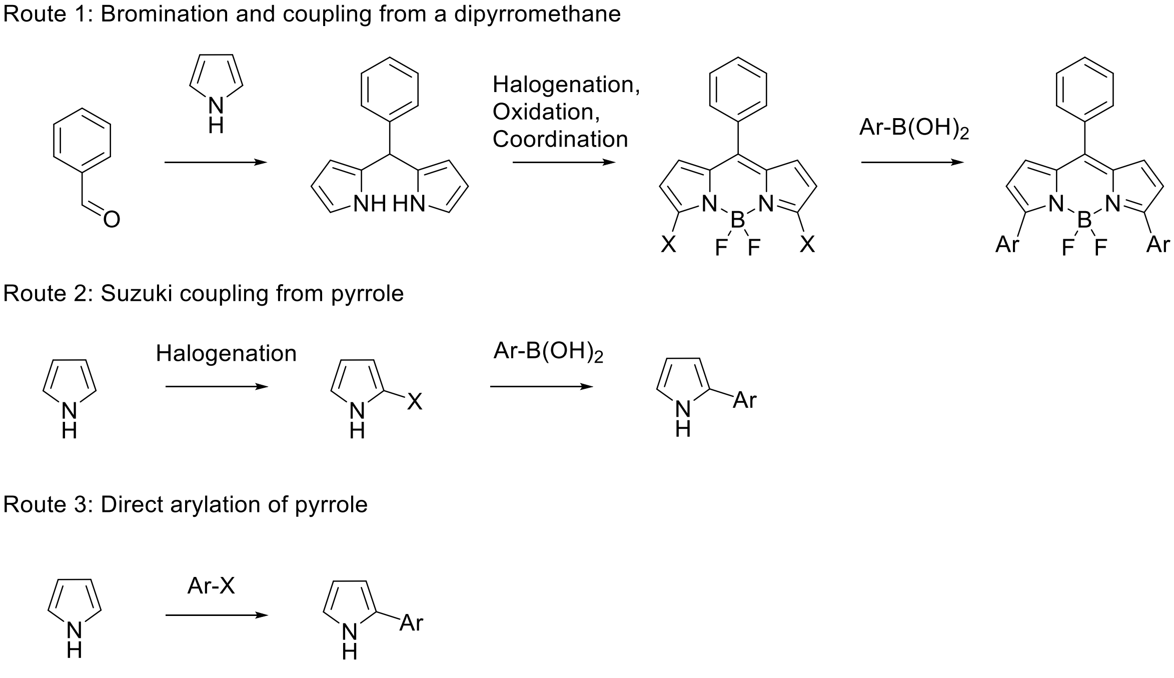

Figure 3.4. Example synthetic routes to an α-substituted pyrrole/BODIPY.

Mono α-substituted BODIPYs have been previously prepared by Hall *et al.*[19] from the synthesis of unsubstituted dipyrromethanes. These were formed by the condensation of an aldehyde with a large excess of pyrrole (used as the solvent), followed by regioselective bromination, oxidation and boron coordination (route 1). The dibrominated BODIPY then undergoes a Suzuki coupling to introduce the aryl substituent in the 3/5-positions. However, in the case of dyes **1**-**4**, two dipyrromethanes would need to be synthesised on each molecule, leading to further complexity regarding regioselectivity and product distribution. As the aldehyde precursors were the product of a 3 - 4 step linear synthesis, it was decided that the pyrrole should be substituted prior to condensation, to maximise overall yields.

Burgess *et al.*[20] prepared 3,5-diaryl BODIPYs using pyrroles synthesised through a Suzuki coupling (route 2) with aryl boronic acids. However, due to the instability of 2-bromopyrrole,[21] this route was carried out from *tert*-butoxycarbonyl-2-bromopyrrole.[22] The direct arylation of pyrrole (route 3) reduces the number of synthetic steps and avoids the use of protecting groups. Sadighi *et al.*[23] studied the direct arylation of (pyrrolyl)zinc chloride with aryl halides using $Pd(OAc)_2$ and bulky dialkylphosphinobiphenyl ligands (2-phenyl-1H-pyrrole was reported in 90% yield). However, this route was not followed as the synthesis of (pyrrolyl)zinc chloride required glove box conditions. Instead, the method developed by Yu *et al.*[24] for the direct arylation of *N*-heteroarenes using diaryliodonium salts was followed. This route (Figure 3.5) was followed to reduce the number of coupling reactions necessary in the overall synthesis, as the reaction did not require transition metal catalysts.

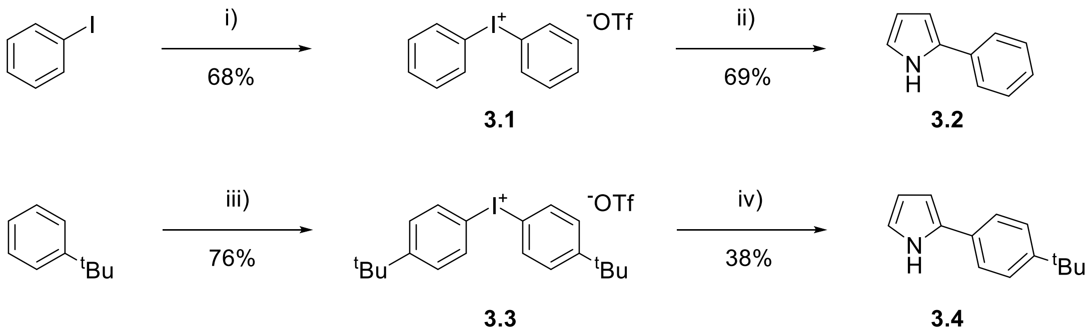

Figure 3.5. Pyrrole synthesis by the direct arylation using diaryliodonium salts; i) a) mCPBA, benzene, DCM; b) TfOH, 68%; ii) NaOH, pyrrole, 69%; iii) a) mCPBA, I_2, DCM; b) TfOH, 76%; iv) NaOH, pyrrole, 38%.

The diaryliodonium triflates were prepared following the one-pot route reported by Olofsson *et al*.[25] (Figure 3.5). In the proposed reaction scheme, mCPBA was used to oxidise iodobenzene to a reactive iodine (III) species, which subsequently underwent ligand exchange with a slight excess of benzene. Trifluoromethanesulfonic acid was used to produce **3.1** in 68% yield. Due to the increased cost of 4-*tert*-butyliodobenzene, for **3.3** the reaction was carried out using *tert*-butylbenzene and molecular iodine. In this reaction, the aryl iodide was formed *in situ* to form the product in 76% yield.[26] For both reactions, the products were isolated by precipitation from the addition of a non-polar solvent to the concentrated reaction mixture. These diaryliodonium salts were used to synthesise arylpyrroles by heating in an excess of pyrrole (used as the solvent) in the presence of NaOH to afford **3.2** and **3.4**, in yields of 69% and 38% respectively, after chromatographic purification. Dye **2** had been poorly soluble in common organic solvents, which was attributed to π-π stacking. Therefore, the bulky *tert*-butyl substituent was introduced to the pyrrole used for **4** to help reduce this stacking.

The synthesis of triphenylamine based dyes has been widely reported in the literature.[4,27] For the synthesis of **2** (detailed in Figure 3.6), the formylation of triphenylamine was carried out by the Vilsmeier-Haack reaction using phosphoryl chloride, to afford **3.5** in 37% yield. This was reacted with bromine in dichloromethane (DCM) at 0 °C to give **3.6** in 59% yield. The aldehyde functional group of **3.6** was oxidised using $KMnO_4$ in refluxing acetone/water to form the anchoring unit, producing **3.7** in 62% yield after an acidic workup. The thiophene π-linkers were introduced by a Suzuki coupling with 5-formyl-2-thienylboronic acid, catalysed by $Pd(PPh_3)_2Cl_2$, that gave **3.8** in 65% yield. **2** was synthesised in a one-pot route by the trifluoracetic acid (TFA) catalysed condensation of **3.2** with **3.8** to give the dipyrromethane. This was oxidised using p-chloranil and boron coordination of the dipyrromethene was subsequently carried out using diisopropylethylamine (DIPEA) and boron trifluoride etherate ($BF_3.OEt_2$). **2** was purified by column chromatography and recrystallisation to give the final product in 21% yield.

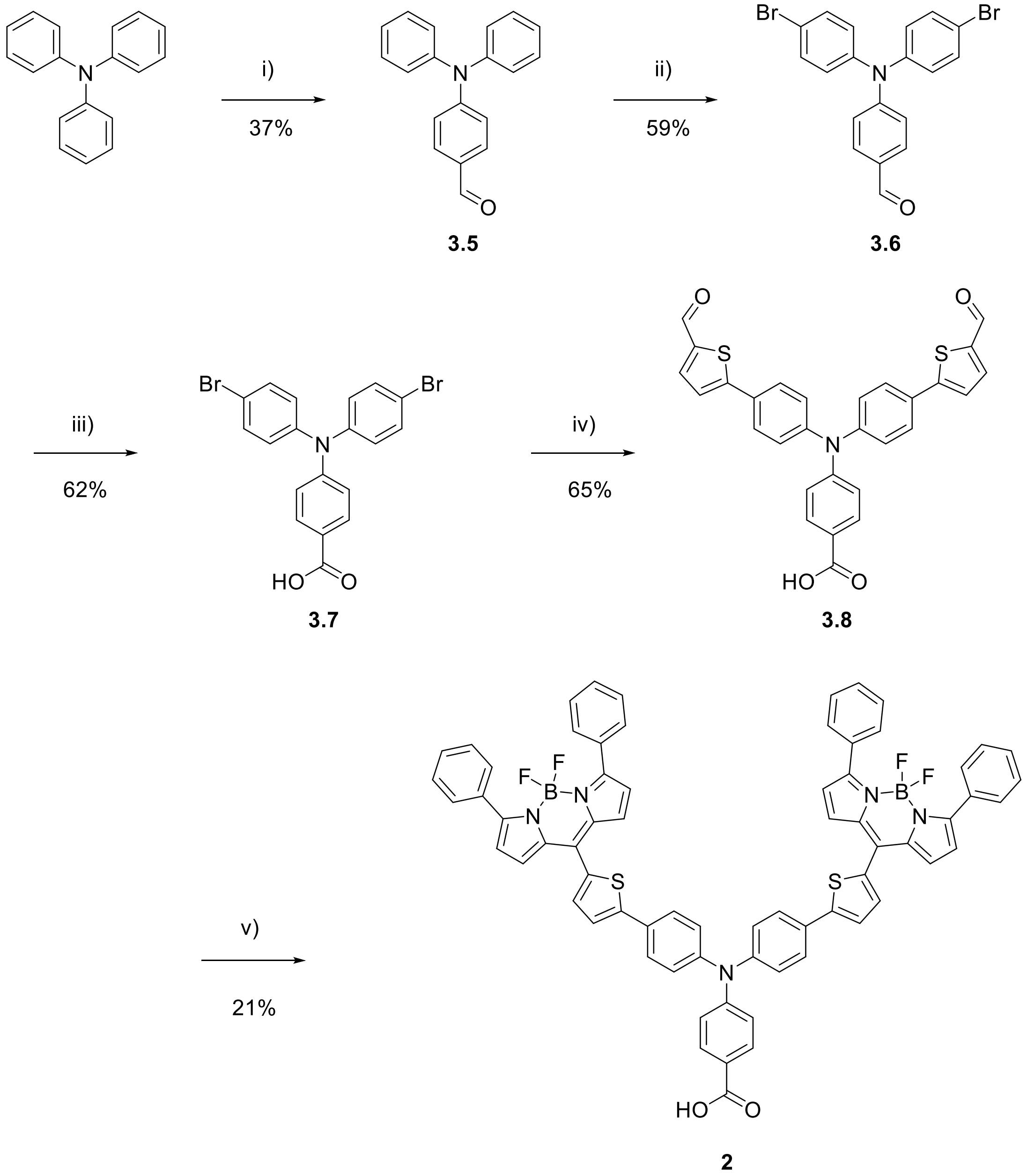

Figure 3.6. Synthesis of **2**; i) $POCl_3$, DMF, 37%; ii) Br_2, DCM, 59%; iii) $KMnO_4$, acetone/H_2O (3:1), 62%; iv) 5-formyl-2-thienyl boronic acid, $Pd(PPh_3)_2Cl_2$, Na_2CO_3, H_2O/DME (1:6), 65%; v) a) 2-phenyl-1H-pyrrole, TFA, DCM; b) p-chloranil; c) DIPEA; d) $BF_3.OEt_2$, 21%.

The synthesis of **4** was performed following similar reactions as for **2** (Figure 3.7). The formylation of triphenylamine was carried out by the same Vilsmeier-Haack reaction using phosphoryl chloride to afford **3.9** in 37% yield. The halogenation reaction carried out for **2** using bromine produced a range of products that required chromatographic separation. As *N*-bromosuccinimide (NBS) is easier to handle, this was used for the bromination of **3.9**, to give **3.10** in quantitative yield after an aqueous workup and recrystallisation. The anchoring unit was then introduced by a Suzuki coupling with carboxyphenylboronic acid, catalysed by $Pd(PPh_3)_2Cl_2$, with a yield of 79%. **4** was synthesised in a one-pot route by the TFA-catalysed condensation of **3.4** with **3.11** to give the dipyrromethane. This was oxidised using p-chloranil and boron coordination of the dipyrromethene was performed using DIPEA and $BF_3.OEt_2$ to produce **4** as a purple solid in 35% yield.

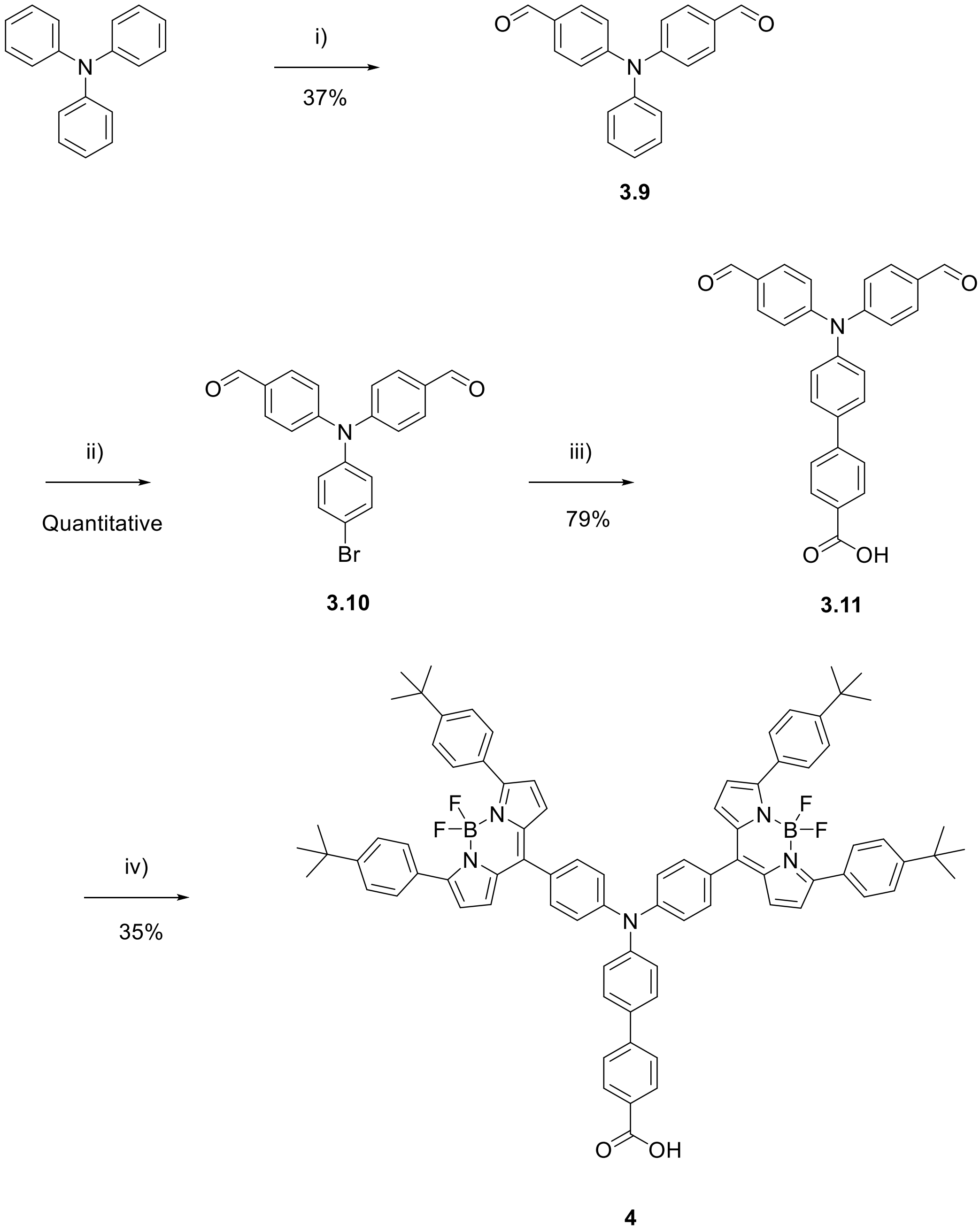

Figure 3.7. Synthesis of **4**; i) $POCl_3$, DMF, 37%; ii) NBS, tetrahydrofuran (THF), quantitative; iii) 4-carboxyphenylboronic acid, $Pd(PPh_3)_2Cl_2$, Na_2CO_3, H_2O/DME (1:3), 79%; iv) a) 2-(4-(*tert*-butyl)phenyl)-1H-pyrrole, TFA, DCM; b) p-chloranil; c) DIPEA; d) $BF_3.OEt_2$, 35%.

The analogous hindered dyes, **1** and **3**, were synthesised following the same routes as for **2** and **4**, using 3-ethyl-2,4-dimethylpyrrole for the final pyrrole condensation. **5** was synthesised in a one-pot reaction starting from the condensation of 3-ethyl-2,4-dimethylpyrrole and 4-carboxybenzaldehyde (Figure 3.8).

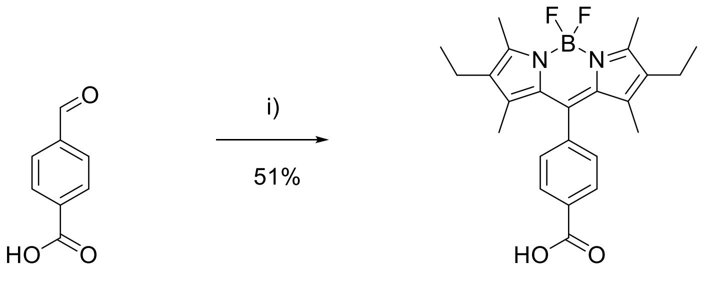

5

Figure 3.8. Synthesis of **5**; i) 2,4-dimethyl-3-ethylpyrrole, TFA, DCM; b) p-chloranil; c) DIPEA; d) $BF_3.OEt_2$, 51%.

3.2.2. Structural Characterisation

2 and **4** have been structurally characterised using ^{1}H NMR/^{13}C NMR spectroscopy. The ^{1}H NMR assignments are summarised in Table 3.1, with protons labelled as shown in Figure 3.9. Homonuclear correlation spectroscopy (COSY) has been used to aid the assignments.

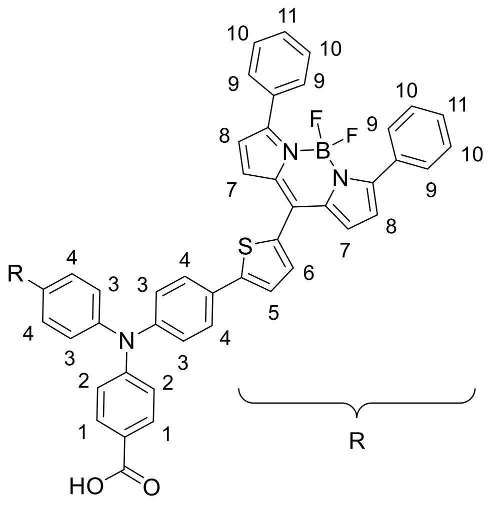

2

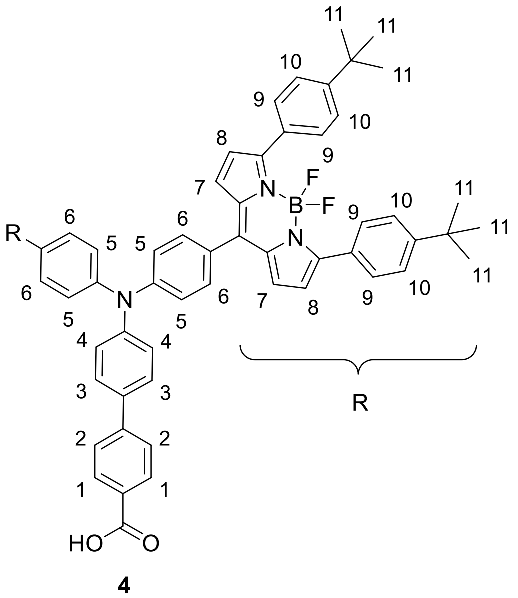

4

Figure 3.9. Proton labelling system used for **2** and **4**.

Table 3.1. ^{1}H NMR assignments for **2** and **4**.

2					**4**				
H$_X$	m, H	δ / ppm	J / Hz	COSY	**H$_X$**	m	δ / ppm	J / Hz	COSY
1	d, 2H	8.01	8.3	a	**1**	d, 2H	8.21	8.3	a
2	d, 2H	7.18	8.1	a	**2**	d, 2H	7.74	8.5	a
3[a]	-	-	-	c	**3**	d, 2H	7.71	8.7	c
4	d, 4H	7.67	8.6	c	**4**	d, 2H	7.41	8.5	c
5	d, 2H	7.55	3.7	d	**5**	d, 4H	7.36	8.6	d
6	d, 2H	7.45	3.7	d	**6**	d, 4H	7.60	8.6	d
7	d, 4H	7.36	4.3	e	**7**	d, 4H	7.03	4.3	e
8	d, 4H	6.68	4.3	e	**8**	d, 4H	6.68	4.3	e
9	d, 8H	7.86	8.1	b	**9**	d, 8H	7.87	8.5	b
10	m, 12H	7.45-7.39	-	b	**10**	d, 8H	7.46	8.6	b
11					**11**	s, 36H	1.35	-	-

Where; H$_X$ = the assigned proton, labelled as in Figure 3.9, δ = the chemical shift of the peak, m = peak multiplicity, H = relative number of protons, *J* = peak coupling constant and COSY = cross-peak as determined using COSY (labelled as in Figure 3.11 and Figure 3.13). [a] = overlaps with CDCl$_3$, observed in the COSY spectrum.

The ^{1}H NMR spectrum of **2** is provided in Figure 3.10 and the corresponding COSY spectrum in Figure 3.11. H$_1$ was assigned to the 2H doublet at 8.01 ppm (*J* = 8.3 Hz), as this is the most deshielded proton due to its close proximity to the carboxylic acid. Additionally, the coupling constant is characteristic of an ortho $^3J_{HH}$ phenyl coupling. From the COSY spectrum, a cross-peak (a) of this to H$_2$ was observed. Therefore, H$_2$ was assigned to the 2H doublet at 7.18 ppm, which is more shielded due to its proximity to the nitrogen lone-pair. H$_3$ cannot be observed directly in the ^{1}H NMR spectrum, as it overlapped with the residual solvent peak of CDCl$_3$. However, a cross-peak (c) could be seen in the COSY spectrum between this peak and H$_4$, which was assigned to the 4H doublet at 7.67 ppm. The two thiophene protons, H$_5$ and H$_6$, were assigned to the two 2H doublets at 7.55 and 7.45 ppm. These were identified due to their smaller coupling constants (*J* = 3.7 Hz, cross-peak d in the COSY spectrum). A smaller coupling constant was also used to distinguish the pyrrole protons, H$_7$ and H$_8$. These were assigned to the two 4H doublets at 7.36 and 6.68 ppm (*J* = 4.3 Hz, coupling e in the COSY spectrum). The BODIPY phenyl ring appeared as an 8H doublet at 7.86 ppm, assigned to proton H$_9$, and a 12H multiplet at 7.45-7.39 ppm. The latter was assigned to an overlap of protons H_{10} and H_{11}, which have a cross-peak in the COSY spectrum (cross-peak b) between the doublet (H_9) and the major peaks in the multiplet.

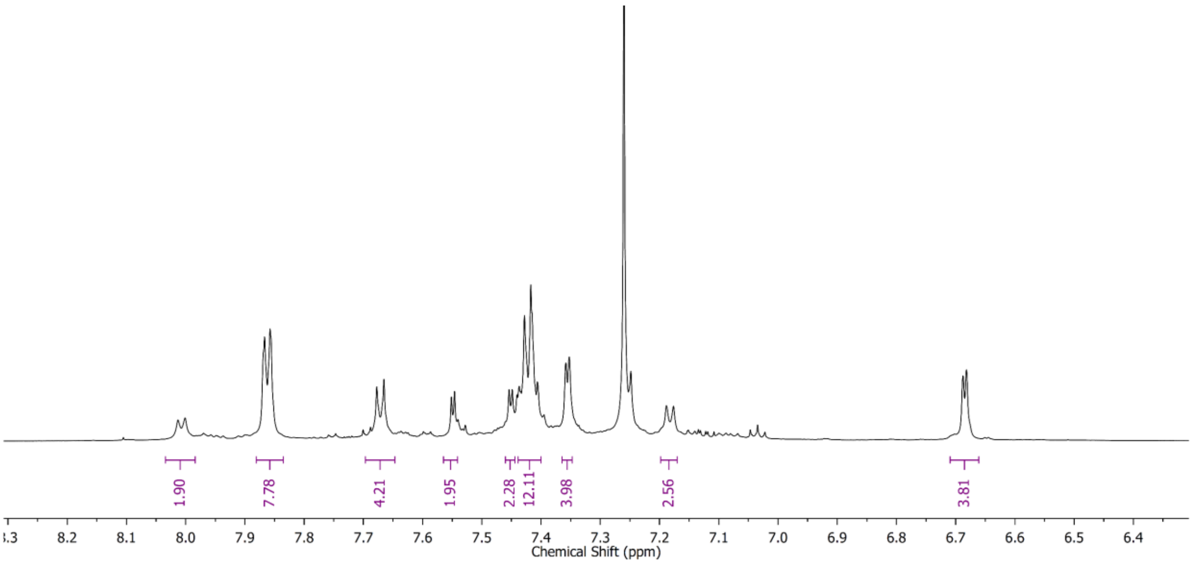

Figure 3.10. Expansion of the aromatic region of the ^{1}H NMR spectrum ($CDCl_3$, 700 MHz) of **2**.

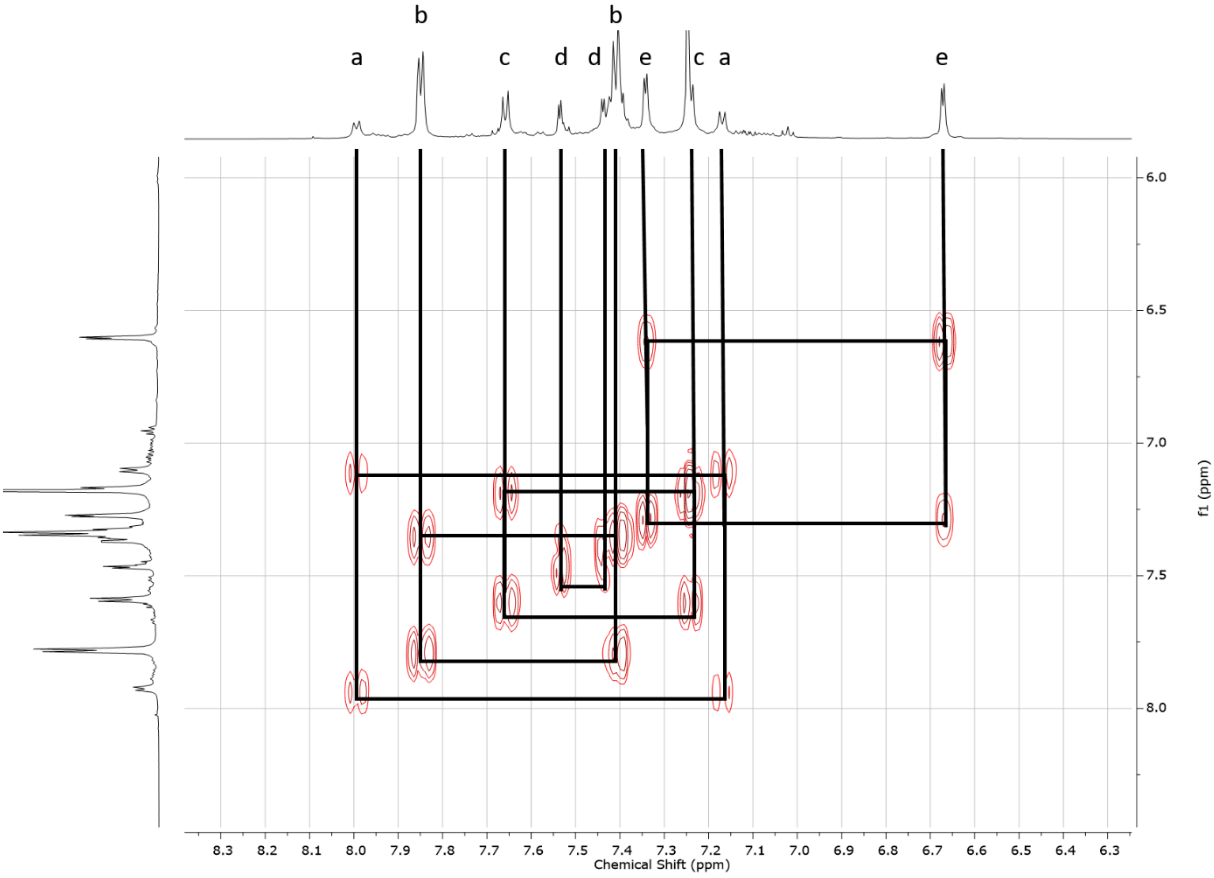

Figure 3.11. Expansion of the aromatic region of the COSY spectrum ($CDCl_3$, 700 MHz) of **2**.

The ^1H NMR spectrum of **4** is provided in Figure 3.12 and the corresponding COSY spectrum in Figure 3.13. The eight phenyl proton environments can be assigned to the peaks with coupling constants ca. 8.5 Hz. H_1 was assigned to the 2H doublet at 8.21 ppm, because this is the most deshielded proton as it is adjacent to the carboxylic acid. From the observed cross-peak to this signal in the COSY spectrum (cross-peak a), H_2 can be assigned to the 2H doublet at 7.74 ppm. H_4 is adjacent to the nitrogen lone pair and thus will be the most shielded of the 2H doublets. Therefore, this has been assigned to the signal at 7.41 ppm. There is a cross-peak (c) in the COSY spectrum between this peak and H_3, which was assigned to the 2H doublet at 7.71 ppm. The two 4H doublets at 7.36 and 7.60 ppm (J = 8.6 Hz, coupling d in the COSY spectrum) have been assigned to H_5 and H_6 respectively. H_5 is more shielded as it is also adjacent to the nitrogen lone pair. H_9 and H_{10} have been assigned to the two 8H doublets at 7.87 and 7.46 ppm (cross-peak b in the COSY spectrum). H_{10} is the more shielded proton environment, as it is closer to the inductive effect of the *tert*-butyl substituent. The two pyrrole protons, H_7 and H_8, can be identified due to their smaller coupling constant (J = 4.3 Hz, cross-peak e in the COSY spectrum). These were assigned to the two 4H doublets at 7.03 and 6.68 ppm respectively. Finally, the *tert*-butyl substituents were assigned to a 36H singlet at 1.35 ppm.

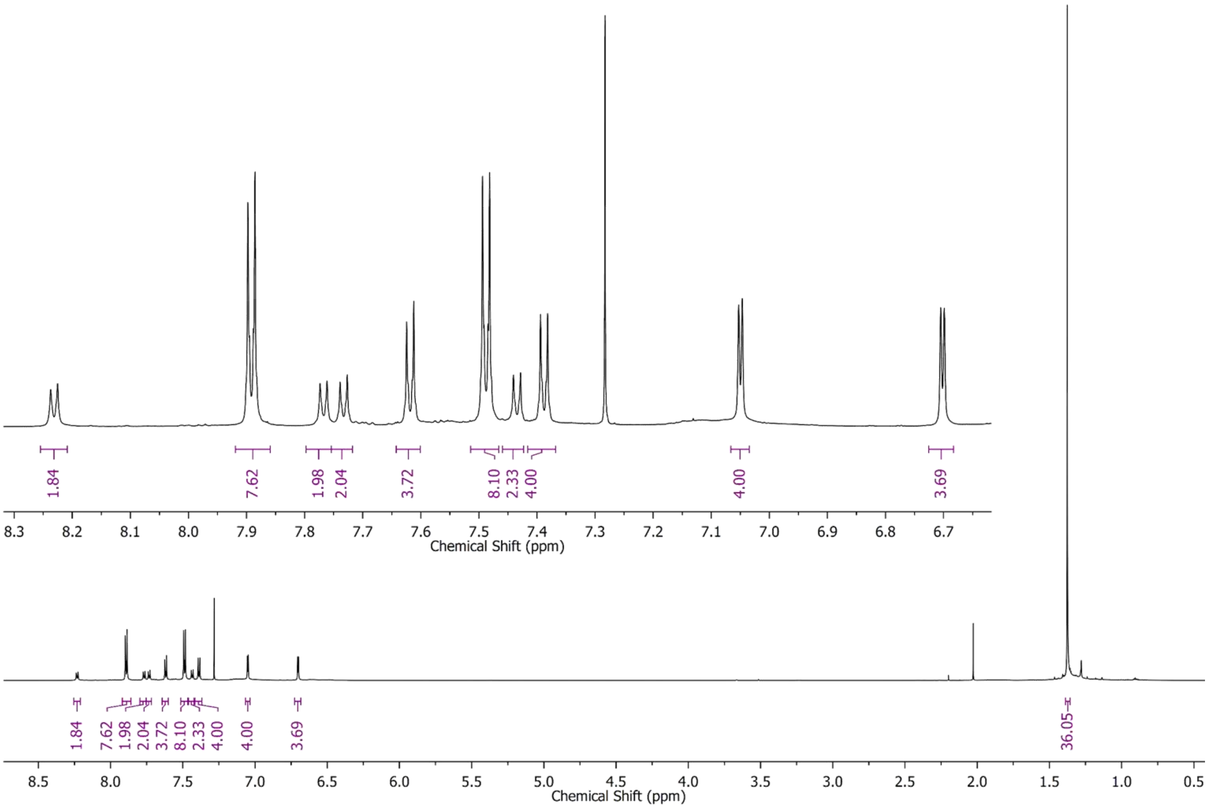

Figure 3.12. ^{1}H NMR spectrum ($CDCl_3$, 700 MHz) of **4**.

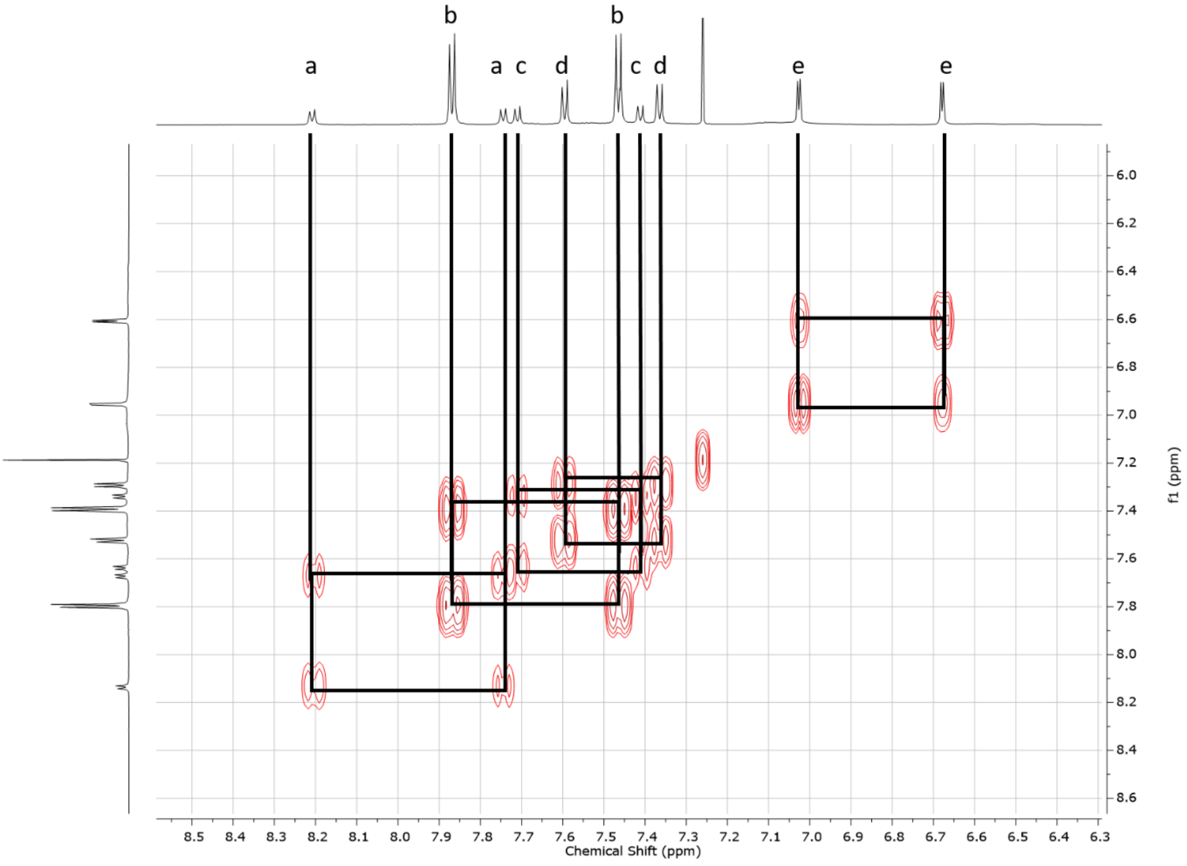

Figure 3.13. Expansion of the aromatic region of the COSY spectrum ($CDCl_3$, 700 MHz) of **4**.

3.2.3. Optical Characterisation – Absorption Spectroscopy

The UV-visible absorption spectra of **1-5** were measured in DCM (Figure 3.14) and are summarised in Table 3.2.

Table 3.2. UV-visible absorption data for **1-5** in DCM.

	λ_{abs} /nm (ε / dm^3 mol^{-1} cm^{-1})
1	540 (112,000), 365 (56,000)
2	565 (65,700), 358 (32,554)
3	526 (81,700), 360 (23,900), 330 (19,600)
4	561 (65,824), 351 (28,237), 308 (41,488)
5	528 (52,000)

λ_{abs} is the wavelength of maximum absorbance and ε is the molar extinction coefficient.

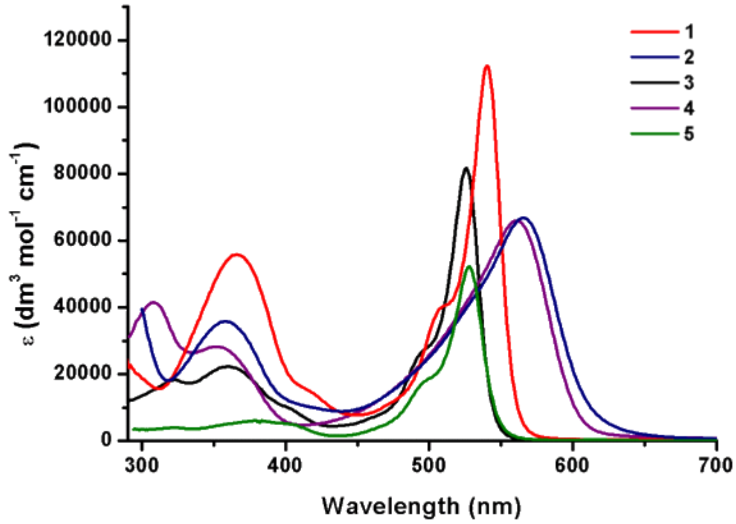

Figure 3.14. UV-visible absorption spectra of **1-5** recorded in DCM.

As the simplest compound of the series, **5** exhibits the typical absorption spectrum of a BODIPY dye. This is characterised by a narrow absorption band at a wavelength greater than 500 nm and a high extinction coefficient that corresponds to a π-π* transition localised on the BODIPY. **3** has a very similar absorption spectrum, with only a small change in λ_{abs} (2 nm) compared to **5**. This suggests there is little electronic coupling between the BODIPY and triphenylamine, as an increase in conjugation would lead to a larger shift of the absorption maxima. This is further supported by the similar shape of the absorption profiles. The extinction coefficient of the transition at ca. 526 nm was higher for **3** compared to **5**, as this π-π* transition is now localised on two BODIPY units. The major difference between the absorption spectra of **3** and **5** was the presence of broad absorption bands at higher energy for **3**, that were not present previously. These are due to electronic transitions primarily localised on the triphenylamine donor unit.

When comparing **1** to **3** and **5**, the characteristic BODIPY absorption profile was still present for all three dyes, but the absorption maxima had shifted to longer wavelengths by 14 nm (for **1** vs. **3** and **5**). There was a significant increase of the extinction coefficient of this lowest energy excitation, alongside an overall broadening of the absorbance. These changes to the absorption spectrum suggest an increase in conjugation of the BODIPY when the thiophene π-linker is present. This could be caused by a reduction in steric hindrance around the BODIPY-thiophene bond, due to the smaller size of the thiophene ring compared with a phenyl ring. This reduction in steric hindrance would allow the BODIPY to rotate to be more in-plane with the thiophene and triphenylamine, increasing orbital overlap and the overall conjugation length of the molecule. However, as the overall characteristic shape of the absorption profile was retained, it is likely that the band was still predominantly a π-π* transition localised on the BODIPY. An increase in the extinction coefficient of the band at higher energy indicates a contribution of the thiophene to the donor/linker based electronic transitions.

While a small increase in donor-acceptor electronic coupling appeared to have occurred for **3**, due to inclusion of the thiophene, the largest difference was seen for **2** and **4**, which have less hindered BODIPYs. For both **2** and **4**, the absorption maxima were shifted toward the NIR by 40 nm compared to **3** and **5** and the overall absorption profile was much broader and less well-defined. There was a reduction of the extinction coefficient, alongside the band broadening. This loss of the typical characteristic features is indicative of a change from a π-π* transition localised on the BODIPY to a more charge-transfer-like transition. The absorption maxima for the lowest energy transition in **2** and **4** were within 4 nm, but **2** had a broader absorption profile (absorbing up to 650 nm), which suggests conjugation increased when the thiophene is present. Removing the methyl substituents in the 1/7-positions of the BODIPY increased the electronic communication between the triphenylamine donors and the BODIPY acceptors. This occured by reducing the steric hindrance for bond rotation around the BODIPY *meso*-position.

In general, the absorption profiles of the dyes broadened and shifted more toward the NIR region as conjugation increased (with increased electronic coupling of the BODIPY acceptor and triphenylamine donor). The inclusion of a thiophene π-linker in **1** caused a bathochromic shift of ca. 15 nm (vs. **3** and **5**) and a broadening of the absorption band. However, the characteristic absorption profile for a BODIPY π-π* transition was retained. In contrast, reducing the steric hindrance for bond rotation around the BODIPY *meso*-position, by modifying the BODIPY, caused a bathochromic shift of ca. 40 nm and a significant broadening of the absorption band with a loss of the characteristic lineshape. On moving from **3** and **5** > **1** > **4** > **2**, it appears that the BODIPY π-π* character decreases and charge transfer character increases.

Generally, the absorption spectra of BODIPY dyes show little solvent dependence.[28] This was investigated for compounds **3** and **4**, which exhibit the largest transformation from a π-π* to a charge-transfer transition. The normalised absorption spectra showed little dependence on solvent polarity, with differences of 4 and 6 nm in the absorption maxima (recorded in DCM and compared to MeCN) for compounds **3** and **4** respectively (Figure 3.15 and Figure 3.16).

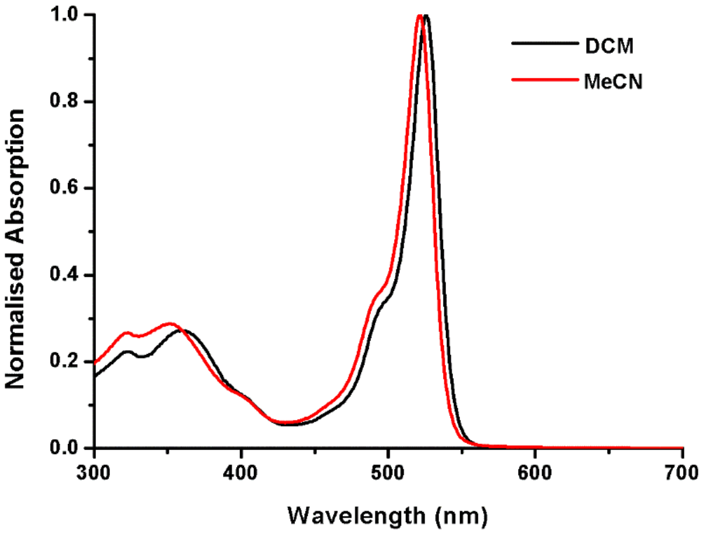

Figure 3.15. Normalised UV-visible absorption spectra of **3** in DCM/MeCN.

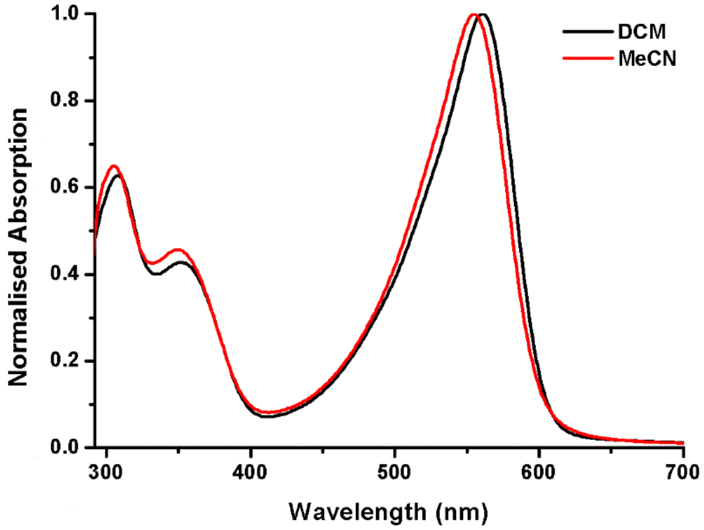

Figure 3.16. Normalised UV-visible absorption spectra of **4** in DCM/MeCN.

3.2.4. Optical Characterisation – Emission Spectroscopy

The photoluminescence of **1-5** was studied in solution and the results are summarised in Table 3.3. The values of $E_{0\text{-}0}$ were estimated from the intercept of the normalised absorption and emission spectra. The overlaid absorption and emission spectra for **2** are shown in Figure 3.17, and the normalised emission spectra of **1** and **3-5** recorded in DCM are shown in Figure 3.18.

Table 3.3. Emission data for **2** in chloroform and **1, 3-5** in dichloromethane (corrected for the detector response) (emission lifetimes ± 0.006).

	λ_{abs} / nm	λ_{em} / nm	$E_{0\text{-}0}$ / eV	Δv / cm^{-1}	τ / ns	Φ^{a}
1	540	560	2.27	507	< 1.5^{b}	0.03
2	565	608	2.11	1252	< 1.5^{b}	-^{c}
3	526	539	2.33	561	5.8	0.38
4	561	600	2.14	1159	2.5	0.15
5	528	547	2.31	658	3.3	0.73^{d}

λ_{abs} is the wavelength of maximum absorbance, λ_{em} is the wavelength of maximum emission, $E_{0\text{-}0}$ is the zero-zero energy (which is the energy difference between the ground and excited states), Δv is the Stokes shift (the separation of λ_{abs} and λ_{em}), τ is the fluoresence lifetime and Φ is the emission quantum yield. [a]Emission quantum yield measurements were carried out in dichloromethane and compared to the quantum yield of Rhodamine 6G in ethanol (0.94). [b]Lifetimes < 1.5 ns are within the instrument response time. [c]Non-emissive in dichloromethane. [d]As reported previously.[29]

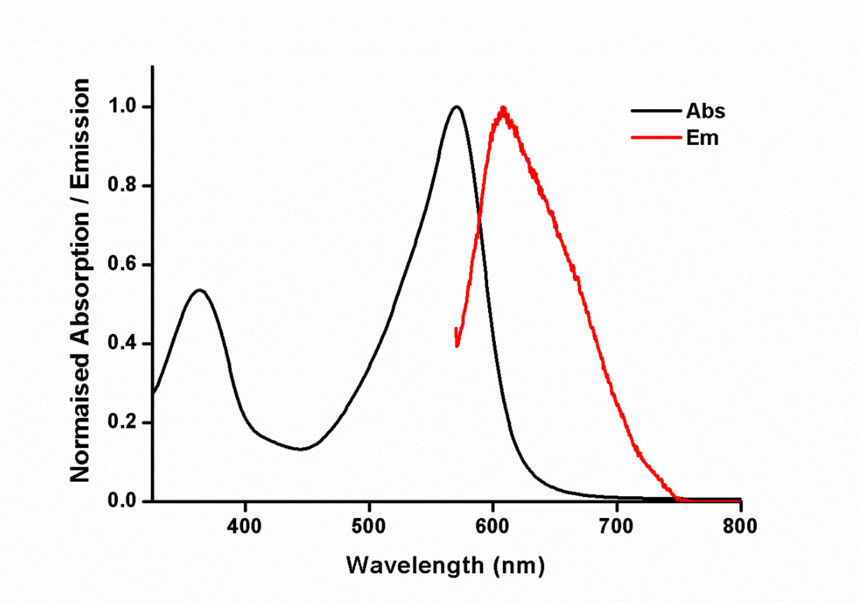

Figure 3.17. Normalised UV-visible absorption/emission spectra of **2** recorded in DCM (absorption) or chloroform (emission, λ_{exc} = 530 nm).

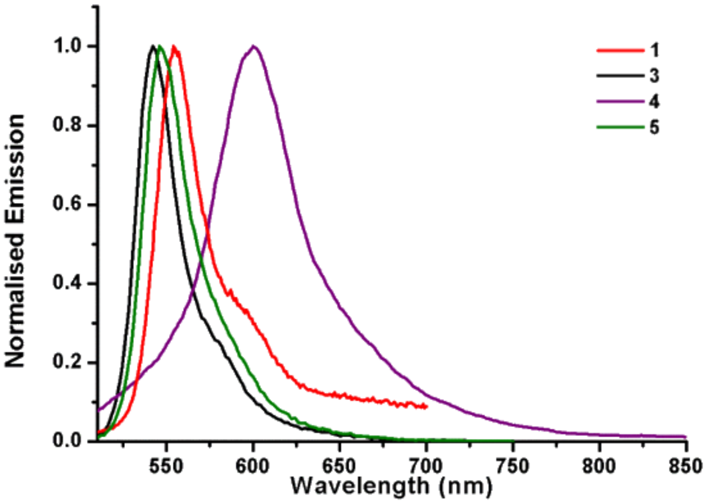

Figure 3.18. Normalised emission spectra of **1, 3, 4** and **5** recorded in DCM.

BODIPY dyes typically exhibit narrow emission bands, that are generally a mirror image of the absorption band. They have a small Stokes shift, which is indicative of little structural change following excitation and vibrational relaxation.[30] For the more sterically hindered dyes **1, 3** and **5** this is the case, where a narrow emission band was seen with a Stokes shift of ca. 500-650 cm$^{-1.}$ In comparison, **2** and **4** had much broader emission bands with larger Stokes shifts of ca. 1200 cm^{-1}.

Emission quantum yields were measured from solutions in DCM using Rhodamine 6G in ethanol as a standard ($\Phi_F = 0.94$). The quantum yield of **5** has been previously reported as 0.73. For BODIPY systems, the quantum yields span a wide range and are very dependent on the nature of the *meso*-substituent. Typical, higher quantum yields are obtained for compounds where rotation around the *meso*-position is restricted.[31] The quantum yields of **1**, **3** and **4** were all lower than **5**, with **3** exhibiting the highest of the new compounds (at $\Phi_F = 0.38$). For **4**, the rotation around the triphenylamine-BODIPY bond was less restricted due to the absence of substituents on the 1/7-positions compared to **3** and there was a decrease in the quantum yield from 0.38 to 0.15. **1** had a much lower quantum yield of 0.03. Rotation around the BODIPY-thiophene bond is less hindered than around the BODIPY-phenyl bond, because of the smaller size of the thiophene ring. It is likely that rotation was more restricted than in **4**, due to the methyl substituents on the 1/7-positions of **1**, yet the quantum yields did not follow the same trend. Alternatively, the donor substituents can quench fluorescence through photoinduced electron transfer to the excited state of the dye. Therefore, the emission of **1** may be quenched due to electron transfer from triphenylamine, which is mediated by the thiophene linker. The bathochromic shift and broadening of the absorption spectrum of **1,** compared to **3**, was consistent with an increase in coupling between the BODIPY and triphenylamine units. The quantum yield of **2** was not measured as it was non-emissive in most solvents (including DCM, which the other samples were recorded in) and it was only very weakly emissive in chloroform. This meant a quantitative comparison could not be made, but qualitatively this was the least emissive sample of the series.

Time-resolved fluorescence spectroscopy was used to study the emission lifetimes, which were determined by single photon counting. Photoinduced electron transfer, facilitated by improved donor-acceptor electronic coupling, would be expected to reduce the emission lifetimes. The lifetime of **4** (2.5 ns) was shorter than **3** (5.8 ns), suggesting that some degree of fluorescence quenching was occurring. This has been attributed to charge transfer from triphenylamine in the absence of the methyl substituents in the 1,7-positions on the BODIPY. For **1** and **2** the emission lifetimes were even shorter. However, a definitive lifetime cannot be reported, as these were recorded as shorter than the instrument response time (< 1.5 ns). This suggests that the thiophene π-linker and reduced BODIPY steric hindrance likely improves electron transfer from triphenylamine to the BODIPY.

As **1**, **3**, **4** and **5** were emissive in multiple solvents, the solvent dependence on the optical properties was studied. This is shown in Figure 3.19 - Figure 3.22 and summarised in Table 3.4. In general, only a small solvent dependence on the wavelength maxima for absorption/emission was observed. The smallest differences were observed for **1** ($\Delta\lambda_{abs}$ = 3 nm, $\Delta\lambda_{em}$ = 5 nm) and the largest differences for **4** and **5** ($\Delta\lambda_{abs}$ = 10 nm (for **4**), $\Delta\lambda_{em}$ = 16 nm (for **4** and **5**)). Only moderate linear correlations could be found between the wavelength maxima and solvent polarity estimated by several methods. The dielectric constant, dipole moment, Kosower's Z values[32] and the Lorentz-Lorenz function[33] were all tested and no single method was equally valid for both absorption and emission. For **3**, the emission lifetime decreased as solvent polarity increased; DCM (5.6 ns) > THF (4.6 ns) > acetone (3.7 ns) > acetonitrile (50 ps < τ_{em} < 1.5 ns). However, the same trend was not observed for **5**, in which the lifetimes were all within a range of 1.4 ns. To more accurately quantify solvent dependence on the absorption/emission properties, a more rigorous test would be needed, with a wider range of solvent polarities. However, this proved difficult, due to the insolubility of these dyes in more non-polar solvents.

Table 3.4. Solvent dependence on the wavelength of maximum absorption/emission, the Stokes shift and emission lifetime (determined by single photon counting, ± 0.006 ns) for **1**, **3**, **4** and **5**.

	Solvent	λabs (nm)	λem (nm)	Δv / cm^{-1}	$τ_{em}$ (ns)
1	Acetone	537	546	306	-
	DCM	536	551	507	<1.5[b]
	MeCN	536	549	441	<1.5[b]
	THF	539	551	404	-
3	Acetone	523	531	288	3.7
	DCM	526	542	561	5.6
	MeCN	522	545	808	<1.5[b]
	THF	524	538	497	4.6
4	Acetone	560	586	792	-
	DCM	561	600	1159	2.5
	MeCN	555	-[a]	-	-
	THF	565	602	1088	-
5	Acetone	522	531	324	4.6
	DCM	528	547	658	3.3
	MeCN	521	533	432	4.7
	THF	526	536	355	3.9

λ_{abs} is the wavelength of maximum absorbance, λ_{em} is the wavelength of maximum emission, E_{0-0} is the zero-zero energy (which is the energy difference between the ground and excited states), Δv is the Stokes shift (the separation of λ_{abs} and λ_{em}), τ is the fluoresence lifetime. [a] Weakly/non-emissive, [b] Lifetimes < 1.5 ns are within the instrument response time.

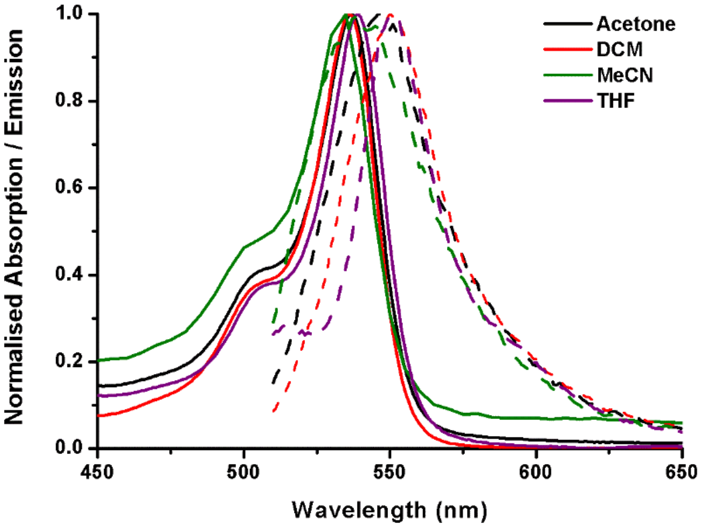

Figure 3.19. Normalised UV-visible absorption/emission spectra of **1** recorded in various solvents (solid lines = absorption, dashed lines = emission).

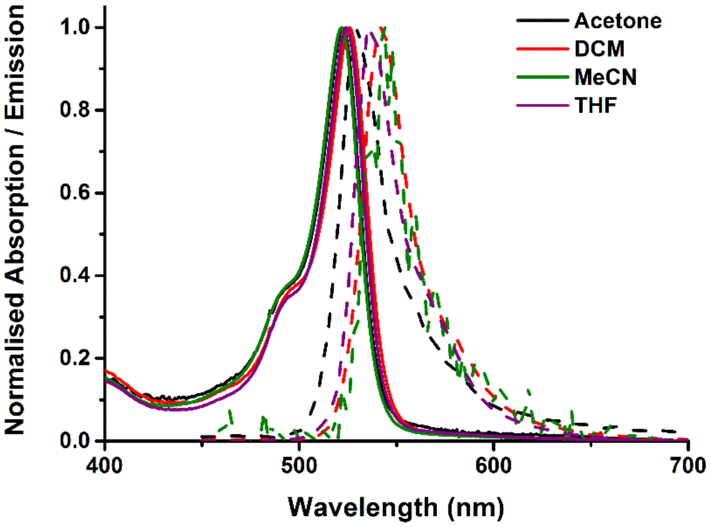

Figure 3.20. Normalised UV-visible absorption/emission spectra of **3** recorded in various solvents (solid lines = absorption, dashed lines = emission).

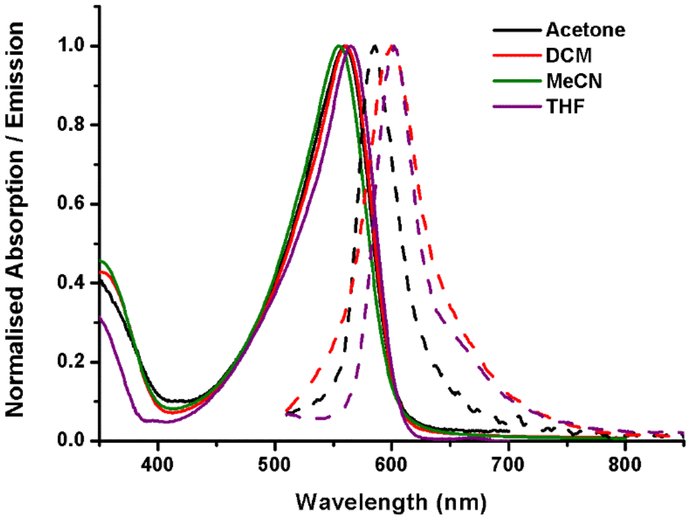

Figure 3.21. Normalised UV-visible absorption/emission spectra of **4** recorded in various solvents (solid lines = absorption, dashed lines = emission).

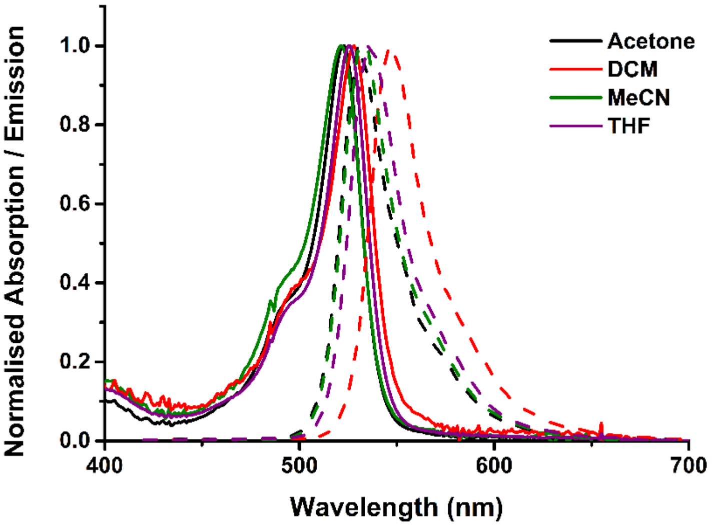

Figure 3.22. Normalised UV-visible absorption/emission spectra of **5** recorded in various solvents (solid lines = absorption, dashed lines = emission).

The shorter-lived emission lifetimes were also measured using a streak-camera setup (an example image is provided in Figure 3.23). However, for **1-5** in solution, the emission lifetimes were longer-lived than the instrument timescale (> 50 ps). The streak-camera setup was also used to study the emission lifetimes of **1-5** when adsorbed onto NiO. Here, the emission was rapidly quenched compared to the dyes in solution, with the emission lifetime occurring on a shorter timescale than the instrument response time (<1 ps). This quenching is evidence of photoinduced electron transfer from the valence band of NiO to the excited dye. It occurs on a rapid timescale, which is common for p-DSCs, where charge transfer is generally efficient (sub-ps).[34]

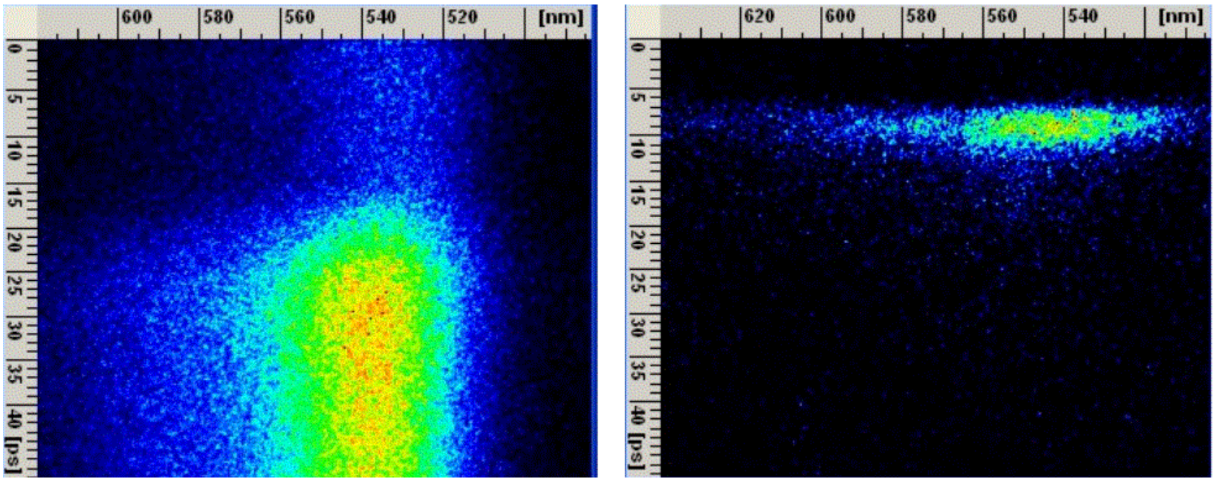

Figure 3.23. Streak camera image of **3** in dichloromethane (left) and adsorbed on NiO (right). The emission lifetime in solution was longer than 50 ps and on NiO the lifetime was shorter than the instrument response time (<1 ps)

3.2.5. Electrochemical Characterisation

The redox potentials of 1 mM solutions of **1-5** in acetonitrile were determined by cyclic voltammetry and differential pulse voltammetry, and the electrochemical data is summarised in Table 3.5. The measurements were calibrated against the Fc/Fc^+ redox couple, used as an internal reference and the potentials were converted to NHE by the addition of 0.63 V.[35] The working electrode used was glassy carbon, the reference electrode was Ag^+/Ag (0.01M $AgNO_3$ in MeCN, calibrated with Fc/Fc^+ as an internal reference) and the counter electrode was a Pt wire

Table 3.5. Summary of electrochemical potentials, **1-5**.

	E_{red} / V		$E_{ox}1$ / V		$E_{ox}2$ / V	
	vs. Fc	vs. NHE	vs. Fc	vs. NHE	vs. Fc	vs. NHE
1[a]	-1.48	-0.85	+0.65[b]	+1.28	+0.75[b]	+1.38
2	-1.29	-0.66	+0.63	+1.26	+0.84[b]	+1.47
3	-1.66	-1.03	+0.62	+1.25	+0.81	+1.44
4	-1.27	-0.64	+0.74	+1.37	+0.99	+1.62
5	-1.63	-1.00	+0.64[b]	+1.27	+0.83[b]	+1.46

E_{red} is the reduction potential and $E_{ox}1$ and $E_{ox}2$ are the first and second oxidation potentials. [a] As previously reported.[16] [b] Unresolved in cyclic voltammogram, peak maximum from DPV.

Cyclic voltammograms of the oxidation and reduction of **2** are provided in Figure 3.24 - Figure 3.25. In the reduction process, the anodic and cathodic peak currents were not equal and the peak separation increased as the scan rate increases. Therefore, this process has been defined as quasi-reversible. Peak currents for the first oxidation process were not equal and the reverse wave for the second process could not be resolved using cyclic voltammetry (thus was determined using DPV), therefore neither process was reversible.

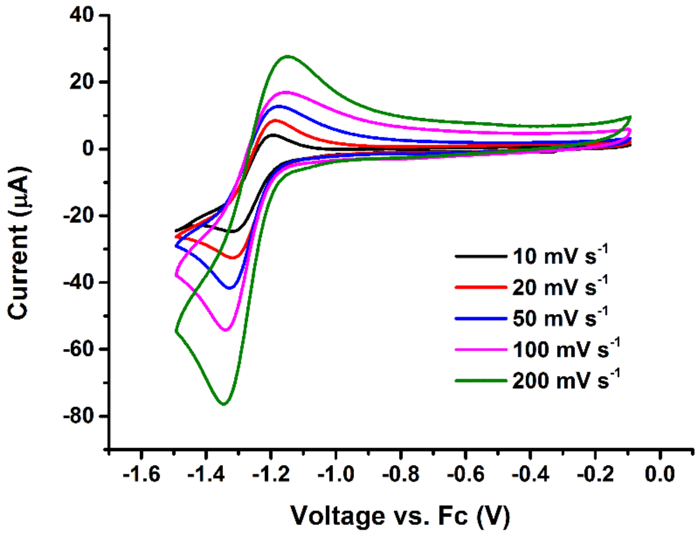

Figure 3.24. Reductive cyclic voltammetry for **2** (1mM) measured in acetonitrile with 100 mM supporting electrolyte (TBA ClO_4).

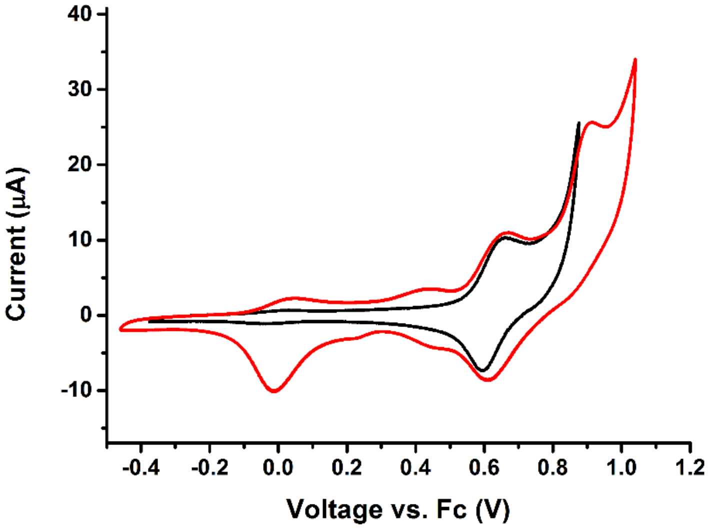

Figure 3.25. Oxidative cyclic voltammetry for **2** (1mM) measured in acetonitrile with 100 mM (TBA ClO_4) supporting electrolyte.

For the reduction of **4** (Figure 3.26), the anodic and cathodic peak currents were equal and peak separation was unaffected by scan rate, consistent with a reversible process. This reversibility, compared to the quasi-reversible process of **2**, could be due to the increased steric bulk of the *tert*-butyl groups protecting the radical species. Scanning in the positive direction revealed two oxidation couples (Figure 3.27) that were close in potential and only distinguishable at higher scan rates, neither of which were reversible.

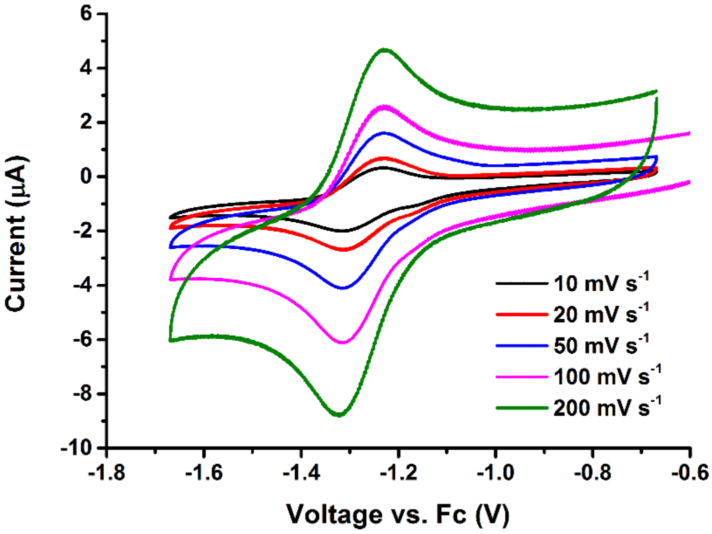

Figure 3.26. Reductive cyclic voltammetry for **4** (1mM) measured in acetonitrile with 500 mM (TBA ClO_4) supporting electrolyte.

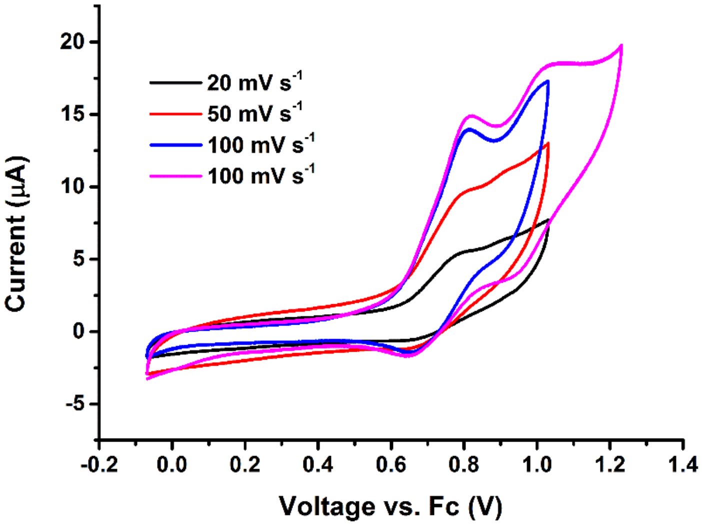

Figure 3.27. Oxidative cyclic voltammetry for **4** (1mM) measured in acetonitrile with 500 mM (TBA ClO_4) supporting electrolyte.

Compound **5** exhibited a quasi-reversible reduction peak (Figure 3.28), at a very similar potential to **3**, where the shift in peak separation on increasing scan rate was small and contained unequal cathodic and anodic peak currents. The oxidation of **5** was broad and accurate redox potentials could not be determined. Instead, DPV was used (Figure 3.29), which revealed two redox couples separated by 190 mV.

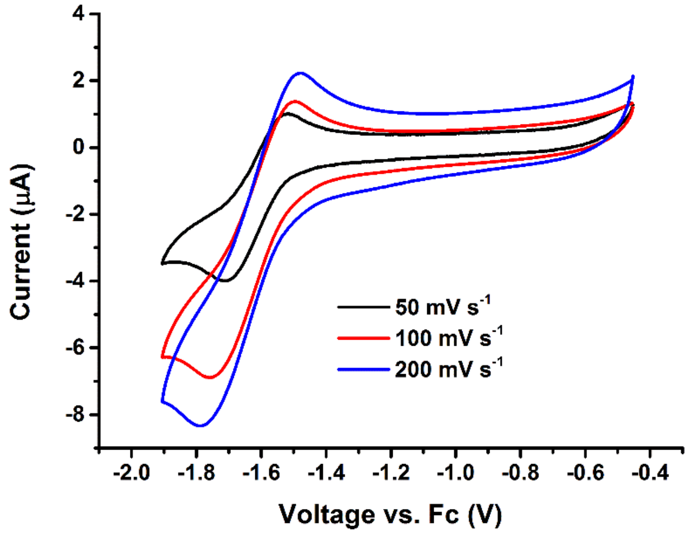

Figure 3.28. Cyclic voltammetry for **5** (1mM) measured in acetonitrile with 500 mM (TBA ClO_4) supporting electrolyte.

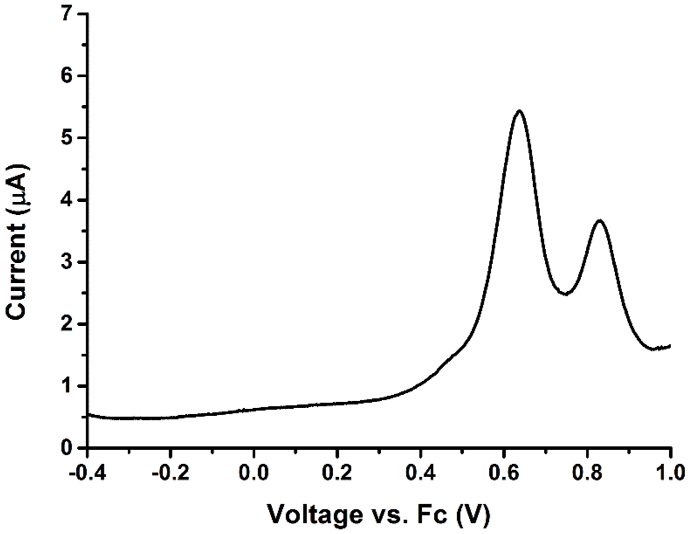

Figure 3.29. DPV of **5** (1mM) measured in acetonitrile with 500 mM (TBA ClO_4) supporting electrolyte.

For each dye **1-5**, scanning in the negative direction gave one reduction peak that has been attributed to reduction of the BODIPY, while scanning in the positive direction gave two oxidation peaks. The first of these has been attributed to oxidation of the BODIPY and the second has been assigned to the oxidation of triphenylamine (or benzoic acid for **5**), by a comparison with model compounds.[36] The reversibility of these processes was dependent on the compound, but, in general, the reduction processes were reversible or quasi-reversible whereas the oxidation peaks were irreversible. In a p-DSC, the dye is reduced by electron transfer from NiO following excitation. Therefore, the most important feature is the reversibility of the reduction process.

By comparing the redox properties, it can be seen that there is little variation in the first oxidation process, which occurred ca. +1.25 V vs. NHE for all compounds (except for **4**, which is shifted by 100 mV to +1.37 V vs. NHE). There is more variation in the second oxidation process, which is based on the triphenylamine donor for **1-4**. The reduction processes of **3** and **5** were very similar (-1.03 and -1.00 V vs. NHE), further supporting the interpretation that the BODIPY acceptor of **3** was electronically decoupled from the triphenylamine donor. This potential is shifted to more positive values for **1** (-0.85 V vs. NHE) and **2** and **4** (-0.66 and -0.64 V vs. NHE). As the LUMO is localised predominantly on the BODIPY in all cases, this shift can be attributed to an improved coupling to the donor, as the linker is introduced or steric hindrance around the BODIPY is reduced.

The redox potentials (determined by electrochemical methods) can be used to calculate driving forces for the electron transfer processes that occur in an operational device. These are a) the electron transfer from the valence band of NiO to the photoexcited dye and b) regeneration of the reduced dye by the redox mediator. These values are summarised in Table 3.6 and represented schematically in Figure 3.30.

Table 3.6. Calculated driving forces for the electron transfer processes occurring within an operational p-DSC. All potentials are reported in V vs. NHE.

	E_{red} / V	E_{0-0} / eV	$E_{red}(S^*/S^-)$ / V	ΔG_{inj} / V	ΔG_{reg} (I^-/I_3^-) / V
1	-0.85	2.27	1.42	-0.88	-0.66
2	-0.66	2.11	1.45	-0.91	-0.47
3	-1.03	2.33	1.30	-0.76	-0.84
4	-0.64	2.14	1.50	-0.96	-0.45
5	-1.00	2.31	1.31	-0.77	-0.81

E_{red} is the ground state reduction potential, E_{0-0} is the zero-zero energy, $E_{red}(S^*/S^-)$ is the excited state reduction potential, ΔG_{inj} is the driving force for charge transfer from NiO to the excited dye and ΔG_{reg} (I^-/I_3^-) is the driving force for regeneration of the reduced dye.

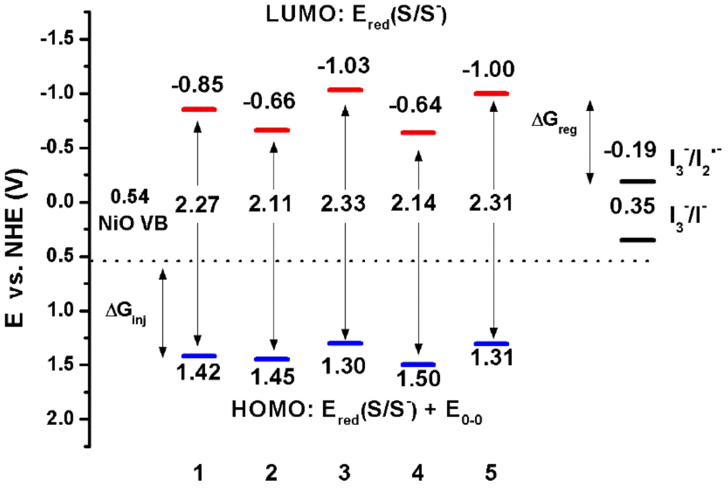

Figure 3.30. HOMO/LUMO energy level diagram for **1-5** alongside the driving forces for electron injection and dye regeneration.

The excited state potentials and driving forces have been calculated as follows:

$$E_{red}(S^*/S^-) = E_{red}(S/S^-) + E_{0-0}$$

Equation 3.1.

$$\Delta G_{inj} = e[E_{VB}(NiO) - E_{red}(S^*/S^-)]$$

Equation 3.2.

$$\Delta G_{reg} = e[E(I_3^-/I_2^{\cdot-}) - E_{red}(S/S^-)]$$

Equation 3.3.

Where E_{VB}(NiO) = 0.54 V vs. NHE[37] and $E(I_3^-/I_2^{\cdot-})$ = -0.19 V vs. NHE.[38]

ΔG_{reg} was highest for the more BODIPY-localised systems (**3** and **5**) and decreased as conjugation increases and the LUMO shifts to more positive potentials. A decrease in this driving force could be expected to favour charge recombination between the reduced dye molecules and holes in the NiO valence band. Qin *et al.*[2] tested a series of triphenylamine-based push-pull dyes with varied HOMO/LUMO energies. They reported efficient regeneration of **P1** (ΔG_{reg} = -0.64 V vs. NHE) and inefficient regeneration of **P3** (ΔG_{reg} = -0.17 V vs. NHE), which had a lower-lying LUMO energy (than **P1**) due to additional malonitrile groups. As the ΔG_{reg} values here were closer to that reported for **P1**, it is likely that regeneration would be thermodynamically favourable for all dyes studied here.

ΔG_{inj} was lower for **3** and **5** and increased as the HOMO shifted to more positive potentials, with the highest driving force for **4** (-0.96 eV). Liu *et al.*[37] designed a series of fluorene based dyes with varying linker units and estimated that $\Delta G_{inj} \approx -0.80$ eV is required for a high hole transfer quantum yield. This could help to explain the lower device efficiencies of **3** and **5** (see **Chapter 3.2.7.**), which had driving forces < -0.80 eV**.**

3.2.6. Computational Studies

HOMO/LUMO distributions were investigated using computational chemistry to help visualise the degree of electronic coupling between the donor/acceptor units. All calculations were carried out using Gaussian 09[39] with either the hybrid B3LYP[40] or CAM-B3LYP[41] exchange functionals and the typical 6-31G(d) basis set. Solvation was treated using the polarisable continuum model (PCM).[42,43] Ground state geometries were optimised and frequency calculations subsequently performed, to ensure that the geometry was a true energy minimum and not a transition state. Afterward, TDDFT calculations were used to calculate the vertical excitation energies.

TDDFT is known to underestimate the vertical excitation energies for systems with significant charge-transfer character.[44] Additionally, it has been recently reported that TDDFT calculations for BODIPY systems tend to overestimate the excitation energies.[45] This lead to difficulties in choosing an appropriate exchange functional/basis set combination. In **Chapter 4.2.5**, calculations were performed on smaller BODIPY compounds using a range of exchange functional/basis set combinations, yet there was only a small variance in the calculated excitation energies. In general, B3LYP/6-31G(d) had the smallest absolute errors, therefore this has been used throughout this chapter (except where noted). While excitation energies were affected by the exchange functional/basis set combination, no significant difference in the calculated orbital distributions was observed for the calculations performed in **Chapter 4** using different methods. The calculations were only used here as a supportive method, to aid the explanation of the experimental results, rather than as a predictive tool where the errors in excitation energies will be more important.

Figure 3.31 summarises the calculations performed on **1-5**. An energy level diagram and the corresponding orbital density plots for the LUMO-1 to the HOMO+1 orbitals are provided. The orbitals predominantly involved in the lowest energy excitation are highlighted in red and these transitions are summarised in Table 3.7.

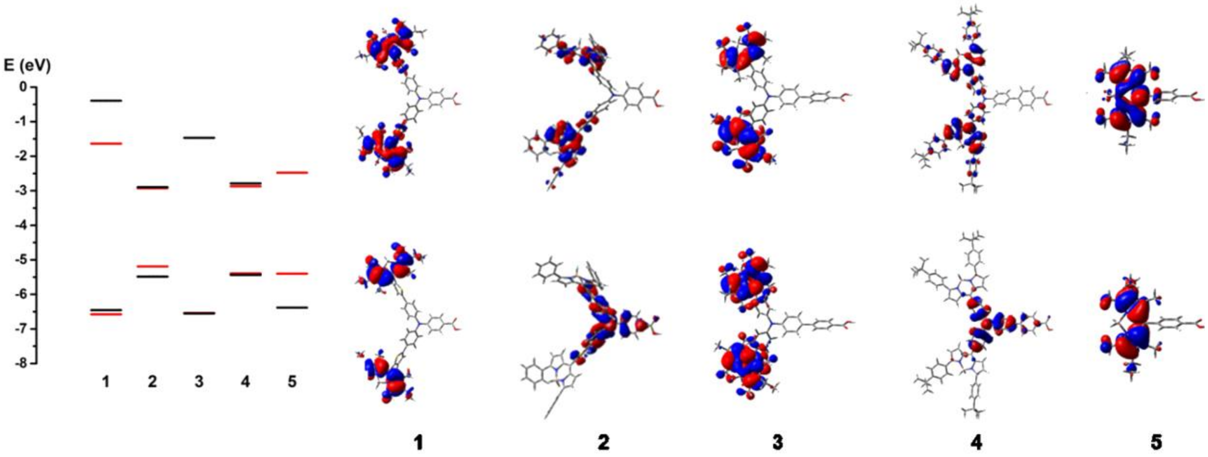

Figure 3.31. Optimised geometry and calculated energy levels for **1**-**5** determined by DFT and TD-DFT (in DCM, solvation treated using the PCM). The orbitals involved in the lowest energy excitation are highlighted in red and the corresponding orbital density plots are provided (bottom = HOMO, top = LUMO).

Experimentally, the absorption spectra of **2** and **4** were consistent with having charge-transfer character (**Chapter 3.2.3**). The calculated HOMO/LUMO distributions for **2** show that the HOMO was distributed across the triphenylamine donor and thiophene π-linkers, while the LUMO was localised on the BODIPY acceptors and the thiophenes. For higher energy orbitals (HOMO-1 and HOMO-2, degenerate in energy), electron density was localised entirely on the BODIPYs. The predicted absorption spectra consisted of excitations that have charge-transfer character, with small contributions from π-π* transitions localised on the BODIPY. Similar features were seen for **4,** where the HOMO was distributed across the triphenylamine donor and benzoic acid anchor and the LUMO was localised on the BODIPY acceptors and the phenyl rings bonded to the BODIPYs. For higher energy orbitals (HOMO-1 and HOMO-2, degenerate in energy), the electron density was localised on the BODIPYs. Predicted excitations again primarily consisted of charge-transfer HOMO-LUMO transitions, with some contribution from π-π* transitions localised on BODIPY. Both of these systems exhibited 'push-pull' characteristics, where charge separation will occur following excitation. This results in the HOMO being localised close to the NiO surface and the LUMO located away from the surface.

Experimentally, the absorption spectra of **1**, **3** and **5** were consistent with π-π* transitions (with some extended conjugation observed for **1**). For **1**, the calculated HOMO/LUMO densities placed the HOMO across the triphenylamine donor/thiophene linkers and the LUMO on the BODIPY acceptors/thiophenes. The HOMO-1 orbital was localised on the BODIPYs, as for **2**. However, unlike **2,** the lowest energy excitation of **1** was predicted to be a π-π* transition from the HOMO-1 to the LUMO, localised on the BODIPY. There were small contributions from charge transfer HOMO to LUMO transitions, but the transitions of **1** primarily had π-π* character. Experimentally, the primary absorption band of **3** and **5** was a π-π* transition localised on the BODIPY. This is supported by calculations, which predict that the HOMO and LUMO for each were localised almost entirely on the BODIPY moieties (there was a small amount of electron density on the phenyl rings of **3**). The lowest energy excitation in each case was from the HOMO to the LUMO, which only had contributions from the π-π* BODIPY transitions.

The dihedral angles between the dipyrromethane plane and the bonded aryl group have been compared to provide a qualitative discussion of donor-acceptor coupling (Table 3.8). A dihedral angle of 90° would put the BODIPY plane perpendicular to the plane of the linker, meaning there could be no orbital overlap and the donor/acceptor would be electronically decoupled. A dihedral angle of 0° would put the BODIPY and linker coplanar, maximising electronic coupling. **3** and **5** had dihedral angles of 87° and 90° respectively, so were the most decoupled of the series. Appending the π-linker for **1** decreased this angle to 84°, possibly due to the smaller size of thiophene compared to benzene. These dihedral angles are smaller in the absence of the 1/7-methyl substituents of the BODIPY. **2** and **4** had dihedral angles of 46° and 53° respectively, with the smaller angle again seen when the thiophene is present. As steric hindrance around the BODIPY *meso*-position decreases (either by inclusion of a π-linker or removing the 1,7-methyl substituents), the ability of the BODIPY to rotate around this bond increases (as seen by smaller dihedral angles). This should increase donor-acceptor coupling, leading to increased charge-transfer character of the predicted transitions (as observed experimentally).

Table 3.7. Calculated principle (singlet) energy transitions determined by TD-DFT for **1-5** and their contributions to the electronic spectra. All transitions were calculated using B3LYP/6-31G(d) in DCM (using the PCM) unless otherwise stated.

Dye	Energy /eV (oscillator strength)	λ /nm	Composition	Contribution (%)
1[a]	2.69 (0.9390)	459	HOMO-1→LUMO	84
	2.70 (0.9257)	458	HOMO-1→LUMO	55
	3.27 (0.2925)	379	HOMO-5→LUMO	3
			HOMO→LUMO	30
			HOMO→LUMO+2	3
	3.29 (0.1342)	376	HOMO→LUMO	52
2	1.92 (0.6845)	645	HOMO→LUMO	95
	2.00 (0.2467)	618	HOMO→LUMO+1	95
	2.36 (0.2470)	525	HOMO-1→LUMO	13
			HOMO-1→LUMO+1	2
			HOMO-2→LUMO	44
3	2.78 (0.4343)	446	HOMO-1→LUMO	45
			HOMO→LUMO+1	47
	2.78 (0.8999)	445	HOMO-1→LUMO	46
			HOMO-1→LUMO	5
			HOMO-1→LUMO	44
	3.47 (0.0224)	357	HOMO-1→LUMO	67
	3.70 (0.0464)	335	HOMO-2→LUMO	48
4	2.09 (0.6505)	592	HOMO→LUMO	99
	2.23 (0.1990)	554	HOMO→LUMO+1	99
	2.34 (0.2488)	529	HOMO-1→LUMO	77
5	2.77 (0.5965)	447	HOMO-1→LUMO	7
			HOMO→LUMO	94
	3.22 (0.1675)	385	HOMO-1→LUMO	92

[a] Calculated using CAM-B3LYP/6-31G(d).

Table 3.8. Average dihedral angles between the BODIPY and the *meso*-substituent, as determined by DFT geometry optimisations.

	BODIPY-Linker Dihedral Angle (°)
1	84
2	46
3	87
4	53
5	90

3.2.7. Device Performances

Devices were constructed from **1-5** by soaking NiO films for 16 hours in a solution of the dye in MeCN (0.3 mM). The electrolyte used was 1 M LiI and 0.1M I_2 in MeCN. The performances of the champion cells (and representative errors for **1, 3, 4** and **5**) are summarised in Table 3.2. These are compared to previously reported values for **P1** as a benchmark.[17] UV-visible absorption spectroscopy was used to confirm the successful adsorption of the dyes onto NiO (Figure 3.32) and to determine the dye loading.

Table 3.9. Photovoltaic performance of champion p-DSCs made from NiO (1.5 μm thickness) sensitised by **1-5**.

	V_{OC} (mV)	J_{SC} (mA cm^{-2})	FF	η (%)	IPCE (%)	Dye loading (mol cm^{-2})
1	95	1.58	0.35	0.05	23	3.35×10^{-5}
2	106	5.87	0.31	0.20	53	1.04×10^{-5}
3	97	1.60	0.38	0.06	27	4.76×10^{-6}
4	109	3.70 ± 0.17	0.35	0.14	44	7.08×10^{-6}
5	95	1.48 ± 0.03	0.36	0.05	20	3.86×10^{-6}
P1	84	5.48	0.34	0.15	64	-

V_{OC} is the open-circuit voltage at the $J = 0$ intercept, J_{SC} is the short-circuit current density at the $V = 0$ intercept, FF is the device fill factor, η is the power conversion efficiency, IPCE is the monochromatic incident photon-to-current conversion efficiency and dye loading is the amount of dye adsorbed onto the NiO surface.

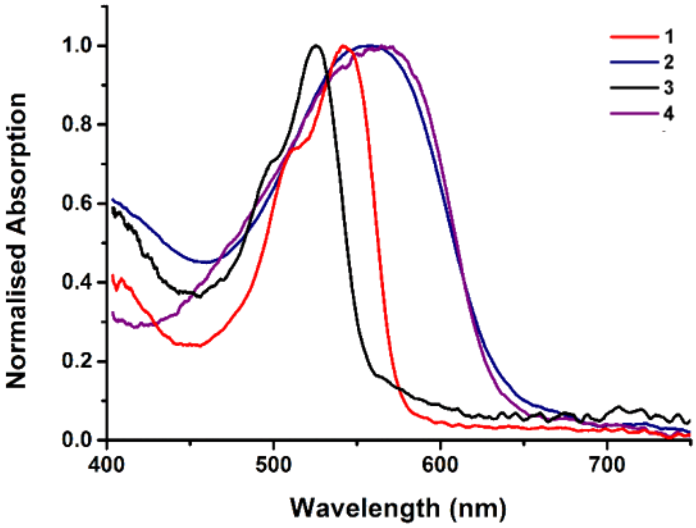

Figure 3.32. Normalised UV-visible absorption spectra for **1-4** adsorbed onto NiO.

For **1-4** adsorbed onto NiO (Figure 3.32), the UV-visible absorption spectra were similar to the dyes in solution (λ_{abs} for each dye was within 2 nm of the dye in solution). There was a general broadening of the absorption profile due to interactions with NiO. **2** and **4** absorbed over a much broader region than **1** and **3**, which was consistent with the solution spectra.

The J-V curves of the champion devices were tested under illumination (Figure 3.33) and in the dark (Figure 3.34). Higher performances were achieved for **2** and **4** compared to **1**, **3** and **5**. For **1**, **3** and **5**, there was little variation in V_{OC} or J_{SC}, with outputs of ca. 95 mV and 1.5 mA cm^{-2} respectively, which appeared to be independent of the dye structure. Surprisingly, **5** performed similar to the more complex dyes **1** and **3**, despite having no donor-acceptor structure. The ground states of **3** and **5** were electronically decoupled from the semiconductor surface and for **1** the absorption was associated with a transition that was decoupled from the surface. It is possible that for these systems, following excitation of the dye, charge transfer from NiO occurs via a through-space interaction with the BODIPY. In comparison, when the HOMO was coupled to the semiconductor surface, then charge transfer from NiO could occur via the triphenylamine donor, following an intramolecular charge transfer from the donor to the acceptor.

Comparatively, devices made from **2** and **4** were more efficient than their more hindered analogues, with three times higher power conversion efficiency obtained for **4** vs. **3** and four times higher for **2** vs. **1**. The highest J_{SC} and power conversion efficiencies were obtained for **2**, where the inclusion of the thiophene π-linker both broadened the absorption band and improved donor/acceptor coupling. Compared to previously reported devices with the benchmark dye **P1**, **4** performed similarly while **2** was more efficient. There was an increase in J_{SC} from 5.48 to 5.87 mA cm^{-2} for **2** compared to **P1**. While the current was lower for **4** (3.70 mA cm^{-2}), similar power conversion efficiencies (0.14% for **4** and 0.15% for **P1**) were obtained due to the higher V_{OC} of **4** (109 vs. 84 mV). The increased J_{SC} for **2**, combined with a higher V_{OC} (106 mV), lead to an improved power conversion efficiency of 0.20% compared to **P1** (0.15%).

It was expected that a longer-lived charge separated state would increase the photocurrent density, by inhibiting recombination between the reduced dye molecules and holes in the valence band of NiO. For these systems, the charge-separated state lifetimes (determined by transient absorption spectroscopy) follow the order of **1** > **2** > **4** > **3** > **5**. In comparison, J_{SC} follows the trend of **2** > **4** > **1** ≈ **3** ≈ **5**, which shows that increasing the lifetime does not necessarily increase the J_{SC}. It appears that for the dyes with limited donor/acceptor coupling, the charge separated state has a longer lifetime. However, the yields of this state are likely to be lower, leading to a lower J_{SC}. Devices constructed from **2** produced the highest J_{SC}, yet the charge separated state lifetime was less than 1 ns, suggesting that regeneration of the reduced dye by the electrolyte is very efficient.

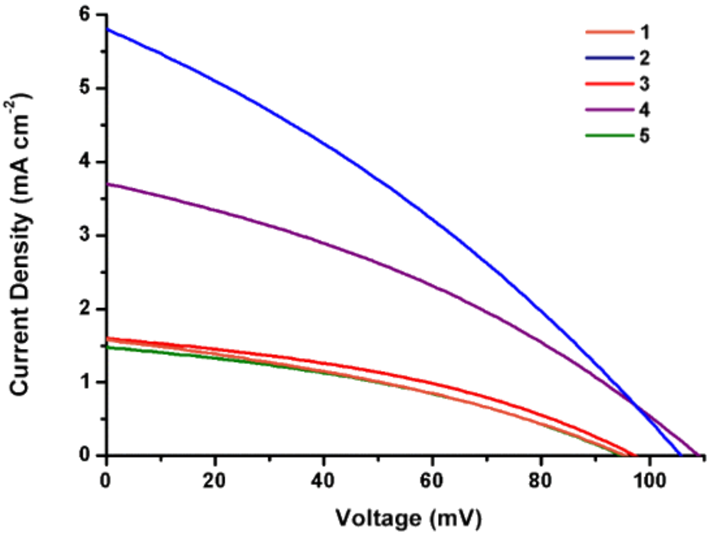

Figure 3.33. J-V curves of p-DSCs constructed using **1-5** tested under illumination (AM1.5, 100 mW cm^{-2}).

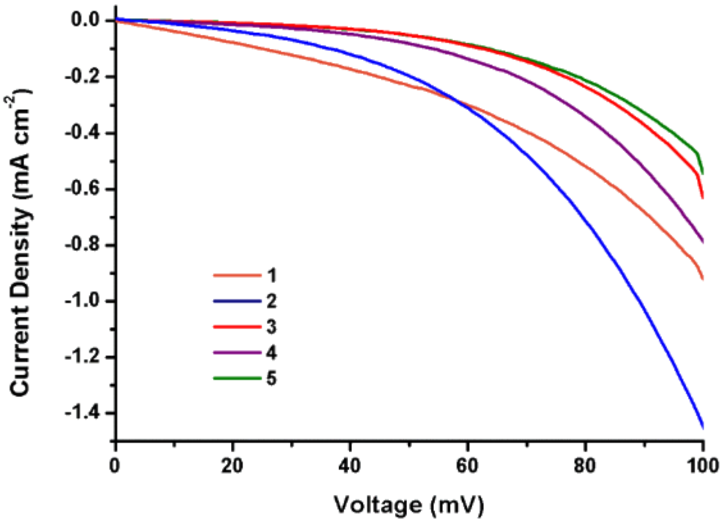

Figure 3.34. J-V curves of p-DSCs constructed using **1-5** tested in the dark.

The IPCE spectra (Figure 3.35) can help to explain the variation in J_{SC} and are used to confirm that excitation of the dye is producing the photocurrent (as the IPCE will match the absorption spectrum of the dye adsorbed onto NiO). For **1**, **3** and **5** the IPCEs were relatively low, at 23%, 27% and 20% respectively. Due to the narrow absorption bands of the dyes, the IPCE only showed a contribution from the dye over a ca. 100 nm region. In comparison, dyes **2** and **4**, which absorbed more broadly over the visible region, had contributions from the dye over a 225 nm range (for **4**) and over the entire 300 nm experimental window (for **2**), producing a higher J_{SC}.

The IPCE of a dye is dependent on several factors:

$$IPCE(\lambda) = LHE(\lambda) \times \eta_{inj}(\lambda) \times \eta_{reg}(\lambda) \times \eta_{CC}(\lambda)$$

Equation 3.4

$$LHE(\lambda) = 1 - 10^{-A(\lambda)}$$

Equation 3.5

Where LHE is the light harvesting efficiency, η_{inj} is the injection efficiency, η_{cc} is the charge collection efficiency and η_{reg} is the regeneration efficiency.

As the LHE is dependent on the optical density of the film, it will be dependent on the dye loading and the extinction coefficient. While these dyes varied in both of those parameters, the optical densities of the NiO films were greater than 1 for each dye (thus LHE > 0.9). Therefore, it is unlikely that LHE was the limiting factor. The ultrafast emission quenching for the adsorbed dyes (Figure 3.23) indicates that electron transfer from NiO to the excited dye was rapid (< ps), despite differences in the rate of intramolecular charge separation and excited state lifetimes. Therefore, η_{inj} is assumed to be efficient. η_{cc} is assumed to be similar for the series, as charge lifetimes were similar.[36] Additionally, the same semiconductor, counter electrode and redox mediator were used, thus charge transport times should be similar. Therefore, it appears that the differences in IPCE were primarily due to differences in regeneration efficiencies.

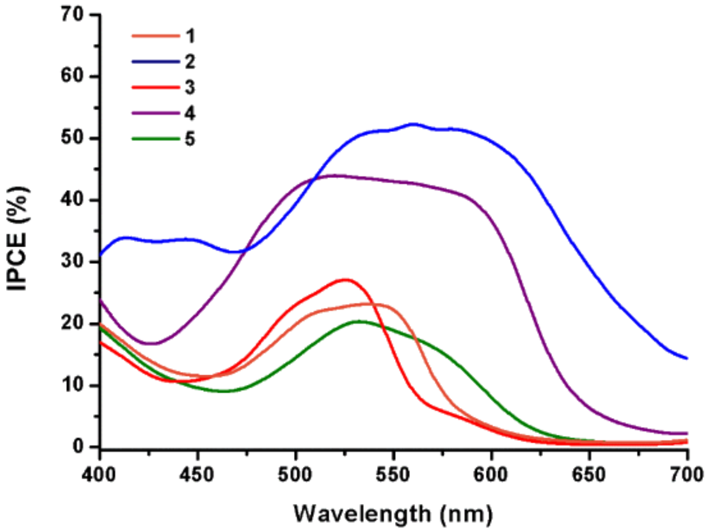

Figure 3.35. IPCE spectra of p-DSCs constructed using **1-5**.

Dye loading was studied using the depletion method, where the absorbance of the dye bath solution was recorded before and after immersion of the NiO films. The change in absorbance could therefore be used to calculate the concentration of dye molecules that had adsorbed onto the NiO surface (Table 3.9) using the known extinction coefficient of the dye. Dye loading amounts were of a similar magnitude and dependent on the donor unit; dyes **4** (7.08×10^{-6} mol cm^{-2}) and **3** (4.76×10^{-6} mol cm^{-2}), which contained the triphenylamine-benzoic acid donor unit, had a lower dye loading than **2** (1.04×10^{-5} mol cm^{-2}) and **1** (3.35×10^{-5} mol cm^{-2}) with the triphenylamine donor.

Surprisingly, the smallest dye (**5**), had the lowest dye loading (3.86×10^{-6} mol cm^{-2}) of the series.

3.2.8. Conclusions

In this chapter, four push-pull triphenylamine-BODIPY dyes and one reference dye have been studied for use in p-type dye-sensitised solar cells, with the highest power conversion efficiency of 0.20% achieved with dye **2**. A method was developed for synthesising donor-acceptor BODIPY dyes, with increased electronic coupling, through the reduction of steric hindrance around the BODIPY *meso*-position.

A comparison of the experimental UV-visible absorption and emission spectra, aided by computational models, revealed a shift in the nature of the main absorption band from a π-π* transition to a charge transfer transition as donor-acceptor coupling was increased. The commonly used thiophene π-spacer served to modestly improve coupling between the donor and acceptor (for **1** compared to **3**). Larger improvements were achieved by reducing steric hindrance around the BODIPY *meso*-position (for **2** vs. **1** and **4** vs. **3**).

p-DSCs were constructed from **1**-**5** and a direct correlation between the charge separated state lifetimes and cell performances was not observed. It was expected that the longer-lived dyes would produce a higher J_{SC}. However, the highest performances were achieved from a dye with a lifetime ($\tau < 1$ ns) that was considerably shorter than the lifetime of **1** (30 ns). Instead, it is possible that decoupling the donor/acceptor units serves to increase the lifetime of the charge-separated state but reduce the yield of formation of this state. Therefore, the dyes with improved coupling have shorter lifetimes and larger yields, leading to a higher J_{SC}.

With regards to future dye design, the most important factor studied here was the electronic coupling of the sensitiser HOMO with the NiO surface. A direct comparison of dyes **1**, **3** and **5** shows that the p-DSC performances were low and essentially independent on dye structure. In each case, the dye HOMO and LUMO were localised on the BODIPY, which is decoupled from the semiconductor surface. For dyes **2** and **4**, the HOMO is localised on the donor group, which was coupled to the semiconductor surface. p-DSCs constructed from these systems performed much more efficiently. Therefore, it is important to avoid decoupling the dye HOMO from NiO to produce efficient devices.

3.3. Experimental

Diphenyliodonium triflate (3.1)

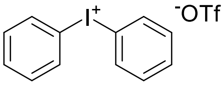

3-Chloroperbenzoic acid (308 mg, 1.785 mmol, 1.1 eqv.) was added to a solution of iodobenzene (0.180 mL, 1.608 mmol, 1 eqv.) in DCM (10 mL). Benzene (0.157 mL, 1.757 mmol, 1.1 eqv.) was added, followed by the dropwise addition of trifluoromethanesulfonic acid (0.428 mL, 4.837 3mol, 3 eqv.). The reaction mixture was stirred at room temperature for 30 minutes before concentrating under vacuum. The addition of diethyl ether resulted in the precipitation of **3.1** as a white solid (527 mg, 68% yield).

^{1}H NMR (300 MHz, $CDCl_3$): δ 8.37 (d, *J* = 7.4 Hz, 4H), 7.80 (t, *J* = 7.4 Hz, 2H), 7.64 (t, *J* = 7.4 Hz, 4H) ppm.

HRMS (ESI): m/z calcd. for $C_{12}H_{10}I$: 280.982, found: 280.980 ($[M]^+$).

Synthesised via the following known method:

M. Bielawski, M. Zhu and B. Olofsson, *Adv. Synth. Catal.*, 2007, **349**, 2610–2618.

2-phenyl-1H-pyrrole (3.2)

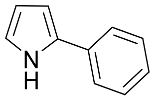

3.1 (527 mg, 1.225 mmol, 1 eqv.) and sodium hydroxide (73.5 mg, 1.838 mmol, 1.5 eqv.) were loaded into a Schlenk tube and purged with 3 vacuum/nitrogen cycles. Pyrrole (2.5 mL) was added and the reaction mixture was heated at 80°C for 18 hours. After cooling to room temperature, ethyl acetate was added (10 mL), the mixture was washed with water (3 x 5 mL) and the organic phase was dried using $MgSO_4$. The crude product was then purified by column chromatography (silica gel, 2:1 hexane:ethyl acetate) to give **3.2** as a white solid (121 mg, 69% yield).

^{1}H NMR (300 MHz, $CDCl_3$): δ 8.46 (s, 1H), 7.50 (d, *J* = 7.4 Hz, 2H), 7.39 (t, *J* = 7.5 Hz, 2H), 7.25 (dd, *J* = 15 Hz, 7.4 Hz, 1H) ppm.

^{13}C NMR ($CDCl_3$, 75 MHz): δ 132.90, 132.26, 129.02, 126.33, 123.98, 118.96, 110.25, 106.08 ppm.

HRMS (ESI): m/z calcd. for $C_{10}H_{10}N$: 144.081, found: 144.080 ($[M+H]^+$).

Synthesised via the following known method:

J. Wen, R.-Y. Zhang, S.-Y. Chen, J. Zhang and X.-Q. Yu, *J. Org. Chem.*, 2012, **77**, 766–771.

Bis(4-tert-butylphenyl)iodonium triflate (3.3)

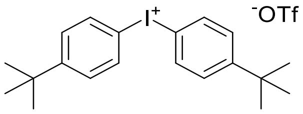

3-Chloroperbenzoic acid (890 mg, 5.16 mmol, 4 eqv.) and iodine (737 mg, 1.29 mmol, 1 eqv.) were dissolved in DCM (15 mL), to which *tert*-butylbenzene (4.5 mL, 12.99 mmol, 10 eqv.) was added. Trifluoromethanesulfonic acid was added dropwise (0.9 mL, 5.16 mmol, 4 eqv.) and the mixture was stirred at room temperature for 30 minutes. The solution was concentrated under reduced pressure and the addition of pentane resulted in the precipitation of **3.3** as a white solid (1.20 g, 76% yield).

^{1}H NMR (300 MHz, $CDCl_3$): δ 7.93 (d, *J* = 8.85 Hz, 4H), 7.45 (d, *J* = 8.85 Hz, 4H), 1.26 (s, 18H) ppm.

HRMS (ESI): m/z calcd. for $C_{20}H_{26}I$; 393.107, found; 393.110 ([M]$^+$).

Synthesised via the following known method:

M. Bielawski, M. Zhu and B. Olofsson, *Adv. Synth. Catal.*, 2007, **349**, 2610–2618.

2-(4-(tert-butyl)phenyl)-pyrrole (3.4)

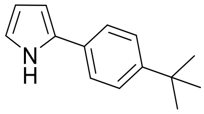

3.3 (1.20 g, 2.21 mmol, 1 eqv.) and sodium hydroxide (190 mg, 4.75 mmol, 2.15 eqv.) were loaded into a Schlenk tube and purged with 3 vacuum/nitrogen. Pyrrole (5 mL) was added and the reaction mixture was heated at 80°C for 18 hours. After cooling to room temperature, ethyl acetate was added (10 mL), the mixture was washed with water (3 × 5 mL) and the organic phase dried using $MgSO_4$. The crude product was then purified by column chromatography (silica gel, 4:1 hexane:ethyl acetate) to afford **3.4** as a white solid (168 mg, 38% yield).

^{1}H NMR (300 MHz, $CDCl_3$): δ 7.47 (m, 4H), 6.83 (m, 1H), 6.47 (m, 1H), 6.19 (m, 1H), 1.34 (s, 9H) ppm.

^{13}C NMR ($CDCl_3$, 75 MHz): δ 149.34, 132.36, 130.21, 125.91, 123.82, 118.57, 110.09, 105.64, 34.64, 31.45 ppm.

FTIR (neat, ATR): v = 3440, 1503, 1268, 1246, 1167, 1127, 1025, 918, 803, 745, 725, 676, 635, 560 cm^{-1}.

HRMS (ESI): m/z calcd. for $C_{14}H_{18}N$; 200.143, found; 200.140 ($[M+H]^+$).

Known compound, synthesised here via a different method:

A. Aliev, D. Almamedova, B. Gasanov and A. Mikhaleva, *Chem. Heterocycl. Compd.*, 1984, **20**, 1117-1119

4-Formyltriphenylamine (3.5)

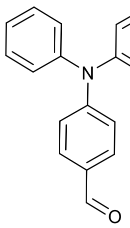

Triphenylamine (10 g, 40 mmol) was dissolved in anhydrous DMF (100 mL) under argon in a three-necked flask and the solution was cooled to 0°C with stirring. Phosphoryl chloride (39 mL, 420 mmol, 11.5 eqv.) was added slowly to the mixture over 1 hour and then the reaction mixture was warmed to 100°C and stirred for 5 hours. After cooling to room temperature, the mixture was carefully neutralised with a 2M NaOH solution. After stirring for a further 30 minutes, the reaction mixture was extracted with ethyl acetate (3 x 200 mL). The organic layer was then dried with Na_2SO_4 and the solvent was evaporated. The crude residue was purified by column chromatography (silica gel, 5:1 petroleum ether:ethyl acetate) to give **3.5** as a beige solid (3.90 g, 36% yield).

^{1}H NMR (300 MHz, $CDCl_3$): δ 9.82 (s, 1H), 7.69 (d, *J* = 8.7 Hz, 2H), 7.41-7.30 (m, 4H), 7.24-7.13 (m, 6H), 7.03 (d, *J* = 8.7 Hz, 2H) ppm.

^{13}C NMR ($CDCl_3$, 75 MHz): δ 190.55, 153.47, 146.27, 131.42, 129.21, 126.43, 125.23, 119.46 ppm.

FTIR (neat, ATR): v = 1688, 1582, 1566, 1503, 1489, 1329, 1304, 1285, 1269, 1220, 1155, 1112, 1075, 824, 756, 695 cm^{-1}.

HRMS (ESI): m/z calcd. for $C_{20}H_{16}NO$; 274.122, found; 274.120 ($[M+H]^+$).

Synthesised via the following known method:

J.-F. Lefebvre, X.-Z. Sun, J. A. Calladine, M. W. George and E. A. Gibson, *Chem. Commun.*, 2014, **50**, 5258–5260.

4,4'-dibromo-4''-formyltriphenylamine (3.6)

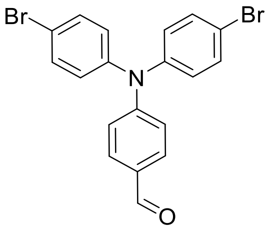

3.5 (1.0 g, mmol) was dissolved in anhydrous DCM (40 mL) under a nitrogen atmosphere. The reaction mixture was cooled to 0°C and bromine (0.375 mL, 7.317 mmol, 2 eqv.) was added dropwise under a flux of nitrogen. The reaction mixture was stirred at room temperature for 6 hours. The reaction was then quenched with aqueous potassium hydroxide and extracted with DCM (3 x 30 mL). The organic phase was washed with water (3 x 20 mL), dried with $MgSO_4$ and evaporated under reduced pressure. The crude residue was purified by column chromatography (silica gel, 1:1 pentane:DCM) to give **3.6** as a yellow solid (930 mg, 59% yield).

^{1}H NMR (300 MHz, $CDCl_3$): δ 9.85 (s, 1H), 7.72 (d, *J* = 8.8 Hz, 2H), 7.46 (d, *J* = 8.8 Hz, 2H), 7.05 (m, 6H) ppm.

^{13}C NMR ($CDCl_3$, 75 MHz): δ 190.48, 152.46, 145.12, 133.04, 131.49, 130.25, 127.50, 120.54, 118.19 ppm.

FTIR (neat, ATR): v = 1700, 1599, 1573, 1485, 1315, 1268, 1220, 1163, 1072, 1005, 817, 656, 530 cm^{-1}.

HRMS (ESI): m/z calcd. for $C_{19}H_{15}Br_2NO$; 429.943, found; 429.941 ($[M+H]^+$).

Synthesised via the following known method:

J.-F. Lefebvre, X.-Z. Sun, J. A. Calladine, M. W. George and E. A. Gibson, *Chem. Commun.*, 2014, **50**, 5258–5260.

4-[bis-(4-bromo-phenyl)-amino]-benzoic acid (3.7)

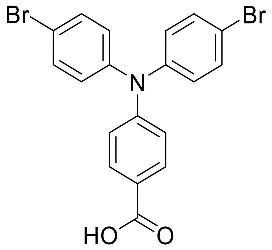

3.6 (250 mg, 0.56 mmol) was suspended in an acetone/water mixture (3:1 v/v, 45/15 mL) and the mixture was heated to reflux. Potassium permanganate (368 mg, 2.24 mmol, 4 eqv.) was slowly added portion wise to the solution, over the course of an hour, and then the mixture was heated at reflex for 4 hours. After cooling to room temperature, the acetone was evaporated and the mixture was diluted with water (40 mL). The solution was filtered to remove any precipitate, which was washed with water. The combined filtrate was acidified with concentrated HCl until precipitation occurred. This precipitate was filtered, washed with water and dried under a flux of air to give **3.7** as a white solid (165 mg, 62% yield).

^{1}H NMR (300 MHz, $CDCl_3$): δ 7.94 (d, *J* = 8.7 Hz, 2H), 7.43 (d, *J* = 8.7 Hz, 4H), 7.04-6.98 (m, 6H) ppm.

^{13}C NMR ($CDCl_3$, 75 MHz): δ 152.05, 145.34, 132.73, 131.71, 127.21, 120.55, 117.78 ppm.

FTIR (neat, ATR): v = 1669, 1603, 1581, 1487, 1313, 1284, 1180, 1072, 1010, 849, 819, 773 cm^{-1}.

HRMS (ESI): m/z calcd. for $C_{19}H_{11}Br_2NO_2$; 443.924, found; 443.920 ($[M-H]^-$).

Synthesised via the following known method:

J.-F. Lefebvre, X.-Z. Sun, J. A. Calladine, M. W. George and E. A. Gibson, *Chem. Commun.*, 2014, **50**, 5258–5260.

4-carboxy-4’,4’’-di-(5-formyl-2-thienyl)triphenylamine (3.8)

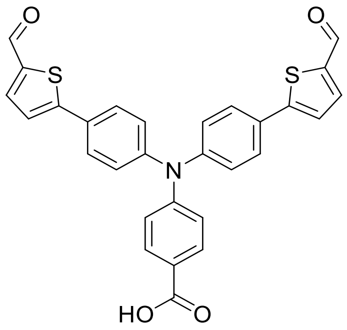

3.7 (163 mg, 0.365 mmol), 5-formyl-2-thienylboronic acid (150 mg, 0.962 mmol, 2.6 eqv.), bis-triphenylphosphinepalladium(II) chloride (13 mg, 1.852 x 10^{-5} mol, 0.05 eqv.) and sodium carbonate (192 mg, 1.811 mmol, 5 eqv.) were loaded into a Schlenk tube and purged with 3 vacuum/nitrogen cycles. The reagents were dissolved in a water/1,2-dimethoxyethane mixture (1:6 v/v, 0.5/3 mL) and this was heated to 90°C for 18 hours. After cooling to room temperature, the reaction mixture was diluted with water (3 mL) and acidified with 0.1M HCl until pH 5. The mixture was extracted with ethyl acetate (3 x 20 mL), the organic phase washed with water (3 x 25mL), dried with $MgSO_4$ and then evaporated under reduced pressure. The crude product was purified by column chromatography (silica gel, 0-2% DCM:MeOH gradient) to give **3.8** as a yellow solid (121 mg, 65% yield).

^{1}H NMR (300 MHz, $CDCl_3$): δ 9.91 (s, 2H), 8.02 (d, *J* = 8.7 Hz, 2H), 7.77 (d, *J* = 4.3 Hz, 2H), 7.65 (d, *J* = 8.7 Hz, 4H), 7.40 (d, J= 4.3 Hz, 2H), 7.22 (d, *J* = 8.8 Hz, 4H), 7.17 (d, *J* = 8.8 Hz, 2H) ppm.

^{13}C NMR ($CDCl_3$, 75 MHz): δ 182.87, 170.38, 153.58, 151.52, 147.34, 142.35, 137.71, 131.99, 129.31, 127.91, 125.69, 123.94, 123.22, 122.21 ppm.

FTIR (neat, ATR): v = 1668, 1591, 1506, 1490, 1445, 1433, 1317, 1267, 1226, 1117, 1058, 801, 770, 673, 545 cm^{-1}.

HRMS (ESI): m/z calcd. for $C_{29}H_{17}NO_4S_2$; 508.068, found; 508.070 ($[M-H]^-$).

Synthesised via the following known method:

J.-F. Lefebvre, X.-Z. Sun, J. A. Calladine, M. W. George and E. A. Gibson, *Chem. Commun.*, 2014, **50**, 5258–5260.

4-(bis(4-(5-(4,4-difluoro-3,5-phenyl-bora-3a,4a-diaza-s-indacene)thiophen-2-yl)phenyl)amino)benzoic acid (2)

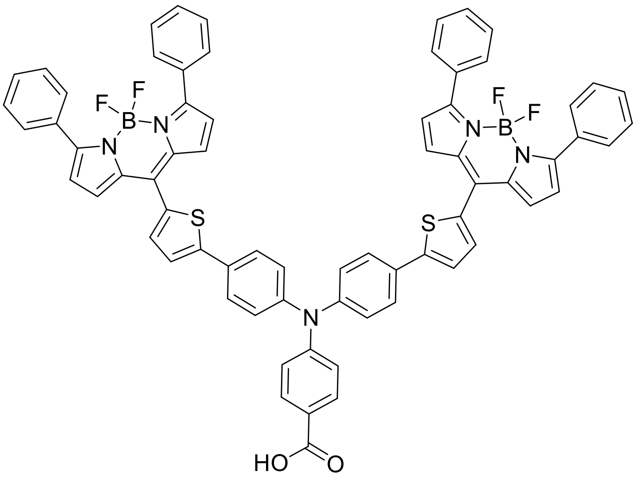

3.2 (53 mg, 0.371 mmol, 4.02 eqv.) and **3.8** (47 mg, 9.22×10^{-5} mol) were loaded into a Schlenk tube and purged with 3 vacuum/nitrogen cycles. Anhydrous DCM (15 mL) was added followed by TFA (1 drop) and the mixture was stirred at room temperature for 18 hours. p-chloranil (47 mg, 0.191 mmol, 4.02 eqv.) was added under a flux of nitrogen and the solution was stirred for a further 30 minutes. DIPEA (0.192 mL, 1.10 mmol, 12 eqv.) was added via syringe and the reaction was stirred for another 10 minutes before adding boron trifluoride etherate (0.228 mL, 1.84 mmol, 20 eqv.). After stirring for four hours, the reaction mixture was washed with water (3 x 10 mL) and the organic layer was dried using $MgSO_4$ and evaporated under reduced pressure. The crude product was purified by column chromatography (silica gel, 0-2% DCM:MeOH gradient) then recrystallised from DCM with the addition of pentane to give **2** as a purple solid (22.5 mg, 21% yield).

^{1}H NMR (700 MHz, $CDCl_3$): δ 7.95 (d, *J* = 8.75 Hz, 2H), 7.79 (dd, *J* = 10, 3 Hz, 8H) 7.61 (d, *J* = 8.5 Hz, 4H), 7.49 (d, *J* = 3.5 Hz, 2H), 7.38 (d, *J* = 3.5 Hz, 2H), 7.36 (d, *J* = 2 Hz, 4H), 7.34 (d, *J* = 2 Hz, 8H), 7.29 (d, *J* = 4.5 Hz, 4H), 7.17 (d, *J* = 8.5 Hz, 4H), 7.12 (d, *J* = 8.75 Hz, 2H), 6.62 (d, *J* = 4.5 Hz, 4H) ppm.

^{13}C NMR (175 MHz, $CDCl_3$): δ 158.8, 151.5, 149.0, 147.1, 146.7, 136.2, 135.7, 134.1, 133.7, 132.8, 132.7, 130.6, 129.6, 129.5, 128.2, 127.4, 125.8, 123.8, 121.7, 120.9, 119.1 ppm.

^{11}B NMR (96 MHz, $CDCl_3$): δ 1.33 (t, *J* = 30 Hz) ppm.

^{19}F NMR (282 MHz, $CDCl_3$): δ -132.35 (q, *J* = 32 Hz) ppm.

FTIR (KBr): v = 3418, 2924, 1651, 1543, 1450, 1381, 1281, 1150, 1072, 764, 964, 610, 463 cm^{-1}.

HRMS (MALDI) m/z: $[M+H]^+$ calcd. for $C_{69}H_{46}B_2F_4N_5O_2S_2$: 1138.32, found: 1138.88.

UV-visible absorption (DCM): λ_{max} (ε, dm^3 mol^{-1} cm^{-1}) = 358 (32,554), 565 (65,700) nm.

4,4'-diformyltriphenylamine (3.9)

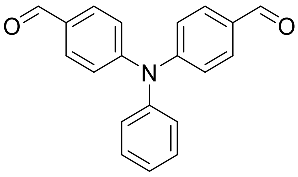

Triphenylamine (10.0 g, 40 mmol) was dissolved in anhydrous DMF (100 mL) under argon in a three-necked flask and the solution was cooled to 0°C with stirring. Phosphoryl chloride (39.0 mL, 420 mmol, 11.5 eqv.) was added slowly to the mixture over 1 hour and then the reaction mixture was warmed to 100°C and stirred for 5 hours under argon. After cooling to room temperature, the mixture was carefully neutralised with a 2M NaOH solution. After stirring for a further 30 minutes, the reaction mixture was extracted with ethyl acetate (3 x 200 mL). The organic layer was dried with Na_2SO_4 and the solvent was evaporated. The crude residue was purified by column chromatography (silica gel, 5:1 petroleum ether:ethyl acetate) to give **3.9** as a beige solid (4.50 g, 37% yield).

^{1}H NMR (300 MHz, $CDCl_3$): δ 9.91 (s, 1H), 7.82-7.76 (m, 2H), 7.46-7.38 (m, 1H), 7.31-7.25 (m, 1H), 7.23-7.16 (m, 3H) ppm.

^{13}C NMR (75 MHz, $CDCl_3$): δ 190.5, 152.0, 145.5, 131.3, 131.3, 130.1, 127.1, 126.3, 122.8, ppm.

FTIR (neat, ATR): v = 1687, 1584, 1505, 1493, 1331, 1291, 1274, 1166, 821, 761, 701, 645, 537 cm^{-1}.

HRMS (ESI): m/z calcd. for $C_{20}H_{17}NO_2$; 302.118, found; 302.120 ($[M+H]^+$).

Known compound, synthesised here via a different method:

1. W. Yang, C. Li, M. Zhang, W. Zhou, R. Xue, H. Liu and Y. Li, *Phys. Chem. Chem. Phys.,* 2016, **18**, 28052-28060
2. Y. Sun, Y. Sun, Q. Pan, G. Li, B. Han, D. Zeng, Y. Zhang and H. Cheng, *Chem. Comm.,* 2016, **52**, 3000-3002

4,4'-[(4-bromophenyl)amino]bis-[benzaldehyde] (3.10)

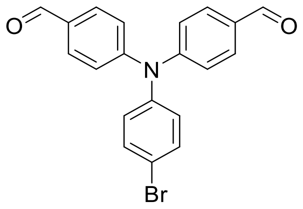

3.9 (500 mg, 1.66 mmol) was dissolved in dry THF (25 mL) under an argon atmosphere. NBS (600 mg, 3.37 mmol) was added under argon at room temperature, then the mixture was heated to reflux for 6 hours. The solvent was evaporated and chloroform (40 mL) was added to the crude residue. The solid was filtered and washed with chloroform. The filtrate was washed with a 10% $NaHCO_3$ aqueous solution (50 mL) and with water (50 mL). The organic layer was dried using $MgSO_4$ and the solvent was evaporated. The product was recrystallised from DCM with the addition of pentane to give **3.10** as a yellow solid (609 mg, quantitative yield).

^{1}H NMR (400 MHz, $CDCl_3$): δ 9.84 (s, 1H), 7.71 (d, *J* = 8.8 Hz, 4H), 7.53 (d, *J* = 8.8 Hz, 2H), 7.21 (d, *J* = 8.8 Hz, 4H), 7.08 (d, *J* = 8.8 Hz, 4H) ppm.

^{13}C NMR (100 MHz, $CDCl_3$): δ 190.4, 151.6, 144.7, 133.3, 131.7, 131.4, 128.7, 123.0, 119.2 ppm.

FTIR (neat, ATR): ν = 1688, 1607, 1573, 1505, 1487, 1309, 1270, 1215, 1164, 1074, 1007, 815, 654, 623 cm^{-1}.

HRMS (ESI): m/z calcd. for $C_{20}H_{16}BrNO_2$; 380.028, found; 380.029 ($[M+H]^+$).

Known compound, synthesised here via a different method:

K. Ghosh, G. Masanta and A. P. Chattopadhyay, *Eur. J. Org. Chem.,* 2009, **26**, 4515-4525

4,4'-[4-(4-carboxyphenyl)phenylamino]bis-[benzaldehyde] (3.11)

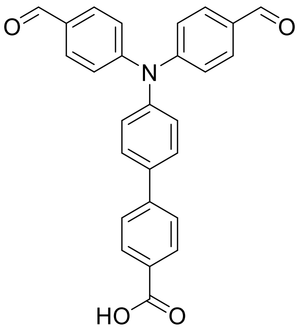

3.10 (84 mg, 0.221 mmol), 4-carboxyphenylboronic acid (120 mg, 0.723 mmol, 3.25 eqv.), bis(triphenylphosphine) palladium(II) dichloride (8 mg, 1.14×10^{-5} mol, 0.05 eqv.) and sodium carbonate (70 mg, 0.660 mmol, 3 eqv.) were loaded in a Schlenk tube and purged with 3 vacuum/nitrogen cycles. Water (1 mL) and 1,2-dimethoxyethane (3 mL) were added and the mixture was heated to reflux for 18 hours under nitrogen. After cooling to room temperature, ethyl acetate (20 mL) and water (10 mL) were added and the mixture was acidified with 0.1 M HCl until pH 5 was reached. The organic phase was extracted with ethyl acetate (3 × 20 mL), washed with water (3 × 25 mL), dried using $MgSO_4$ and evaporated. The product was purified by column chromatography (silica gel, 0 – 2% DCM/MeOH gradient) to give **3.11** as a yellow solid (110 mg, 79% yield).

^{1}H NMR (300 MHz, $CDCl_3$): δ 9.95 (s, 1H), 8.23 (d, *J* = 8.2 Hz, 2H), 7.84 (d, *J* = 8.7 Hz, 4H), 7.73 (d, *J* = 8.2 Hz, 2H), 7.69 (d, *J* = 8.7 Hz, 2H), 7.26-7.32 (m, 6H) ppm.

^{13}C NMR (75 MHz, $CDCl_3$): δ 190.6, 151.8, 145.7, 145.0, 137.3, 131.6, 131.4, 128.9, 126.9, 123.2 ppm.

FTIR (neat, ATR): v = 1685, 1588, 1506, 1429, 1323, 1267, 1164, 1121, 829, 776, 707 cm^{-1}.

HRMS (ESI): m/z calcd. for $C_{27}H_{19}NO_4$; 420.124, found; 420.120 ($[M-H]^-$).

4-(bis(4-(5-(4,4-difluoro-3,5-(4-*tert*-butyl)phenyl-bora-3a,4a-diaza-s-indacene)phenyl)amino)-[1,1'-biphenyl]-4-carboxylic acid (4)

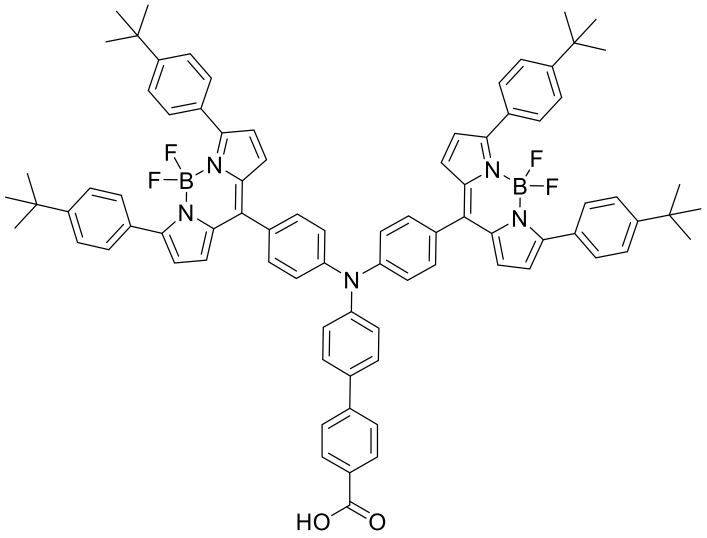

3.4 (158 mg, 0.795 mmol, 4.5 eqv.) and **3.11** (75 mg, 0.176 mmol) were loaded into a Schlenk tube and purged with 3 vacuum/nitrogen cycles. Anhydrous DCM (2 mL) and TFA (2 drops) were added and the mixture was stirred for 16 hours in the dark. p-chloranil (85 mg, 0.342 mmol, 2.0 eqv.) was added under a flux of nitrogen and the mixture was stirred for another 30 minutes. DIPEA (0.38 mL, 2.18 mmol, 10 eqv.) was added and the mixture was stirred under nitrogen for 10 minutes. Finally, boron trifluoride etherate (0.45 mL, 1.51 mmol, 10 eqv.) was added and the mixture was stirred under nitrogen for a further 2 hours. DCM (20 mL) was added to the mixture and the organic layer was washed with water (3 × 10 mL), dried on MgSO$_4$ and evaporated. The crude residue was purified by column chromatography (silica gel, 0 – 2% DCM/MeOH gradient) and recrystallised from DCM with the addition of pentane to give **4** as a purple solid (78 mg, 35% yield).

^{1}H NMR (700 MHz, CDCl$_3$): δ 8.23 (d, J = 8.4 Hz, 2H), 7.89 (d, J = 8.5 Hz, 8H), 7.77 (d, J = 8.5 Hz, 2H), 7.73 (d, J = 8.7 Hz, 2H), 7.62 (d, J = 8.6 Hz, 4H), 7.49 (d, J = 8.6 Hz, 8H), 7.43 (d, J = 8.6 Hz, 2H), 7.39 (d, J = 8.6 Hz, 4H), 7.05 (d, J = 4.3 Hz, 4H), 6.70 (d, J = 4.3 Hz, 4H), 1.10 (s, 36H) ppm.

^{1}H NMR (175 MHz, CDCl$_3$): δ 170.3, 158.5, 152.6, 148.8, 145.6, 145.4, 142.8, 136.2, 130.9, 130.3, 129.8, 129.4, 129.2, 128.8, 128.0, 126.8, 126.2, 125.3, 123.1, 120.9, 34.8, 31.3 ppm.

^{11}B NMR (96 MHz, CDCl$_3$): δ 1.55 (t, J = 30.1 Hz).

^{19}F NMR (282 MHz, CDCl$_3$): δ -132.66 (q, J = 32.2 Hz).

FTIR (KBr): v = 3418, 3127, 2963, 1595, 1568, 1541, 1504, 1472, 1400, 1385, 1285, 1276, 1221, 1184, 1146, 1113, 1070, 1059, 1016, 989, 970, 883, 841, 793, 73.7, 698, 567 cm^{-1}.

HRMS (ESI): m/z calcd. for $C_{83}H_{76}B_2F_4N_5O_2$; 1272.612, found; 1272.610 ($[M-H]^-$).

UV-visible absorption (DCM): λ_{max} (ε, dm^3 mol^{-1} cm^{-1}) = 308 (41,488), 351 (28,237), 561 (65,824) nm.

4-(2,6-diethyl-4,4-difluoro-1,3,5,7-bora-3a,4a-diaza-s-indacene)benzoic acid (5)

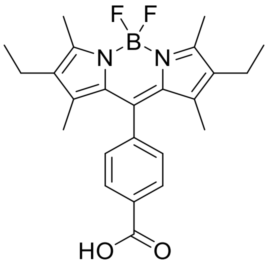

4-carboxybenzaldehyde (50 mg, 0.333 mmol) was loaded into a Schlenk tube and purged with 3 vacuum/nitrogen cycles. 2,4-dimethyl-3-ethylpyrrole (0.1 mL, 0.733 mmol) and anhydrous DCM (2 mL) were then added. TFA (one drop) was added and the mixture was stirred under argon, at room temperature, in the dark, for 3 hours. p-chloranil (90 mg, 0.366 mmol) was added under argon and the mixture was stirred for 45 minutes. DIPEA (1 mL, 5.74 mmol) was added and the mixture was stirred under argon for 30 minutes. Finally, boron trifluoride etherate (0.83 mL, 6.73 mmol) was added and the mixture was stirred under argon for a further hour. DCM (10 mL) was added to the mixture and the organic layer was washed with water (3 x 5 mL), dried using $MgSO_4$ and evaporated. The product was purified by column chromatography (silica gel, 0 – 2% DCM/MeOH gradient) to give **5** as a red solid (72 mg, 51% yield).

^{1}H NMR (300 MHz, $CDCl_3$): δ 8.25 (d, *J* = 8.4 Hz, 2H), 7.45 (d, *J* = 8.4 Hz, 2H), 2.54 (s, 6H), 2.30 (q, *J* = 7.5 Hz, 4H), 1.27 (s, 6H), 0.98 (t, *J* = 7.5 Hz, 6H) ppm.

^{13}C NMR (100 MHz, $CDCl_3$): δ 171.8, 156.4, 154.5, 141.8, 138.6, 138.2, 133.3, 131.1, 130.3, 129.0, 17.2, 14.7, 12.7, 12.0 ppm.

FTIR (KBr): v = 3262, 2965, 2872, 1692, 1610, 1541, 1476, 1404, 1319, 1277, 1190, 1117, 1076, 978, 862, 795, 739, 660, 534 cm^{-1}.

HRMS (ESI): m/z calcd. for $C_{24}H_{29}BF_2N_2O_2$; 425.221, found; 425.220 ($[M+H]^+$).

UV-visible absorption (DCM): λ_{max} (ε, $dm^3\ mol^{-1}\ cm^{-1}$) = 528 (51,964) nm.

Known compound, synthesised here via a different method:

B. Brizet, V. Goncalves, C. Bernhard, P. D. Harvey, F. Denat and C. Goze*, Chem. Eur. J.*, 2014, **20**, 12933-12944

3.4. References

1 P. Qin, H. Zhu, T. Edvinsson, G. Boschloo, A. Hagfeldt and L. Sun, *J. Am. Chem. Soc.*, 2008, **130**, 8570–8571.

2 P. Qin, J. Wiberg, E. A. Gibson, M. Linder, L. Li, T. Brinck, A. Hagfeldt, B. Albinsson and L. Sun, *J. Phys. Chem. C*, 2010, **114**, 4738–4748.

3 M. Wild, J. Griebel, A. Hajduk, D. Friedrich, A. Stark, B. Abel and K. R. Siefermann, *Sci. Rep.*, 2016, **6**, 26263.

4 M. Liang and J. Chen, *Chem. Soc. Rev.*, 2013, **42**, 3453–3488.

5 C.-H. Chang, Y.-C. Chen, C.-Y. Hsu, H.-H. Chou and J. T. Lin, *Org. Lett.*, 2012, **14**, 4726–4729.

6 F. Brunner, N. Marinakis, C. Wobill, M. Willgert, C. D. Ertl, T. Kosmalski, M. Neuburger, B. Bozic-Weber, T. Glatzel, E. C. Constable and C. E. Housecroft, *J. Mater. Chem. C*, 2016, **4**, 9823–9833.

7 Y. Pellegrin, L. Le Pleux, E. Blart, A. Renaud, B. Chavillon, N. Szuwarski, M. Boujtita, L. Cario, S. Jobic, D. Jacquemin and F. Odobel, *J. Photochem. Photobiol. A Chem.*, 2011, **219**, 235–242.

8 J. Warnan, Y. Pellegrin, E. Blart, L. Zhang, A. Brown, L. Hammarström, D. Jacquemin and F. Odobel, *Dye. Pigment.*, 2014, **105**, 174–179.

9 I. R. Perera, T. Daeneke, S. Makuta, Z. Yu, Y. Tachibana, A. Mishra, P. Bäuerle, C. A. Ohlin, U. Bach and L. Spiccia, *Angew. Chem. Int. Ed.*, 2015, **54**, 3758–3762.

10 A. Nattestad, M. Ferguson, R. Kerr, Y.-B. Cheng and U. Bach, *Nanotechnology*, 2008, **19**, 295304.

11 L. Zhu, H. Bin Yang, C. Zhong and C. M. Li, *Dye. Pigment.*, 2014, **105**, 97–104.

12 M. Weidelener, A. Mishra, A. Nattestad, S. Powar, A. J. Mozer, E. Mena-Osteritz, Y.-B. Cheng, U. Bach and P. Bäuerle, *J. Mater. Chem.*, 2012, **22**, 7366–7379.

13 K. A. Click, D. R. Beauchamp, B. R. Garrett, Z. Huang, C. M. Hadad and Y. Wu, *Phys. Chem. Chem. Phys.*, 2014, **16**, 26103–26111.

14 L. Le Pleux, A. L. Smeigh, E. Gibson, Y. Pellegrin, E. Blart, G. Boschloo, A. Hagfeldt, L. Hammarström and F. Odobel, *Energy Environ. Sci.*, 2011, **4**, 2075–

2084.

15 C. J. Wood, M. Cheng, C. A. Clark, R. Horvath, I. P. Clark, M. L. Hamilton, M. Towrie, M. W. George, L. Sun, X. Yang and E. A. Gibson, *J. Phys. Chem. C*, 2014, **118**, 16536–16546.

16 J.-F. Lefebvre, X.-Z. Sun, J. A. Calladine, M. W. George and E. A. Gibson, *Chem. Commun.*, 2014, **50**, 5258–5260.

17 L. Li, E. A. Gibson, P. Qin, G. Boschloo, M. Gorlov, A. Hagfeldt and L. Sun, *Adv. Mater.*, 2010, **22**, 1759–1762.

18 A. B. Nepomnyashchii, S. Cho, P. J. Rossky and A. J. Bard, *J. Am. Chem. Soc.*, 2010, **132**, 17550–17559.

19 R. B. Alnoman, S. Rihn, D. C. O'Connor, F. A. Black, B. Costello, P. G. Waddell, W. Clegg, R. D. Peacock, W. Herrebout, J. G. Knight and M. J. Hall, *Chem. Eur. J.*, 2016, **22**, 93–96.

20 A. Burghart, H. Kim, M. B. Welch, L. H. Thoresen, J. Reibenspies, K. Burgess, F. Bergström and L. B.-Å. Johansson, *J. Org. Chem.*, 1999, **64**, 7813–7819.

21 H. M. Gilow and D. E. Burton, *J. Org. Chem.*, 1981, **46**, 2221–2225.

22 W. Chen, E. K. Stephenson, M. P. Cava and Y. A. Jackson, *Org. Synth.*, 1992, **70**, 151–154.

23 R. D. Rieth, N. P. Mankad, E. Calimano and J. P. Sadighi, *Org. Lett.*, 2004, **6**, 3981–3983.

24 J. Wen, R.-Y. Zhang, S.-Y. Chen, J. Zhang and X.-Q. Yu, *J. Org. Chem.*, 2012, **77**, 766–771.

25 M. Bielawski, M. Zhu and B. Olofsson, *Adv. Synth. Catal.*, 2007, **349**, 2610–2618.

26 D. M. Hossain, Y. Ikegami and T. Kitamura, *J. Org. Chem.*, 2006, **71**, 9903–9905.

27 Y.-S. Yen, W.-T. Chen, C.-Y. Hsu, H.-H. Chou, J. T. Lin and M.-C. P. Yeh, *Org. Lett.*, 2011, **13**, 4930–4933.

28 N. Boens, V. Leen, W. Dehaen, L. Wang, K. Robeyns, W. Qin, X. Tang, D. Beljonne, C. Tonnelé, J. M. Paredes, M. J. Ruedas-Rama, A. Orte, L. Crovetto,

E. M. Talavera and J. M. Alvarez-Pez, *J. Phys. Chem. A*, 2012, **116**, 9621–9631.

29 M. Brellier, G. Duportail and R. Baati, *Tetrahedron Lett.*, 2010, **51**, 1269–1272.

30 A. C. Benniston and G. Copley, *Phys. Chem. Chem. Phys.*, 2009, **11**, 4124–4131.

31 A. Loudet and K. Burgess, *Chem. Rev.*, 2007, **107**, 4891–4932.

32 E. M. Kosower, *J. Am. Chem. Soc.*, 1958, **80**, 3253–3260.

33 S. Stalke, D. A. Wild, T. Lenzer, M. Kopczynski, P. W. Lohse and K. Oum, *Phys. Chem. Chem. Phys.*, 2008, **10**, 2180–2188.

34 A. Morandeira, G. Boschloo, A. Hagfeldt and L. Hammarström, *J. Phys. Chem. B*, 2005, **109**, 19403–19410.

35 V. V. Pavlishchuk and A. W. Addison, *Inorganica Chim. Acta*, 2000, **298**, 97–102.

36 G. H. Summers, J.-F. Lefebvre, F. A. Black, E. Stephen Davies, E. A. Gibson, T. Pullerits, C. J. Wood and K. Zidek, *Phys. Chem. Chem. Phys.*, 2016, **18**, 1059–1070.

37 Z. Liu, D. Xiong, X. Xu, Q. Arooj, H. Wang, L. Yin, W. Li, H. Wu, Z. Zhao, W. Chen, M. Wang, F. Wang, Y. B. Cheng and H. He, *ACS Appl. Mater. Interfaces*, 2014, **6**, 3448–3454.

38 E. A. Gibson, L. Le Pleux, J. Fortage, Y. Pellegrin, E. Blart, F. Odobel, A. Hagfeldt and G. Boschloo, *Langmuir*, 2012, **28**, 6485–6493.

39 Gaussian 09, Revision D.01, M. J. Frisch, G. W. Trucks, H. B. Schlegel, G. E. Scuseria, M. A. Robb, J. R. Cheeseman, G. Scalmani, V. Barone, G. A. Petersson, H. Nakatsuji, X. Li, M. Caricato, A. Marenich, J. Bloino, B. G. Janesko, R. Gomperts, B. Mennucci, H. P. Hratchian, J. V. Ortiz, A. F. Izmaylov, J. L. Sonnenberg, D. Williams-Young, F. Ding, F. Lipparini, F. Egidi, J. Goings, B. Peng, A. Petrone, T. Henderson, D. Ranasinghe, V. G. Zakrzewski, J. Gao, N. Rega, G. Zheng, W. Liang, M. Hada, M. Ehara, K. Toyota, R. Fukuda, J. Hasegawa, M. Ishida, T. Nakajima, Y. Honda, O. Kitao, H. Nakai, T. Vreven, K. Throssell, J. A. Montgomery, Jr., J. E. Peralta, F. Ogliaro, M. Bearpark, J. J. Heyd, E. Brothers, K. N. Kudin, V. N. Staroverov, T. Keith, R. Kobayashi, J. Normand, K. Raghavachari, A. Rendell, J. C. Burant, S. S. Iyengar, J. Tomasi,

M. Cossi, J. M. Millam, M. Klene, C. Adamo, R. Cammi, J. W. Ochterski, R. L. Martin, K. Morokuma, O. Farkas, J. B. Foresman, and D. J. Fox, Gaussian, Inc., Wallingford CT, 2016.

40 A. D. Becke, *J. Chem. Phys.*, 1993, **98**, 1372–1377.

41 T. Yanai, D. P. Tew and N. C. Handy, *Chem. Phys. Lett.*, 2004, **393**, 51–57.

42 S. Miertuš, E. Scrocco and J. Tomasi, *Chem. Phys.*, 1981, **55**, 117–129.

43 M. Cossi and V. Barone, *J. Chem. Phys.*, 2001, **115**, 4708–4717.

44 A. Dreuw and M. Head-Gordon, *Chem. Rev.*, 2005, **105**, 4009–4037.

45 M. R. Momeni and A. Brown, *J. Chem. Theory Comput.*, 2015, **11**, 2619–2632.

Chapter 4 – A Novel Pyrrole Anchoring Unit for BODIPY/Cationic Dyes

4.1. Introduction

4.1.1. Multidentate anchored dyes

As discussed in **Chapter 3**, most dyes for p-DSCs use carboxylic acids as anchoring units. In non-aqueous media (as is the case for most p-DSCs), this is generally not a problem for dye stability. However, with thoughts of moving toward making a p-type dye-sensitised photoelectrochemical cell (pDSPEC), the stability of the dye in an aqueous environment is crucial. It has been previously reported that dyes anchored through carboxylic acids can desorb from NiO in the presence of water.[1,2]

Two commonly used methods for improving dye stability, are a) to replace the carboxylic acid with anchors less prone to hydrolysis (such as phosphonates)[3] or b) to use multiple carboxylic anchoring groups. The first route (a) will be discussed in **Chapter 6**, while the second route (b) has been investigated here. **PMI-6T-TPA**, as investigated by Bach *et al.,*[4] contains two carboxylic acid anchoring groups and has been used as a sensitiser for aqueous p-DSCs over a pH range of 8.15 - 10.91.[5] Therefore, using multiple carboxylates can be a successful route for improving stability. However, it is proposed that the long hydrophobic chains present on **PMI-6T-TPA** are also likely to improve its resistance to hydrolysis. The dye **BH4**, containing two of the same thiophene-PMI chains on one triphenylamine donor (with a single carboxylic acid anchor), was stable at pH 0 for several hours.[6] This could present an issue for an aqueous device, as although the hydrophobic chains may protect the dye/semiconductor from degradation, they could also hinder dye/catalyst interactions.

4.1.2. Motivation

In this chapter, a novel pyrrole-based anchoring motif has been developed and successfully incorporated into three dyes (Figure 4.1). By testing n-heterocycles as a replacement for triphenylamine, the donor ability could be tuned. For dyes **6** and **7**, a BODIPY chromophore was chosen to provide a distinct spectroscopic handle, having been thoroughly characterised for dyes **1-5** in **Chapter 3**. The linker unit has been varied between phenyl and thiophene groups, to probe the effect this has on device performances. For **8**, a cationic indolium acceptor unit has been used as the electron acceptor. This was successfully used previously for the dye **CAD 3**,[7] which produced a record J_{SC} of 8.21 mA cm^{-2}. These dyes are relatively simple and do not follow the typical triphenylamine-based ‘push-pull’ structure. This was intended as a further test to investigate whether smaller molecular dyes can produce efficient devices.

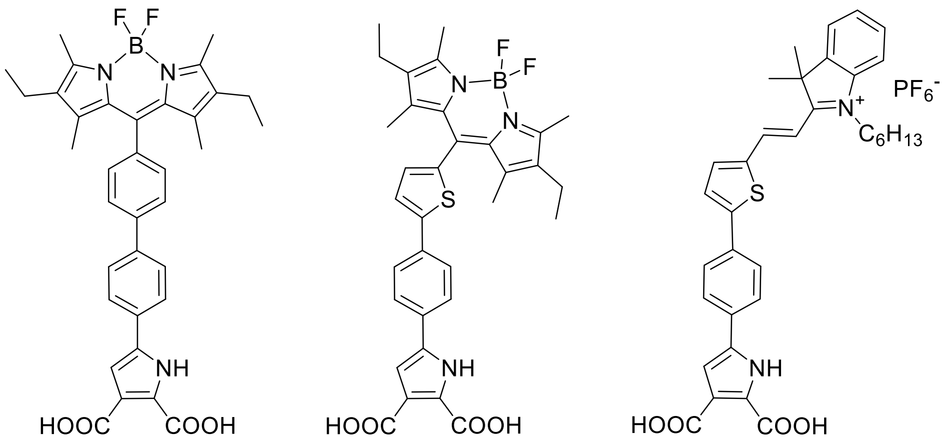
6 **7** **8**

Figure 4.1. Chemical structure of the pyrrole-anchored dyes discussed in this chapter.

4.2. Results and Discussion

4.2.1. Synthesis

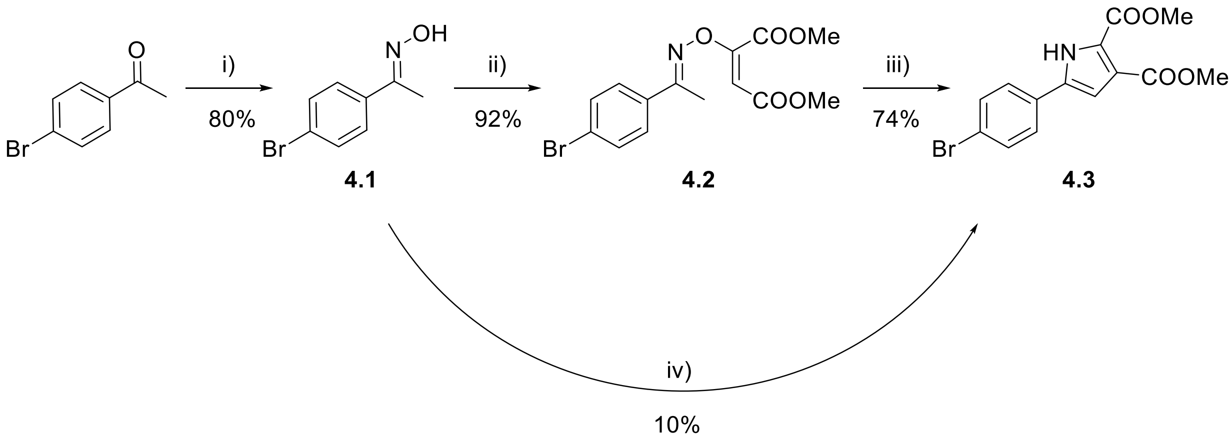

Figure 4.2. Synthesis of the dicarboxylate pyrrole anchor via a one or two-pot route. i) $HONH_2$, pyridine, EtOH, 80%; ii) DABCO, dimethyl acetylenedicarboxylate, DCM, 92%; iii) toluene, microwave irradiation (170 °C, 45 minutes), 74%; iv) DABCO, dimethyl acetylenedicarboxylate, toluene, microwave irradiation (85 °C, 15 minutes then 170 °C, 45 minutes), 10%.

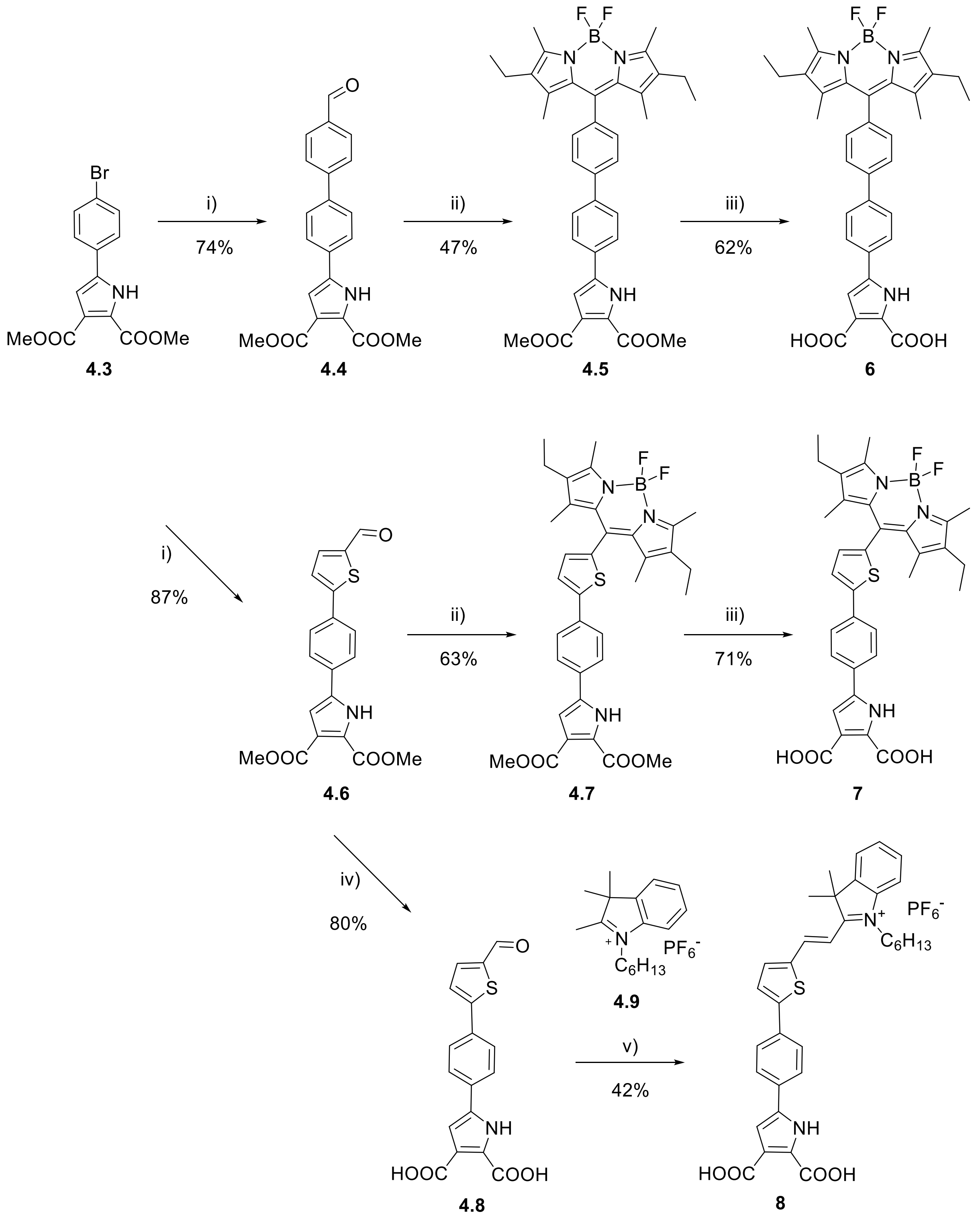

Figure 4.3. Synthesis of **6-8**. i) 5-formyl-2-thienylboronic acid or 4-formylphenylboronic acid, Na_2CO_3, $Pd(PPh_3)_2Cl_2$, H_2O, DME, 74% or 87%; ii) a) 2,4-dimethyl-3-ethylpyrrole, TFA, DCM; b) p-chloranil; c) DIPEA; d) $BF_3{\cdot}OEt_2$, 47% or 63%; iii) a) TMSBr, MeCN; b) MeOH; c) DIPEA, DCM, rt, 15 min; d) $BF_3{\cdot}OEt_2$, 62% or 71%; iv) MeOH/H_2O, NaOH, 80%; v) piperidine, MeCN, 42%.

The synthetic route to **6-8** started with the synthesis of the pyrrole anchoring unit, following a method previously reported by Ngwerume *et al*.[8] **4.1** was prepared from the addition of hydroxylamine to 4-bromoacetophenone and was purified by an aqueous workup to give the product in 80% yield. Two routes were tested for synthesising **4.3**. The first route was a one-pot formation of the vinyl oxime by the DABCO catalysed addition of the oxime to the alkyne (at 85 °C, 15 minutes), followed by thermal rearrangement (170 °C, 45 minutes) to the pyrrole. The second route was a two-step synthesis, where the vinyl oxime (**4.2**) was synthesised at room temperature overnight and isolated prior to thermal rearrangement. The one-pot route only produced the pyrrole in low yield (≤ 10%) after chromatographic purification, possibly due to hydrolysis of the vinyl oxime that is more likely to occur at higher temperatures. Following the two-step route, **4.2** was synthesised by the DABCO catalysed addition of dimethyl acetylenedicarboxylate to **4.1,** to afford the product as a colourless oil in 92% yield as an E:Z isomer mixture (10:1 estimated from ^{1}H NMR). The thermal rearrangement of **4.2** to **4.3** was carried out by heating a solution of the vinyl oxime in anhydrous toluene at 170 °C for 45 minutes in a microwave reactor. This gave the product as a white solid in 74% yield after chromatographic purification.

From **4.3**, the two aldehyde precursors **4.4** and **4.6** were synthesised via Suzuki couplings with 4-formylphenyl boronic acid and 5-formyl-2-thienyl boronic acid, in yields of 74% and 63% respectively. The two ester-protected BODIPY dyes, **4.5** and **4**.**7**, were synthesised from these aldehydes by the condensation of 2,4-dimethyl-3-ethylpyrrole, catalysed by TFA, to form the dipyrromethane. These were oxidised to the dipyrromethene using p-chloranil. Deprotonation was achieved using DIPEA and boron was coordinated using boron trifluoride diethyl etherate to give **4.5** and **4.7** in yields of 47% and 63% respectively.

Hydrolysis of the methyl esters to produce the final dyes, **6** and **7**, proved difficult. The complete hydrolysis of both anchors required harsh conditions (12 hours reflux in methanolic NaOH) under which the BODIPY was not stable. Trimethylsilyl bromide (TMSBr) is commonly used as a selective reagent for the hydrolysis of phosphonate esters.[9] Here, it was used for the hydrolysis of the carboxylate esters of **4.5** and **4.7** via refluxing with a large excess (40 eqv.) of TMSBr for 7 days in acetonitrile under an inert atmosphere. The BODIPY was stable (as monitored by UV-visible absorption spectroscopy) during the initial reflux. However, after the addition of methanol to hydrolyse the silyl esters, decoordination of boron was observed. Immediate treatment of the crude product with diisopropylethylamine and boron trifluoride in anhydrous DCM reformed the coordinated BODIPY. Due to the high polarity of the products, chromatographic purification on silica or alumina gel was not successful. Therefore, size exclusion chromatography (Sephadex, MeOH eluent) followed by recrystallisation was employed to yield the hydrolysed dyes **6** and **7**.

Anchor hydrolysis/deprotection is often the final synthetic step in dye synthesis for p-DSCs,[10,11] as if an acid group is present during all steps of a synthetic route, the increased polarity can cause difficulties with purification. However, in this case, the difficulties encountered with hydrolysing the anchoring unit and the poor stability of the BODIPY under typical hydrolysis conditions lead us to investigate a synthetic route where the anchor is hydrolysed prior to condensation of the acceptor group. BODIPY synthesis leads to a diverse range of products that need to be separated chromatographically. As the doubly hydrolysed pyrrole would not easily move on silica/alumina, an alternative acceptor unit was chosen as a comparison. The cationic indolium unit had been previously successfully used in p-DSCs,[7,12] therefore, this acceptor group was chosen for **8**.

The synthesis of **8** started from the hydrolysis of **4.6** in refluxing methanolic NaOH, followed by an acidic workup and extraction with ethyl acetate, to give **4.8** in 80% yield. No further purification was required. 1-hexyl-2,3,3-trimethyl-*3H*-indol-1-ium PF_6 (**4.9**) was synthesised in two steps from the alkylation of 2,3,3-trimethylindolenine using iodohexane and a subsequent anion exchange of the iodide salt with $NaPF_6$. This gave the alkylated PF_6 salt (**4.9**) in an overall yield of 65%. **8** was synthesised by the Knoevenagel condensation, catalysed by piperidine, of **4.8** and **4.9** in refluxing anhydrous acetonitrile. Purification was achieved through a series of recrystallisations. The aldehyde starting material was insoluble in DCM, therefore after an aqueous workup, the crude residue was dissolved in DCM and filtered to remove any unreacted aldehyde. The unreacted indolium (an excess of 2.5 eqv. was used in the reaction) was soluble in diethyl ether and was removed by three sequential recrystallisations from DCM with the slow diffusion of diethyl ether. This was followed by a final recrystallisation from DCM, with the addition of pentane, to give **8** as a purple solid in 42% yield.

4.2.2. Structural Characterisation

6-**8** have been structurally characterised using ^{1}H NMR/^{13}C NMR spectroscopy. The ^{1}H NMR assignments are summarised in Table 4.1, with protons labelled as shown in Figure 4.4. Due to the limited solubility of **6** and **7** following ester hydrolysis, these have been characterised as their methyl-ester protected forms (**4.5** and **4.7**).

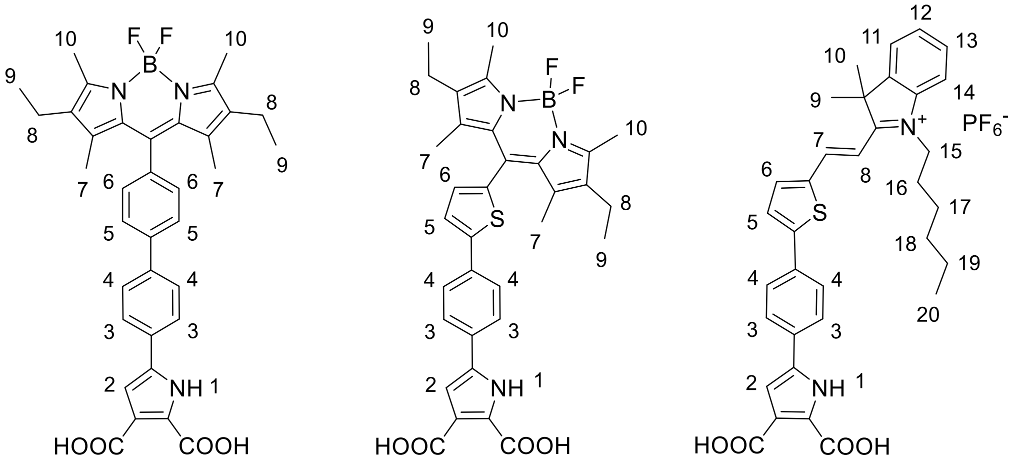

6 **7** **8**

Figure 4.4. Proton labelling system for **6**-**8**.

As the BODIPYs were structurally simpler than the cationic dye **8**, their spectra could be assigned through comparison of the ^{1}H NMR spectra (Figure 4.5 and Figure 4.6) with the spectra of the precursors. The ^{1}H NMR spectrum of **8** was more complex (Figure 4.7) and the assignment was aided using COSY to identify the coupled protons (Figure 4.8).

Table 4.1. ^{1}H NMR assignments for **4.5, 4.7** (300 MHz, $CDCl_3$) and **8** (700 MHz, DMSO-d6).

4.5				**4.7**				**8**				
H_x	m, H	δ / ppm	J / Hz	**H_x**	m, H	δ / ppm	J / Hz	**H_x**	m, H	δ / ppm	J / Hz	COSY
1	s, 1H	9.60	-	**1**	s, 1H	9.52	-	**1**	s, 1H	11.82	-	-
2	d, 1H	7.01	2.9	**2**	d, 1H	6.98	3.1	**2**	d, 1H	7.01	1.8	-
3[a]	d, 2H	7.77	8.3	**3**	d, 2H	7.70	8.3	**3**	d, 2H	8.04	8.3	c
4	d, 2H	7.68	8.3	**4**	d, 2H	7.59	8.3	**4**	d, 2H	7.82	8.3	c
5[a]	d, 2H	7.77	8.3	**5**	d, 1H	7.40	3.6	**5**	d, 1H	8.21	4.1	b
6	d, 2H	7.38	8.0	**6**	d, 1H	6.97	3.6	**6**	d, 1H	7.92	4.1	b
7	s, 6H	1.36	-	**7**	s, 6H	1.63	-	**7**	d, 1H	8.72	15.6	a
8	q, 4H	2.31	7.5	**8**	q, 4H	2.33	7.5	**8**	d, 1H	7.28	15.6	a
9	t, 6H	0.99	7.5	**9**	t, 6H	1.01	7.5	**9 - 10**	s, 6H	1.80	-	-
10	s, 6H	2.55	-	**10**	s, 6H	2.54	-	**11-14**	m, 2H m, 2H	7.88 7.51	- -	d
								15	t, 2H	4.63	7.2	-
								16-19	m, 4H m, 4H	1.57 1.33	- -	- -
								20	t, 3H	0.87	6.8	-

Where; H_X = the assigned proton, labelled as in Figure 4.4, δ = the chemical shift of the peak, m = peak multiplicity, H = relative number of protons, *J* = peak coupling constant and COSY = cross-peak as determined using COSY (labelled as in Figure 4.8). [a] Signals overlapped as a 4H doublet.

The ^{1}H NMR spectrum of **4.5** is provided in Figure 4.5. The four phenyl proton environments appeared as three doublets with integrations of 4:2:2. Two of the signals overlapped to form the region with an integration of 4H. H_3 and H_4 were assigned to the peaks at 7.77 and 7.68 ppm respectively, as these have similar chemical shifts as the phenyl peaks of **4.7** (Figure 4.6). An additional phenyl signal at 7.38 ppm was assigned to H_6, while H_5 overlapped with the peak at 7.77 ppm, to produce an integration of 4. These peaks have a coupling constant of 8 - 8.3 Hz, which is indicative of a $^3J_{HH}$ ortho-coupling in phenyl protons. H_2 appeared as a doublet at 7.01 ppm, with a smaller coupling constant of 2.9 Hz and the pyrrole proton H_1 was assigned to the broad singlet at 9.60 ppm. In the aliphatic region, the methyl substituents of the BODIPY appeared as two 6H singlets at 2.55 and 1.36 ppm. The ethyl substituents appeared as a 4H quartet and a 6H triplet, at 2.31 and 0.99 ppm respectively, with a coupling constant of 7.5 Hz.

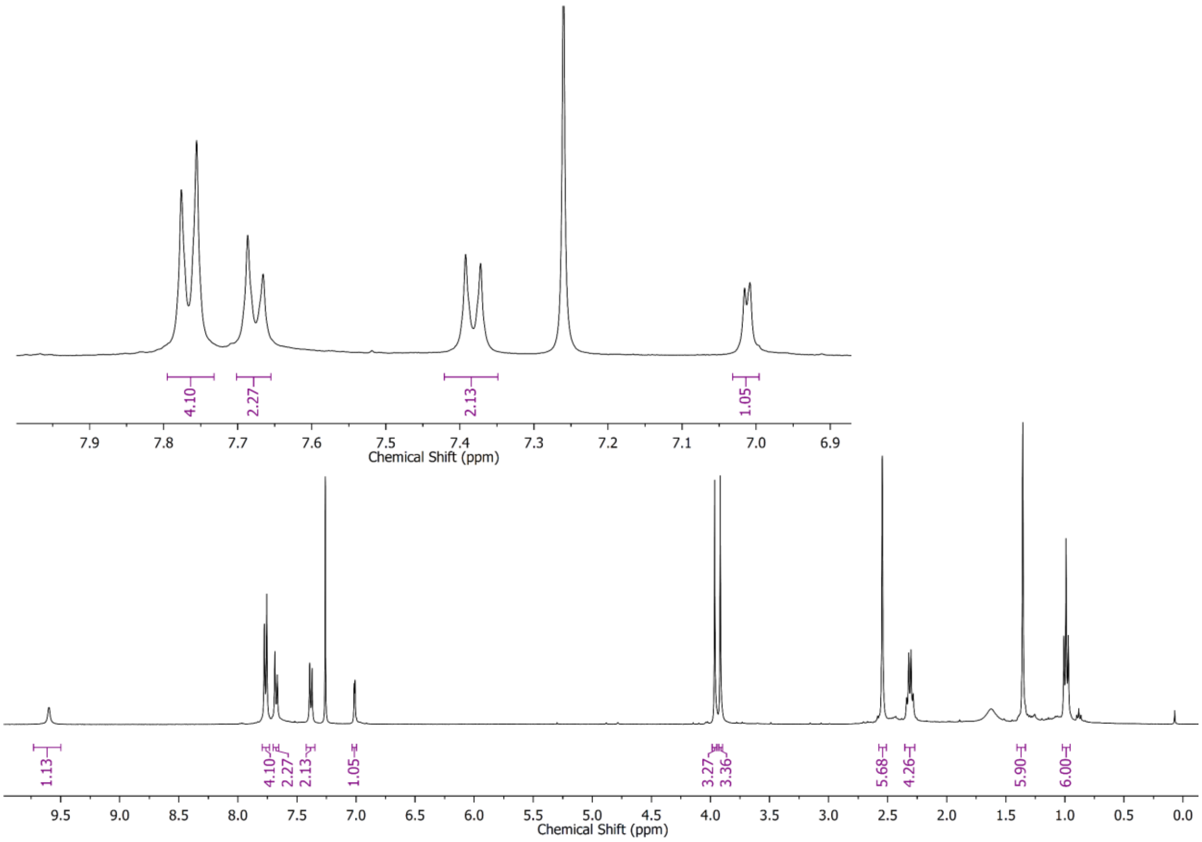

Figure 4.5. ^{1}H NMR spectrum of **4.5** (300 MHz, CDCl$_3$).

The ^{1}H NMR spectrum of **4.7** is provided in Figure 4.6. The two phenyl environments were assigned to the two 2H doublets at 7.70 and 7.59 ppm, for H_3 and H_4 respectively, with a coupling constant of 8.3 Hz. H_2 on the pyrrole heterocycle was assigned to a 1H doublet at 6.98 ppm, with a coupling constant of 3.1 Hz, due to its similarity to the analogous proton in **4.5**. This reveals that the electronic properties of the heterocycle appear largely unaffected by differences in the π-linker. The two thienyl protons, H_5 and H_6, appeared as 1H doublets at 7.40 and 6.97 ppm respectively, with the latter overlapping slightly with H_2. Again, the pyrrole proton H_1 was assigned to a broad singlet at 9.52 ppm. In the aliphatic region, the methyl substituents of the BODIPY appeared as two 6H singlets at 2.54 and 1.63 ppm. The ethyl substituents appeared as a 4H quartet and a 6H triplet, at 2.33 and 1.01 ppm respectively, with a coupling constant of 7.5 Hz.

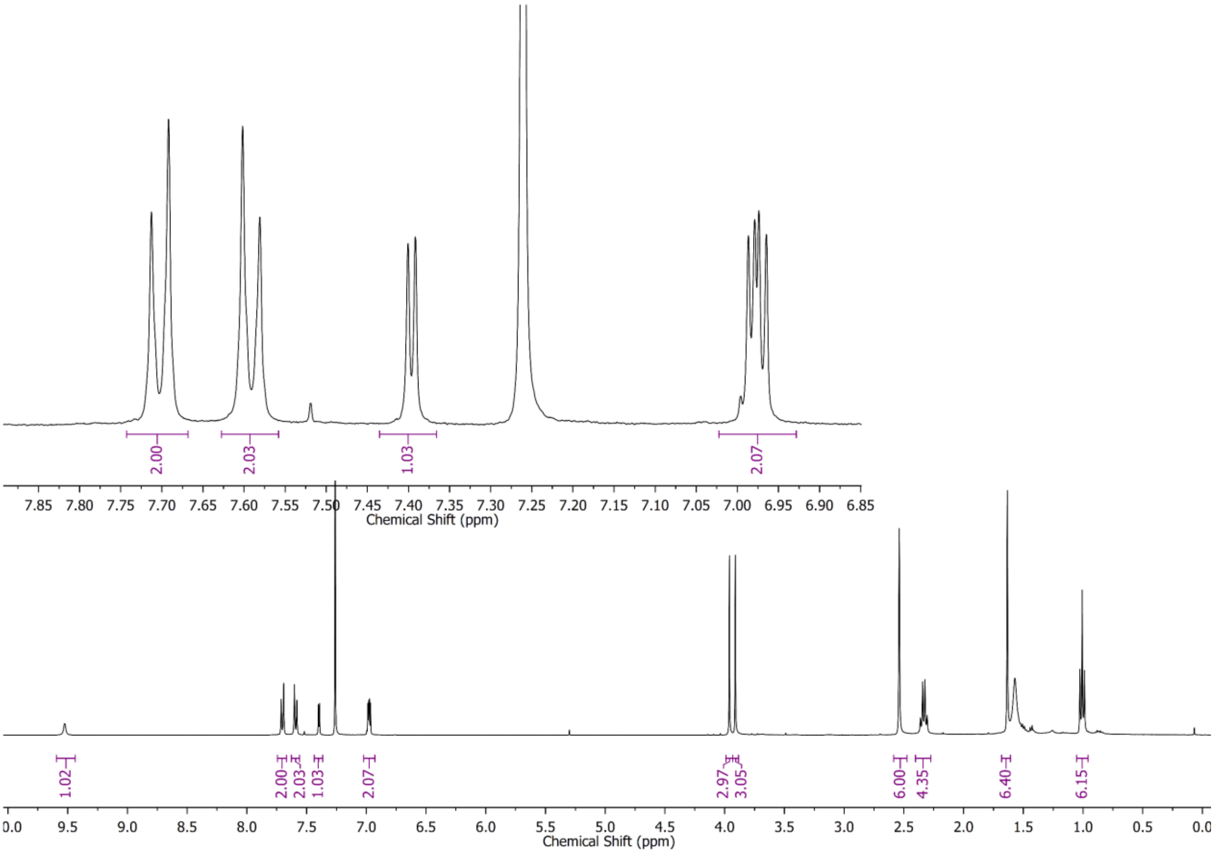

Figure 4.6. ^{1}H NMR spectrum of **4.7** (300 MHz, $CDCl_3$).

The ^{1}H NMR spectrum of **8** is provided in Figure 4.7. While most peaks were sufficiently resolved to measure coupling constants and assign them to specific protons, COSY was used to confirm these couplings (Figure 4.8). The two 1H doublets at 8.72 and 7.28 ppm have been assigned to H_7 and H_8 respectively, as the large coupling constant (coupling a in the COSY spectrum) of 15.6 Hz is indicative of a vicinal alkene coupling. As this coupling is large and isomerism is not seen in the ^{1}H NMR spectrum, **8** has been assigned as the (E)-isomer, which possibly forms due to steric reasons. The thienyl protons, H_5 and H_6, were assigned as the two 1H doublets at 8.21 and 7.92 ppm with a coupling constant of 4.1 Hz (coupling b). H_3 and H_4, the linker phenyl protons, were assigned to the two 2H doublets with a coupling constant of 8.3 Hz at 8.04 and 7.82 ppm (coupling c). The aromatic protons on the indolium phenyl ring (H_{11}-H_{14}) were not well defined and appeared as two 2H multiplets at 7.91-7.86 and 7.65-7.59 ppm, with a coupling that was observed using COSY (coupling d). Only a few of the protons in the aliphatic region appeared as isolated signals. H_9 and H_{10} appeared as an equivalent 6H singlet at 1.80 ppm, H_{15} has been assigned to a 2H triplet (with *J* = 7.2 Hz) at 4.63 ppm and H_{20} appeared as a 3H triplet (with *J* = 6.8 Hz) at 0.87 ppm. The remainder of the hexyl chain (H_{16}-H_{19}) have been assigned to two 4H multiplets at 1.59-1.54 and 1.39-1.27 ppm.

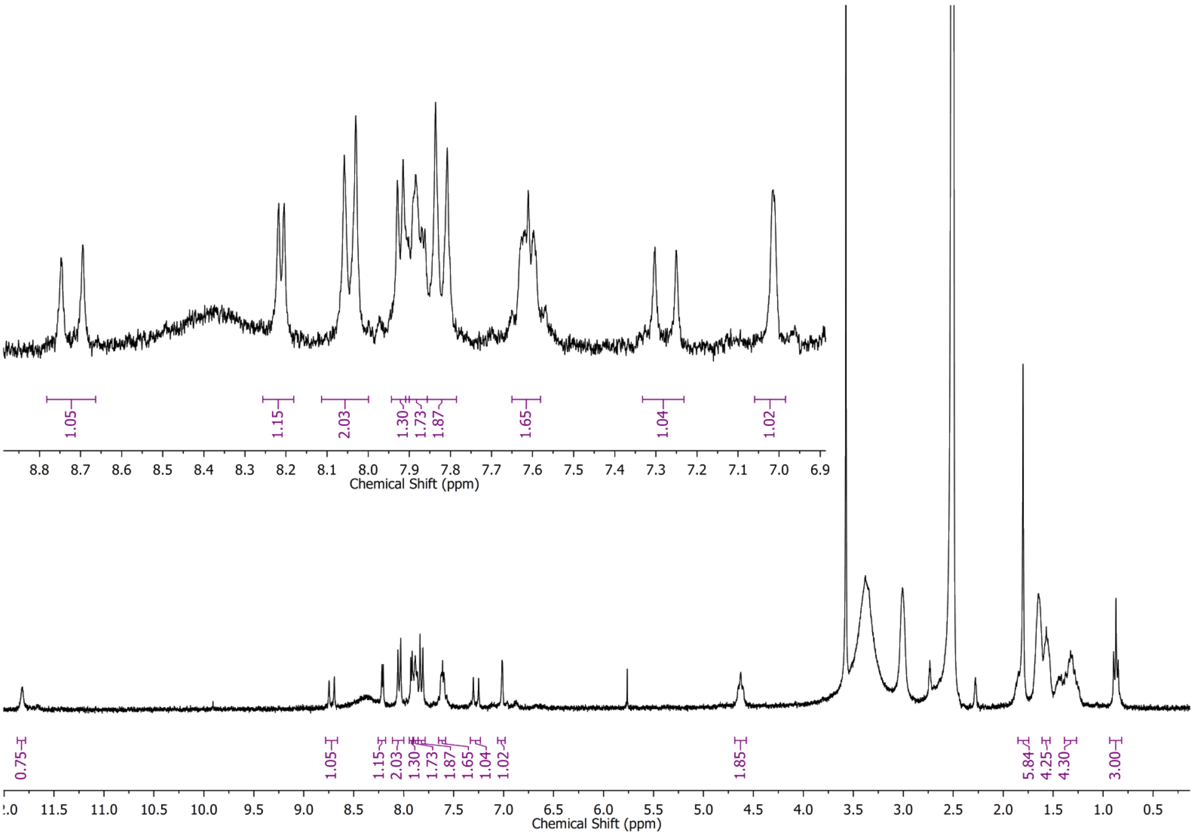

Figure 4.7. ^1H NMR spectrum of **8** (300 MHz, DMSO-d_6).

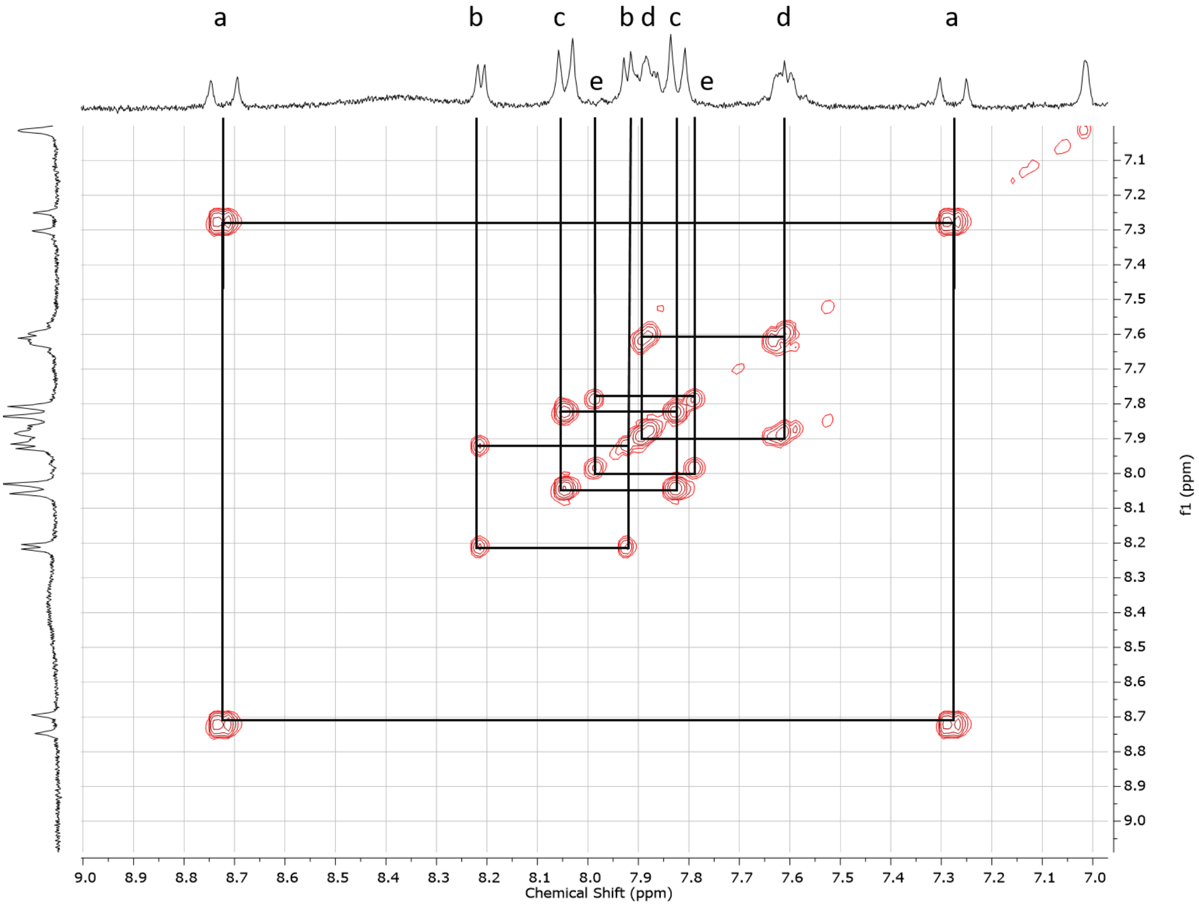

Figure 4.8. Expansion of the aromatic region of the COSY (700 MHz, DMSO-d$_6$) spectrum of **8,** overlaid with the original ^{1}H NMR spectrum (300 MHz, DMSO-d$_6$).

Due to the low solubility of **8,** a long integration time was necessary to collect a ^{13}C spectrum. It appeared that the sample was not stable during the prolonged measurement and had started to decompose; an 8-scan 300 MHz spectrum, recorded before and after the scans on the 700 MHz spectrometer (Figure 4.9), showed the formation of new peaks at 9.90, 8.00 and 6.98 ppm. The protons at 8.00 and 6.98 ppm were coupled, as shown by a COSY cross-peak (coupling e, Figure 4.10). This decomposition was possibly the hydrolysis of the alkene, to reform the aldehyde precursor (as indicated by the new sharp singlet peak at 9.90 ppm), upon prolonged dissolution in a hygroscopic solvent. While this was cause for concern regarding dye stability, all solvents used in the device preparation were anhydrous, so this decomposition would be hopefully minimal.

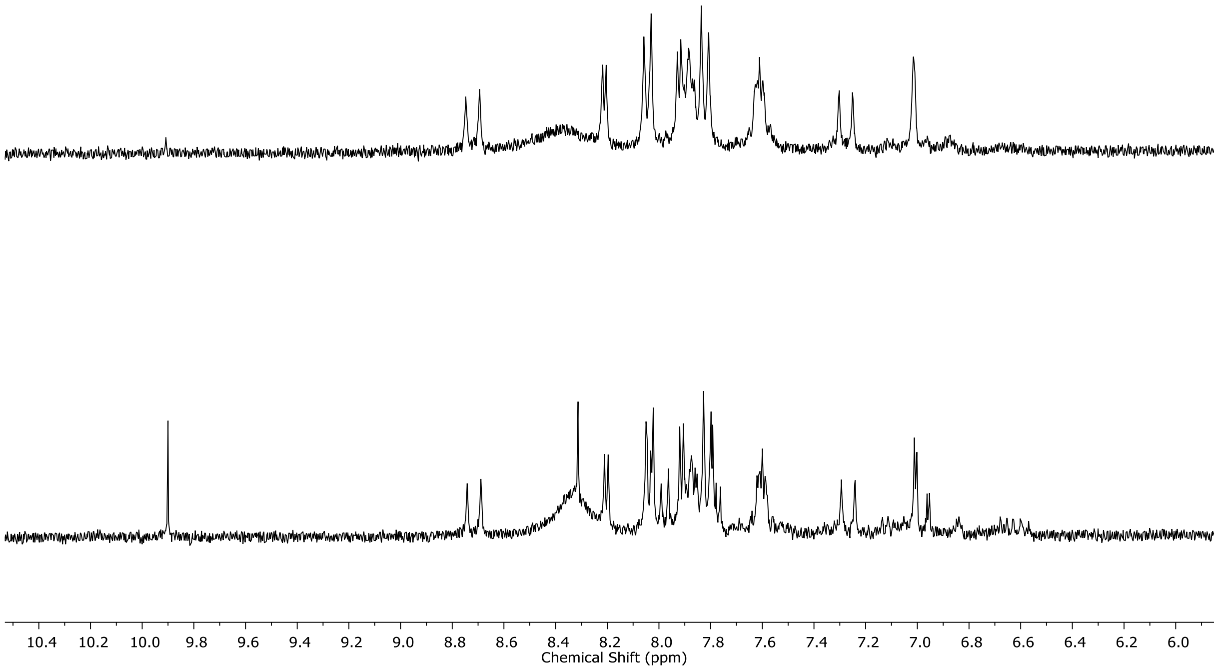

Figure 4.9. Expansion of the aromatic region of the ^{1}H NMR spectra of **8** (300 MHz, DMSO-d_6), obtained before (top) and after (bottom) experiments recorded at 700 MHz.

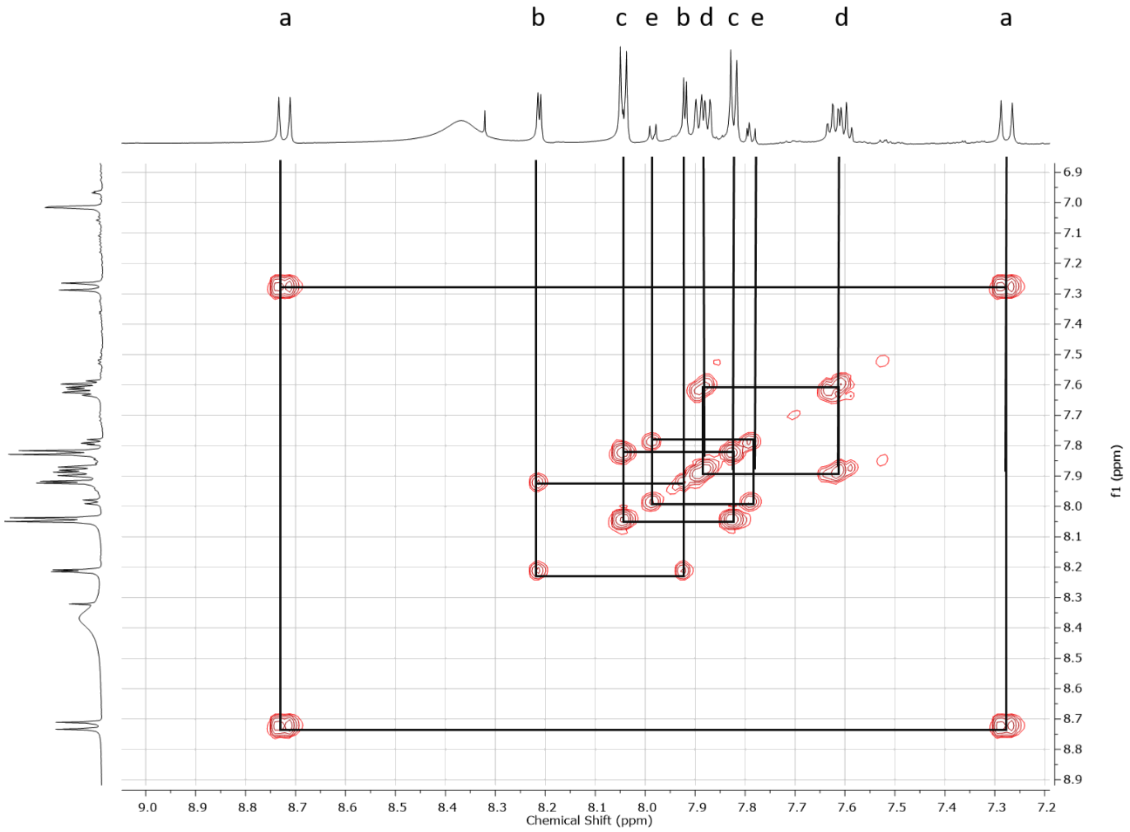

Figure 4.10. Expansion of the aromatic region of the COSY spectrum of **8**, overlaid with the ^{1}H NMR spectrum, both obtained using a 700 MHz spectrometer (in DMSO-d_6, after decomposition had occurred).

4.2.3. Optical Characterisation

The UV-visible absorption spectra of **4.5**, **4.7** and **8** measured in DCM is shown in Figure 4.11 and summarised in Table 4.2.

Table 4.2. UV-visible absorption and emission data for **4.5**, **4.7** and **8** recorded in DCM.

	λ_{abs} / nm (ε / dm^3 mol^{-1} cm^{-1})	λ_{em} / nm	$E_{0\text{-}0}$ / eV	Δv / cm^{-1}
4.5	324 (29,500), 526 (52,000)	540	2.33	493
4.7	341 (33,000), 541 (51,500)	555	2.27	466
8	332 (6000), 532 (12,000)	682	2.05	4134

Where λ_{abs} is the wavelength of maximum absorbance, λ_{em} is the wavelength of maximum emission, $E_{0\text{-}0}$ is the zero-zero energy (which is the energy difference between the ground and excited states) and Δv is the Stokes shift (the separation of λ_{abs} and λ_{em}).

For **4.5** and **4.7**, the absorption spectra were typical of BODIPY compounds; they exhibit a narrow absorption band with $\lambda_{max} > 500$ nm and a high extinction coefficient, which is attributed to a π-π* transition localised on BODIPY. The wavelength of maximum absorption and extinction coefficient for **4.5** were very similar to that of compound **5** studied in **Chapter 3** ($\lambda_{max} = 528$ nm, $\varepsilon = 52,000$ dm^3 mol^{-1} cm^{-1}). Switching the linker unit from phenyl (**4.5**) to thiophene (**4.7**) caused a red shift of 15 nm of λ_{max}. This suggests that the thiophene influences the electron donor/acceptor coupling, which has an effect on the absorption spectrum. The extinction coefficient was essentially the same and no broadening of the absorption band was observed. A more in-depth investigation into the tuning of donor/acceptor coupling in BODIPY dyes and the effect this has on their optical properties was carried out in **Chapter 3**. In this study, it appeared that replacing phenyl with thiophene facilitated increased electronic communication between the linker and BODIPY. This is possibly because the smaller size of thiophene restricts rotation around the BODIPY *meso*-position less than phenyl.

The absorption spectrum of **8** was much broader than that of the BODIPY based dyes, with an absorption band in the UV-region and a more intense absorption band spanning from 400-700 nm. The band in the visible region was less intense than for the BODIPY analogues ($\varepsilon = 12,000$ dm^3 mol^{-1} cm^{-1}). Compared to the analogous triphenylamine push-pull dye **CAD3**,[7] which contained the same indolium acceptor, the extinction coefficient was significantly lower ($\lambda_{max} = 614$ nm, $\varepsilon = 94580$ dm^3 mol^{-1} cm^{-}

[1]). However, **CAD3** has a much larger conjugated π-system and two indolium acceptors.

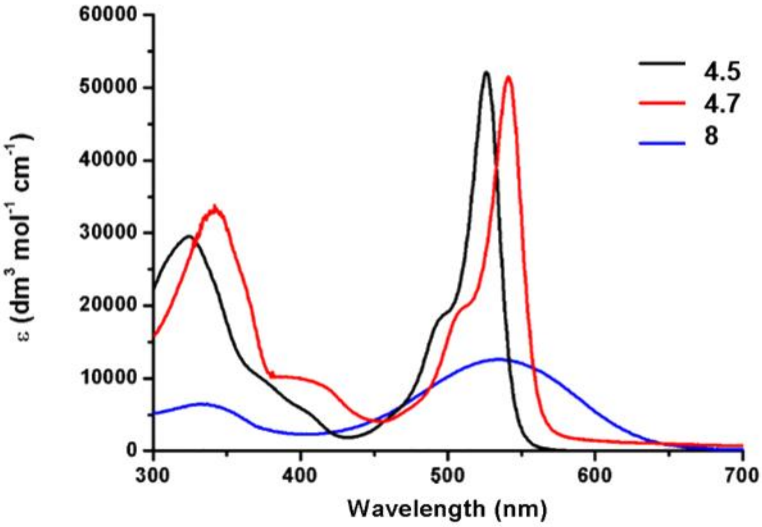

Figure 4.11. UV-visible absorption spectra of **4.5**, **4.7** and **8** recorded in DCM.

The solvent effect on the absorption spectra of **6-8** was investigated (Figure 4.12 - Figure 4.14) by comparing the optical properties in DCM and MeCN. There was a small hypsochromic shift upon increasing the solvent polarity that was slightly higher for **7** (7 nm) compared to **6** (5 nm), but the effect was small in both cases. This is consistent with a small reorganisation of electron density upon excitation (as predicted by supportive calculations, see **Chapter 4.2.3**). There was a larger shift of 15 nm for **8** (Figure 4.14) that was expected, as this absorption band was predicted to contain more charge-transfer character (**Chapter 4.2.3**). There was no change in λ_{max} for **6** (Figure 4.12) and **7** (Figure 4.13) compared to the methyl ester-protected dyes. This is consistent with a BODIPY-localised transition, which is decoupled from the pyrrole anchoring unit. Therefore, this transition is unaffected by the change in electron density on the heterocycle.

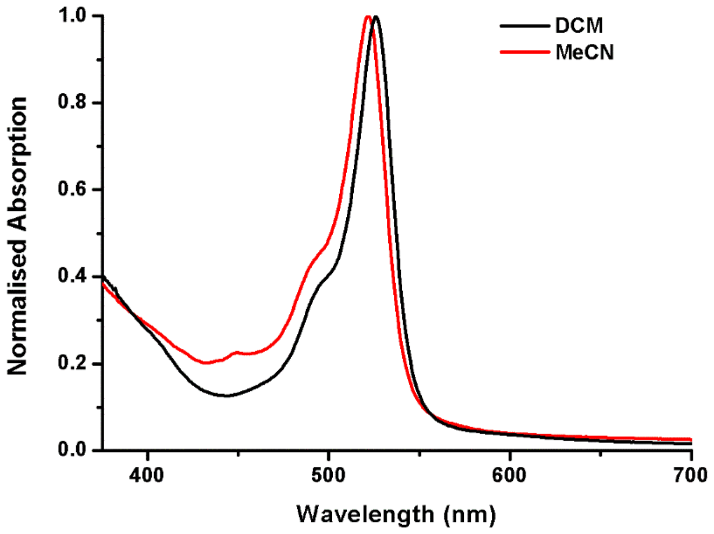

Figure 4.12. Normalised UV-visible absorption spectra of **6** recorded in DCM/MeCN.

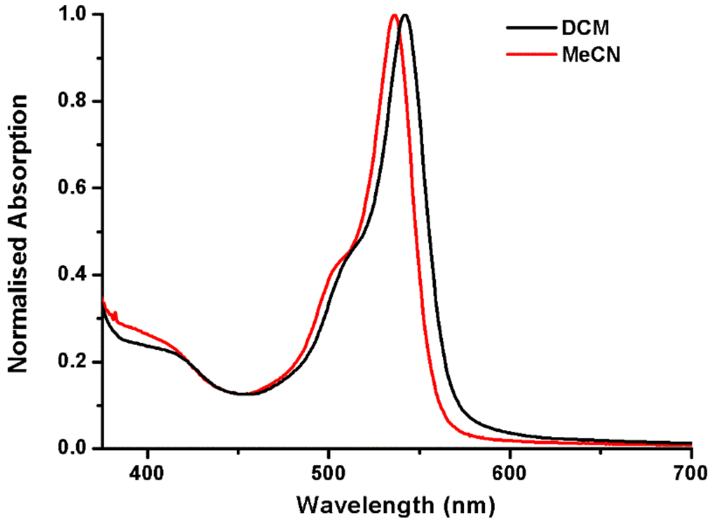

Figure 4.13. Normalised UV-visible absorption spectra of **7** recorded in DCM/MeCN.

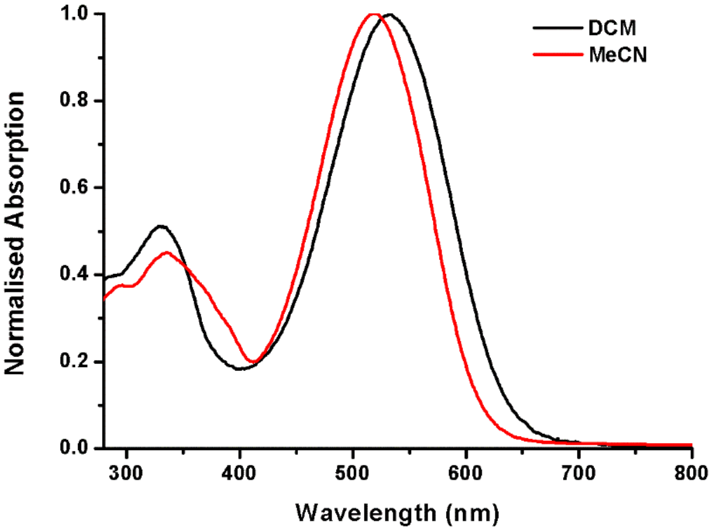

Figure 4.14. Normalised UV-visible absorption spectra of **8** recorded in DCM/MeCN.

The emission of **6-8** was measured in DCM (Figure 4.15 - Figure 4.17) and the key features are summarised in Table 4.2. For the BODIPY dyes **4.5** (Figure 4.15) and **4.7** (Figure 4.16), the emission spectra were roughly mirror images of the S_0-S_1 transition, with emission maxima of 540 (**4.5**) and 555 (**4.7**) nm. Both exhibited small Stokes shifts (493 (**4.5**) and 466 (**4.7**) cm^{-1}), which is typical of BODIPY compounds. Qualitatively, **4.5** was more emissive than **4.7**. This could possibly be due to quenching resulting from electron transfer from the thiophene, or increased rates of non-radiative decay. **8** exhibited a broad emission band (Figure 4.17), which mirrored the absorption profile and had a much larger Stokes shift of 4134 cm^{-1} compared to the BODIPY analogues. This is indicative of a larger structural reorganisation following excitation.

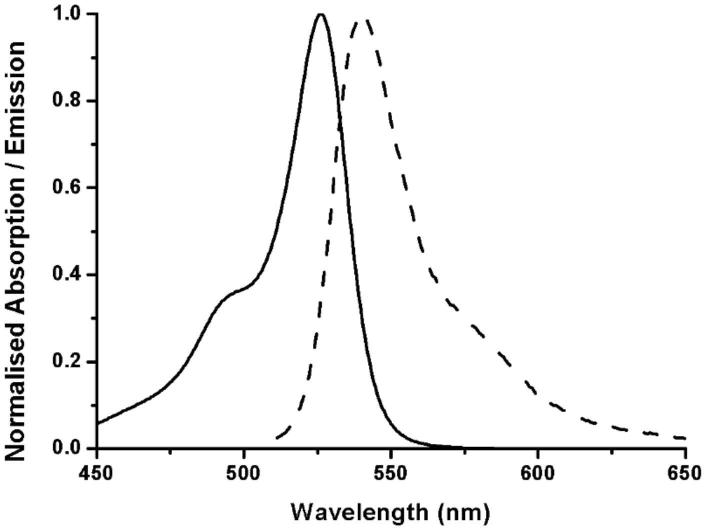

Figure 4.15. Normalised UV-visible absorption (solid line) and emission (dashed line) spectra of **4.5** recorded in DCM.

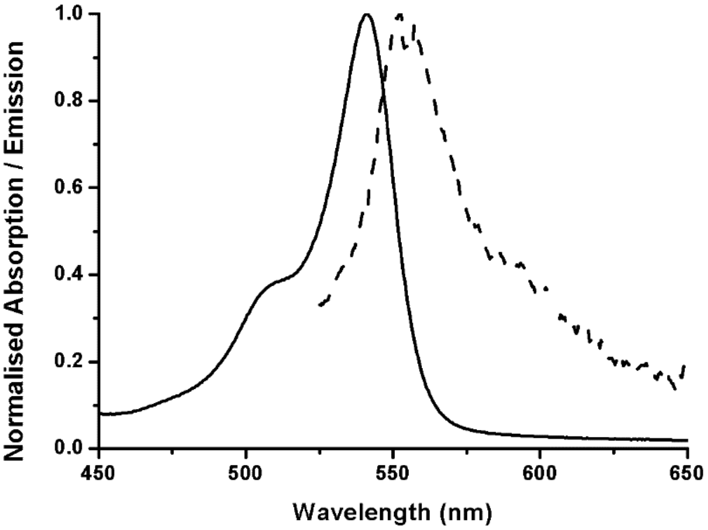

Figure 4.16. Normalised UV-visible absorption (solid line) and emission (dashed line) spectra of **4.7** recorded in DCM.

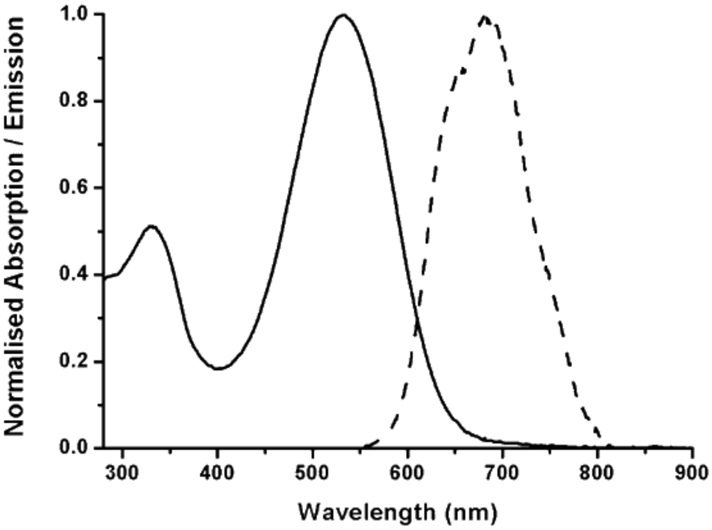

Figure 4.17. Normalised UV-visible absorption (solid line) and emission (dashed line) spectra of **8** recorded in DCM.

4.2.4. Computational Studies

Orbital distributions of **6**-**8** were calculated using Gaussian 09[13] with the B3LYP (**6** and **7**) or CAM-B3LYP (**8**) exchange functional[14] and the 6-31G(d) basis set. Energy level diagrams and orbital distributions are shown in Figure 4.18 - Figure 4.20 and the identity of the lowest energy excitations are summarised in Table 4.3.

Table 4.3. Wavelengths, oscillator strengths (*f*) and compositions of selected transitions derived from TD-DFT calculations.

	Excitation	λ / nm	*f*	Composition	Character
6	S1	441	0.432	HOMO → LUMO	BODIPY π→ π *
7	S1	444	0.387	HOMO → LUMO	BODIPY π → π*
8	S1	517	1.8159	HOMO → LUMO (83%) HOMO - 1 → LUMO (12%)	Charge transfer

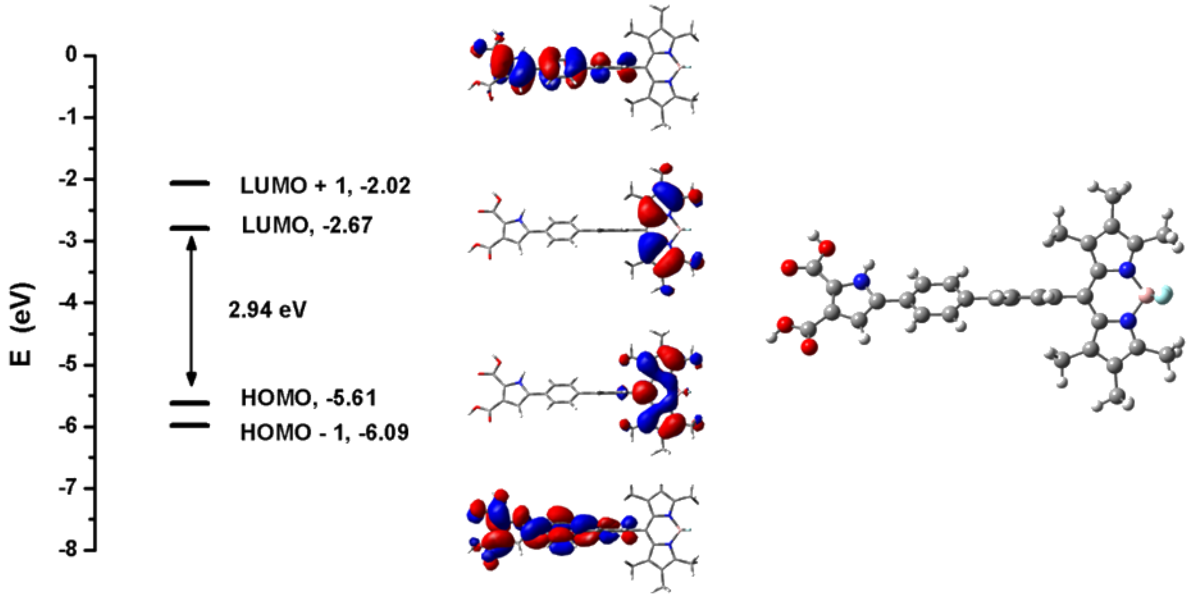

Figure 4.18. Optimised geometry and calculated energy levels for select orbitals of **6** in DCM, determined by DFT/TD-DFT (using the PCM for solvation) using B3LYP/6-31G(d).

For **6** (Figure 4.18) and **7** (Figure 4.19), the HOMO and LUMO are localised on the BODIPY, which is in agreement with the experimental UV-visible absorption spectra. The LUMO of **7** was more conjugated compared to **6,** as some electron density is present on the thiophene π-linker. The dihedral angle between the plane of the BODIPY and the π-linker was 88° for **6** and 82° for **7**, so the smaller size of the thiophene allows the BODIPY to rotate more easily around the *meso*-position. As for the dyes in **Chapter 3** which were synthesised using 3-ethyl-2,4-dimethylpyrrole (**1**, **3** and **5**), there appeared to be limited electron coupling between the BODIPY acceptor and the anchor/donor groups. Therefore, it was expected that these dyes would be poorly coupled to the semiconductor.

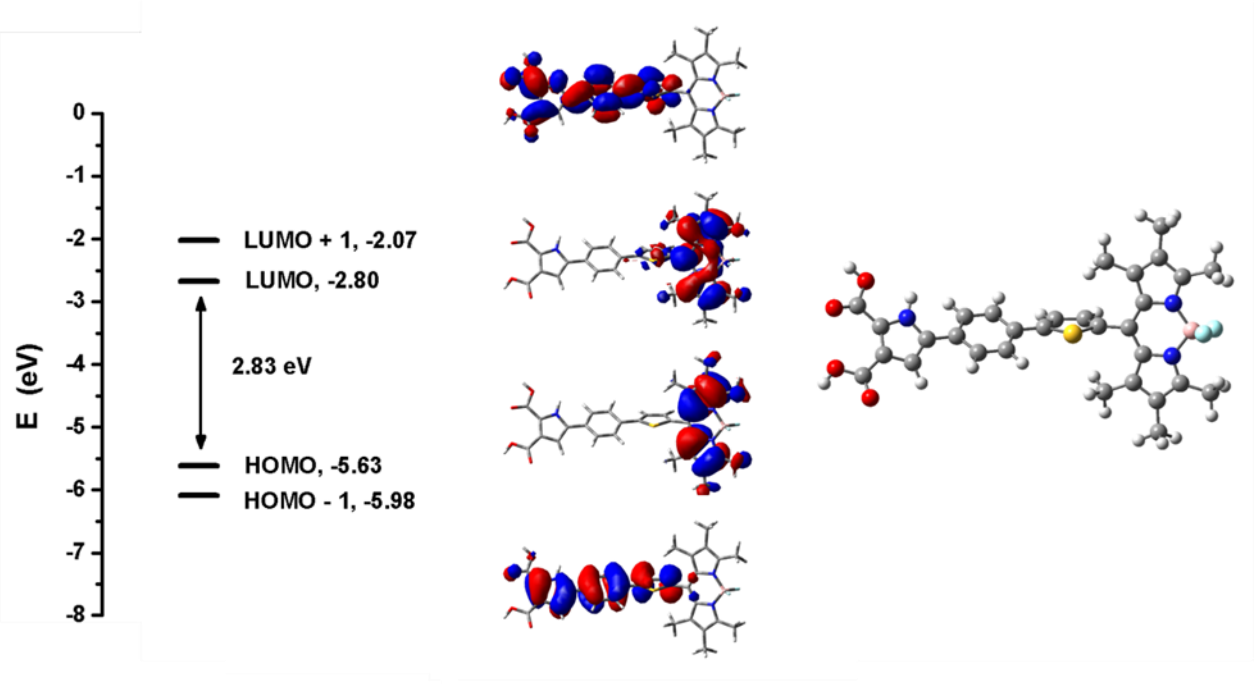

Figure 4.19. Optimised geometry and calculated energy levels for select orbitals of **7** in DCM, determined by DFT/TD-DFT (using the PCM for solvation) using B3LYP/6-31G(d).

The HOMO/LUMO distributions of **8** (Figure 4.20) show that electron density is delocalised across the entire conjugated π-system and that the excitation is a charge-transfer process. The HOMO was predominantly located on the anchor/linker, with some electron density on the indolium acceptor, while the LUMO was delocalised across the linker/acceptor, with some electron density on the anchor. The calculated lowest energy excitation (517 nm) was predominantly comprised of contributions from a HOMO to LUMO transition. This shows that there is some push-pull character to this dye. Therefore, electron density would be drawn away from the NiO surface following excitation of the dye, which was expected to reduce recombination. However, due to the small size of **8**, this spatial charge-separation is limited.

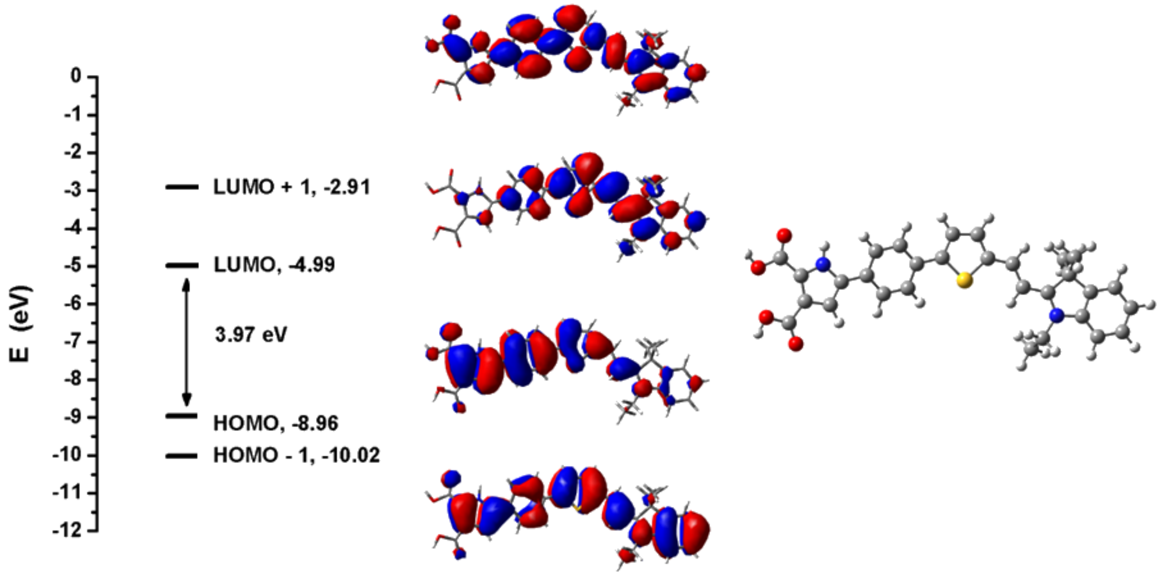

Figure 4.20. Optimised geometry and calculated energy levels for select orbitals of **8** in DCM, determined by DFT/TD-DFT (using the PCM for solvation) using CAM-B3LYP/6-31G(d). To reduce computational cost, the hexyl chain has been replaced with an ethyl chain.

As mentioned in **Chapter 3**, it has been recently reported that TD-DFT calculations for BODIPY systems tend to overestimate the excitation energies.[15] Taking **6** as an example, TD-DFT calculations (using B3LYP/6-31G(d)) predicted the wavelength of the lowest energy excitation to be 447 nm (2.77 eV), while experimentally this was determined to be 526 nm (2.35 eV). This error (0.42 eV) was greater than that typically expected and accepted for TD-DFT methods (0.1 - 0.3 eV), but in the same range (> 0.3 eV) as the nine different functionals that were tested by Brown *et al*.[15] Simulations of the absorption spectra were carried out with a range of different exchange-correlation functionals, in an attempt to more accurately simulate the experimental spectra. In addition to B3LYP, two functionals with increasing Hartree-Fock exchange were tested; from 20% with B3LYP to 35% and 50% using B35LYP and BHandHLYP[16] respectively. Additionally, the long-range functional CAM-B3LYP[17] and M062X were also used. The lowest energy excitations calculated for **6**, using a range of exchange functionals, are shown in Figure 4.21 and summarised in Table 4.4.

Table 4.4. Identity of the lowest energy excitation of **6**, calculated using a range of exchange correlation functionals containing different amounts of Hartree-Fock exchange.

Exchange Functional.	% HF	λ / nm	E / eV	ΔE / eV
B3LYP	20	447	2.77	0.42
B35LYP	35	432	2.87	0.51
BHaHLYP	50	425	2.92	0.56
CAM-B3LYP	20	439	2.82	0.47
M062X	54	442	2.81	0.45

% HF is the percentage Hartree Fock character that the exchange functional uses, λ and E are the wavelength and energy of the calculated lowest energy excitation and ΔE is the energy difference between the calculated and experimental value.

For all calculations summarised in Table 4.4, the geometry was optimised using the different exchange functionals with the 6-31G(d) basis set. After confirming that the optimised geometries were true energy minima (using frequency calculations), TD-DFT calculations were performed in DCM, with solvation treated using the PCM. As can be seen from the absolute errors, there was no improvement over B3LYP on increasing the Hartee-Fock exchange or through using CAM-B3LYP/M062X. Additionally, the simpler exchange functionals PBE and BLYP were tested, as these had also been shown by Brown *et al.* to reduce the overestimation in excitation energy. However, for these systems, calculations using those exchange functionals predicted charge-transfer transitions at wavelengths > 650 nm. These were excluded as they did not correlate with the experimental results.

In the work of Brown *et al.*,[15] the BODIPYs investigated had little substitution in the *meso*-position. It is possible that improvements were not seen for the systems described here due to the increased complexity of these molecules. Importantly, there was no change in the geometry or orbital distributions simulated using different methods, as these are dependent on the ground-state optimisation and not the TD-DFT calculation. Therefore, the results previously discussed are suitable as a qualitative visualisation of the orbital distributions.

For **8,** there was a much greater correlation between the calculated and experimental excitation energies (Figure 4.22) than for **6** and **7**. As mentioned previously, TD-DFT methods tend to underestimate excitation energies for charge-transfer transitions.[18] Therefore, the long-range corrected CAM-B3LYP[17] functional is often used for these systems, which varies the amount of HF exchange at different ranges. Here, B3LYP/6-31G(d) underestimated the excitation energy with an error of 0.38 eV, while CAM-B3LYP/6-31G(d) had an error of 0.07 eV. The excitation calculated using both exchange functionals corresponded to a HOMO – LUMO charge transfer transition from the anchoring unit/linker to the linker/acceptor.

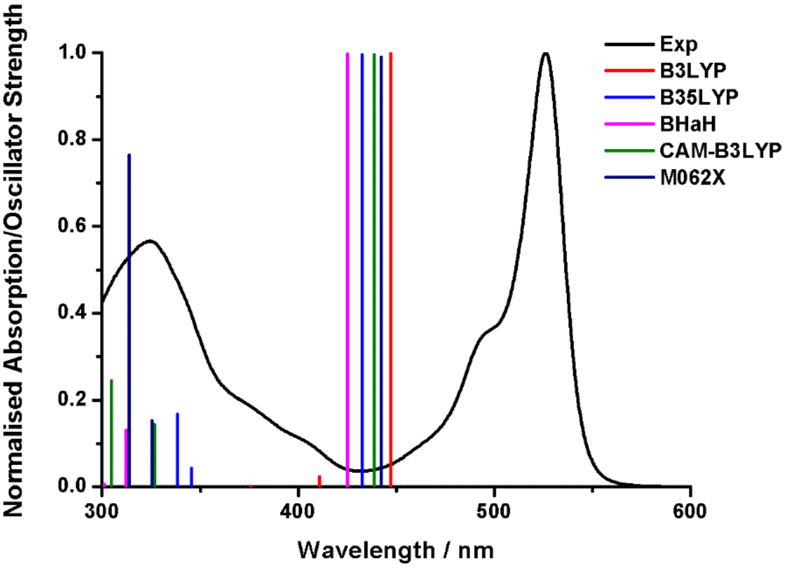

Figure 4.21. Lowest energy excitations calculated using a variety of computational methods, compared to the experimentally obtained absorption spectrum for **6**.

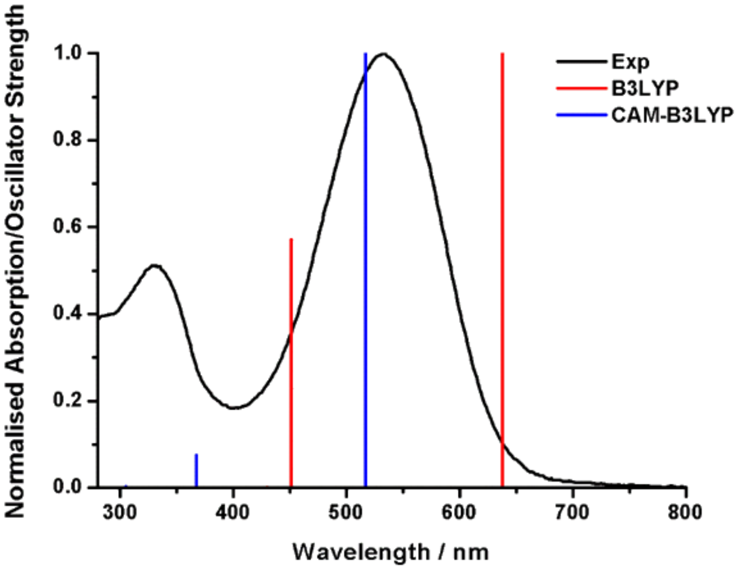

Figure 4.22. Calculated energies of the two lowest energy excitations compared to the experimentally obtained absorption spectrum for **8**.

4.2.5. Device Performances

p-DSCs were constructed from **6**-**8** by soaking NiO films (average thickness of 1.5 µm) for 16 hours in a solution of the dye (0.3 mM) in MeCN (**6** and **7**) or DCM (**8**). The electrolyte used was 1 M LiI and 0.1M I_2 in MeCN. The performances are summarised in Table 4.5.

Table 4.5. Photovoltaic performance of p-DSCs based on NiO sensitised with **6-8**. The performance of **8** has been compared to previously reported indolium dyes containing a triphenylamine donor (**CAD1** and **CAD2**).[12] For **6** and **7**, standard deviations for J_{SC}, V_{OC}, FF and η are provided in parenthesis (as determined for 3 devices).

	A	J_{SC} / mA cm^{-2}	V_{OC} / mV	FF	η / %	IPCE / %	APCE / %
6	1.25	0.53 (0.09)	53 (6)	0.30 (0.0035)	0.009 (5.3 x 10^{-4})	5	5
7	1.50	1.17 (0.11)	61 (3)	0.32 (0.02)	0.023 (4.7 x 10^{-3})	11	11
8	1.20	3.96	84	0.31	0.105	38	41
CAD1	-	3.32	87	0.33	0.09	25	33
CAD2	-	3.25	96	0.33	0.10	17	29

A is the film absorptivity of the dye-sensitised NiO, J_{SC} is the short-circuit current density at the V = 0 intercept, V_{OC} is the open-circuit voltage at the *J* = 0 intercept, FF is the device fill factor, η is the power conversion efficiency, IPCE is the monochromatic incident photon-to-current conversion efficiency and APCE is the monochromatic absorbed photon-to-current conversion efficiency.

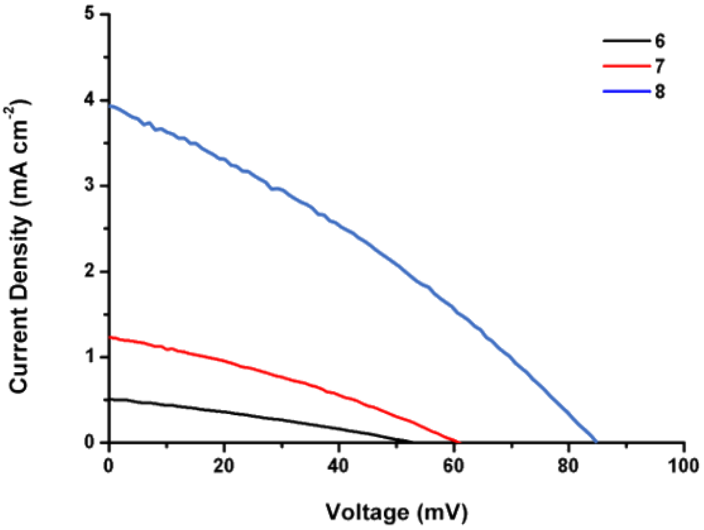

Figure 4.23. J-V curves of p-DSCs constructed using **6-8** and tested under illumination (AM1.5, 100 mW cm^{-2}).

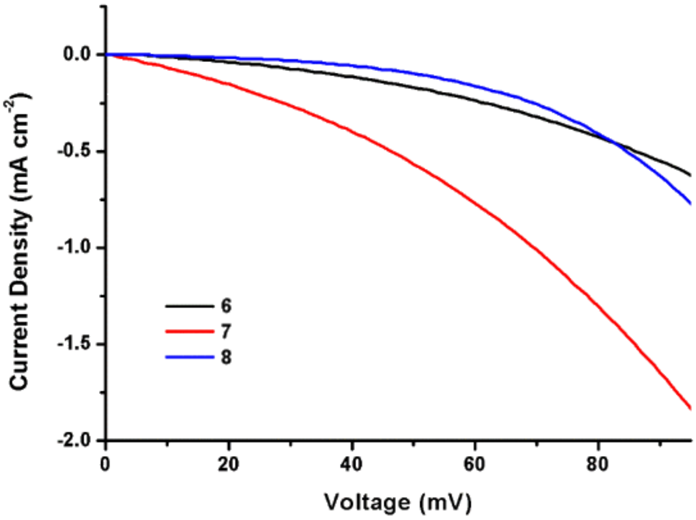

Figure 4.24. J-V curves of p-DSCs constructed using **6-8** and tested in the dark.

From the J-V curves tested under illumination (Figure 4.23), it can be seen that dyes **6** and **7** performed poorly compared to typical triphenylamine based push-pull dyes with BODIPY[19] acceptors (**Chapter 3.2.7**). These dyes produced low photocurrent densities, despite their strong absorbance. A film absorptivity greater than 1 will give a LHE > 90% (See Equation 2.20). Therefore, the low currents were due to low quantum yields for the charge transfer processes (either regeneration, injection or charge collection; see Equation 2.17). As the HOMO for both **6** and **7** were decoupled from the NiO surface, it is possible that the injection quantum yield is a limiting factor. The voltages for **6** and **7** were lower than those typically generated in p-DSCs (ca. 100 mV), possibly due to increased recombination at the electrolyte/NiO interface causing an upward shift in the Fermi level of NiO. The higher dark currents for **6** and **7** compared to **8** (Figure 4.24), which produced a voltage more typical of p-DSCs (84 mV), are consistent with this explanation. The fill factor of these devices was low, which is typical of p-DSCs.[20] Switching from a phenyl to the thiophene linker, twice the J_{SC} and maximum IPCE were achieved for **7**. This is possibly due to improved electronic coupling between NiO and the dye HOMO, as seen in the DFT calculations (**Chapter 4.2.4**).

In comparison, **8** performed more efficiently, generating a J_{SC} of ca. 4 mA cm^{-2} and an overall efficiency four times higher than the BODIPY analogues. The improved photovoltage could be due to reduced recombination at the electrolyte/NiO interface.

This can be attributed to the increased steric bulk of the dye, due to the presence of the hexyl chain, which has been previously reported in a series of analogous dyes (**CAD1** and **CAD2**, Figure 4.25).[12] Interestingly, while **6** and **7** performed worse than their triphenylamine-based analogues, **8** performed more efficiently than **CAD1** and **CAD2**. This improved performance can be attributed to a higher J_{SC}. **8** has a lower extinction coefficient than **CAD1** or **CAD2** ($\varepsilon \approx 24{,}000$ dm^3 mol^{-1} cm^{-1}), which would be expected to limit the J_{SC} by producing a lower film absorptivity. However, the smaller size of **8** resulted in a higher dye loading (dye loading = 17.2 > 6.7 > 2.6 x 10^{-6} mol cm^{-2} for **8**, **CAD1** and **CAD2** respectively) which compensated for this.

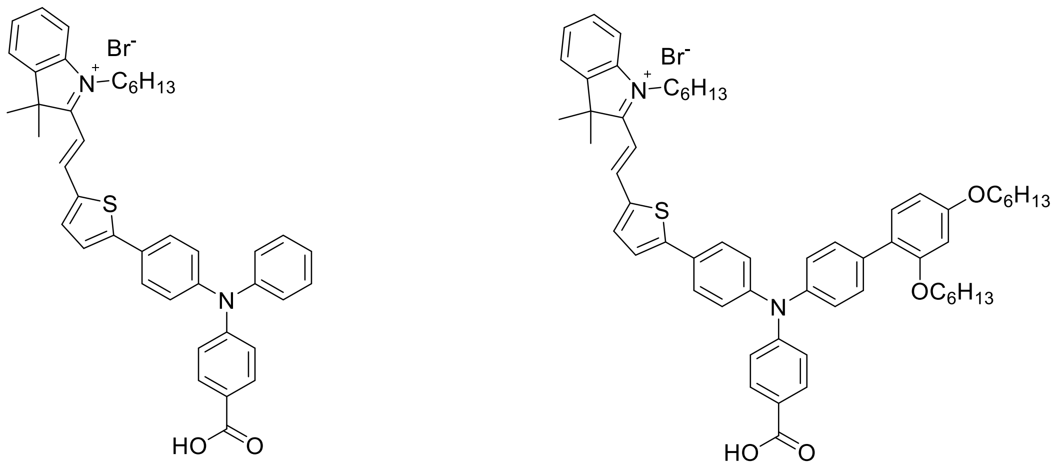

CAD1 **CAD2**

Figure 4.25. Chemical structure of previously reported triphenylamine-based cationic indolium dyes **CAD1** and **CAD2**.[12]

The IPCE spectra are shown in Figure 4.26. The spectral response has the same shape as the absorption spectra of the dyes. This is consistent with photoinduced electron transfer from NiO to the dye driving the production of a photocurrent. The IPCE were much lower for **6** and **7** (5 and 11% respectively at 545 nm) than **8** (38% at 525 nm), which is in agreement with the lower J_{SC}. The J_{SC} produced from **6** was very low and similar to what can be achieved from a non-sensitised NiO film with an iodine based electrolyte[21] through the photolysis of triiodide.[22] This can be observed in the IPCE from the current response at 400 nm, which will contain a contribution from both the photolysis of triiodide and from photoexcitation of the dye. This value was higher for **8** as the broader absorption of the dye on NiO (Figure 4.27) means there was a higher contribution from excitation of the dye at these wavelengths, compared to **6** and

7. Devices constructed using **8** produced a higher IPCE than the previously reported dyes **CAD1** and **CAD2**. The APCE can be used to compare dyes that differ in their absorptivity. For **6** and **7**, the IPCE and APCE were the same. There was a slight increase in the APCE for **8** and this was higher than both **CAD1** and **CAD2**, suggesting that the dye more efficiently converts absorbed photons to a photocurrent.

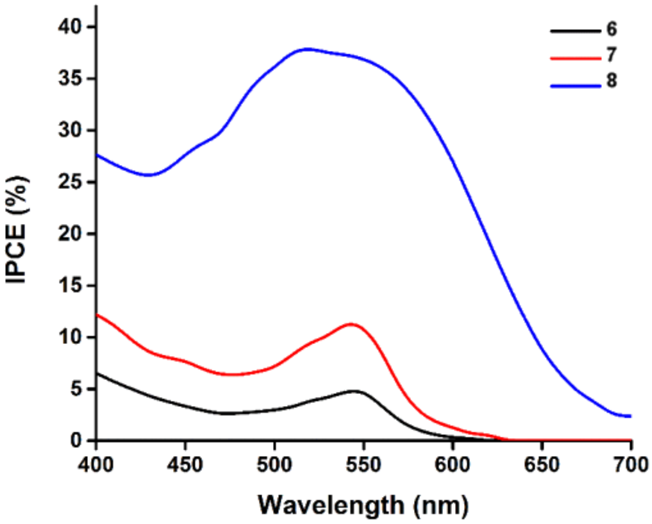

Figure 4.26. IPCE spectra of p-DSCs constructed using **6-8**.

The UV-visible absorption spectra of each dye adsorbed onto NiO (Figure 4.27) confirmed that the dyes have adsorbed onto the surface following hydrolysis. Each film was rinsed with solvent after removing from the dye bath, to remove any physisorbed molecules. Therefore, the absorptivity was due to covalently attached dye molecules. There was a small hypsochromic shift of the absorption maxima of each dye upon binding to NiO (**6**: 526 to 520 nm, **7**: 541 to 539 nm, **8**: 532 to 525 nm). The underlying broad absorption band, tailing from the UV-region across the visible and NIR region, is from Ni^{III} sites in the NiO film.[23] The IPCE spectra match that of the dye adsorbed onto NiO, with a broad spectral response across the visible region for **8** and narrower bands for **6** and **7**. Despite having a lower extinction coefficient than **6** or **7**, the NiO films sensitised with **8** had a similar optical density (Table 4.5), suggesting a greater surface coverage with the indolium based dye.

FTIR spectroscopy was used to investigate the binding of the anchoring unit to NiO (Figure 4.28). We would expect predominantly bidentate binding (either chelating or bridging) of the carboxylic acid to NiO. Therefore, the carbonyl bands of the dye will be lost upon binding. In the ATR spectra of **8,** a band was present at 1700 cm^{-1} that has been assigned to the carbonyl groups. This band disappeared in the spectra of **8**/NiO, indicating that the dye was adsorbed onto the NiO surface through the carboxylic acid groups.

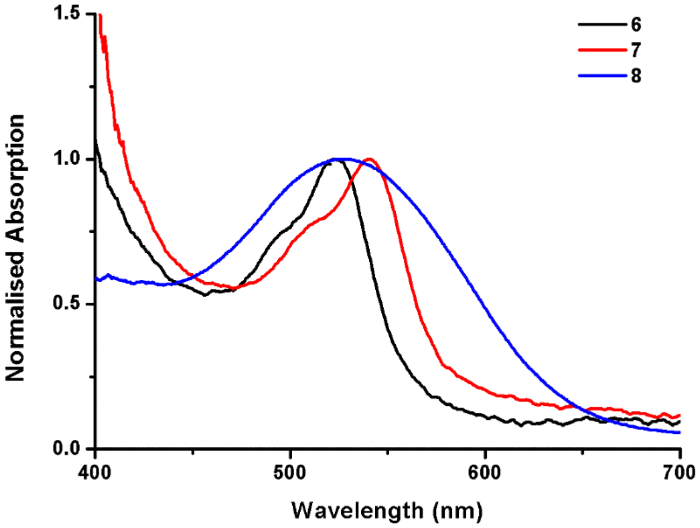

Figure 4.27. UV-visible absorption spectra of **6-8** adsorbed onto NiO, normalised to the absorption maxima of each dye.

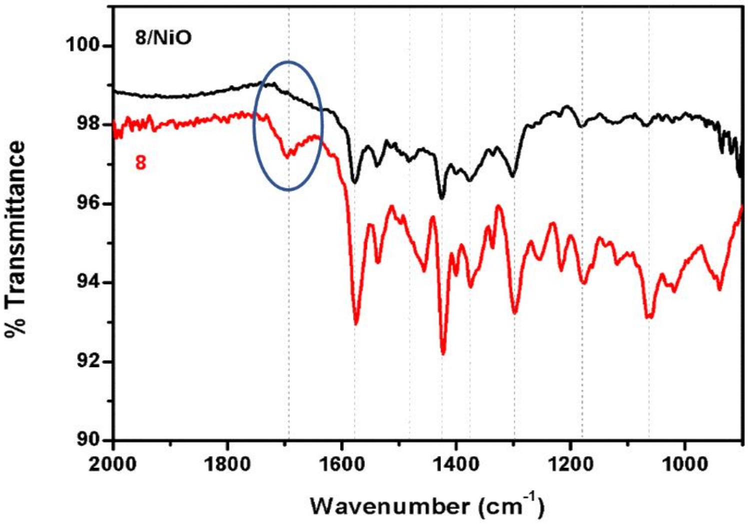

Figure 4.28. Comparison of FTIR spectra for **8** as a solid (red, ATR) and **8** adsorbed onto NiO (black, KBr) showing the disappearance of the highlighted carbonyl band at 1695 cm^{-1} upon binding.

4.2.6. Conclusions

In this chapter, three dyes have been designed and synthesised based on a dicarboxylate pyrrole anchoring unit and BODIPY/indolium acceptors, without the typical triphenylamine donor unit. Devices constructed using the BODIPY dyes performed poorly, compared to triphenylamine-BODIPY analogues (**Chapter 3.2.7**). More efficient devices were obtained using the thiophene linker, possibly due to improved electronic communication between the dye and NiO. A possible explanation for the low efficiencies of **6** and **7** is a high amount of recombination between the redox electrolyte and NiO. This was observed by the high dark currents and low V_{OC}.

More promising results were obtained from **8**, which has been attributed to the suppression of electrolyte/NiO recombination and a broader spectral response. Devices constructed from **8** performed more efficiently than the previously reported triphenylamine-indolium analogues with one acceptor group (**CAD1** and **CAD2**). The higher efficiency was due to a higher J_{SC}, which has been attributed to an increased dye loading for **8** compared to the bulkier triphenylamine-based dyes. The small footprint and broad spectral response of **8** make it a promising candidate for co-sensitisation.

In general, a route was developed in this chapter to synthesising a novel multidentate pyrrole-based anchoring group. However, difficulties with the hydrolysis of this anchoring group limits the design of other sensitisers that incorporate this unit. This prompted an investigation into alternative routes for introducing anchoring groups, which will be discussed in **Chapter 6**. Furthermore, the low p-DSC efficiencies obtained using **6** and **7** support the hypothesis that decoupling the dye HOMO from the NiO surface is detrimental to device performances.

4.3. Experimental

1-(4-Bromophenyl)ethanone oxime (4.1)

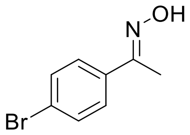

Pyridine (0.8 mL, 10 mmol) was added to a solution of 4-bromoacetophenone (2.0 g, 10 mmol) and hydroxylamine hydrochloride (700 mg, 10 mmol) in ethanol (50 mL) and the solution was heated to reflux for 18 hours. After cooling to room temperature, the solvent was evaporated under reduced pressure. The crude residue was dissolved in ethyl acetate (50 mL) and washed with water. The organic layer was dried over $MgSO_4$ and evaporated to give **4.1** as a white solid (1.72 g, 80% yield).

^{1}H NMR ($CDCl_3$, 300 MHz): δ 8.17 (d, *J* = 8.7 Hz, 2H), 8.04 (d, *J* = 8.7 Hz, 2H), 3.96 (s, 3H) ppm.

^{13}C NMR ($CDCl_3$, 75 MHz): δ 155.38, 135.51, 131.80, 127.72, 123.70, 12.14 ppm.

FTIR (neat, ATR): v = 3210 (br), 2359, 1669, 1590, 1488, 1395, 1366, 1310, 1071, 1007, 928, 821, 777, 717, 555 cm^{-1}.

Synthesised via the following known method:

S. Ngwerume and J. E. Camp, *J. Org. Chem.*, 2010, **75**, 6271–6274

Dimethyl 2-(((1-(4-bromophenyl)ethylidene)amino)oxy)maleate (4.2)

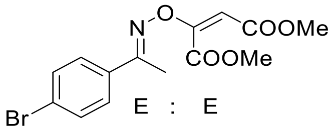

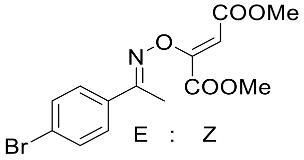

Dimethyl acetylenedicarboxylate (0.64 mL, 5.21 mmol, 1.3 eqv.) in anhydrous DCM (5 mL) was added dropwise over 15 min to a stirred solution of **4.1** (850 mg, 3.97 mmol, 1 eqv.) and DABCO (45 mg, 0.397 mmol, 10 mol %) in anhydrous DCM (15 mL) at –10 °C. The reaction temperature was maintained at –10 °C for 1 hour and the solution was then stirred for 16 hours, with warming to room temperature. The solvent was evaporated under reduced pressure and the product purified by column chromatography (silica gel, 5:1 petrol:ethyl acetate) to afford **4.2** as a colourless oil (1.31 g, 92% yield).

(*E*)-isomer: ^{1}H NMR ($CDCl_3$, 300 MHz): δ 7.39 (m, 4H), 5.95 (s, 1H), 3.75 (s, 3H), 3.58 (s, 3H), 2.31 (s, 3H) ppm.

^{13}C NMR ($CDCl_3$, 75 MHz): δ 164.6, 162.5, 158.9, 153.0, 133.3, 131.6, 128.0, 124.5, 105.8, 52.6, 51.5, 13.2 ppm.

Note: Sample obtained in a 10:1 ratio of E:E vs. E:Z isomers, as determined by ^{1}H NMR analysis (in comparison with previously reported spectra).

Synthesised via the following known method:

S. Ngwerume and J. E. Camp, *J. Org. Chem.*, 2010, **75**, 6271–6274

Dimethyl 5-(4-Bromophenyl)-1H-pyrrole-2,3-dicarboxylate (4.3)

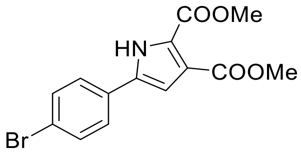

4.2 (200 mg, 0.562 mmol) was loaded into a microwave tube and purged with three vacuum/argon cycles. Anhydrous toluene (4 mL) was added and the solution was heated using microwave irradiation (170 °C, 45 min). After cooling to room temperature, the solvent was evaporated under reduced pressure and the residue was purified by column chromatography (silica gel, 4:1 petrol:ethyl acetate) to give **4.3** as a white solid (140 mg, 74% yield).

^{1}H NMR ($CDCl_3$, 400 MHz): δ 9.96 (s, 1H), 7.52 (d, *J* = 8.8 Hz, 2H), 7.44 (d, *J* = 8.8 Hz, 2H), 6.89 (d, *J* = 3.1 Hz, 1H), 3.88 (s, 3H), 3.87 (s, 3H) ppm.

^{13}C NMR ($CDCl_3$, 100 MHz): δ 164.1, 160.6, 133.7, 132.2, 131.0, 126.3, 122.9, 122.2, 121.5, 110.9, 52.3, 51.9 ppm.

FTIR (neat, ATR): v = 3305, 1728, 1690, 1452, 1380, 1264, 1217, 1151, 1009, 808, 794, 770, 708, 654, 571 cm^{-1}.

Synthesised via the following known method:

S. Ngwerume and J. E. Camp, *J. Org. Chem.*, 2010, **75**, 6271–6274

Dimethyl 5-(4'-formyl-[1,1'-biphenyl]-4-yl)-1H-pyrrole-2,3-dicarboxylate (4.4)

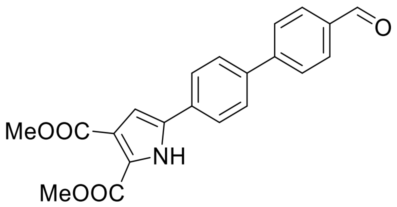

4.3 (73 mg, 0.216 mol), 4-formylphenylboronic acid (60 mg, 0.259 mmol, 1.2 eqv.), bis-triphenylphosphinepalladium(II) chloride (12.6 mg, 1.80×10^{-5} mol, 0.08 eqv.) and Na_2CO_3 (33.7 mg, 0.318 mmol, 1.5 eqv.) were loaded into a Schlenk tube and purged with three vacuum/nitrogen cycles. Water (0.5 mL) and then 1,2-dimethoxyethane (2.5 mL) were added and the mixture was heated to 90 °C for 18 hours under nitrogen. After cooling to room temperature, water (3 mL) was added and the mixture was acidified with 0.1 M HCl until pH 5 was reached. The organic phase was extracted with EtOAc (3 × 50 mL), dried over $MgSO_4$ and the solvent was evaporated under reduced pressure. The residue was purified by column chromatography (silica gel, 0 – 2% MeOH in DCM gradient) to give **4.4** as a white solid (58 mg, 74% yield).

^{1}H NMR ($CDCl_3$, 400 MHz): δ 10.10 (s, 1H,), 9.65 (br s, 1H), 8.01 (d, *J* = 8.4 Hz, 2H), 7.81 (d, *J* = 8.3 Hz, 2H), 7.75 (d, *J* = 8.6 Hz, 2H), 7.70 (d, *J* = 8.6 Hz, 2H), 7.04 (d, *J* = 3.2 Hz, 1H), 3.98 (s, 3H), 3.94 (s, 3H) ppm.

^{13}C NMR ($CDCl_3$, 100 MHz): δ 191.9, 164.3, 160.7, 146.1, 139.6, 135.6, 134.1, 130.5, 130.4, 128.3, 127.6, 125.5, 123.3, 121.8, 111.3, 52.5, 52.1 ppm.

MS (ESI$^+$): calcd. for $C_{21}H_{18}NO_5$: 364.118, found: 364.118 ([M+H]+).

MS (ESI$^-$): calcd. for $C_{21}H_{16}NO_5$: 362.103, found: 362.103 ([M-H]$^-$).

Dimethyl 5-(phenyl-4-phenyl-(2,6-diethyl-4,4-difluoro-1,3,5,7-tetramethyl-4-bora-3a,4a-diaza-s-indecene)-1H-pyrrole-2,3-dicarboxylate (4.5)

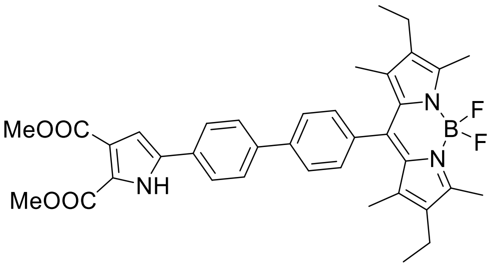

4.4 (25 mg, 6.88×10^{-5} mol) was loaded into a Schlenk tube and purged with three vacuum/nitrogen cycles. Anhydrous DCM (2 mL) was added followed by 2,4-dimethyl-3-ethylpyrrole (30 µL, 2.22×10^{-4} mol, 3.2 eqv.) and TFA (1 drop). The mixture was stirred for 5 hours under nitrogen. *p*-Chloranil (16.9 mg, 6.87×10^{-5} mol, 1.0 eqv.) was added under a flux of nitrogen and the mixture was stirred for 1 hour. DIPEA (100 µL, 5.74×10^{-4} mol, 8.3 eqv.) was added and the mixture was stirred for 15 min. Boron trifluoride etherate (100 µL, 8.10×10^{-4} mol, 11.8 eqv.) was added and the mixture was stirred for a further 1 hour. DCM (25 mL) was added to the mixture and the organic layer was washed with water (3 × 30 mL), dried over $MgSO_4$ and evaporated under reduced pressure. The residue was purified by column chromatography (silica gel, 0 – 2% MeOH in DCM gradient). Recrystallisation from DCM with the addition of pentane gave **4.5** as a red solid (20 mg, 47% yield).

^{1}H NMR ($CDCl_3$, 400 MHz, 25 °C): δ 9.64 (s br, 1H), 7.80 (d, *J* = 8.3 Hz, 4H), 7.71 (d, *J* = 8.3 Hz, 2H), 7.41 (d, *J* = 8.3 Hz, 2H), 7.04 (d, *J* = 2.9 Hz, 1H), 3.99 (s, 3H), 3.95 (s, 3H), 2.57 (s, 6H), 2.34 (q, *J* = 7.5 Hz, 4H), 1.38 (s, 6H), 1.02 (t, *J* = 7.5 Hz, 6H) ppm.

^{13}C NMR ($CDCl_3$, 100 MHz, 25 °C): δ 164.3, 160.7, 154.8, 145.4, 138.7, 135.6, 134.2, 133.7, 133.4, 131.8, 129.8, 129.3, 126.5, 125.4, 123.7, 123.1, 121.8, 111.1, 76.8, 52.5, 52.1, 17.3, 14.7, 12.7, 11.4 ppm.

FTIR (KBr): v = 2961, 2922, 2853, 1715, 1541, 1475, 1456, 1315, 1261, 1186, 1157, 1115, 1069, 976, 826, 765, 733, 708 cm^{-1}.

HRMS (TOF-ESI^{+}): calcd. for $C_{37}H_{38}BF_2N_3NaO_4$: 660.282, found: 660.284 ([M+Na]$^{+}$).

UV-visible absorption (CH_2Cl_2): λ_{max} (ε, dm^{3} mol^{-1} cm^{-1}) = 324 (29,500), 526 (52,000) nm.

5-(phenyl-4-phenyl-(2,6-diethyl-4,4-difluoro-1,3,5,7-tetramethyl-4-bora-3a,4a-diaza-s-indecene)-1H-pyrrole-2,3-dicarboxylic acid (6)

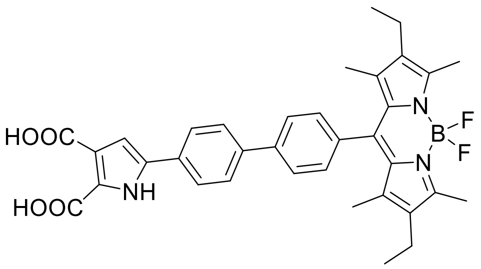

4.5 (10 mg, 1.57×10^{-5} mol) was dissolved in dry MeCN (20 mL) in a Schlenk tube purged with three vacuum/nitrogen cycles. TMS-Br (0.12 mL, 62.74×10^{-5} mol, 40 eqv.) was added and the mixture was stirred at reflux for 7 days. Acetonitrile was evaporated under reduced pressure and the crude residue was stirred in MeOH (10 mL) overnight. MeOH was evaporated under reduced pressure and the residue was dissolved in dry DCM (10 mL), followed by the addition of DIPEA (29 µL, 1.66×10^{-4} mol, 10.5 eqv.). The reaction mixture was stirred under nitrogen for 15 min, then boron trifluoride etherate (35 µL, 2.84×10^{-4} mol, 18 eqv.) was added and the mixture was stirred under nitrogen for an additional hour. The organic layer was washed with water (3 × 10 mL), dried over $MgSO_4$ and the solvent evaporated under reduced pressure. The residue was purified by size exclusion chromatography on Sephadex LH-20 with a MeOH eluent. Crystallisation from DCM with the addition of pentane gave **6** as a red solid (5.9 mg, 62% yield).

^1H NMR (CD_3OD, 400 MHz): δ 7.96 (d, *J* = 8.5 Hz, 2H), 7.90 (d, *J* = 8.2 Hz, 2H), 7.86 (m, 2H), 7.43 (d, *J* = 8 Hz, 2H), 7.09 (d, *J* = 3.9 Hz, 1H), 2.49 (s, 6H), 2.36 (q, *J* = 7.6 Hz, 4H), 1.43 (s, 6H), 1.01 (t, *J* = 7.6 Hz, 6H) ppm.

HRMS (TOF-ESI$^-$): calcd. for $C_{35}H_{33}BF_2N_3O_4$: 608.254, found: 608.243 ($[M-H]^-$).

UV-visible absorption (CH_2Cl_2): λ_{max} (relative intensity (%)) = 512 (41), 536 (100) nm.

Dimethyl 5-(4-(5-formylthiophen-2-yl)phenyl)-1H-pyrrole-2,3-dicarboxylate (4.6)

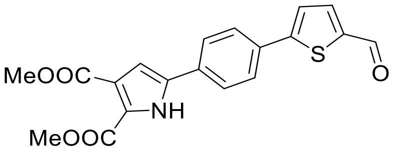

4.3 (52 mg, 0.154 mmol), 5-formyl-2-thienylboronic acid (36 mg, 0.231 mmol, 1.5 eqv.), bis-triphenylphosphinepalladium(II) chloride (9 mg, 1.28×10^{-5} mol, 0.08 eqv.) and Na_2CO_3 (24 mg, 0.226 mmol, 1.5 eqv.) were loaded into a Schlenk tube and purged with three vacuum/nitrogen cycles. Water (0.5 mL) and then 1,2-dimethoxyethane (3 mL) were added and the mixture was heated to 90 °C for 18 hours under nitrogen. After cooling, the mixture was filtered and the filtrate acidified with 0.1 M HCl until pH 5 was reached. The organic phase was extracted with EtOAc (3 × 50 mL), dried over $MgSO_4$ and the solvent was evaporated under reduced pressure. The residue was purified by column chromatography (silica gel, 0 – 2% MeOH in DCM gradient) to give **4.6** as a yellow solid (14 mg, 63% yield).

^1H NMR ($CDCl_3$, 400 MHz): δ 9.91 (s, 1H), 9.61 (br s, 1H, H), 7.78-7.70 (m, 3H), 7.62 (d, *J* = 8.5 Hz, 2H), 7.45 (d, *J* = 4.0 Hz, 1H), 7.00 (d, *J* = 3.1 Hz, 1H), 3.95 (s, 3H), 3.94 (s, 3H) ppm.

^{13}C NMR ($CDCl_3$, 100 MHz, 25 °C): δ 182.9, 164.2, 160.7, 153.2, 142.9, 137.5, 133.8, 133.0, 131.1, 127.3, 125.5, 124.5, 123.4, 121.8, 111.5, 52.5, 52.2 ppm.

MS (ESI$^+$): calcd. for $C_{19}H_{16}NO_5S$: 370.075, found: 370.072 ($[M+H]^+$).

MS (ESI$^-$): calcd. for $C_{19}H_{14}NO_5S$: 368.059, found: 368.060 ($[M-H]^-$).

Dimethyl 5-(phenyl-4-thienyl-(2,6-diethyl-4,4-difluoro-1,3,5,7-tetramethyl-4-bora-3a,4a-diaza-s-indecene)-1H-pyrrole-2,3-dicarboxylate (4.7)

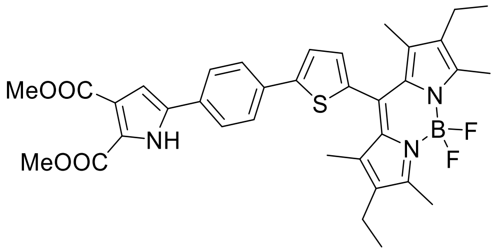

4.6 (25 mg, 6.77×10^{-5} mol) was loaded into a Schlenk tube and purged with three vacuum/nitrogen cycles. Anhydrous DCM (2 mL) was added, followed by 2,4-dimethyl-3-ethylpyrrole (28 µL, 2.07×10^{-4} mol, 3.1 eqv.) and TFA (1 drop). The mixture was stirred for 5 hours under nitrogen. *p*-Chloranil (16.6 mg, 6.75×10^{-5} mol, 1.0 eqv.) was added under a flux of nitrogen and the mixture was stirred for 1 hour. DIPEA (71 µL, 4.08×10^{-4} mol, 6.0 eqv.) was added and the mixture was stirred for 15 min. Finally, boron trifluoride etherate (84 µL, 6.81×10^{-4} mol, 10.1 eqv.) was added and the mixture was stirred for an additional hour. DCM (25 mL) was added to the mixture and the organic layer was washed with water (3 x 30 mL), dried over $MgSO_4$ and evaporated under reduced pressure. The residue was purified by column chromatography (silica gel, 0 – 2% MeOH in DCM gradient). Recrystallisation from DCM with the addition of pentane gave **4.7** as a red solid (27 mg, 63% yield).

^{1}H NMR ($CDCl_3$, 400 MHz): δ 9.56 (s br, 1H), 7.73 (d, *J* = 8.3 Hz, 2H), 7.62 (d, *J* = 8.3 Hz, 2H), 7.41 (d, *J* = 3.6 Hz, 1H), 7.01 (d, *J* = 3.0 Hz, 1H), 7.00 (d, *J* = 3.6 Hz, 1H), 3.99 (s, 3H), 3.94 (s, 3H), 2.57 (s, 6H), 2.36 (q, *J* = 7.5Hz, 4H), 1.66 (s, 6H), 1.04 (t, *J* = 7.5Hz, 6H) ppm.

^{13}C NMR ($CDCl_3$, 100 MHz, 25 °C): δ 164.3, 160.7, 154.0, 140.5, 140.1, 138.5, 135.4, 134.33, 133.0, 130.9, 129.7, 129.2, 127.9, 127.5, 125.4, 123.1, 121.8, 111.1, 52.5, 52.1, 17.3, 14.8, 12.7, 12.1 ppm.

FTIR (KBr): v = 2956, 2920, 2849, 1751, 1713, 1645, 1539, 1456, 1379, 1315, 1294, 1261, 1217, 1186, 1159, 1117, 1072, 972, 808, 746 cm^{-1}.

HRMS (TOF-ESI$^+$): calcd. for $C_{35}H_{36}BF_2N_3NaO_4S$: 666.239, found: 666.238 ([M+Na]$^+$).

UV-visible absorption (CH_2Cl_2): λ_{max} (ε, dm^3 mol^{-1} cm^{-1}) = 341 (33,000), 541 (51,500) nm.

5-(phenyl-4-thienyl-(2,6-diethyl-4,4-difluoro-1,3,5,7-tetramethyl-4-bora-3a,4a-diaza-s-indecene)-1H-pyrrole-2,3-dicarboxylic acid (7)

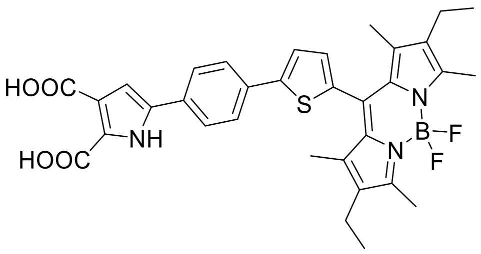

4.7 (11 mg, 2.02×10^{-5} mol) was dissolved in dry MeCN (20 mL) in a Schlenk tube and purged with three vacuum/nitrogen cycles. TMS-Br (0.16 mL, 80.80×10^{-5} mol, 40 eqv.) was added via syringe and the mixture was stirred at reflux for 7 days. MeCN was evaporated under reduced pressure and the crude residue was stirred in MeOH (10 mL) overnight. MeOH was evaporated under reduced pressure and the residue was dissolved in dry DCM (10 mL), followed by the addition of DIPEA (29 µL, 1.66×10^{-4} mol, 8.2 eqv.). The reaction mixture was stirred under nitrogen for 15 min, then boron trifluoride etherate (35 µL, 2.84×10^{-4} mol, 14 eqv.) was added and the mixture was stirred under nitrogen for an additional hour. The organic layer was washed with water (3 × 10 mL), dried over $MgSO_4$ and evaporated under reduced pressure. The residue was purified by size exclusion chromatography on Sephadex LH-20 with a MeOH eluent. Crystallisation from DCM, with the addition of pentane, gave **7** as a red solid (7.5 mg, 71% yield).

^{1}H NMR (CD_3OD, 400 MHz, 25 °C): δ 7.80 (4H, m), 7.58 (d, *J* = 3.7 Hz, 1H), 7.11 (m, 2H), 2.52 (s, 6H), 2.42 (q, *J* = 7.5Hz, 4H), 1.73 (s, 6H, H_{Me}), 1.05 (t, *J* = 7.5Hz, 6H) ppm.

HRMS (TOF-ESI$^-$): calcd. for $C_{33}H_{31}BF_2N_3O_4S$: 614.210, found: 614.218 ([M-H]$^-$).

UV-visible absorption (CH_2Cl_2): λ_{max} (relative intensity (%)) = 324 (80), 407 (23), 499 (45), 526 (100) nm.

5-(4-(5-Formylthiophen-2-yl)phenyl)-1H-pyrrole-2,3-dicarboxylic acid (4.8)

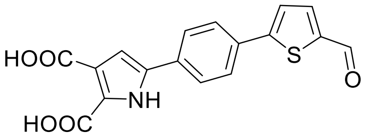

To a suspension of **4.6** (58 mg, 0.157 mmol) in MeOH (20 mL) was added NaOH (150 mg, 3.75 mmol, 24 eqv.) in water (20 mL). The orange solution which formed was heated at reflux for 12 hours. After cooling to room temperature, the solution was neutralised using 0.1 M HCl and extracted with EtOAc (4 x 50 mL). The combined organic layers were washed with brine (2 x 50 mL), dried over $MgSO_4$ and the solvent was evaporated under reduced pressure to give **4.8** as a yellow solid (43 mg, 80% yield).

^{1}H NMR (DMSO-d_6, 300 MHz): δ 12.83 (br s, 1H), 9.91 (s, 1H), 8.07-8.01 (m, 3H), 7.83 (d, *J* = 9.1 Hz, 2H), 7.81 (d, *J* = 4.2 Hz, 1H), 7.22 (d, *J* = 2.8 Hz, 1H) ppm.

^{13}C NMR (DMSO-d_6, 75 MHz): δ 184.5, 169.0, 161.3, 152.5, 142.4, 139.7, 135.1, 132.2, 131.5, 127.0, 126.9, 126.8, 125.9, 119.9, 112.2 ppm.

HRMS (ESI): m/z calcd. for $C_{17}H_{10}NO_5S$: 340.028, found: 340.028 ($[M-H]^-$).

1-hexyl-2,3,3-trimethyl-3H-indol-1-ium hexafluorophosphate (4.9)

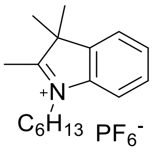

2,3,3-trimethyl-3H-indole (1g, 6.28 mmol, 1 eqv.) was dissolved in 1-iodohexane (1.86 mL, 12.56 mmol, 2 eqv.) and heated at 110 °C for 18 hours under a nitrogen atmosphere. After cooling to room temperature, diethyl ether (20 mL) was added and the precipitate formed was filtered, washed with diethyl ether and dried under vacuum to give 1-hexyl-2,3,3-trimethyl-3H-indol-1-ium iodide as a pink solid (1.9 g, 83% yield).

1-hexyl-2,3,3-trimethyl-3H-indol-1-ium iodide (200 mg, 0.54 mmol) and $NaPF_6$ (250 mg, 1.08 mmol, 2 eqv.) were dissolved in methanol (10 mL) and heated at reflux for 18 hours. After cooling to room temperature, the solvent was evaporated and the crude residue dissolved in DCM. The excess $NaPF_6$ was filtered and the filtrate was evaporated and recrystallised from DCM, with the addition of pentane, to give **4.9** as a red solid (165 mg, 79% yield).

^{1}H NMR ($CDCl_3$, 300 MHz): δ 7.76–7.40 (m, 4H), 4.65 (t, *J* = 7.8 Hz, 2H), 3.10 (s, 3H), 1.98-1.85 (m, 2H), 1.64 (s, 3H), 1.53-1.37 (m, 2H), 1.37-1.21 (m, 4H), 0.85 (t, *J* = 6.9 Hz, 3H) ppm.

^{13}C NMR ($CDCl_3$, 75 MHz): δ 195.79, 141.76, 140.91, 130.31, 129.61, 123.46, 115.23, 54.80, 49.02, 31.20, 27.96, 26.47, 22.92, 22.44, 14.82, 13.98 ppm.

^{19}F NMR ($CDCl_3$, 282 MHz): δ -72.15 (d, *J* = 713.1 Hz) ppm.

^{31}P NMR ($CDCl_3$, 121 MHz): δ -144.40 (sept, *J* = 711.8 Hz) ppm.

FTIR (neat, ATR): v = 2958, 2931, 2856, 1653, 1629, 1471, 1460, 1015, 829, 766, 556 cm^{-1}.

Iodide salt synthesised via the following known method:

E. Ronchi, R. Ruffo, S. Rizzato, A. Albinati, B. Alberto, L. Beverina and G. A. Pagani, *Org. Lett.*, 2011, **13**, 3166-3169

(E)-2-(2-(5-(4-(4,5-dicarboxy-1H-pyrrol-2-yl)phenyl)thiophen-2-yl)vinyl)-1-hexyl-3,3-dimethyl-3H-indol-1-ium hexafluorophosphate (8)

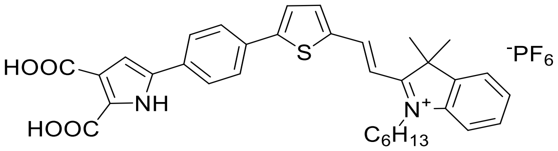

4.8 (43 mg, 0.126 mmol, 1 eqv.) and **4.9** (120 mg, 0.31 mmol, 2.5 eqv.) were loaded into a Schlenk tube and purged with three vacuum/nitrogen cycles. Dry MeCN (15 mL) and piperidine (17 µL, 0.172 mmol, 1.36 eqv.) were added and the solution was heated to reflux for 48 hours. After cooling to room temperature, the solvent was evaporated and the crude residue dissolved in DCM (20 mL) and washed with water (3 x 30 mL) and brine (1 x 20 mL). The organic layer was dried over $MgSO_4$, filtered and the solvent was evaporated under reduced pressure. The residue was purified from three sequential recrystallisations from DCM by the layering of diethyl ether, followed by a final recrystallisation from DCM with the slow diffusion of pentane. The solid was filtered, washed with pentane and dried under vacuum to give **8** as a purple solid (38 mg, 42%).

^{1}H NMR (DMSO-d_6, 300 MHz): δ 11.82 (br s, 1H), 8.72 (d, *J* = 15.6 Hz, 1H), 8.21 (d, *J* = 4.1 Hz, 1H), 8.04 (d, *J* = 8.3 Hz, 2H), 7.92 (d, *J* = 4.2 Hz, 1H), 7.91 – 7.86 (m, 2H), 7.82 (d, *J* = 8.4 Hz, 2H), 7.65 – 7.58 (m, 2H), 7.28 (d, *J* = 15.6 Hz, 1H), 7.01 (d, *J* = 1.8 Hz, 1H), 4.63 (t, *J* = 7.2 Hz, 2H), 1.80 (s, 6H), 1.58 – 1.54 (m, 2H), 1.39 – 1.27 (m, 4H), 0.87 (t, *J* = 6.8 Hz, 3H) ppm.

^{13}C NMR (DMSO-d_6, 175 MHz): δ 184.4, 180.9, 166.1, 163.6, 154.3, 146.4, 144.0, 142.0, 141.3, 139.6, 133.5, 131.4, 131.1, 129.6, 129.4, 126.9, 126.8, 126.1, 126.0, 122.4, 115.3, 111.5, 111.20, 110.17, 52.3, 44.2, 31.3, 28.6, 26.3, 26.0, 22.7, 22.4, 22.1, 14.3 ppm.

FTIR (KBr): ν = 2359, 2324, 1695, 1576, 1537, 1456, 1425, 1373, 1298, 1254, 1219, 1175, 1113, 1063, 1020, 937, 835, 802, 772 cm^{-1}.

HRMS (ESI): m/z calcd. for $C_{34}H_{35}N_2O_4S$: 567.231, found: 567.233 (M^+).

UV-visible absorption (CH_2Cl_2): λ_{max} (ε, dm^3 mol^{-1} cm^{-1}) = 332 (6000), 532 (12,000) nm.

4.4. References

1 M. Bräutigam, M. Schulz, J. Inglis, J. Popp, J. G. Vos and B. Dietzek, *Phys. Chem. Chem. Phys.*, 2012, **14**, 15185-15190.

2 M. Bräutigam, P. Weyell, T. Rudolph, J. Dellith, S. Krieck, H. Schmalz, F. H. Schacher and B. Dietzek, *J. Mater. Chem. A*, 2014, **2**, 6158–6166.

3 M. A. Gross, C. E. Creissen, K. L. Orchard and E. Reisner, *Chem. Sci.*, 2016, **7**, 5537–5546.

4 A. Nattestad, A. J. Mozer, M. K. R. Fischer, Y.-B. Cheng, A. Mishra, P. Bäuerle and U. Bach, *Nat. Mater.*, 2010, **9**, 31–35.

5 W. Xiang, J. Marlow, P. Bäuerle, U. Bach and L. Spiccia, *Green Chem.*, 2016, **18**, 6659–6665.

6 K. A. Click, D. R. Beauchamp, Z. Huang, W. Chen and Y. Wu, *J. Am. Chem. Soc.*, 2016, **138**, 1174–1179.

7 C. J. Wood, G. H. Summers and E. A. Gibson, *Chem. Commun.*, 2015, **51**, 3915–3918.

8 S. Ngwerume and J. E. Camp, *J. Org. Chem.*, 2010, **75**, 6271–6274.

9 K. Muthukumaran, R. S. Loewe, A. Ambroise, S. I. Tamaru, Q. Li, G. Mathur, D. F. Bocian, V. Misra and J. S. Lindsey, *J. Org. Chem.*, 2004, **69**, 1444–1452.

10 M. Weidelener, A. Mishra, A. Nattestad, S. Powar, A. J. Mozer, E. Mena-Osteritz, Y.-B. Cheng, U. Bach and P. Bäuerle, *J. Mater. Chem.*, 2012, **22**, 7366–7379.

11 Z. Liu, W. Li, S. Topa, X. Xu, X. Zeng, Z. Zhao, M. Wang, W. Chen, F. Wang, Y.-B. Cheng and H. He, *ACS Appl. Mater. Interfaces*, 2014, **6**, 10614–22.

12 C. J. Wood, M. Cheng, C. A. Clark, R. Horvath, I. P. Clark, M. L. Hamilton, M. Towrie, M. W. George, L. Sun, X. Yang and E. A. Gibson, *J. Phys. Chem. C*, 2014, **118**, 16536–16546.

13 Gaussian 09, Revision D.01, M. J. Frisch, G. W. Trucks, H. B. Schlegel, G. E. Scuseria, M. A. Robb, J. R. Cheeseman, G. Scalmani, V. Barone, G. A. Petersson, H. Nakatsuji, X. Li, M. Caricato, A. Marenich, J. Bloino, B. G. Janesko, R. Gomperts, B. Mennucci, H. P. Hratchian, J. V. Ortiz, A. F. Izmaylov,

J. L. Sonnenberg, D. Williams-Young, F. Ding, F. Lipparini, F. Egidi, J. Goings, B. Peng, A. Petrone, T. Henderson, D. Ranasinghe, V. G. Zakrzewski, J. Gao, N. Rega, G. Zheng, W. Liang, M. Hada, M. Ehara, K. Toyota, R. Fukuda, J. Hasegawa, M. Ishida, T. Nakajima, Y. Honda, O. Kitao, H. Nakai, T. Vreven, K. Throssell, J. A. Montgomery, Jr., J. E. Peralta, F. Ogliaro, M. Bearpark, J. J. Heyd, E. Brothers, K. N. Kudin, V. N. Staroverov, T. Keith, R. Kobayashi, J. Normand, K. Raghavachari, A. Rendell, J. C. Burant, S. S. Iyengar, J. Tomasi, M. Cossi, J. M. Millam, M. Klene, C. Adamo, R. Cammi, J. W. Ochterski, R. L. Martin, K. Morokuma, O. Farkas, J. B. Foresman, and D. J. Fox, Gaussian, Inc., Wallingford CT, 2016.

14 A. D. Becke, *J. Chem. Phys.*, 1993, **98**, 1372–1377.

15 M. R. Momeni and A. Brown, *J. Chem. Theory Comput.*, 2015, **11**, 2619–2632.

16 J. Guthmuller and B. Champagne, *J. Chem. Phys.*, 2007, **127**, 164507.

17 T. Yanai, D. P. Tew and N. C. Handy, *Chem. Phys. Lett.*, 2004, **393**, 51–57.

18 A. Dreuw and M. Head-Gordon, *Chem. Rev.*, 2005, **105**, 4009–4037.

19 G. H. Summers, J.-F. Lefebvre, F. A. Black, E. Stephen Davies, E. A. Gibson, T. Pullerits, C. J. Wood and K. Zidek, *Phys. Chem. Chem. Phys.*, 2016, **18**, 1059–1070.

20 F. Odobel, Y. Pellegrin, E. A. Gibson, A. Hagfeldt, A. L. Smeigh and L. Hammarström, *Coord. Chem. Rev.*, 2012, **256**, 2414–2423.

21 M. Awais, E. Gibson, J. G. Vos, D. P. Dowling, A. Hagfeldt and D. Dini, *ChemElectroChem*, 2014, **1**, 384–391.

22 E. A. Gibson, L. Le Pleux, J. Fortage, Y. Pellegrin, E. Blart, F. Odobel, A. Hagfeldt and G. Boschloo, *Langmuir*, 2012, **28**, 6485–6493.

23 G. Boschloo and A. Hagfeldt, *J. Phys. Chem. B*, 2001, **105**, 3039–3044.

Chapter 5 – Bay Annulated Indigo as a New Chromophore for p-DSCs

5.1. Introduction

In the previous chapters, the dyes were designed with a donor-acceptor structure, where the chromophore (either a BODIPY or indolium group) was synthesised by a condensation reaction onto an aldehyde.[1–4] An alternative approach to promote charge-separation is to design 'dyad' dyes, consisting of chromophores covalently linked to secondary electron acceptors. Typically, this is carried out by functionalising the chromophore with an anchoring unit, then attaching a secondary electron acceptor through sequential halogenation and coupling reactions. This approach has been widely studied for p-DSCs, with the dyads often utilising a perylene monoimide chromophore with acceptors such as naphthalene diimide or C_{60}.[5–9]

The diketopyrrolopyrrole (DPP) chromophore is a building block that has recently attracted attention for incorporation into DSCs (both n and p-type).[10–15] The DPP dyes used for p-DSCs (Figure 5.1) could be readily halogenated, allowing access to coupling reactions to introduce anchoring groups and electron acceptors. A structurally similar chromophore that has also been used for p-DSCs is isoindigo (Figure 5.1, **ISO-Br** and **ISO-NDI**).[16] While these dyes are photosensitisers for NiO, their low extinction coefficients ($\varepsilon < 20{,}000$ M^{-1} cm^{-1}) could limit device the solar cell efficiency. Additionally, the DPP and isoindigo cores are not readily available and need to be synthesised in several steps.

Indigo, one of the oldest known blue dyes, is readily available from commercial sources and is relatively inexpensive. However, the direct use of indigo as a starting material is hindered due to limited solubility. In a recent report by the group of Liu *et al.*,[17] indigo was functionalised by reacting with 2-thienylacetyl chloride to produce bay-annulated indigo (BAI, Figure 5.2). In this structure, the two pyrrole groups are incorporated into a conjugated, planar structure with two flanking thiophenes. These thiophene units can be readily functionalised through aromatic substitution reactions and the solubility is improved compared to indigo due to the suppression of hydrogen-bonding interactions. The increased conjugation for BAI compared to indigo leads to a higher extinction coefficient ($\varepsilon = 26800$ M^{-1} cm^{-1} for BAI vs. 22140 M^{-1} cm^{-1} for indigo).[18] This unit was incorporated into fluorene and benzodithiophene containing polymers, which were used as organic semiconductors.

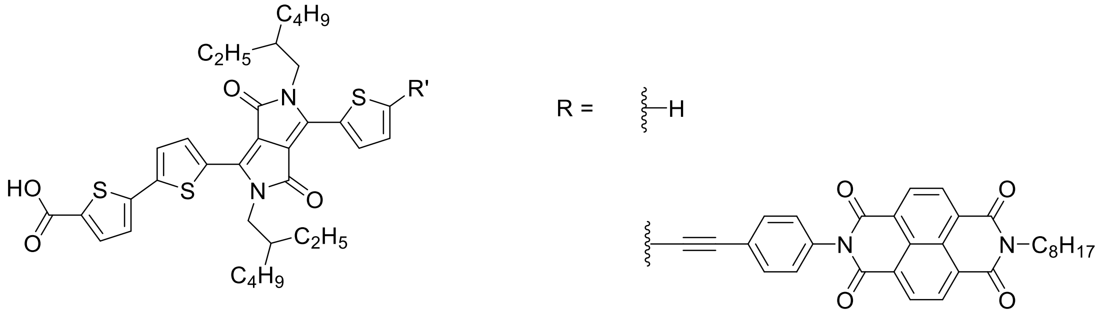

Th-DPP / Th-DPP-NDI

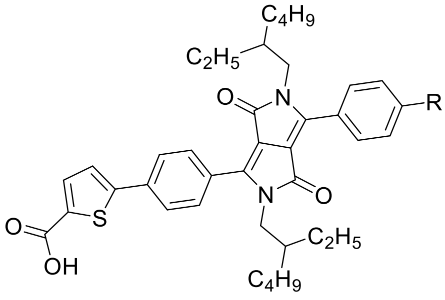

DPP-Br / DPP-NDI

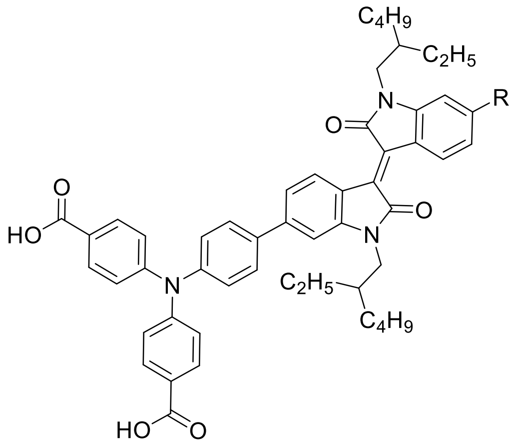

ISO-Br / ISO-NDI

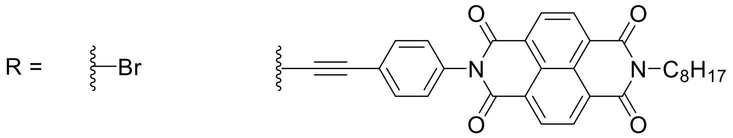

Figure 5.1. Diketopyrrollopyrole and isoindigo-based dyads used for p-DSCs, synthesised by Odobel *et al.*[10,11,13,16]

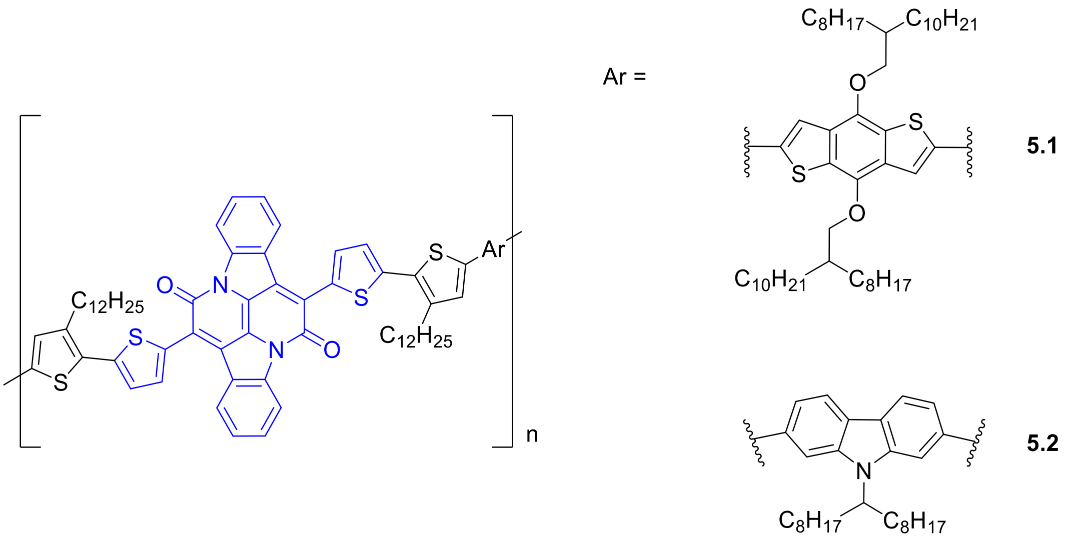

Figure 5.2. Conjugated polymers based on BAI used as organic semiconductors, synthesised by Liu *et al*.[17] The BAI core is highlighted in blue.

Despite having many favourable properties for DSC applications (a large extinction coefficient, high solubility and amenability to functionalisation), the BAI chromophore has not yet been used for either n-type or p-type cells. Therefore, this chapter discusses the development of BAI-based dyes for p-DSCs.

5.2. Results and Discussion

5.2.1. Synthesis

The synthetic route used to functionalise indigo is shown in Figure 5.3. Following a literature procedure,[17] with some modifications, the BAI core (**5.3**) was synthesised in one step by reacting indigo with 2-thienylacetyl chloride in refluxing xylene. The published purification method was to filter the precipitated product after cooling the reaction mixture. However, due to the greatly increased solubility of BAI in xylene compared to indigo (which is only sparingly soluble at room temperature), most of the product appeared to remain in solution. Therefore, the solvent was instead evaporated and the crude residue dissolved in DCM and filtered, to remove any unreacted indigo (which is insoluble in DCM). After again evaporating the solvent, **5.3** could be isolated in 65% yield by precipitating in acetone. This was halogenated using two equivalents of NBS to produce **5.4** in an 80% yield, which was purified by washing with acetone after precipitating with methanol. To avoid an asymmetric Suzuki coupling, the initial plan was to halogenate **5.3** on only one thiophene. However, due to the high reactivity of the thienyl groups, this proved difficult to carry out, despite several attempted methods of reacting with a stoichiometric amount of NBS (such as high dilution, low reaction temperature, slow addition of NBS). 4-carboxyphenylboronic acid was used for the Suzuki coupling to provide a simple anchoring unit, to initially test the suitability of BAI-based dyes for p-DSCs. The reaction was monitored by TLC and a consumption of the boronic acid was observed. No new coloured product could be detected that had remained in solution and a blue precipitate had formed during the reaction. This precipitate was washed with DCM to remove any excess starting material and solubility tests were carried out. However, this precipitate was insoluble in every solvent tested. While **5.4** was relatively soluble in chlorinated solvents, it is not surprising that the solubility decreased after desymmetrisation of the product and the introduction of a polar acidic group. As the product was too insoluble to characterise or functionalise it further, this route was abandoned in favour of attempts to make a more soluble compound.

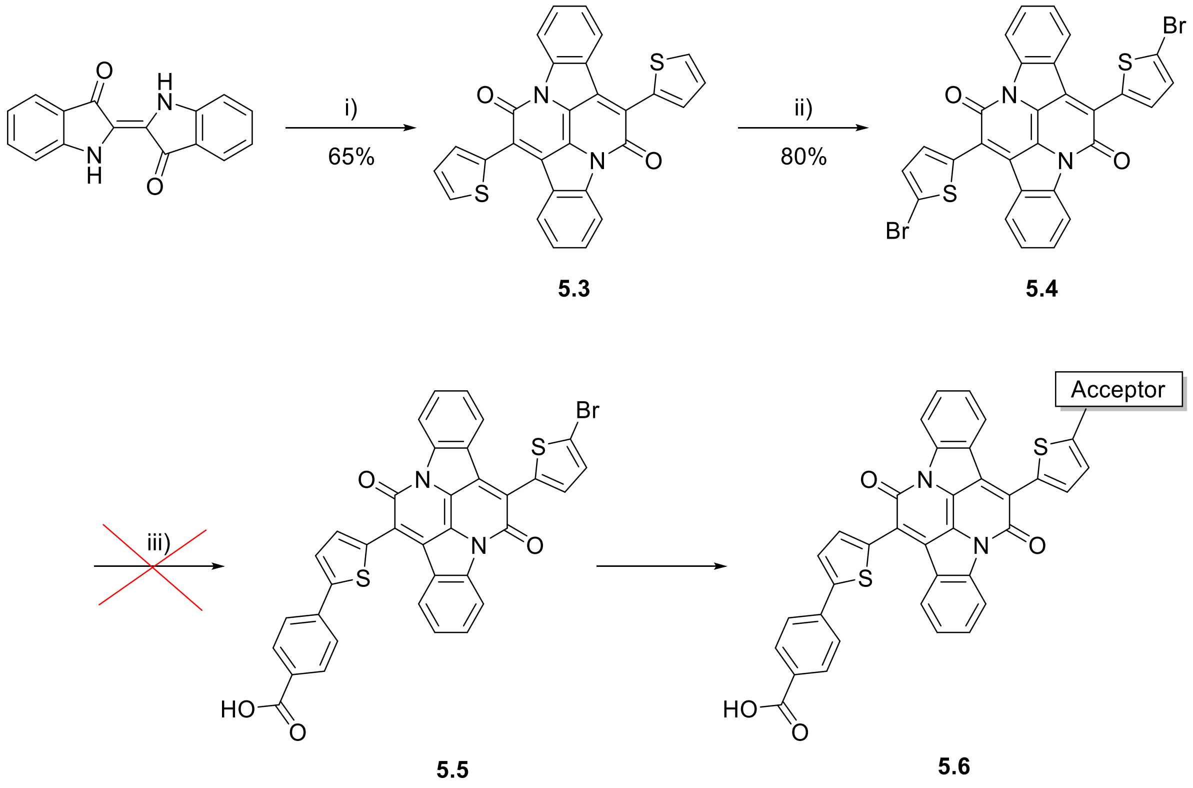

Figure 5.3. Synthesis and functionalisation of BAI. i) 2-thienylacetyl chloride, xylene, 65%; ii) NBS, DCM, 80%; iii) 4-carboxyphenylboronic acid, K_2CO_3, $Pd(PPh_3)_4$, toluene/DMF.

As the previously reported BAI polymers (**5.1** and **5.2**)[17] had been functionalised with long alkyl chains to improve their solubility, a similar approach was tested using a dihexyl fluorene-based anchoring unit (**5.7**, Figure 5.4). So that the products of the Suzuki coupling could be characterised, the fluorene unit contained a carbonyl group rather than an acid. This could be oxidised as a final step, after a sequential Suzuki coupling to introduce an electron acceptor. Alternatively, the carbonyl could have been reacted with cyanoacetic acid in a Knoevenagel reaction to produce an n-type dye. The oxidation of **5.7** was tested using silver nitrate, however, the product of the reaction was insoluble in organic solvents and could not be extracted from the aqueous reaction mixture.

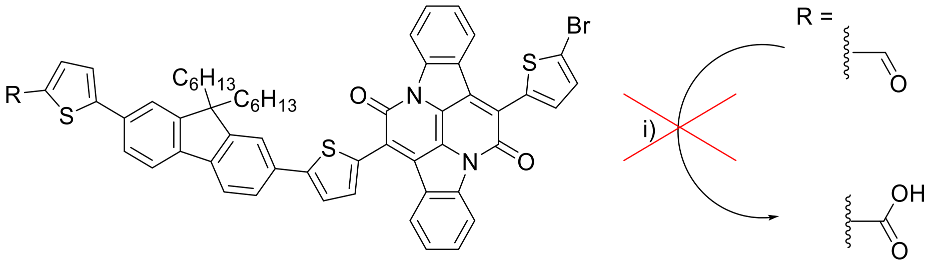

5.7

5.8

Figure 5.4. Attempted oxidation of a BAI-fluorene compound. i) Ag_2O, NaOH, H_2O/EtOH.

The cause of the insolubility of these compounds is likely to be π-π stacking of the conjugated cores. One method to reduce stacking is to functionalise the planar core with sterically demanding groups. **5.3** could not be functionalised on the phenyl rings, as the thiophenes were the more reactive functional group. Therefore, this functionalisation needed to be carried out on indigo prior to bay-annulation. Liu *et al*. have improved the solubility of the BAI core by appending 2-ethylhexyloxy chains (**EHBAI**, Figure 5.5).[19] As this core was reported to be highly soluble in common organic solvents, **EHBAI** was chosen for further investigation, beginning with the introduction of an anchoring group. The synthetic route to this compound is provided in Figure 5.6.

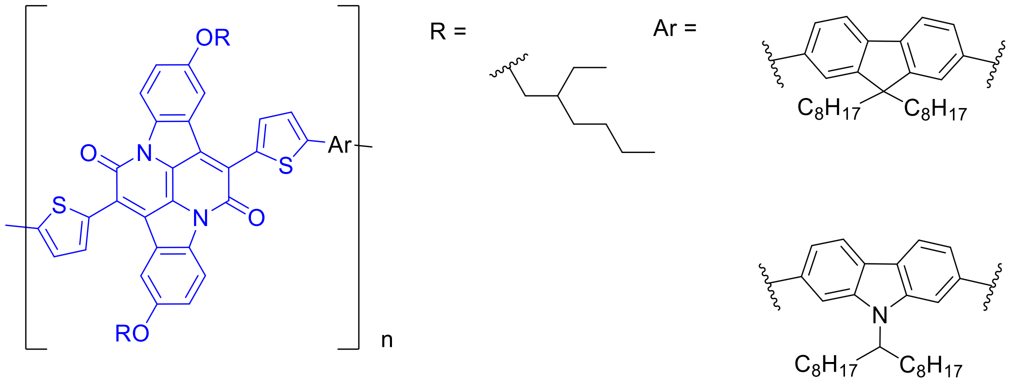

5.9

5.10

Figure 5.5. Conjugated polymers based on **EHBAI** used as electrochromic materials, synthesised by Liu *et al*.[19] The EHBAI core is highlighted in blue.

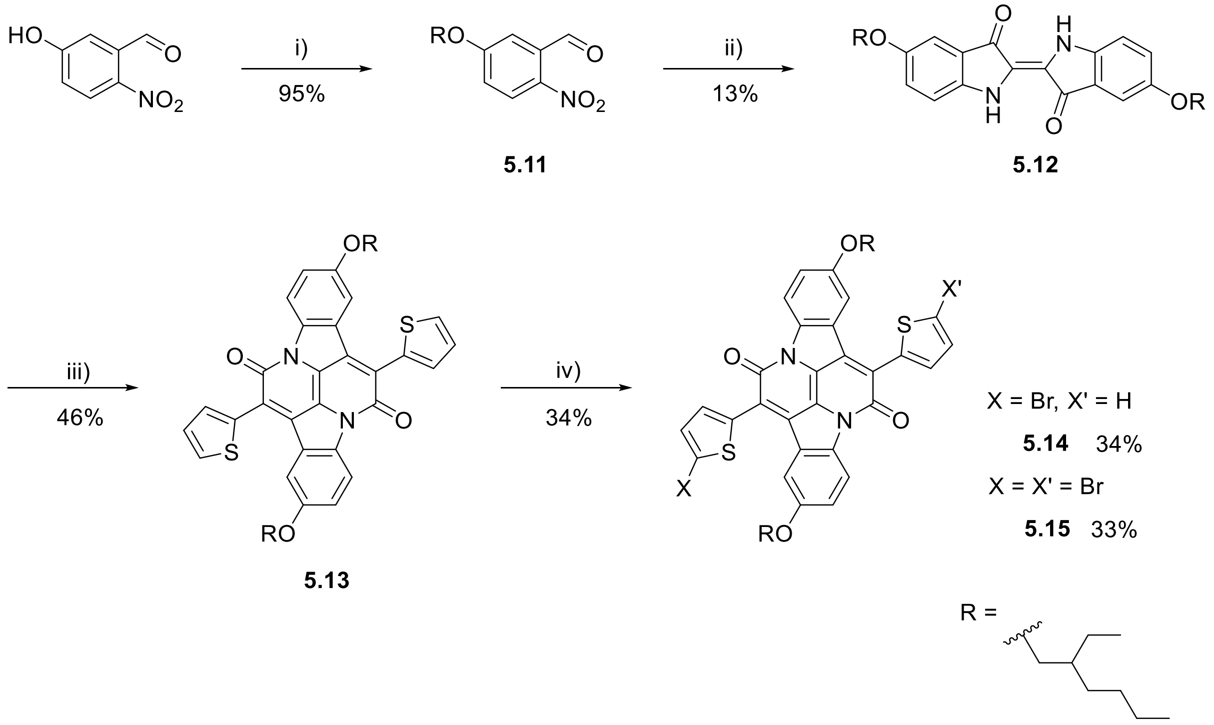

Figure 5.6. Synthesis and asymmetric halogenation of EHBAI. i) 2-ethylhexyl bromide, K_2CO_3, 18-crown-6, DMF, 95%; ii) NaOH, acetone/water, 13%; iii) 2-thienylacetyl chloride, xylene, 46%; iv) NBS, $CHCl_3$, 34%.

The first step was the alkylation of 5-hydroxy-2-nitrobenzaldehyde using 2-ethylhexyl bromide, which gave **5.11** in a yield of 95%. **5.12** was produced by the Baeyer–Drewson reaction of **5.11** and acetone in 13% yield after recrystallisation. This was reacted with 2-thienylacetyl chloride in refluxing xylene, to give the bay annulated product (**5.13**) in 46% yield after purification by recrystallisation. To avoid an asymmetric Suzuki coupling, **5.13** was brominated on one thiophene by reacting with a slight excess (1.1 eqv.) of NBS. While the reaction was not selective, the desired product (**5.14**) could be separated from the bis-brominated product (**5.15**) using column chromatography. **5.14** was isolated in a yield of 34% (with **5.15** obtained in 33% yield as a by-product). The two different products could be identified and characterised using ^{1}H NMR spectroscopy (Figure 5.7).

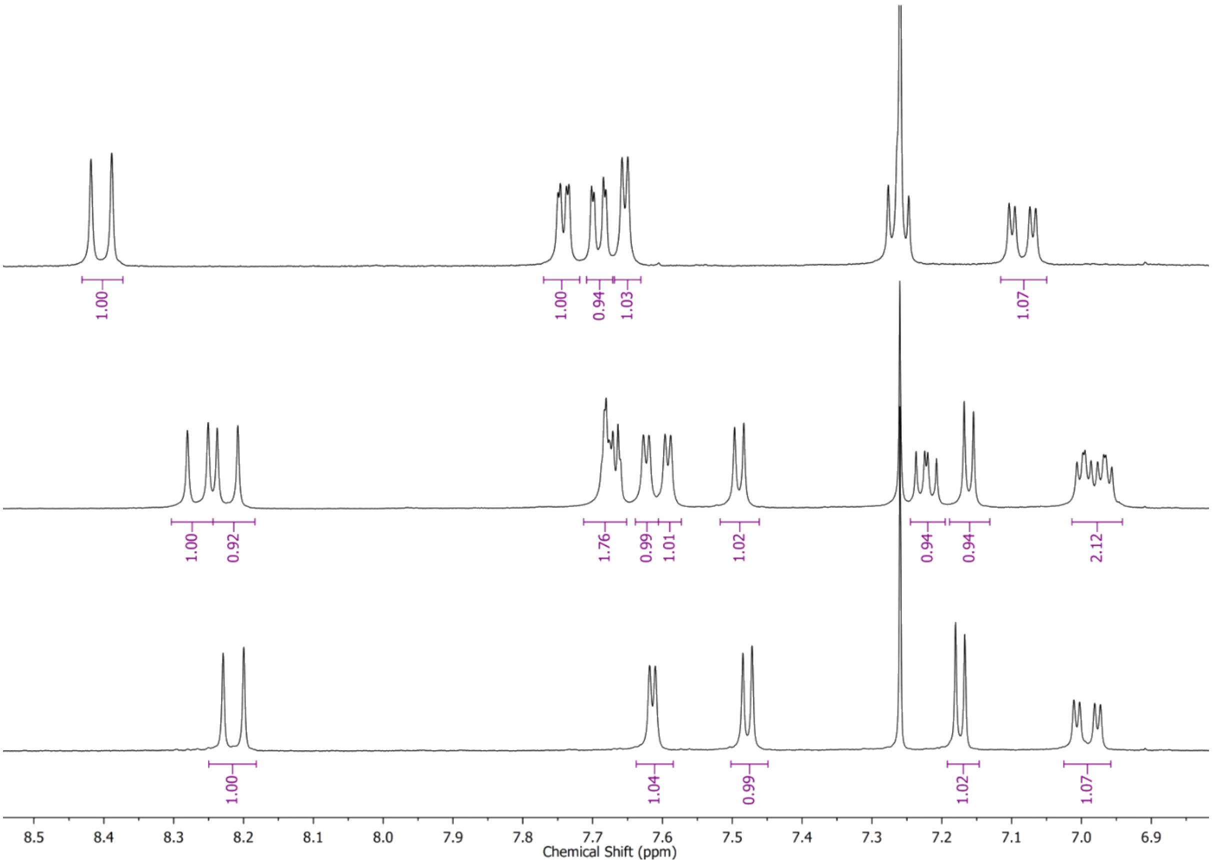

Figure 5.7. ^{1}H NMR spectra (300 MHz, $CDCl_3$) of **5.13** (top), **5.14** (middle) and **5.15** (bottom).

The ^{1}H NMR spectrum of **5.13** showed six proton environments; two doublets (*J* = 8.9 and 2.5 Hz) and a double doublet (*J* = 8.9, 2.5 Hz) corresponding to the phenyl ring and two double doublets (*J* = 5.1, 1.2 and 3.1, 1.2 Hz) corresponding to the thiophenes. A third peak, corresponding to the missing thiophene environment, overlapped with the residual solvent peak for $CDCl_3$ but should be a double doublet (*J* = 5.1, 3.1 Hz). This overlapping peak has been previously reported using a spectrometer with a higher frequency.[19]

There were five proton environments in the ^{1}H NMR spectrum of **5.15**, indicating a symmetric functionalisation. The splitting pattern of the three phenyl environments were unchanged, but they were all shifted upfield due to the mesomeric effect of bromine. The two thiophene peaks now appeared as doublets with a ${}^3J_{HH}$ coupling of 4 Hz, which confirms the bromination position.

The spectrum of **5.14** is more complex, as the desymmetrisation leads to an increase in the number of distinct proton environments. The total integration of the aromatic region gives eleven protons, indicating that the bromination has occurred on only one position. The spectrum was assigned with the aid of COSY and will be discussed in more depth in the following section (**Chapter 6.2.2**).

As **5.14** could be isolated, this offered the possibility of carrying out one Suzuki coupling to introduce the anchor/acceptor group, followed by sequential halogenation and coupling reactions to introduce the other component. Initially, a simple structure was proposed with a benzoic acid anchoring group, to test the suitability of BAI-based dyes for p-DSCs. If the model complex proved a viable dye, then at a later stage a more complex dye containing a secondary electron acceptor could be developed. An anchoring group containing BAI dye (**9**) was synthesised from **5.14** via a Suzuki coupling with 4-carboxyphenylboronic acid (Figure 5.8).

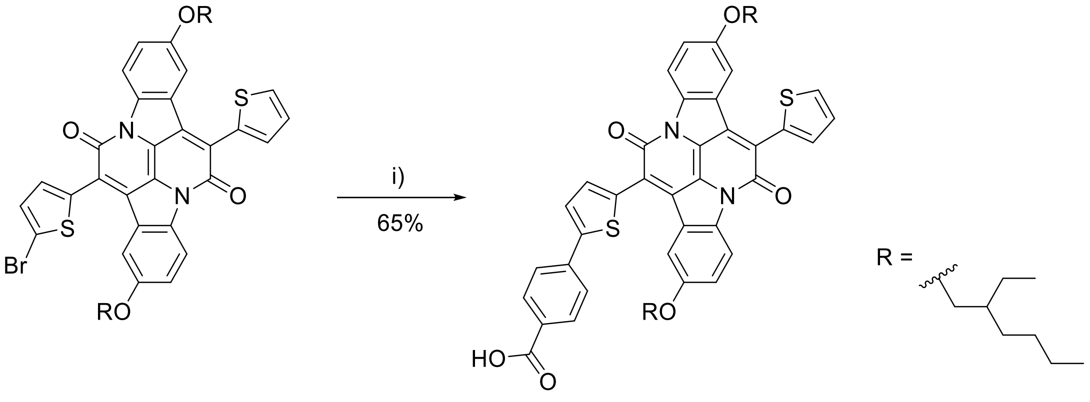

5.14 **9**

Figure 5.8. Synthesis of **9**. i) 4-carboxyphenylboronic acid, K_2CO_3, $Pd(PPh_3)_4$, dioxane/water, 65%.

When the starting material had been fully consumed (as determined from TLC analysis), the solvent was evaporated and the crude residue was purified by column chromatography. While the starting material was readily soluble in chlorinated solvents and eluted with DCM, the product from this reaction was insoluble in DCM and eluted using a 95:5:1 toluene/methanol/acetic acid mixture in 65% yield. Conversion to the product was confirmed using ${}^1H$ NMR spectroscopy (Figure 5.9), by the appearance of two new 2H doublet peaks corresponding to benzoic acid at 8.18 and 7.84 ppm. Like the product of the Suzuki reaction between **5.4** and 4-carboxyphenylboronic acid, the solubility was greatly decreased after the reaction. However, it was possible to achieve limited solubility for **9** in mixed solvent systems (such as $CHCl_3$/BuOH). The solubility was improved by adding acids or bases to the suspension of **9** in $CHCl_3$. This suggests that the insolubility was primarily due to aggregation or dimerization caused by hydrogen bonding interactions between the carboxylic acid and the carbonyl groups (on both the acid group and the core).

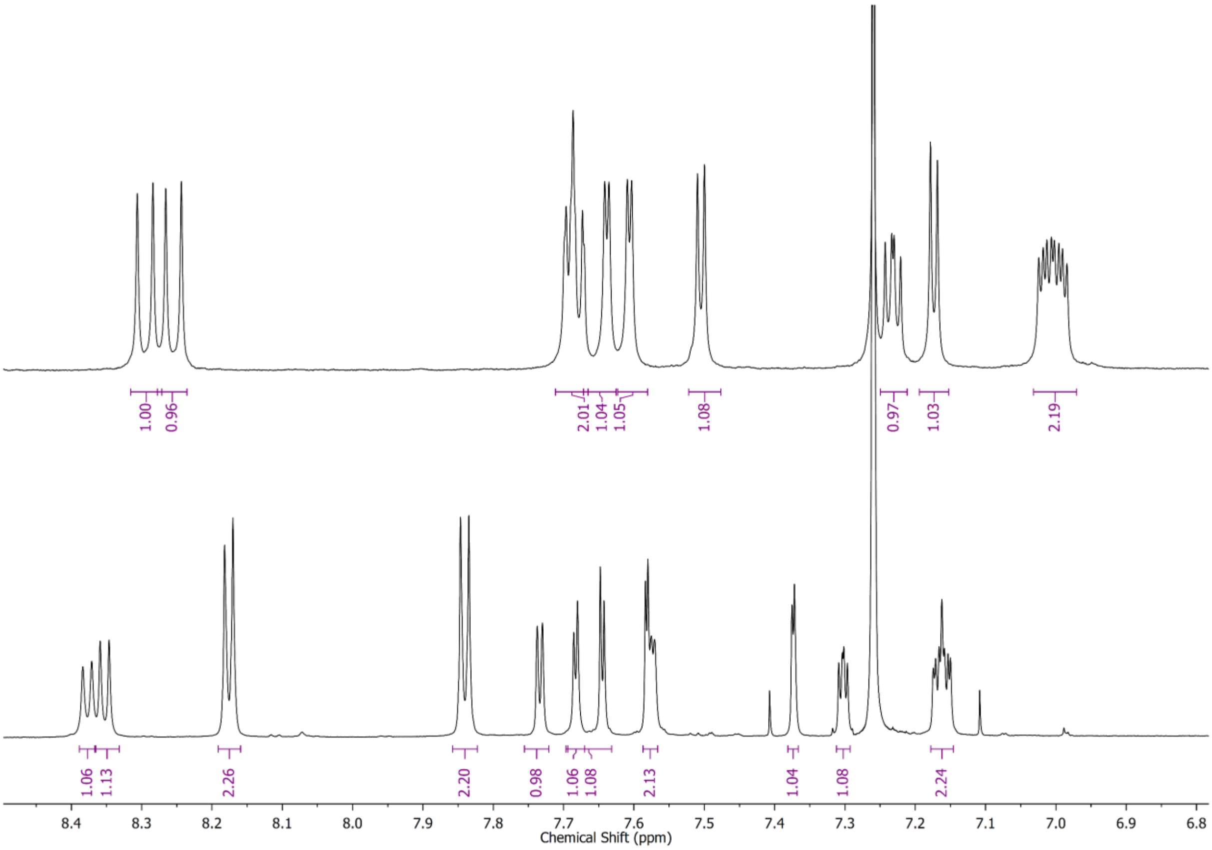

Figure 5.9. ^{1}H NMR spectra of **5.14** (top, 300 MHz, $CDCl_3$) and **9** (bottom, 700 MHz, $CDCl_3$/TFA).

5.2.2. Structural Characterisation

The structure of **9**, and the precursor (**5.14**), have been fully characterised and assigned using ^{1}H NMR spectroscopy (Figure 5.11 and Figure 5.13) and COSY (Figure 5.12 and Figure 5.14). The assignments are provided in Table 5.1 and Table 5.2 according to the labelling system shown in Figure 5.10.

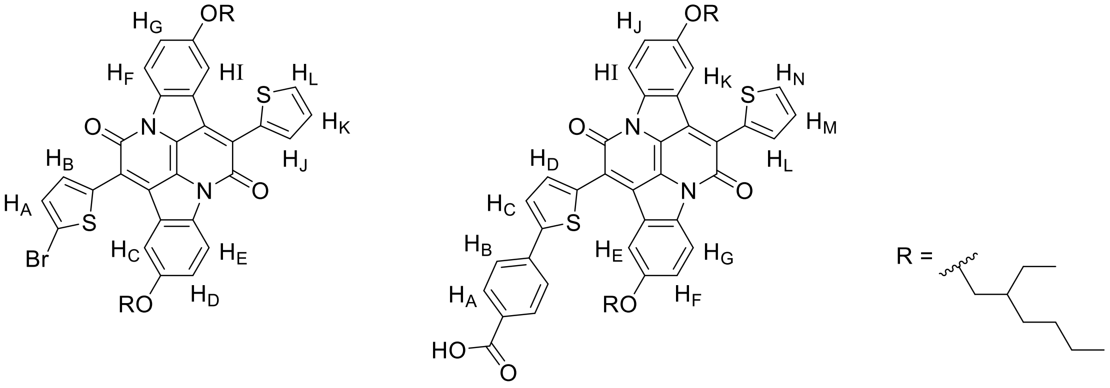

5.14 **9**

Figure 5.10. Proton labelling system for **EHBAI-Br** and **9**.

Table 5.1. Assignment of the aromatic region of the ^{1}H NMR spectrum of **5.14** (400 MHz, $CDCl_3$).

Peak	δ / ppm	m	H	$^nJ_{HH}$ / Hz	COSY	H_X
1	8.30	d	1	8.9	a	H_E
2	8.25	d	1	8.9	b	H_F
3	7.68	m (2 x dd)	2	-[a]	c/d	H_J/H_L
4	7.64	d	1	2.5	e	H_C
5	7.61	d	1	2.5	f	H_I
6	7.50	d	1	3.9	g	H_A
7	7.23	dd	1	5.1, 3.6	c/d	H_K
8	7.17	d	1	3.9	g	H_B
9	7.00	m (2 x dd)	2	-[a]	a,b,e,f	H_D/H_G

Where; δ = the chemical shift of the peak, m = peak multiplicity, H = relative number of protons, $^nJ_{HH}$ = peak coupling constant, COSY = cross-peak as determined using COSY (labelled as in Figure 5.12) and H_X = the assigned proton (labelled as in Figure 5.10). [a] Could not be determined as peaks overlap.

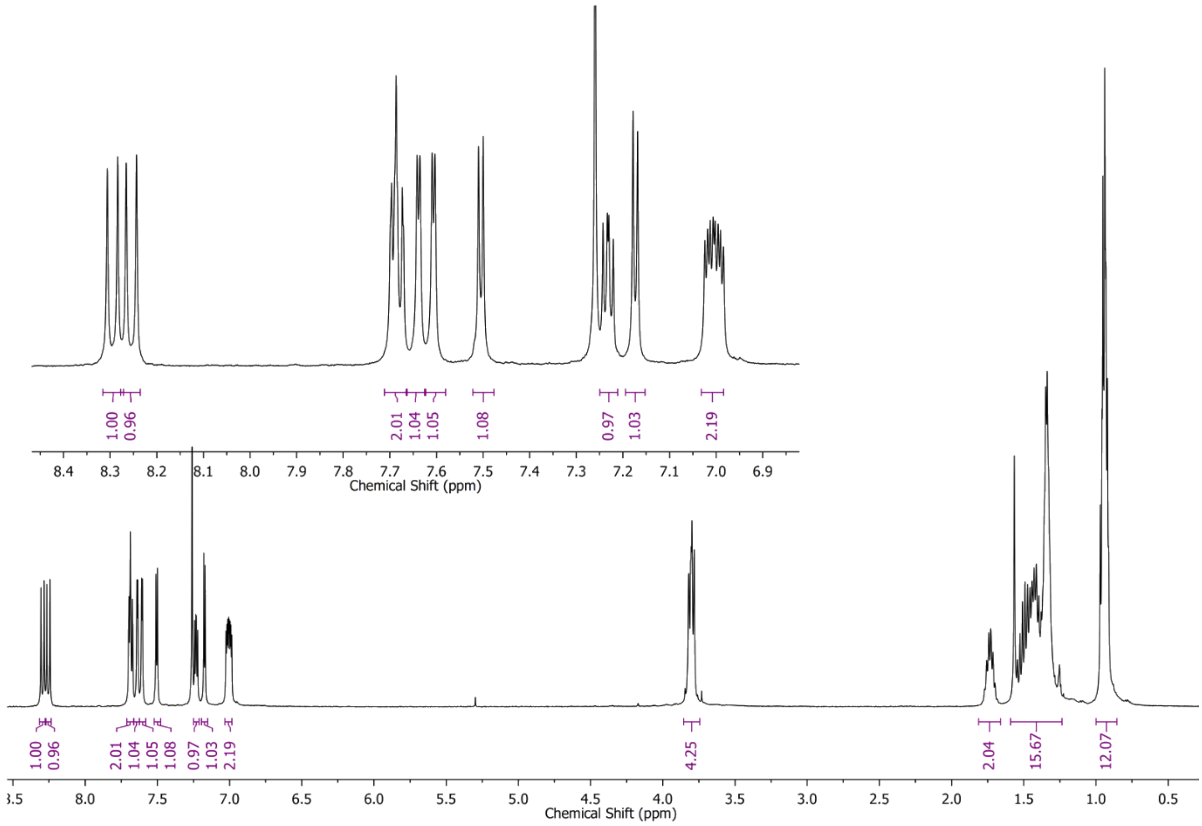

Figure 5.11. ^{1}H NMR spectrum (CDCl$_3$, 400 MHZ) of **5.14**.

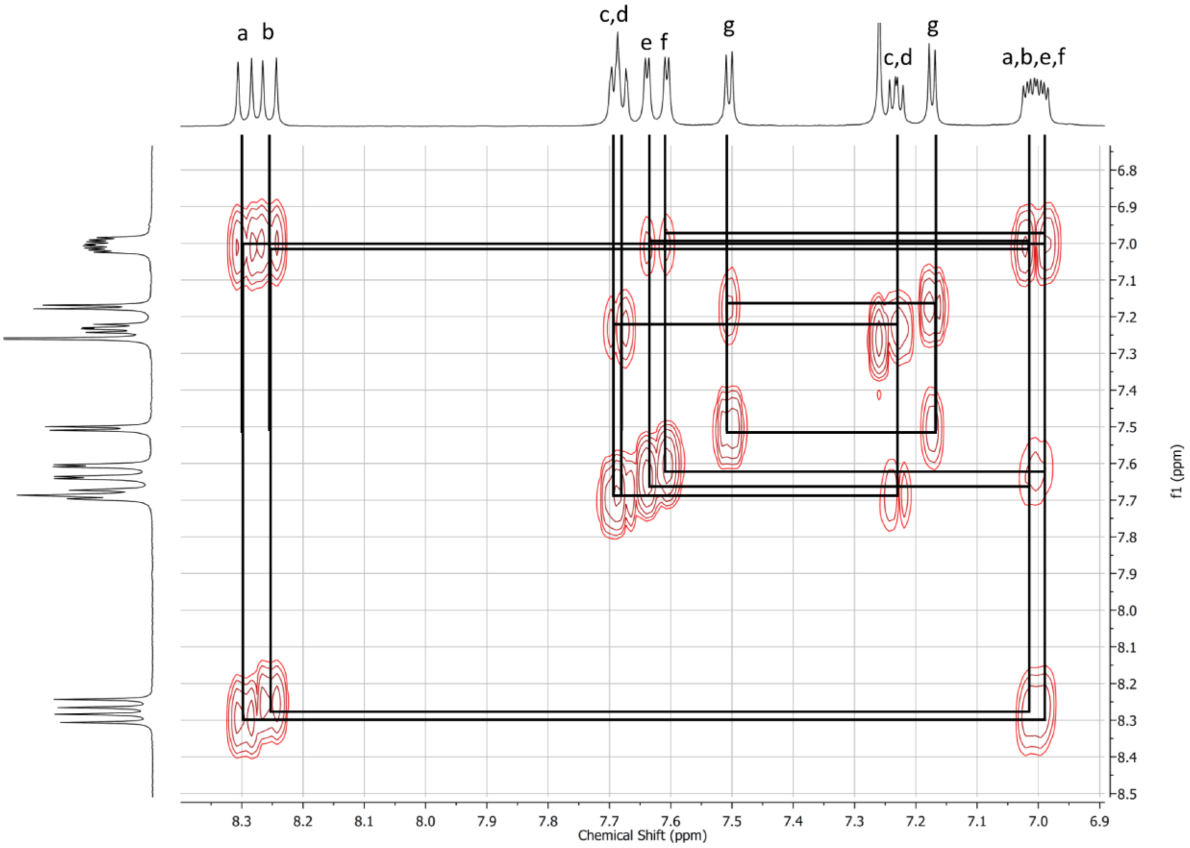

Figure 5.12. COSY spectrum (CDCl$_3$, 400 MHZ) of **5.14**.

The aromatic region of **5.14** should contain a total of eleven distinct proton signals, but there were only nine different environments, two of which had an integration of 2H. The phenyl rings contribute five of these environments; the two 1H doublets at 8.30 and 8.25 ppm with *J* = 8.9 Hz, the two 1H doublets at 7.64 and 7.61 ppm with *J* = 2.5 Hz and the 2H multiplet at 7.00 ppm. The peaks at 8.30 and 8.25 ppm correspond to H_E and H_F respectively, as the coupling constant of 8.9 Hz is indicative of a $^3J_{HH}$ ortho coupling. Protons H_C and H_I have been assigned as the two peaks at 7.64 and 7.61 ppm, as the coupling constant of 2.5 Hz suggests a $^4J_{HH}$ meta coupling. These four protons have a cross-peak in the COSY spectrum to the multiplet at 7.00 ppm, which indicates this is an overlap of two double doublets (with *J* = 8.9, 2.5 Hz) corresponding to H_D and H_G.

The remaining four proton environments correspond to the thiophenes. The two protons on the brominated thiophene (H_A and H_B) have been assigned to the two 1H doublets at 7.50 and 7.17 ppm (with *J* = 3.9 Hz, cross-peak g in the COSY spectrum), as these were the only thiophene protons with just one adjacent proton. The three protons on the other thiophene therefore correspond to the two remaining proton environments; a 1H double doublet (*J* = 5.1, 3.6 Hz) at 7.23 ppm and a 2H multiplet at 7.68 ppm. The double doublet has been assigned to H_K, as the magnitude of the two coupling constants suggests two different $^3J_{HH}$ couplings to adjacent protons. This proton environment is coupled to the 2H multiplet at 7.68 ppm, which is therefore an overlap of two double doublets (with *J* = 5.1, ≈ 1.2 and 3.6, ≈ 1.2 Hz) corresponding to H_J and H_L. These assignments were used to aid the characterisation of **9** (assignments summarised in Table 5.2).

Table 5.2. Assignment of the aromatic region of the ^{1}H NMR spectrum of **9** (700 MHz, $CDCl_3$/TFA).

Peak	δ / ppm	m	H	$^nJ_{HH}$ / Hz	COSY	H_X
1	8.38	d	1	8.8	a	H_G
2	8.35	d	1	8.8	b	H_I
3	8.18	d	2	8.1	c	H_A
4	7.84	d	2	8.1	c	H_B
5	7.73	d	1	5.1	d	H_N
6	7.68	d	1	3.8	e	H_C
7	7.65	d	1	3.8	e	H_D
8	7.58	m (2 x d)	2	-[a]	f / g	H_L / H_E
9	7.37	d	1	2.5	h	H_K
10	7.30	dd	1	5.1, 3.4	d, g	H_M
11	7.16	m (2 x dd)	2	-[a]	a,b,f,h	H_F / H_J

Where; δ = the chemical shift of the peak, m = peak multiplicity, H = relative number of protons, $^nJ_{HH}$ = peak coupling constant, COSY = cross-peak as determined using COSY (labelled as in Figure 5.14) and H_X = the assigned proton (labelled as in Figure 5.10). [a] Could not be determined as peaks overlap.

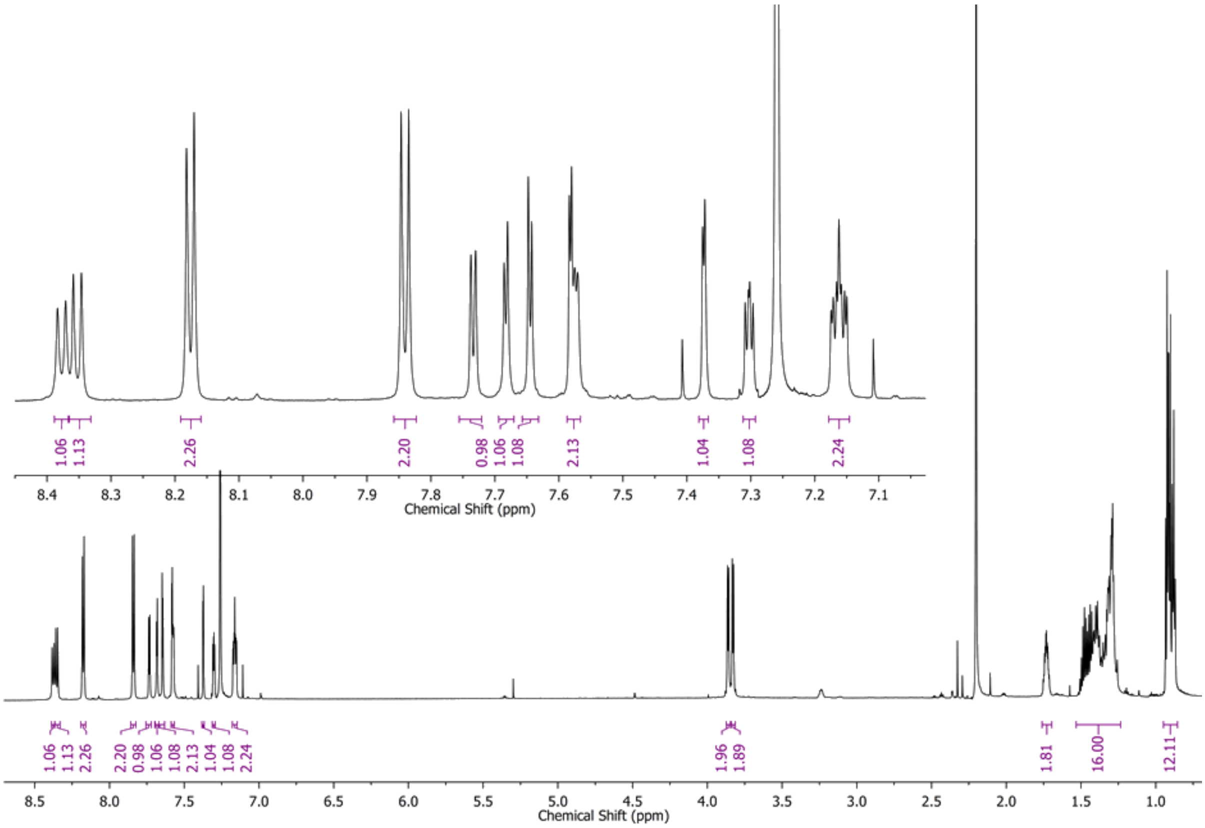

Figure 5.13. ^{1}H NMR spectrum (CDCl$_3$/TFA, 700 MHZ) of **9**.

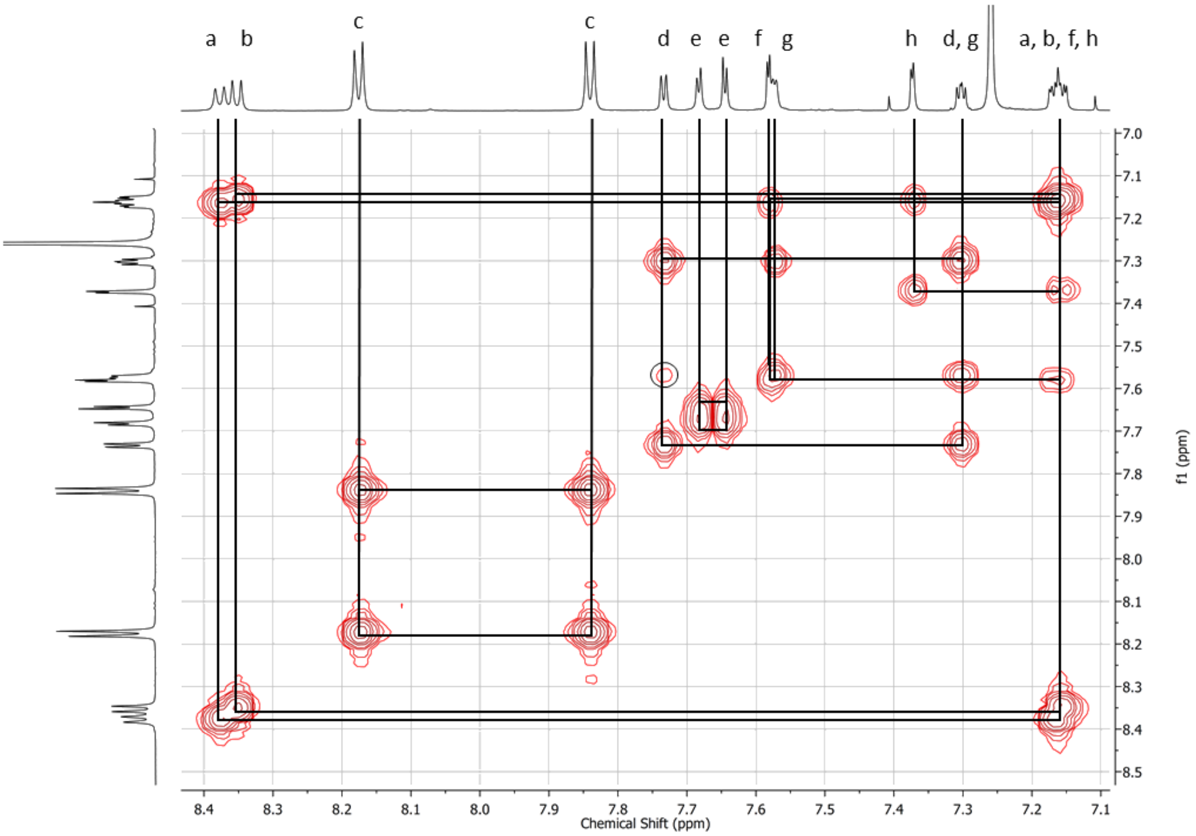

Figure 5.14. COSY spectrum (CDCl$_3$/TFA, 700 MHZ) of **9**.

The aromatic region of **9** (Figure 5.13) should contain thirteen different proton environments, but here there were eleven different signals, with two consisting of overlapping peaks. The new benzoic acid anchoring unit corresponds to the two 2H doublets at 8.18 and 7.84 ppm (J = 8.1 Hz), with the coupling confirmed using COSY (Figure 5.14). The phenyl protons on the core correspond to the two 1H doublets (J = 8.8 Hz) at 8.38 / 8.35 ppm, the overlapping 2H signal at 7.16 ppm and two 1H doublets (J = 2.5 Hz) at 7.37 and 7.58 ppm (the latter overlaps with a thienyl peak). Again, the 8.8 Hz coupling is indicative of a $^3J_{HH}$ ortho interaction and the 2.5 Hz coupling is due to a $^4J_{HH}$ meta coupling. These couplings have been confirmed using COSY, which showed a cross-peak between the overlapping 2H signal at 7.16 ppm (H_F/H_J) and the overlapping 2H signal at 7.58 ppm, which was therefore partly comprised of a phenyl signal.

Two of the thienyl protons appeared as 1H doublets at 7.68 and 7.65 ppm (J = 3.8 Hz), which correspond with the thiophene functionalised with benzoic acid. The double doublet at 7.30 ppm (J = 5.1, 3.4 Hz) corresponds to proton H_M, as this has two different $^3J_{HH}$ couplings. In the COSY spectrum, there were two cross-peaks corresponding to this signal, which show it was coupled to the 1H doublet at 7.73 ppm (J = 5.1 Hz) and the overlapping 2H signal at 7.58 ppm. This signal was therefore comprised of two overlapping doublets. A $^4J_{HH}$ coupling was not observed for the thienyl protons on the non-functionalised thiophene, but a very weak cross-peak was present in the COSY spectrum (which has been circled in Figure 5.14).

The structure was also investigated using IR spectroscopy (Figure 5.15). The spectrum for **9** contains a broad stretch around 3500 cm^{-1} which was absent in the spectrum for the precursor and is indicative of an acidic O-H bond. The carbonyl region ca. 1600 cm^{-1} was more intense for **9**, due to the presence of an additional carbonyl bond. These peaks were quite broad and less defined than for **5.14**, possibly due to hydrogen bonding interactions

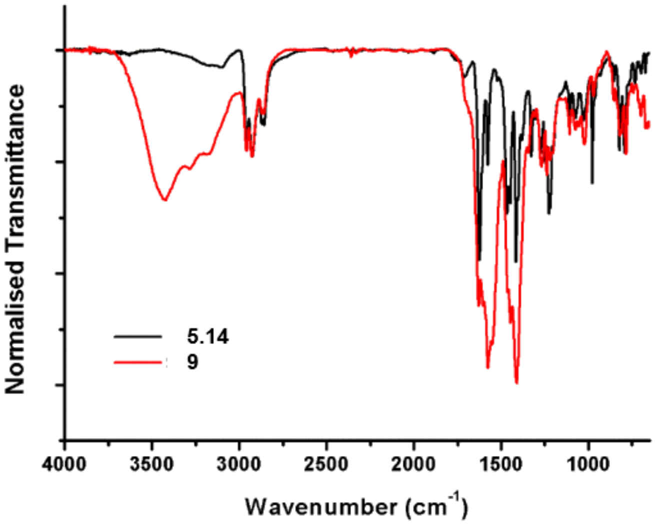

Figure 5.15. Overlaid FTIR spectra of **5.14** and **9** recorded in transmittance mode as KBr disks, normalised to the C-H stretch (2900 cm^{-1}) and baseline corrected.

5.2.3. Optical and Electrochemical Characterisation

The UV-visible absorption and emission spectra of **9** were measured in $CHCl_3$/TFA (99:1 v/v) and the results are shown in Figure 5.16 and Table 5.3. Electrochemistry was performed using a glassy carbon working electrode modified with **9** (deposited from a 2.16 x 10^{-5} M solution in $CHCl_3$/TFA (99:1 v/v)). The results are shown in Figure 5.25 – 5.26 and in Table 5.3.

Table 5.3. UV-visible absorption and emission data for **9** in $CHCl_3$/TFA (99:1 v/v). Electrochemical data recorded using a glassy carbon electrode modified with **9** (deposited from a 2.16 x 10^{-5} M solution in $CHCl_3$/TFA (99:1 v/v)), a platinum counter electrode and a SCE reference electrode. The supporting electrolyte was 0.5 M TBA PF_6 in $CHCl_3$ and all potentials were calibrated and referenced vs. Fc/Fc^+.

λ_{abs} / nm (ε / M^{-1} cm^{-1})	λ_{em} (nm)	$E_{0\text{-}0}$[a] (eV)	$E_{1/2}$Ox (V)	$E_{1/2}$Red (V)	$E_{1/2}(S^*/S^-)$[b] (V)	ΔG_{inj}[c] (eV)	$\Delta G_{reg}(I^-/I_3^-)$[d] (eV)
567 (49,650), 303 (71,375)	653	2.00	0.93	-1.25	0.75	-0.87	-0.43

λ_{abs} is the wavelength of maximum absorption, λ_{em} is the wavelength of maximum emission, $E_{0\text{-}0}$ is the zero-zero energy, $E_{1/2}$Ox and $E_{1/2}$Red are the ground state oxidation and reduction potentials (as determined using DPV), $E_{1/2}(S^*/S^-)$ is the excited state reduction potential, ΔG_{inj} is the driving force for charge transfer from NiO to the excited dye and $\Delta G_{reg}(I^-/I_3^-)$ is the driving force for regeneration of the reduced dye. [a] Determined from the intersection of the overlaid absorption and emission spectra. [b] Determined according to the equation: $E_{1/2}(S^*/S^-) = E_{1/2}\text{Red} + E_{0\text{-}0}$. [c] Determined according to the equation: $\Delta G_{inJ} = E_{VB}(\text{NiO}) - E_{1/2}(S^*/S^-)$, where E_{VB}(NiO) ≈ -0.12 V vs. Fc.[20] [d] Determined according to the equation: $\Delta G_{reg}(I^-/I_3^-) = E(I_3^-/I_2^{\cdot-}) - E_{1/2}\text{Red}$, where $E(I_3^-/I_2^{\cdot-})$ = -0.82 V vs. Fc.[21]

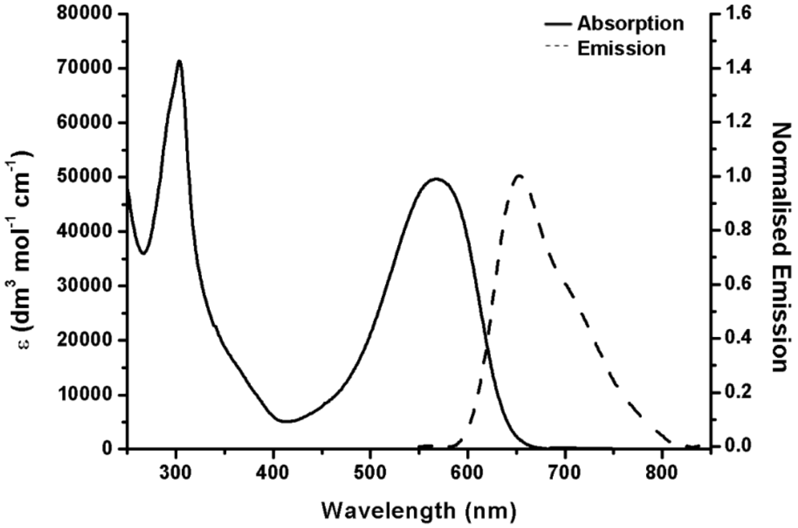

Figure 5.16. Normalised UV-visible absorption and emission spectra for **9** recorded in $CHCl_3$/TFA (99:1 v/v).

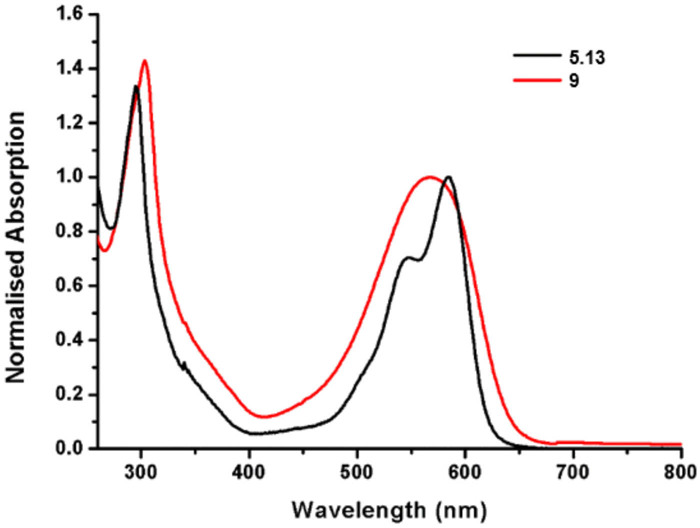

Figure 5.17. Normalised UV-visible absorption spectra of **5.13** (in $CHCl_3$) and **9** (in $CHCl_3$/TFA (99:1 v/v)).

The UV-visible absorption spectra of **9**, compared to the symmetric core (**5.13**), is provided in Figure 5.17. The two peaks visible in the absorption spectrum of **5.13** have been previously attributed to a π-π* transition (584 nm) and an intramolecular charge transfer (547 nm). In comparison, the absorption spectrum of **9** was less well-defined and broader than **5.13**. The broad absorption band at longer wavelengths is particularly suitable for p-DSCs, with the intention of constructing tandem devices.

A linear relationship between concentration and absorption was observed for the absorption spectra of **9** recorded in $CHCl_3$/TFA (99:1, v/v), over a concentration range of $1.16 \times 10^{-6} – 2.16 \times 10^{-5}$ M. Figure 5.18 shows the change in UV-visible absorption spectra of **9** recorded in $CHCl_3$/pyridine (10:1, v/v) across the same concentration range, which had a non-linear relationship between concentration and absorption. As concentration increased, an absorption band at 570 nm appeared and became more intense. Overlaying the normalised spectra (Figure 5.19) highlights that as the concentration increases, the band at 570 nm becomes more intense than the π-π* transition at 610 nm. This hypsochromic shift could be attributed to H-aggregation, which occurs when chromophores stack. This has often been observed in perylenes which have a similar planar, conjugated aromatic core.[22,23]

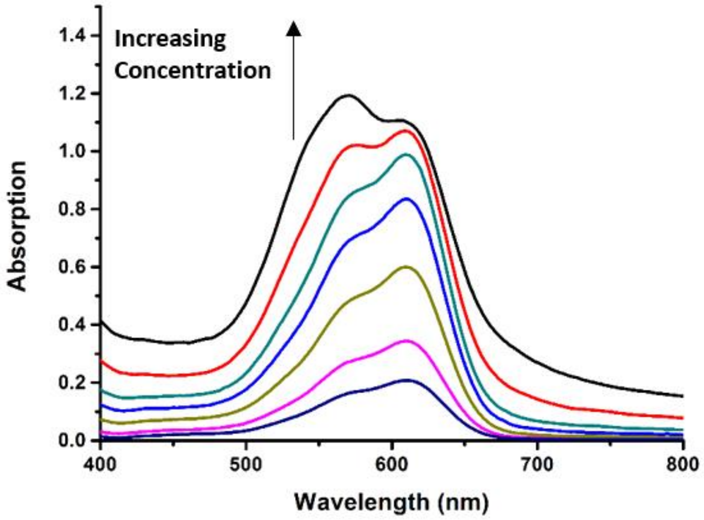

Figure 5.18. Overlaid UV-visible absorption spectra of **9** in $CHCl_3$/pyridine (10:1 v/v) with a concentration range of 1.16 x 10^{-6} – 2.16 x 10^{-5} M.

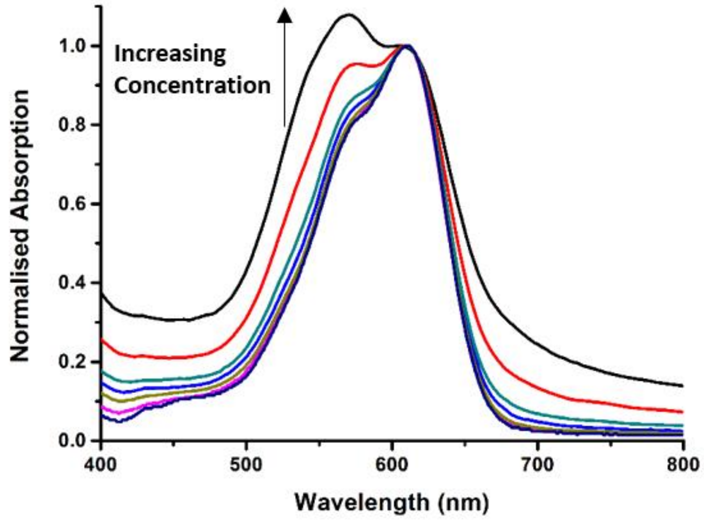

Figure 5.19. UV-visible absorption spectra (normalised to the absorption band at 610 nm) of **9** in $CHCl_3$/pyridine (10:1 v/v) with a concentration range of 1.16 x 10^{-6} – 2.16 x 10^{-5} M.

The overlaid UV-visible absorption and emission spectra of **9** are provided in Figure 5.16 (recorded in $CHCl_3$/TFA) and Figure 5.20 (recorded in $CHCl_3$/pyridine). In both solvent systems, the emission band was roughly a mirror image of the absorption profile, with a shoulder peak observed in the emission spectrum. The peak maxima were separated by a Stokes shift of 1423.38 and 2322.75 cm^{-1} for $CHCl_3$/pyridine and $CHCl_3$/TFA respectively. The emission spectra obtained from multiple excitation wavelengths were compared (Figure 5.21 and Figure 5.22) and the shape of the emission band remained unchanged. A comparison of the normalised absorption and excitation spectra recorded for various emission wavelengths (Figure 5.23 and Figure 5.24) showed a reasonable agreement, indicating that the emissive species in each case was the same.

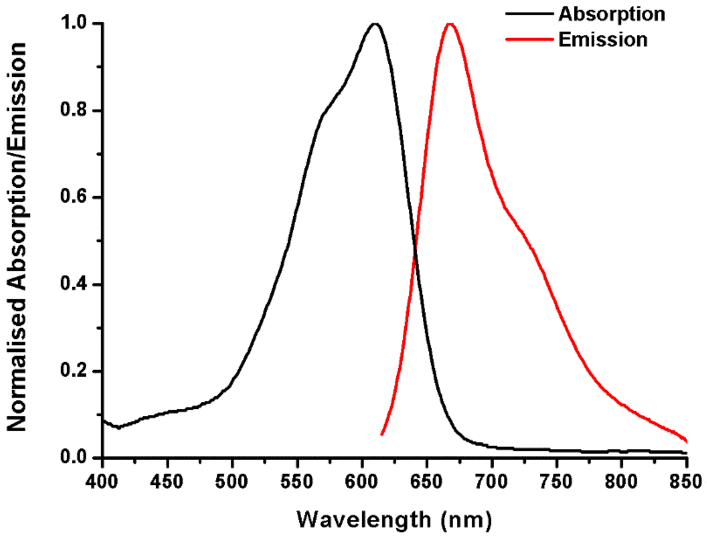

Figure 5.20. Normalised UV-visible absorption and emission spectra for **9** recorded in $CHCl_3$/pyridine (10:1 v/v).

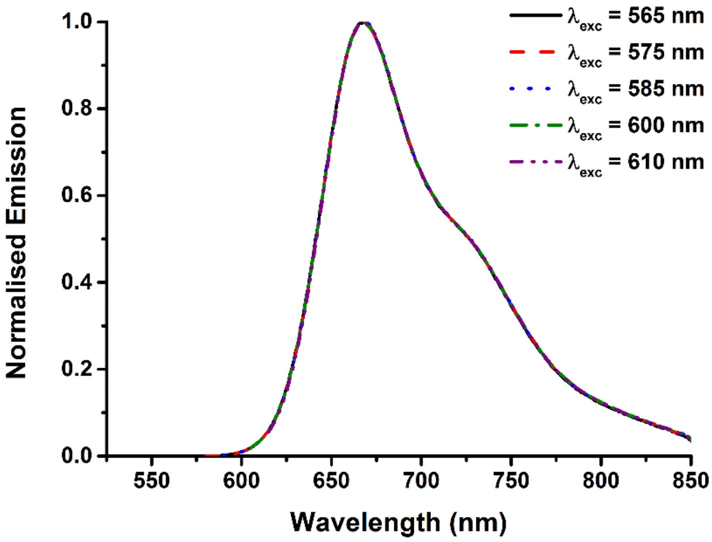

Figure 5.21. Normalised emission spectra for **9** recorded in $CHCl_3$/pyridine (10:1 v/v) with various excitation wavelengths.

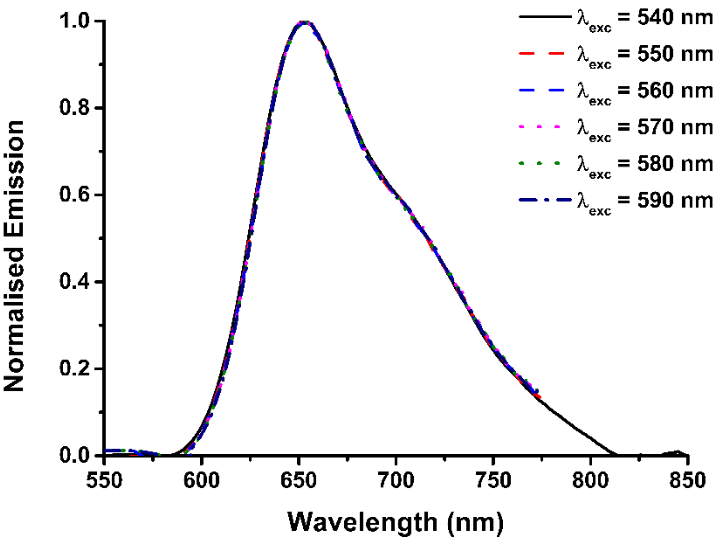

Figure 5.22. Normalised emission spectra for **9** recorded in $CHCl_3$/TFA (99:1 v/v) with various excitation wavelengths.

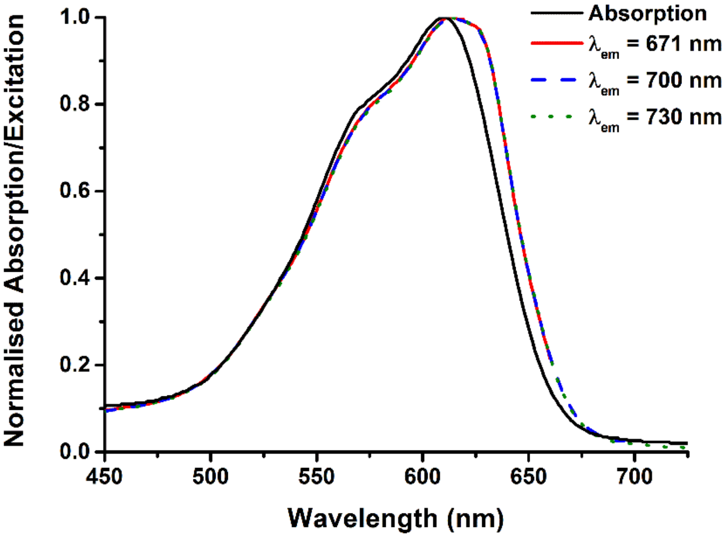

Figure 5.23. Normalised excitation spectra for **9** recorded in $CHCl_3$/pyridine (10:1 v/v) with various emission wavelengths.

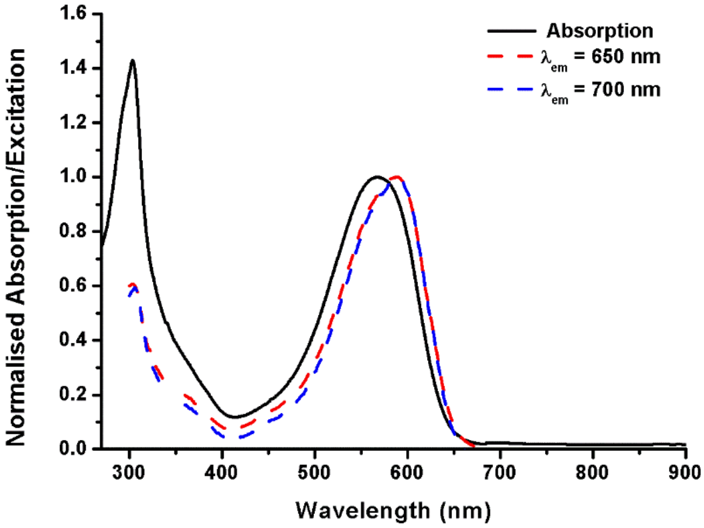

Figure 5.24. Overlaid normalised absorption and excitation spectra for **9** recorded in $CHCl_3$/TFA (99:1 v/v) with various emission wavelengths.

The ground state oxidation and reduction potentials of **9** were determined using DPV (Figure 5.25 – 5.26 and Table 5.3). The electrochemistry was performed with **9** immobilised on a glassy carbon electrode, as the dye was insoluble in single-solvent systems. Additionally, a sufficiently high concentration could only be achieved through the addition of acids/bases, which would complicate the electrochemical measurements. From this study, NiO-dye charge transfer (ΔG_{inj}) and dye regeneration (ΔG_{reg}) driving forces have been determined (Table 5.3). Liu *et al*. proposed that ΔG_{inj} > -0.8 eV is required for efficient charge separation,[20] therefore photoinduced charge transfer from NiO to **9** should be efficient (ΔG_{inJ} = -0.87 eV). There must be a sufficient driving force for dye regeneration to compete with charge recombination between the reduced dye and NiO. ΔG_{reg} (**9**) = -0.43 eV, which is comparable to previously reported values for **P1** (ΔGreg = -0.64 eV)[1] and thus should be sufficient to promote dye regeneration. These values are similar to the driving forces calculated for the BODIPY dyes (**1-5**) studied in Chapter 3 (see **Chapter 3.2.5**).

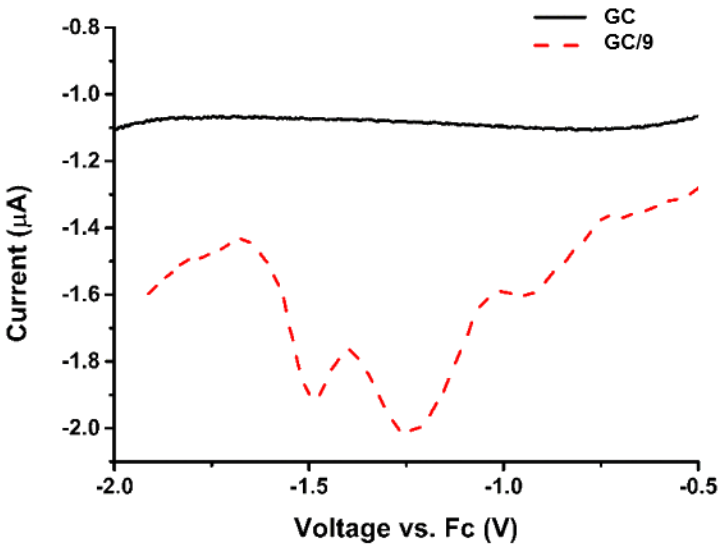

Figure 5.25. Reductive DPV (100 mV s^{-1} scan rate) recorded in 0.5 M TBA PF_6 ($CHCl_3$), performed using a pristine glassy carbon working electrode (black line) compared to a glassy carbon working electrode modified with **9** (red line).

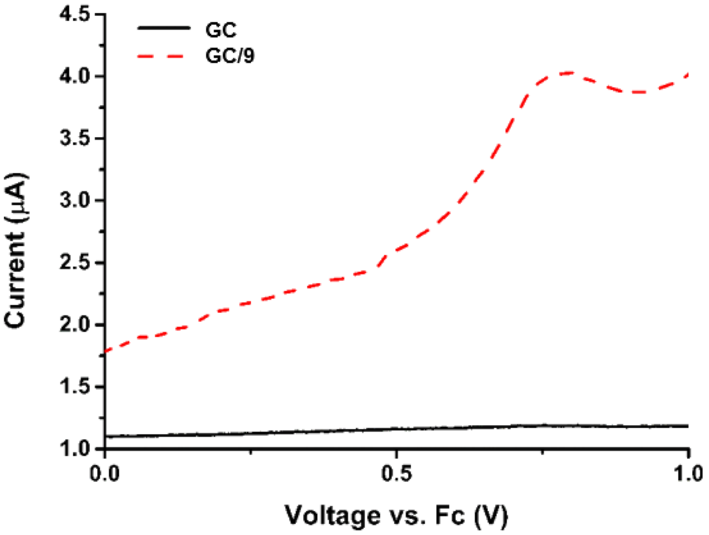

Figure 5.26. Oxidative DPV (100 mV s^{-1} scan rate) recorded in 0.5 M TBA PF_6 ($CHCl_3$), performed using a pristine glassy carbon working electrode (black line) compared to a glassy carbon working electrode modified with **9** (red line).

5.2.4. Computational Studies

Theoretical calculations were used to determine the molecular orbital distributions within **9,** to visualise the electronic transitions that will occur when the dye is integrated into a p-DSC. Theoretical energy levels and the corresponding molecular orbital distributions were calculated using the hybrid B3LYP[24] exchange functional and a 6-31G(d,p) basis set. Solvation was treated using the PCM. Initially, the ground state geometries were optimised (in $CHCl_3$), then frequency calculations were performed to check this was a true energy minimum. TDDFT calculations were then used to determine the vertical excitation energies.

The HOMO-LUMO orbital distributions, alongside the calculated energy levels are provided in Figure 5.27. Both the HOMO and LUMO were delocalised across the entire conjugated system and there was no 'push-pull' character within the molecule. This lack of a charge transfer to the periphery of the dye could be detrimental to p-DSC performance, as there is no spatial separation to hinder charge recombination.

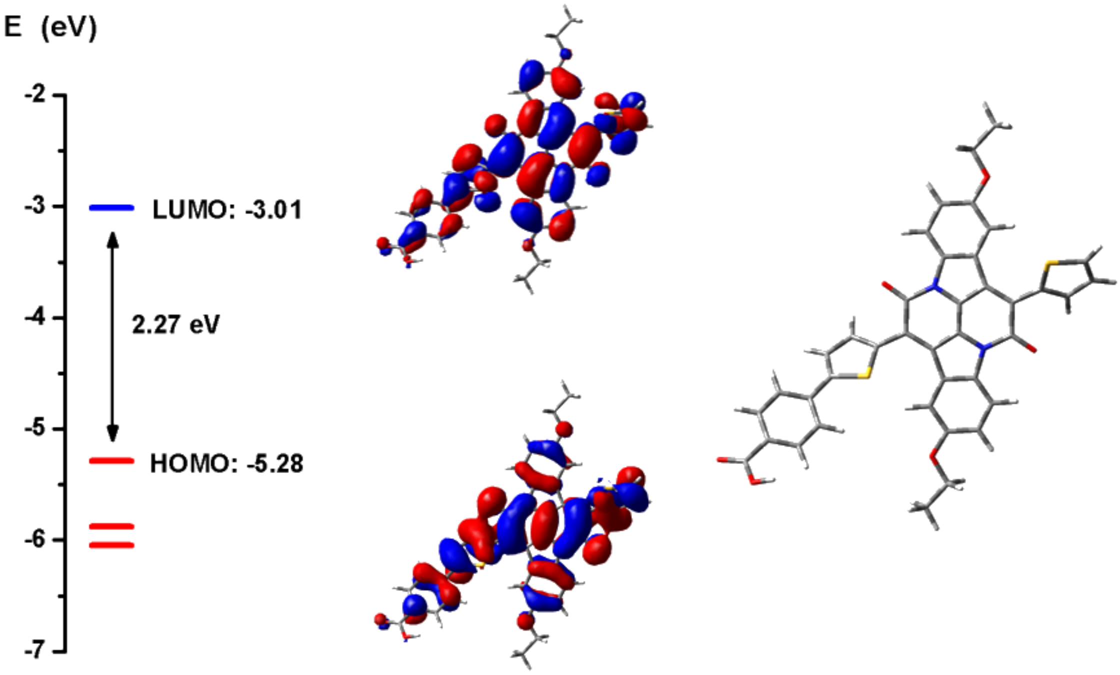

Figure 5.27. Optimised geometry, calculated energy level diagram and orbital distribution (top = LUMO, bottom = HOMO) for **9** in $CHCl_3$ using B3LYP/6-31G(d,p).

TTDFT was used to calculate the electronic transitions which were compared to the experimentally obtained absorption spectrum. The calculated transitions are summarised in Table 5.4 and a comparison of the calculated and experimental transitions is provided in Figure 5.28.

Table 5.4. Calculated singlet energy transitions for **9** determined by TDDFT (calculated using B3LYP/6-31G(d,p) in $CHCl_3$ using the PCM) and the contributions from specific orbitals. *f* is the calculated oscillator strength.

	Energy / eV (λ / nm)	*f*	Composition (contribution / %)
9	2.0306 (611)	0.9914	H → L (99)
	2.5441 (487)	0.0103	H - 2 → L (97)

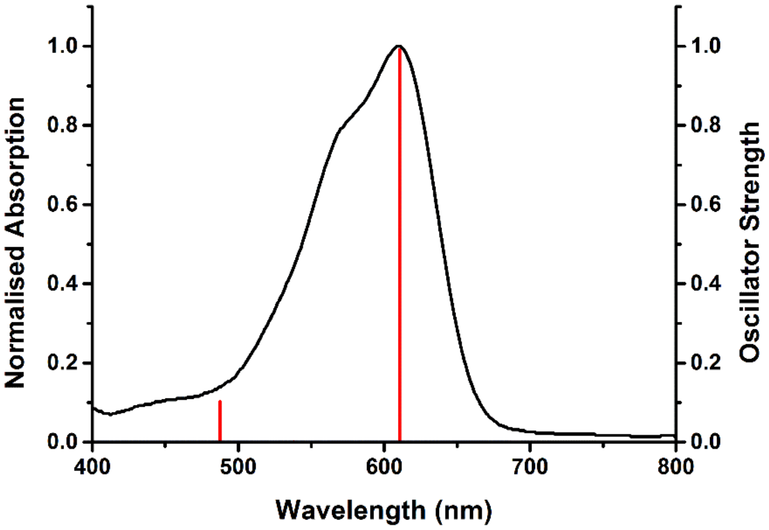

Figure 5.28. Normalised UV-visible absorption spectra (recorded in $CHCl_3$/pyridine, 10:1 v/v) overlaid with the electronic transitions calculated using TDDFT (B3LYP/6-31G(d,p), $CHCl_3$ solvation using the PCM model).

There was a good agreement between the calculated lowest energy excitation and the experimentally obtained absorption maxima for **9** (Figure 5.28). This transition corresponds with a HOMO to LUMO π-π* transition, which has very little charge transfer character. A weaker transition at higher energy was attributed to a HOMO-2 to LUMO transition, which has more charge transfer character, as the HOMO-2 orbital is predominantly located on the benzoic acid anchor and nearest thiophene. Here there is more of a shift in electron density onto the conjugated core. However, the calculated intensity was ten times lower than for the major transition.

5.2.5. Device Performances

The performance of **9**, when utilised in a p-DSC, was tested and compared to similar structures in the literature, alongside **P1** as a benchmark. Devices were constructed from **9** and **P1** by immersing NiO films (1.5 µm thickness) in a solution of the dye for 16 hours (0.3mM in MeCN for **P1** and a saturated solution in 1:1 v/v $CHCl_3$/BuOH containing 1 mM chenodeoxycholic acid for **9**). The electrolyte used was 1 M LiI and 0.1 M I_2 in MeCN. The performances are summarised in Table 5.5 and compared to previously reported values for **DPP-Br** and **Th-DPP** (Figure 5.1).

Table 5.5. Photovoltaic performance of champion p-DSCs constructed using **9** and **P1** using NiO films from the same batch (1.5 µm thickness). The values for **DPP-Br**[11] and **Th-DPP**[13] are as previously reported. Average performances with standard deviations for **9** and **P1**, as determined for 4 devices, for J_{sc}, V_{oc}, FF and η are provided in parenthesis.

	J_{sc} / mA cm^{-2}	V_{oc} / mV	FF	η / %	IPCE / %	APCE / %
9	1.13 (0.82 ± 0.22)	79 (78 ± 2)	0.33 (0.32 ± 0.003)	0.029 (0.021 ± 5.9 x 10^{-4})	7.8	10.4
DPP-Br	0.88	70	0.33	0.020	6.0	-[a]
Th-DPP	0.26	74	0.53	0.008	< 5.0	-[a]
P1	1.93 (1.71 ± 0.28)	99 (94 ± 7)	0.33 (0.34 ± 0.020)	0.063 (0.055 ± 9.9 x 10^{-3})	31.0	32.6

J_{sc} is the short-circuit current density at the $V = 0$ intercept, V_{oc} is the open-circuit voltage at the $J = 0$ intercept, *FF* is the device fill factor, η is the power conversion efficiency. [a] Not reported.

The J-V curves of the highest performing devices under illumination are provided in Figure 5.29 and the corresponding dark-current curves are shown in Figure 5.30. **9** performed modestly (producing a J_{SC} higher than 1 mA cm^{-2}), but worse than **P1**. However, there is room for optimisation here, as the results for **P1** were lower than the reported record.[25] This could be approached by optimising the film preparation or electrolyte composition (however, the concentrations used here were the same as for the record device). The photovoltage obtained for **9** was lower than for **P1**, which possibly arises through increased recombination between the electrolyte and NiO. This explanation is supported by the higher dark currents for **9** than **P1** (Figure 5.30). While the aliphatic chains present on **9** are often reported to inhibit electrolyte/NiO recombination,[26,27] the low dye loading (discussed later) could limit this effect. Despite performing worse than **P1**, the cell results for **9** were higher than the structurally related 'first-generation' DPP dyes (**DPP-Br/Th-DPP**), which shows that BAI is a promising chromophore on which to base a more structurally complex dye.

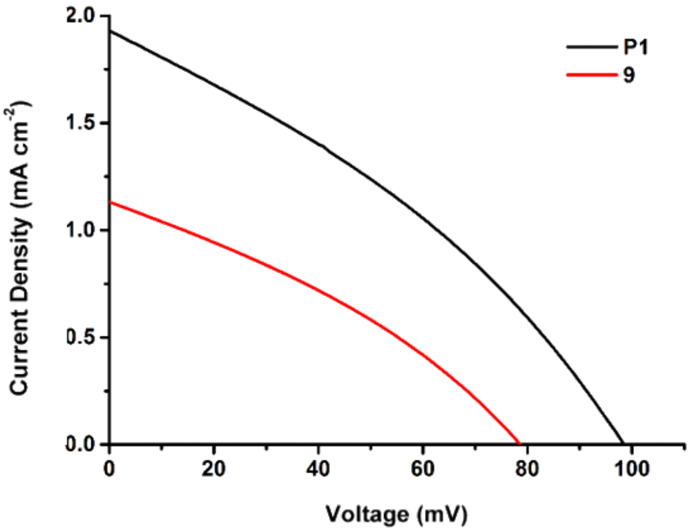

Figure 5.29. J-V curves of p-DSCs constructed using **9** and **P1** measured under illumination (AM1.5, 100 mW cm^{-2}).

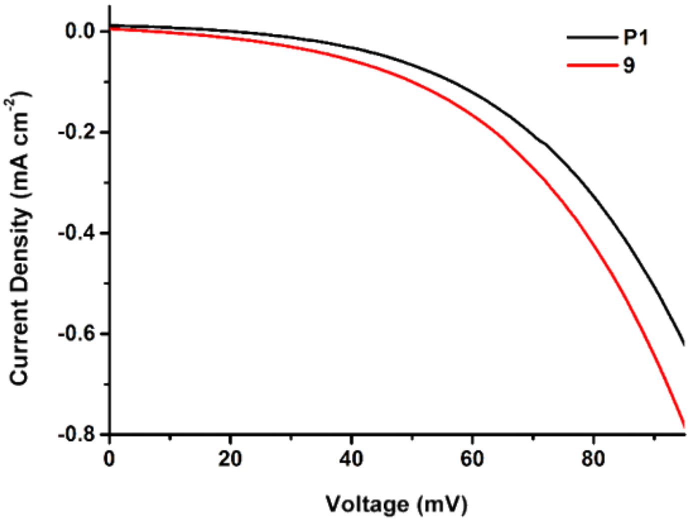

Figure 5.30. J-V curves of p-DSCs constructed using **9** and **P1** measured in the dark.

The IPCE spectra for **9** and **P1** are provided in Figure 5.31. The contribution to the photocurrent from excitation of the dye is clear from the IPCE response at longer wavelengths (with the maxima at 550 nm). However, this was much lower than the devices made using **P1** (ca. 8% for **9** vs 31% for **P1**). Most of the photocurrent produced from cells made using **9** comes from the photodissociation of triiodide (the band < 450 nm), whereas for **P1** this band was comparable to the spectral response of the dye. **9** had a slightly narrower wavelength range over which photocurrent is produced, however, this did stretch further into the NIR region than for **P1**. One possible reason for the lower IPCE is a lower LHE, as the NiO film sensitised with **9** had a lower optical density than for **P1** (A = 1.2 vs. 1.6). This was reflected in the higher APCE/IPCE ratio for **9** than **P1**. Additionally, it is possible that dye regeneration by the redox mediator is less efficient for **9**, due to the lack of charge-transfer within the dye (see Figure 5.27).

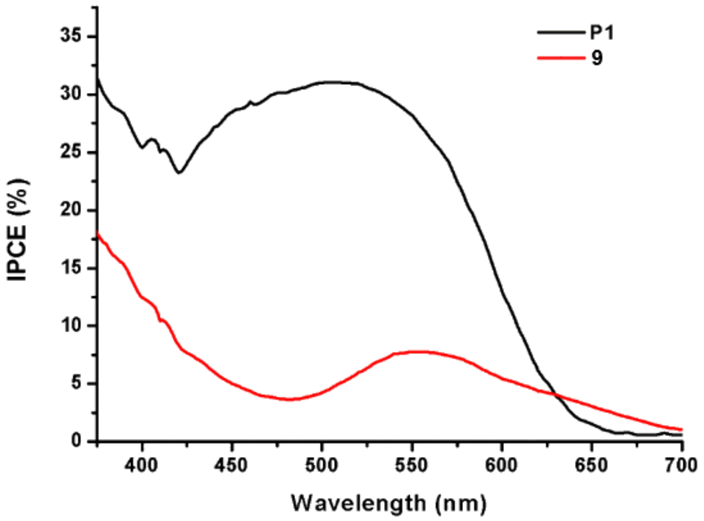

Figure 5.31. IPCE spectra of p-DSCs constructed using **9** and **P1**.

The devices were also analysed using charge extraction (Figure 5.32)[28] and small amplitude square wave light-modulated photovoltage experiments (Figure 5.33 - Figure 5.34). In the charge extraction measurement (Figure 5.32), the cell was illuminated at open circuit until a steady state of charge was reached. The illumination was then turned off, causing a decay of the charge due to recombination between NiO and the electrolyte. After a set delay time (which was varied to measure the extracted charge at various photovoltages), the cell was switched to short circuit and the charges remaining in the film were extracted. At the same charge-density, the V_{OC} was slightly higher for **9** than **P1**. This suggests that the Fermi level was slightly deeper, which is typically associated with a positive shift in the valence band edge. However, this is opposite to the trend that was anticipated from the dark current curves.

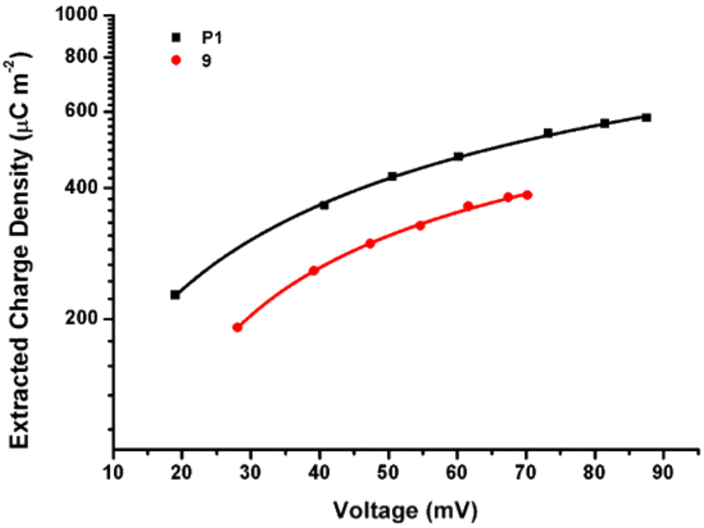

Figure 5.32. Extracted charge density as a function of photovoltage for p-DSCs constructed using **9** and **P1**.

Charge lifetime measurements (Figure 5.33) show that, at the same photovoltage, lifetimes were higher for **9** than **P1**. As the dark current measurements suggest greater electrolyte/NiO recombination for **9**, this could mean that the dye/NiO recombination rate was slower for **9** than **P1**. To remove the effect of any shift in the valence band edge, the charge lifetime was plotted as a function of extracted charge density (Figure 5.34). For each dye, the charge lifetimes were longer at lower charge densities, as there is a lower concentration of holes in the NiO valence band to recombine. Charge lifetimes at the same charge density were considerably higher for **9** compared to **P1**. This suggests that recombination between holes in the NiO with the reduced species in the electrolyte was slower for **9** than **P1**. However, this did not increase the V_{OC} at 1 sun illumination. Reasons for this could be that fewer charges were injected into the NiO, or charge-recombination between the reduced dye with charges in the NiO could be faster for **9** compared to **P1**. Additionally, this discrepancy could be due to the small charge values recorded in this experiment.

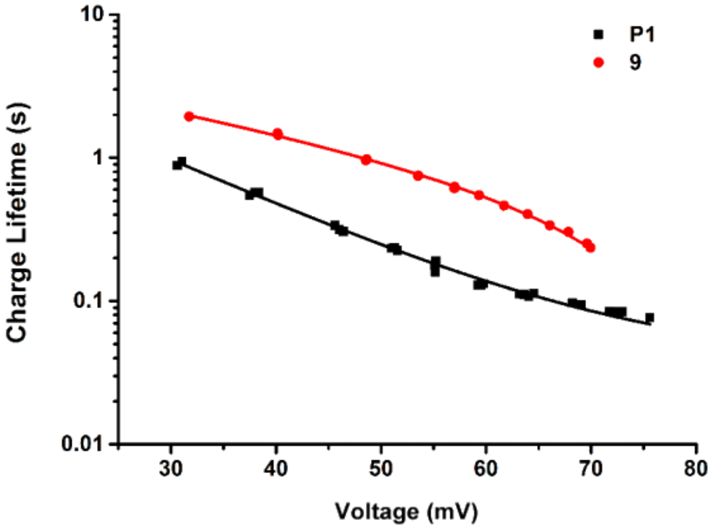

Figure 5.33. Charge lifetime as a function of photovoltage for p-DSCs constructed using **9** and **P1**.

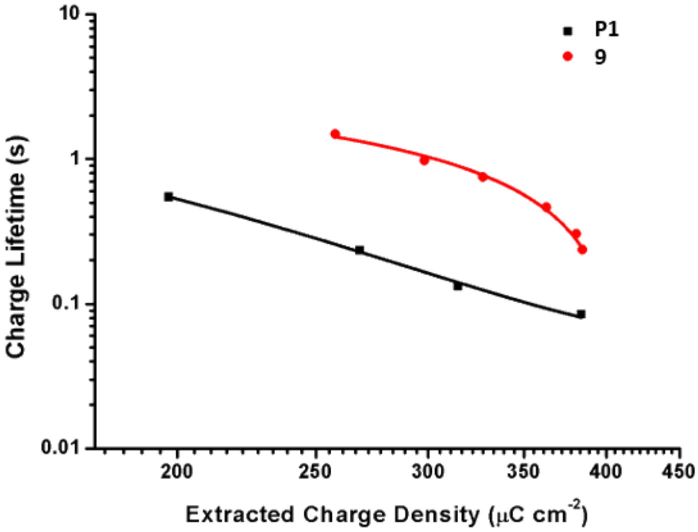

Figure 5.34. Charge lifetime as a function of extracted charge density for p-DSCs constructed using **9** and **P1**.

Poor dye loading was possibly a major reason for the lower p-DSC performance of **9**. A comparison of the UV-visible absorption spectra of **9** and **P1** adsorbed onto NiO films of the same thickness is provided in Figure 5.35.

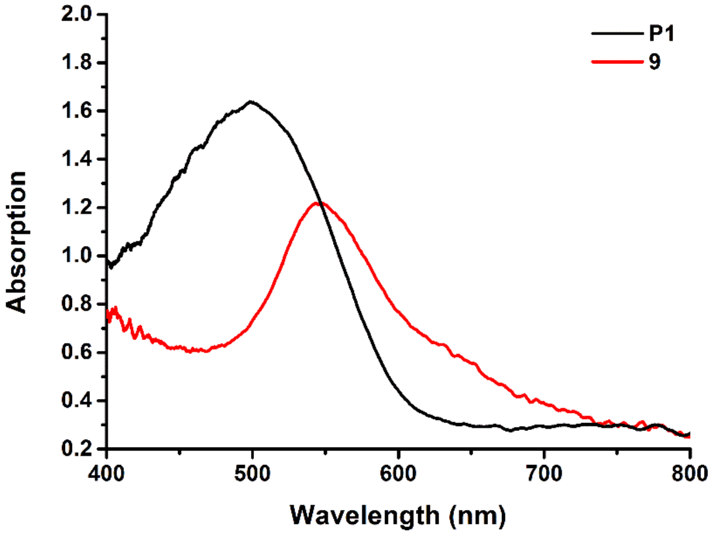

Figure 5.35. UV-Visible absorption spectra of NiO films (1.5 µm thick) sensitised with **9** and **P1**.

Assuming that the extinction coefficient of the immobilised dye is not significantly changed from the values calculated from solution, dye loading can be calculated from the following equations:

$$A(\lambda) = \Gamma_{pro}\sigma(\lambda)$$

Equation 5.1.

$$\sigma(\lambda) = \varepsilon(\lambda) * 1000\ cm^3/dm^3$$

Equation 5.2.

Where Γ_{pro} is the number of moles of dye per square centimetre of projected surface area (mol cm^{-2}), A is the film absorbance, σ is the absorption cross-section (cm^2 mol^{-1}) and ε is the molar extinction coefficient for the dye in solution.

Using 58,000 M^{-1} cm^{-1} as the extinction coefficient for **P1**,[25] dye loading was estimated as 22.4 nmol cm^{-2}. In comparison, **9** had a lower dye loading of 12.1 nmol cm^{-2}. The branched ethylhexyl chains were necessary to improve the solubility of the BAI core, to allow functionalisation with an anchoring group. However, the added steric bulk, in addition to the limited solubility of **9** in the dye-bath solvent, likely contributed to the low dye loading. This will reduce the LHE of the device, which will reduce the J_{SC} produced. Much larger dyes have been reported with higher dye loadings, such as **BH4**[27] (Figure 5.36) which has a reported dye loading of 22 nmol cm^{-2} for NiO films with thickness between 1.6 – 1.8 µm. It is possible that for **9**, the anchoring unit is too short and positioned too close to the bulky alkyl chains, thereby hindering adsorption onto NiO.

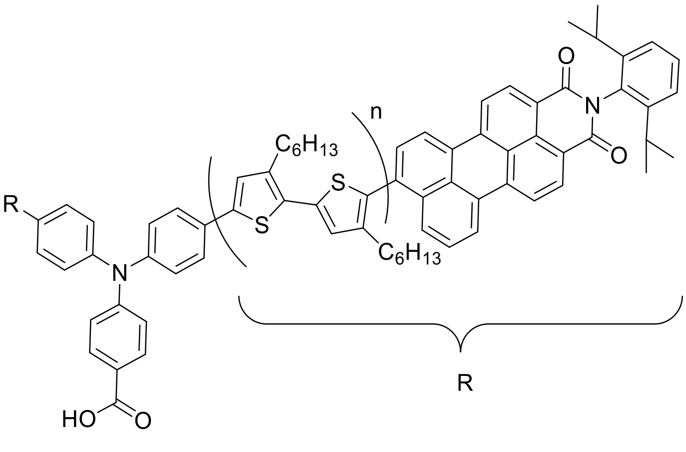

BH4 (n = 2)

Figure 5.36. Chemical structure of **BH4**[27].

While the p-DSC performances of **9** were quite low, it is a promising structure when compared to the performances of the ‘first generation’ DPP dyes published by Odobel *et al*.[11,13] Table 5.6. summarises the performances of these compared to the improved ‘second generation’ dyes containing an additional electron acceptor (NDI).[11,13]

Table 5.6. Photovoltaic performance of p-DSCs constructed using **9** compared to **DPP-Br/DPP-NDI**[11] and **Th-DPP/Th-DPP-NDI**[13] as previously reported.

	J_{sc} / mA cm^{-2}	V_{oc} / mV	FF	η / %	IPCE / %
9	1.13	79	0.33	0.029	7.8
DPP-Br	0.88	70	0.33	0.020	6.0
DPP-NDI	1.79	81	0.34	0.048	25.0
Th-DPP	0.26	74	0.53	0.008	< 5.0
Th-DPP-NDI	7.38	147	0.32	0.35	55.0

J_{sc} is the short-circuit current density at the $V = 0$ intercept, V_{oc} is the open-circuit voltage at the $J = 0$ intercept, *FF* is the device fill factor, η is the power conversion efficiency.

When compared to the other dyes that do not contain an NDI acceptor, p-DSCs made from **9** performed more efficiently, especially compared to **Th-DPP**. As **DPP-Br** contains a peripheral bromine substituent, the electronegativity will impart some degree of push-pull nature, even without the NDI group present. This is possibly why it performs more efficiently than **Th-DPP**. In both cases, when NDI is present, the p-DSC performances were greatly improved. The solar cell characteristics for devices incorporating **Th-DPP-NDI** were comparable to record devices reported by other groups.[1,27,20] The significant differences between **DPP-NDI** and **Th-DPP-NDI** have been attributed to the thiophene bridges improving electronic coupling between NiO and the dye compared to the phenyl groups.

If **9** could be functionalised with an NDI group, then improved performances should also be seen. Ideally, due to the increased extinction coefficient of the BAI core compared to DPP, a higher J_{SC} could be obtained. Taking into consideration the solubility issues encountered during the synthesis of **9**, it would be beneficial to perform the Suzuki coupling with an ester protected anchoring group, so that sequential halogenation and coupling reactions could be performed. A model EHBAI-NDI dyad (Figure 5.37) has been investigated using DFT methods, and the NDI group does appear to impart charge transfer character onto the dye (Figure 5.38). This should produce a longer-lived charge separated state and improve the J_{SC}.

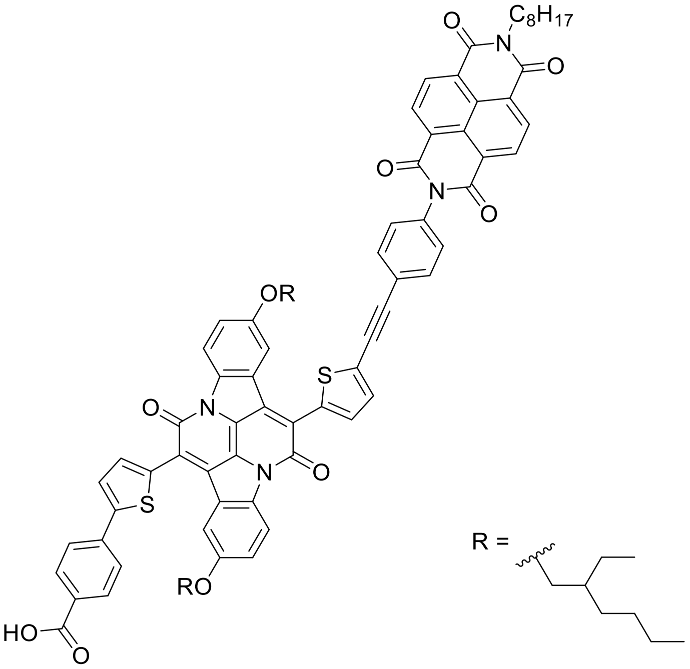

Figure 5.37. Possible structure of a BAI-NDI dyad.

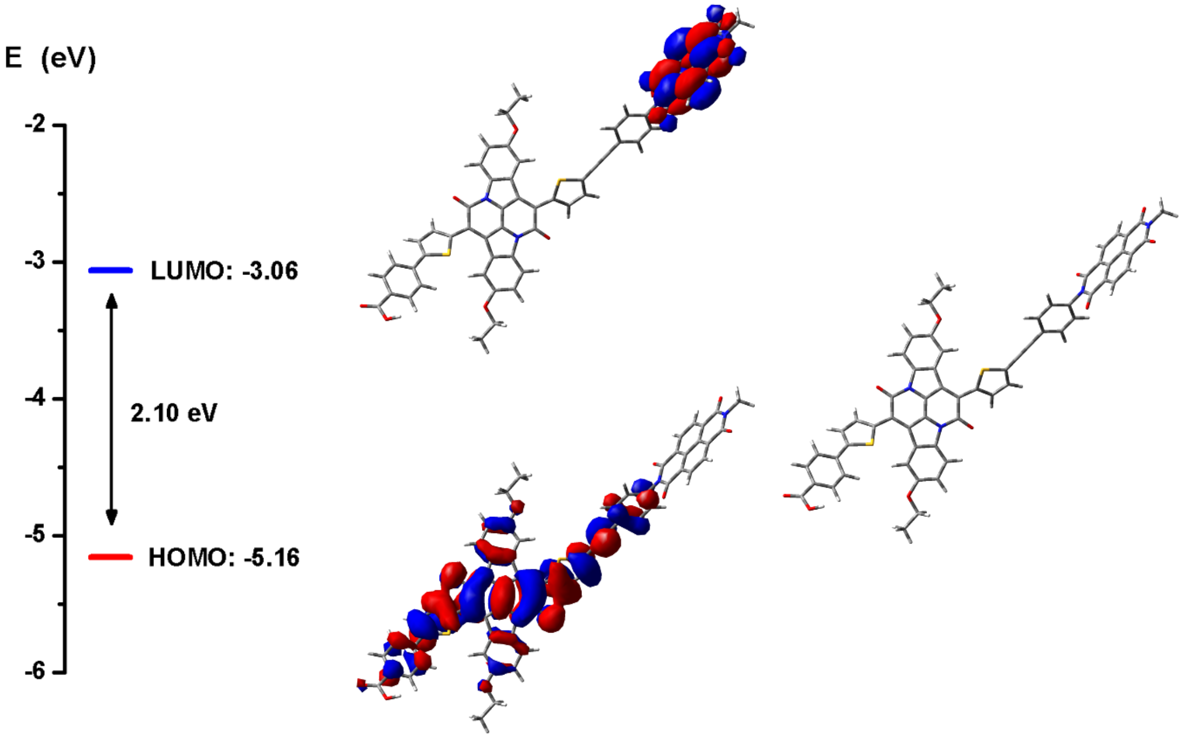

Figure 5.38. Optimised geometry, calculated energy level diagram and orbital distribution (top = LUMO, bottom = HOMO) for the BAI-NDI dyad in $CHCl_3$ using B3LYP/6-31G(d,p).

5.2.6. Conclusions

In this chapter, the BAI chromophore was found to be a suitable chromophore to develop dyes for p-DSCs. Due to its limited solubility, BAI derived from indigo could not be used. However, a BAI core containing solubilising branched alkyl chains was successfully functionalised with an anchoring group, which allowed covalent bonding to NiO. The characterisation of this dye was hindered by its low solubility in most solvents, which possibly arises from both hydrogen bonding interactions and aggregation caused by π-π stacking.

p-DSCs constructed using **9** produced reasonable photocurrent densities (J_{sc} = 1.13 mA cm^{-2}), which were higher than other first-generation DPP dyes reported. The performances seem to be limited by low dye loading and dye aggregation. It is also possible that the lack of push-pull character could be hindering the photoelectrochemical properties. This could be improved by introducing an additional electron acceptor unit, such as NDI, an approach which has been successful for related DPP dyes. These results have highlighted several challenges for integrating BAI dyes into p-DSCs and have formed the foundations for a longer study in the future.

5.3. Experimental

5-((2-ethylhexyl)oxy)-2-nitrobenzaldehyde (5.11)

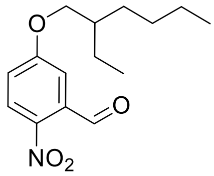

5-hydroxy-2-nitrobenzaldehyde (2.5 g, 14.96 mmol, 1 eqv.), K_2CO_3 (6.2 g, 44.88 mmol, 3 eqv.) and 18-crown-6 (30 mg, 0.11 mmol, 0.75 mol %) were loaded into a two-neck round bottom flask and purged with three vacuum/nitrogen cycles. Anhydrous DMF (30 mL) and 2-ethylhexyl bromide (4.3 g, 22.44 mmol, 1.5 eqv.) were added and the mixture was heated at 80 °C for 36 hours. After cooling to room temperature, the solution was filtered and evaporated. The residue was purified using column chromatography (silica gel, 2:1 petroleum ether/DCM) to give **5.11** as a light-yellow oil (3.97 g, 95% yield).

^{1}H NMR (400 MHz, $CDCl_3$): δ 10.49 (s, 1H), 8.15 (d, *J* = 9.1 Hz, 1H), 7.32 (d, *J* = 2.8 Hz, 1H), 7.14 (dd, *J* = 9.1, 2.8 Hz, 1H), 3.98 (m, 2H), 1.82-1.72 (m, 1H), 1.52-1.40 (m, 4H), 1.35-1.28 (m, 4H), 0.96-0.89 (m, 6H) ppm.

^{13}C NMR (101 MHz, CDCl3): δ 188.80, 164.00, 142.07, 134.49, 127.36, 118.96, 113.88, 71.92, 39.29, 30.45, 29.10, 23.83, 23.09, 14.16, 11.17 ppm.

IR (neat, ATR): v = 2959, 2929, 2363, 1699, 1581, 1515, 1462, 1386, 1328, 1285, 1323, 1071, 1016, 848, 748 cm^{-1}.

Synthesised via the following known method:

B. He, W. T. Neo, T. L. Chen, L. M. Klivansky, H. Wang, T. Tan, S. J. Teat, J. Xu and Y. Liu, *ACS Sustain. Chem. Eng.*, 2016, **4**, 2797–2805.

6,6'-bis((2-ethylhexyl)oxy)-indigo (5.12)

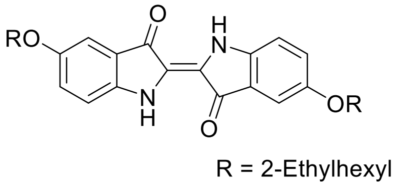

5.11 (2.3 g, 8.23 mmol, 1 eqv.) was dissolved in an acetone/water mixture (1:1 v/v, 50 mL) and heated to 60 °C. NaOH (540 mg, 13.5 mmol, 1.6 eqv.) dissolved in water (4 mL) was added dropwise over 10 minutes. The solution was heated to 60 °C with vigorous stirring for four hours, then cooled to room temperature and poured into water (500 mL). The solution was filtered, washed thoroughly with water then recrystallised from DCM with the addition of petroleum ether to give **5.12** as a blue solid (570 mg, 13% yield).

^{1}H NMR (400 MHz, $CDCl_3$): 8.71 (s, 2H), 7.19 (d, *J* = 2.5 Hz, 2H), 7.13 (dd, *J* = 8.7, 2.6 Hz, 2H), 6.96 (d, *J* = 8.7 Hz, 2H), 3.84 (d, *J* = 5.9 Hz, 4H), 1.80-1.67 (m, 2H), 1.53-1.38 (m, 8H), 1.35-1.28 (m, 8H), 0.99-0.87 (m, 12H) ppm.

^{13}C NMR (101 MHz, $CDCl_3$, partial due to low solubility): δ 154.54, 126.02, 113.22, 106.81, 71.58, 39.52, 30.67, 29.22, 24.02, 23.21, 18.59, 14.24, 11.25 ppm.

IR (neat, ATR): v = 3372, 2958, 2925, 2859, 2339, 1613, 1485, 1467, 1401, 1267, 1223, 1133, 1107, 1063, 816, 778, 694, 525 cm^{-1}.

Synthesised via the following known method:

B. He, W. T. Neo, T. L. Chen, L. M. Klivansky, H. Wang, T. Tan, S. J. Teat, J. Xu and Y. Liu, *ACS Sustain. Chem. Eng.*, 2016, **4**, 2797–2805.

2,9-Bis((2-ethylhexyl)oxy)-7,14-di(thiophen-2-yl)diindolo-[3,2,1-de:3',2',1'-ij][1,5]naphthyridine-6,13-dione (5.13)

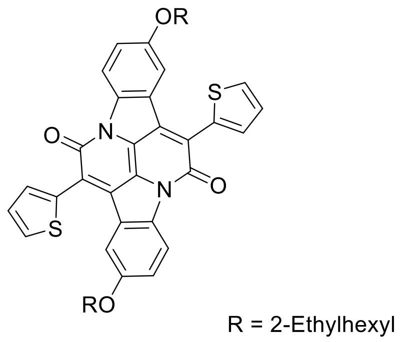

5.12 (200 mg, 0.386 mmol) was dissolved in xylene (10 mL) under a nitrogen atmosphere and heated to reflux. 2-Thiopheneacetyl chloride (248 mg, 1.54 mmol, 4 eqv.) dissolved in xylene (3 mL) was added dropwise over 30 minutes and then the heating was continued for an additional hour. After cooling to room temperature, the solvent was evaporated under reduced pressure and the residue was recrystallised from DCM, with the addition of pentane, to give **5.13** as a purple solid (130 mg, 46% yield).

^{1}H NMR (400 MHz, CDCl$_3$): 8.42 (d, *J* = 8.9 Hz, 2H), 7.75 (d, *J* = 3.6 Hz, 2H), 7.70 (dd, *J* = 5.1, 1.2 Hz, 2H), 7.66 (d, *J* = 2.5 Hz, 2H), 7.28 (d, *J* = 3.7 Hz, 2H), 7.10 (dd, *J* = 9.0, 2.5 Hz, 2H), 3.83 (d, *J* = 5.8 Hz, 4H), 1.73 (m, 2H), 1.49-1.41 (m, 8H), 1.33 (m, 8H), 0.95-0.90 (m, 12H) ppm.

IR (neat, ATR): v = 3101, 1958, 1927, 2339, 1623, 1575, 1462, 1445, 1416, 1383, 1352, 1276, 1256, 1223, 1203, 1107, 1077, 1055, 1031, 965, 854, 813, 793, 769, 727, 705, 673, 625 cm^{-1}.

Synthesised via the following known method:

B. He, W. T. Neo, T. L. Chen, L. M. Klivansky, H. Wang, T. Tan, S. J. Teat, J. Xu and Y. Liu, *ACS Sustain. Chem. Eng.*, 2016, **4**, 2797–2805.

7-(5-bromothiophen-2-yl)-2,9-bis((2-ethylhexyl)oxy)-14-(thiophen-2-yl)diindolo[3,2,1-de:3',2',1'-ij][1,5]naphthyridine-6,13-dione (5.14)

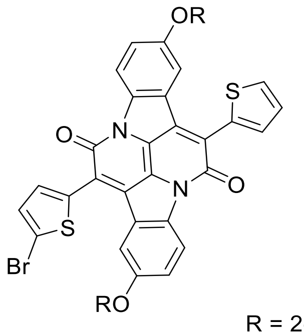

R = 2-Ethylhexyl

5.13 (50 mg, 68.4 µmol, 1 eqv.) was dissolved in CHCl$_3$ (10 mL). NBS (13 mg, 71.8 µmol, 1.1 eqv.) was added and the solution was stirred for 2 hours, before quenching the reaction with the addition of water (50 mL). The organic layer was washed with water (2 x 50 mL) then brine (2 x 50 mL), dried using MgSO$_4$ and evaporated. The product was purified using column chromatography (silica gel, DCM) to give **5.14** as a purple solid (19 mg, 34% yield). The bis-brominated product (**5.15**) was also isolated as a purple solid (20 mg, 33% yield).

^{1}H NMR (400 MHz, CDCl$_3$): 8.30 (d, *J* = 8.9 Hz, 1H), 8.25 (d, *J* = 8.9 Hz, 1H), 7.72-7.66 (m, 2H), 7.64 (d, *J* = 2.5 Hz, 1H), 7.61 (d, *J* = 2.5 Hz, 1H), 7.50 (d, *J* = 3.9 Hz, 1H), 7.23 (dd, *J* = 5.1, 2.6 Hz, 1H), 7.17 (d, *J* = 3.9 Hz, 1H), 7.04-6.97 (m, 2H), 3.84-3.77 (m, 4H), 1.73 (m, 2H), 1.55-1.39 (m, 8H), 1.34 (m, 8H), 0.98-0.89 (m, 12H) ppm.

^{13}C NMR (101 MHz, CDCl$_3$): 158.03, 157.96, 130.51, 130.25, 129.88, 129.73, 129.12, 128.95, 127.01, 126.77, 126.33, 122.29, 118.20, 110.94, 71.54, 39.42, 30.59, 29.23, 23.93, 23.22, 14.28, 11.24 ppm.

IR(KBr): v = 2955, 2926, 2872, 1711, 1624, 1578, 1466, 1447, 1416, 1404, 1383, 1327, 1275, 1246, 1227, 1219, 1202, 1107, 1073, 1030, 978, 854, 822, 795, 768, 733, 698, 673, 571, 503 cm^{-1}.

4-(5-(2,9-bis((2-ethylhexyl)oxy)-6,13-dioxo-14-(thiophen-2-yl)-6,13-dihydrodiindolo[3,2,1-de:3',2',1'-ij][1,5]naphthyridin-7-yl)thiophen-2-yl)benzoic acid (9)

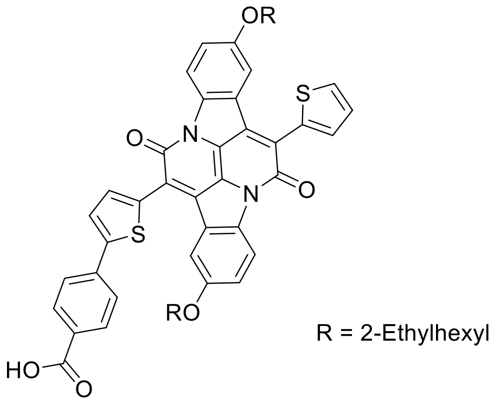

5.14 (41 mg, 50.6 µmol, 1 eqv.), 4-carboxyphenylboronic acid (13 mg, 75.9 µmol, 1.5 eqv.), K_2CO_3 (28 mg, 20.24 µmol, 4 eqv.) and $Pd(PPh_3)_4$ (3 mg, 2.53 µmol, 5 mol %) were loaded into a Schlenk tube and purged with 3 vacuum/nitrogen cycles. A degassed mixture of dioxane and water (4:1 v/v, 12 mL / 3 mL) was added and the solution was heated to 90 °C for 24 hours. After cooling to room temperature, the solvent was evaporated under reduced pressure and the product purified using column chromatography (silica gel, 95:5:1 toluene/methanol/acetic acid) to give **9** as a blue solid (28 mg, 65% yield).

^{1}H NMR (700 MHz, $CDCl_3$/TFA): δ 8.38 (d, *J* = 8.8 Hz, 1H), 8.35 (d, *J* = 8.9 Hz, 1H), 8.18 (d, *J* = 8.1 Hz, 2H), 7.84 (d, *J* = 8.2 Hz, 2H), 7.73 (d, *J* = 5.1 Hz, 1H), 7.68 (d, *J* = 3.8 Hz, 1H), 7.65 (d, *J* = 3.7 Hz, 1H), 7.58 (m, 2H), 7.37 (d, *J* = 2.5 Hz, 1H), 7.30 (dd, *J* = 5.2, 3.4 Hz, 1H), 7.16 (m, 2H), 3.86 (d, *J* = 5.9 Hz, 2H), 3.83 (d, *J* = 5.9 Hz, 2H), 1.76 – 1.70 (m, 2H), 1.53 – 1.24 (m, 16H), 0.95 – 0.85 (m, 12H) ppm.

^{13}C NMR (176 MHz, $CDCl_3$/TFA): δ 179.63, 158.72, 147.35, 139.57, 137.70, 137.61, 132.96, 132.47, 132.24, 132.08, 131.41, 130.71, 130.33, 127.36, 126.92, 125.91, 124.99, 123.09, 119.13, 118.91, 118.84, 118.73, 112.04, 71.80, 71.70, 39.08, 30.32, 28.97, 28.94, 23.66, 22.99, 22.97, 20.65, 14.01, 13.97, 10.94, 10.91 ppm.

IR (KBr): v = 3429, 3285, 3175, 2959, 2926, 2872, 2858, 1628, 1603, 1576, 1551, 1462, 1447, 1409, 1308, 1269, 1238, 1219, 1206, 1107, 1072, 1055, 1022, 972, 856, 820, 812, 785, 743, 700, 671, 662, 640, 621, 526 cm^{-1}.

HRMS (ESI): m/z calcd. for $C_{51}H_{49}N_2O_6S_2$: 849.3038, found: 849.3037 ($[M-H]^-$).

UV-visible absorption ($CHCl_3$/TFA 99:1, v/v): λ_{max} (ε, $dm^3\ mol^{-1}\ cm^{-1}$) = 567 (49,650), 303 (71,375) nm.

5.4. References

1 C. J. Wood, G. H. Summers and E. A. Gibson, *Chem. Commun.*, 2015, **51**, 3915–3918.

2 G. H. Summers, J.-F. Lefebvre, F. A. Black, E. Stephen Davies, E. A. Gibson, T. Pullerits, C. J. Wood and K. Zidek, *Phys. Chem. Chem. Phys.*, 2016, **18**, 1059–1070.

3 G. H. Summers, G. Lowe, J.-F. Lefebvre, S. Ngwerume, M. Bräutigam, B. Dietzek, J. E. Camp and E. A. Gibson, *ChemPhysChem*, 2017, **18**, 406–414.

4 F. A. Black, C. J. Wood, S. Ngwerume, G. H. Summers, I. P. Clark, M. Towrie, J. E. Camp and E. A. Gibson, *Faraday Discuss.*, 2017, **198**, 449–461.

5 L. Le Pleux, A. L. Smeigh, E. A. Gibson, Y. Pellegrin, E. Blart, G. Boschloo, A. Hagfeldt, L. Hammarström and F. Odobel, *Energy Environ. Sci.*, 2011, **4**, 2075–2084.

6 E. A. Gibson, A. L. Smeigh, L. Le Pleux, J. Fortage, G. Boschloo, E. Blart, Y. Pellegrin, F. Odobel, A. Hagfeldt and L. Hammarström, *Angew. Chem. Int. Ed.*, 2009, **48**, 4402–4405.

7 E. A. Gibson, A. L. Smeigh, L. Le Pleux, L. Hammarström, F. Odobel, G. Boschloo and A. Hagfeldt, *J. Phys. Chem. C*, 2011, **115**, 9772–9779.

8 A. Morandeira, J. Fortage, T. Edvinsson, L. Le Pleux, E. Blart, G. Boschloo, A. Hagfeldt, L. Hammarström and F. Odobel, *J. Phys. Chem. C*, 2008, **112**, 1721–1728.

9 A. L. Smeigh, L. Le Pleux, J. Fortage, Y. Pellegrin, E. Blart, F. Odobel and L. Hammarström, *Chem. Commun.*, 2012, **48**, 678-680.

10 L. Favereau, J. Warnan, Y. Pellegrin, E. Blart, M. Boujtita, D. Jacquemin and F. Odobel, *Chem. Commun.*, 2013, **49**, 8018-8020.

11 Y. Farré, L. Zhang, Y. Pellegrin, A. Planchat, E. Blart, M. Boujtita, L. Hammarström, D. Jacquemin and F. Odobel, *J. Phys. Chem. C*, 2016, **120**, 7923–7940.

12 L. Zhang, L. Favereau, Y. Farre, E. Mijangos, Y. Pellegrin, E. Blart, F. Odobel and L. Hammarström, *Phys. Chem. Chem. Phys.*, 2016, **18**, 18515-18527.

13 Y. Farré, M. Raissi, A. Fihey, Y. Pellegrin, E. Blart, D. Jacquemin and F. Odobel, *ChemSusChem*, 2017, **10**, 2618–2625.

14 J. Yum, T. W. Holcombe, Y. Kim, K. Rakstys, T. Moehl, J. Teuscher, J. H. Delcamp, M. K. Nazeeruddin and M. Grätzel, *Sci. Rep.*, 2013, **3**, 2446.

15 Y. Hao, Y. Saygili, J. Cong, A. Eriksson, W. Yang, J. Zhang, E. Polanski, K. Nonomura, S. M. Zakeeruddin, M. Grätzel, A. Hagfeldt and G. Boschloo, *ACS Appl. Mater. Interfaces*, 2016, **8**, 32797–32804.

16 D. Ameline, S. Diring, Y. Farre, Y. Pellegrin, G. Naponiello, E. Blart, B. Charrier, D. Dini, D. Jacquemin and F. Odobel, *RSC Adv.*, 2015, **5**, 85530–85539.

17 B. He, A. B. Pun, D. Zherebetskyy, Y. Liu, F. Liu, L. M. Klivansky, A. M. McGough, B. A. Zhang, K. Lo, T. P. Russell, L. Wang and Y. Liu, *J. Am. Chem. Soc.*, 2014, **136**, 15093–15101.

18 J. Seixas de Melo, A. P. Moura and M. J. Melo, *J. Phys. Chem. A*, 2004, **108**, 6975–6981.

19 B. He, W. T. Neo, T. L. Chen, L. M. Klivansky, H. Wang, T. Tan, S. J. Teat, J. Xu and Y. Liu, *ACS Sustain. Chem. Eng.*, 2016, **4**, 2797–2805.

20 Z. Liu, W. Li, S. Topa, X. Xu, X. Zeng, Z. Zhao, M. Wang, W. Chen, F. Wang, Y.-B. Cheng and H. He, *ACS Appl. Mater. Interfaces*, 2014, **6**, 10614–22.

21 F. Odobel, Y. Pellegrin, E. A. Gibson, A. Hagfeldt, A. L. Smeigh and L. Hammarström, *Coord. Chem. Rev.*, 2012, **256**, 2414–2423.

22 S. Yagai, T. Seki, T. Karatsu, A. Kitamura and F. Würthner, *Angew. Chem. Int. Ed.*, 2008, **47**, 3367–3371.

23 H. Langhals, *Helv. Chim. Acta*, 2005, **88**, 1309–1343.

24 A. D. Becke, *J. Chem. Phys.*, 1993, **98**, 1372–1377.

25 L. Li, E. A. Gibson, P. Qin, G. Boschloo, M. Gorlov, A. Hagfeldt and L. Sun, *Adv. Mater.*, 2010, **22**, 1759–1762.

26 C. J. Wood, M. Cheng, C. A. Clark, R. Horvath, I. P. Clark, M. L. Hamilton, M. Towrie, M. W. George, L. Sun, X. Yang and E. A. Gibson, *J. Phys. Chem. C*, 2014, **118**, 16536–16546.

27 K. A. Click, D. R. Beauchamp, B. R. Garrett, Z. Huang, C. M. Hadad and Y. Wu, *Phys. Chem. Chem. Phys.*, 2014, **16**, 26103–26111.

28 N. Duffy, L. Peter, R. M. G. Rajapakse and K. G. U. Wijayantha, *Electrochem. Commun.*, 2000, **2**, 658–662.

29 P. Qin, H. Zhu, T. Edvinsson, G. Boschloo, A. Hagfeldt and L. Sun, *J. Am. Chem. Soc.*, 2008, **130**, 8570–8571.

30 S. A. Trammell and T. J. Meyer, *J. Phys. Chem. B*, 1999, **103**, 104–107.

Chapter 6 – Investigating the Anchoring Units of p-DSCs using Click Chemistry

6.1. Introduction

6.1.1. Anchoring units for dyes used in p-DSCs

For an efficient p-DSC, the dye must be strongly adsorbed onto the semiconductor surface, to promote efficient charge transfer from the semiconductor to the dye. Therefore, the dye should possess an anchoring group which can react with surface hydroxyl groups on the metal oxide to form covalent bonds. For n-type devices, the most commonly studied anchoring units are carboxylic and cyanoacetic acids, but a wide range of others including phosphonates, sulfonates and catechol have been used.[1,2] For p-type devices, the range of anchors which have been studied is much smaller, with carboxylic acids predominantly used. However, a few other examples have been reported in the literature.

Odobel and co-workers compared a series of ruthenium polypyridine complexes with various anchoring units; carboxylic acid, carbodithioic acid, catechol and methyl phosphonic acid (Figure 6.1).[3]

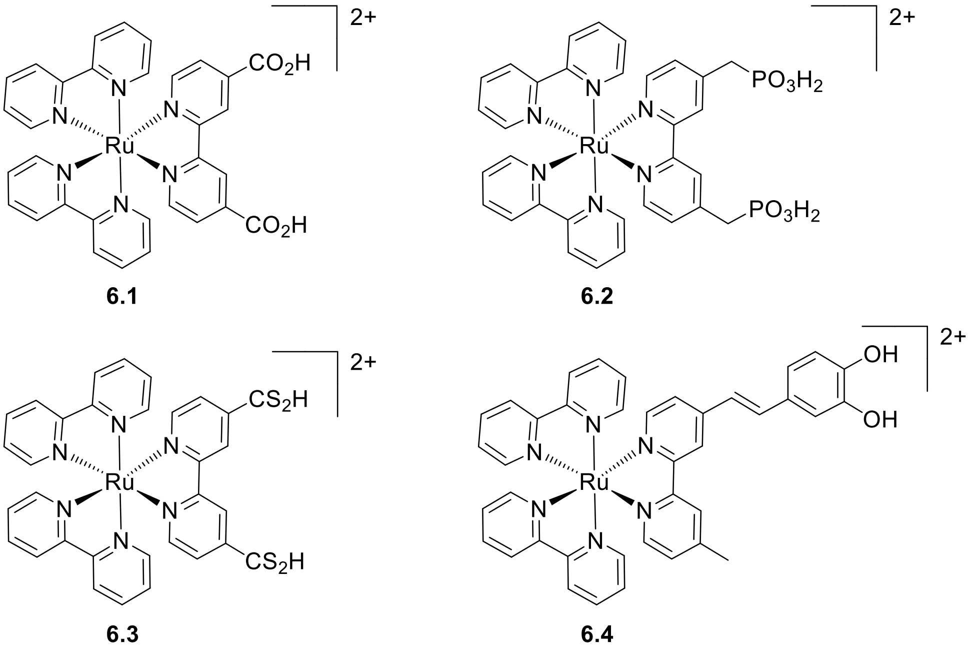

Figure 6.1. Ruthenium tris(bipyridine) complexes studied by Odobel *et al.*[3]

Binding constants were measured and followed the trend of CO_2H > PO_3H_2 > catechol > CS_2H, with two orders of magnitude difference between the weaker catechol/CS_2H binding constants and the carboxylic acid. The photovoltaic performances were all relatively similar ($\eta < 0.025\%$, $J_{sc} < 0.80$ mA cm^{-2}) therefore, no strong conclusions could be determined as to the anchor effect. Additionally, the complexes were not truly structurally analogous. For example, the anchors of the phosphonate complex were decoupled from the bipyridine ligand and for the catechol complex there was only one anchoring unit (however, this was still a bidentate anchoring mode). For a more accurate comparison, the only structural difference should be the type of anchoring group used. Housecroft *et al.*[4] reported the synthesis of ruthenium tris-bipyridine dyes anchored using carboxylic or phosphonic acid, that are structurally analogous except for the acid group. However, despite synthesising both dyes, only p-DSC results for the phosphonate were reported.

Wang and co-workers replaced the carboxylic acid anchoring unit of **P1** with a pyridine group (Figure 6.2).[5,6] Pyridine was chosen as it is less electron withdrawing than the carboxylic acid. This was expected to draw less electron density away from the donor, which hinders charge separation. Also, the electron rich character is expected to aid charge transfer between the dye and semiconductor. Slight improvements were made over **P1** when measured in the same conditions (**CW2**; J_{sc} = 4.05 mA cm^{-2}, V_{oc} = 117.9 mV, FF = 0.34, η = 0.160%, **P1**; J_{sc} = 4.67 mA cm^{-2}, V_{oc} = 92.9 mV, FF = 0.33, η = 0.143%), but these are lower than the highest performances recorded for **P1**.[7] This improvement was attributed to a positive shift in the valence band edge of NiO and a reduction in NiO/dye recombination. However, again the chemical structure of **CW2** and **P1** are quite different, as the former contains an additional phenyl ring.

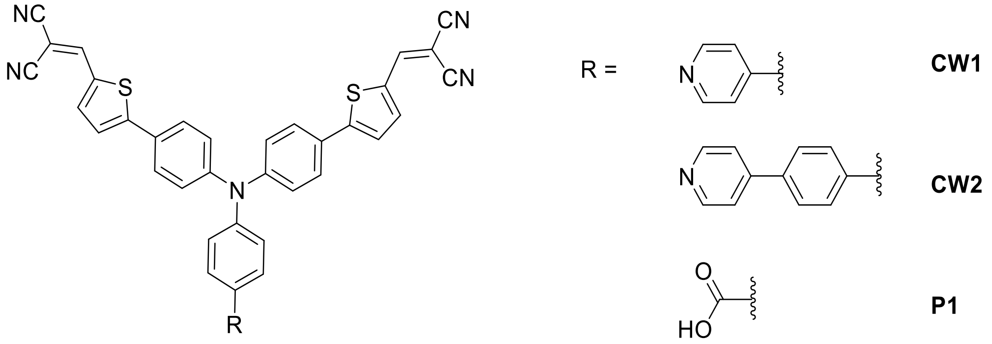

Figure 6.2. Pyridine anchored dyes studied by Wang *et al.*[5,6]

6.1.2. Motivation

The dyes used for p-DSCs which have performed the most efficiently are synthesised through linear synthetic routes.[8–12] These typically follow a series of sequential halogenations and coupling reactions, often starting from triphenylamine. Following this approach, it is difficult to tune individual components (such as the anchor, donor and acceptor groups) without following separate linear routes for each new dye. This is particularly true for the anchoring group, which is generally synthesised either via oxidation of a carbonyl introduced using the Vilsmeier formylation[10–13] or the hydrolysis of tert-butyl benzoate.[8,13] The latter route limits the dye structure to one containing triphenylamine, following the synthetic route established by Bäuerle *et al.* (Figure 6.3).[14] A more modular approach would be desirable, where the chromophore and anchoring group could be synthesised separately and then assembled, using the minimum number of reactions possible.

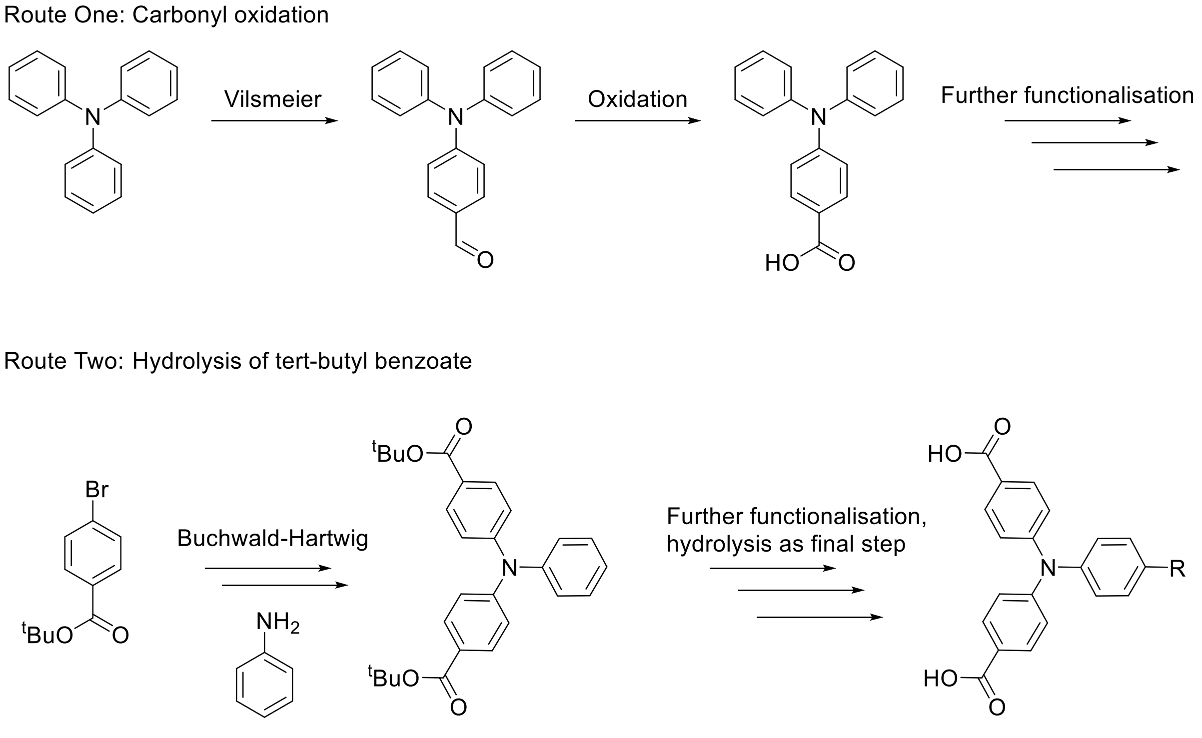

Figure 6.3. General synthetic routes followed for anchor functionalisation of p-type dyes.

‘Click chemistry’ is a term defined by Sharpless[15] to describe the concept of a reaction in which two molecular building blocks are joined in a high-yielding, selective reaction that has simple conditions and few by-products. The copper-catalysed azide-alkyne cycloaddition (CuAAC),[16] independently discovered in 2002 by the groups of Sharpless[17] and Meldal,[18] is the most popular and widely used click reaction. By following this modular approach, a range of anchoring groups with azide functionalities could be synthesised and coupled with an alkyne containing chromophore via a CuAAC. This will facilitate the development of a new synthetic route to introduce anchoring groups as one of the final steps in dye synthesis, which will allow the design of a more diverse range of sensitisers.

As discussed in Chapter 4, a major limitation that arose during the design of a new anchoring system was the instability of the dye under harsh hydrolysis conditions. Porphyrins are often derivatised using ‘click’ reactions[19] and they are typically robust to anchor group hydrolysis.[20] They have also been successfully used for p-DSCs[21,22] and provide a distinct spectroscopic handle for anchoring studies. Therefore, for these reasons, a porphyrin has been chosen as the chromophore. In this chapter, three porphyrins were functionalised (Figure 6.4) with a carboxylic acid, a phosphonate and a coumarin-based anchoring system. The effect of the anchoring group on dye adsorption and p-DSC performances has been studied. The carboxylic acid was chosen as this is the most widely used anchor for p-DSCs. The phosphonate has been used as a direct comparison, as these are widely used for TiO_2 and are reported to be much more stable toward desorption than their carboxylate counterparts.[2,23] Finally, the coumarin anchor was chosen as a multidentate binding mode between the carboxylic acid and the ketone could be possible, which should improve the anchoring stability. Charge transfer from NiO to coumarin based dyes has been previously reported and occurs on the fs timescale. Therefore, this anchoring group should facilitate efficient photoinduced charge transfer from NiO to the porphyrin.

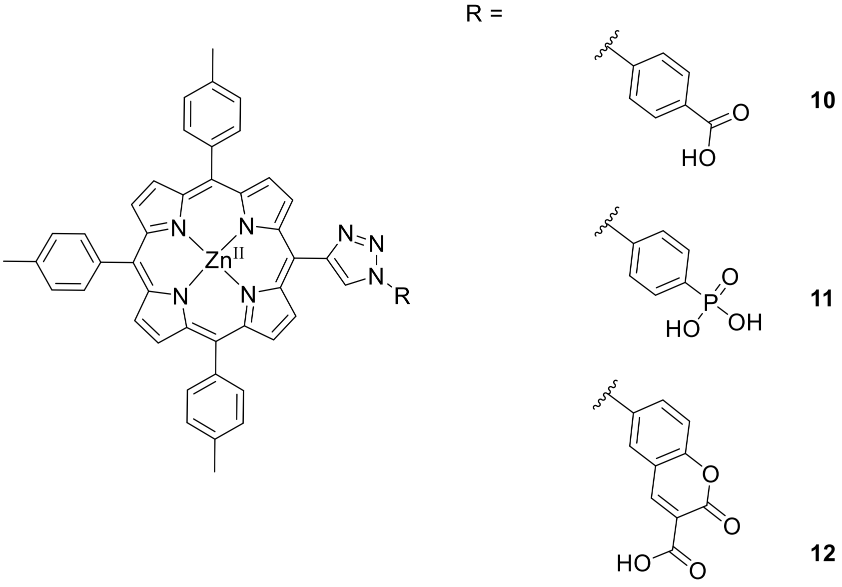

Figure 6.4. Chemical structure of the porphyrins studied.

6.2. Results and Discussion

6.2.1. Synthesis

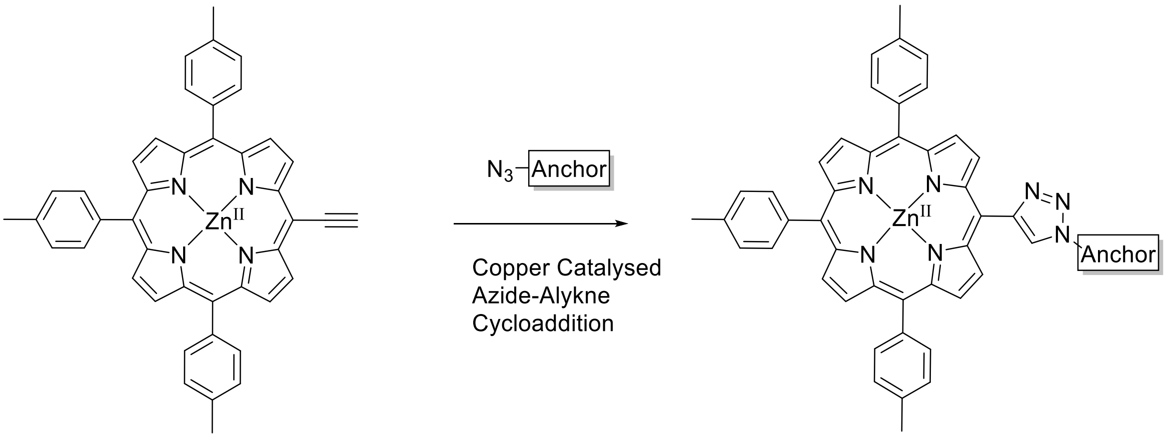

Figure 6.5. General synthetic route to the triazole-bridged anchored porphyrins.

A generalised synthetic route used to prepare **10-12** is provided in Figure 6.5. The alkyne fragment chosen was 5-ethynyl-10,15,20-tri-p-tolyl-porphyrin and the anchors were functionalised with the azide group. The porphyrin was coordinated with zinc to stop copper insertion occuring during the click reaction and the tolyl groups were used to help reduce porphyrin stacking. This was intended to improve solubility and suppress aggregation when the dye was adsorbed onto NiO. The alkyne group was synthesised as a direct *meso*-substituent using TMS-propynal, rather than using TMS-ethynyl-benzaldehyde, which is more commonly used.[24–26] This was intended to improve electronic coupling between the porphyrin core and the anchor, as *meso*-phenyl rings in tetra-aryl porphyrins are non-planar.[27]

Initially, three other porphyrins were also proposed (**6.5** – **6.7**, Figure 6.6), but ultimately the synthesis of these proved to be unfeasable, which will be discussed in this section.

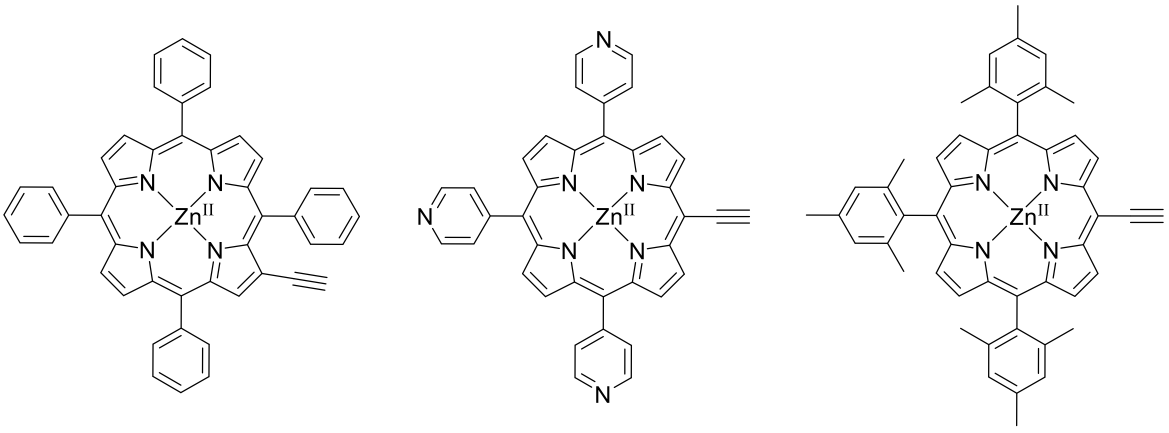

6.5 **6.6** **6.7**

Figure 6.6. Chemical structure of other target porphyrins initially designed.

When synthesising an asymmetric porphyrin from mixed aldehyde precursors, the desired porphyrin will exist as one of six possible products. These can be difficult to isolate and purify, depending on the relative differences in polarity of the two aldehydes. This typically leads to low yields (< 10%) following extensive chromatographic purification. In comparison, symmetric porphyrins are generally simpler to prepare and isolate, with higher optimised yields (ca. 35%). If a symmetric porphyrin could be synthesised and functionalised with a β-alkyne group (**6.5**, Figure 6.6), then both the anchor and chromophore could be more easily tuned. Additionally, it has been reported that electronic communication between the porphyrin core and substituents through the β-positions is greater than for *meso*-substituents.[28–30] This would improve coupling between NiO and the dye through the anchor.

Natali and co-workers have shown *meso*-tetrakis(1-methyl-pyridinium-4-yl)-porphyrin to be an efficient hydrogen evolving catalyst, when coupled with a photosensitiser (Ru(bpy)$_3$) and using ascorbic acid as a sacrificial donor in solution.[31] The sacrificial donor could be replaced by anchoring to a semiconductor, so this porphyrin (**6.6**,

Figure 6.6) could be potentially utilised for both p-DSCs and photoelectrochemical hydrogen evolution. When using porphyrins as a sensitiser, it is important to supress aggregation, which leads to self-quenching of the porphyrin excited state.[32] Bulky mesityl substituents (**6.7**, Figure 6.6) are often used to hinder this aggregation by blocking porphyrin stacking.

6.5 was successfully prepared following the synthetic scheme shown in Figure 6.7. Tetraphenylporphyrin was halogenated using 1.5 eqv. NBS to produce the mono β-brominated porphyrin in 65% yield, which was quantitatively metallated using $Zn(OAc)_2.2H_2O$ to give **6.8**. The alkyne group of **6.9** was introduced via a Sonogashira coupling with TMS-acetylene in 42% yield after purification, which could be deprotected in high yield using TBAF. However, while **6.5** was successfully synthesised, the click reaction did not work. The major product obtained after a CuAAC reaction of the porphyrin alkyne with 4-azidobenzoic acid was the Glaser coupled product (**6.11**, Figure 6.8) rather than the click product (**6.10**, Figure 6.8). This was despite rigorously deoxygenated conditions, as the CuAAC is catalysed by a Cu(I) salt and the Glaser coupling catalysed by a Cu(II) salt. Even using a Cu(II) salt and an excess of ascorbate, which has been reported to generate triazole products in nearly quantitative yield,[16] produced only trace amounts of **6.10** compared to **6.11**.

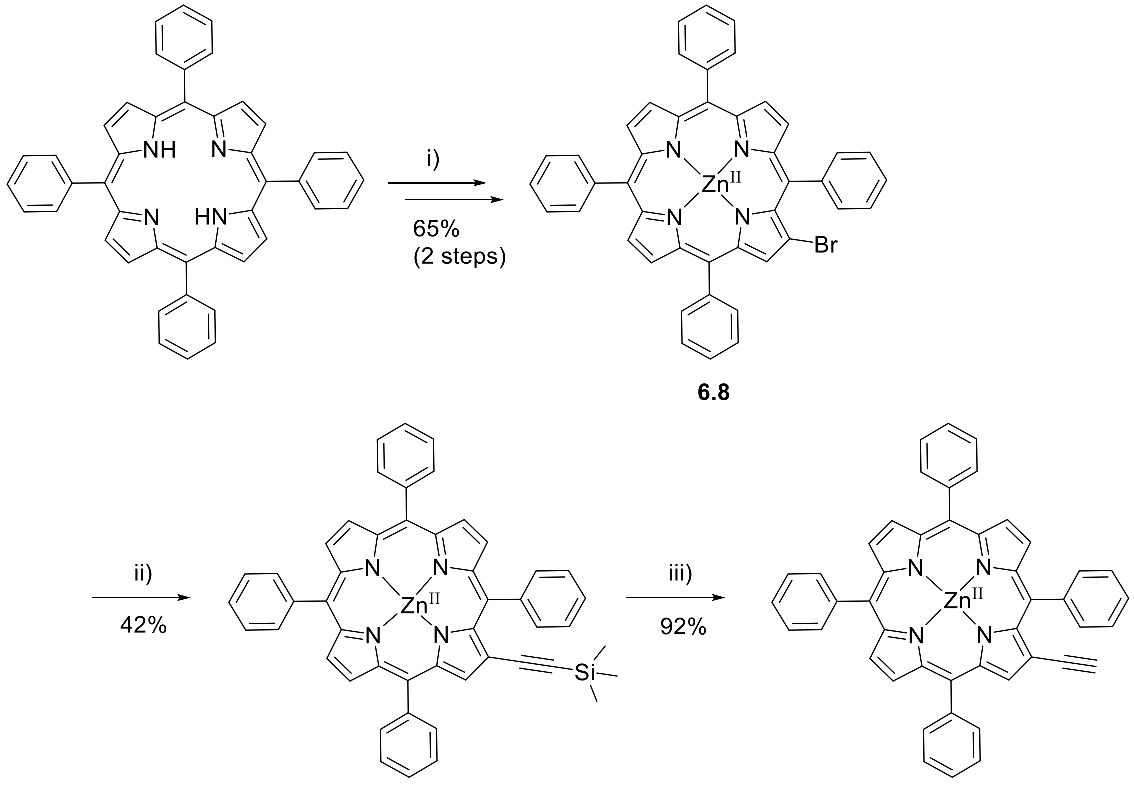

6.8

6.9

6.5

Figure 6.7. Synthetic routes to β-ethynyl tetraphenylporphyrin. i) a) NBS, $CHCl_3$, 65%, b) $Zn(OAc)_2.2H_2O$, $CHCl_3$/MeOH, quantitative; ii) TMS-acetylene, $Pd(PPh_3)_4$, CuI, DMF/TEA, 42%; iii) TBAF, $CHCl_3$, 92%.

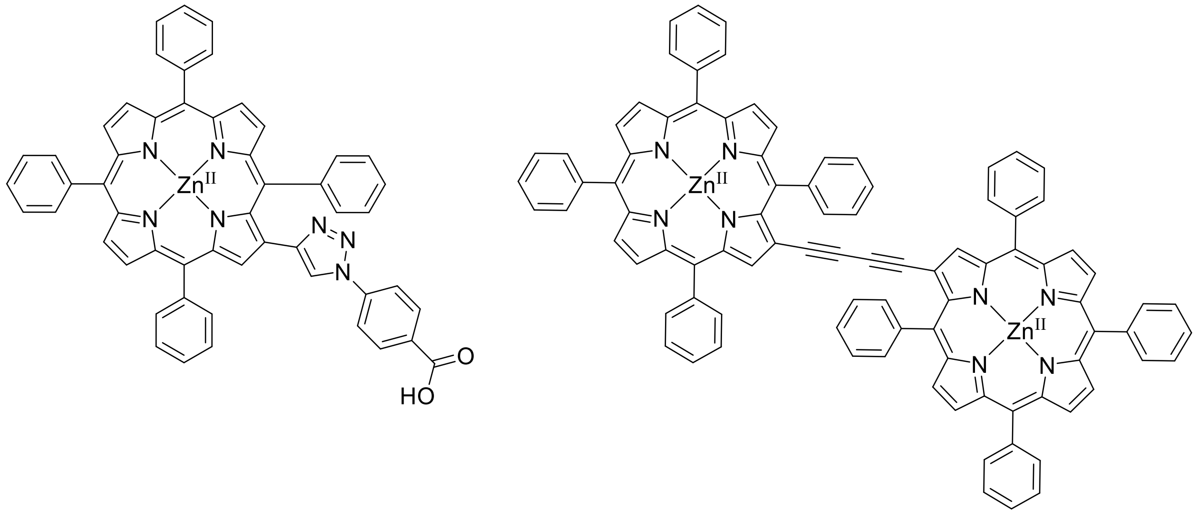

6.10

6.11

Figure 6.8. Desired β-triazole-anchored click product (left) vs. Glaser coupled porphyrin dimer (right).

The synthesis of **6.6** was attempted through both the Adler-Longo and Lindsey methods (Figure 6.9).

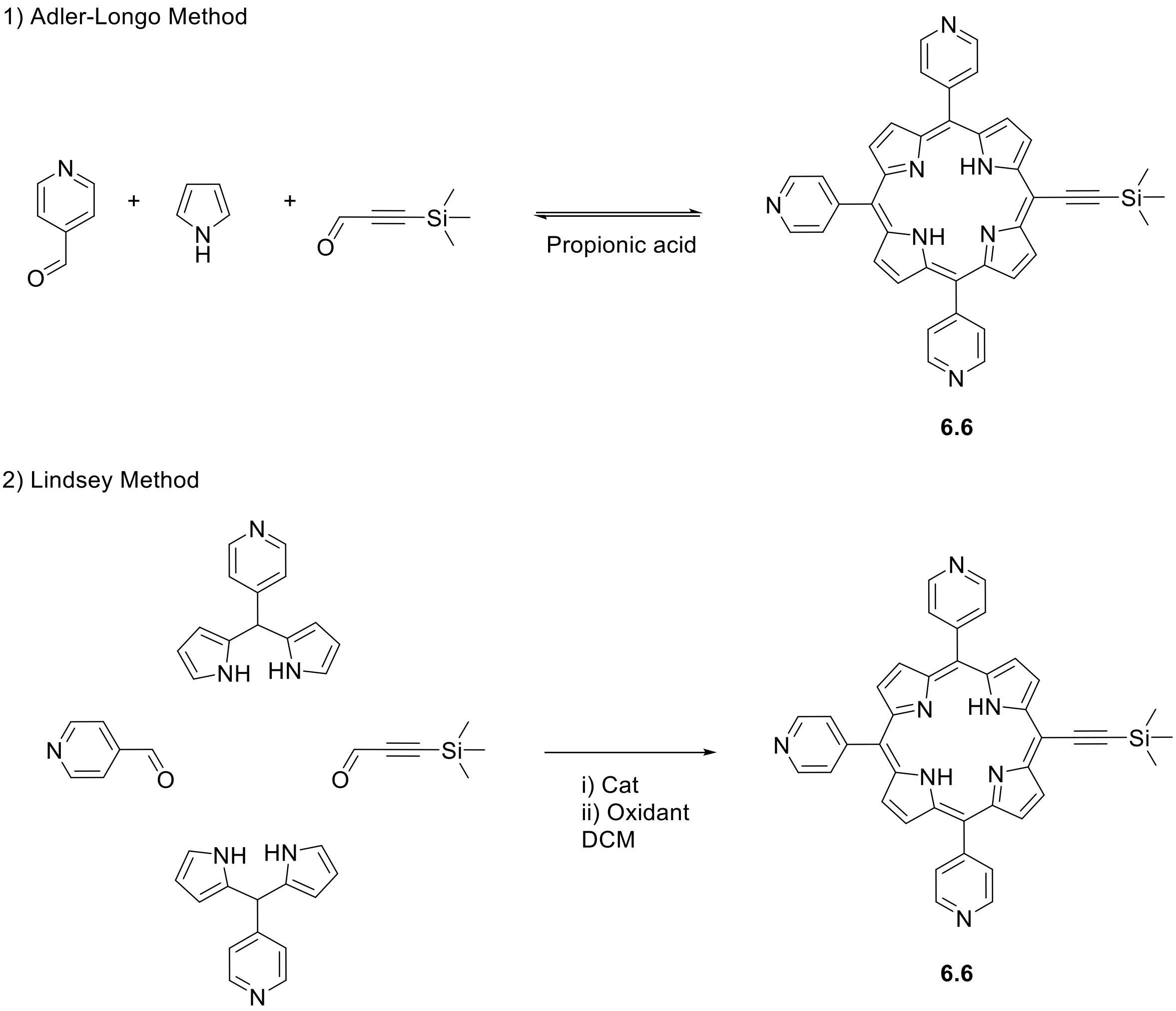

Figure 6.9. Attempted synthetic routes to the A_3B 5-(TMS-ethynyl)-10,15,20-tri(pyridin-4-yl)-porphyrin.

The Adler-Longo method involves the reaction of pyrrole and an aldehyde in refluxing propionic acid, using atmospheric oxygen as an oxidant, which was originally used to prepare tetraphenylporphyrin in 20% yield.[33] This method is suitable for porphyrins that will precipitate in cooled propionic acid, but for porphyrins that will remain soluble, the high boiling point of propionic acid makes isolation difficult. The Lindsey method involves the reaction of pyrrole and the desired aldehyde at room temperature in anhydrous, deoxygenated solvent (usually $CHCl_3$ or DCM) with catalytic amounts of a Lewis acid catalyst. An oxidant (typically p-chloranil or DDQ) is then used to oxidise the porphyrinogen to the porphyrin. Yields of 50% were obtained for tetraphenylporphyrin using this method which has the advantage of simpler purification and a wider substrate scope compared to the Adler-Longo method.[34] The Lindsey method can be carried out using mixed aldehydes or pre-formed dipyrromethanes. The latter route reduces the amount of porphyrin products formed from six to three, which can simplify purification.

The synthesis of **6.6** was initially attempted using Lindsey conditions. The reaction was first carried out in anhydrous DCM from mixed aldehydes (4-pyridine carboxaldehyde and TMS-propynal) using $BF_3.OEt_2$ (0.1 eqv.) as a catalyst, but only polypyrrolic products were obtained. Another reaction under the same conditions using 4-pyridyl dipyrromethane, 4-pyridine carboxaldehyde and TMS-propynal also failed to produce any porphyrin products. It has been previously suggested[35] that $BF_3.OEt_2$ can coordinate to a pyridyl nitrogen, thereby deactivating the catalyst. Increasing the amount of catalyst from 0.1 to 6 to 40 eqv. did not produce any porphyrin products, nor did changing the catalyst to TFA. Following the Adler-Longo method did produce a range of porphyrin products. However, these proved difficult to isolate as they remained soluble in propionic acid at room temperature, requiring evaporation of the solvent and repeated precipitations from methanol. ^1H NMR analysis of the isolated porphyrins showed only small amounts of the TMS peak, possibly due to instability of the aldehyde under the harsh reaction conditions.

The Lindsey method was followed in an attempt to synthesise **6.7** (Figure 6.10). The initial reaction of pyrrole, mesitaldehyde and mesityl dipyrromethane carried out in anhydrous DCM, using $BF_3.OEt_2$ as a catalyst, produced only the trans A_2B_2 porphyrin. The solvent dependence of the synthesis of tetramesitylporphyrin (TMP) has been studied by Lindsey *et al.*,[36] who found the porphyrin was synthesised in a 31% yield in $CHCl_3$ compared to 0% in DCM. The large difference was attributed to the ethanol content of the $CHCl_3$ used, which was present as a stabiliser (0.75% v/v). They found that TMP was synthesised in similar yields (25%) in DCM with added ethanol, but that the reaction failed to proceed in absolute $CHCl_3$. The reaction of pyrrole, mesitaldehyde and mesityl dipyrromethane was repeated in DCM containing ethanol (0.75% v/v) and the desired A_3B porphyrin (**6.7**) was formed and isolated. However, the major product was again the trans A_2B_2 porphyrin, possibly due to steric effects hindering the condensation of mesitaldehyde with the dipyrromethane. Due to this, scaling up the reaction proved difficult and so an alternative porphyrin was used.

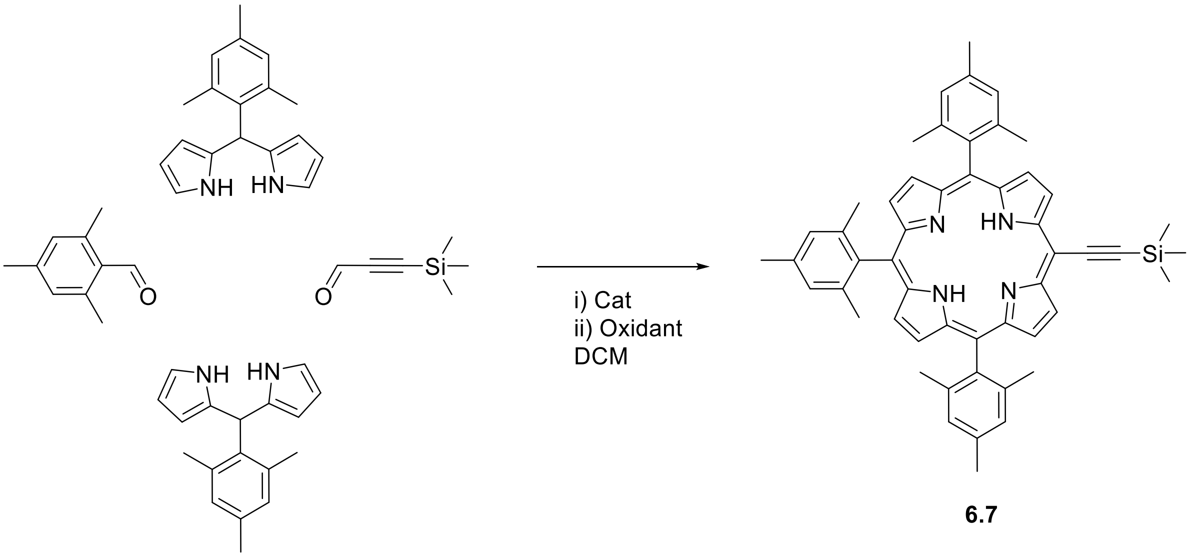

6.7

Figure 6.10. Attempted synthetic route to the A_3B 5-ethynyl-10,15,20-trimesityl-porphyrin.

While the synthesis of the three previously discussed porphyrins was ultimately unsuccessful, 5-ethynyl-10,15,20-tri-p-tolylporphyrin (**6.12**) was successfully prepared in quantities large enough to investigate the click reactions (Figure 6.11).

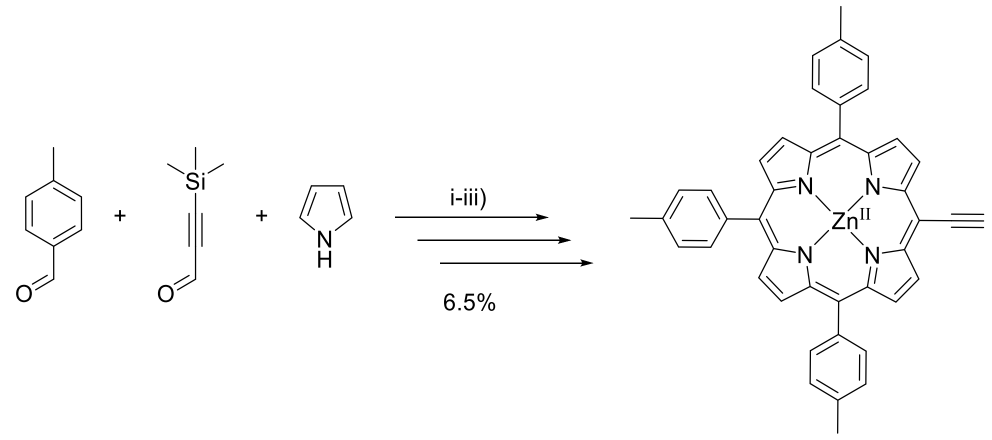

6.12

Figure 6.11. Synthesis of zinc 5-ethynyl-10,15,20-tri-p-tolylporphyrin. i) a) DCM/EtOH, $BF_3.OEt_2$, b) p-chloranil, 6.5%; ii) $Zn(OAc)_2.2H_2O$, DCM/MeOH, quantitative; iii) NaOH, THF/MeOH, quantitative.

Firstly, 5-(TMS-ethynyl)-10,15,20-tri-p-tolylporphyrin was prepared following the Lindsey method for the reaction of p-tolualdehyde, TMS-propynal and pyrrole in DCM/EtOH (0.75% v/v) catalysed by $BF_3.OEt_2$. p-Chloranil was used as an oxidant and the product was obtained in 6.5% yield after purification by column chromatography. The porphyrin was metallated by reacting with $Zn(OAc)_2.2H_2O$ in DCM/MeOH. The reaction could be monitored by UV-visible absorption spectroscopy, as the number of Q-bands changes from four to two. After evaporation of the solvent, the crude product was treated with 2M aqueous NaOH in THF/MeOH to deprotect the alkyne. **6.12** could be extracted with DCM in quantitative yield for the two steps. The reaction progress could be easily followed using ^1H NMR spectroscopy; the change from a free base to a zinc porphyrin can be seen by the loss of the broad 2H singlet at -2.41 ppm, corresponding to the internal pyrrole protons. The alkyne deprotection can be followed by the loss of a 9H singlet at 0.61 ppm corresponding to the TMS group and the formation of a 1H singlet at 4.12 ppm due to the alkyne proton (Figure 6.12).

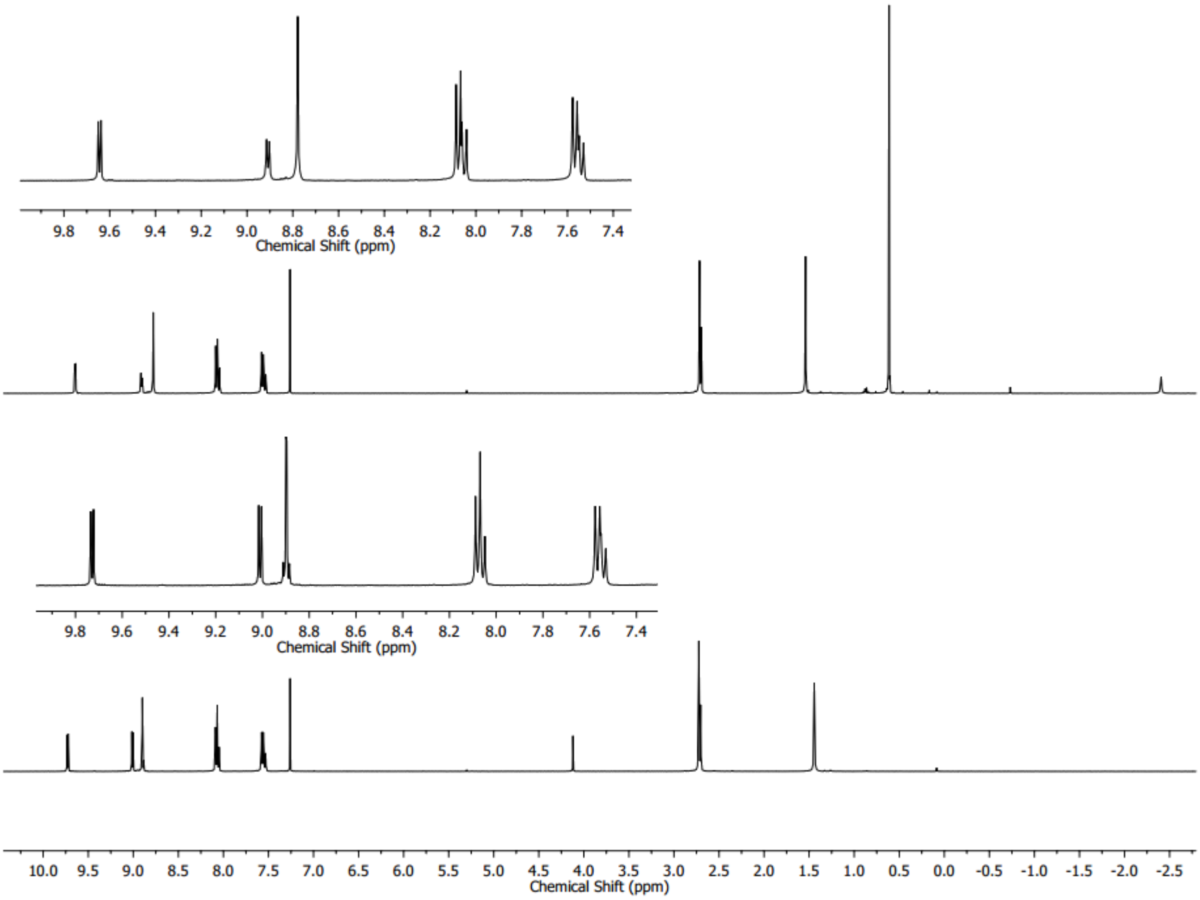

Figure 6.12. ^1H NMR spectra of 5-(TMS-ethynyl)-10,15,20-tri-p-tolylporphyrin (top) and zinc 5-ethynyl-10,15,20-tri-p-tolylporphyrin (**6.12**, bottom).

As the porphyrin contained the alkyne fragment, it was necessary to functionalise the anchors with azides to carry out the click reactions. It would have been possible to synthesise an azido porphyrin and functionalise the anchors with alkyne groups, but this route was chosen to minimise the number of necessary Sonogashira couplings. Figure 6.13 outlines the synthesis of the three anchoring groups studied which consist of benzoic acid, phenylphosphonic acid and coumarin-3-carboxylic acid. The latter two were used in the click reaction as esters to avoid any solubility issues and to reduce the polarity of the final porphyrin for purification. The anchors for these were hydrolysed as the final synthetic step.

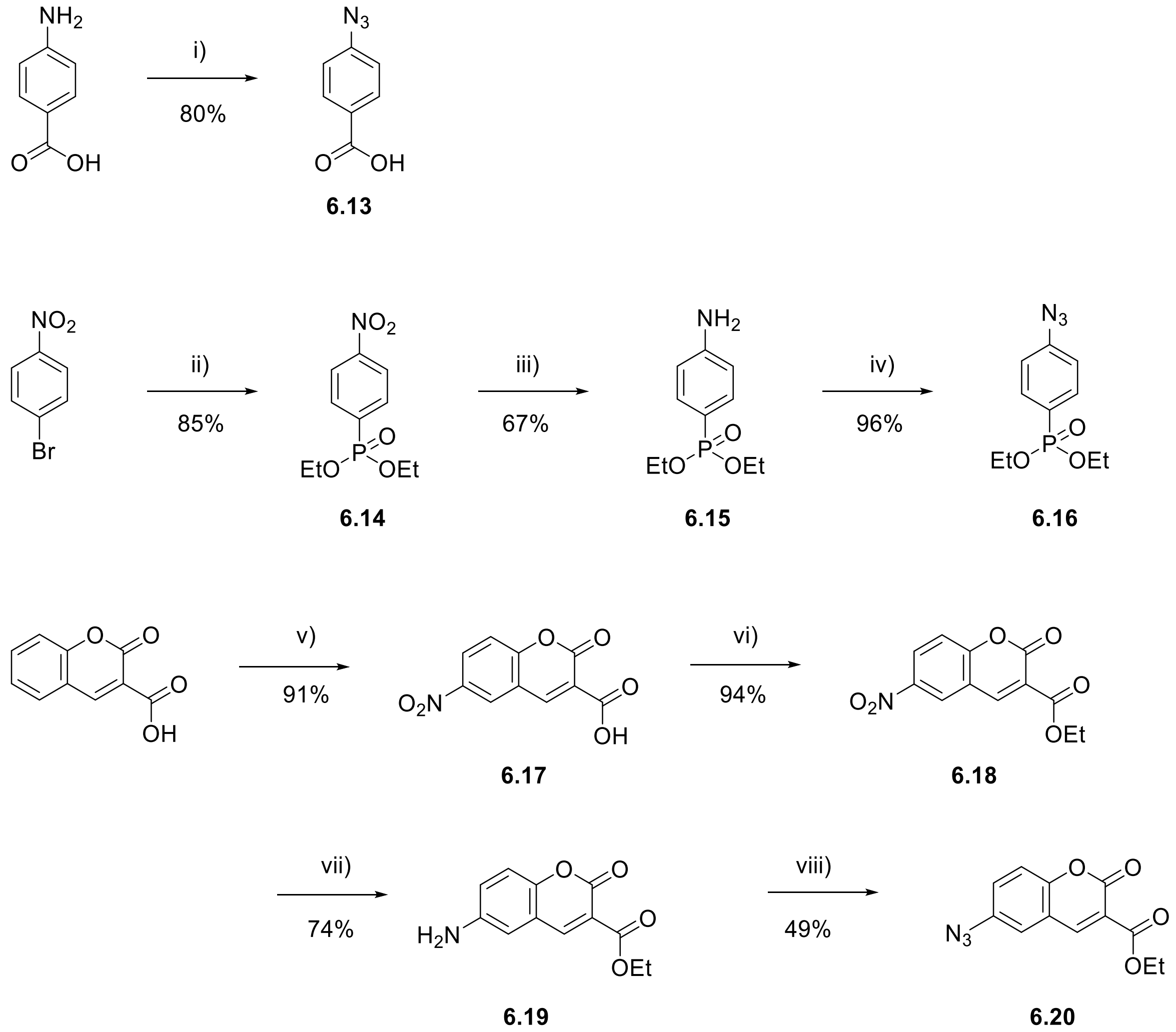

Figure 6.13. Synthesis of the azide functionalised anchor fragments. i) a) H_2SO_4 (4 M), $NaNO_2$, b) NaN_3, 80%; ii) KOAc, $Pd(OAc)_2$, dppf, diethyl phosphite, TEA, THF, 85%; iii) $SnCl_2.2H_2O$, EtOH, 67%; iv) a) acetic acid (9 M), $NaNO_2$, b) NaN_3, 96%; v) H_2SO_4/HNO_3 (1:1, v/v), 91%; vi) $EtOH/H_2SO_4$ (20:1, v/v), 94%; vii) $SnCl_2.2H_2O$, EtOAc, 74%; viii) H_2SO_4 (4 M), $NaNO_2$, b) NaN_3, 49%.

4-Azidobenzoic acid (**6.13**) was synthesised from 4-aminobenzoic acid by sequential reaction with sodium nitrite and sodium azide in sulfuric acid. The desired product precipitated from the reaction mixture and was obtained in 80% yield after washing with water and drying under vacuum. The synthesis of the phosphonate anchor began with the Hirao coupling of 1-bromo-4-nitrobenzene and diethyl phosphite, following a literature procedure,[37] to give **6.14** in 85% yield. This was followed by the reduction of the nitro group to an amine using $SnCl_2.2H_2O$, which produced **6.15** in 67% yield after an aqueous workup. While these two steps could be consolidated into one by carrying out the Hirao coupling on 4-bromoaniline, this reaction did not proceed in high yield and only trace amounts of the desired product could be detected. This is possibly because the electron rich nature of the aryl halide hinders oxidative addition to the palladium catalyst. Finally, **6.15** was converted to the azide by sequential reaction with sodium nitrite and sodium azide in acetic acid. Unlike 4-azidobenzoic acid, the azide did not precipitate from the reaction, but **6.16** was obtained in 96% yield after extraction with diethyl ether and careful evaporation of the solvent.

The initial reaction in the synthesis of **6.20** was the nitration of coumarin-3-carboxylic acid. This was carried out by stirring the coumarin in a mixture of sulfuric and nitric acid overnight. **6.17** was isolated in 91% yield, after neutralising with NaOH. There are five possible regioisomers for **6.17** and this product has been assigned as 6-nitro-coumarin-3-carboxylic acid using 2D NMR spectroscopy (see **Chapter 6.2.2**). The next step was the esterification of the carboxylic acid, by refluxing in ethanol/H_2SO_4, to form **6.18** in 94% yield. The acid group was esterified because 6-amino/azido coumarin-3-carboxylic acid were poorly soluble in organic solvents. They were therefore difficult to extract from the nitro reduction or azide formation reactions, which were both carried out in acidic aqueous solvents. **6.18** was reduced to the amine using $SnCl_2.2H_2O$ in refluxing ethyl acetate, to give **6.19** in 74% yield after an aqueous workup. **6.19** was converted to the azide by sequential treatment with sodium nitrite and sodium azide in sulfuric acid. **6.20** precipitated from the reaction in 49% yield.

Figure 6.14 summarises the click reactions and anchor group hydrolysis used to synthesise **10-12**.

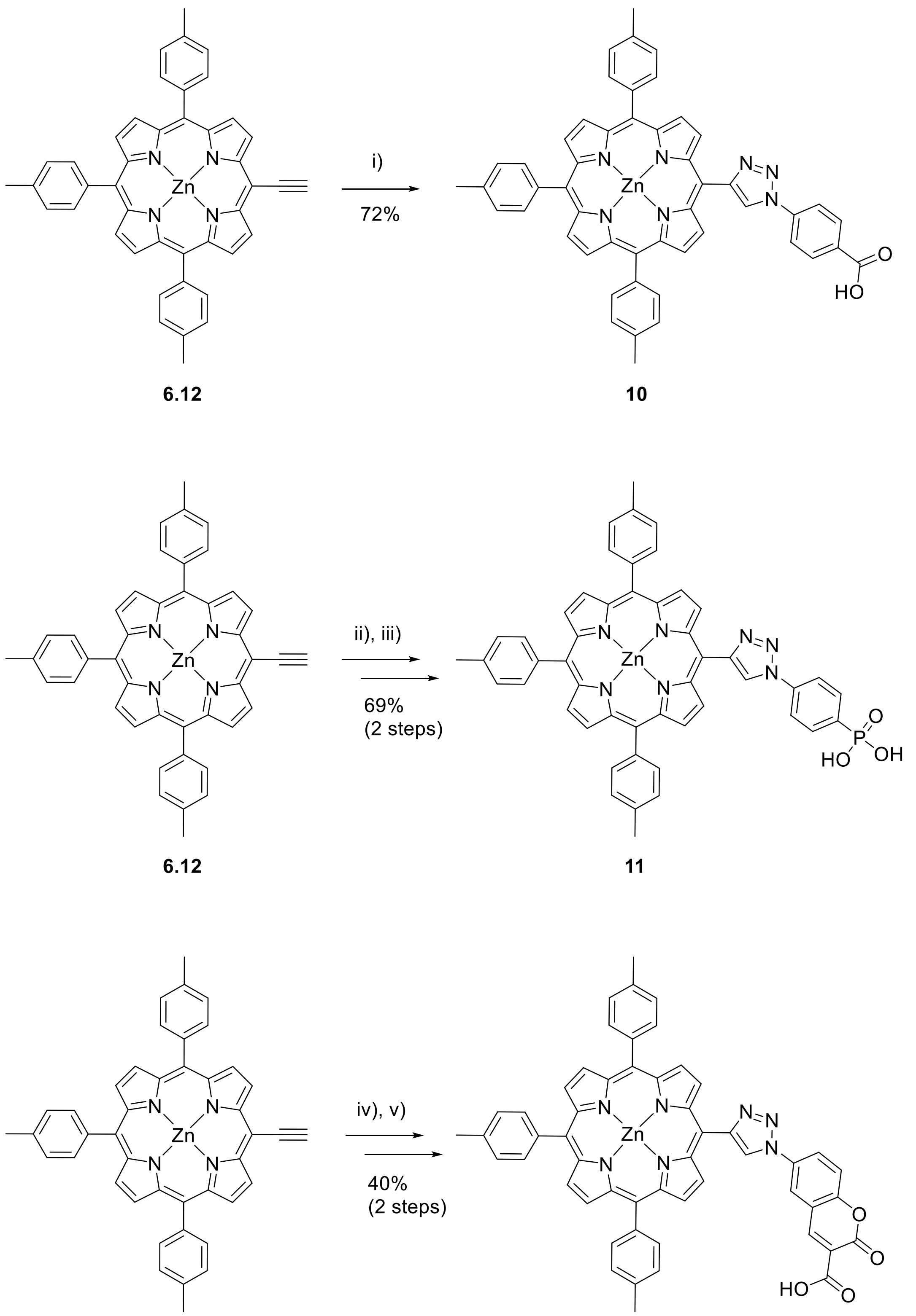

Figure 6.14. CuAAC reactions and anchor group hydrolysis of **10**-**12**. i) 4-azidobenzoic acid, CuI, toluene, 72%; ii) a) diethyl (4-azidophenyl)phosphonate, $CuSO_4.5H_2O$, NaAsc, DMF, b) DCM, TFA, c) $Zn(OAc)_2.2H_2O$, DCM/MeOH (4:1, v/v), 79%; iii) a) $CHCl_3$, TMS-Br, TEA, b) $Zn(OAc)_2.2H_2O$, DCM/MeOH (4:1, v/v), 87%; iv) ethyl 6-azido-coumarin-3-carboxylate, $CuSO_4.5H_2O$, NaAsc, DMF, b) DCM, TFA, c) $Zn(OAc)_2.2H_2O$, DCM/MeOH (4:1, v/v), 45%; v) KOH, THF/MeOH/H_2O (2:1:1, v/v), 90%.

Click chemistry is widely used in the synthesis of porphyrin derivatives,[19] but there are few examples for a *meso*-ethynyl porphyrin.[38–42] The reactions performed by Odobel,[38] Haumesser[41] and Shen[42] were used to synthesise porphyrin-porphyrin dimers, via the reaction of a *meso*-ethynyl porphyrin and an azido porphyrin. Odobel *et al.*[38] reacted a *meso*-ethynyl porphyrin and a *meso*-azido porphyrin in THF/H_2O (3:1, v:v), catalysed by (SIMes)CuBr, to produce a porphyrin dimer in 18% yield. Haumesser[41] and Shen[42] prepared porphyrin dimers using $CuSO_4.5H_2O$ and ascorbic acid in DMF, with yields of 30% and 98% respectively. The lower yield was obtained for a *meso*-azido porphyrin compared to a β-azido porphyrin. Maeda *et al*.[39,40] carried out a range of click reactions of *meso*-ethynyl porphyrins with benzyl bromide using CuCl in toluene at elevated temperatures (100 °C). The products were isolated in yields > 61% and no regioisomers were detected, despite the higher temperature, which has been attributed to the large steric effect of the porphyrin.

The conditions followed by Haumesser, Shen and Maeda (substituting CuCl with CuI) were screened for the reaction of **6.12** and 4-azidobenzoic acid (to synthesise **10**), as well as the conditions typically used for *meso*-ethynyl porphyrins[20] (CuI, DIPEA, THF). The only route which proved successful was the reaction carried out using CuI in toluene at 100 °C, which produced **10** in 72% yield. These conditions were tested for **11** and **12** but proved unsuccessful, possibly due to the limited solubility of **6.16** and **6.20** in toluene. The same reactions carried out in a mixed DMF/toluene solvent system were also unsuccessful. **11** and **12** were successfully prepared using $CuSO_4.5H_2O$ and sodium ascorbate in DMF, with yields of 79% and 45% respectively, after demetallation with TFA and metallation using $Zn(OAc)_2.2H_2O$ in DCM/MeOH. The products had initially appeared to contain a paramagnetic species, as the ^1H NMR spectra of **11** and **12** were considerably broadened compared to **10**. A broadening/splitting of the Soret band was also observed using UV-visible absorption spectroscopy. This was originally attributed to copper exchange during the click reaction, which prompted the demetallation of these porphyrins to confirm the formation of the products via ^1H NMR spectroscopy of the free base derivatives of **11** and **12**. However, as will be discussed in the next section (**Chapter 6.2.2**), this was later determined to be due to the coordination of the triazole to zinc causing self-assembly of the porphyrins.

Lindsey *et al.*[43] reported the synthesis of porphyrins with arylphosphonic acid substituents. They found that the treatment of zinc porphyrins with TMS-Br at room temperature, which are typical conditions for phosphonate cleavage, caused demetallation of the porphyrin alongside cleavage of the phosphonate esters. However, the esters could be deprotected by treatment of the porphyrin with TMS-Br and TEA in refluxing chloroform, without affecting the metallation state. The hydrolysis of **11** was performed using TMS-Br and TEA in refluxing chloroform and while it was minimised, a small amount of the porphyrin was demetallated (as observed by UV-visible absorption spectroscopy). After reaction with an excess of $Zn(OAc)_2.2H_2O$, the product was isolated in 87% yield after recrystallisation. **12** was hydrolysed by treatment with an excess of KOH in 2:1:1 THF:MeOH:H_2O and was isolated as a precipitate in 90% yield after acidifying the reaction mixture.

6.2.2. Structural Characterisation

As mentioned previously, NMR spectroscopy was used to identify the product of the nitration of coumarin-3-carboxylic acid. Figure 6.15 shows the possible regioisomers for **6.17**. The ^1H NMR spectrum of the product obtained from the nitration of coumarin-3-carboxylic acid is provided in Figure 6.16.

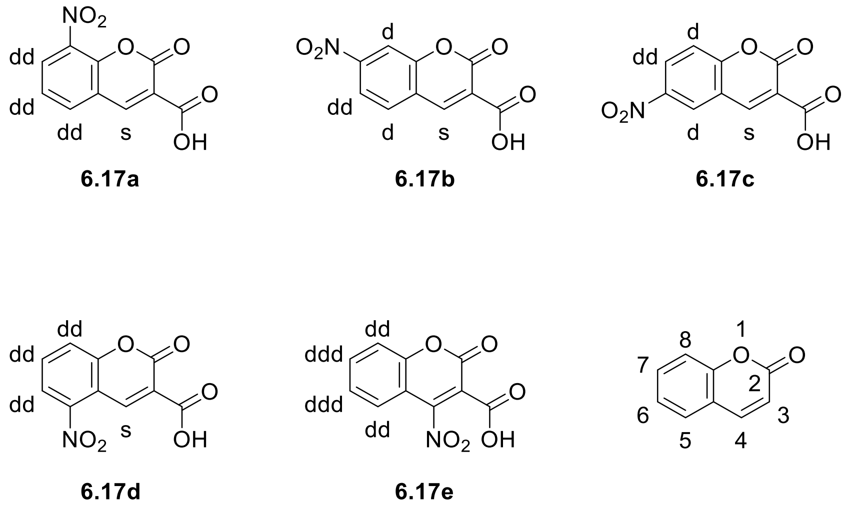

6.17a **6.17b** **6.17c**

6.17d **6.17e**

Figure 6.15. Possible regioisomers for the nitration of coumarin-3-carboxylic acid (protons are labelled with the expected ^1H NMR splitting pattern) and the IUPAC numbering system for a coumarin ring used throughout this discussion.

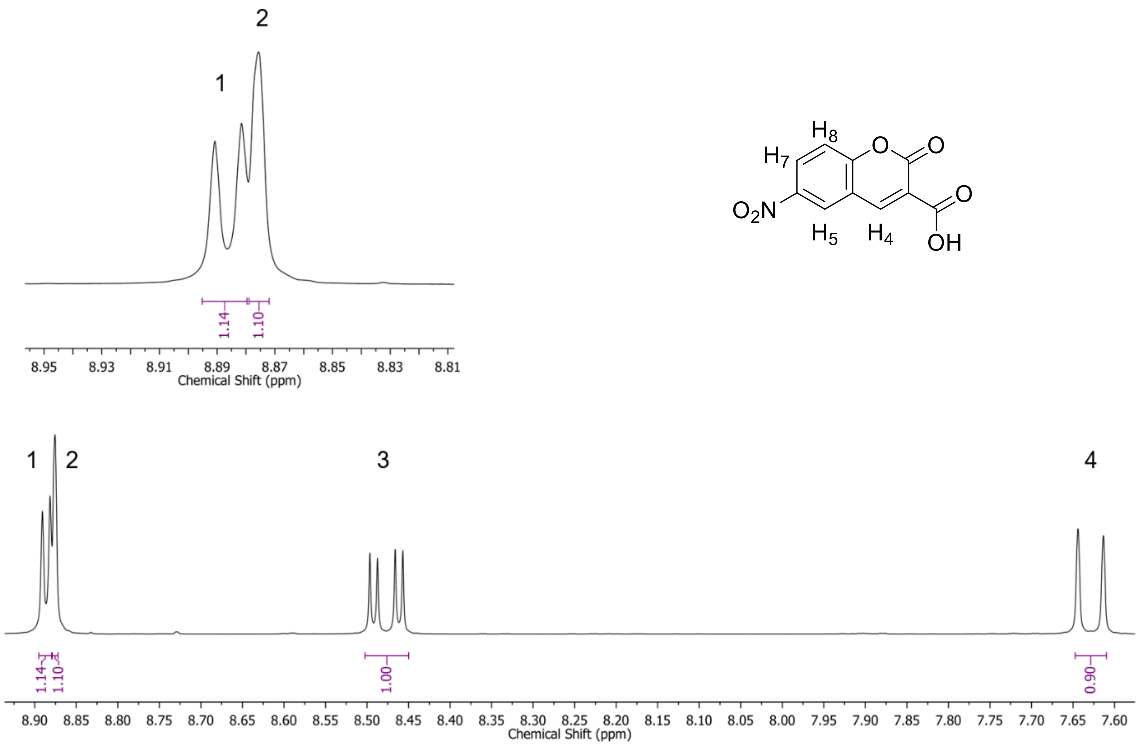

Figure 6.16. Assigned ^{1}H NMR spectrum of 6-nitro-coumarin-3-carboxylic acid.

Four distinct proton environments can be seen in the spectrum that correspond to a singlet, two doublets and a double doublet. The two possible regioisomers that matched these splitting patterns were **6.17b** and **6.17c**. However, while the ^{1}H NMR and COSY spectra can be used to narrow the possible regioisomers to 6/7-nitro-coumarin-3-carboxylic acid, they cannot be used to distinguish between the two. This was performed using a combination of HSQC and HMBC (Figure 6.17).

The cross-peak at 8.88/147.5 ppm in the HSQC spectrum identifies which peak corresponds with the carbon (C_4) coupled to the singlet (H_4) in the ^{1}H NMR spectrum. By comparing this to the HMBC spectrum, it was possible to identify which proton signal corresponds to H_5. The magnitude of the coupling constant for this signal could then be used to identify the correct regioisomer. If the product was **6.17b**, then H_5 would be a doublet with $^{3}J_{HH} \approx$ 8-9 Hz, but if the product was **6.17c**, then H_5 would be a doublet with $^{4}\mathrm{J}_{HH} \approx$ 3-4 Hz . The cross-peak at 8.89/147.5 ppm in the HMBC spectrum (that is absent in the HSQC spectrum) showed that H_5 was a doublet with J = 2.8 Hz, therefore assigning this compound to 6-nitro-coumarin-3-carboxylic acid (**6.17c**). Additionally, while a NMR spectrum has not been reported for the direct nitration of coumarin-3-carboxylic acid, this does match with spectra previously reported for the same compound synthesised via other methods.[44] The ^1H NMR spectrum has therefore been assigned to 6-nitro-coumarin-3-carboxylic acid (**6.17c**), with the proton assignment provided in Figure 6.16.

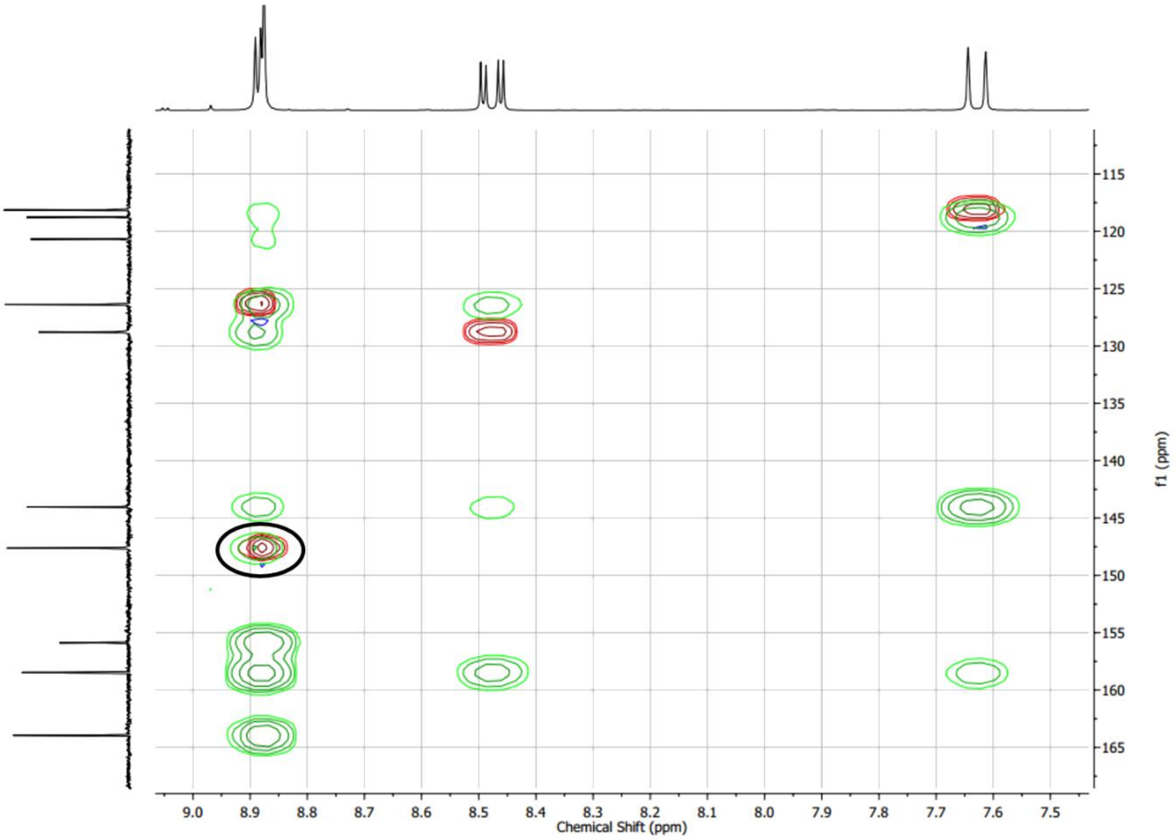

Figure 6.17. Overlaid HSQC (red contours) and HMBC (green contours) spectra of 6-nitro-coumarin-3-carboxylic acid. The black circle highlights the cross-peak that was used to assign the spectra to the product nitrated at C_6 and not C_7.

The most de-shielded doublet at 8.89 ppm (1) with J = 2.8 Hz has been assigned to H_5, as this proton is adjacent to the electron withdrawing NO_2 group and has a distinctive $^4J_{HH}$ meta coupling. The singlet at 8.88 ppm (2) has been assigned to H_4, because this is the only proton that is not coupled to another and it is downfield due to being on an electron poor ring adjacent to a carboxylic acid. The double doublet at 8.48 ppm (3) was assigned to H_7 as it is also de-shielded, due to being adjacent to the nitro group. It is coupled to two other protons with J = 9.2, 2.8 Hz which are indicative of $^3J_{HH}$ ortho and $^4J_{HH}$ meta couplings. Finally, the more shielded doublet at 7.63 ppm (4) with J = 9.2 Hz has been assigned to H_8, as it has a $^3J_{HH}$ ortho coupling to H_7 and is further away from the nitro group. While the coupled protons can be clearly assigned from the different coupling constants, these have been confirmed using COSY (Figure 6.18).

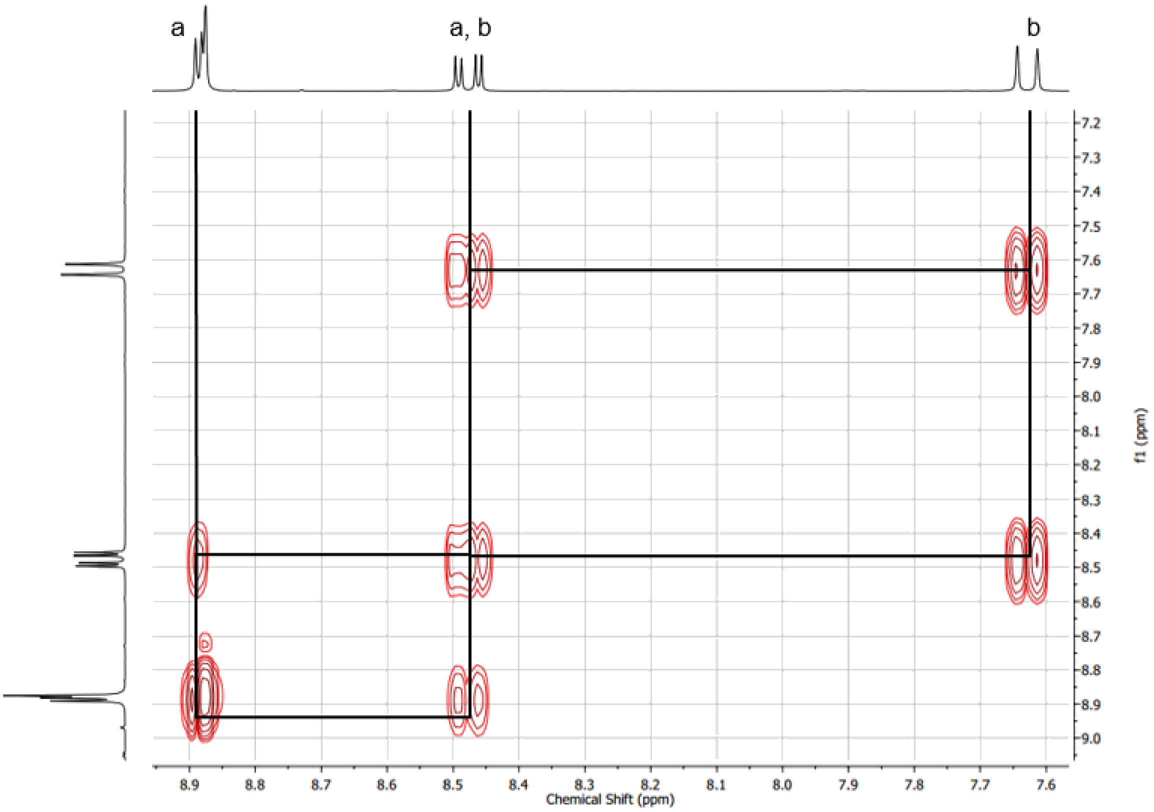

Figure 6.18. COSY spectrum of 6-nitro-coumarin-3-carboxylic acid. The labels indicate which protons are coupled.

^{1}H NMR spectroscopy was used to identify and characterise the structures of **10-12** (Figure 6.20). The peaks have been assigned (Table 6.1) according to the labelling system provided in Figure 6.19. Due to limited solubility and issues with aggregation, **11** and **12** have been characterised in their ester forms. As will be discussed later, due to issues with self-assembly of the triazole unit and the coordinated metal of the porphyrin, **11** and **12** have been characterised as free-base porphyrins.

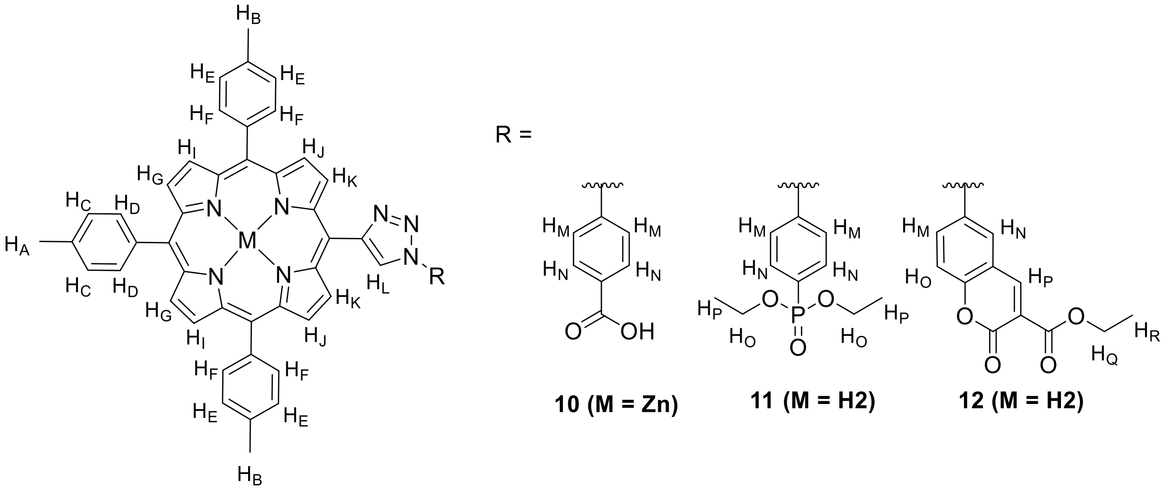

Figure 6.19. Proton labelling system used for **10-12**.

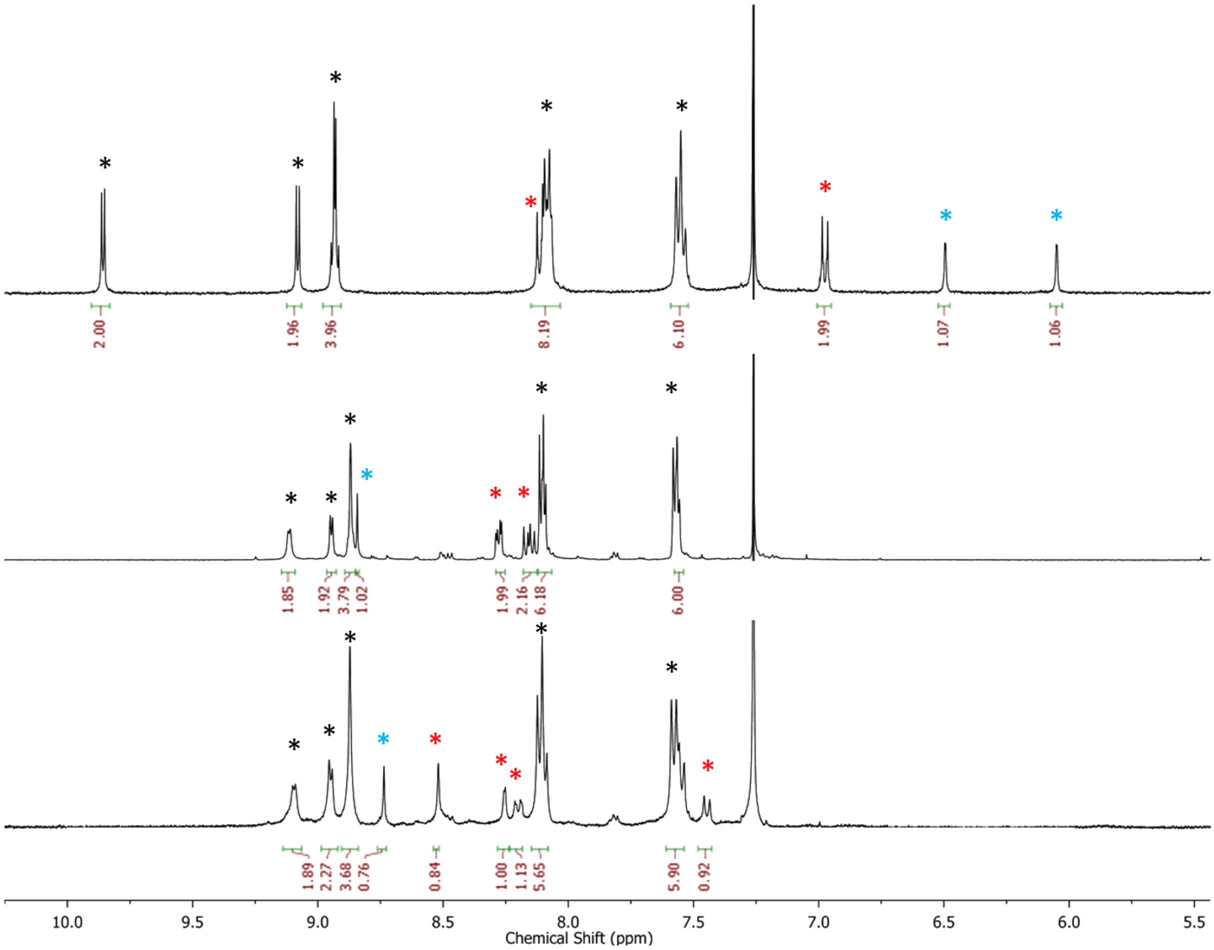

Figure 6.20. ^{1}H NMR spectra of **10** (top), **11** (middle) and **12** (bottom) recorded in $CDCl_3$ (400 MHz). For **10**, M = Zn while for **11** and **12** M = H_2. The peaks are colour coded according to their identity; black = porphyrin pyrrole/phenyl peaks, red = anchor peaks, blue = triazole peaks.

Table 6.1. Assignment of the ^{1}H NMR spectra of **10-12** (CDCl$_3$, 400 MHz).

	10			**11**			**12**		
H$_X$	δ / ppm	m / H	$^nJ_{HH}$ / Hz	δ / ppm	m	$^nJ_{HH}$ / Hz	δ / ppm	m	$^nJ_{HH}$ / Hz
A	2.70	s, 3H	-	2.71	s, 3H	-	2.69	s, 3H	-
B	2.72	s, 6H	-	2.72	s, 6H	-	2.72	s, 6H	-
C/E	8.16-8.04	m, 8H	-[a,b]	8.13-8.08	m, 6H	-[a]	8.15-8.06	m, 6H	-[a]
D/F	7.60-7.49	m, 6H	-[a]	7.58-7.55	m, 6H	-[a]	7.61-7.52	m, 6H	-[a]
G/I	8.98-8.88	m, 4H	-	8.89-8.85	m, 4H	-	8.92-8.82	m, 4H	-
J	9.86	d, 2H	4.8	9.11	d, 2H	4.8	9.10	d, 2H	4.9
K	9.08	d, 2H	4.8	8.95	d, 2H	4.8	8.95	d, 2H	4.9
L	6.97 / 6.49	d, 1H / d, 1H	1.5 / 1.5	8.84	s, 1H	-	8.74	s, 1H	-
M	8.16-8.04	m, 8H	-[a, b]	8.28	dd, 2H	8.5, 3.2	8.25	br s, 1H	-
N	6.97	d, 2H	8.8	8.16	dd, 2H	12.8, 8.5	8.20	br d, 1H	8.9
O	-	-	-	4.31-4.15	m, 4H	-	7.45	d, 1H	8.9
P	-	-	-	1.41	t, 6H	7.1	8.52	s, 1H	-
Q	-	-	-	-	-	-	4.45	q, 2H	7.1
R	-	-	-	-	-	-	1.44	t, 3H	7.1

Where; H$_X$ = the assigned proton (labelled as in Figure 6.19), δ = the chemical shift of the peak, m = peak multiplicity, H = relative number of protons and $^nJ_{HH}$ = peak coupling constant. [a] Could not be determined as peaks overlap. [b] H$_M$ (for **10**) overlaps with the 6H multiplet corresponding to H$_C$/H$_E$ (appears as an 8H multiplet of three overlapping doublets).

The ^{1}H NMR spectra of **10-12** is shown in Figure 6.20. In each case, the signals for the porphyrin core (colour coded in black) were similar. Due to the desymmetrisation, the pyrrole protons appeared as three different environments; two 2H doublets and a 4H multiplet. Similarly, the tolyl protons appeared as two 6H multiplets, that were each comprised of two overlapping 4H and 2H doublets. The chemical shifts of the tolyl peaks were mostly unaffected by the nature of the anchoring group/metallation state of the porphyrin, but for **10** the pyrrole peaks were considerably more deshielded than for **11** and **12**. This is due to the loss of electron density on the conjugated porphyrin ring after binding to zinc.

The signals corresponding to the anchoring unit are highlighted in red. For **10**, these appeared as two 2H doublets (with J = 8.8 Hz), one of which overlapped with a signal corresponding to the porphyrin tolyl groups. For **11**, these appeared as two 2H double doublets, with J = 12.8 / 8.5 Hz and 8.5 / 3.2 Hz respectively. The 8.5 Hz coupling corresponds to a $^3J_{HH}$ coupling of the two adjacent protons, while the couplings of 12.8 and 3.2 Hz correspond to $^3J_{PH}$ and $^4J_{PH}$ couplings respectively. There were four proton environments visible for the anchoring unit of **12**; these all have an integration of one and appeared as two singlets and two doublets (with J = 8.9 Hz). One pair of these singlets and doublets both appeared to be broadened, as the weak $^4J_{HH}$ coupling (that split these into a doublet and double doublet respectively for the coumarin precursors) was not fully resolved.

For **11** and **12**, the triazole proton appeared as a 1H singlet at 8.84 and 8.74 ppm respectively. This is similar to previously reported porphyrins with a bridging triazole group, where the triazole singlet appears in the range of 8.55 – 9.33 ppm.[20,41,42] However, for **10**, the triazole was shifted upfield in comparison and appeared as two 1H doublets (with J = 1.5 Hz) at 6.97 and 6.49 ppm. This is not indicative of a mixture of regioisomers, due to the 1:1 integral ratio and absence (or broadening) of any other aromatic peaks. The weak splitting of these peaks suggests a $^4J_{HH}$ coupling, possibly indicative of a protonated triazole, which could arise due to a zwitterionic interaction (Figure 6.21). The chemical shift of these peaks (6.97 and 6.49 ppm) are similar to a porphyrin appended to an unfunctionalised *meso*-triazole group (6.57 ppm) reported by the group of Osuka.[39]

This zwitterionic interaction could also explain why the ^{1}H NMR spectrum of **10** (when M = Zn) is clearly defined, whereas for **11** and **12** the peaks were considerably broadened compared to the free-base derivatives (Figure 6.22). This broadening has been observed for triazole-functionalised porphyrins due to self-assembly of the triazole subunits with zinc.[45] The dynamic exchange between the monomeric and self-assembled species occurs on a shorter timescale to the NMR measurement,[46] leading to peak averaging, which causes the broadened signals. If the triazole is protonated (as is possibly the case with **10**), then the loss of one nitrogen lone-pair and a decrease in the electron density of the ring will hinder this self-assembly. This self-assembly of **11** and **12** did not hinder other characterisation techniques, as they were performed in coordinating solvents (THF or MeCN) that will compete with the triazole for coordination to the zinc porphyrin.

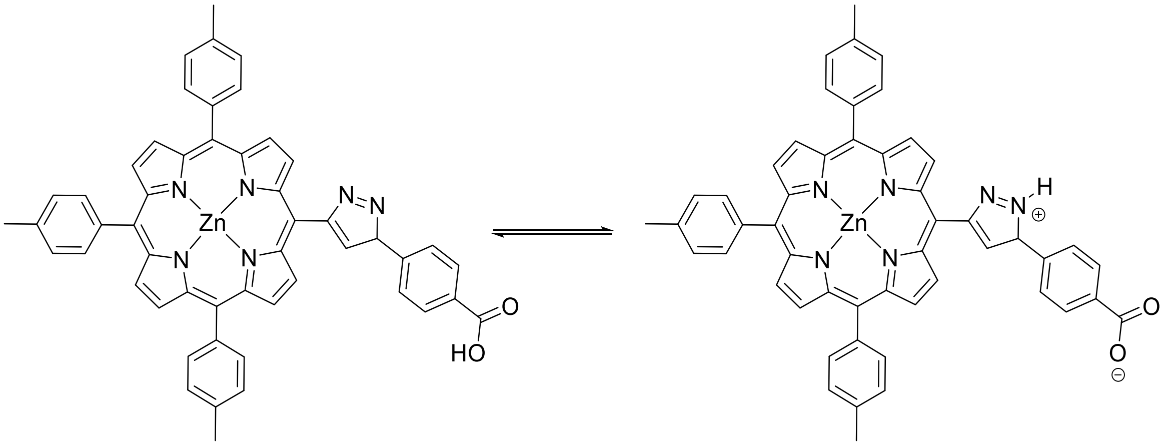

Figure 6.21. Possible zwitterionic structure of **10**.

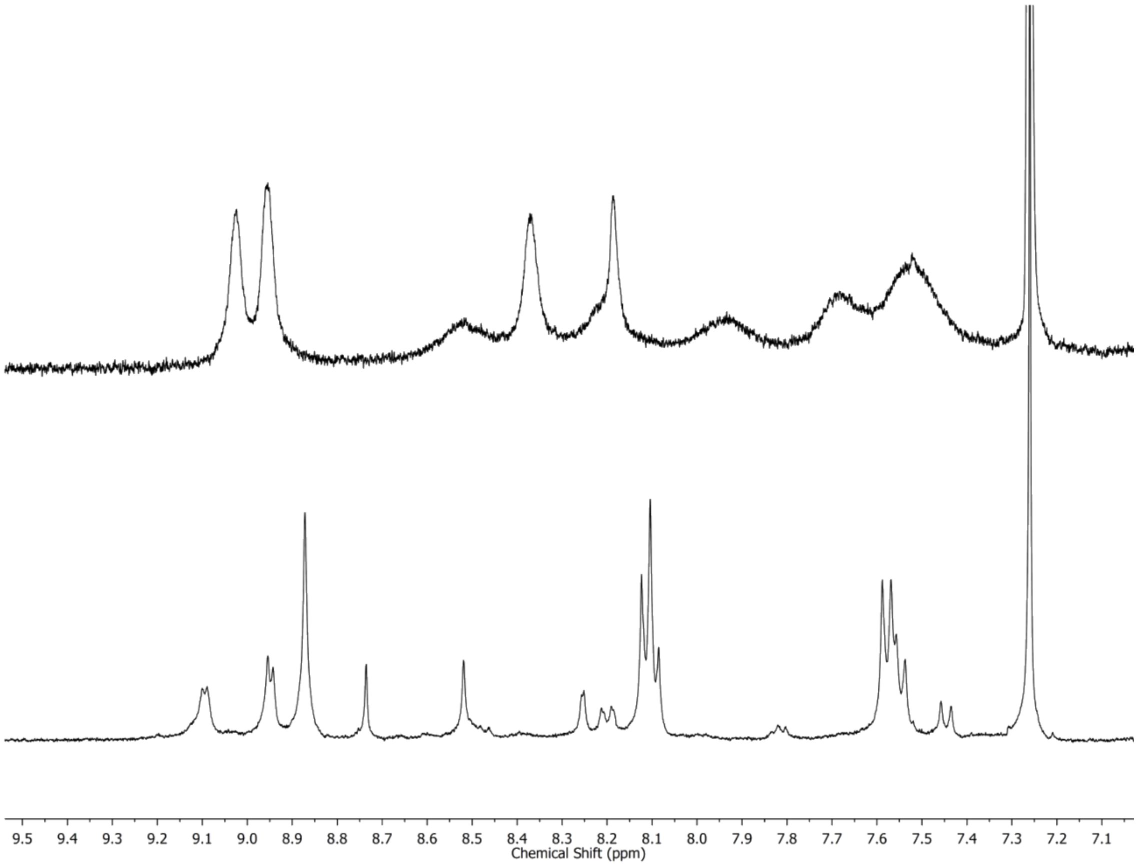

Figure 6.22. ^{1}H NMR spectrum of **12** in $CDCl_3$ (400 MHz). Top, M = Zn; bottom, M = H_2.

6.2.3. Optical Characterisation

The UV-visible absorption (Figure 6.23) and emission (Figure 6.24 - Figure 6.26) spectra of **10-12** were measured in THF and are summarised in Table 6.2.

Table 6.2. UV-visible absorption and emission data for **9-11** in THF.

	λ_{abs} / nm (ε / M^{-1} cm^{-1})	λ_{em} / nm (relative intensity[a])	E_{0-0} / eV
10	423 (333,330), 554 (11,150), 597 (3750)	606 (1.0), 657 (0.99)	1.97
11	424 (326,565), 556 (13,670), 598 (5875)	610 (1.0), 659 (0.89)	1.98
12	424 (273,520), 557 (15,820), 598 (6775)	609 (1.0), 659 (0.82)	1.98

Where λ_{abs} is the wavelength of maximum absorbance, λ_{em} is the wavelength of maximum emission and E_{0-0} is the zero-zero energy (which is the energy difference between the ground and excited states). [a] Relative intensities from the emission spectra excited at 420 nm.

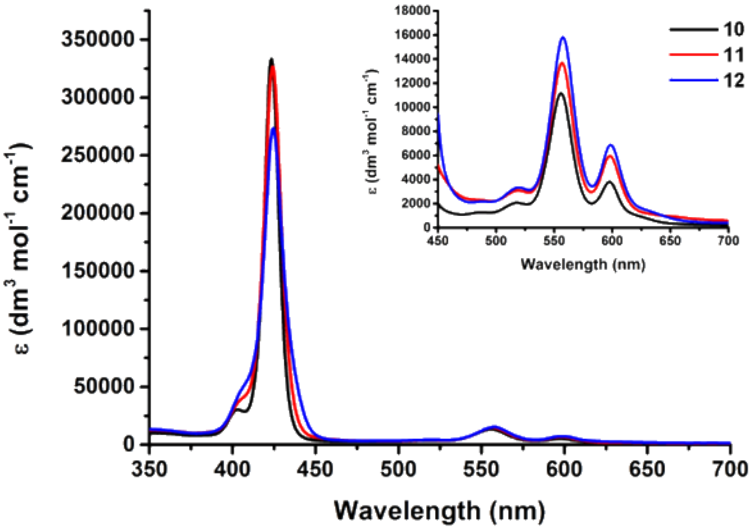

Figure 6.23. UV-visible absorption spectra of **10-12** recorded in THF.

The absorption spectra of **10-12** are typical of metalloporphyrins, with three major bands in the visible region.[47–49] The most intense band (ca. 420 nm) is the Soret (or B) band and the two bands at higher energy are the Q bands. Free-base porphyrins have four distinct Q bands, therefore metallation can be monitored by the change from four to two bands (alongside a small red-shift of the Soret band). The Soret bands of **10** and **11** were very similar, with a small decrease in intensity and a slight broadening for **11**. For **12** there was a larger decrease in the peak intensity and an increased broadening compared to **10** and **11**. To compare the intensity of bands with different band widths, oscillator strengths (f) have been previously used.[50,51] Here the trend in f_{Soret} was **11** (1.295) ≈ **12** (1.294) > **10** (1.124) which is different to the trend in $\varepsilon_{\text{Soret}}$ of **10** > **11** > **12**. The intensity of the Q bands follows the trend **12** > **11** > **10** and there was little variation in band width. For all three porphyrins, the peak maxima of the Soret and Q bands were within a range of 1 and 3 nm respectively.

The steady state emission spectra of **10-12** (Figure 6.24 - Figure 6.26) show two bands at 606-610 nm and 657-659 nm. These are due to fluorescence from the Q-band states and can be detected following excitation into either the Soret (420 nm) or Q_{0-1} (550 nm) bands.[52] From an excitation at 420 nm, the two bands were of essentially equal intensity for **10** (relative intensity 1.0 vs. 0.99) but the intensity of the lower energy band decreased for **11** (1.0 vs. 0.89) and **12** (1.0 vs. 0.82). For **10** and **11**, the emission spectra were mostly independent of the excitation wavelength, but for **12**, emission from the second band was more intense when excited at 550 nm (relative intensity 1.0 vs. 0.95). When excited at 420 nm, each porphyrin showed a very weak emission band at ca. 460 nm that could be emission from the Soret band, but the intensity was minimal compared to the Q-band emission.

Quantum yields were not determined, but for samples measured under the same instrumental settings with identical absorptions at the excitation wavelength, the relative intensities of the band at ca. 610 nm follows the trend **10** (1.0) > **11** (0.64) > **12** (0.59). Compared to the absorption spectra, the most emissive porphyrin was **10**, which had the narrowest absorption band, while the least emissive porphyrin was **12**, which had the broadest band. No additional emission band could be attributed to the coumarin; coumarin 3-carboxylic acid has an emission band at 350 nm (λ_{Exc} = 286 nm),[53] so it would not have been observed during these measurements.

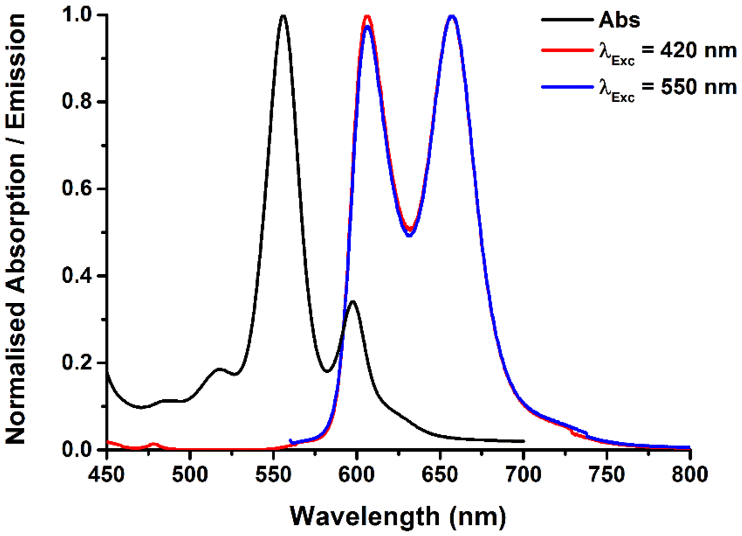

Figure 6.24. Normalised absorption and emission spectra of **10** recorded in THF.

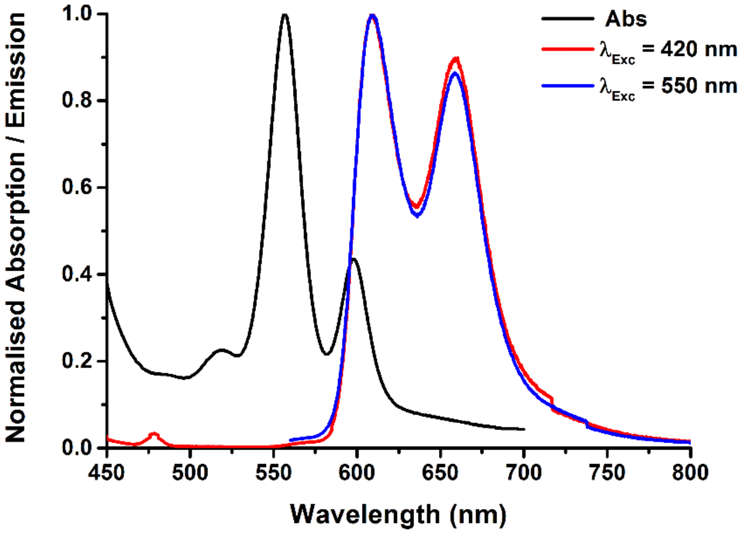

Figure 6.25. Normalised absorption and emission spectra of **11** recorded in THF.

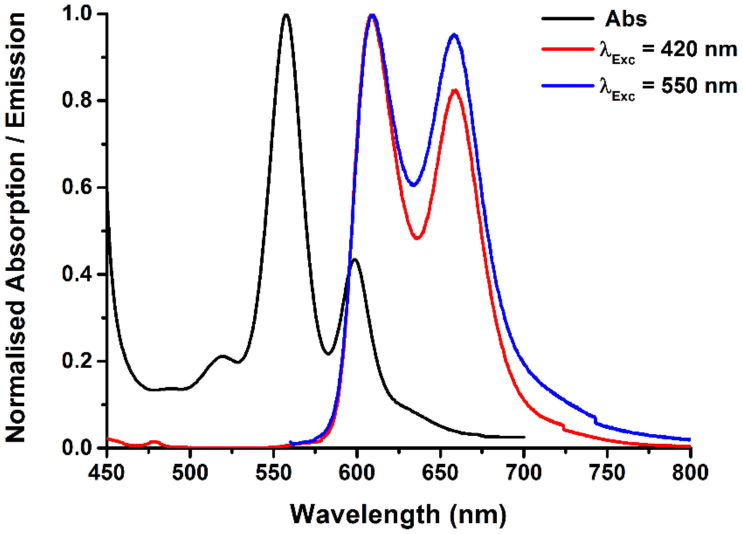

Figure 6.26. Normalised absorption and emission spectra of **12** recorded in THF.

The uncorrected excitation spectra were recorded for both emission bands and are shown in Figure 6.27 - Figure 6.29. A good agreement of the absorption and excitation spectra was obtained for both the Soret and Q-bands, indicating that the emissive species for both bands was the same.

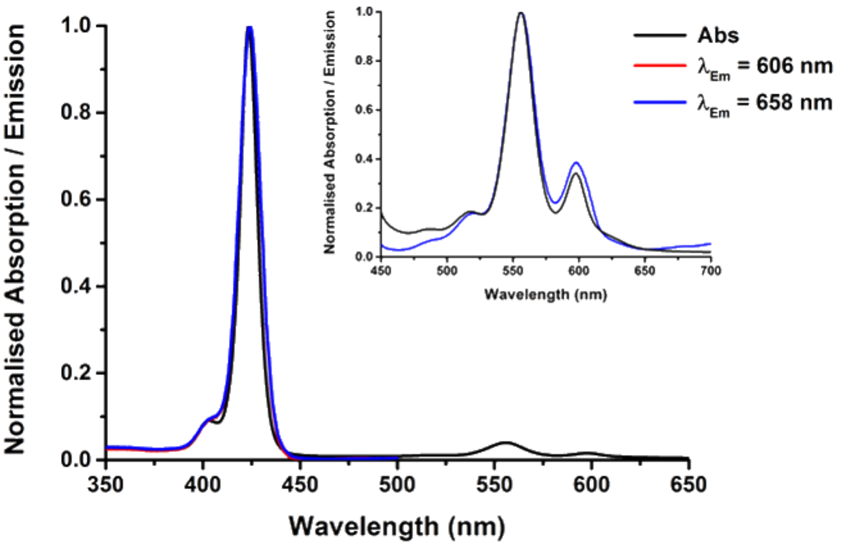

Figure 6.27. Normalised absorption and excitation spectra of **10** recorded in THF.

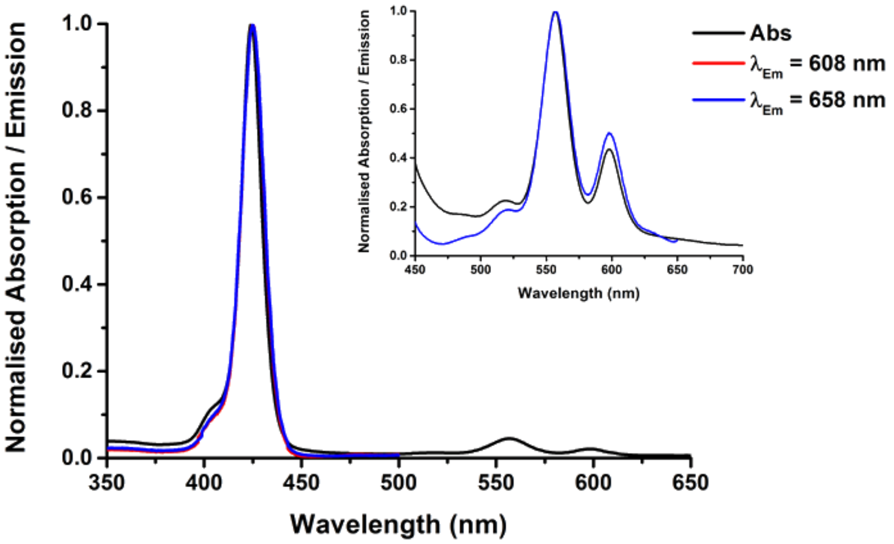

Figure 6.28. Normalised absorption and excitation spectra of **11** recorded in THF.

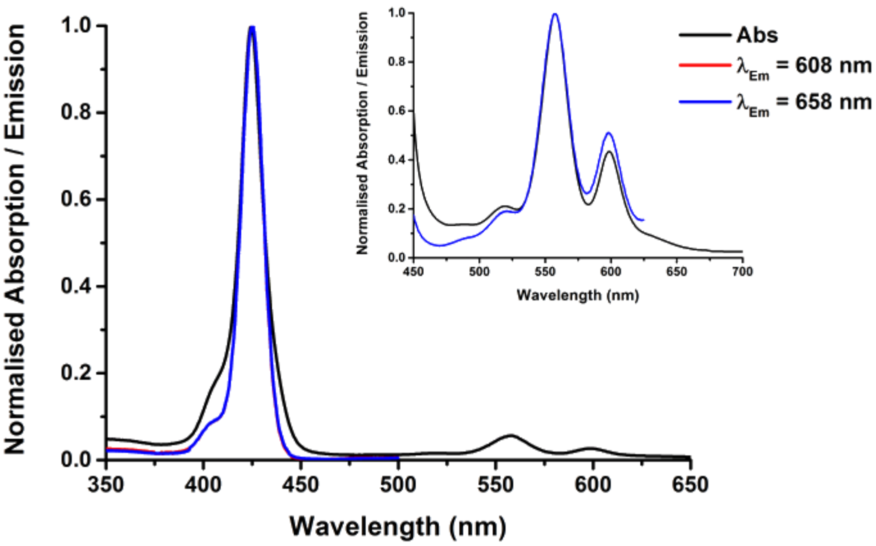

Figure 6.29. Normalised absorption and excitation spectra of **12** recorded in THF.

The zero-zero energy of a molecule is the energy difference between the electronic ground state and the vibrational ground state of the excited species. An estimate of this energy is used to calculate the excited state redox potentials. It is typically calculated by taking the intercept of the normalised absorption and emission spectra. E_{0-0} can be used to estimate the electrochemical driving forces for the electron transfer processes in a DSC (see **Chapter 3.2.5**). For porphyrins that do not have a clear overlap of the absorption and emission spectra, different methods have been used to calculate E_{0-0}.[54] Here it has been calculated using either the median wavelength values between corresponding absorption/emission bands (method A) or from the intercept of Lorentzian fits of the absorption/emission bands (method B, an example fit is provided in Figure 6.30). These were calculated for the singlet Q_{0-1} and Q_{0-0} states, which are summarised in Table 6.3. The values obtained from both methods were similar and the average excited state energies were mostly independent on the nature of the anchoring group.

Table 6.3. $E_{0\text{-}0}$ values for **10-12** determined using the median wavelength between corresponding absorption/emission peaks (method A) or the intercept-method using Gaussian fits (method B).

		$E_{0\text{-}0}$ / eV		
Transition.	Method	**10**	**11**	**12**
$Q_{0\text{-}1}$	A	2.13	2.13	2.13
	B	2.11	2.11	2.11
$Q_{0\text{-}0}$	A	1.97	1.97	1.97
	B	1.98	1.99	1.99

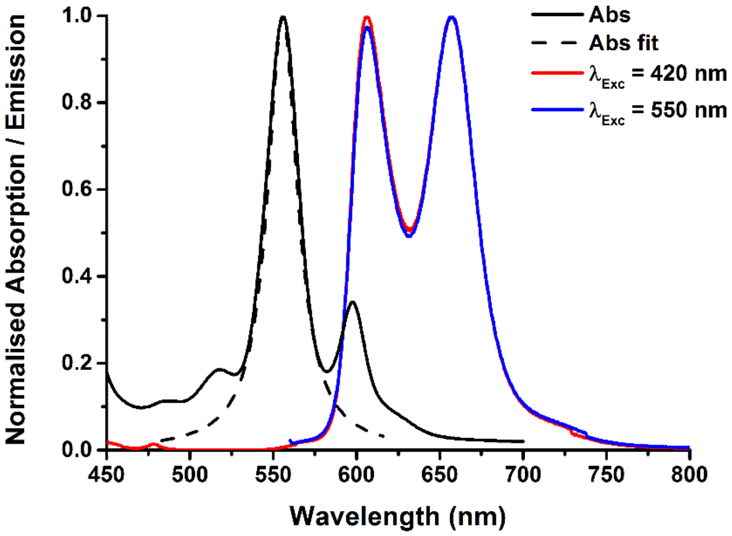

Figure 6.30. Normalised absorption and emission spectra of **10** recorded in THF overlaid with the fit of the $Q_{0\text{-}1}$ absorption transition (fit to a Lorentzian function).

6.2.4. Electrochemistry

The redox potentials of **10**-**12** were determined using cyclic voltammetry and DPV. All electrochemistry was carried out with a 1 mM analyte concentration and was measured in acetonitrile with 500 mM $LiClO_4$ supporting electrolyte (working electrode: glassy carbon; reference electrode: $Ag/AgNO_3$ calibrated with Fc/Fc^+ as an internal reference, counter electrode: Pt). Due to the limited solubility of **11** and **12** in acetonitrile, these were studied as esters.

Table 6.4. Summary of electrochemical potentials recorded for **10-12** as determined by CV, unless otherwise stated. The potentials were referenced against the Fc/Fc+ redox couple and converted to NHE by the addition of 0.63 V.[55]

	E_{red}[a] / V vs.		$E_{ox}1$ / V vs.		$E_{ox}2$ / V vs.		$E_{ox}3$[a] / V vs.		$E_{ox}4$[a] / V vs.	
	Fc	NHE	Fc	NHE	Fc	NHE	Fc	NHE	Fc	NHE
10	-1.77	-1.14	+0.30	+0.93	+0.49	+1.12	+0.79	+1.42	+0.94	+1.57
11	-1.74	-1.11	+0.32	+0.95	+0.42	+1.05	+0.65	+1.28	+0.89	+1.52
12	-1.87	-1.24	+0.29	+0.92	+0.41	+1.04	+0.68	+1.31	+0.87	+1.50

E_{red} is the reduction potential and E_{ox} is the oxidation potential. [a] Potential obtained using DPV.

Cyclic voltammograms of the oxidation and reduction processes for **10** are provided in Figure 6.31 – Figure 6.33. On initially scanning to 0.6 V vs. Fc, two oxidation peaks were observed, separated by 190 mV. These have been defined as quasi-reversible, because the peak separation for the first process is dependent on scan rate and for the second process, the anodic and cathodic peak currents were not equal. Upon increasing the oxidative scan window a third process was revealed, with a peak current five times higher than the first two processes, that was irreversible. Only one irreversible reductive process (Figure 6.33) was observed in the potential window examined. As few of the peak potentials could be determined using cyclic voltammetry, these were instead measured using DPV (Figure 6.39 - Figure 6.40).

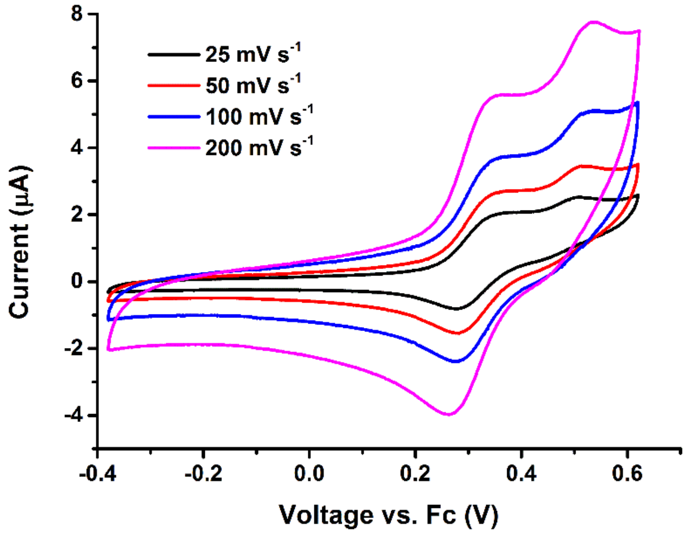

Figure 6.31. Oxidative cyclic voltammetry for **10** showing the first two redox processes.

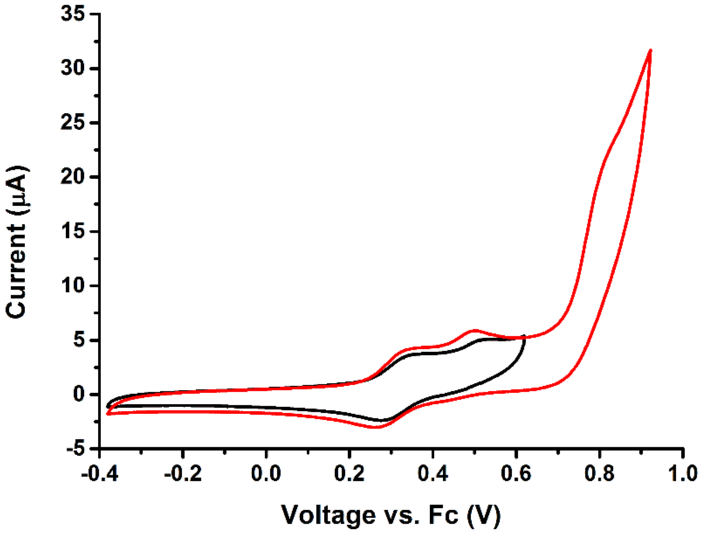

Figure 6.32. Oxidative cyclic voltammetry for **10** showing the first three redox processes (100 mV s^{-1} scan rate).

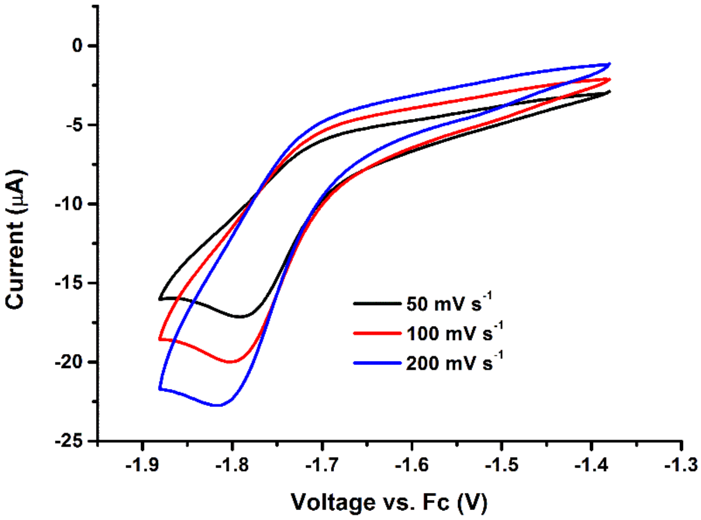

Figure 6.33. Reductive cyclic voltammetry for **10**.

The oxidation and reduction processes for **11** are shown in Figure 6.34 – Figure 6.36. As for **10**, upon scanning to 0.6 V vs. Fc, two oxidation peaks were observed. These had a smaller separation of 100 mV and were quasi-reversible, because the anodic and cathodic peak currents for both were not equal. Upon increasing the oxidative scan window a third process was again revealed, but unlike for **10** the peak current of this wave was roughly equal to the first two processes. As for **10**, only one reductive process (Figure 6.36) was observed, which was quasi-reversible, as a return wave was present at higher scan rates, but the peak currents were different. At a scan rate of 100 mV s^{-1} a shoulder peak was seen on the reductive wave, but this was not resolved at slower or faster scan rates. The peak potentials were determined using DPV (Figure 6.39 - Figure 6.40).

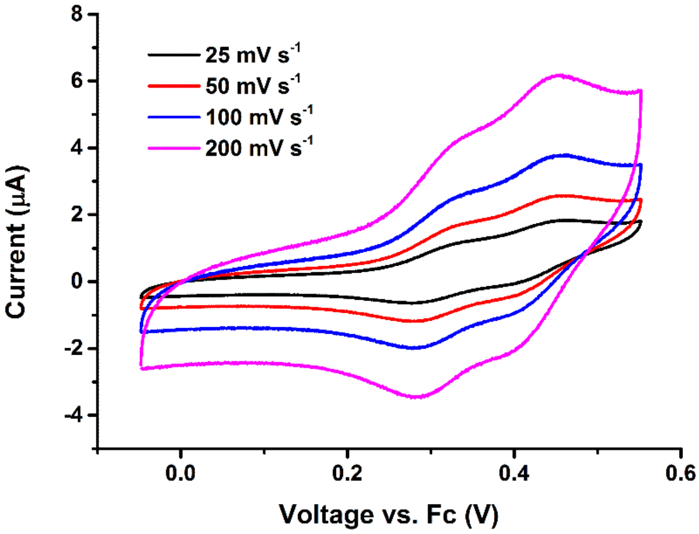

Figure 6.34. Oxidative cyclic voltammetry for **11** showing the first two redox processes.

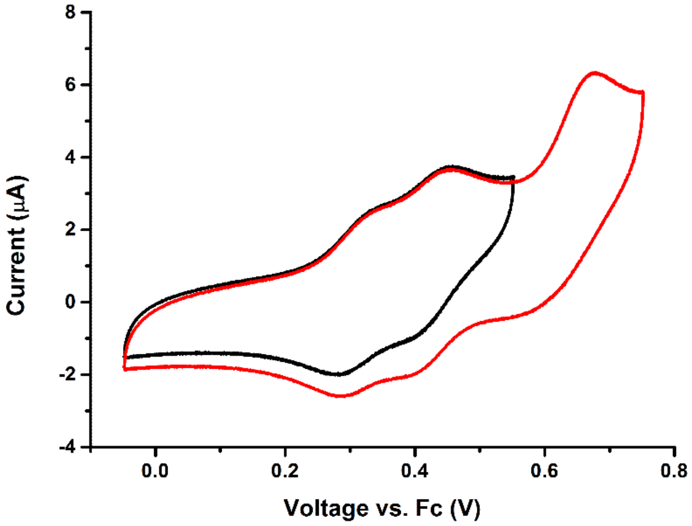

Figure 6.35. Oxidative cyclic voltammetry for **11** showing the first three redox processes (100 mV s^{-1} scan rate).

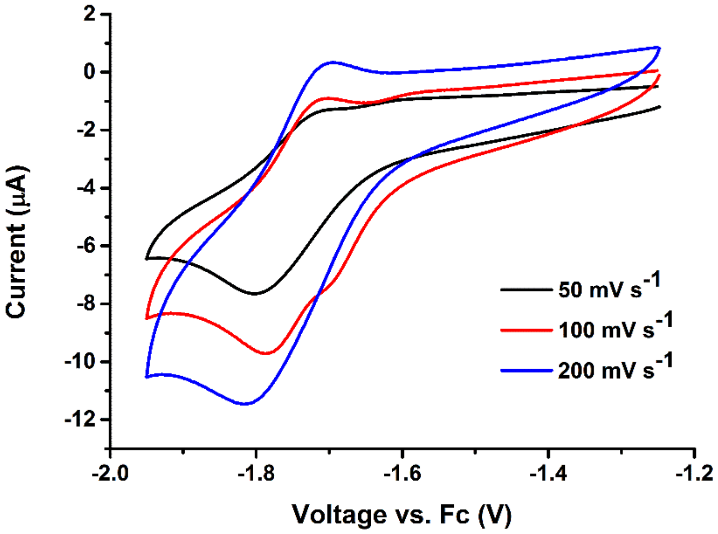

Figure 6.36. Reductive cyclic voltammetry for **11**.

Cyclic voltammograms of the oxidation process for **12** are provided in Figure 6.37 and Figure 6.38. Two quasi-reversible processes can be seen with a peak separation of 120 mV, which was lower than for **10** but slightly larger than **11**. As for **10** and **11**, upon increasing the potential window an irreversible oxidation process was observed, with a peak current roughly twice the size of the first two processes. The reduction process could not be resolved using cyclic voltammetry, as a broad reduction was recorded that overlapped with the solvent window. Therefore, this potential was determined using DPV (Figure 6.39 - Figure 6.40).

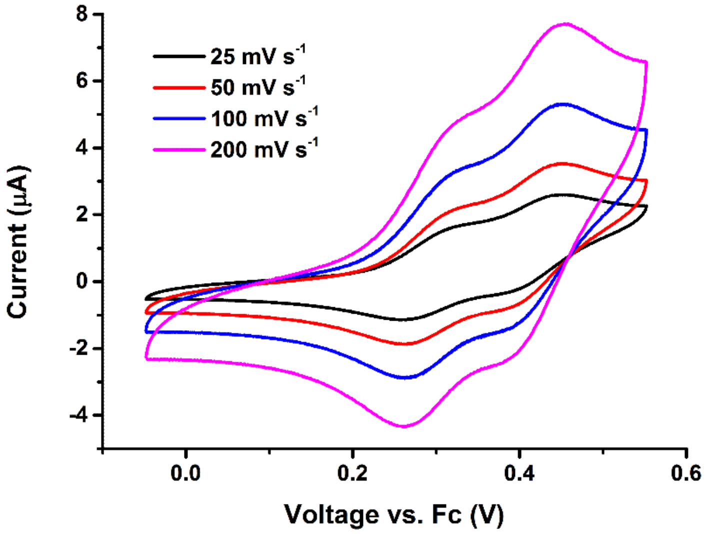

Figure 6.37. Oxidative cyclic voltammetry for **12** showing the first two redox processes.

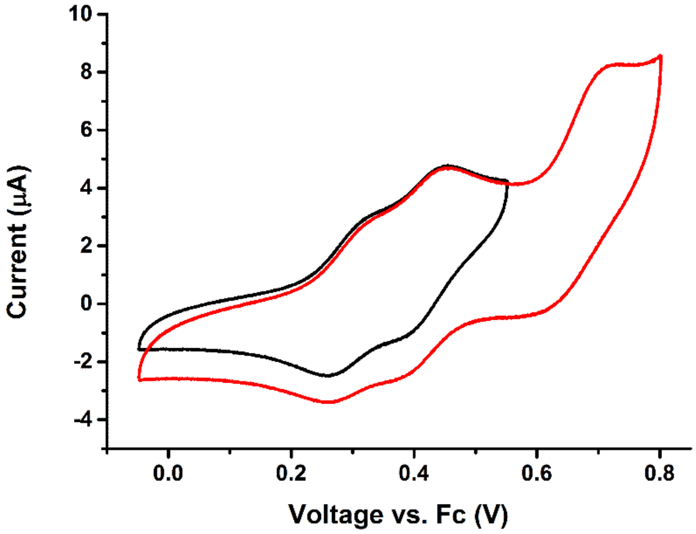

Figure 6.38. Oxidative cyclic voltammetry for **12** showing the first three redox processes (100 mV s^{-1} scan rate).

DPV was used to measure the peak potentials of the oxidation (Figure 6.39) and reduction (Figure 6.40) processes of **10-12**. In each case there were three well resolved oxidation processes and a fourth that is generally broader and less well-defined (except for **12**). This fourth process could not be resolved using cyclic voltammetry for any of the samples. There was little variation in the first oxidation potential; all three porphyrins were oxidised between +0.29 and +0.32 V vs. Fc, with **12** the easiest to oxidise (+0.29 V vs. Fc) and **11** the hardest (+0.32 V vs. Fc). The reduction processes occur within a potential range of -1.74 to -1.87 V vs. Fc, with **11** reduced at lower potentials (-1.74 V vs. Fc) and **12** requiring the highest potential (-1.87 V vs. Fc).

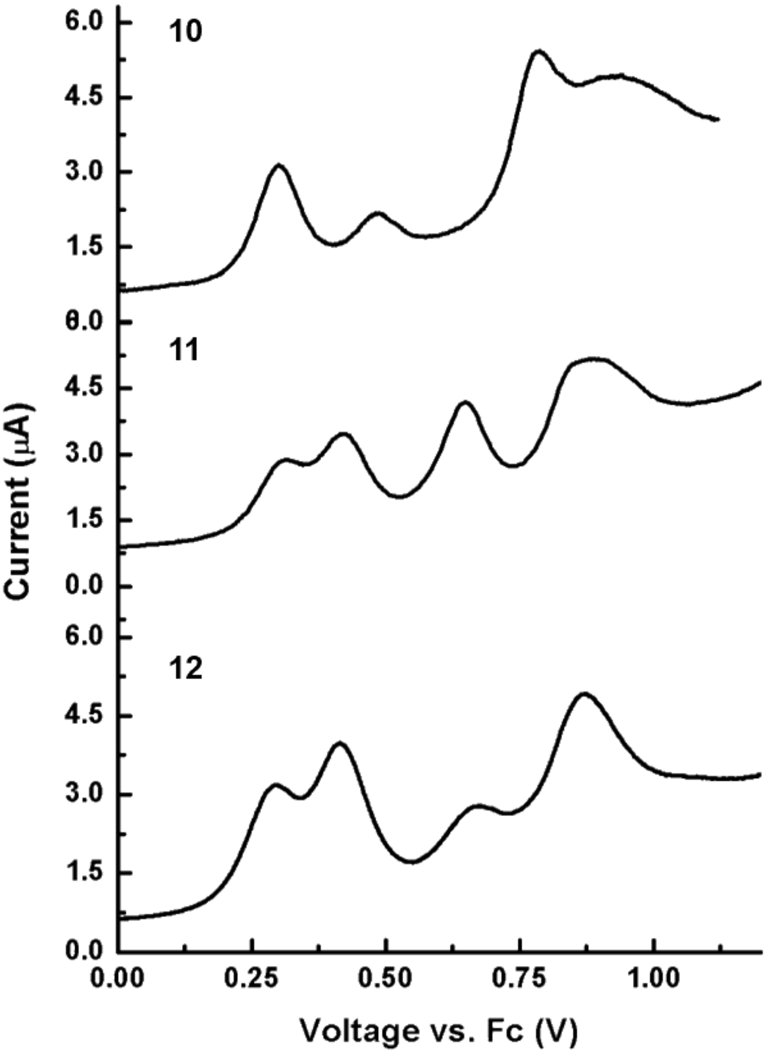

Figure 6.39. Comparison of oxidative DPV for **10-12** (100 mv s^{-1} scan rate).

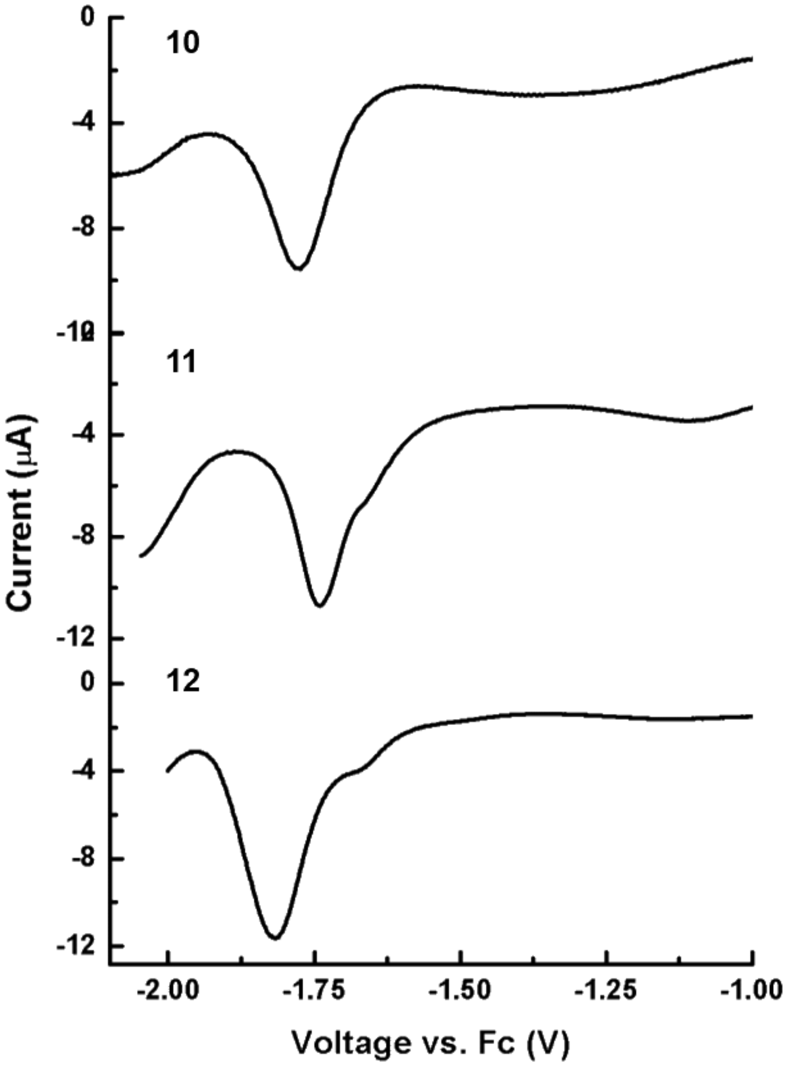

Figure 6.40. Comparison of reductive DPV for **10-12** (100 mv s^{-1} scan rate).

As discussed earlier (**Chapter 3.2.5**), these redox potentials can be used to calculate driving forces for the electron transfer processes that occur in an operational device. Specifically, they are used to calculate the driving force for electron transfer from the valence band of NiO to the photoexcited dye and regeneration of the reduced dye by the redox mediator. These driving forces were calculated using Equation 3.1 – Equation 3.3. They are summarised in Table 6.5 and represented schematically in Figure 6.41.

Table 6.5. Calculated electrochemical driving forces for the electron transfer processes occurring within an operational p-DSC. All potentials are reported in V vs. NHE.

	E_{red} / V	E_{0-0} / eV	$E_{red}(S^*/S^-)$ / V	ΔGinj / V	ΔG_{reg} (I^-/I_3^-) / V
10	-1.14	1.97	0.83	-0.29	-0.95
11	-1.11	1.98	0.87	-0.33	-0.92
12	-1.24	1.98	0.74	-0.20	-1.05

E_{red} is the ground state reduction potential, E_{0-0} is the zero-zero energy, $E_{red}(S^*/S^-)$ is the excited state reduction potential, ΔG_{inj} is the driving force for charge transfer from NiO to the excited dye and ΔG_{reg} (I^-/I_3^-) is the driving force for regeneration of the reduced dye.

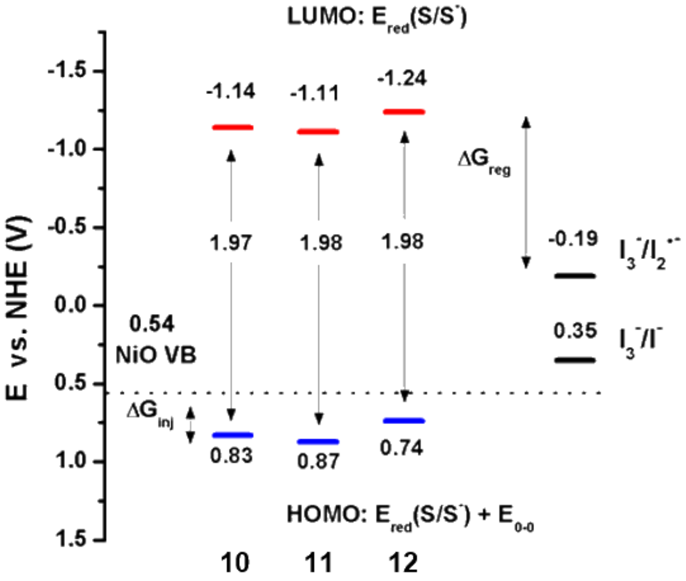

Figure 6.41. HOMO/LUMO energy level diagram for **10-12** alongside driving forces for electron injection and dye regeneration.

ΔG_{reg} is high in all cases, with the highest driving force of -1.05 eV for **12** and the lowest of -0.92 eV for **10**. These are higher than any of the BODIPY dyes studied in Chapter 3 (**1-5**), which were efficiently regenerated. This suggests that regeneration will not be a limiting factor to device performances. ΔG_{inj} was highest for **11** at -0.33 eV and lowest for **12** at -0.20 eV, as the HOMO was higher in potential. These driving forces are similar to a porphyrin (**ZnP$_{ref}$**, Figure 6.42) studied by Odobel and co-workers[21] (ΔG_{inJ} =-0.30 eV and ΔG_{reg} = -1.09 eV). Liu *et al.*[56] proposed that ca. -0.8 eV of driving force is needed for a high quantum yield for hole injection. As ΔG_{inj} for these porphyrins (and those of Odobel *et al.*) were lower than this, this could contribute to the low performances typically obtained from porphyrin sensitised p-DSCs.[21,22]

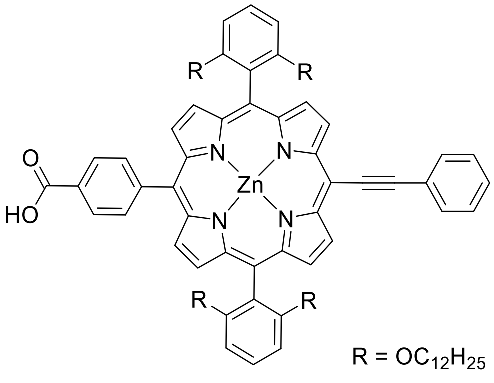

ZnP_{ref}

Figure 6.42. *Meso*-anchored porphyrin studied by Odobel *et al*.[21] for use in p-DSCs.

6.2.5. Computational Studies

Theoretical energy levels and the corresponding molecular orbital distributions were calculated using the hybrid B3LYP[57] exchange functional and a 6-311G(d,p) basis set. Solvation was treated using the PCM.[58] Initially, the ground state geometries were optimised (in THF) then frequency calculations were performed to check this was a true energy minimum. TDDFT calculations were then used to determine the vertical excitation energies.

The orbital distributions for HOMO-1 through to LUMO+2, alongside the calculated energy levels, are shown in Figure 6.43 - Figure 6.45 and the energies are summarised in Table 6.6.

Table 6.6. Calculated energy levels for **10**-**12** (calculated using B3LYP/6-311G(d,p) in THF using the PCM).

	Calculated energy / eV		
	10	**11**	**12**
LUMO +2	-2.15	-1.87	-2.55
LUMO +1	-2.54	-2.54	-2.61
LUMO	-2.60	-2.60	-2.90
HOMO	-5.22	-5.23	-5.27
HOMO-1	-5.54	-5.55	-5.55

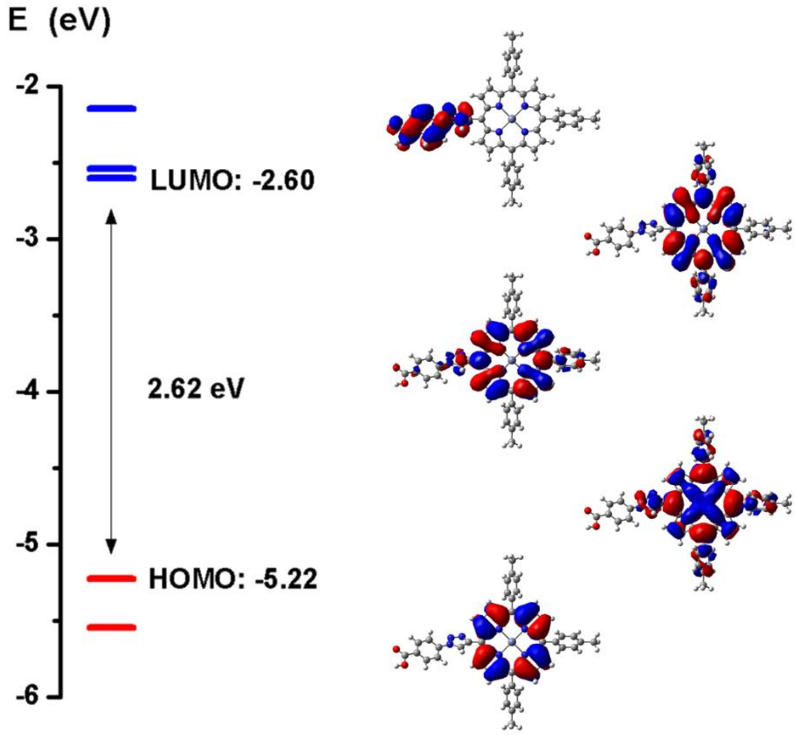

Figure 6.43. Optimised geometry, calculated energy level diagram and orbital distribution (LUMO+2 to HOMO-1, top to bottom) for **10** in THF using B3LYP/6-311G(d,p).

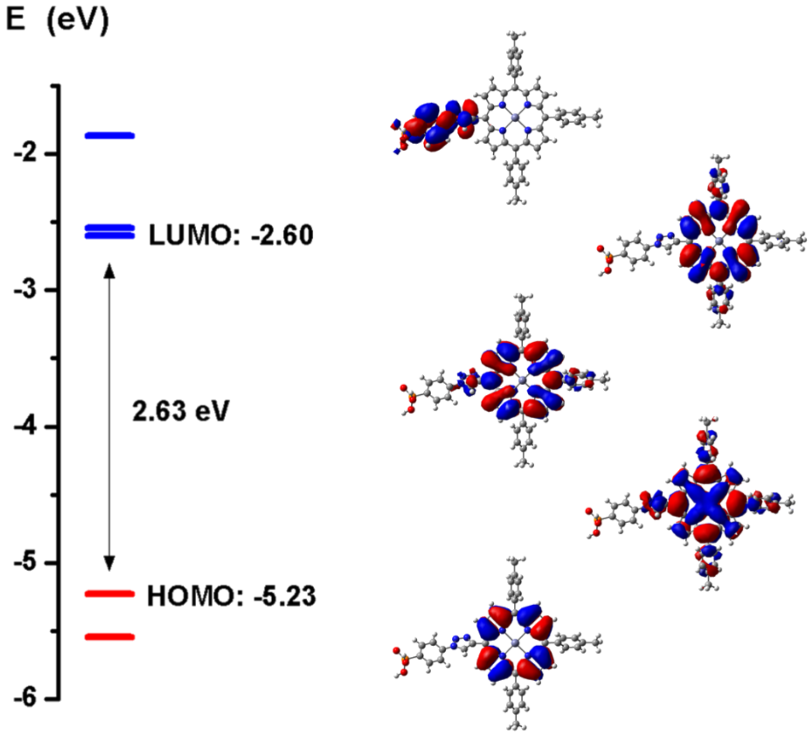

Figure 6.44. Optimised geometry and calculated energy level diagram (LUMO+2 to HOMO-1, top to bottom) for **11** in THF using B3LYP/6-311G(d,p).

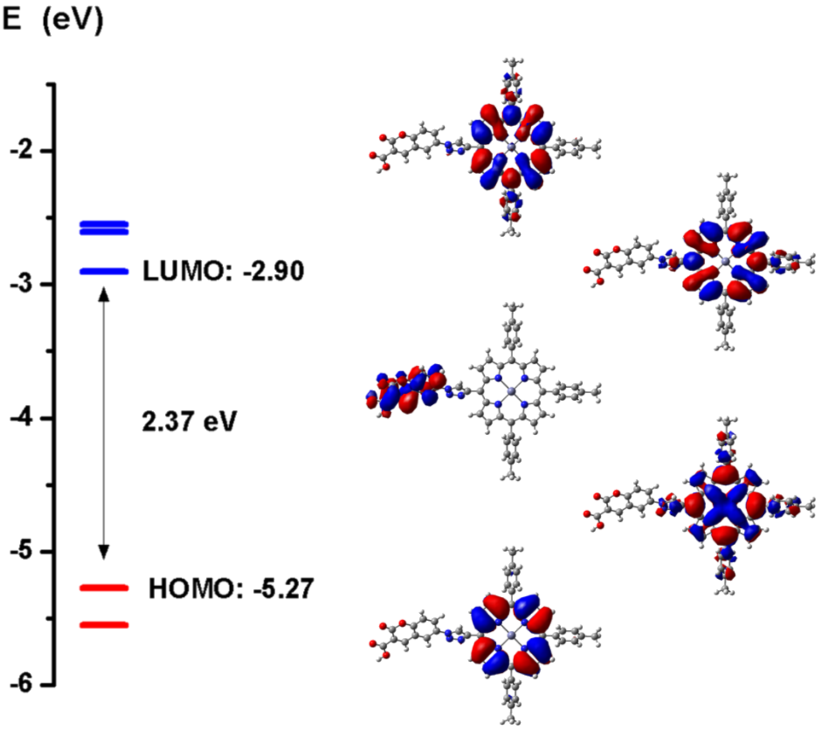

Figure 6.45. Optimised geometry and calculated energy level diagram (LUMO+2 to HOMO-1, top to bottom) for **12** in THF using B3LYP/6-311G(d,p).

In each case, there were four orbitals localised on the porphyrin core; the HOMO-1 to LUMO+1 for **10** and **11** and the HOMO-1/HOMO and LUMO+1/+2 for **12**. The calculated energies of these orbitals were within 0.05 eV. In the HOMO for all three porphyrins, the electron density was located on the porphyrin core and the four *meso*-substituents (with electron density on the triazole, but not the anchor). For the unoccupied porphyrin orbitals, the lower energy orbital was localised on the core and the *meso*-substituents in the x-axis, while the higher energy orbital was distributed across the core and y-axis substituents. The major difference between the three porphyrins was the unoccupied orbital associated with the anchor. For **10** and **11,** this was the LUMO+2 which was higher in energy for the phosphonate than the carboxylic acid, but for **12** this orbital was lower in energy than the porphyrin orbitals and was the LUMO. For **10** and **11** this orbital had electron density on the triazole, thus the anchor and porphyrin are coupled. However, for **12**, there was no electron density on the triazole in the LUMO, therefore the anchor and porphyrin are seemingly decoupled.

TDDFT was used to compare the experimentally obtained absorption spectra and the calculated electronic transitions. The calculated energies are summarised in Table 6.7 and these transitions, overlaid with the experimental UV-visible absorption spectra, are shown in Figure 6.46 - Figure 6.48.

There was a reasonable agreement between the calculated and experimental absorption spectra (Figure 6.46 - Figure 6.48), with lower intensity transitions calculated at lower energy (corresponding to the Q-bands) and higher intensity transitions at higher energy (the Soret band). In each case, the calculated Q-band transitions were predominantly from HOMO to LUMO (or LUMO+1, the lowest porphyrin orbital, for **12**) and HOMO to LUMO+1 (+2 for **12**) transitions. The Soret band transitions were primarily due to excitations to the higher energy porphyrin orbitals. This agrees with the theory that the Soret band is from S_0-S_2 transitions and the Q-bands from S_0-S_1. For **10** and **12**, the orbital localised on the anchoring group was not involved with any of the excitations, but for **11**, there was a small charge-transfer contribution to the Soret band from a porphyrin to anchor transition.

Table 6.7. Select calculated singlet energy transitions for **10-12** determined by TDDFT (calculated using B3LYP/6-311G(d,p) in THF using the PCM) and the contributions from specific orbitals. *f* = caculated oscillator strength.

	Energy / eV (λ / nm)	*f*	Composition (contribution / %)
10	2.161 (574)	0.1052	H-1→L+1 (28), H→L (71)
	2.182 (568)	0.0501	H→L+1 (71)
	2.936 (422)	1.4149	H-1→L (48), H→L (5) H→L+1 (23)
	2.976 (416)	1.6117	H-1→L (14), H-1→L+1 (49) H→L+1 (7)
11	2.164 (573)	0.0987	H-1→L+1 (29), H→L (70)
	2.184 (568)	0.0495	H→L+1 (65)
	2.926 (424)	1.1138	H-1→L (23), H-1→L+1 (21), H→L+1 (12), H→L+2 (35)
	2.9560 (419)	1.6423	H-1→L (36), H→L (12), H→L+1 (18)
12	2.1895 (566)	0.0765	H-1→L+2 (31), H→L+1 (68)
	2.2069 (562)	0.0338	H→L+2 (63)
	2.9727 (417)	1.6556	H-1→L+1 (60), H→L+2 (35)
	2.9818 (416)	1.8212	H-1→L+2 (65)

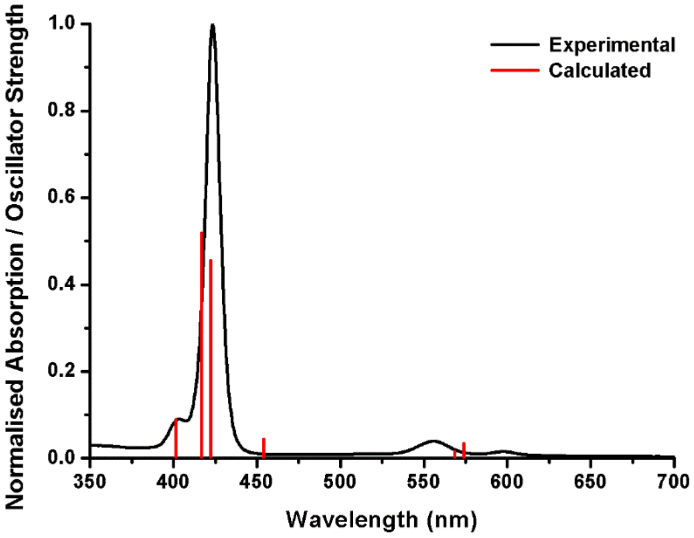

Figure 6.46. Experimental absorption spectrum and calculated principle energy transitions for **10** (in THF using B3LYP/6-311G(d,p) with solvation treated using the PCM).

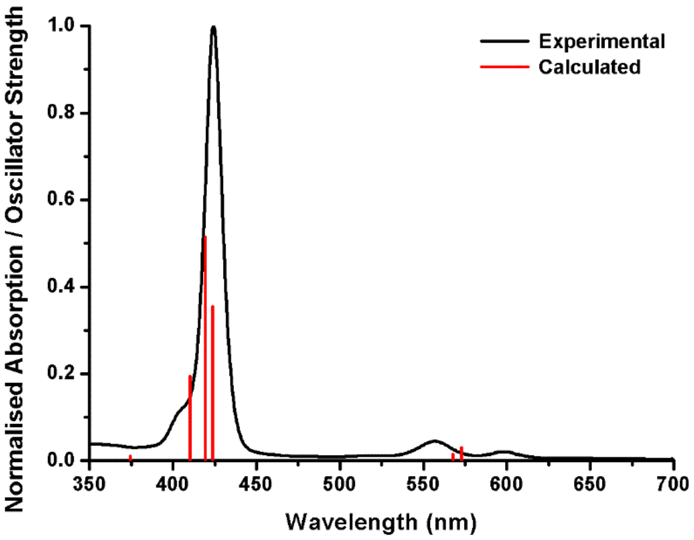

Figure 6.47. Experimental absorption spectrum and calculated principle energy transitions for **11** (in THF using B3LYP/6-311G(d,p) with solvation treated using the PCM).

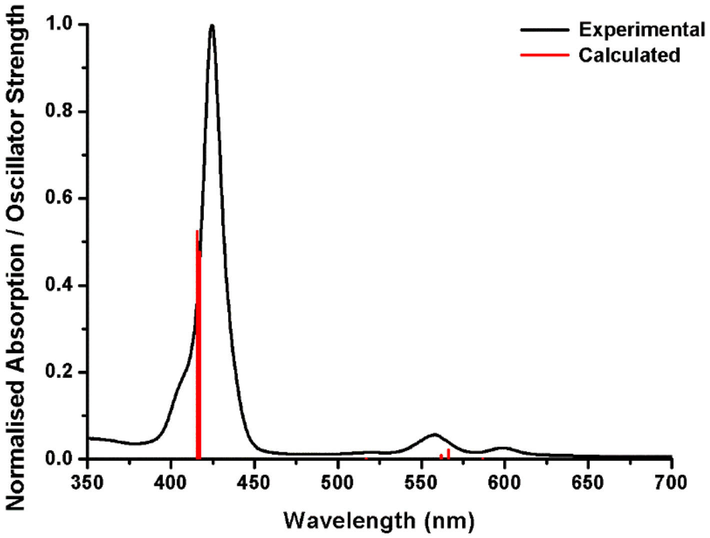

Figure 6.48. Experimental absorption spectrum and calculated principle energy transitions for **12** (in THF using B3LYP/6-311G(d,p) with solvation treated using the PCM).

6.2.6. Dye Adsorption Studies – Adsorption Isotherms

To investigate how the chemical structure of the different anchoring groups affects the dyes affinity to NiO, dye loading studies were performed (Figure 6.49). The concentration dependence on dye loading was investigated by measuring the equilibrium surface concentration from a range of initial dye bath concentrations (20 – 300 µM). Surface concentration at full monolayer coverage (Γ_{max}) and binding constants (K), as determined using the Langmuir adsorption isotherm model, are summarised in Table 6.8.

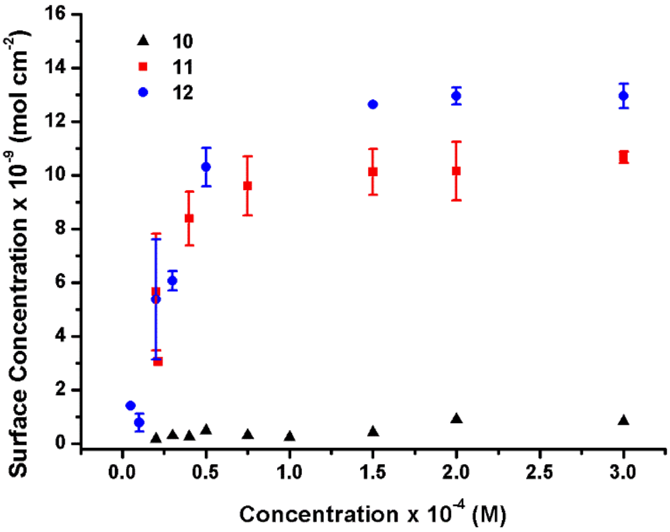

Figure 6.49. Equilibrium surface concentration of three-layer (1.5 µm thick) NiO films as a function of dye bath concentration (films immersed for 18 hours in a THF solution of the dye). The surface concentration was determined using the absorbance of the soret band (ca. 420 nm) at lower dye bath concentrations and the highest energy Q-band (ca. 550 nm) at higher concentrations.

Table 6.8. Binding constants (K_L) and surface concentration at full monolayer coverage (Γ_{max}) as determined using the Langmuir adsorption isotherm model (Non-linear fitting, equation 6.7). Data is reported as an average value with standard errors in parenthesis.

	10	**11**	**12**
K_L (M^{-1})	-[a]	6.65×10^4 (5.35×10^3)	2.81×10^4 (8.04×10^3)
Γ_{max} (mol cm^{-2})[b]	8.41×10^{-10} (7.65×10^{-12})	1.07×10^{-8} (2.16×10^{-10})	1.30×10^{-8} (4.47×10^{-10})

[a] Could not be fit to the Langmuir model. [b] Γ_{max} reported as the surface concentration from adsorption with a dye bath concentration of 300 µM.

The equilibrium surface concentration was calculated using the modified Beer-Lambert law (Equation 6.1),[59] which assumes that dye-NiO interactions do not significantly modify the absorption coefficient determined from solution.

$$A(\lambda) = \Gamma_{pro}\sigma(\lambda)$$

Equation 6.1.

$$\sigma(\lambda) = \varepsilon(\lambda) \times 1000\, cm^3/dm^3$$

Equation 6.2.

Where: A(λ) is the absorbance of the film, Γ_{pro} is the number of moles of dye per square centimetre of projected surface area (mol cm^{-2}), σ(λ) is the absorption cross section (cm^2 mol^{-1}) and ε(λ) is the molar extinction coefficient for the dye in solution (M^{-1} cm^{-1}).

For **11** and **12** the dye loading depended on the concentration of the dye bath, with the absorption of the film (and corresponding surface concentration) increasing as the dye bath concentration increased (Figure 6.49). The surface concentration reached a plateau between 75 and 150 µM. Giovannetti *et al.*[60] observed changes in the shape of the Q-bands at higher dye bath concentrations, for the adsorption of a porphyrin onto TiO_2, indicating aggregation is occurring. Here, there was no change to the shape of the absorption spectra upon increasing dye bath concentration. This suggests there was little interaction between the adsorbed dye molecules and that only a monolayer had formed. The dye loading was higher for **12** (1.30×10^{-8} mol cm^{-2}) than **11** (1.07×10^{-8} mol cm^{-2}), possibly due to the larger footprint of the phosphonate than the coumarin. There was a much lower dye loading for **10** than **11** or **12**, which was surprising as there were only small steric differences between the three dyes (with **10** being the smallest). As carboxylic acids are so prevalent in the literature, it is intriguing that **10** had the lowest dye loading. It is possible that there were alternative anchoring modes competing with the acid for **10**, which were not present for **11** and **12**.

For **11** and **12**, the equilibrium data could be analysed using isotherm models, but for **10**, the film absorbances were comparatively much lower at each dye bath concentration studied (Figure 6.50). The low dye uptake and high error associated with the measurements performed at lower dye bath concentrations made accurate analysis of the data impossible. All further thermodynamic/kinetic analysis of the adsorption process has been carried out for just **11** and **12**.

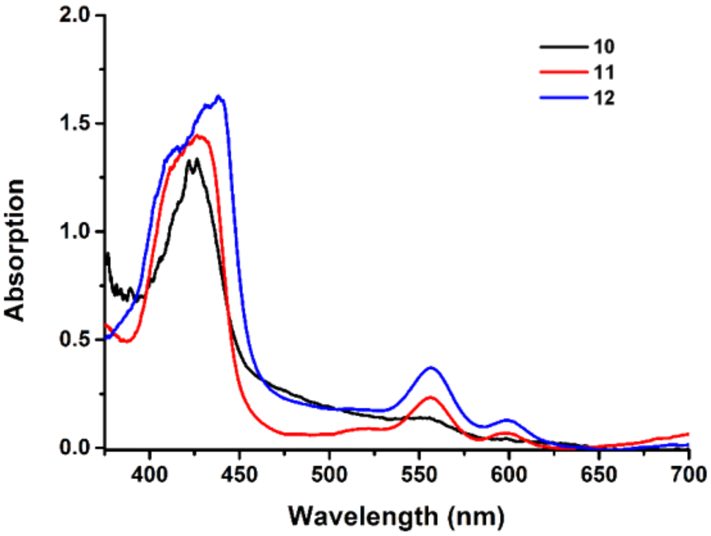

Figure 6.50. UV-visible absorption spectra of **10-12** adsorbed onto NiO (18 hours adsorption from a 300 µM THF dye bath).

The equilibrium data for **11** and **12** have been analysed using the Freundlich (Equation 6.3) and Langmuir (Equations 6.4 and 6.5) isotherms.

$$Q_e = K_F {C_e}^{1/n}$$

Equation 6.3.

$$Q_e = \frac{(K_L C_e)}{(1 + a_L C_e)}$$

Equation 6.4.

$$Q_e = \frac{(Q_0 a_L C_e)}{(1 + a_L C_e)}$$

Equation 6.5.

Where Q_e is the amount of dye adsorbed onto NiO at equilibrium, K_F and n are the Freundlich constants (that represent adsorption capacity and intensity respectively), C_e is the concentration of the dye bath, K_L and a_L are the Langmuir constants (that represent adsorption capacity and energy of adsorption respectively) and Q_0 is the theoretical saturation capacity of the NiO monolayer.[61]

These equations can be linearised as follows:

$$lnQ_e = lnK_F + \left(\frac{1}{n}\right) lnC_e$$

Equation 6.6.

$$\frac{C_e}{Q_e} = \left(\frac{1}{K_L}\right) + \left(\frac{a_L}{K_L}\right) C_e$$

Equation 6.7.

$$\frac{C_e}{Q_e} = \left(\frac{1}{Q_0 a_L}\right) + \left(\frac{1}{Q_0}\right) C_e$$

Equation 6.8.

To evaluate which model would be more suitable in describing the equilibrium data, it was initially fit to the linear forms of the Freundlich (Equation 6.6) and Langmuir (Equation 6.7) isotherms. The fitting parameters are summarised in Table 6.9 and the linear fits are shown in Figure 6.51 - Figure 6.54.

Table 6.9. Fitting parameters for the linear forms of the Freundlich (Equation 6.6) and Langmuir (Equation 6.7) adsorption isotherms of **11** and **12**.

Fitting		**11**	**12**
Langmuir (Equation 6.7)	K_L	7.44×10^{-4}	4.23×10^{-4}
	a_L	6.65×10^{4}	2.81×10^{4}
	Q_0 (mol cm^{-2})	1.12×10^{-8}	1.51×10^{-8}
	R^2	0.99943	0.98364
Freundlich (Equation 6.6)	K_F	1.05×10^{-7}	2.88×10^{-7}
	n	3.57	3.14
	R^2	0.64943	0.72953

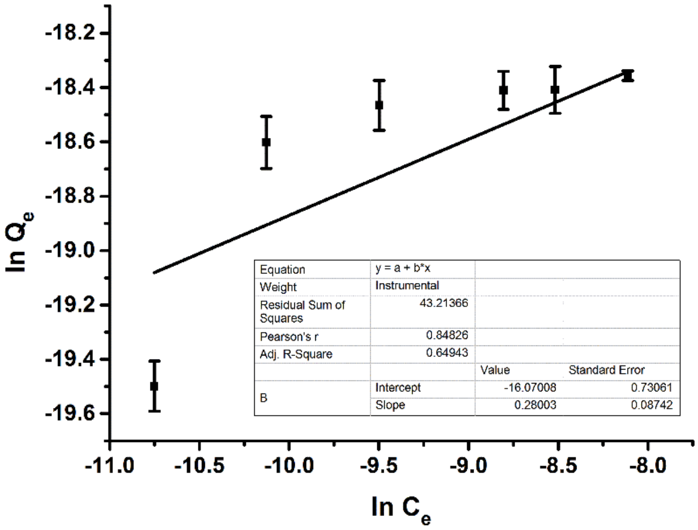

Equation	y = a + b*x		
Weight	Instrumental		
Residual Sum of Squares	43.21366		
Pearson's r	0.84826		
Adj. R-Square	0.64943		
		Value	Standard Error
B	Intercept	-16.07008	0.73061
	Slope	0.28003	0.08742

Figure 6.51. The adsorption data for **11** modelled by the linear form of the Freundlich isotherm (Equation 6.6).

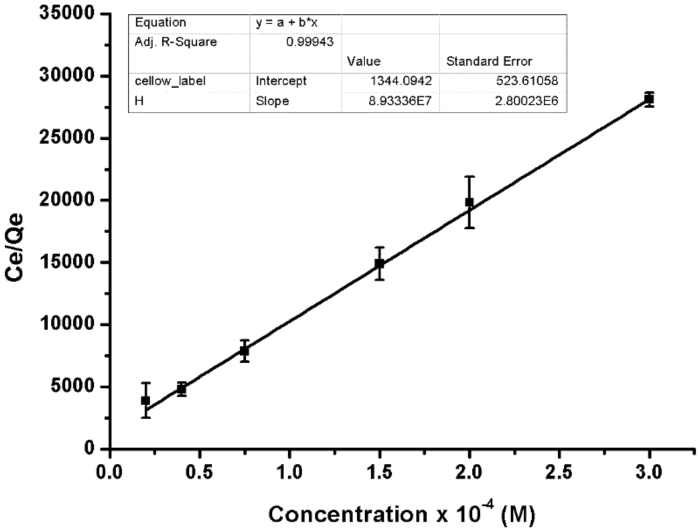

Equation	y = a + b*x		
Adj. R-Square	0.99943		
		Value	Standard Error
cellow_label	Intercept	1344.0942	523.61058
H	Slope	8.93336E7	2.80023E6

Figure 6.52. The adsorption data for **11** modelled by the linear form of the Langmuir isotherm (Equation 6.7).

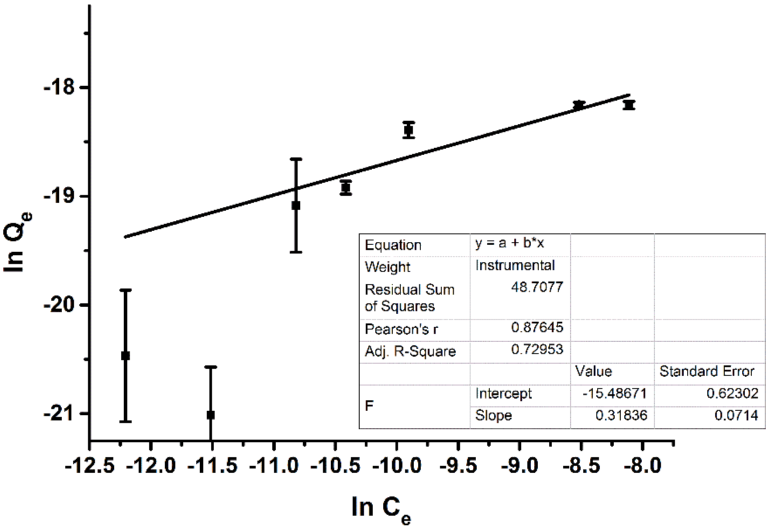

Figure 6.53. The adsorption data for **12** modelled by the linear form of the Freundlich isotherm (Equation 6.6).

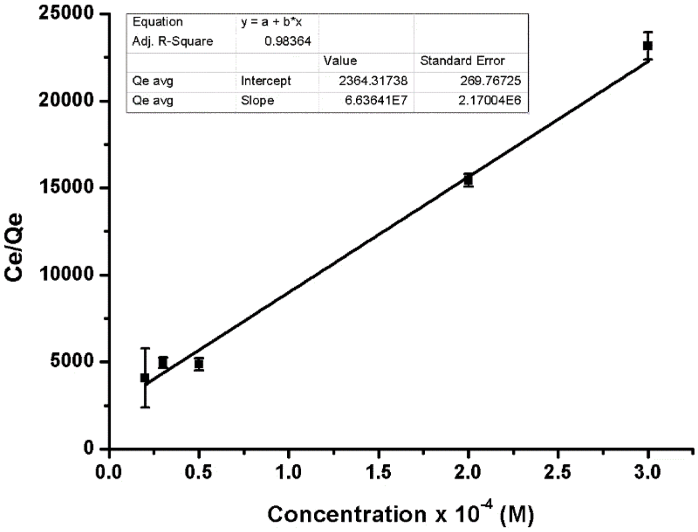

Figure 6.54. The adsorption data for **12** modelled by the linear form of the Langmuir isotherm (Equation 6.7).

As seen by the higher R^2 values, the data was more accurately modelled using the Langmuir isotherm. At high concentrations, a reasonable linear trend was seen for the Freundlich isotherm (Figure 6.51 and Figure 6.53), but this did not accurately model the lower dye bath concentrations. Comparatively, the Langmuir isotherm accurately described the adsorption process across the entire concentration range.

The Langmuir adsorption isotherm is one of the simplest models for the adsorption of molecules on a solid surface. It has been routinely used to describe dye adsorption onto semiconductor surfaces[3,60,62,63] and is based on four assumptions:

1. Only a monolayer of adsorbent forms on the solid surface.
2. All adsorption sites are uniform and equally accessible.
3. There is no interaction between adsorbed molecules.
4. All adsorption occurs through the same mechanism.

When fitting the non-linear data to a Langmuir isotherm, if Q_0 is experimentally known, then Equation 6.4 can be used. If a clear plateau has not been reached, then Equation 6.3 can be used and in this case the ratio of K_L/a_L gives Q_0. The equilibrium adsorption data for **11** and **12** was fit to both the linear and non-linear form of the Langmuir isotherm and the fitting parameters are summarised in Table 6.8.

Table 6.10. Fitting parameters for the Langmuir adsorption isotherms of **11** and **12** fit to the linear and non-linear equations. Data is fit to average values with instrumental weighting of experimental errors. Standard errors of the linear regression are reported in parenthesis.

Fitting		**11**	**12**
Linear (Equation 6.7)	K_L	7.44 x 10^{-4}	4.23 x 10^{-4}
	a_L	6.65 x 10^{4} (5.35 x 10^{3})	2.81 x 10^{4} (8.04 x 10^{3})
	Q_0 (mol cm^{-2})	1.12 x 10^{-8}	1.51 x 10^{-8}
	R^2	0.99943	0.98364
Non-linear 1 (Equation 6.4)	K_L	6.68 x 10^{-4} (8.61 x 10^{-5})	4.49 x 10^{-4} (9.07 x 10^{-5})
	a_L	5.90 x 10^{4} (8.90 x 10^{3})	3.02 x 10^{4} (7.80 x 10^{3})
	Q_0 (mol cm^{-2})	1.13 x 10^{-8}	1.49 x 10^{-8}
	R^2	0.95503	0.92199
Non-linear 2 (Equation 6.5) (Q_0 from linear fit)	a_L	6.81 x 10^{4} (4.20 x 10^{3})	2.61 x 10^{4} (3.06 x 10^{3})
	R^2	0.97382	0.95875
Non-linear 2 (Equation 6.5) (Q_0 from non-linear fit)	a_L	6.03 x 10^{4} (4.24 x 10^{3})	2.72 x 10^{4} (3.30 x 10^{3})
	R^2	0.95933	0.95691

As discussed previously, the linear form of the Langmuir isotherm (Equation 6.6) accurately describes the adsorption data (Figure 6.52 and Figure 6.54). The binding constant was determined to be 6.65 (± 0.5) x 10^4 M^{-1} and 2.81 (± 0.8) x 10^4 M^{-1} for **11** and **12** respectively. This indicates that the phosphonate anchoring group has a higher affinity for NiO than the coumarin anchor. The binding constant for **11** is larger than for the phosphonate-anchored ruthenium trisbipyridine complex studied by Odobel *et al.*[3] (**6.2**, Figure 6.1, K = 1.7 x 10^4 M^{-1}). In the same report, a larger binding constant of 1.8 x 10^5 M^{-1} was calculated for the ruthenium complex anchored using carboxylic acid groups (**6.1**). Wu *et al.*[64] studied the adsorption behaviour of **P1** onto NiO and reported a binding constant of 3.54 (± 0.16) x 10^5 M^{-1}. As the two reported binding constants for dyes containing carboxylic anchoring groups are on the order of 10^5 M^{-1}, it is surprising that the binding of **10** was so poor. It is possible that **10** was instead binding through the triazole instead of the acid. This could explain the lower dye loading compared to **11** and **12**, because anchoring through the triazole could cause the porphyrin to lie flat onto the NiO surface, reducing the amount of dye that would be able to adsorb.

The adsorption data was also fit using the non-linear forms of the Langmuir isotherm (Equation 6.4 and Equation 6.5). Using Equation 6.5 and substituting the surface concentration at 300 µM (approximated as Γ_{max}) as Q_0 did not accurately model the data (R^2 ca. 0.8, data not shown). This suggests that the theoretical saturation capacity was not reached at the higher dye bath concentrations. Modelling the data using Equation 6.4 was more accurate (Figure 6.55 and Figure 6.56), with reasonable fits to the isotherm and values of a_L and Q_0 in agreement with the linear form. The data was also accurately modelled using Equation 6.5, where the value of Q_0 was used as determined from the linear and non-linear fits. The binding constants, as determined from the various methods, were in the range of 6.03 - 6.81 x 10^4 M^{-1} and 2.61 – 3.02 x 10^4 M^{-1} for **11** and **12** respectively, with the values agreeing within error.

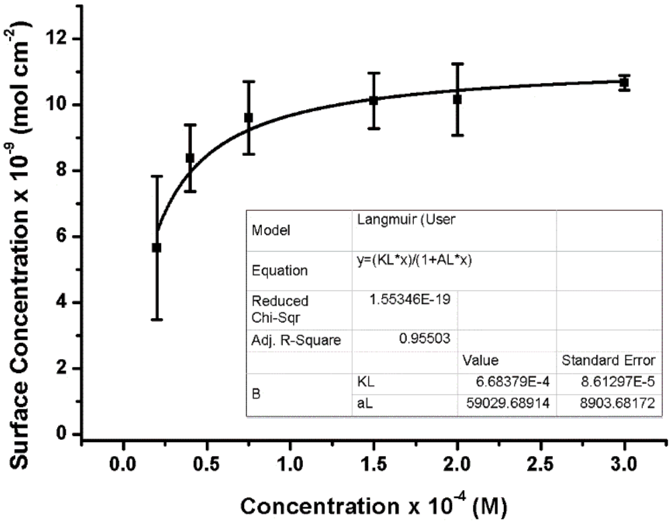

Model	Langmuir (User		
Equation	y=(KL*x)/(1+AL*x)		
Reduced Chi-Sqr	1.55346E-19		
Adj. R-Square	0.95503		
		Value	Standard Error
B	KL	6.68379E-4	8.61297E-5
	aL	59029.68914	8903.68172

Figure 6.55. The adsorption data for **11** modelled by the non-linear form of the Langmuir isotherm (Equation 6.4).

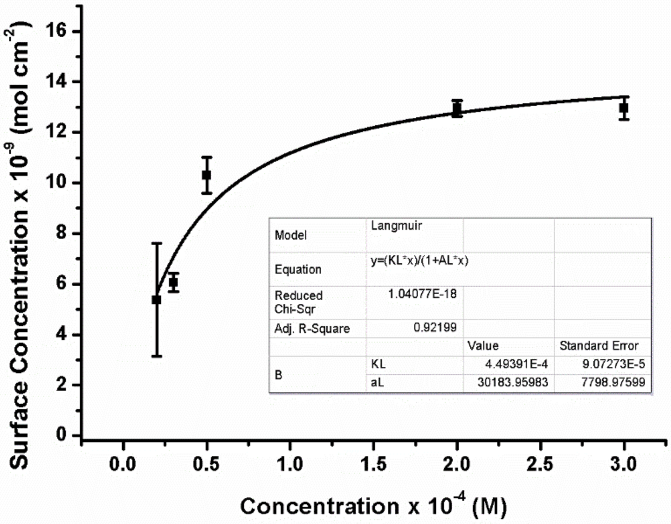

Model	Langmuir		
Equation	y=(KL*x)/(1+AL*x)		
Reduced Chi-Sqr	1.04077E-18		
Adj. R-Square	0.92199		
		Value	Standard Error
B	KL	4.49391E-4	9.07273E-5
	aL	30183.95983	7798.97599

Figure 6.56. The adsorption data for **12** modelled by the non-linear form of the Langmuir isotherm (Equation 6.4).

The surface area occupied by each dye molecule on NiO can be calculated using Q_0. BET analysis of F108 templated NiO gave a specific surface area of 40.6 (±0.8) m^2 g^{-1}.[65] The average weight of a NiO film with surface area of 0.196 cm^2 and thickness of 1.5 µm is 0.3 mg. Multiplying the BET surface area with the NiO mass gives a surface area of 121.8 cm^2 for each film. The surface area occupied by each dye molecule can be calculated by dividing the NiO surface area by Q_0 x Avogadro's number, which gives 1.81 and 1.34 nm^2 for **11** and **12** respectively. Dividing the average NiO crystal size (determined using pXRD and the Scherrer equation in the same study) of 20 nm by these values gives ratios of 11 and 13 dye molecules per NiO crystal, for **11** and **12** respectively.

6.2.7. Dye Adsorption Studies – Adsorption Kinetics

The Langmuir adsorption isotherms were used to describe the adsorption process in an equilibrium situation. Studying the kinetics of adsorption provides additional insight into this process. NiO films were immersed in a 300 µM solution of the dye (the same concentration used for the solar cell studies) and the surface concentration was determined at regular intervals from the film absorbance (using Equation 6.1). The evolution of surface concentration over time is provided in Figure 6.57 - Figure 6.58

and the kinetic parameters for dye uptake, fit to various kinetic models, are summarised in Table 6.11.

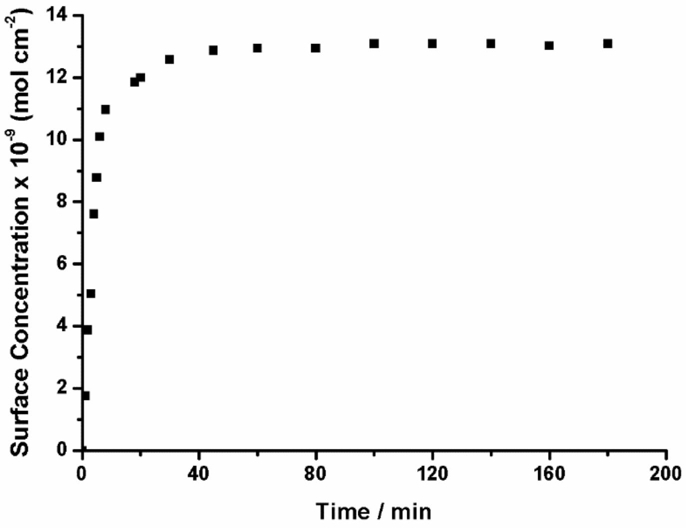

Figure 6.57. Surface concentration of a three-layer (1.5 µm thick) NiO film as a function of time (film immersed in a 300 µM THF solution of the dye) for **11**. The surface concentration was determined using the absorbance of the Soret band (ca. 420 nm) at lower surface concentrations and the highest energy Q-band (ca. 550 nm) at higher concentrations.

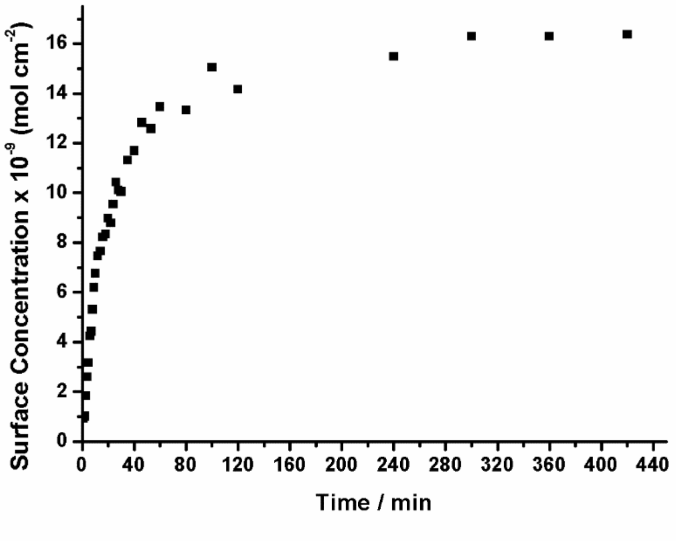

Figure 6.58. Surface concentration of a three-layer (1.5 µm thick) NiO films as a function of time (film immersed in a 300 µM THF solution of the dye) for **12**. The surface concentration was determined using the absorbance of the Soret band (ca. 420 nm) at lower surface concentrations and the highest energy Q-band (ca. 550 nm) at higher concentrations.

For the adsorption of both **11** and **12** onto NiO, there was an initial fast uptake of dye followed by a slower uptake, until a plateau is reached. For the uptake of **11** by NiO, the surface concentration reached 75% of the final saturated value in the first 10 minutes. A saturated surface concentration was then reached after 40 minutes. The uptake of **12** by NiO was much slower, with the surface concentration reaching 50% of the final value over 20 minutes in the initial fast uptake process. A saturated surface concentration was then reached after 280 minutes, which was seven times slower than for **11**.

The adsorption of a dye onto NiO can be represented by:

$$NiO + Dye \rightarrow NiO\colon Dye$$

Equation 6.9.

Where: NiO represents an adsorption site on NiO and NiO:Dye represents a dye molecule adsorbed onto NiO.

The reaction rate (r) of Equation 6.9 can be represented by:

$$r = \frac{d[NiO\colon Dye]}{dt} = k[NiO]^n[Dye]^m$$

Equation 6.10.

Where: k is the reaction constant, n and m are reaction orders, [NiO:Dye] is the amount of adsorbed dye at a given time, [NiO] and [Dye] are the concentrations of free adsorption sites and dye respectively.

From the Langmuir isotherm (Figure 6.49) the highest dye loading was 1.30 x 10^{-8} mol cm^{-2} for **12**. The surface concentration can be converted to a volume concentration using Equation 6.11:

$$Vol.\ conc. = \frac{Surface\ conc.}{Film\ thickness}$$

Equation 6.11

The NiO films have an average thickness of 1.5 µm, therefore the maximum volume concentration of **12** was 8.66 x 10^{-5} mol cm^{-3}. These 1.5 µm thick films have a surface area of 0.196 cm^2, therefore the volume is 2.94 x 10^{-5} mol cm^{-3}. Taking the volume concentration as 8.66 x 10^{-5} mol cm^{-3}, the total amount of adsorbed dye is 2.55 x 10^{-9} mol. The adsorption kinetics have been measured using a 10 mL dye bath with a dye concentration of 300 µM, therefore the initial amount of dye is 3 x 10^{-6} mol and a decrease of 2.55 x 10^{-9} mol during the experiment is a change of 8.5 x 10^{-4} %.

As the change in dye concentration is negligible compared to the change in the number of adsorption sites, it can therefore be set as constant. Equation 6.10 can thus be dealt with as a pseudo rate law and rewritten as follows:

$$r = k'[NiO]^n$$

Equation 6.12.

The kinetics have been analysed using pseudo-first and second-order kinetics. The pseudo-first-order rate equation is provided by:

$$\frac{dq}{dt} = k_1(q_e - q)$$

Equation 6.13.

Where q_e is the amount of dye adsorbed at equilibrium conditions, q is the amount of dye adsorbed at a given time and k_1 is the first-order rate constant. This equation can be integrated to give:

$$ln\left(\frac{q_e - q}{q_e}\right) = -k_1 t$$

Equation 6.14.

The pseudo-second-order rate law can be expressed as:

$$\frac{dq}{dt} = k_2(q_e - q)^2$$

Equation 6.15.

Where k_2 is the second-order rate constant. This can be integrated to give the following:

$$\frac{1}{(q_e - q)} = \frac{1}{q_e} + k_2 t$$

Equation 6.16.

Which can then be rearranged to obtain a linear form:

$$\frac{t}{q} = \frac{1}{k_2 q_e^2} + \frac{1}{q_e} t$$

Equation 6.17.

Additionally, the initial adsorption rate (h) can be defined as:

$$h = k_2 q_e^2$$

Equation 6.18.

The adsorption kinetics for the uptake of **11** and **12** onto NiO have been modelled using these pseudo-first and second-order rate equations (Figure 6.59 - Figure 6.62) and the fitting parameters are summarised in Table 6.11.

Table 6.11. Kinetic parameters for the uptake of **11** and **12** onto NiO modelled using pseudo-first and second-order kinetic models. Values are reported with standard errors from the linear regression in parenthesis.

		11	**12**
1st order	R^2	0.90403	0.92613
	K (min^{-1})	0.075 (0.007)	0.403 (0.077)
2nd order	R^2	0.99946	0.99805
	K_2 (cm^2 mol^{-1} min^{-1})	2.46 x 10^7 (5.26 x 10^3)	2.97 x 10^6 (3.63 x 10^3)
	q_e (mol cm^{-2})	1.34 x 10^{-8} (2.37 x 10^{-6})	1.71 x 10^{-8} (2.15 x 10^{-6})
	h (mol cm^{-2} min^{-1})	4.39 x 10^{-9} (2.96 x 10^{-8})	8.68 x 10^{-10} (1.68 x 10^{-8})

Where K is the first order rate constant, K_2 is the second order rate constant, q_e is the amount of dye adsorbed at equilibrium conditions and h is the initial adsorption rate.

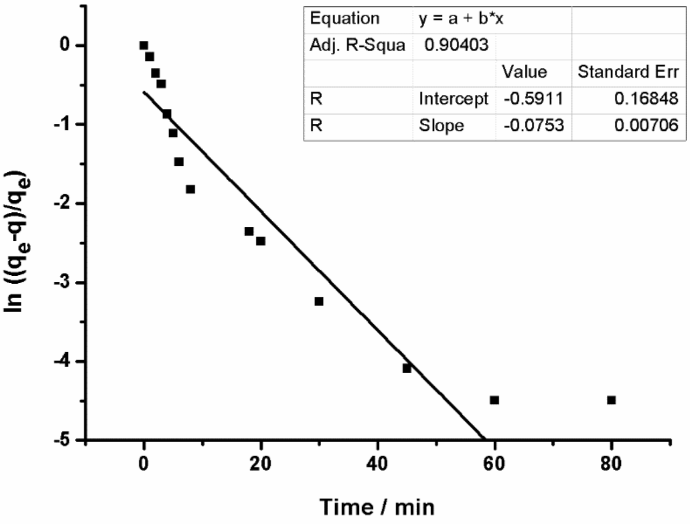

Figure 6.59. Kinetic data for the uptake of **11** onto NiO modelled using the pseudo-first-order rate equation (Equation 6.14).

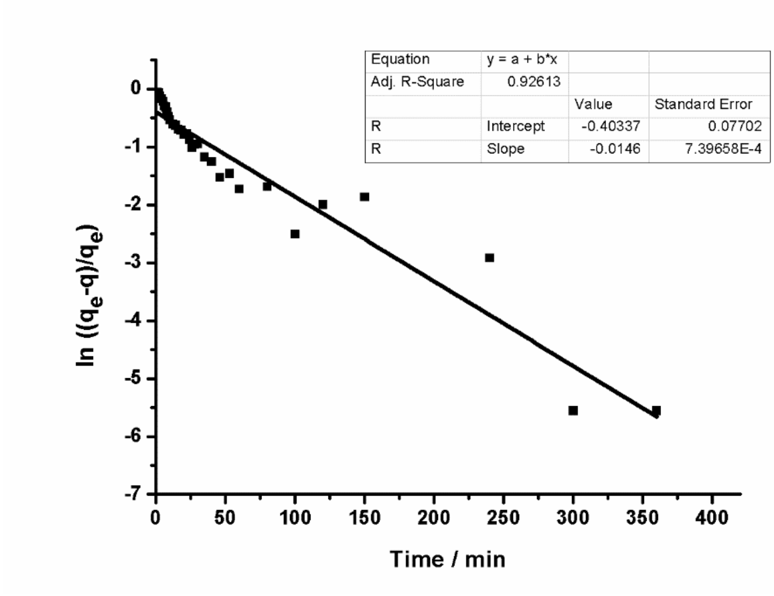

Figure 6.60. Kinetic data for the uptake of **12** onto NiO modelled using the pseudo-first-order rate equation (Equation 6.14).

A pseudo-first-order model has been previously used to model the uptake of **N719**[66] and a porphyrin[60] onto TiO_2 and the uptake of **P1** onto NiO.[65] However, in this case, the pseudo-first-order model did not accurately describe the kinetic data (Figure 6.59 and Figure 6.60). If the reaction does have a first order dependence on a reactant, then a plot of ln ((q_e-q)/q_e) vs. time should be linear. Two linear relationships can be seen here; an initial part with a larger gradient at shorter times (t < 10 min), then another at longer times with a lower gradient. The linear regressions were lower here than for the second-order model (R^2 = 0.904 - 0.926 vs 0.998 - 0.999).

The pseudo-second-order model has been used to describe the uptake of an azo dye[63] and catechol-thiophene sensitisers[67] onto TiO_2. This was successfully used to model the adsorption of **11** and **12** onto NiO (Figure 6.61 and Figure 6.62), as plots of t/q_e vs. time were linear, with high R^2 values. Pseudo-second-order rate constants of 2.46 x 10^7 and 2.97 x 10^6 cm^2 mol^{-1} min^{-1} were calculated for **11** and **12** respectively. This indicates that the phosphonate anchor has both a higher affinity for NiO (as determined by the Langmuir adsorption studies) and that the adsorption of the phosphonate occured with a higher rate. It has been suggested that a second-order kinetic process for dye adsorption indicates the rate-limiting step is a chemisorption process, where an adsorbate-adsorbent electron exchange takes place.[63,67]

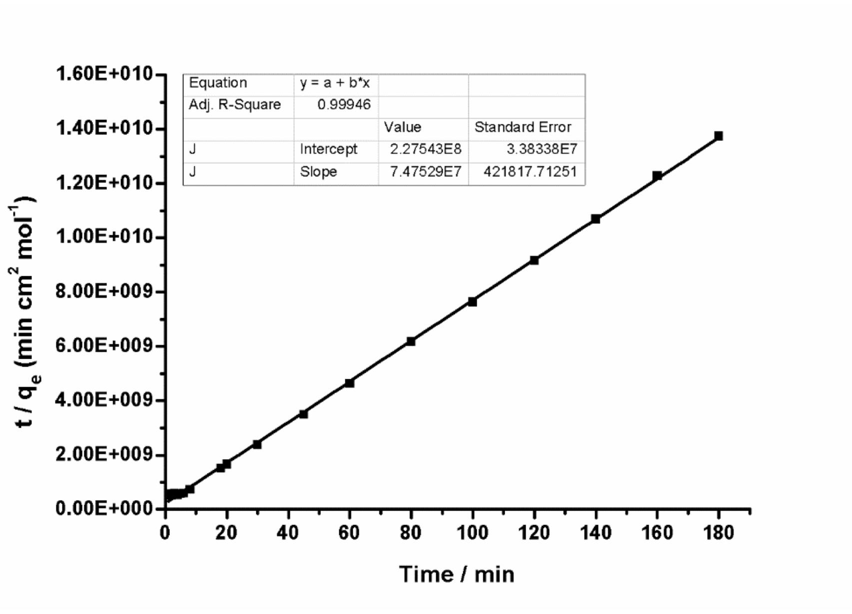

Figure 6.61. Kinetic data for the uptake of **11** onto NiO modelled using the pseudo-second-order rate equation (Equation 6.17).

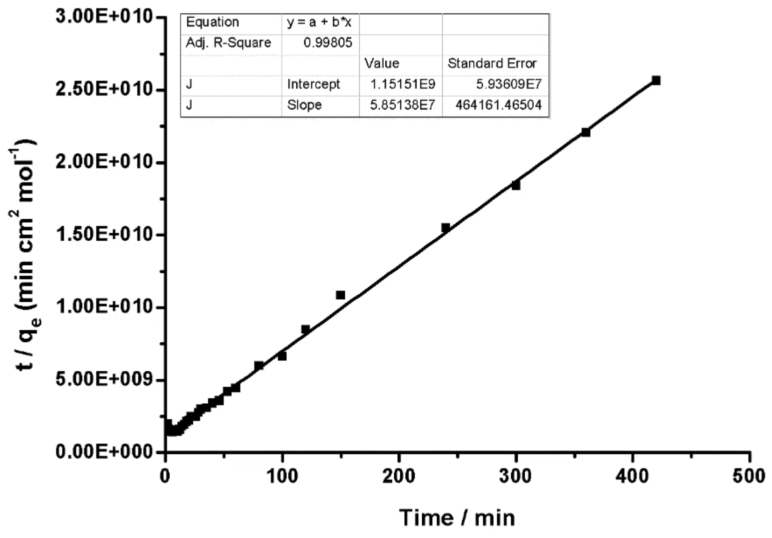

Figure 6.62. Kinetic data for the uptake of **12** onto NiO modelled using the pseudo-second-order rate equation (Equation 6.17).

6.2.8. Device Performances

Devices were constructed from **10-12** by soaking the 1.5 µm thick NiO films for 18 hours in a solution of the dye in THF (0.3 mM). The electrolyte used was 1 M LiI and 0.1 M I_2 in MeCN. The performances of the champion cells and representative standard deviations are summarised in Table 6.12 and compared to previously reported values for **ZnP$_{ref}$** (Figure 6.42)^{21} as a benchmark.

Table 6.12. Photovoltaic performance of champion p-DSCs constructed using **10-12**. Average performances and standard deviations as determined for 5 devices constructed from the same batch of cells for JSC, VOC, FF and η are provided in parenthesis.

	JSC / mA cm^{-2}	VOC / mV	FF	η / %	IPCE / % (λ / nm)
10	0.28 (0.26 ± 0.05)	57 (54 ± 3)	0.35 (0.32 ± 0.016)	0.006 ((4.8 ± 0.9) x 10^{-4})	5.4 (430), 1.0 (570), 0.6 (610)
11	0.45 (0.43 ± 0.02)	74 (72 ± 3)	0.35 (0.34 ± 0.014)	0.012 ((10.8 ± 0.7) x 10^{-3})	8.2 (430), 2.9 (570), 1.8 (610)
12	0.51 (0.51 ± 0.04)	76 (74 ± 6)	0.37 (0.36 ± 0.006)	0.014 ((13.0 ± 0.8) x 10^{-4})	9.8 (430), 3.5 (570), 2.2 (610)
ZnPref	0.19	98	0.35	0.006	-

JSC is the short-circuit current density at the $V = 0$ intercept, VOC is the open-circuit voltage at the $J = 0$ intercept, *FF* is the device fill factor, η is the power conversion efficiency; IPCE is the monochromatic incident photon-to-current conversion efficiency.

The J-V curves for the champion devices were measured under illumination (Figure 6.63) and in the dark (Figure 6.64). Only modest performances were achieved for any of the dyes, with the highest VOC and JSC (76 mV and 0.51 mA cm^{-2} respectively) obtained for **12**. The trend in both VOC and JSC followed the order of **12** > **11** > **10**, which was the same trend followed for dye loading and thus film absorbance. The trend in JSC is consistent with the differences in optical density, as the films with a higher absorbance will have an increased LHE and therefore produce a higher JSC. Examination of the J-V curves measured in the dark (Figure 6.64) shows that the dark current was higher for **10** than **11** or **12**, which were almost identical. This also helps to explain the trend in JSC, as net currents are equal to the photocurrent produced under illumination minus the dark current (see Equation 2.21). The dark currents are due to recombination between the redox electrolyte and NiO. As the dark currents have an inverse relationship with dye loading, it is likely that the reduced surface coverage of **10** did not protect the NiO surface from recombination to the same extent as **11** or **12**. The higher dark current for **10** leads to a lower VOC, as increased recombination causes the Fermi-level of NiO to be less positive (thereby reducing the energy gap between E_F-NiO and the redox potential of the electrolyte).

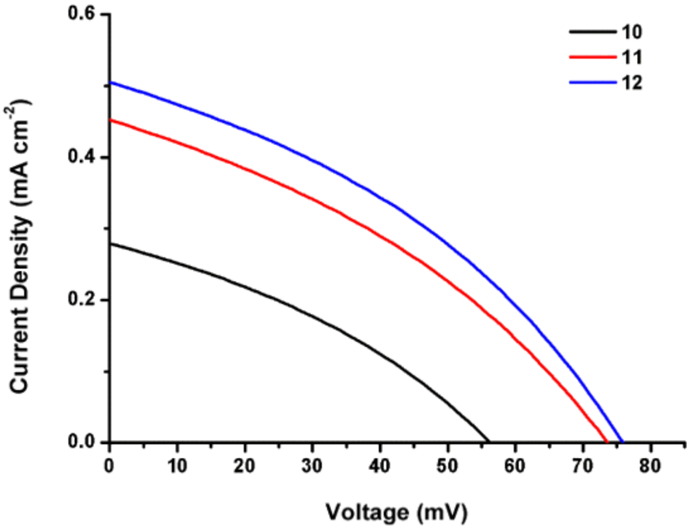

Figure 6.63. J-V curves of p-DSCs constructed using **10-12** measured under illumination (AM 1.5, 100 mW cm^{-2}).

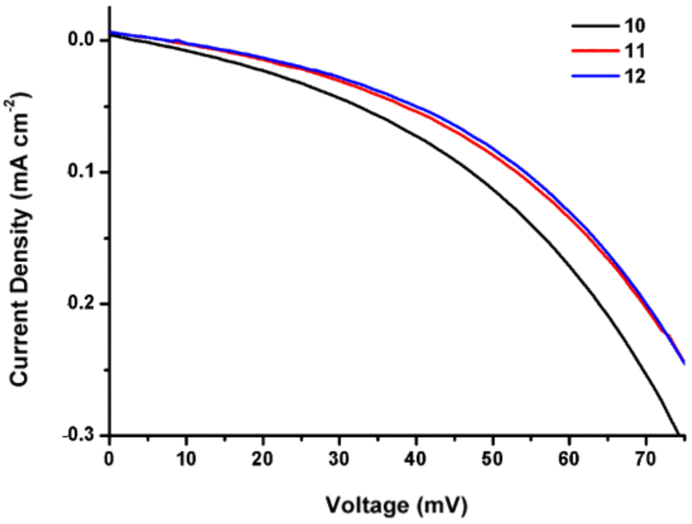

Figure 6.64. J-V curves of p-DSCs constructed using **10-12** measured in the dark.

The IPCE spectra of the highest-performing devices are shown in Figure 6.65. The IPCE at 430 nm, which corresponds to the porphyrin Soret band, is indicative of contributions to the photocurrent from dye excitation. This contribution is lowest for **10** and almost masked by the IPCE from the photolysis of triiodide. For **11** and **12**, the IPCE at 430 nm is higher (8.2 and 9.8% respectively) and contribution from the Q-bands can also be observed.

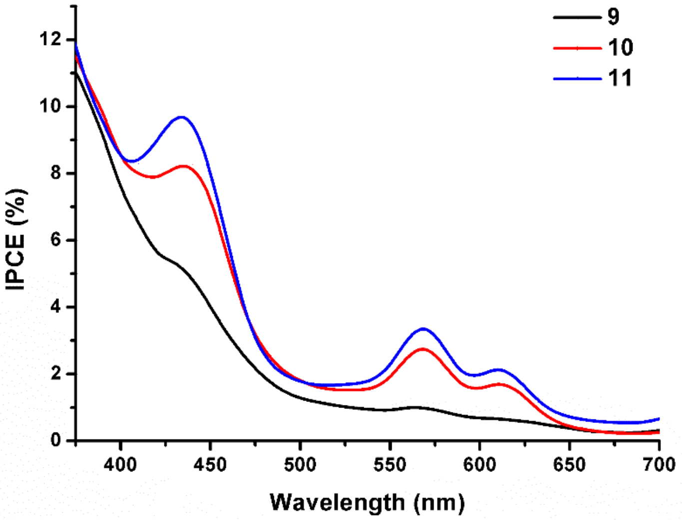

Figure 6.65. IPCE spectra of p-DSCs constructed using NiO films sensitised with **10-12** (0.3 mM in THF, 18 hours).

The devices were also analysed using small amplitude square wave modulated photovoltage (Figure 6.66 and Figure 6.68) and charge extraction (Figure 6.67)[68] experiments. From the charge extraction measurement (Figure 6.67), the V_{OC} at the same extracted charge density follows the trend **10** > **11** > **12**. This indicates a positive shift in the valence band position. Additionally, it appears that the charge lifetime of **10** is higher (Figure 6.66). These two factors would be expected to reduce the dark current and increase J_{SC}. However, care must be taken in comparing devices with different charge densities, as the amount of injected charge will effect $E_{F,NiO}$ (Equation 2.13).

Combining these measurements gives the charge lifetime as a function of extracted charge density (Figure 6.68), which corrects for any shifts in the valence band. For each dye, the charge lifetimes were longer at lower charge densities, as there was a lower concentration of holes in the NiO valence band to recombine with the electrolyte.

Charge lifetimes (at the same charge density) follows the trend of **12** > **11** > **10**, suggesting that the suppression of recombination, as dye coverage increases, leads to a higher J_{SC}.

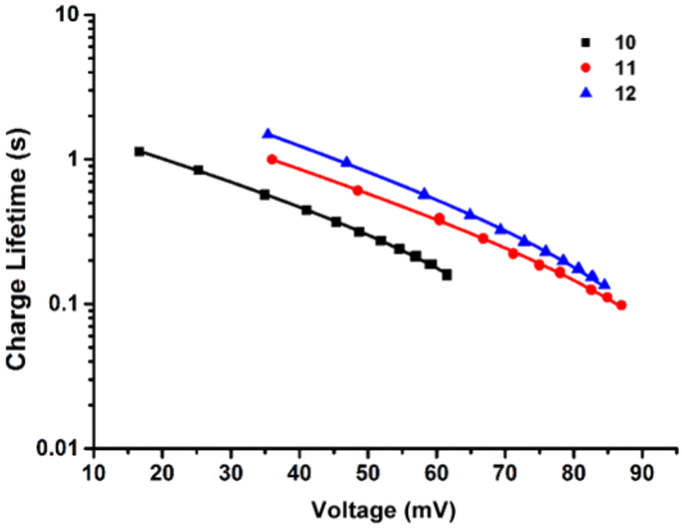

Figure 6.66. Charge lifetime as a function of photovoltage for p-DSCs constructed using **10**-**12**.

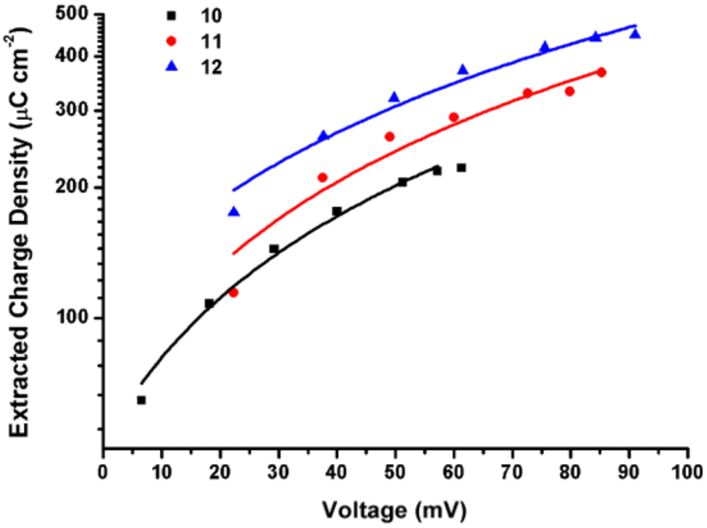

Figure 6.67. Extracted charge density as a function of photovoltage for p-DSCs constructed using **10**-**12**.

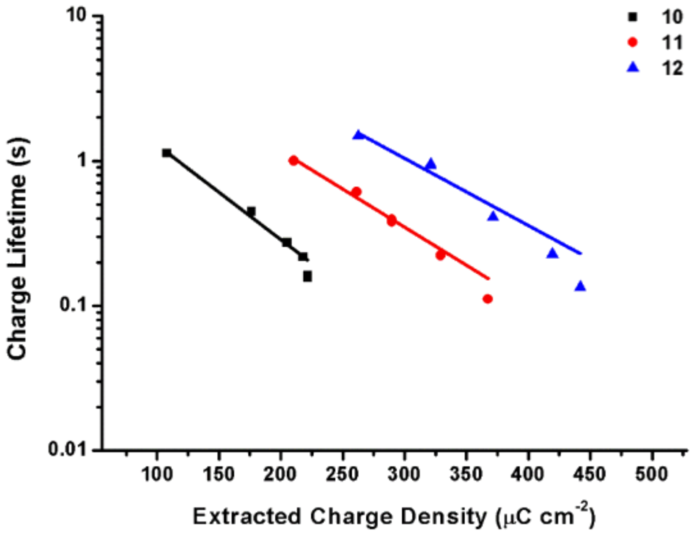

Figure 6.68. Charge lifetime as a function of extracted charge density for p-DSCs constructed using **10-12**.

While the performances of **10-12** were relatively low, these results are similar to previously reported p-DSCs that use porphyrins which do not contain a secondary electron acceptor. A close structural analogue that has been previously reported is **ZnP** (Figure 6.42) by Odobel *et al.*[21] and the photovoltaic properties are summarised in Table 6.12 alongside those for **10-12**. p-DSCs made using **ZnP** produced an efficiency of 0.006%, comparable to **10** and lower than **11** and **12**, with a lower J_{SC} (0.19 mA cm^{-2}) but a higher V_{OC} (98 mV). The same porphyrin core was synthesised with a secondary NDI electron acceptor (Figure 6.69), which performed more efficiently in p-DSCs (J_{SC} = 1.38 mA cm^{-2}, V_{OC} = 127 mV, FF = 32 %, η = 0.012 %). The authors attributed this increased performance to a longer-lived charge separated state with NDI present. Transient absorption experiments showed that recombination between NiO and the excited dye occurred on a 50-100 ps time scale for NiO/**ZnP**$_{\mathbf{ref}}$, whereas for NiO/**ZNP-NDI** most of the excited species had decayed on a < 2 ns time scale. They believe the longer lifetime for **ZNP-NDI** leads to more efficient regeneration of the excited dye by the redox electrolyte and a higher J_{SC}. The higher V_{OC} for **ZNP-NDI** can also be explained by reduced recombination, as fewer electrons in the NiO valence band will increase the energy gap between the NiO fermi-level and the redox potential of the electrolyte.

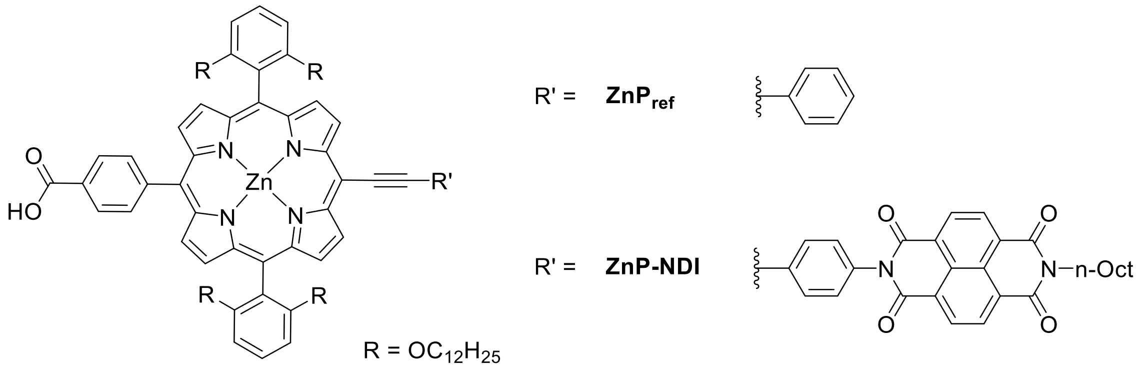

Figure 6.69. Chemical structure of **ZnP$_{ref}$** and **ZNP-NDI** synthesised and tested in p-DSCs by Odobel *et al.*[21,22]

Haining and co-workers tested NiO devices sensitised using zinc tetra(carboxyphenyl) porphyrin (**ZnTCPP**, Figure 6.70).[69] These devices performed modestly (J_{SC} = 0.5 mA cm^{-2}, V_{OC} = 120 mV, FF = 40 %, η = 0.02 %) and the authors postulated that the limiting factor was a fast hole recombination process. To try and overcome this limitation, they tested a supramolecular system with **ZnTCPP** coordinated to N-methyl-2-(4'-pyridyl)-3,4-fulleropyrrolidine (**C$_{60}$PPy**). This was inspired by previous reports of supramolecular interactions between porphyrins and C_{60} derivatives, which showed a fast porphyrin to C_{60} charge transfer process and a long lifetime for the reduced fullerene.[70,71] NiO films sensitised using **ZnTCPP/C$_{60}$PPy** performed more efficiently than the porphyrin alone (J_{SC} = 1.5 mA cm^{-2}, V_{OC} = 158 mV, FF = 38 %, η = 0.09 %). The authors attributed this increased performance to a suppression of recombination between the reduced dye and NiO. However, time-resolved experiments were not carried out to confirm an increase in charge-separated state lifetime.

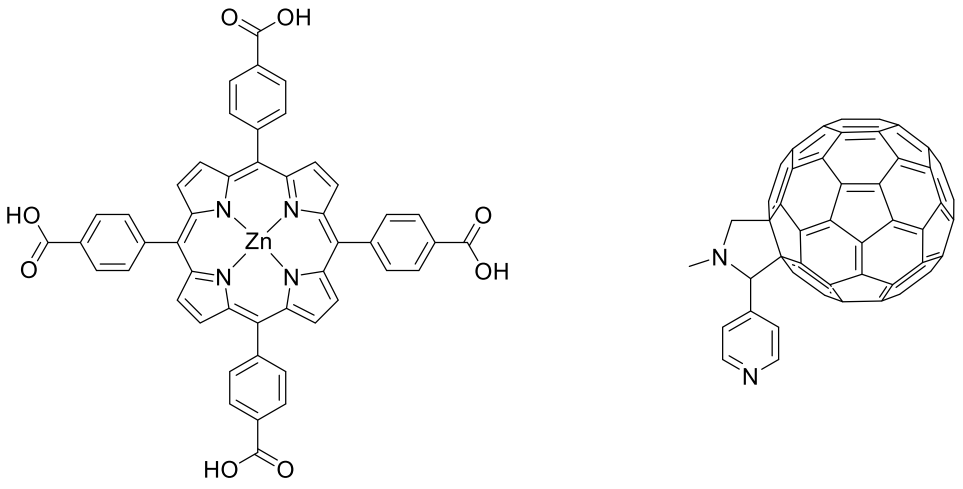

ZnTCPP **C_{60}PPy**

Figure 6.70. Chemical structure of **ZnTCPP** and **C_{60}PPy** synthesised and tested in p-DSCs by Haining *et al.*[69]

This supramolecular system was tested to try and improve the performances of **12** (Figure 6.71). **C_{60}PPy** was synthesised following a literature procedure[72] via the Prato reaction; 4-pyridinecarboxaldehyde and N-methylglycine were reacted with C_{60} in refluxing toluene to form the pyrrolidinofullerene. This was coordinated to the porphyrin through a sequential adsorption process, where the porphyrin was first adsorbed onto NiO and then the dyed film was immersed in a toluene solution of **C_{60}PPy** overnight. **C_{60}PPy** cannot be directly observed using UV-visible absorption spectroscopy, as the major absorption band is in the UV-region (λ_{max} = 310 nm) which overlaps with the absorption from FTO/NiO, while a less intense absorption (λ_{max} = 431 nm) overlaps with the porphyrin Soret band. However, a red-shift of the porphyrin Soret and Q-bands has been previously reported as evidence for the formation of supramolecular interactions between a porphyrin and C_{60} (Figure 6.72).[73] The photovoltaic performances of p-DSCs sensitised using **12** with and without the presence of **C_{60}PPy** are summarised in Table 6.13.

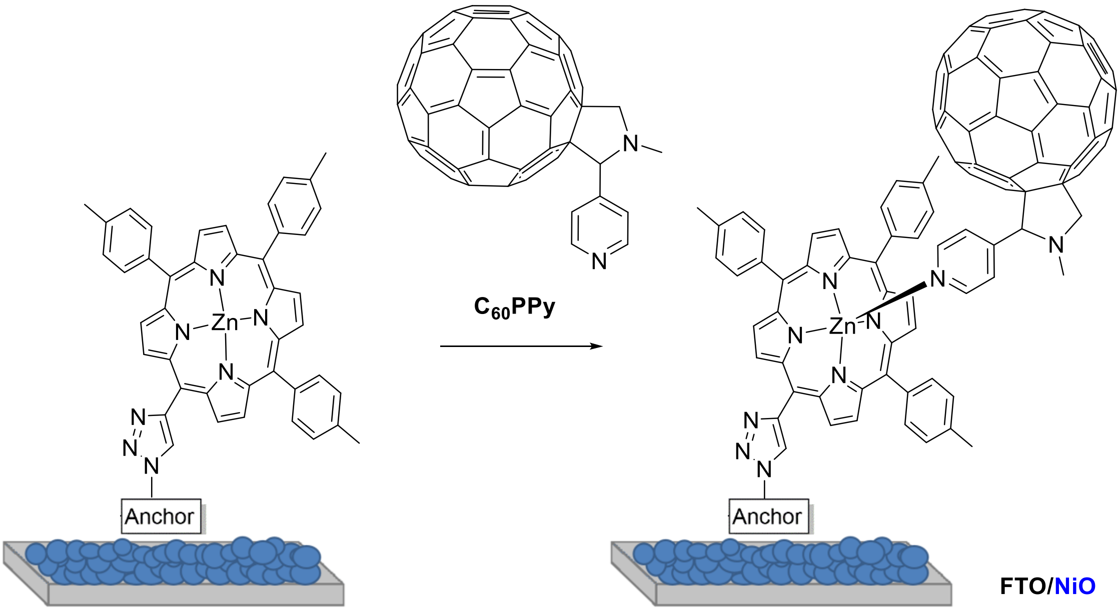

Figure 6.71. Schematic representation of the adsorbed supramolecular porphyrin-**C_{60}PPy** conjugate.

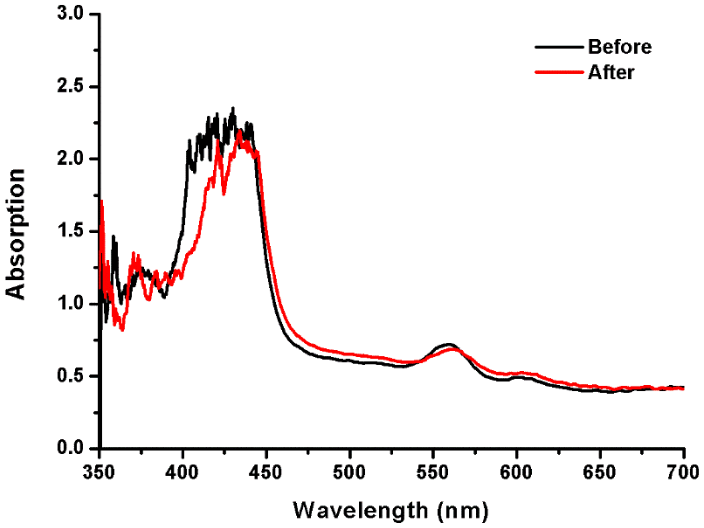

Figure 6.72. UV-visible absorption spectra of a 1.5 µm thick NiO film dyed with **12** before and after immersion in a dye bath of **C_{60}PPy** (0.3 mM in toluene, 16 hours).

Table 6.13. Photovoltaic performance of p-DSCs constructed using **12** with and without **C_{60}PPy**. Standard deviations as determined for 3 devices constructed from the same batch of cells for J_{SC}, V_{OC}, FF and η are provided in parenthesis.

	J_{SC} / mA cm^{-2}	V_{OC} / mV	FF	η / %
12	0.51 (0.51 ± 0.04)	76 (74 ± 6)	0.37 (0.36 ± 0.006)	0.014 ($(13.0 \pm 0.8) \times 10^{-4}$)
12/C_{60}PPy	0.42 (0.35 ± 0.08)	46 (45 ± 0.5)	0.32 (0.31 ± 0.007)	0.006 ($(5.0 \pm 1.2) \times 10^{-3}$)

J_{SC} is the short-circuit current density at the $V = 0$ intercept, V_{OC} is the open-circuit voltage at the $J = 0$ intercept, FF is the device fill factor, η is the power conversion efficiency.

The J-V curves measured under illumination are shown in Figure 6.73. While Haining and co-workers[69] observed improved performances for the supramolecular porphyrin-**C_{60}PPy** system, in this case, **12** performed worse when the fullerene was coordinated. There was a 0.09 mA cm^{-2} decrease in J_{SC} and a 30 mV decrease in V_{OC}, combined with a reduced fill factor for the optimum device. This produced an efficiency that was less than half the value of **12**-sensitised NiO alone. The J-V measurements performed in the dark (Figure 6.74) show a large increase in the dark current when **C_{60}PPy** is present. This suggests that the reduced V_{OC} is due to an increase in recombination, possibly as **C_{60}PPy** has introduced an additional recombination pathway. As pyridine rings can anchor to semiconductor surfaces,[5,74,75] it is possible that **C_{60}PPy** is both coordinated to the porphyrin and anchored to free binding sites on NiO. If this is the case, then the fullerenes anchored to the surface could intercept electrons from the reduced porphyrin and recombine with NiO, instead of being regenerated by the redox electrolyte, which could explain the decreased J_{SC}.

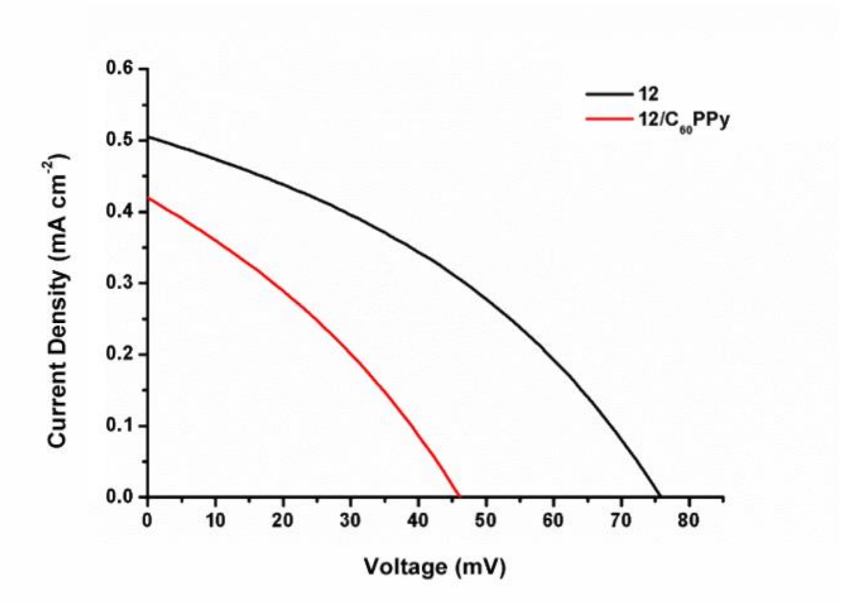

Figure 6.73. J-V curves of p-DSCs constructed using **12** with and without **C60PPy** measured under illumination (AM1.5, 100 mW cm^{-2}).

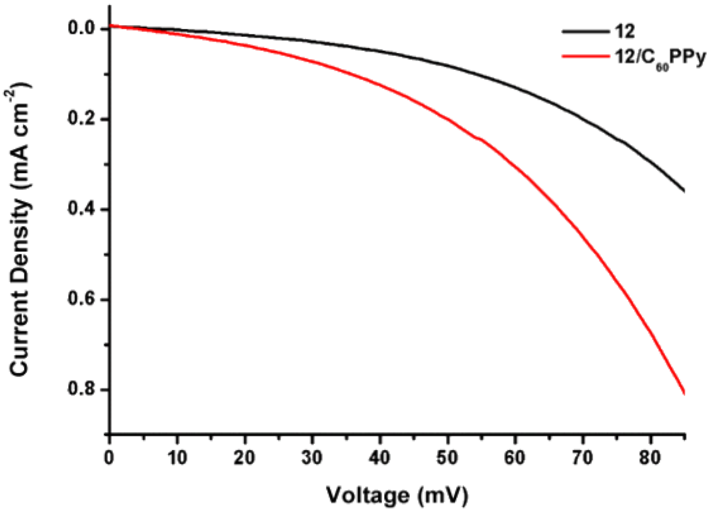

Figure 6.74. J-V curves of p-DSCs constructed using **12** with and without **C60PPy** measured in the dark.

The porphyrins developed in this chapter have only one anchoring group, but **ZnTCPP** contains four carboxylic acids capable of binding to NiO. Haining *et al.*[69] provided evidence, in the form of XPS and FTIR measurements, to indicate that the majority of **ZnTCPP** adsorbs to NiO ‘lying down’ in a flat orientation. This would effectively cover the NiO surface with porphyrin rings, blocking **C60PPy** from binding directly to the surface. As the porphyrin is only anchored through one group for **12**, it could possibly 'stand up' and point away from the surface, thereby leaving binding sites accessible to **C60PPy**. To try and replicate this concept of surface coverage, the **12**-sensitised NiO films were dyed overnight in an ethanolic solution of chenodeoxycholic acid (cheno, Figure 6.75) prior to coordination with **C_{60}PPy**. Cheno is routinely added to dye baths as a co-adsorbent to prevent dye aggregation as its carboxylic acid group allows efficient adsorption onto NiO. The smaller size of cheno compared to **12** could allow it to bind to sites that the larger porphyrin could not. The NiO films were sensitised in a sequential process; first with the porphyrin, then cheno and finally **C_{60}PPy**. The UV-visible absorption spectra of a NiO film after immersion in each solution is provided in Figure 6.76. There was a large reduction in the porphyrin film absorptivity after immersion in the cheno dye bath, indicating that cheno had displaced some of the porphyrin molecules. A red-shift of the Soret band was again seen after immersion in the solution of **C_{60}PPy**, which indicated the successful coordination of the fullerene to the porphyrin. The photovoltaic properties of p-DSCs constructed using **12**-sensitised NiO with and without treatment with cheno/**C_{60}PPy** are summarised in Table 6.14.

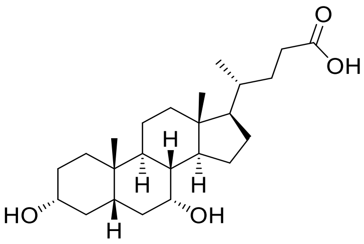

Figure 6.75. Chemical structure of chenodeoxycholic acid.

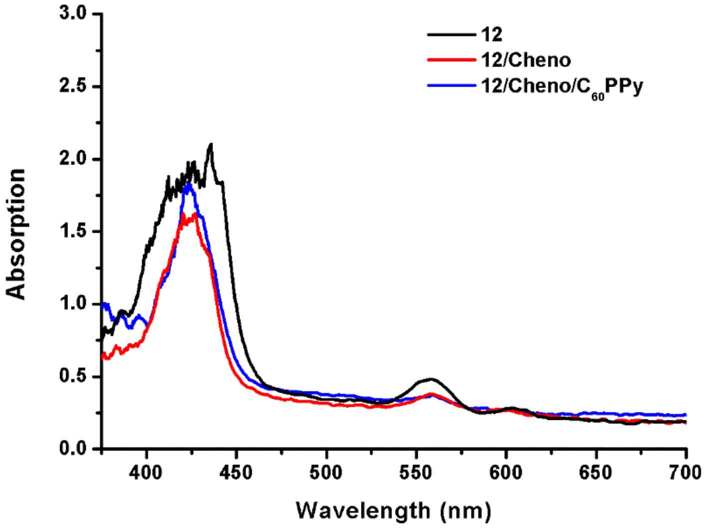

Figure 6.76. UV-visible absorption spectra of a 1.5 µm thick NiO film dyed with **12** before and after sequential immersion in a dye bath of cheno (ethanol, 0.3 mM, 16 hours) and then **C_{60}PPy** (toluene, 0.3 mM, 16 hours).

Table 6.14. Photovoltaic performance of p-DSCs constructed using **12** with and without cheno/**C_{60}PPy**. Standard deviations as determined for 5 devices constructed from the same batch of cells for J_{SC}, V_{OC}, FF and η are provided in parenthesis.

	J_{SC} / mA cm^{-2}	V_{OC} / mV	FF	η / %
12	0.51 (0.51 ± 0.04)	76 (74 ± 6)	0.37 (0.36 ± 0.006)	0.014 ((13.0 ± 0.8) x 10^{-4})
12/C_{60}PPy	0.42 (0.35 ± 0.08)	46 (45 ± 0.5)	0.32 (0.31 ± 0.007)	0.006 ((5.0 ± 1.2) x 10^{-3})
12/Cheno//C_{60}PPy	0.55 (0.51 ± 0.02)	80 (77 ± 4)	0.35 (0.34 ± 0.011)	0.015 ((1.3 ± 0.1) x 10^{-2})

J_{SC} is the short-circuit current density at the $V = 0$ intercept, V_{OC} is the open-circuit voltage at the $J = 0$ intercept, *FF* is the device fill factor, η is the power conversion efficiency.

The J-V curves measured under illumination are shown in Figure 6.77. Despite the reduction in film absorptivity after treatment with cheno (and corresponding reduction in LHE), devices made using the cheno/**C_{60}PPy** treated films slightly outperformed the untreated films. There was an increase in both J_{SC} and V_{OC} which, despite a reduced FF, gave a slightly higher efficiency. The J-V measurements performed in the dark (Figure 6.78) show a reduced dark current for **12**/cheno/**C_{60}PPy**. This suggests that the high dark current (and reduced J_{SC} and V_{OC}) for **12/C_{60}PPy** was due to **C_{60}PPy** anchored onto the NiO surface facilitating recombination. The reduced dark current for **12**/cheno/**C₆₀PPy** indicates that cheno effectively blocks the redox electrolyte from recombining with the NiO surface.

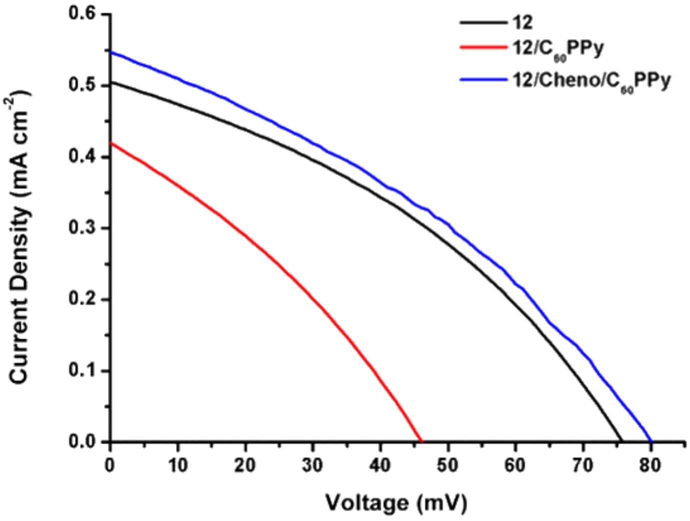

Figure 6.77. J-V curves of p-DSCs constructed using **12** with and without cheno/**C₆₀PPy** measured under illumination (AM 1.5, 100 mW cm^{-2}).

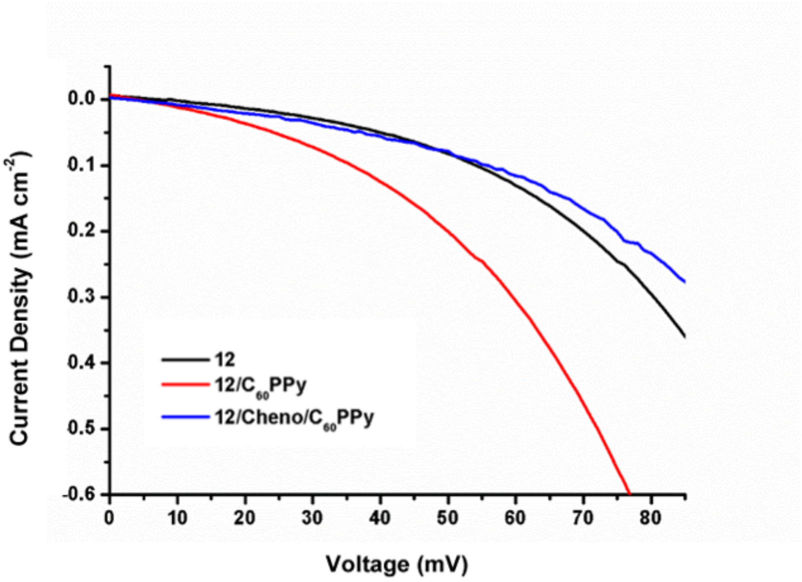

Figure 6.78. J-V curves of p-DSCs constructed using **12** with and without cheno/**C₆₀PPy** measured in the dark.

The IPCE spectra of the highest performing devices for **12** and **12**/cheno/**C$_{60}$PPy** are shown in Figure 6.79. In general, the IPCE profile was lower for **12/**cheno/**C$_{60}$PPy** than **12**, except for at the maximum absorption of the Soret band. This is to be expected, as the IPCE of a device is dependent on its LHE (see Equation 2.18) and the film absorption was reduced after treatment with cheno. The IPCE is the product of the LHE, the injection efficiency and the charge collection efficiency. For **12**/cheno/**C$_{60}$PPy** the LHE was lower and the injection efficiency was assumed to be similar for both systems, as the dye is the same for both. Therefore, one or both of the charge collection and regeneration efficiencies must be higher for the supramolecular system. The charge collection efficiency is dependent on the probability of the holes in NiO reaching the conducting substrate, rather than recombining with the electrolyte or the reduced dye. In comparison, the regeneration efficiency is determined by the competition between regeneration of the reduced dye by the redox mediator and recombination between the reduced dye and holes in NiO. It is possible that both factors have been improved in this system, as cheno is expected to reduce the electrolyte/NiO recombination and **C$_{60}$PPy** is expected to reduce the dye/NiO recombination by extending charge lifetimes.

Comparing the shape of the IPCE for both systems, the Soret band is more clearly pronounced for **12**/cheno/**C$_{60}$PPy** than **12** alone. For **12**/cheno/**C$_{60}$PPy** the IPCE between 330-400 nm, which is caused by the photolysis of triiodide,[76] is reduced. This was likely due to cheno blocking the electrolyte from reaching the NiO surface, thereby hindering electron transfer from NiO to the diiodide radical. Therefore, for **12**/cheno/**C$_{60}$PPy** the porphyrin provided a larger contribution to the photocurrent than in devices made using only **12**. As the LHE was lower for **12**/cheno/**C$_{60}$PPy**, but the IPCE are similar, the APCE will be higher (see Equation 2.19); the APCE at 440 nm = 10.03 % for **12** and 11.87 % for **12**/cheno/**C$_{60}$PPy.**

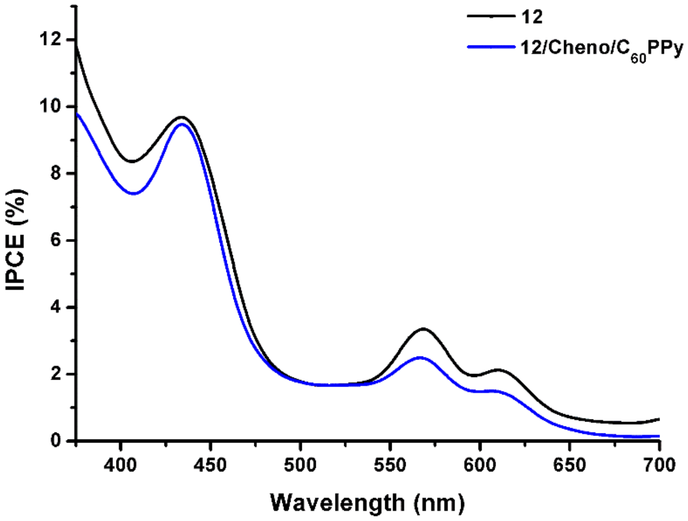

Figure 6.79. IPCE spectra of p-DSCs constructed using NiO films sensitised with **12** (THF, 0.3 mM, 18 hours) with and without the sequential adsorption of cheno (ethanol, 0.3 mM, 16 hours) and then **C_{60}PPy** (toluene, 0.3 mM, 16 hours).

Charge extraction measurements (Figure 6.80) show a higher extracted charge at the same photovoltage for the system without cheno/**C_{60}PPy**, suggesting reduced recombination. This contradicts the dark current measurements (Figure 6.78), where the current is lower for cheno/**C_{60}PPy**, suggesting a reduction in recombination. However, the dark current measurement is a combination of any shifts in $E_{VB,NiO}$ and $E_{F,NiO}$ and any reduction in recombination. Charge lifetime measurements (Figure 6.81) show that the lifetimes were mostly similar for both systems, which would suggest that recombination rates were similar. It is difficult to compare systems with different dye loadings, as different amounts of charge injection from NiO will affect the charge density within the NiO valence band. Therefore, it is necessary to compare the charge lifetimes as a function of charge density (Figure 6.82). Charge lifetimes were shorter for **12**/cheno/**C_{60}PPy** than **12** at the same charge density, which suggests there was more recombination for **12**/cheno/**C_{60}PPy**. As was seen for **12**/**C_{60}PPy** (Figure 6.74), it is possible that the presence of **C_{60}PPy** introduced a new recombination pathway that was not fully blocked by using cheno.

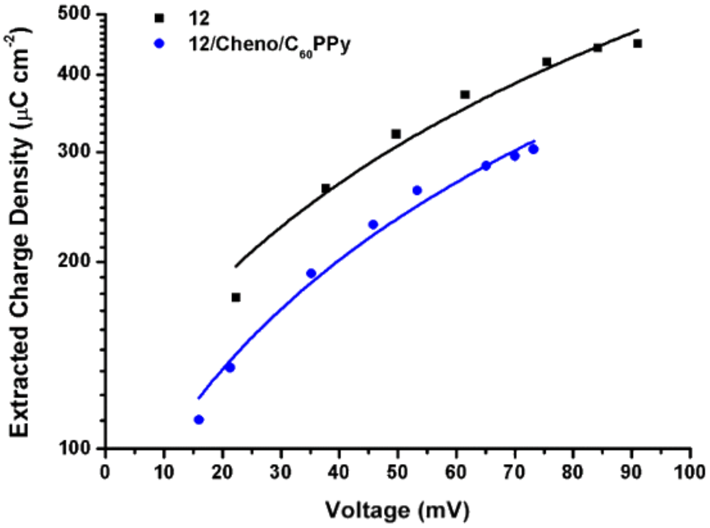

Figure 6.80. Extracted charge density as a function of photovoltage for p-DSCs constructed using **12** and **12**/cheno/**C_{60}PPy**.

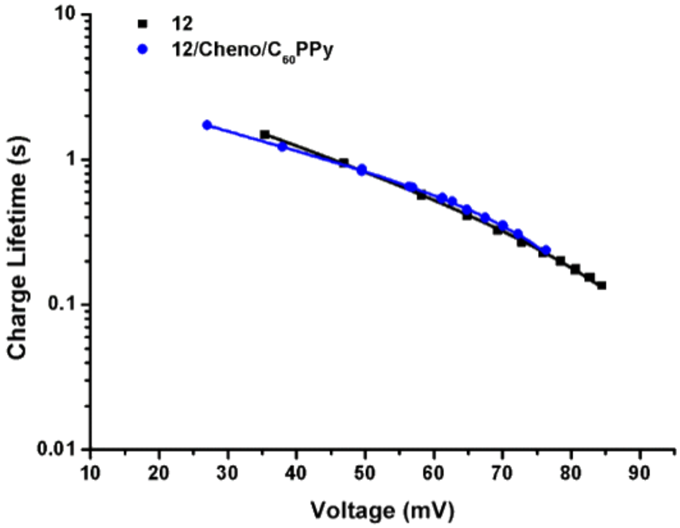

Figure 6.81. Charge lifetime as a function of photovoltage for p-DSCs constructed using **12** and **12**/cheno/**C_{60}PPy**.

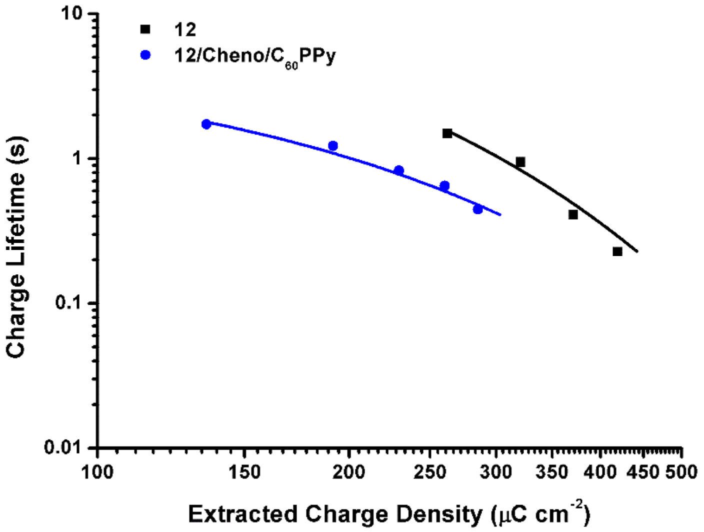

Figure 6.82. Charge lifetime as a function of extracted charge density for p-DSCs constructed using **12** and **12**/cheno/**C60PPy**.

While using **C60PPy** alone caused a reduction in p-DSC performances, the combination of cheno/**C60PPy** produced a small improvement, despite a reduction in film absorption. From the IPCE measurements (Figure 6.79), this improvement appears to be due to a higher APCE compensating for the reduced LHE. Further improvements can be imagined by optimising the porphyrin:cheno ratio, to block the surface sites not occupied by porphyrin molecules without displacing the dye. This would lead to a higher LHE, which coupled with the higher charge collection efficiency would improve the device IPCE/J_{SC}, leading to a higher PCE.

6.2.9. Conclusions

In this chapter, three novel porphyrins have been synthesised with varying anchoring groups, using ‘click’ methodology. The influence of the anchoring group on dye adsorption was studied using adsorption isotherms and kinetic measurements. The adsorption behaviour was modelled using the Langmuir isotherm model and binding constants of 6.65×10^4 and 2.81×10^4 M^{-1} were determined for **11** and **12** respectively. As the dye loading for the porphyrin containing a carboxylic acid was an order of magnitude lower, a binding constant could not be determined. For a 1.5 µm thick NiO film, dye loadings of 8.41×10^{-10} mol cm^{-2} (**10**), 1.07×10^{-8} mol cm^{-2} (**11**) and 1.30 x 10-

^{8} mol cm^{-2} (**12**) were determined. NMR studies suggest that **10** is zwitterionic and thus could be binding to NiO through the protonated triazole, which could explain the lower dye loading. For **11** and **12**, the adsorption kinetics were also studied and modelled using a pseudo-second order rate model. Rate constants of 2.46 x 10^{7} and 2.97 x 10^{6} cm^{2} mol^{-1} min^{-1} were determined for **11** and **12** respectively, which shows that adsorption occurs more rapidly for the anchor that has a higher affinity for NiO.

All three dyes were tested in p-DSCs and performed relatively poorly, but these results were comparable or higher to other porphyrins tested in the literature, which do not contain a secondary electron acceptor. IPCE measurements confirmed that excitation of the porphyrin was contributing toward the photocurrent for each device. p-DSC performances followed the trend of **12** > **11** > **10**, which has been attributed to higher dye loading increasing the LHE, thereby increasing the J_{SC}. In an attempt to improve the solar cell performances, a supramolecular system was tested, where the porphyrin was coordinated to a pyridyl-functionalised fullerene (**C_{60}PPy**). This was intended to extend charge lifetimes and therefore increase the J_{SC}. p-DSCs made using **12**/**C_{60}PPy** had a lower PCE, mainly due to a lower V_{OC}, which has been attributed to an increase in recombination when the fullerene is present. It was speculated that this was due to the fullerene anchoring directly to NiO and introducing an alternative recombination pathway. Cheno was used to block the free surface sites prior to the coordination of **C_{60}PPy**, to try and block this anchoring. After dying with cheno, there was a reduction in the film absorptivity due to porphyrin displacement. However, devices made using **12**/cheno/**C_{60}PPy** slightly outperformed **12** alone, which was due to an improved APCE. This has been tentatively attributed to an improvement in the charge collection and regeneration efficiencies, due to an increased charge lifetime when the fullerene is present.

While the devices constructed in this chapter performed somewhat poorly, the distinct spectroscopic properties of the porphyrins allowed a detailed investigation of the adsorption behaviour of various anchoring groups. In this chapter, synthetic routes have been developed to several azide-functionalised anchors, which were successfully linked to a chromophore via a CuAAC. This will aid the design of future dyes, as more efficient chromophores could be developed and linked to the different anchors.

6.3. Experimental

4-Azidobenzoic acid (6.13)

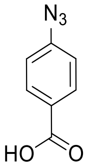

4-Aminobenzoic acid (200 mg, 1.45 mmol) was dissolved in a water/H_2SO_4 mixture (10 mL / 3 mL), cooled to 0 °C in an ice bath and maintained at this temperature, with stirring, for the duration of the reaction. A solution of sodium nitrite (106 mg, 1.54 mmol, 1.06 eqv.) in water (3 mL) was added in portions over 10 minutes and stirring was continued for an additional 20 minutes. A solution of sodium azide (120 mg, 1.85 mmol, 1.28 eqv.) in water (3 mL) was then added and the solution was stirred for 30 minutes. The white suspension was filtered, rinsed with water and dried under vacuum to give **6.13** as a white solid (189 mg, 80% yield).

^{1}H NMR (400 MHz, $CDCl_3$): δ 8.11 (d, *J* = 8.7 Hz, 2H), 7.11 (d, *J* = 8.7 Hz, 2H) ppm.

^{13}C NMR (101 MHz, $CDCl_3$): δ 170.41, 145.82, 132.21, 125.72, 119.10 ppm.

FTIR (neat, ATR): v = 3550 (br), 2668, 2104, 1677, 1601, 1577, 1507, 1425, 1282, 1176, 1118, 930, 856, 766, 689 cm^{-1}.

Synthesised via the following known method:

Z. H. Mohamed, N. A. El-Koussi, N. M. Mahfouz, D. F. Youssef, G. A. Abdel Jaleel and S. A. Shouman, *Eur. J. Med. Chem.*, 2015, **97**, 75-82

Diethyl (4-nitrophenyl)phosphonate (6.14)

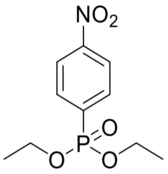

1-Bromo-4-nitrobenzene (500 mg, 2.48 mmol, 1 eqv.), KOAc (24 mg, 0.248 mmol, 0.1 eqv.), Pd(OAc)$_2$ (28 mg, 0.124 mmol, 5 mol %) and dppf (137 mg, 0.248 mmol, 0.1 eqv.) were loaded into a Schlenk tube and purged with 3 vacuum/nitrogen cycles. Diethyl phosphite (0.32 mL, 2.48 mmol, 1 eqv.), triethylamine (0.37 mL, 2.69 mmol, 1.09 eqv.) and anhydrous THF (10 mL) were added and the solution was heated to 68 °C for 4 hours. After cooling to room temperature, the solvent was evaporated under reduced pressure and purified using column chromatography (silica gel, 1:1 petroleum ether/ethyl acetate) to give **6.14** as a yellow oil (547 mg, 85% yield).

^{1}H NMR (300 MHz, CDCl$_3$): δ 8.30 (dd, *J* = 8.8, 3.3 Hz, 2H), 8.00 (dd, *J* = 12.7, 8.9 Hz, 2H), 4.24 – 3.98 (m, 4H), 1.34 (t, *J* = 7.1 Hz, 6H) ppm.

^{13}C NMR (75 MHz, CDCl$_3$): δ 150.28, 150.23, 133.03, 132.89, 123.47, 123.26, 62.84, 62.76, 16.39, 16.31 ppm.

Synthesised via the following known method:

M. Kalek, M. Jezowska and J. Stawinski, *Adv. Synth. Catal.*, 2009, **351**, 3207–3216.

Diethyl (4-aminophenyl)phosphonate (6.15)

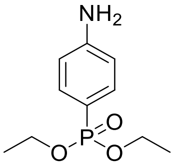

6.14 (540 mg, 2.08 mmol) and $SnCl_2.2H_2O$ (2.35 g, 10.4 mmol, 5 eqv.) were dissolved in EtOH (10 mL) and the solution was heated to reflux for 4 hours. After cooling to room temperature, the solution was neutralised using a saturated aqueous solution of $NaHCO_3$. The organic layer was extracted with DCM, washed with water (3 x 50 mL) then brine (2 x 50 mL) and dried over $MgSO_4$. The solvent was evaporated to give **6.15** as a light yellow solid (320 mg, 67% yield).

^{1}H NMR (400 MHz, $CDCl_3$): δ 7.58 (dd, *J* = 12.8, 8.5 Hz, 2H), 6.69 (dd, *J* = 8.5, 3.5 Hz, 2H), 4.13 – 3.96 (m, 4H), 1.30 (t, *J* = 7.1 Hz, 6H) ppm.

^{13}C NMR (101 MHz, $CDCl_3$): δ 150.14, 150.11, 133.72, 133.61, 114.34, 114.18, 61.76, 61.71, 16.37, 16.30 ppm.

FTIR (neat, ATR): v = 3433, 3344, 3230, 2983, 2904, 2361, 1641, 1601, 1514, 1212, 1130, 1020, 958, 773, 670, 547 cm^{-1}.

Known compound, synthesised here via a different method:

V. Penicaud, C. Maillet, P. Pascal, M. Pipelier and B. Bujoli, *Eur. J. Org. Chem.*, 1999, 7, 1745-1748

Diethyl (4-azidophenyl)phosphonate (6.16)

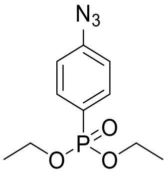

6.15 (310 mg, 1.35 mmol) was dissolved in acetic acid (9 M, 10 mL) and cooled to 0 °C in an ice bath. A saturated aqueous solution (1 mL) of sodium nitrite (140 mg, 2.03 mmol, 1.5 eqv.) was added and the mixture was stirred for 1 hour. A saturated aqueous solution (1 mL) of sodium azide (132 mg, 2.03 mmol, 1.5 eqv.) was added dropwise at 0 °C, then the solution was warmed to room temperature and stirred for an additional hour. The solution was diluted with water (20 mL), neutralised with the addition of $NaHCO_3$ then extracted with diethyl ether (100 mL). The organic layer was washed with water (3 x 30 mL) then brine (2 x 50 mL) and dried over $MgSO_4$. The solvent was carefully evaporated to give **6.16** a light orange oil (330 mg, 96% yield).

^{1}H NMR (400 MHz, $CDCl_3$): δ 7.79 (dd, *J* = 12.9, 8.7 Hz, 2H), 7.10 (dd, *J* = 8.7, 3.4 Hz, 2H), 4.18 – 4.05 (m, 4H), 1.32 (t, *J* = 7.1 Hz, 6H) ppm.

^{13}C NMR (101 MHz, $CDCl_3$): δ 144.50, 144.46, 133.91, 133.80, 133.79, 133.68, 119.38, 119.25, 119.22, 119.09, 62.48, 62.43, 62.36, 62.30, 16.64, 16.57, 16.51, 16.44 ppm.

FTIR (neat, ATR): ν = 2982, 2363, 2128, 2098, 1594, 1499, 1292, 1245, 1048, 1015, 958, 829, 792, 758, 704, 604, 538 cm^{-1}.

6-Nitro-coumarin-3-carboxylic acid (6.17)

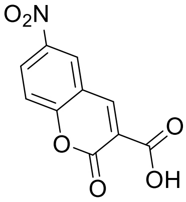

Coumarin-3-carboxylic acid (2.50 g, 13.125 mmol) was added, in portions over 10 minutes, to a mixture of sulfuric and nitric acid (4 mL, 1:1, v/v), which was cooled to 0 °C in an ice bath. The temperature was maintained for 1 hour and then the solution was stirred overnight, with warming to room temperature. The solution was diluted with water (15 mL), then neutralised with 2 M NaOH(aq) until precipitation occurred. The precipitate was filtered, rinsed with water and dried under vacuum to give **6.17** as a white solid (2.80 g, 91% yield).

^{1}H NMR (300 MHz, DMSO-d$_6$): δ 8.88 (d, *J* = 2.8 Hz, 1H), 8.87 (s, 1H), 8.47 (dd, *J* = 9.1, 2.8 Hz, 1H), 7.62 (d, *J* = 9.1 Hz, 1H) ppm.

^{13}C NMR (75 MHz, DMSO-d$_6$): δ 163.94, 158.47, 155.87, 147.62, 144.03, 128.79, 126.38, 120.68, 118.78, 118.14 ppm.

FTIR (neat, ATR): ν = 3253 (br), 1717, 1616, 1534, 1522, 1479, 13498, 1230, 1203, 1124, 1008, 978, 854, 799, 728, 672, 602 cm^{-1}.

Known compound, synthesised here via a different method:

I. Kempen, M. Hemmer, S. Counerotte, L. Pochet, P. Tullio, J.-M. Foidart, S. Blacher, A. Noel, F. Frankenne and B. Pirotte, *Eur. J. Med. Chem.*, 2008, **43**, 2735-2750

Ethyl 6-nitro-coumarin-3-carboxylate (6.18)

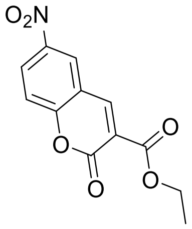

6.17 (1.0 g, 4.25 mmol) was suspended in a mixture of EtOH and H_2SO_4 (50 mL / 2.5 mL) and the solution was heated to reflux, with a calcium hydride trap, for 3 hours until a clear solution had formed. The solution was cooled to room temperature, ethanol was evaporated under reduced pressure and the resulting slurry was neutralised using a saturated aqueous solution of $NaHCO_3$. The precipitate was filtered, washed thoroughly with water and dried under vacuum to give **6.18** as a white solid, which was used without further purification (1.0 g, 94% yield).

^{1}H NMR (400 MHz, $CDCl_3$): δ 8.58 (s, 1H), 8.56 (d, *J* = 2.6 Hz, 1H), 8.49 (dd, *J* = 9.1, 2.6 Hz, 1H), 7.50 (d, *J* = 9.1 Hz, 1H), 4.44 (q, *J* = 7.2 Hz, 2H), 1.43 (t, *J* = 7.1 Hz, 3H) ppm.

^{13}C NMR (101 MHz, $CDCl_3$): δ 162.17, 158.46, 155.05, 146.98, 144.37, 128.71, 125.31, 120.76, 118.21, 117.94, 62.69, 14.32 ppm.

FTIR (neat, ATR): ν = 2360, 1771, 1759, 1688, 1616, 1569, 1526, 1479, 1344, 1296, 1254, 1218, 1092, 1017, 985, 847, 793, 752, 664, 608 cm^{-1}.

Known compound, synthesised here via a different method:

I. Kempen, M. Hemmer, S. Counerotte, L. Pochet, P. Tullio, J.-M. Foidart, S. Blacher, A. Noel, F. Frankenne and B. Pirotte, *Eur. J. Med. Chem.*, 2008, **43**, 2735-2750

Ethyl 6-amino-coumarin-3-carboxylate (6.19)

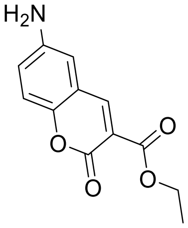

6.18 (994 mg, 4.23 mmol) and $SnCl_2.2H_2O$ (4.77 g, 21.15 mmol, 5 eqv.) were dissolved in EtOAc (10 mL) and the solution was heated to reflux for 4 hours. The solution was cooled to room temperature and neutralised by the addition of solid $NaHCO_3$. The organic layer was washed with water (2 x 20 mL), brine (2 x 20 mL) and then dried using $MgSO_4$. The organic layer was evaporated to give **6.19** as a yellow solid (641 mg, 74% yield).

^{1}H NMR (400 MHz, $CDCl_3$): δ 8.39 (s, 1H), 7.18 (d, *J* = 8.8 Hz, 1H), 6.98 (dd, *J* = 8.8, 2.8 Hz, 1H), 6.80 (d, *J* = 2.7 Hz, 1H), 4.41 (q, *J* = 7.1 Hz, 2H), 3.80 (br s, 2H), 1.41 (t, *J* = 7.1 Hz, 3H) ppm.

^{13}C NMR ($CDCl_3$, 75 MHz): δ 164.58, 148.65, 122.28, 117.59, 111.94, 62.34, 14.43 ppm.

FTIR (neat, ATR): v = 3402, 3328, 3230, 3065, 2359, 1747, 1569, 1495, 1379, 1239, 1131, 1036, 796 cm^{-1}.

Known compound, synthesised here via a different method:

H. K. Chaudhari, A. Pahelkar and B. S. Takale, *Tett. Lett.*, 2017, **58**, 4107-4110

Ethyl 6-azido-coumarin-3-carboxylate (6.20)

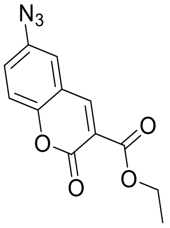

To a stirred solution of ethyl **6.19** (234 mg, 1.0 mmol) in H_2SO_4 (4 M, 26 mL), cooled to 0 °C in an ice bath, was added a solution of sodium nitrite (138 mg, 2 mmol, 2.0 eqv.) in water (3 mL). The solution was stirred for 30 minutes then a solution of sodium azide (120 mg, 1.85 mmol, 1.85 eqv.) in water (3 mL) was added and the solution was stirred at 0 °C for 1 hour, then overnight with warming to room temperature. The precipitate was filtered, rinsed with water and dried under vacuum to give **6.20** as a light orange solid (127 mg, 49% yield).

^{1}H NMR (400 MHz, DMSO-d$_6$): δ 8.73 (s, 1H), 7.73 (d, *J* = 2.4 Hz, 1H), 7.50 – 7.40 (m, 2H), 4.29 (q, *J* = 7.1 Hz, 2H), 1.31 (t, *J* = 7.1 Hz, 3H) ppm.

^{13}C NMR (101 MHz, DMSO-d$_6$): δ 162.86, 156.19, 152.11, 148.19, 136.49, 125.82, 119.80, 119.19, 119.02, 118.29, 61.81, 14.52 ppm.

FTIR (neat, ATR): v = 3406, 2115, 1751, 1712, 1575, 1490, 1376, 1288, 1248, 1142, 1024, 820, 769, 646, 619 cm^{-1}.

5,10,15-tri-p-tolyl-20-((trimethylsilyl)ethynyl)porphyrin

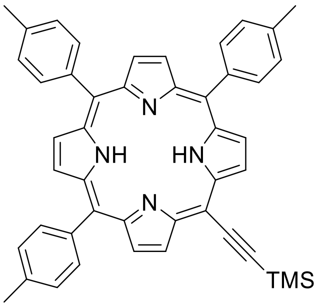

A solution of anhydrous DCM (2 L) containing EtOH (0.75%, v/v) was degassed for 30 minutes with nitrogen, followed by the addition of p-tolualdehyde (1.42 mL, 12.04 mmol, 1.5 eqv.), 3-(trimethylsilyl)-2-propynal (1.18 mL, 7.98 mmol, 1.0 eqv.) and pyrrole (1.38 mL, 19.89 mmol, 2.50 eqv.). $BF_3.OEt_2$ (0.25 mL, 1.98 mmol, 0.25 eqv.) was added, then the solution was stirred at room temperature, in the dark, for 8 hours. p-chloranil (3.69 g, 15 mmol, 1.90 eqv.) was added and the solution was stirred for 16 hours. The solution was concentrated under reduced pressure, to ca. 200 mL, and filtered through a short plug of silica, eluting with DCM. Silica gel (50 g) was added to this filtrate and the product was then purified by column chromatography (silica gel, 3:1 petroleum ether:DCM (v/v) eluent) to give the product as a purple solid (315 mg, 6.5% yield).

^{1}H NMR (400 MHz, $CDCl_3$): δ 9.64 (d, *J* = 4.8 Hz, 2H), 8.91 (d, *J* = 4.7 Hz, 2H), 8.78 (s, 4H), 8.08 (d, *J* = 8.0 Hz, 4H), 8.05 (d, *J* = 8.0 Hz, 2H), 7.57 (d, *J* = 7.6 Hz, 2H), 7.54 (d, *J* = 7.6 Hz, 1H), 2.72 (s, 6H), 2.70 (s, 3H), 0.61 (s, 9H), -2.41 (s, 2H) ppm.

^{13}C NMR (101 MHz, $CDCl_3$): δ 162.86, 156.19, 152.11, 148.19, 136.49, 125.82, 119.80, 119.19, 119.02, 118.29, 61.81, 14.52 ppm.

FTIR (neat, ATR): v = 3318, 2359, 1751, 1710, 1472, 1436, 1378, 1343, 1249, 1183, 1109, 1023, 843, 799, 730, 691 cm^{-1}.

Known compound, synthesised here via a different method:

J.-W. Seo, S. Y. Jang, D. Kim and H.-J. Kim, *Tetrahedron*, 2008, **64**, 2733-2739

5-ethynyl-10,15,20-tri-p-tolyl-zinc-porphyrin (6.12)

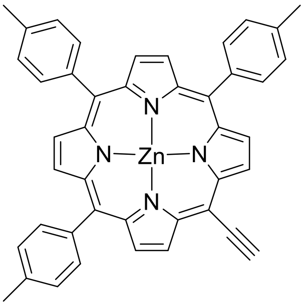

5,10,15-tri-p-tolyl-20-((trimethylsilyl)ethynyl)porphyrin.(335 mg, 4.95×10^{-4} mol, 1.0 eqv.) and $Zn(OAc)_2.2H_2O$ (226 mg, 1.24 mmol, 2.5 eqv.) were dissolved in DCM/MeOH (30 mL / 10 mL) and stirred in the dark, at room temperature, for 18 hours. The solvent was then evaporated under reduced pressure and replaced with THF/MeOH (15 mL / 15 mL). 2M aqueous NaOH (3 mL) was added and stirring was continued for 1 hour in the dark before the solvent was evaporated. DCM (50 mL) and water (50 mL) were added and the organic layer was extracted with DCM, washed with brine (2 × 50 mL) and dried over $MgSO_4$. The solvent was evaporated to give **6.12** as a purple solid (330 mg, 99% yield).

^{1}H NMR (400 MHz, $CDCl_3$): δ 9.73 (d, *J* = 4.7 Hz, 2H), 9.01 (d, *J* = 4.6 Hz, 2H), 8.94 – 8.87 (m, 4H), 8.11 – 8.02 (m, 6H), 7.57 (d, *J* = 7.8 Hz, 4H), 7.54 (d, *J* = 8.1 Hz, 2H), 4.12 (s, 1H), 2.72 (s, 6H), 2.70 (s, 3H) ppm.

^{13}C NMR (101 MHz, $CDCl_3$): δ 152.81, 150.93, 150.25, 150.15, 139.75, 139.62, 137.40, 134.48, 134.38, 133.26, 132.44, 131.97, 130.95, 127.52, 127.45, 123.35, 122.15, 86.28, 83.45, 21.69 ppm.

FTIR (neat, ATR): v = 3265, 2359, 1496, 1436, 1379, 1340, 1241, 1210, 1182, 1071, 998, 795, 675, 624 cm^{-1}.

4-(4-(10,15,20-tri-p-tolyl-zinc-porphyrin-5-yl)-1H-1,2,3-triazol-1-yl)benzoic acid (10)

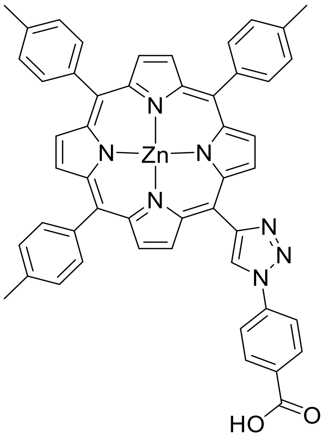

6.12 (50 mg, 7.5 × 10^{-5} mol, 1 eqv.), **6.13** (16 mg, 9.8 × 10^{-5} mol, 1.3 eqv.) and CuI (3 mg, 1.5 × 10^{-5} mol, 0.2 eqv.) were loaded into a Schlenk tube and purged with three vacuum/nitrogen cycles. Anhydrous, degassed toluene (5 mL) was added and the solution was heated at 100 °C, with stirring, for 24 hours. The solution was cooled to room temperature, evaporated under reduced pressure and purified by column chromatography (silica gel, DCM eluent) to give the product as a purple solid (45 mg, 72% yield).

^{1}H-NMR (400 MHz, $CDCl_3$): δ 9.85 (d, *J* = 4.7 Hz, 2H), 9.08 (d, *J* = 4.7 Hz, 2H), 8.97-8.89 (m, 4H), 8.14-8.05 (m, 8H), 7.58-7.52 (m, 6H), 6.97 (d, *J* = 8.8 Hz, 2H), 6.49 (d, *J* = 1.5 Hz, 1H), 6.05 (d, *J* = 1.5 Hz, 1H), 2.72 (s, 6H), 2.70 (s, 3H) ppm.

UV-visible absorption (THF): λ_{max} (dm^3 mol^{-1} cm^{-1}) = 423 (333,330), 554 (11,150), 597 (3750) nm.

Diethyl (4-(4-(10,15,20-tri-p-tolyl-zinc-porphyrin-5-yl)-1H-1,2,3- triazol-1-yl) phenyl)phosphonate

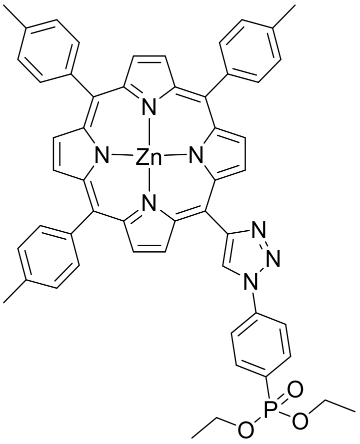

6.12 (30 mg, 45 µmol, 1 eqv.), **6.16** (17 mg, 67.5 µmol, 1.5 eqv.), $CuSO_4.5H_2O$ (1.2 mg, 4.5 µmol, 0.1 eqv.) and sodium ascorbate (4.5 mg, 22.5 µmol, 0.5 eqv.) were loaded into a Schlenk tube and purged with 3 vacuum/nitrogen cycles. Anhydrous DMF (5 mL) was degassed with bubbling nitrogen for 1 hour, then added to the solids via syringe and the solution was stirred in the dark for 36 hours. The solvent was evaporated and the product purified using column chromatography (silica gel, DCM to DCM/methanol (1.5%) gradient) to give the product as a purple powder, which appeared to contain a mixture of zinc and copper as the coordinated metal.

The porphyrin mixture was dissolved in DCM (30 mL), TFA (0.5 mL) was added and the solution stirred in the dark for 30 minutes until demetallation was complete (as observed by the change in number of Q-bands from two to four). TEA (1 mL) was added and the solution was stirred for 30 minutes. The solution was washed with water, dried using $MgSO_4$ and evaporated. An excess of $Zn(OAc)_2.2H_2O$ (80 mg) was added, the residue was dissolved in DCM/methanol (20/5 mL) and the solution stirred in the dark overnight. When the metallation was complete the solvent was evaporated, the residue dissolved in DCM, filtered through a short plug of celite and evaporated. Recrystallisation from DCM with the addition of pentane gave the product as a purple powder (33 mg, 79% yield).

^{1}H-NMR (400 MHz, $CDCl_3$): δ 9.11 (d, *J* = 4.8 Hz, 2H), 8.95 (d, *J* = 4.8 Hz, 2H), 8.89 – 8.85 (m, 4H), 8.84 (s, 1H), 8.28 (dd, *J* = 8.5, 3.2 Hz, 2H), 8.16 (dd, *J* = 12.8, 8.5 Hz, 2H), 8.13 – 8.08 (m, 6H), 7.58 – 7.55 (m, 6H), 4.31 - 4.15 (m, 4H), 2.72 (s, 6H), 2.71 (s, 2H), 1.41 (t, *J* = 7.2 Hz, 6H) ppm.

(4-(4-(10,15,20-tri-p-tolyl-zinc-porphyrin-5-yl)-1H-1,2,3-triazol-1-yl) phenyl)phosphonic acid (11)

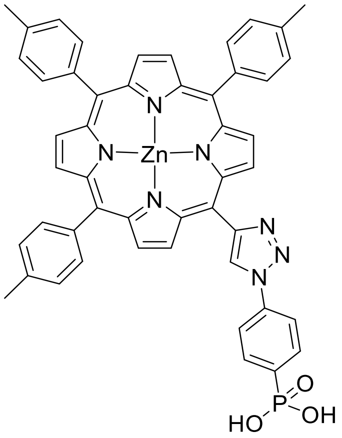

Diethyl (4-(4-(10,15,20-tri-p-tolyl-zinc-porphyrin-5-yl)-1H-1,2,3-triazol-1-yl)phenyl) phosphonate (15 mg, 16.2 µmol, 1 eqv.) was dissolved in anhydrous chloroform (5 mL) under a nitrogen atmosphere. TMS-Br (33 µL, 0.25 mmol, 15.4 eqv.) and TEA (33 µL, 0.315 mmol, 19.4 eqv.) were added and the solution heated to reflux for 4 hours. The solution was cooled to room temperature, the solvent evaporated, an excess of $Zn(OAc)_2.2H_2O$ (20 mg) added and the residue dissolved in DCM/methanol (10 mL / 5 mL). The solution was stirred overnight in the dark and then the solvent was evaporated. DCM (20 mL) and water (100 mL) were added, leading to the formation of a dark precipitate. The solution was filtered and the precipitate was rinsed with water (200 mL) and DCM (50 mL). The precipitate was recrystallised from THF with the addition of pentane, then dried under vacuum, to give **11** as a purple powder (13 mg, 87% yield).

UV-visible absorption (THF): λ_{max} (dm^3 mol^{-1} cm^{-1}) = 424 (326,565), 556 (13,670), 598 (5875) nm.

Ethyl 6-(4-(10,15,20-tri-p-tolyl-zinc-porphyrin-5-yl)-1H-1,2,3-triazol-1-yl) coumarin-3-carboxylate

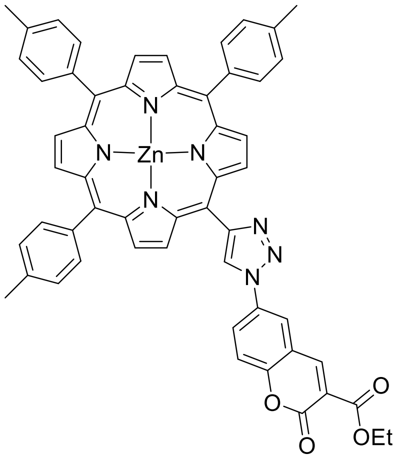

6.12 (40 mg, 60 µmol, 1 eqv.), **6.20** (16 mg, 90 µmol, 1.5 eqv.), $CuSO_4.5H_2O$ (1.6 mg, 6 µmol, 0.1 eqv.) and sodium ascorbate (6 mg, 30 µmol, 0.5 eqv.) were loaded into a Schlenk tube and purged with 3 vacuum/nitrogen cycles. Anhydrous DMF (8 mL) was degassed with bubbling nitrogen for 1 hour, then added to the solids via syringe and the solution was stirred in the dark for 36 hours. The solvent was evaporated and the product purified using column chromatography (silica gel, DCM to DCM/methanol (0.5%) gradient) to yield the product as a purple powder, which appeared to contain a mixture of zinc and copper as the coordinated metal.

The porphyrin mixture was dissolved in DCM (30 mL), TFA (0.5 mL) was added and the solution stirred in the dark for 30 minutes until demetallation was complete (as observed by the change in number of Q-bands from two to four). TEA (1 mL) was added and the solution was stirred for 30 minutes. The solution was washed with water, dried using $MgSO_4$ and evaporated. An excess of $Zn(OAc)_2.2H_2O$ (50 mg) was added, the residue was dissolved in DCM/methanol (20/5 mL) and the solution stirred in the dark overnight. When the metallation was complete the solvent was evaporated, the residue dissolved in DCM, filtered through a short plug of celite and evaporated. Recrystallisation from DCM with the addition of pentane gave the product as a purple powder (25 mg, 45% yield).

^{1}H-NMR (400 MHz, $CDCl_3$): δ 9.10 (d, *J* = 4.9 Hz, 2H), 8.95 (d, *J* = 4.9 Hz, 2H0, 8.92 – 8.82 (m, 4H0, 8.74 (s, 1H), 8.52 (s, 1H), 8.25 (s, 1H), 8.20 (d, *J* = 8.9 Hz, 1H), 8.15 – 8.06 (m, 6H), 7.61 – 7.52 (m, 6H), 7.45 (d, *J* = 8.9 Hz, 1H), 4.45 (q, *J* = 7.1 Hz, 2H), 2.72 (s, 6H), 2.69 (s, 3H), 1.44 (t, *J* = 7.1 Hz, 3H) ppm.

6-(4-(10,15,20-tri-p-tolyl-zinc-porphyrin-5-yl)-1H-1,2,3-triazol-1-yl)-coumarin-3-carboxylic acid (12)

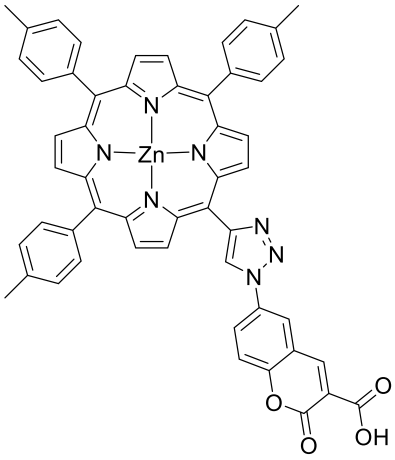

Ethyl 6-(4-(10,15,20-tri-p-tolyl-zinc-porphyrin-5-yl)-1H-1,2,3-triazol-1-yl)-coumarin-3-carboxylate (10 mg, 10.8 µmol, 1 eqv.) and KOH (35 mg, 0.62 mmol, 57 eqv.) were dissolved in THF/methanol/water (14 mL / 7 mL / 7 mL) and the mixture stirred at room temperature overnight. The solvent was evaporated, water (10 mL) was added and the solution was acidified using 1 M HCl until precipitation occurred. The suspension was filtered, washed thoroughly with water, rinsed with cold DCM then dried under vacuum to give **12** as a purple solid (9 mg, 90% yield).

UV-visible absorption (THF): λ_{max} (dm^3 mol^{-1} cm^{-1}) = 424 (273,520), 557 (15,820), 598 (6775) nm.

6.4. References

1 A. Hagfeldt, G. Boschloo, L. Sun, L. Kloo and H. Pettersson, *Chem. Rev.*, 2010, **110**, 6595–6663.

2 L. Zhang and J. M. Cole, *ACS Appl. Mater. Interfaces*, 2015, **7**, 3427–3455.

3 Y. Pellegrin, L. Le Pleux, E. Blart, A. Renaud, B. Chavillon, N. Szuwarski, M. Boujtita, L. Cario, S. Jobic, D. Jacquemin and F. Odobel, *J. Photochem. Photobiol. A Chem.*, 2011, **219**, 235–242.

4 F. Brunner, N. Marinakis, C. Wobill, M. Willgert, C. D. Ertl, T. Kosmalski, M. Neuburger, B. Bozic-Weber, T. Glatzel, E. C. Constable and C. E. Housecroft, *J. Mater. Chem. C*, 2016, **4**, 9823–9833.

5 J. Cui, J. Lu, X. Xu, K. Cao, Z. Wang, G. Alemu, H. Yuang, Y. Shen, J. Xu, Y. Cheng and M. Wang, *J. Phys. Chem. C*, 2014, **118**, 16433–16440.

6 G. Alemu, J. Cui, K. Cao, J. Li, Y. Shen and M. Wang, *RSC Adv.*, 2014, **4**, 51374–51380.

7 L. Li, E. A. Gibson, P. Qin, G. Boschloo, M. Gorlov, A. Hagfeldt and L. Sun, *Adv. Mater.*, 2010, **22**, 1759–1762.

8 A. Nattestad, A. J. Mozer, M. K. R. Fischer, Y.-B. Cheng, A. Mishra, P. Bäuerle and U. Bach, *Nat. Mater.*, 2010, **9**, 31–35.

9 K. A. Click, D. R. Beauchamp, B. R. Garrett, Z. Huang, C. M. Hadad and Y. Wu, *Phys. Chem. Chem. Phys.*, 2014, **16**, 26103–26111.

10 P. Qin, H. Zhu, T. Edvinsson, G. Boschloo, A. Hagfeldt and L. Sun, *J. Am. Chem. Soc.*, 2008, **130**, 8570–8571.

11 P. Qin, J. Wiberg, E. A. Gibson, M. Linder, L. Li, T. Brinck, A. Hagfeldt, B. Albinsson and L. Sun, *J. Phys. Chem. C*, 2010, **114**, 4738–4748.

12 F. Wu, L. Zhu, S. Zhao, Q. Song and C. Yang, *Dye. Pigment.*, 2016, **124**, 93–100.

13 F. Wu, S. Zhao, C. Zhong, Q. Song and L. Zhu, *RSC Adv.*, 2015, **5**, 93652–93658.

14 M. Weidelener, A. Mishra, A. Nattestad, S. Powar, A. J. Mozer, E. Mena-Osteritz, Y.-B. Cheng, U. Bach and P. Bäuerle, *J. Mater. Chem.*, 2012, **22**, 7366–7379.

15 H. C. Kolb, M. G. Finn and K. B. Sharpless, *Angew. Chem. Int. Ed.*, 2001, **40**, 2004–2021.

16 L. Liang and D. Astruc, *Coord. Chem. Rev.*, 2011, **255**, 2933–2945.

17 V. V. Rostovtsev, L. G. Green, V. V. Fokin and K. B. Sharpless, *Angew. Chem. Int. Ed.*, 2002, **41**, 2596–2599.

18 C. W. Tornøe, C. Christensen and M. Meldal, *J. Org. Chem.*, 2002, **67**, 3057–3064.

19 K. Ladomenou, V. Nikolaou, G. Charalambidis and A. G. Coutsolelos, *Coord. Chem. Rev.*, 2016, **306**, 1–42.

20 V. Nikolaou, K. Karikis, Y. Farré, G. Charalambidis, F. Odobel and A. G. Coutsolelos, *Dalt. Trans.*, 2015, **44**, 13473–13479.

21 L. Zhang, L. Favereau, Y. Farre, A. Maufroy, Y. Pellegrin, E. Blart, M. Hissler, D. Jacquemin, F. Odobel and L. Hammarström, *RSC Adv.*, 2016, **6**, 77184–77194.

22 A. Maufroy, L. Favereau, F. B. Anne, Y. Pellegrin, E. Blart, M. Hissler, D. Jacquemin and F. Odobel, *J. Mater. Chem. A*, 2015, **3**, 3908–3917.

23 G. Guerrero, J. G. Alauzun, M. Granier, D. Laurencin and P. H. Mutin, *Dalt. Trans.*, 2013, **42**, 12569-12585.

24 M. A. Fazio, O. P. Lee and D. I. Schuster, 2008, **10**, 4979–4982.

25 V. S. Shetti and M. Ravikanth, *Eur. J. Org. Chem.*, 2010, **2010**, 494–508.

26 G. De Miguel, M. Wielopolski, D. I. Schuster, M. A. Fazio, O. P. Lee, C. K. Haley, A. L. Ortiz, L. Echegoyen, T. Clark and D. M. Guldi, *J. Am. Chem. Soc.*, 2011, **133**, 13036–13054.

27 S. J. Silvers and A. Tulinsky, *J. Am. Chem. Soc.*, 1967, **89**, 3331–3337.

28 H. Liu, F. Duclairoir, B. Fleury, L. Dubois, Y. Chenavier and J.-C. Marchon, *Dalt. Trans.*, 2009, **19**, 3793-3799.

29 G. Y. Gao, J. V. Ruppel, D. B. Allen, Y. Chen and X. P. Zhang, *J. Org. Chem.*, 2007, **72**, 9060–9066.

30 C.-W. Lee, H.-P. Lu, C.-M. Lan, Y.-L. Huang, Y.-R. Liang, W.-N. Yen, Y.-C. Liu, Y.-S. Lin, E. W.-G. Diau and C.-Y. Yeh, *Chem. Eur. J.*, 2009, **15**, 1403–1412.

31 M. Natali, A. Luisa, E. Iengo and F. Scandola, *Chem. Commun.*, 2014, **50**, 1842-1844.

32 T. Higashino and H. Imahori, *Dalt. Trans.*, 2015, **44**, 448–463.

33 A. D. Adler, F. R. Longo, J. D. Finarelli, J. Goldmacher, J. Assour and L. Korsakoff, *J. Org. Chem.*, 1967, **32**, 476–476.

34 J. S. Lindsey, I. C. Schreiman, H. C. Hsu, P. C. Kearney and A. M. Marguerettaz, *J. Org. Chem.*, 1987, **52**, 827–836.

35 C. M. Lemon, E. Karnas, M. G. Bawendi and D. G. Nocera, *Inorg. Chem.*, 2013, **52**, 10394–10406.

36 J. S. Lindsey and R. W. Wagner, *J. Org. Chem.*, 1989, **54**, 828–836.

37 M. Kalek, M. Jezowska and J. Stawinski, *Adv. Synth. Catal.*, 2009, **351**, 3207–3216.

38 M. Séverac, L. Le Pleux, A. Scarpaci, E. Blart and F. Odobel, *Tetrahedron Lett.*, 2007, **48**, 6518–6522.

39 A. Osuka, C. Maeda, S. Yamaguchi, C. Ikeda and H. Shinokubo, *Org. Lett.*, 2008, **10**, 549–552.

40 C. Maeda, P. Kim, S. Cho, J. K. Park, J. M. Lim, D. Kim, J. Vura-Weis, M. R. Wasielewski, H. Shinokubo and A. Osuka, *Chem. Eur. J.*, 2010, **16**, 5052–5061.

41 J. Haumesser, J. P. Gisselbrecht, L. Karmazin-Brelot, C. Bailly, J. Weiss and R. Ruppert, *Organometallics*, 2014, **33**, 4923–4930.

42 D. M. Shen, C. Liu and Q. Y. Chen, *Eur. J. Org. Chem.*, 2007, 1419–1422.

43 K. Muthukumaran, R. S. Loewe, A. Ambroise, S. I. Tamaru, Q. Li, G. Mathur, D. F. Bocian, V. Misra and J. S. Lindsey, *J. Org. Chem.*, 2004, **69**, 1444–1452.

44 B. S. Creaven, D. A. Egan, K. Kavanagh, M. McCann, A. Noble, B. Thati and M. Walsh, *Inorganica Chim. Acta*, 2006, **359**, 3976–3984.

45 D. A. Roberts, T. W. Schmidt, M. J. Crossley and S. Perrier, *Chem. Eur. J.*, 2013, **19**, 12759–12770.

46 R. T. Stibrany, J. Vasudevan, S. Knapp, J. A. Potenza, T. Emge and H. J. Schugar, *J. Am. Chem. Soc.*, 1996, **118**, 3980–3981.

47 A. Harriman and M. C. Richoux, *J. Phys. Chem.*, 1983, **87**, 4957–4965.

48 M. Nappa and J. S. Valentine, *J. Am. Chem. Soc.*, 1978, **100**, 5075–80.

49 G. D. Dorough, J. R. Miller and F. M. Huennekens, *J. Am. Chem. Soc.*, 1951, **73**, 4315–4320.

50 S. Zakavi and S. Hoseini, *RSC Adv.*, 2015, **5**, 106774–106786.

51 M. Gouterman, *J. Chem. Phys.*, 1959, **30**, 1139-1160.

52 D. J. Quimby and F. R. Longo, *J. Am. Chem. Soc.*, 1975, **97**, 5111–5117.

53 A. Varlan and M. Hillebrand, *Cent. Eur. J. Chem.*, 2011, **9**, 624–634.

54 A.-M. Manke, K. Geisel, A. Fetzer and P. Kurz, *Phys. Chem. Chem. Phys.*, 2014, **16**, 12029–42.

55 V. V. Pavlishchuk and A. W. Addison, *Inorganica Chim. Acta*, 2000, **298**, 97–102.

56 Z. Liu, D. Xiong, X. Xu, Q. Arooj, H. Wang, L. Yin, W. Li, H. Wu, Z. Zhao, W. Chen, M. Wang, F. Wang, Y. B. Cheng and H. He, *ACS Appl. Mater. Interfaces*, 2014, **6**, 3448–3454.

57 A. D. Becke, *J. Chem. Phys.*, 1993, **98**, 1372–1377.

58 S. Miertuš, E. Scrocco and J. Tomasi, *Chem. Phys.*, 1981, **55**, 117–129.

59 S. A. Trammell and T. J. Meyer, *J. Phys. Chem. B*, 1999, **103**, 104–107.

60 R. Giovannetti, M. Zannotti, L. Alibabaei and S. Ferraro, *Int. J. Photoenergy*, 2014, **2014**, 1-9.

61 İ. Tosun, *Int. J. Environ. Res. Public Health*, 2012, **9**, 970–984.

62 T.-Y. Kim, J.-W. Lee, E.-M. Jin, J.-Y. Park, J.-H. Kim and K.-H. Park, *Measurement*, 2013, **46**, 1692–1697.

63 P. J. Holliman, B. Vaca Velasco, I. Butler, M. Wijdekop and D. A. Worsley, *Int. J. Photoenergy*, 2008, **2008**, 1-7.

64 G. Natu, Z. Huang, Z. Ji and Y. Wu, *Langmuir*, 2012, **28**, 950–956.

65 M. Zannotti, C. J. Wood, G. H. Summers, L. A. Stevens, M. R. Hall, C. E. Snape, R. Giovanetti and E. A. Gibson, *ACS Appl. Mater. Interfaces*, 2015, **7**, 24556–24565.

66 C. R. Lee, H. S. Kim, I. H. Jang, J. H. Im and N. G. Park, *ACS Appl. Mater. Interfaces*, 2011, **3**, 1953–1957.

67 B.-K. An, W. Hu, P. L. Burn and P. Meredith, *J. Phys. Chem. C*, 2010, **114**, 17964–17974.

68 N. Duffy, L. Peter, R. M. G. Rajapakse and K. G. U. Wijayantha, *Electrochem. Commun.*, 2000, **2**, 658–662.

69 H. Tian, J. Oscarsson, E. Gabrielsson, S. K. Eriksson, R. Lindblad, B. Xu, Y. Hao, G. Boschloo, E. M. J. Johansson, J. M. Gardner, A. Hagfeldt, H. Rensmo and L. Sun, *Sci. Rep.*, 2014, **4**, 4282.

70 H. Yamada, H. Imahori, Y. Nishimura, I. Yamazaki and S. Fukuzumi, *Adv. Mater.*, 2002, **14**, 892–895.

71 H. Yamada, H. Imahori, Y. Nishimura, I. Yamazaki, T. K. Ahn, S. K. Kim, D. Kim and S. Fukuzumi, *J. Am. Chem. Soc.*, 2003, **125**, 9129–9139.

72 M. Prato, M. Maggini, C. Giacometti, G. Scorrano, G. Sandonà and G. Farnia, *Tetrahedron*, 1996, **52**, 5221–5234.

73 F. D’Souza and O. Ito, *Chem. Commun.*, 2009, **0**, 4913–4928.

74 Y. Dong, L. Wei, R. Fan, Y. Yang and P. Wang, *RSC Adv.*, 2016, **6**, 39972–39981.

75 L. A. Martini, G. F. Moore, R. L. Milot, L. Z. Cai, S. W. Sheehan, C. A. Schmuttenmaer, G. W. Brudvig and R. H. Crabtree, *J. Phys. Chem. C*, 2013, **117**, 14526–14533.

76 E. A. Gibson, L. Le Pleux, J. Fortage, Y. Pellegrin, E. Blart, F. Odobel, A. Hagfeldt and G. Boschloo, *Langmuir*, 2012, **28**, 6485–6493.

Chapter 7 – Conclusions and Future Work

The work presented in this thesis has been a multidisciplinary study of organic dyes for NiO-based p-type dye-sensitised solar cells. A range of novel dyes have been synthesised and characterised using structural, photophysical and electrochemical methods to probe their suitability for use in p-DSCs.

A series of donor-acceptor triphenylamine-BODIPY dyes were synthesised following the ‘push-pull’ design (**1**-**4**, Chapter 3) to investigate the effect of donor-acceptor coupling on p-DSC performances. Through the use of thiophene π-linkers and mono-substituted BODIPYs, the charge-transfer character of these dyes could be tuned. The BODIPY dyes with more charge-transfer character (**2** and **4**) had a broader spectral response which stretched further into the NIR region. p-DSCs constructed using **2** achieved a higher power conversion efficiency (0.20%) than the structurally analogous benchmark dye, **P1**. It was concluded that lower PCEs were obtained for the systems where the dye HOMO was decoupled from the semiconductor surface, due to poor charge-transfer efficiencies.

In Chapter 4, a multidentate pyrrole-based anchoring unit was developed and three dyes were studied containing BODIPY and indolium acceptors. The BODIPY dyes (**6** and **7**) performed poorly when integrated into p-DSCs, likely because of inefficient charge-transfer from NiO. The indolium-based dye (**8**) performed much more efficiently, with a higher PCE than the analogous triphenylamine-based dyes containing the same acceptor group. The small footprint and broad spectral response of **8** make this dye a promising candidate for applications in co-sensitisation. The synthetic difficulties encountered in this work regarding anchor-group hydrolysis prompted an investigation into developing new methods for introducing anchoring groups (Chapter 6).

The work presented in Chapter 5 aimed to develop a new chromophore for use in p-DSCs. Previously, the synthesis of bay-annulated indigo (BAI) had been reported for use in OPVs and organic semiconductors. The high extinction coefficient and apparent ease of functionalisation of this molecule made it a promising candidate for use in DSCs. A simple, first-generation dye was developed containing a benzoic acid anchoring group (**9**) and this was integrated into p-DSCs. Fairly poor performances were obtained for these devices, which has been attributed to low dye loading and dye aggregation. Despite this, the p-DSCs made using this dye performed more efficiently than structurally analogous dyes reported in the literature. Therefore, this remains a promising candidate for further functionalisation and study. The poor solubility of this dye following coupling of the anchoring group further highlighted the necessity of developing new methods of anchor group functionalisation.

In Chapter 6, a synthetic method was developed to introduce anchoring groups through copper-catalysed ‘click chemistry’. Using this method, azide-functionalised anchoring group fragments were designed containing a carboxylic acid, a phosphonic acid and a coumarin-based anchor. These were coupled together with an alkyne-functionalised porphyrin, chosen as a distinct spectroscopic handle, to give three triazole-bridged porphyrin dyes (**10**-**12**). The adsorption of these dyes onto NiO was investigated using Langmuir adsorption isotherms and kinetic studies. Increased dye loading was obtained for the porphyrins anchored using the phosphonic acid and coumarin-based anchors compared to the carboxylic acid. The phosphonate anchor had a higher binding constant and rate constant for adsorption than the coumarin-based anchor. p-DSCs constructed using these dyes performed poorly, however, the performances were comparable to other previously reported porphyrin-sensitised NiO devices. The synthetic methods developed in this chapter can be combined with a more suitable chromophore, such as the BAI chromophore studied in Chapter 5, to facilitate the design of a highly efficient dye.

In conclusion, this thesis has described the synthesis and characterisation of organic dyes for use in p-DSCs. BAI was shown to be a promising candidate to design dyes for p-DSCs, due to a high extinction coefficient and broad spectral response at longer wavelengths. Functionalisation of the chromophore was hindered due to the limited solubility of the dye following the conventional method of introducing an anchoring group (a Suzuki coupling of an aryl-carboxylic acid). The synthetic routes developed in Chapter 6 could potentially circumvent this issue, as the phosphonate and coumarin anchors developed in that chapter were hydrolysed as a final synthetic step. Thus, the BAI core could be coupled to an ester-protected anchoring group using click chemistry, which should produce a dye with improved solubility compared to **9** (which was directly coupled to benzoic acid). This improved solubility would allow the further halogenation and coupling reactions necessary to append a secondary electron acceptor, which is expected to increase the lifetime of the charge separated state (as has been seen for analogous work involving DPP-based dyes). Finally, the branched alkyl chains (which were necessary to solubilise the BAI core) appeared to hinder the adsorption of the dye onto NiO. An alternative route, to potentially avoid this issue, is to append the BAI core with *tert*-butyl phenol groups, drawing inspiration from studies on perylene-based chromophores. These should improve solubility by hindering π-π stacking, without interacting with the semiconductor surface to the same extent as the long alkyl chains. The investigations presented in this thesis should therefore serve as the foundations for further development of the previously discussed BAI-based sensitiser, which remains a promising chromophore to be utilised for designing highly efficient devices.

Appendix 1

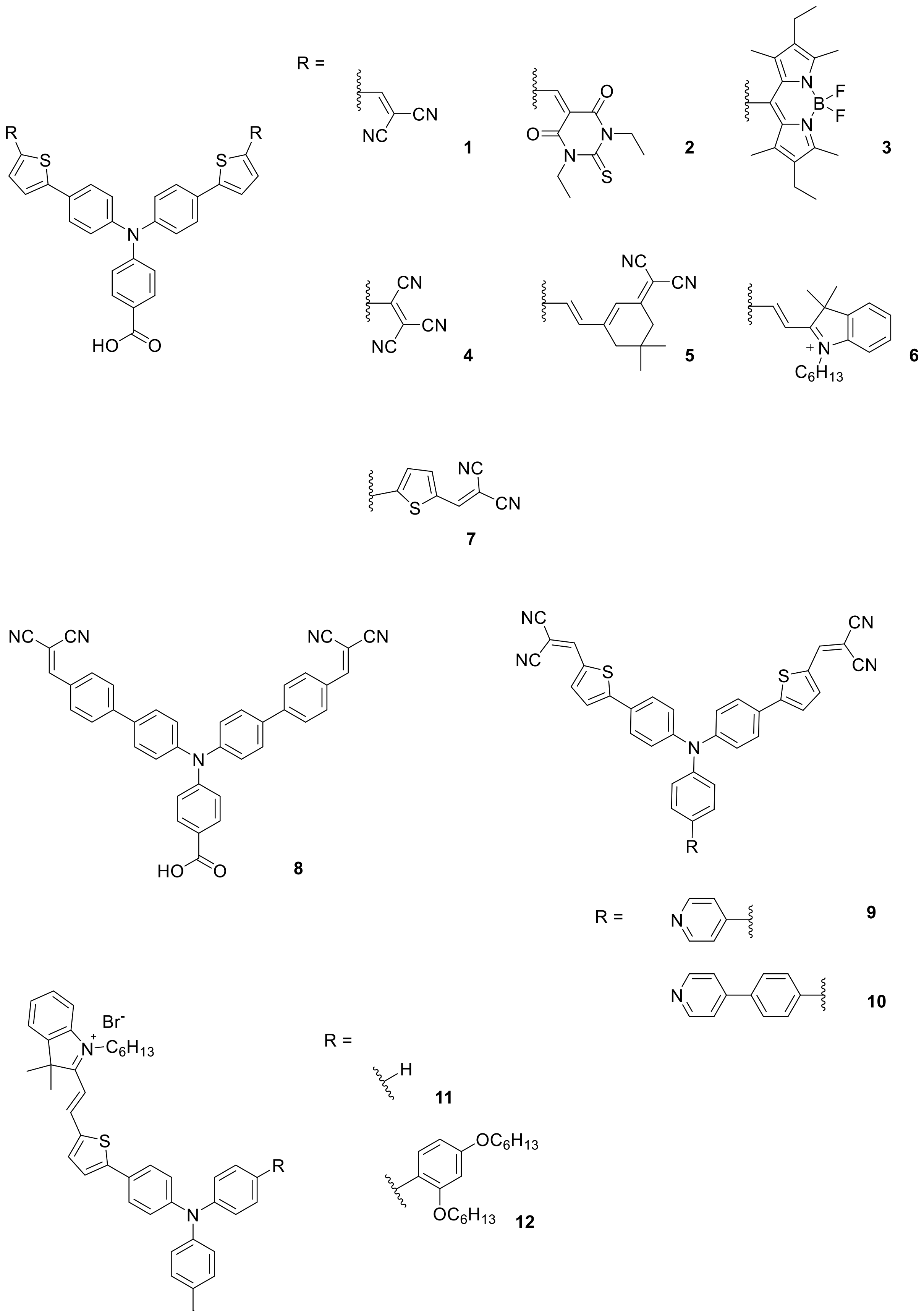

Figure A1.1. Chemical structure of dyes (**1-12**) tested for p-DSCs, summarised in Table A1.1.

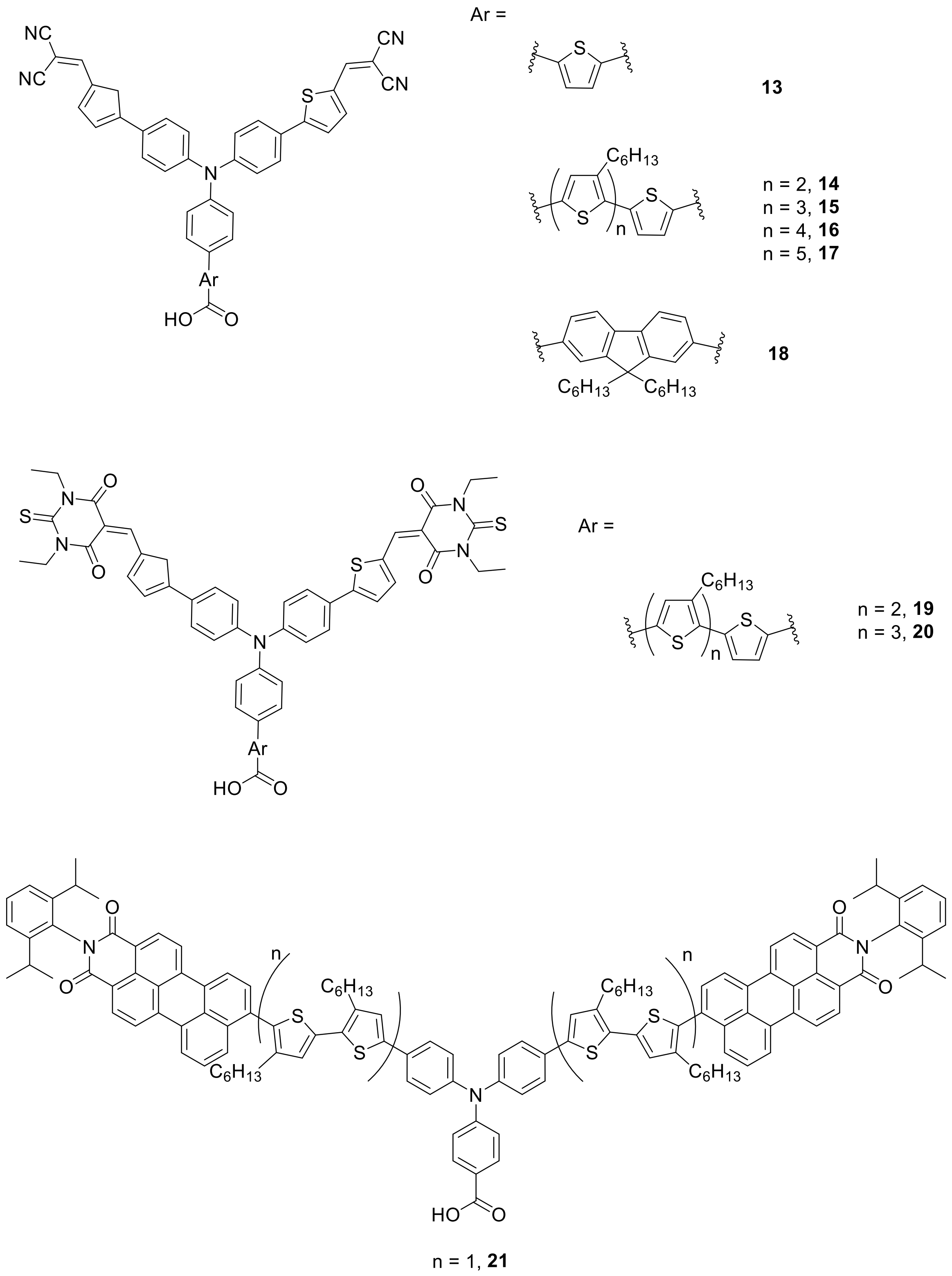

13

n = 2, **14**
n = 3, **15**
n = 4, **16**
n = 5, **17**

18

n = 2, **19**
n = 3, **20**

n = 1, **21**
n = 2, **22**
n = 3, **23**

Figure A1.2. Chemical structure of dyes (**13-23**) tested for p-DSCs, summarised in Table A1.1.

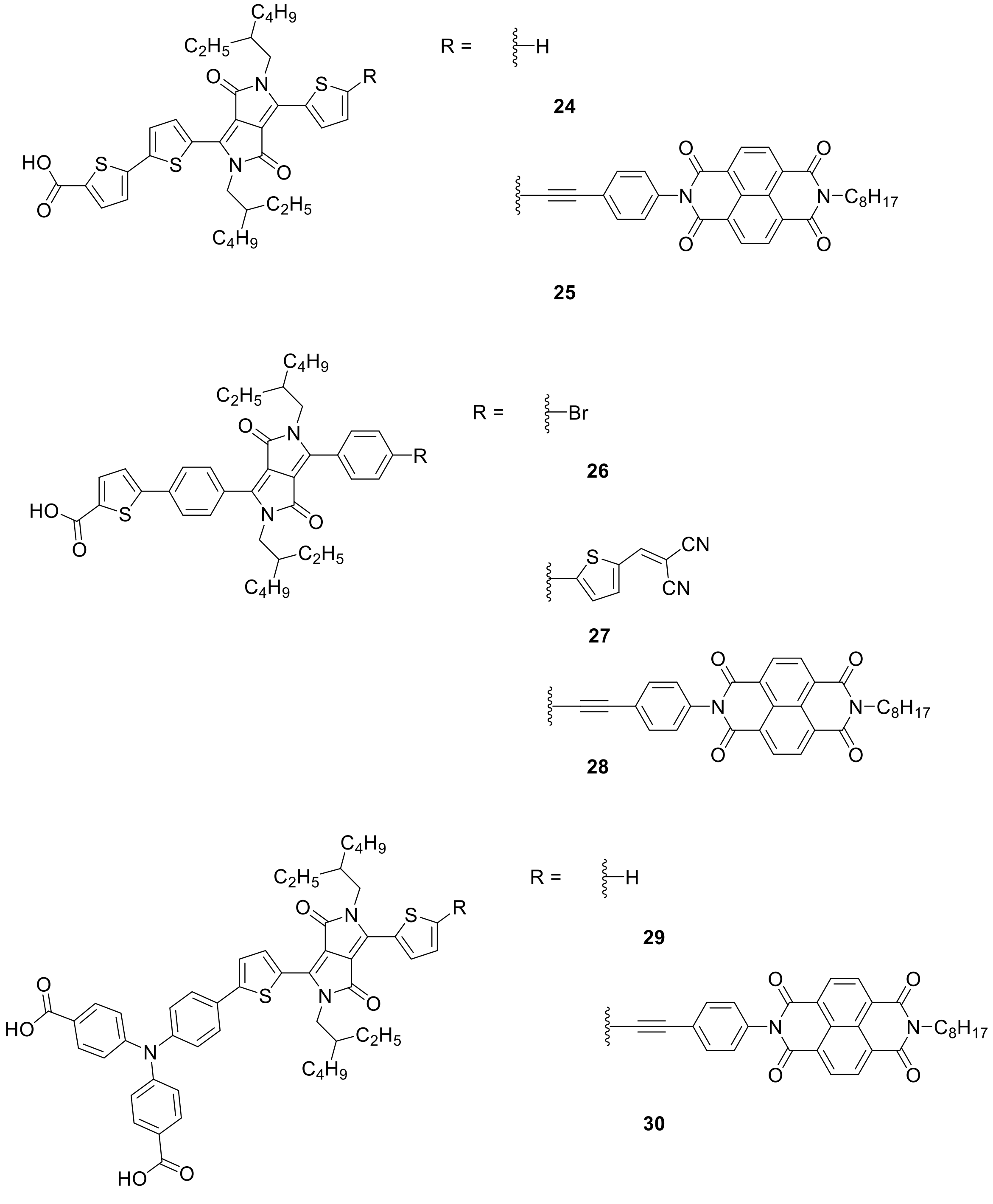

Figure A1.3. Chemical structure of dyes (**24-30**) tested for p-DSCs, summarised in Table A1.1.

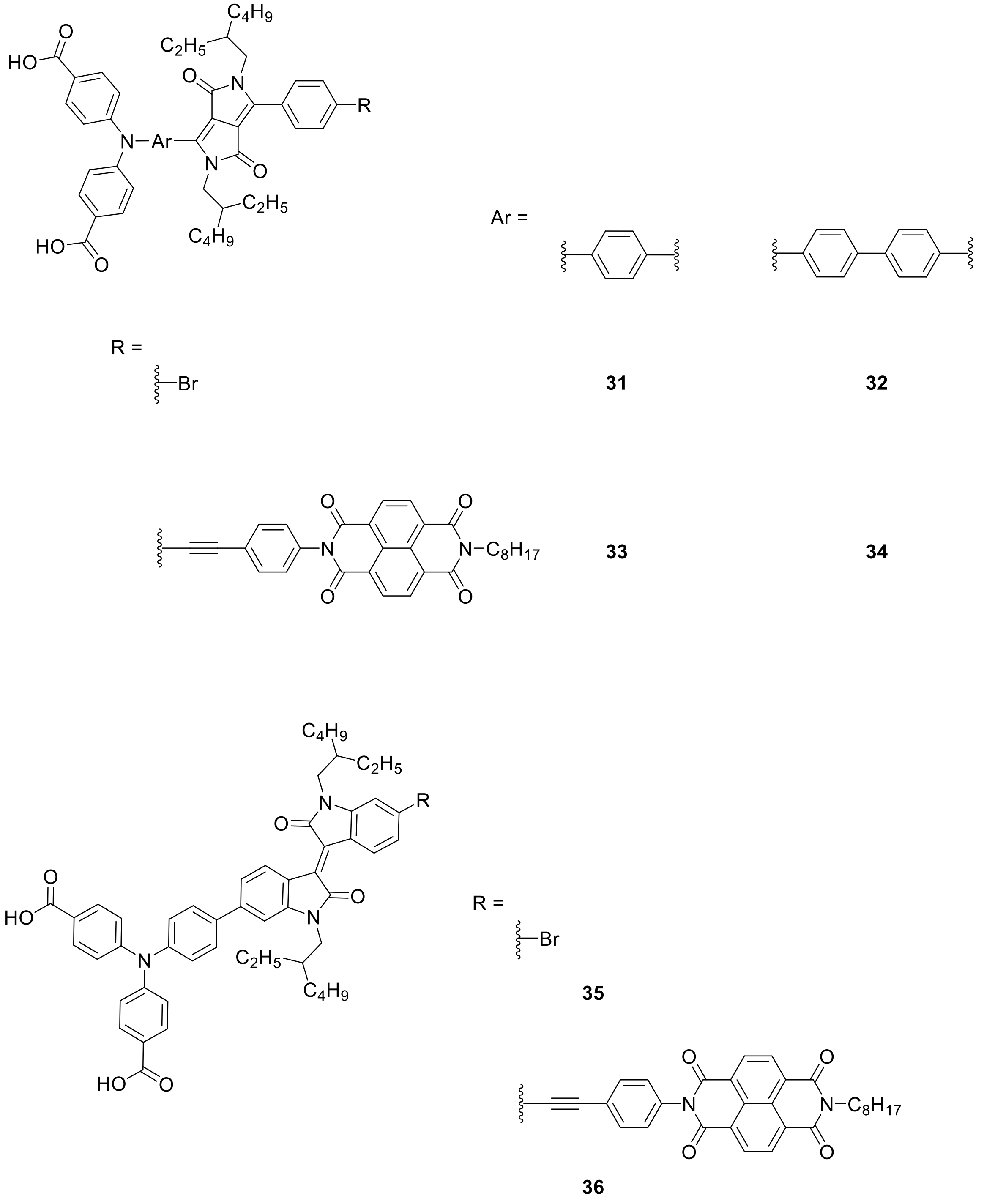

Figure A1.4. Chemical structure of dyes (**31-36**) tested for p-DSCs, summarised in Table A1.1.

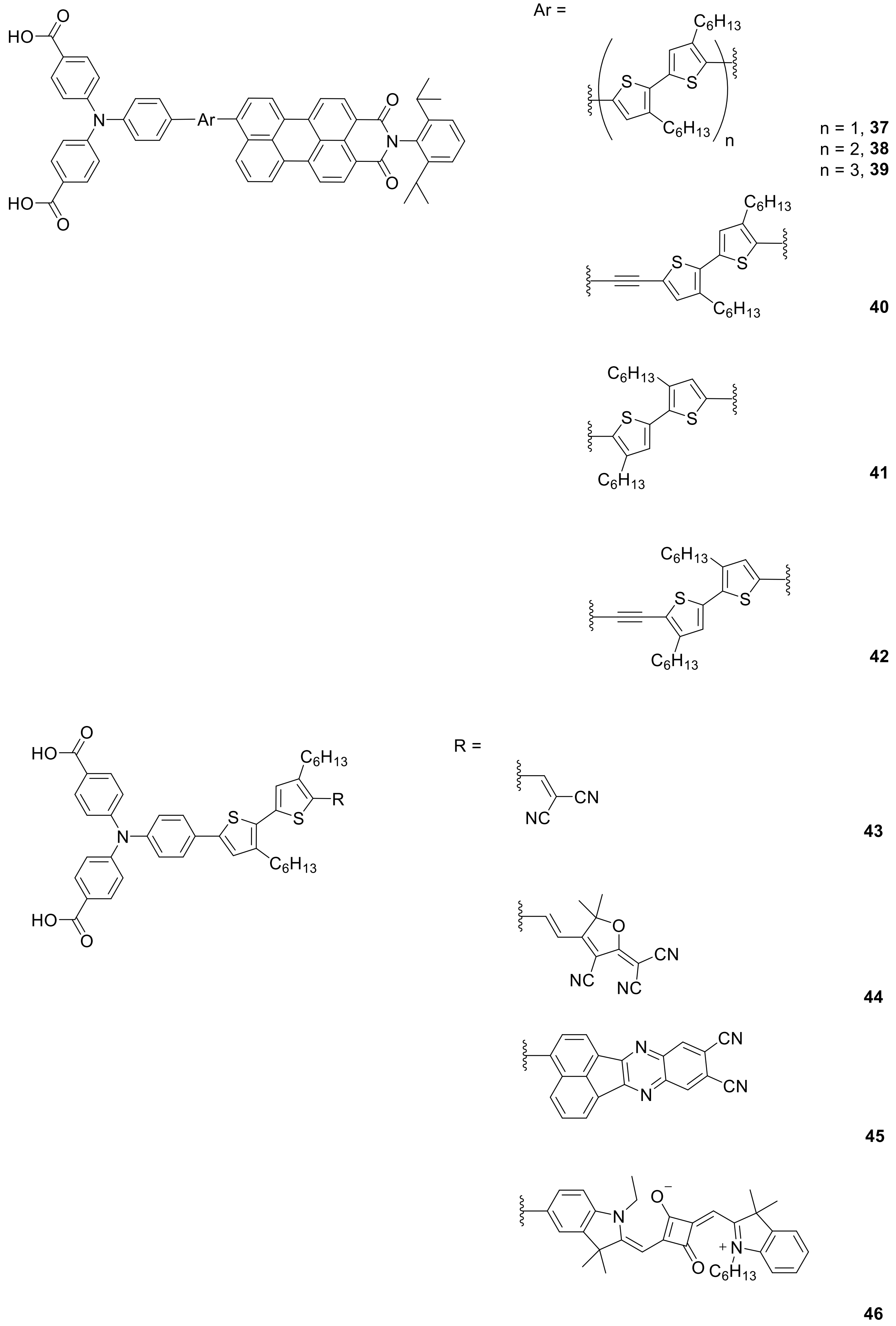

Figure A1.5. Chemical structure of dyes (**37**-**46**) tested for p-DSCs, summarised in Table A1.1.

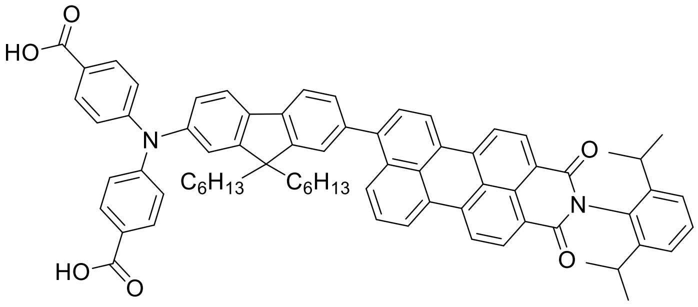

47

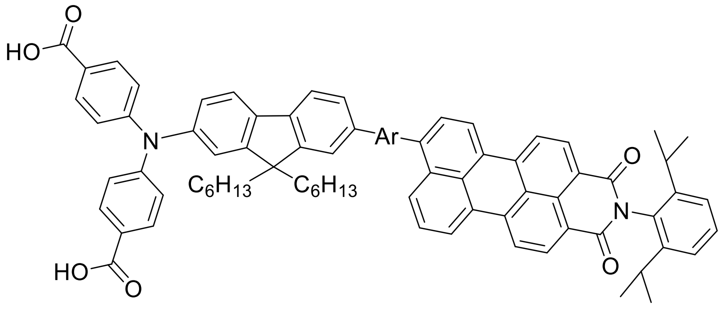

Ar =

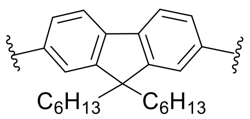

48

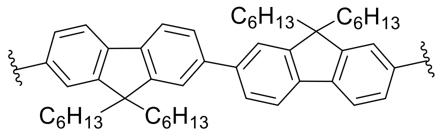

49

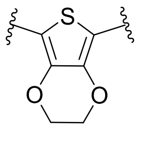

50

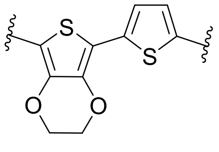

51

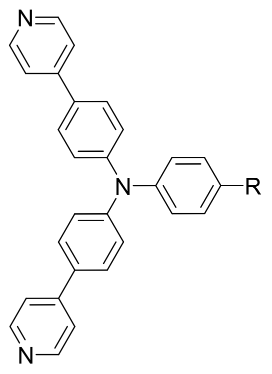

R =

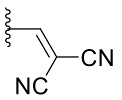

52

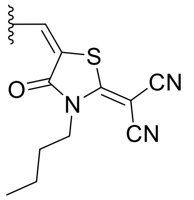

53

Figure A1.6. Chemical structure of dyes (**47**-**53**) tested for p-DSCs, summarised in Table A1.1.

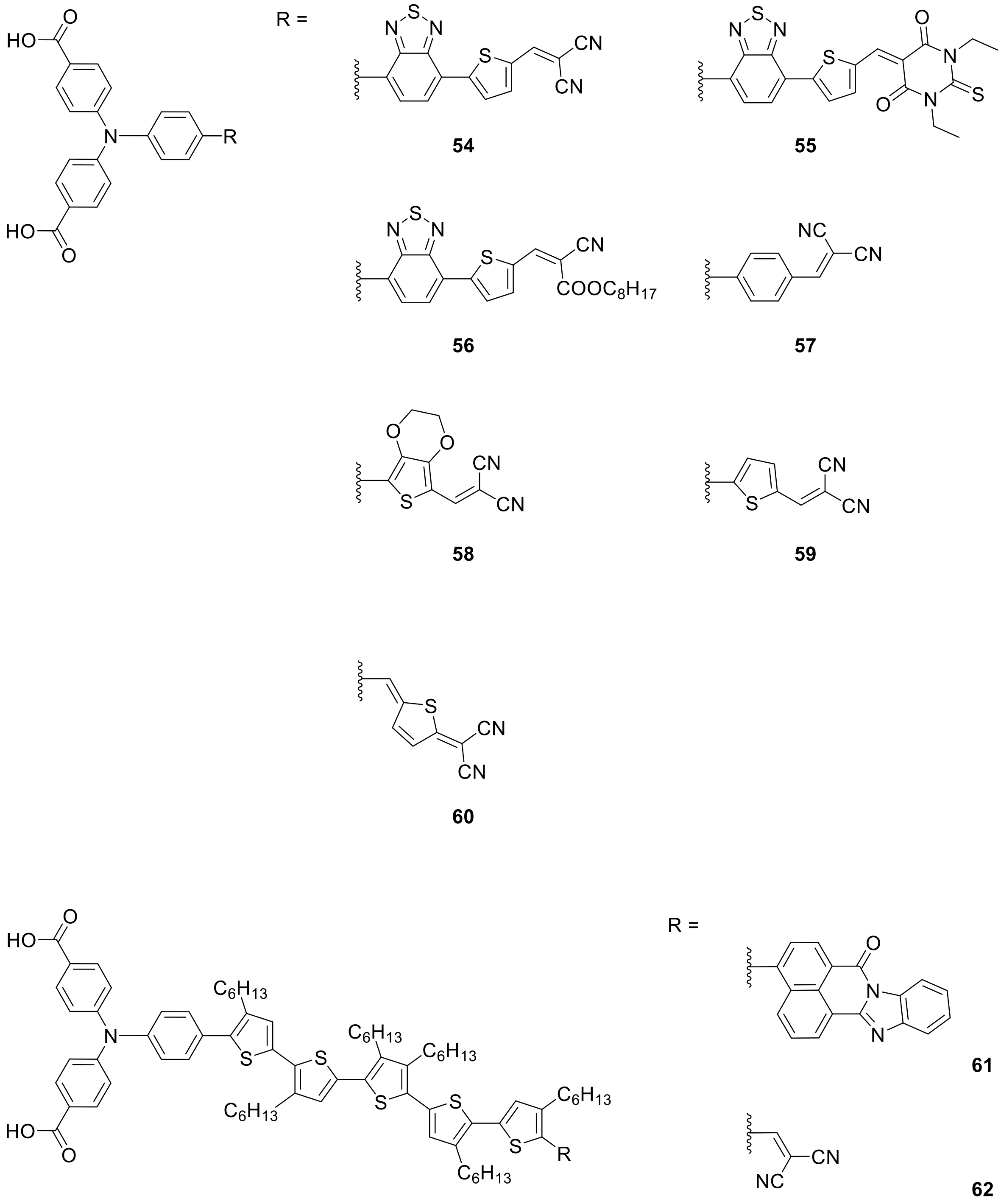

Figure A1.7. Chemical structure of dyes (**54-62**) tested for p-DSCs, summarised in Table A1.1.

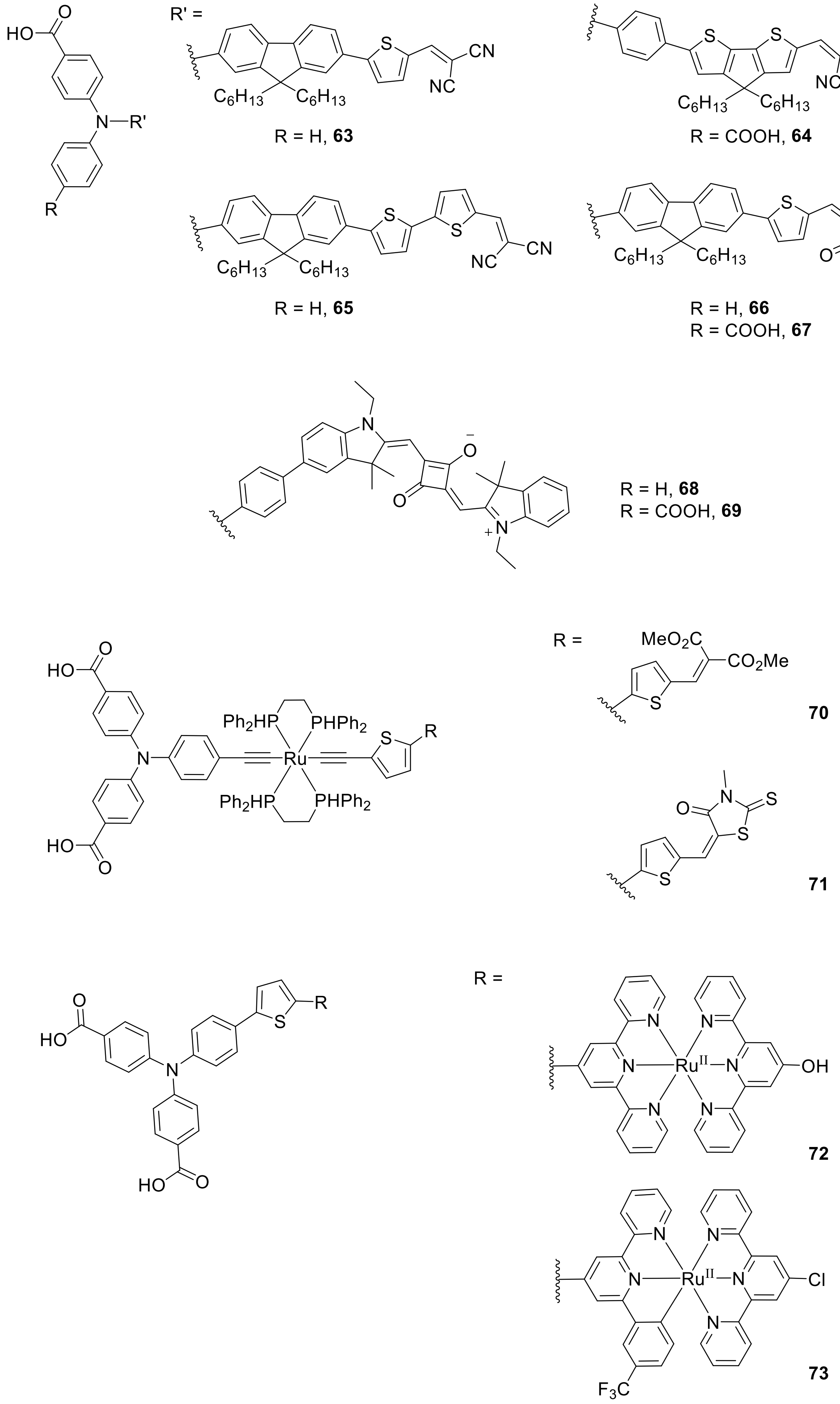

Figure A1.8. Chemical structure of dyes (**63**-**73**) tested for p-DSCs, summarised in Table A1.1.

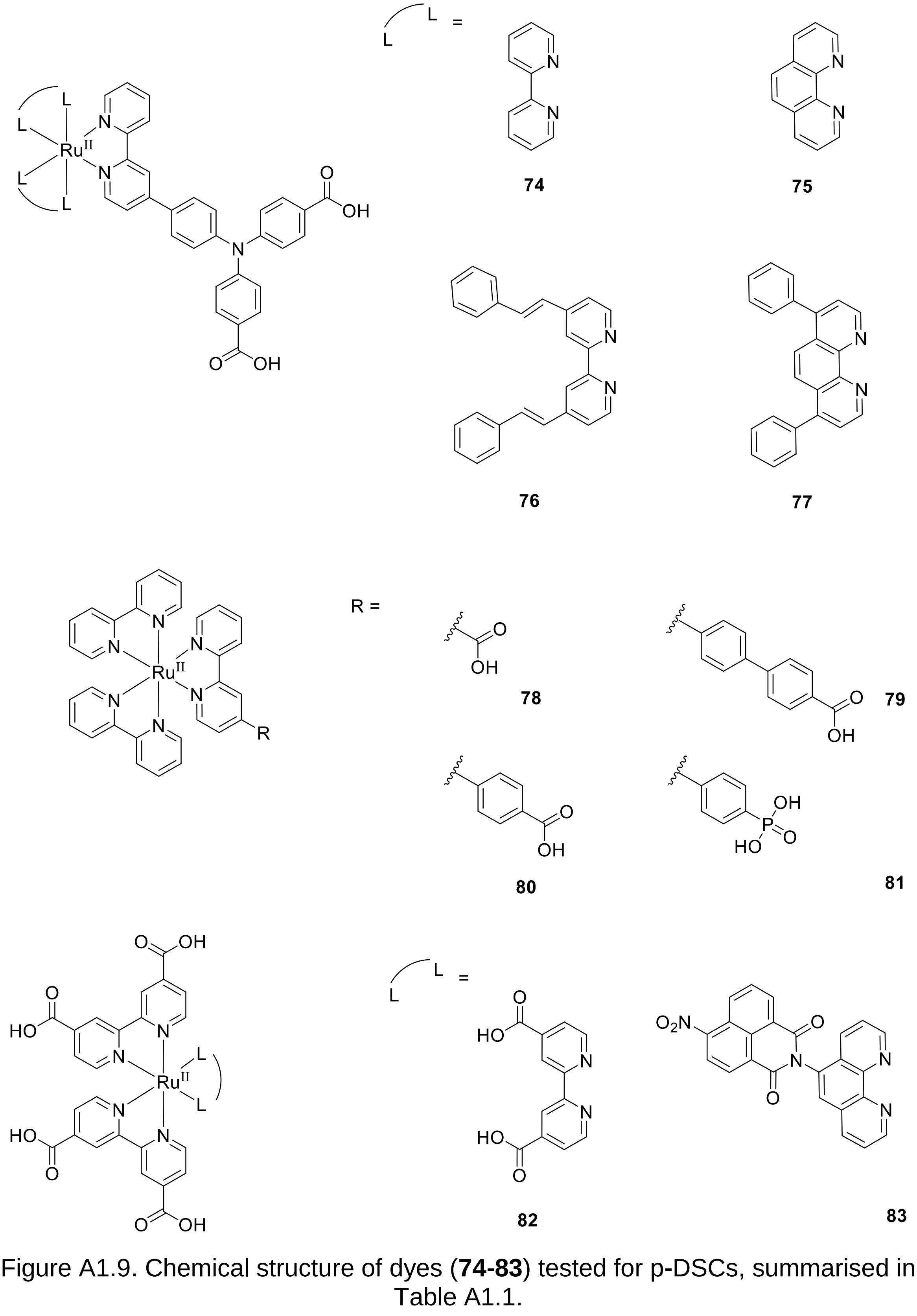

Figure A1.9. Chemical structure of dyes (**74-83**) tested for p-DSCs, summarised in Table A1.1.

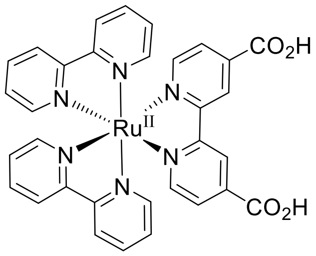

84

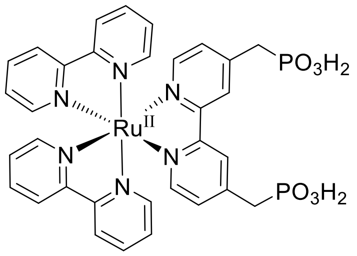

85

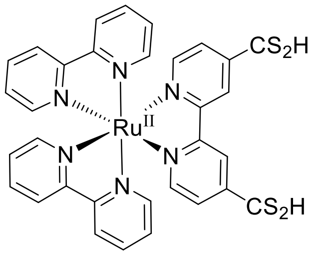

86

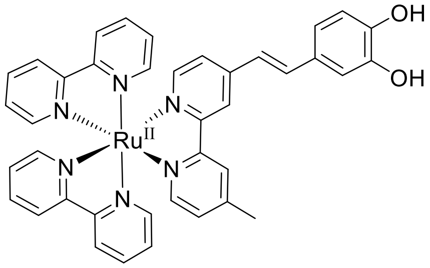

87

Figure A1.10. Chemical structure of dyes (**84-87**) tested for p-DSCs, summarised in Table A1.1.

Table A1.1. Summarised photovoltaic performance of NiO based p-DSCs reported in the literature (with an I^-/I_3^- electrolyte).

Dye	V_{OC} (mV)	J_{SC} (mA cm^{-2})	FF	η (%)	IPCE (%)	Ref
1	84	5.48	0.34	0.15	63	[1]
2	63	3.37	0.31	0.07	32	[2]
3	79	3.15	0.31	0.08	28	[3]
4	55	1.36	0.34	0.03	6	[2]
5	80	3.37	0.35	0.09	26	[2]
6	101	8.21	0.31	0.25	50	[4]
7	94	2.53	0.27	0.065	40	[5]
8	100	2.48	0.36	0.09	44	[6]
9	99	2.66	0.35	0.093	28	[7]
10	118	4.05	0.34	0.16	42	[7]
11	87	3.32	0.33	0.09	25	[8]
12	96	3.25	0.33	0.1	17	[8]
13	125	2.82	0.31	0.11	32	[9]
14	121	5.01	0.3	0.184	27	[10]
15	133	5.57	0.31	0.23	25	[11]
16	124	4.51	0.33	0.186	23	[10]

17	133	4.02	0.33	0.178	22	[10]
18	123	1.69	0.29	0.06	20	[9]
19	152	3.94	0.35	0.21	22	[11]
20	152	6.74	0.31	0.32	26	[11]
21	97	4.30	0.31	0.13	- [a]	[12]
22	128	7.40	0.3	0.28	- [a]	[12]
23	95	4.40	0.31	0.13	- [a]	[12]
24	74	0.26	0.53	0.008	< 2	[13]
25	147	7.38	0.32	0.35	55	[13]
26	125	0.75	0.37	0.03	8	[14]
27	135	1.51	0.32	0.07	22	[14]
28	81	1.79	0.34	0.048	25	[14]
29	81	0.70	0.25	0.01	5	[13]
30	123	4.04	0.32	0.16	30	[13]
31	90	2.03	0.33	0.062	34	[15]
32	100	1.89	0.33	0.063	25	[15]
33	76	1.72	0.32	0.041	22	[15]
34	84	1.44	0.33	0.04	17	[15]
35	87	0.82	0.34	0.025	7	[16]
36	96	1.27	0.33	0.04	5	[16]
37	153	2.06	0.29	0.09	- [a]	[17]
38	176	3.40	0.32	0.19	- [a]	[17]
39	218	5.35	0.35	0.41	- [a]	[17]
40	147	2.24	0.3	0.1	22	[18]
41	122	1.06	0.29	0.04	8	[18]
42	136	1.23	0.28	0.05	10	[18]
43	111	0.62	0.27	0.02	5	[19]
44	88	0.27	0.27	0.01	< 1	[19]
45	163	1.66	0.28	0.08	22	[19]
46	133	0.43	0.47	0.03	2	[19]
47	96	5.70	0.38	0.207	50	[20]
48	117	7.57	0.41	0.353	70	[20]
49	115	6.68	0.4	0.308	58	[20]
50	111	4.00	0.36	0.16	48	[21]

51	109	3.80	0.36	0.15	42	[21]
52	124	2.36	0.37	0.11	20	[22]
53	130	2.97	0.35	0.14	30	[22]
54	131	2.83	0.34	0.126	13	[23]
55	121	4.16	0.33	0.166	17	[23]
56	134	2.32	0.33	0.103	8	[23]
57	97	1.04	0.37	0.037	14	[24]
58	90	1.74	0.38	0.06	18	[24]
59	94	1.43	0.37	0.05	12	[24]
60	120	8.20	0.34	0.33	57	[25]
61	110	1.40	0.37	0.056	12	[26]
62	105	1.00	0.35	0.038	8	[26]
63	105	1.59	0.36	0.06	16	[27]
64	131	2.05	0.32	0.09	24	[27]
65	115	1.39	0.36	0.06	15	[27]
66	113	1.38	0.34	0.05	14	[27]
67	122	2.18	0.35	0.09	17	[27]
68	117	1.22	0.37	0.056	6	[28]
69	140	1.92	0.42	0.113	18	[28]
70	104	2.25	0.34	0.079	18	[29]
71	77	1.50	0.33	0.038	7	[29]
72	96	2.91	0.32	0.09	14	[30]
73	93	1.96	0.39	0.07	9	[30]
74	100	2.75	0.36	0.10	- [a]	[31]
75	89	2.66	0.31	0.074	- [a]	[32]
76	93	3.43	0.33	0.104	- [a]	[31]
77	92	2.69	0.34	0.085	- [a]	[32]
78	63	0.44	0.36	0.009	2	[33]
79	82	1.84	0.34	0.051	9	[33]
80	79	1.16	0.36	0.033	5	[33]
81	95	4.06	0.36	0.139	- [a]	[34]
82	110	0.09	0.43	0.004	- [a]	[35]
83	95	0.16	0.36	0.006	- [a]	[35]
84	85	0.63	0.34	0.019	- [a]	[36]

85	95	0.78	0.34	0.025	- [a]	[36]
86	75	0.25	0.34	0.0065	- [a]	[36]
87	85	0.65	0.32	0.018	- [a]	[36]

V_{OC} is the open-circuit voltage at the $J = 0$ intercept, J_{SC} is the short-circuit current density at the $V = 0$ intercept, FF is the device fill factor, η is the power conversion efficiency and IPCE is the monochromatic incident photon-to-current conversion efficiency. [a] Not reported.

References.

1 L. Li, E. A. Gibson, P. Qin, G. Boschloo, M. Gorlov, A. Hagfeldt and L. Sun, *Adv. Mater.*, 2010, **22**, 1759–1762.

2 P. Qin, J. Wiberg, E. A. Gibson, M. Linder, L. Li, T. Brinck, A. Hagfeldt, B. Albinsson and L. Sun, *J. Phys. Chem. C*, 2010, **114**, 4738–4748.

3 J.-F. Lefebvre, X.-Z. Sun, J. A. Calladine, M. W. George and E. A. Gibson, *Chem. Commun.*, 2014, **50**, 5258–5260.

4 C. J. Wood, G. H. Summers and E. A. Gibson, *Chem. Commun.*, 2015, **51**, 3915–3918.

5 L. Zhu, H. Yang, C. Zhong and C. M. Li, *Chem. - An Asian J.*, 2012, **7**, 2791–2795.

6 P. Qin, M. Linder, T. Brinck, G. Boschloo, A. Hagfeldt and L. Sun, *Adv. Mater.*, 2009, **21**, 2993–2996.

7 J. Cui, J. Lu, X. Xu, K. Cao, Z. Wang, G. Alemu, H. Yuang, Y. Shen, J. Xu, Y. Cheng and M. Wang, *J. Phys. Chem. C*, 2014, **118**, 16433–16440.

8 C. J. Wood, M. Cheng, C. A. Clark, R. Horvath, I. P. Clark, M. L. Hamilton, M. Towrie, M. W. George, L. Sun, X. Yang and E. A. Gibson, *J. Phys. Chem. C*, 2014, **118**, 16536–16546.

9 L. Zhu, H. Bin Yang, C. Zhong and C. M. Li, *Dye. Pigment.*, 2014, **105**, 97–104.

10 F. Wu, S. Zhao, C. Zhong, Q. Song and L. Zhu, *RSC Adv.*, 2015, **5**, 93652–93658.

11 F. Wu, L. Zhu, S. Zhao, Q. Song and C. Yang, *Dye. Pigment.*, 2016, **124**, 93–100.

12 K. A. Click, D. R. Beauchamp, B. R. Garrett, Z. Huang, C. M. Hadad and Y. Wu, *Phys. Chem. Chem. Phys.*, 2014, **16**, 26103–26111.

13 Y. Farré, M. Raissi, A. Fihey, Y. Pellegrin, E. Blart, D. Jacquemin and F. Odobel, *ChemSusChem*, 2017, **10**, 2618–2625.

14 L. Favereau, J. Warnan, Y. Pellegrin, E. Blart, M. Boujtita, D. Jacquemin and F. Odobel, *Chem. Commun.*, 2013, **49**, 8018–8020.

15 Y. Farré, L. Zhang, Y. Pellegrin, A. Planchat, E. Blart, M. Boujtita, L. Hammarström, D. Jacquemin and F. Odobel, *J. Phys. Chem. C*, 2016, **120**, 7923–7940.

16 D. Ameline, S. Diring, Y. Farre, Y. Pellegrin, G. Naponiello, E. Blart, B. Charrier, D. Dini, D. Jacquemin and F. Odobel, *RSC Adv.*, 2015, **5**, 85530–85539.

17 A. Nattestad, A. J. Mozer, M. K. R. Fischer, Y.-B. Cheng, A. Mishra, P. Bäuerle and U. Bach, *Nat. Mater.*, 2010, **9**, 31–35.

18 M. Weidelener, A. Mishra, A. Nattestad, S. Powar, A. J. Mozer, E. Mena-Osteritz, Y.-B. Cheng, U. Bach and P. Bäuerle, *J. Mater. Chem.*, 2012, **22**, 7366–7379.

19 M. Weidelener, S. Powar, H. Kast, Z. Yu, P. P. Boix, C. Li, K. Müllen, T. Geiger, S. Kuster, F. Nüesch, U. Bach, A. Mishra and P. Bäuerle, *Chem. - An Asian J.*, 2014, **9**, 3251–3263.

20 Z. Liu, W. Li, S. Topa, X. Xu, X. Zeng, Z. Zhao, M. Wang, W. Chen, F. Wang, Y.-B. Cheng and H. He, *ACS Appl. Mater. Interfaces*, 2014, **6**, 10614–10622.

21 Z. Liu, D. Xiong, X. Xu, Q. Arooj, H. Wang, L. Yin, W. Li, H. Wu, Z. Zhao, W. Chen, M. Wang, F. Wang, Y. B. Cheng and H. He, *ACS Appl. Mater. Interfaces*, 2014, **6**, 3448–3454.

22 B. Jin, W. Wu, X. Zhang, F. Guo, Q. Zhang and J. Hua, *Chem. Lett.*, 2013, **42**, 1271–1272.

23 F. Wu, J. Liu, X. Li, Q. Song, M. Wang, C. Zhong and L. Zhu, *Eur. J. Org. Chem.*, 2015, **2015**, 6850–6857.

24 Z. Ji, G. Natu, Z. Huang and Y. Wu, *Energy Environ. Sci.*, 2011, **4**, 2818–2821.

25 Q.-Q. Zhang, K.-J. Jiang, J.-H. Huang, C.-W. Zhao, L.-P. Zhang, X.-P. Cui, M.-J. Su, L.-M. Yang, Y.-L. Song and X.-Q. Zhou, *J. Mater. Chem. A*, 2015, **3**, 7695–7698.

26 E. Sheibani, L. Zhang, P. Liu, B. Xu, E. Mijangos, G. Boschloo, A. Hagfeldt, L. Hammarström, L. Kloo and H. Tian, *RSC Adv.*, 2016, 18165–18177.

27 Y.-S. Yen, W.-T. Chen, C.-Y. Hsu, H.-H. Chou, J. T. Lin and M.-C. P. Yeh, *Org.*

Lett., 2011, **13**, 4930–4933.

28 C.-H. Chang, Y.-C. Chen, C.-Y. Hsu, H.-H. Chou and J. T. Lin, *Org. Lett.*, 2012, **14**, 4726–4729.

29 S. Lyu, Y. Farré, L. Ducasse, Y. Pellegrin, T. Toupance, C. Olivier and F. Odobel, *RSC Adv.*, 2016, **6**, 19928–19936.

30 C. J. Wood, K. C. D. Robson, P. I. P. Elliott, C. P. Berlinguette and E. A. Gibson, *RSC Adv.*, 2014, **4**, 5782–5791.

31 M. He, Z. Ji, Z. Huang and Y. Wu, *J. Phys. Chem. C*, 2014, **118**, 16518–16525.

32 Z. Ji, G. Natu and Y. Wu, *ACS Appl. Mater. Interfaces*, 2013, **5**, 8641–8648.

33 Z. Ji, G. Natu, Z. Huang, O. Kokhan, X. Zhang and Y. Wu, *J. Phys. Chem. C*, 2012, **116**, 16854–16863.

34 N. Marinakis, M. Willgert, E. C. Constable and C. E. Housecroft, *Sustain. Energy Fuels*, 2017, **0**, 1–10.

35 J. C. Freys, J. M. Gardner, L. D'Amario, A. M. Brown and L. Hammarström, *Dalt. Trans.*, 2012, **41**, 13105.

36 Y. Pellegrin, L. Le Pleux, E. Blart, A. Renaud, B. Chavillon, N. Szuwarski, M. Boujtita, L. Cario, S. Jobic, D. Jacquemin and F. Odobel, *J. Photochem. Photobiol. A Chem.*, 2011, **219**, 235–242.